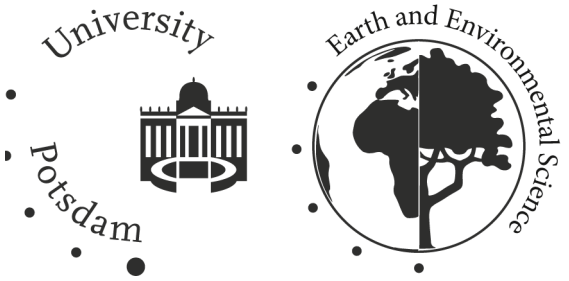

Institut für Erd- und Umweltwissenschaften

^{40}Ar/^{39}Ar Geochronology of ICDP PALEOVAN Drilling Cores

Dissertation

von

Jonathan Franz Engelhardt

Zur Erlangung des akademischen Grades

Doctor Rerum Naturalium

≫Dr. rer. nat.≪

in der Wissenschaftsdisziplin *Geochemie*

Die Dissertation wurde eingereicht an der

Mathematisch-Naturwissenschaftlichen Fakultät

der Universität Potsdam

Potsdam, den 16. Juli 2018

.
.
.

Ärmlich brennt das Licht der Lupinen.
Dein Blick spurt im Nebel:
die auf Widerruf gestundete Zeit
wird sichtbar am Horizont.

.
.
.

aus: Ingeborg Bachmann, *Die gestundete Zeit*

Published online at the
Institutional Repository of the University of Potsdam:
https://doi.org/10.25932/publishup-42953
https://nbn-resolving.org/urn:nbn:de:kobv:517-opus4-429539

Frequent Abbreviations

ACs	Alder Creek Sanidine
AR	Ahlat Ridge
ARM	Anhysteric Remanent Magnetization
BSE	Backscattered Electrons
CL	Cathodoluminescnce
CLICIT	Cadmium-Lined In-Core Irradiation Tube
CMS	Cobb Mountain Subchron
CPO	Crystallographic Preferred Orientation
EDX	Energy Dispersive X-ray Spectroscopy
EKP	Erzurum-Kars Plateau
EMPA	Electron Microprobe Analyser
FCs	Fish Canyon Sanidine
ICDP	International Continental Scientific Drilling Program
JFE	Jonathan Franz Engelhardt
LIF	Lithium Fluoride
LSC	Liquid Scintillation Counting
MDF	Mass Discrimination Factor
MGTF	Multi Grain Total Fusion
MIS	Marine Isotope Stage
MRP	Mass Resolution Power
NB	Northern Basin
NGRIP	North Greenland Ice Core Project
NRM	Natural Remanent Magnetization
OSTR	Oregon State TRIGA Reactor
PE	Polyethylene
PET	Pentaerythritol
RPI	Relative Paleointensity
SBF	Southern Boundary Fault
SEM	Scanning Electron Microscopy
SGTF	Single Grain Total Fusion
SWH	Stepwise Heating
TAP	Thallium Acid Phthalate
TFEG	Thermal Field-emission Gun
TOC	Total Organic Carbon
TRIGA	Training, Research, Isotopes and General Atomistic
VADM	Virtual Axial Dipole Momentum
WDX	Wavelength Dispersive X-ray Spectroscopy
XRD	X-ray Diffraction
XRF	X-ray Fluorescence

Constants Used for $^{40}Ar/^{39}Ar$ Dating

$^{40}Ar/^{36}Ar_{Atm}$	298.56 ± 0.31		Isotopic Composition of Atmospheric Argon
$^{38}Ar/^{36}Ar_{Atm}$	0.1885 ± 0.0003		Isotopic Composition of Atmospheric Argon
$\lambda_{^{40}K}$	$(5.463 \pm 0.107) \times 10^{-10}$	[1/a]	Decay Constant
$\lambda_{^{39}Ar}$	$(2.940 \pm 0.016) \times 10^{-7}$	[1/h]	Decay Constant
$\lambda_{^{37}Ar}$	$(8.230 \pm 0.012) \times 10^{-4}$	[1/h]	Decay Constant
$\lambda_{^{36}Cl}$	$(2.257 \pm 0.015) \times 10^{-6}$	[1/a]	Decay Constant
$\gamma_{^{40}K}$	3.31 ± 0.06	$[g^{-1}\ sec^{-1}]$	Decay Activity
$\beta^-_{^{40}K}$	27.890 ± 0.300	$[g^{-1}\ sec^{-1}]$	Decay Activity
K_{AMU}	39.0983 ± 0.0001	[AMU]	Atomic Weight
t_a	3.1556925445×10^7	[sec]	Solar Year

Allgemeine Zusammenfassung

Die PALEOVAN−Bohrkampagne des internationalen kontinentalen Bohrprogramms ICDP wurde im Sommer 2010 realisiert. Das übergeordnete Ziel dieser Kampagne war die Entnahme eines Klimaarchivs im Osten Anatoliens. Als Archiv dienen Süßwasserablagerungen am Grund des Vansees. PALEOVAN Bohrkerne bieten lakustrine Ablagerungen von zwei Lokalitäten des Sees, und zwar der Ahlat Ridge und des Northern Basins. Durch das Zusammenstellen bestmöglicher Bohrkernbestände aus sieben parallelen Bohrungen auf der Ahlat Ridge, konnte die nahezu vollständige Aufzeichnung der Geschichte des Sees gewonnen werden. Dieses detaillierte Archiv zeichnete sensible Klimafaktoren auf. Als Beispiele sind zu nennen: die Variationen organischen Kohlenstoffs, das Verhältnis von Kalium zu Kalzium und die Anteile arborealer Pollen gegenüber dem Gesamtpollenbestand. Stellvertreterdaten für Klimavariationen (sogenannte Proxies) ähneln in ihrem Muster sehr stark den bekannten Klimavariationen aus Eisbohrkernen des Grönlandeises. Da das Timing der Klimavariationen in den Grönlandeiskernen durch Datierungen mithilfe im Eis gespeicherter Gasphasen und orbitaler Modellberechnungen sehr genau bekannt ist, konnten Sedimentolog*innen des PALEOVAN−Teams ein klimastratigraphisches Altersmodell aus den Proxies berechnen. Die Kernaufgabe der hier vorgelegten Dissertation ist es, eingelagerte pyroklastische Ablagerungen mithilfe der $^{40}Ar/^{39}Ar$−Methode zu datieren und das Altersmodell zu diskutieren. Die Notwendigkeit der $^{40}Ar/^{39}Ar$−Datierungen war besonders gegeben, da vorab publizierte radiometrische Datierungen von ICDP−PALEOVAN Bohrkernen statistisch nicht ausreichend beschrieben wurden und vorhandene Abweichungen gegenüber dem Altersmodell undiskutiert blieben.

An der westlichen und nördlichen Küste des Sees befinden sich zwei Stratovulkane: Nemrut und Süphan. Beide Vulkane haben über die Dauer der kompletten Seegeschichte pyroklastisches Material im See abgelagert. Feldspäte und vulkanische Gläser aus rhyolitischen und trachytischen Auswurfprodukten wurden auf ihre Zusammensetzung untersucht und es wurde ihre Eignung für eine Anwendung der $^{40}Ar/^{39}Ar$−Geochronologie festgestellt. Die Abwesenheit hoher Kaliumkonzentrationen in Feldspäten aus geeigneten pyroklastischen Lagen bedeutet, dass Kristalle eine Mindestgröße von ca. 500 Mikrometer benötigen, um Analysen an einzelnen Kristallen durchführen zu können. Nicht alle Proben liefern ausreichend Kristalle dieser groben Korngröße. Somit wurde eine Methode gewählt, die Mehrkorn und Einzelkornanalysen miteinander kombiniert. Die bevorzugte Methode des schrittweisen Ausheizens war nur mit drei Proben möglich. Grund dafür ist, dass der geringe Kaliumgehalt und das junge geologische Alter große Mengen (ca. 20 mg) einschluss− und korrosionsfreier Feldspäte benötigten. Die geringen Probenmengen (25% Aliquot von üblicherweise 5 cm^3 Probenmaterial) und die Omnipräsenz von Schmelzeinschlüssen in den Feldspäten legten nahe, auf die Methodik des schlagartigen Ausheizens von Einzel− und Mehrkornproben zu setzen. $^{40}Ar/^{39}Ar$−Datierungen an einzelnen Feldspäten haben den Vorteil, dass sich ein vorhandener Überschuss von ^{40}Ar oder Kontaminationen detritischer Körner leicht feststellen lassen und in der Altersberechnung berücksichtigt werden können. Mehrkornanalysen zeigen diese Hürden nur bei intensiver Kontamination und bergen die Gefahr, radiometrische Alter zu bestimmen, die von dem tatsächlichen geologischen Alter abweichen, weil sie zu alt sind. $^{40}Ar/^{39}Ar$−Datierungen in dieser Dissertation wurden deshalb für die meisten Proben mithilfe von Mehrkornanalysen und (wenn vorhanden) in Kombination mit wenigen Einzelkornanalysen durchgeführt.

Bis auf die Resultate zweier Proben sind die radiometrischen Alter der Feldspäte statistisch gesehen identisch zu den Altersabschätzungen des klimastratigraphischen Altersmodells. Abweichungen zeigen ausschließlich ältere radiometrische Alter einzelner Kornfraktionen. Die beiden abweichenden Proben sind ebenfalls älter als das Altersmodell. Eine statistische Auswertung mittels t−Tests beweist die Abweichungen der radiometrischen von den klimastratigraphischen Altersdaten. Das Altersmodell wurde mit jedem der radiometrischen Alter innerhalb eines stratigraphischen Einzugsbereichs von ± 10 Metern verglichen. Die Konkordanz der Altershinweise aus unterschiedlichen Klimaproxies und aus geophysikalischen Altershinweisen (durch das Identifizieren zeitlich bekannter Variationen des Erdmagnetfelds) legen nahe, dass beiden Abweichungen fehlerhafte $^{40}Ar/^{39}Ar$−Datierungen zugrunde liegen. Zwei mögliche Ursachen werden in Betracht gezogen: (1) unregelmäßiges beziehungsweise vereinzeltes Auftreten von überschüssigem ^{40}Ar im Zusammenhang mit Schmelz− und Fluideinschlüssen oder (2) Kontamination der Probe mit älteren, xenokristischen Feldspäten durch eine zügige (im Zeitraum von Tagen) Kombination von magmatischer Assimilation und Auswurf des Materials. Ebenfalls nicht auszuschließen ist eine detritische Kontamination. Die normalverteilten $^{40}Ar/^{39}Ar$−Werte der Proben sind allerdings untypisch für eine detritische Kontamination.

Je ein Aliquot der selektierten Kristallfraktionen wurde intensiv auf vorhandene Zonierungen untersucht. Alle untersuchten Feldspatproben zeigen Elementzonierungen, die sich einteilen lassen. Die Zonierungen sind entweder kompositionelle Zonierungen der Hauptzusammensetzung („C-type – compositional type“), pseudo-oszillatorische Zonierungen gewisser Spurenelementkonzentrationen („PO-type“), konzentrische Zonierungen von Spurenelementkonzentrationen („CC-type – concentric type“) und chaotisch-fleckige Zonierungsmuster („R-type – resorbed and patchy“). Proben, deren $^{40}Ar/^{39}Ar$−Alter abweichen, zeigen Zonierungen in ihrer Hauptzusammensetzung (C-type), fleckige Zonierungen (R-type) oder zeigen eine Mischung aus unterschiedlichen Zonierungstypen (C-type und PO-type). Feldspäte, die ausschließlich eine Zonierung ihrer Spurenelmente (PO-type) zeigen, liegen typischerweise in kleineren Korngrößen vor und markieren Zusammensetzungen, die typisch sind für die spätesten Phasen der magmatischen Entwicklung von Feldspäten in peralkalinen Gesteinen. Diese Kristalle sind in der Regel arm an Schmelzeinschlüssen und nur selten korrodiert. Die vorliegende Arbeit weist Feldspäte, die keine Zonierung in ihrer Hauptzusammensetzung, sondern nur pseudo-oszillatorische Spurenelementvariationen aufzeigen, als ideale Chronometer für die Anwendung der $^{40}Ar/^{39}Ar$−Methode an Quartären, kaliumarmen Feldspäten aus.

Um Abweichende Proben erneut zu analysieren und um stratigraphische Abschnitte zu datieren, die nicht erfolgreich beprobt werden konnten, wurden fünf Proben datiert, indem die $^{40}Ar/^{39}Ar$−Methode auf vulkanisches Glas angewendet wurde. Hohe Gehalte an atmosphärischem Argon (in der Regel > 98 %) führten allerdings zu ungenauen radiometrischen Altersbestimmungen, die aufgrund ihrer großen Fehler keine Abweichungen vom Altersmodell zeigen. Die Gläser zeigen Hinweise darauf, dass Variationen in den Altern der Feldspäte auf die Gegenwart eines Ar-Reservoirs in Schmelzeinschlüssen zurückzuführen sein könnte, das weder radiogen noch atmosphärisch ist. Ob eine Verknüpfung der Ar-Isotopien in vulkanischen Gläsern und in Porenwässern gegeben ist, bleibt offen. Instrumentelle und methodische Hürden lassen nur eine Vermutung zu, dass Porenwässer und vulkanische Gläser in ihren Ar-Isotopendaten eine Verknüpfung zeigen könnten.

Ein neues Alterstiefenmodell, das ebenfalls auf der Interpolation von Altershinweisen durch Klimaproxies und geophysikalischer Daten basiert wird in dieser Arbeit ebenfalls vorgelegt. Im Gegensatz zu bestehenden „Spline“-Interpolationen wurde in dieser Dissertation eine PCHIP-Interpolation bevorzugt. Abgesehen von abweichenden Proben wurden allen Proben, die mithilfe der $^{40}Ar/^{39}Ar-$Methode an Feldspäten datiert sind, zusätzlich ein klimastratigraphisches Modellalter zugewiesen. Diese Modellalter bieten die Grundlage dafür, das Alter des in der Datierung benutzten Mineralstandards (Alder Creek Sanidine) nachrechnen zu können. Die erfolgreiche klimastratigraphische Kalibrierung des Standards beweist, dass Alterstiefenmodelle aus den PALEOVAN-Bohrkernen genau sind, und dass alle verwendeten Chronometer innerhalb der angezeigten Varianzen ein synchrones Timing zulassen.

Die Dissertation bietet petrochemische Charakterisierungen der entnommenen Proben an und diskutiert nachvollziehbar mögliche Provenanzen der Pyroklastite. 41 von 57 entnommenen Proben lassen sich Nemrut zuordnen. Kriterien, die für eine Zuordnung herangezogen wurden, werden aufgezeigt und diskutiert. Eine mögliche Korrelation der datierten Proben zu pyroklastischen Einheiten, die in der Literatur an den Hängen der Stratovulkane im Detail beschrieben wurden, wird ebenfalls diskutiert. Die beprobten pyroklasitischen Lagen haben geringe Mächtigkeiten (in der Regel < 40 cm) und liegen mittleren bis kleineren Eruptionen zugrunde. Diese Eruptionen hinterlassen keine oder nur schwer definierbare pyroklastische Einheiten von geringer Mächtigkeit an Land. Eine genaue Korrelation ist mit den hier präsentierten Daten deshalb nicht oder nur sehr vage möglich.

Abweichende radiometrische Alter aus Datierungen von Feldspat könnten im Zusammenhang mit vererbtem ^{40}Ar aus Xenokristallen stehen. Um diese Hypothese zu testen, wurden diffusionsabhängige Konzentrationsschwankungen von Barium in zonierten Feldspäten untersucht. Da das diffusive Verhalten von Barium in Feldspat bekannt ist, kann durch die Analyse des Konzentrationsgradienten die Dauer der magmatischen Entwicklung ab der Bildung der untersuchten Zonierung berechnet werden. Diese Zeitspanne wurde genutzt, um zu modellieren, ob Xenokristalle während einer unvollständigen Assimilation komplett entgast werden. Dafür wurde angenommen, dass das diffusive Angleichen von unterschiedlichen Bariumkonzentrationen maximale Werte für die Dauer von der Assimilation bis zum Auswurf liefert. Die Modellierung zeigt, dass vererbtes ^{40}Ar aus Xenokristallen keinen Anteil an den abweichenden Altern haben. Allerdings sind die erhobenen Diffusionsgradienten am Rande der benötigten analytischen Auflösung, und eine Überschätzung der Dauer der magmatischen Prozesse kann nicht ausgeschlossen werden. Die Diffusionsprofile sind ein weiterer Hinweis dafür, dass unregelmäßige beziehungsweise vereinzelte Quellen von überschüssigem ^{40}Ar die schwierigste Hürde für $^{40}Ar/^{39}Ar-$Datierungen an ICDP-PALEOVAN Bohrkernen darstellen.

Die vorgelegte Arbeit bietet nicht nur $^{40}Ar/^{39}Ar-$Datierungen, um das vorhandene Altersmodell kritisch zu diskutieren, sondern zeigt, wie Abweichungen statistisch zu erfassen sind, welche mineralogischen Beobachtungen in die Interpretation abweichender radiometrischer Alter miteinbezogen werden sollten und wie die Synchronizität verschiedener Chronometer getestet werden kann. Die Korrektheit des klima-stratigraphischen Timings der PALEOVAN Kerne ist mit dieser Arbeit nachgewiesen. Vergleiche der Proxydaten zu anderen Klimaarchiven deren Auflösung sogar höher als die der Milankovitchzyklen ist (die Auflösung der Dnsgaard-Oeschger Ereignisse), existieren für viele Kerne des PALEOVAN-Archivs. Die Kerne aus dem PALEO-

VAN Projekt repräsentieren damit ein Schlüsselarchiv für die Rekonstruktion des Klimas im Nahen Osten. Dieses Archiv bietet ein klima-stratigraphisches Altersmodell von bemerkenswerter Genauigkeit und Auflösung.

Abstract

The scientific drilling campaign PALEOVAN was conducted in the summer of 2010 and was part of the international continental drilling programme (ICDP). The main goal of the campaign was the recovery of a sensitive climate archive in the East of Anatolia. Lacustrine deposits underneath the lake floor of 'Lake Van' constitute this archive. The drilled core material was recovered from two locations: the Ahlat Ridge and the Northern Basin. A composite core was constructed from cored material of seven parallel boreholes at the Ahlat Ridge and covers an almost complete lacustrine history of Lake Van. The composite record offered sensitive climate proxies such as variations of total organic carbon, K/Ca ratios, or a relative abundance of arboreal pollen. These proxies revealed patterns that are similar to climate proxy variations from Greenland ice cores. Climate variations in Greenland ice cores have been dated by modelling the timing of orbital forces to affect the climate. Volatiles from melted ice aliquots are often taken as high-resolution proxies and provide a base for fitting the according temporal models. Colleagues from the PALEOVAN scientific team fitted proxy data from Lake Van to the ice core data and constructed an age model that based on the fitting. Embedded volcaniclastic layers had to be dated radiometrically in order to provide independent age constraints to this climate-stratigraphic age model. Solving this task by an application of the $^{40}Ar/^{39}Ar$ method was the main objective of this thesis. Earlier efforts to apply the $^{40}Ar/^{39}Ar$ dating resulted in inaccuracies that could not be explained satisfactorily.

Two stratovolcanos are located at the western and the northern shore of Lake Van: Nemrut and Süphan. Both volcanoes have deposited volcaniclastic materials into the lake's basin throughout the entire lacustrine history of Lake Van. Feldspars and volcanic glasses from rhyolitic and trachytic tephra were analysed for their chemical composition in order to evaluate their suitability as target materials for the $^{40}Ar/^{39}Ar$ method. The absence of K-rich feldspars in suitable tephra layers implied that crystals needed to be 500 μm in size minimum, in order to apply single-crystal $^{40}Ar/^{39}Ar$ dating. Some of the samples did not contain any of these grain sizes or only very few crystals of that size. In order to overcome this problem this study applied a combined single-crystal and multi-crystal approach with different crystal fractions from the same sample. The preferred method of a stepwise heating analysis of an aliqoute of feldspar crystals has been applied to three samples. The Na-rich crystals and their young geological age required 20 mg of inclusion-free, non-corroded feldspars. Small sample volumes (usually 25 % aliquots of 5 cm^3 of sample material – a spoon full of tephra) and the widespread presence of melt-inclusion led to the application of combined single- and multigrain total fusion analyses. $^{40}Ar/^{39}Ar$ analyses on single crystals have the advantage of being able to monitor the presence of excess ^{40}Ar and detrital or xenocrystic contamination in the samples. Multigrain analyses may hide the effects from these obstacles. The results from the multigrain analyses are therefore discussed with respect to the findings from the respective cogenetic single crystal ages. Some of the samples in this study were dated by $^{40}Ar/^{39}Ar$ on feldspars on multigrain separates and (if available) in combination with only a few single crystals.

$^{40}Ar/^{39}Ar$ ages from two of the samples deviated statistically from the age model. All other samples resulted in identical ages. The deviations displayed older ages than those obtained from the age model. t-Tests compared radiometric ages with available age control points from various proxies and from the relative paleointensity of the earth magnetic field within a stratigraphic

range of ± 10 m. Concordant age control points from different relative chronometers indicated that deviations are a result of erroneous $^{40}Ar/^{39}Ar$ ages. The thesis argues two potential reasons for these ages: (1) the irregular appearance of ^{40}Ar from rare melt- and fluid- inclusions and (2) the contamination of the samples with older crystals due to a rapid combination of assimilation and ejection. The contamination with older crystals by detrital processes cannot be excluded due to the analysis of multigrain fractions. However, this process appears unlikely because apparent ages are normally distributed.

Another aliquot of feldspar crystals that underwent separation for the application of $^{40}Ar/^{39}Ar$ dating was investigated for geochemical inhomogeneities. Magmatic zoning is ubiquitous in the volcaniclastic feldspar crystals. Four different types of magmatic zoning were detected. The zoning types are compositional zoning (C-type zoning), pseudo-oscillatory zoning of trace element concentrations (PO-type zoning), chaotic and patchy zoning of major and trace element concentrations (R-type zoning) and concentric zoning of trace elements (CC-type zoning). Samples that deviated in $^{40}Ar/^{39}Ar$ ages showed C-type zoning, R-type zoning or a mix of different types of zoning (C-type and PO-type). Feldspars showing PO-type zoning typically represent the smallest grain size fractions in the samples. The constant major element compositions of these crystals are interpreted to represent the latest stages in the compositional evolution of feldspars in a peralkaline melt. PO-type crystals contain less melt- inclusions than other zoning types and are rarely corroded. This thesis concludes that feldspars that show PO-type zoning are most promising chronometers for the $^{40}Ar/^{39}Ar$ method, if samples provide mixed zoning types of Quarternary anorthoclase feldspars.

Five samples were dated by applying the $^{40}Ar/^{39}Ar$ method to volcanic glass. High fractions of atmospheric Ar (typically $> 98\%$) significantly hampered the precision of the $^{40}Ar/^{39}Ar$ ages and resulted in rough age estimates that widely overlap the age model. Ar isotopes indicated that the glasses bore a chorine-rich Ar-end member. The chlorine-derived ^{38}Ar indicated chlorine-rich fluid-inclusions or the hydration of the volcanic glass shards. This indication strengthened the evidence that irregularly distributed melt-inclusions and thus irregular distributed excess ^{40}Ar influenced the problematic feldspar $^{40}Ar/^{39}Ar$ ages. Whether a connection between a corrected initial $^{40}Ar/^{36}Ar$ ratio from glasses to the $^{40}Ar/^{36}Ar$ ratios from pore waters exists remains unclear.

This thesis offers another age model, which is similarly based on the interpolation of the temporal tie points from geophysical and climate-stratigraphic data. The model used a PCHIP-interpolation (piecewise cubic hermite interpolating polynomial) whereas the older age model used a spline-interpolation. Samples that match in ages from $^{40}Ar/^{39}Ar$ dating of feldspars with the earlier published age model were additionally assigned with an age from the PCHIP-interpolation. These modelled ages allowed a recalculation of the Alder Creek sanidine mineral standard. The climate-stratigraphic calibration of an $^{40}Ar/^{39}Ar$ mineral standard proved that the age versus depth interpolations from PAELOVAN drilling cores were accurate, and that the applied chronometers recorded the temporal evolution of Lake Van synchronously.

Petrochemical discrimination of the sampled volcaniclastic material is also given in this thesis. 41 from 57 sampled volcaniclastic layers indicate Nemrut as their provenance. Criteria that served for the provenance assignment are provided and reviewed critically. Detailed correlations of selected PALEOVAN volcaniclastics to onshore samples that were described in detail by earlier

studies are also discussed. The sampled volcaniclastics dominantly have a thickness of < 40 cm and have been ejected by small to medium sized eruptions. Onshore deposits from these types of eruptions are potentially eroded due to predominant strong winds on Nemrut and Süphan slopes. An exact correlation with the data presented here is therefore equivocal or not possible at all.

Deviating feldspar $^{40}Ar/^{39}Ar$ ages can possibly also be explained by inherited ^{40}Ar from feldspar xenocrysts contaminating the samples. In order to test this hypothesis diffusion couples of Ba were investigated in compositionally zoned feldspar crystals. The diffusive behaviour of Ba in feldspar is known, and gradients in the changing concentrations allowed for the calculation of the duration of the crystal's magmatic development since the formation of the zoning interface. Durations were compared with degassing scenarios that model the Ar-loss during assimilation and subsequent ejection of the xenocrystals. Diffusive equilibration of the contrasting Ba concentrations is assumed to generate maximum durations as the gradient could have been developed in several growth and heating stages. The modelling does not show any indication of an involvement of inherited ^{40}Ar in any of the deviating samples. However, the analytical set-up represents the lower limit of the required spatial resolution. Therefore, it cannot be excluded that the degassing modelling relies on a significant overestimation of the maximum duration of the magmatic history. Nevertheless, the modelling of xenocrystal degassing evidences that the irregular incorporation of excess ^{40}Ar by melt- and fluid inclusions represents the most critical problem that needs to be overcome in dating volcaniclastic feldspars from the PALEOVAN drill cores.

This thesis provides the complete background in generating and presenting $^{40}Ar/^{39}Ar$ ages that are compared to age data from a climate-stratigraphic model. Deviations are identified statistically and then discussed in order to find explanations from the age model and/or from $^{40}Ar/^{39}Ar$ geochronology. Most of the PALEOVAN stratigraphy provides several chronometers that have been proven for their synchronicity. Lacustrine deposits from Lake Van represent a key archive for reconstructing climate evolution in the eastern Mediterranean and in the Near East. The PALEOVAN record offers a climate-stratigraphic age model with a remarkable accuracy and resolution.

Contents

List of Figures

List of Tables

1 Thesis Organization and Author Contributions

This study constitutes a monograph that includes the quotation of one peer-reviewed and published article. The article depicts the primordial attempt to submit a thesis in a cumulative form. A peer-review of a second article did not warrant publication and the author decided to submit the thesis in monograph form that includes the already published article as a quote, which represents chapter 4.

This thesis is a result of a project that has been funded by the 'Deutsche Forschungsgesellschaft (DFG)'. The project has the title 'Lake Van Drilling Project "PALEOVAN", a long continental record in Eastern Turkey: Geochronology, palynostratigraphy and environmental response on volcanic events' and is part of the DFG priority program 'International Continental Drilling Program (ICDP)'. The funding of this DFG project was granted to R. Oberhänsli (University of Potsdam) and to T. Litt (University of Bonn) and involved hiring a post-doctoral position at the University of Bonn (N. Pickarski) and a doctoral candidate at the University of Potsdam (the author of the given thesis).

The thesis represents the outcome of one from two major aims of the granted DFG project: radioisotopic dating of volcaniclastic material in the PALEOVAN drilling cores via the $^{40}Ar/^{39}Ar$ method. The author of the given thesis has written and compiled all chapters in the role of first and responsible author. The detailed contributions to the particular chapters of the monograph are compiled in the following. Support in operations of analytic instruments is furthermore detailed with respect to the particular chapters.

Prof. Dr. Roland Oberhänsli and Dr. Masafumi Sudo supervised Jonathan Franz Engelhardt during conduction of the doctoral fellpwship. Prof. Dr. Uwe Altenberger mentored the doctoral candidate.

Introduction(Chapter 2)

This chapter introduces the PALEOVAN drilling campaign and the role of the here presented doctoral study. J. F. Engelhardt (JFE) wrote the chapter and is responsible for all figures. R. Oberhänsli and M. Sudo commented on this introduction and provided editing.

Instrumental Methods (Chapter 3)

A methodology chapter provides detailed insights to most instrumental analyses conducted during this doctoral project. Together with appendix A all instrumental methods that had been applied in this study are explained. JFE wrote the chapter and illustrated all figures. R. Oberhänsli and M. Sudo provided editing. M. Sudo contributed to the detailed methodology of the $^{40}Ar/^{39}Ar$ method.

Feldspar $^{40}Ar/^{39}Ar$ dating of ICDP PALEOVAN cores (Chapter 4)

Material sampling was conducted by JFE under support of N. Pickarski, T. Litt and R.Oberhänsli in the IODP core repository at MARUM, University of Bremen. JFE operated all instrumental analyses presented in this study. The work included preparation for sample irradiation prior to $^{40}Ar/^{39}Ar$ analyses. M. Sudo, C. Günther, and U. Altenberger introduced the author into laboratory processes and supported instrumental operations. M. Stockhecke provided insights into the establishment of the climatostratigraphic age model and supported the discussion about the comparison of temporal constraints from radioisotopic and climatostratigraphic methods. R. Oberhänsli contributed to the petrological and mineralogical discussion from compositional analyses of feldspars. The $^{40}Ar/^{39}Ar$ methodology and the discussion about insights from $^{38}Ar_{Cl}$ and $^{37}Ar_{Ca}$ was supported by M. Sudo. The chapter is published as: *Engelhardt J. F., Sudo M., Stockhecke M. and Oberhänsli R. (2017) Feldspar $^{40}Ar/^{39}Ar$ dating of ICDP PALEOVAN cores. Geochim. Cosmochim. Acta 217, 144–170.* Text and illustrations are the responsibility of JFE. All co-authors discussed the results and reviewed the manuscript. Fred Jourdan and two anonymous reviewers provided an international peer-review. Chris Hall officiated as associate editor.

$^{40}Ar/^{39}Ar$ dating of volcanic glass from ICDP Lake Van cores (Chapter 5)

F. Wilke operated electron beam analyses of volcanic glass. $^{40}Ar/^{39}Ar$ analyses were conducted as stated in the above paragraph. Multi-linear correlations of ^{40}Ar, $^{38}Ar_{Cl}$, $^{37}Ar_{Ca}$, and $^{39}Ar_K$ used a MATLAB script compiled by JFE. A total least squares method from Petráš and Bednárová (2010) was implemented for error propagation. M. Müller assisted and operated some of the $^{40}Ar/^{39}Ar$analyses. M. Sudo adjusted instruments and contributed to discussion about Ar isotope systematics. F. Wilke also supported this discussion and contributed to interpretations of the alteration indices. R. Oberhänsli participated in the interpretation of radioisotopic ages and the potential pore water compositions in the samples. This chapter has originally been submitted for publication to Terra Nova as: *Engelhardt J. F., Sudo M., Wilke F. and Oberhänsli R. $^{40}Ar/^{39}Ar$ dating of volcanic glass from ICDP Lake Van cores.* Terra Nova did not warrant publication and JFE reworked the manuscript by considering the majority of the suggested improvements.

Recalibration of an $^{40}Ar/^{39}Ar$ Standard Validates Chronostratigraphy in ICDP Lake Van Record (Chapter 6)

JFE calculated an age model relative to the stratigraphic depth and modelled ages for all volcaniclastic samples. The model uses exclusively climatostratigraphic and paleomagnetic temporal constraints. R. Oberhänsli provided editing of the manuscript and gave instructive criticism. All figures and the text have been established by JFE.

Tephra provenance (Chapter 7)

A. Musiol conducted XRF analyses. JFE prepared samples for the XRF analyses. Electron microprobe data has been obtained by JFE. M. Müller assisted some electron microprobe analyses. C. Günther adjusted the microprobe for analyses on pyroxenes. M. Sudo and R. Oberhänsli

commented on the manuscript of the chapter and provided editing. Responsibility for all images and text is by JFE.

Modelling Retention of Inherited ^{40}Ar in Volcaniclastic Anorthoclase(Chapter 8)

Electron microprobe analyses have been conducted by JFE. L. Morales and S. Mayanna conducted EBSD analyses of mounted feldspars. J. Guillemoteau designed a deterministic inversion procedure that deconvolved results from spatially averaged results. The inherent optimization of fitting a gradient in Ba concentration has furthermore been computed by J. Guillemoteau. JFE calculated temperture-time scenarios from Ba diffusion couples and Ar degassing scenarios. JFE has the responsibilty on all figures and the text.

2 Introduction

The current public discussion about global warming illustrates the desire of a detailed knowledge about the climate of the past. Lacustrine sediments offer paleoenvironmental and paleomagnetic archives that provide insights into abiotic and biotic processes. The east of Anatolia is particularly sensitive to global climate changes. Seasonally occurring jet streams steer cyclone tracks that are responsible in supplying moist air masses from the Mediterranean towards Anatolia (Fig. 2.1). The Subtropical high pressure systems control the expansion of dry continental air masses to North-eastern Europe and towards the Middle East (Akçar and Schlüchter, 2005; Litt et al., 2009). Therefore, the climate-sensitive region of Eastern Anatolia was estimated to correlate in climate signals to other environmental and climatologic archives such as ice-cores, marine sediments and speleothems (Bar-Matthews et al., 2003; Fleitmann, 2003; Litt et al., 2009). Lake Van represents the third largest terminate Lake on the planet (Reimer et al., 2009), following the Caspian Sea and Lake Issykkul. The lake's large volume and depths suggest that deepest sedimentary deposits might archive multiple glacial-interglacial cycles (Degens et al., 1984). Litt et al. (2007) suggested that drilling lacustrine sediments in an International Continental Drilling Project (ICDP) from Lake Van, could provide climatic and environmental data for East Anatolia and the Near East of unprecedented duration and quality. Accordingly, the ICDP PALEOVAN drilling campaign was conducted in summer 2010 at two different drill sites: on the Ahlat Ridge (AR) and in the Northern Basin (NB).

In the next section of this chapter a geographic and geologic background is provided. The subsequent section leads into the aims of this study and introduces the potential of $^{40}Ar/^{39}Ar$ geochronology on recovered volcaniclastics from ICDP PALEOVAN cores.

2.1 Geographic and geologic background

The following subsections provide basic information about the local topography and offers an introduction into the tectonic setting of the Lake Van area, the volcanism on the Eastern Anatolian Plateau, and the lake sediments of Lake Van.

2.1.1 Topography of the lake van area

Lake Van is located on the south of the Eastern Anatolian Plateau, which has an average elevation of ca. 2 km above sea level (asl) and a spatial extent of ca. 150,000 km^2 (Şengör et al., 2003; Keskin, 2007). The present-day surface of the lake covers about 3755 km^2. Lake Van has a maximum depth of about 450 m. Its lake level is at an elevation of 1648 m asl.

The Erciş Gulf represents the lake's Northeast and does not exceed a depth > 100 m. Three main basins represent the deepest part of Lake Van. They are named in an NW-SE direction: Northern Basin, Tatvan Basin, and Devebonyu Basin. An escarpment and the Northern Ridge separate the Northern Basin from the Tatvan Basin (Fig. 2.2). The Ahlat Ridge subdivides the most northern part of the Tatvan Basin from the Ahlat Subbasin.

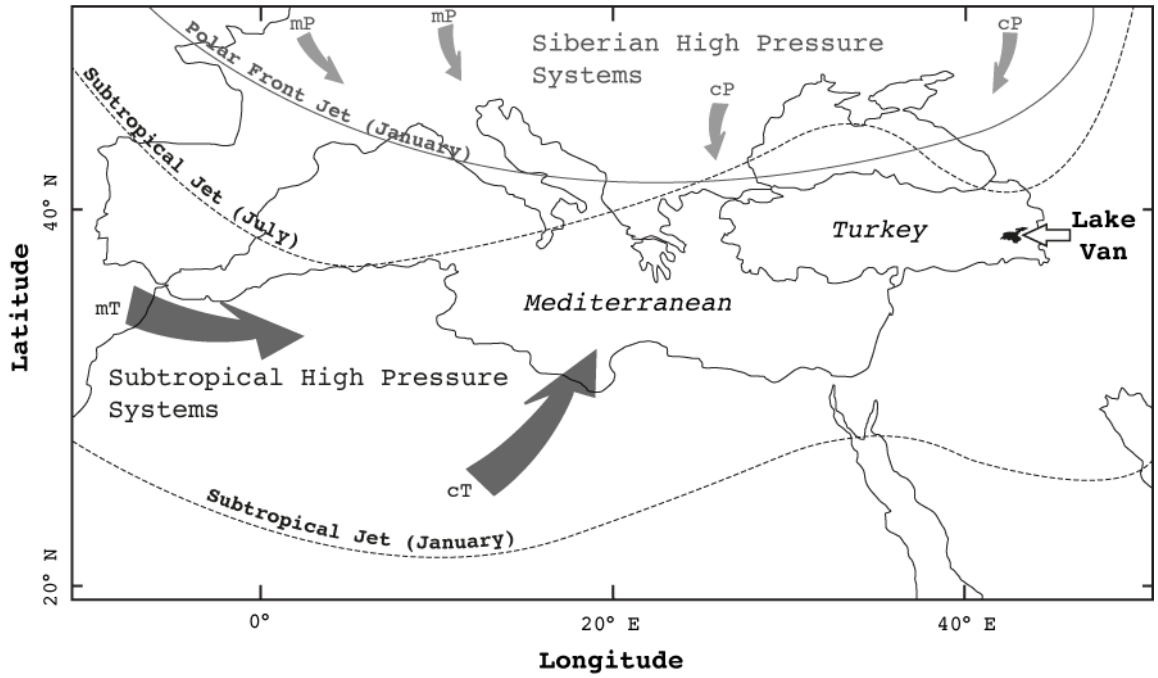

Figure 2.1: A sketched map showing the location of Lake Van in the Mediterranean region. Its sensitive location with respect to global climate variations is indicated by the averaged positions for the subtropical and polar jets. cP: Continental Polar Air Mass; mP: Marine Polar Air Mass; mT: Marine Tropical Air Mass; cT: Continental Tropical Air Mass. The map has been drawn after Wigley and Farmer (1982), Akçar and Schlüchter (2005), and Litt et al. (2009).

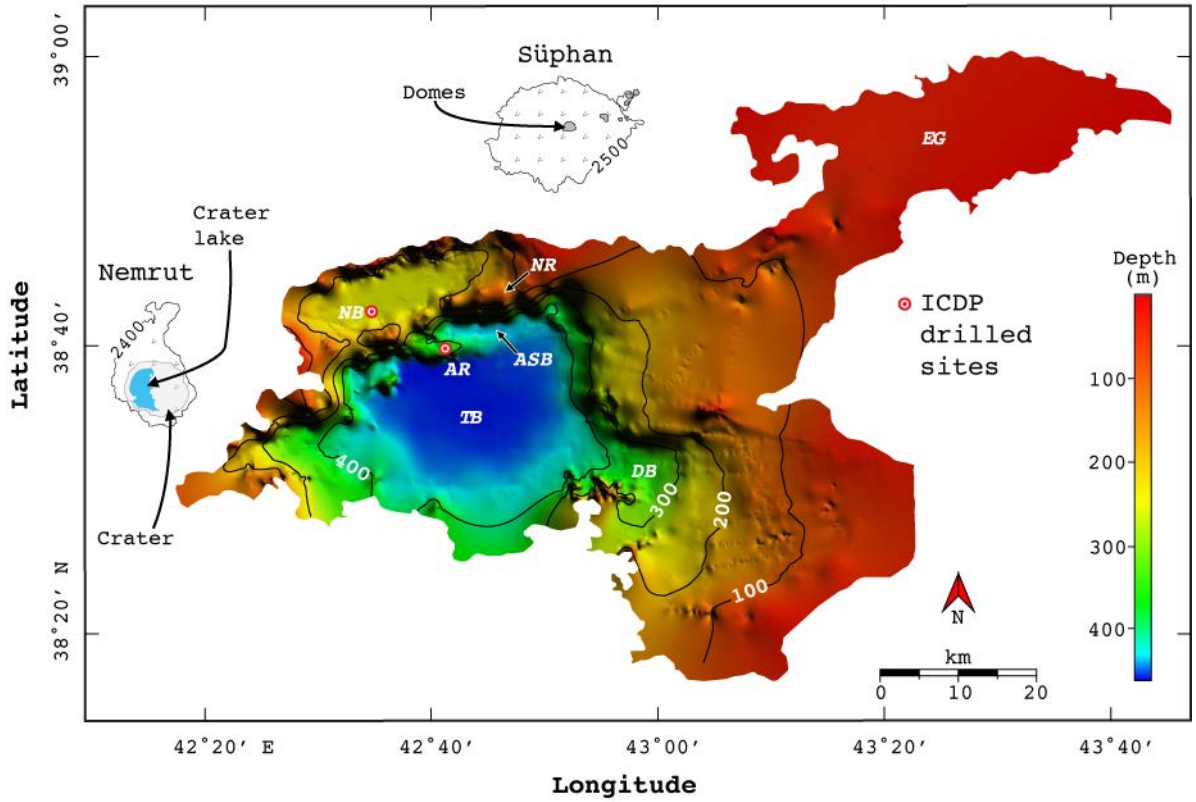

Figure 2.2: Bathymetric map of Lake Van. Colours indicate the lake's depth below lake surface. NB marks the ICDP drill location in the Northern Basin and AR on the Ahlat Ridge. Volcanic edifices of Nemrut and Süphan are marked with two contour lines (representing elevation in meters above sea level). The bathymetric map was provided by Cukur et al. (2014a). ASB: Ahlat Subbasin; DB: Devebonyu Basin; NR: Northern Ridge; TB: Tatvan Basin; EG: Erciş Gulf.

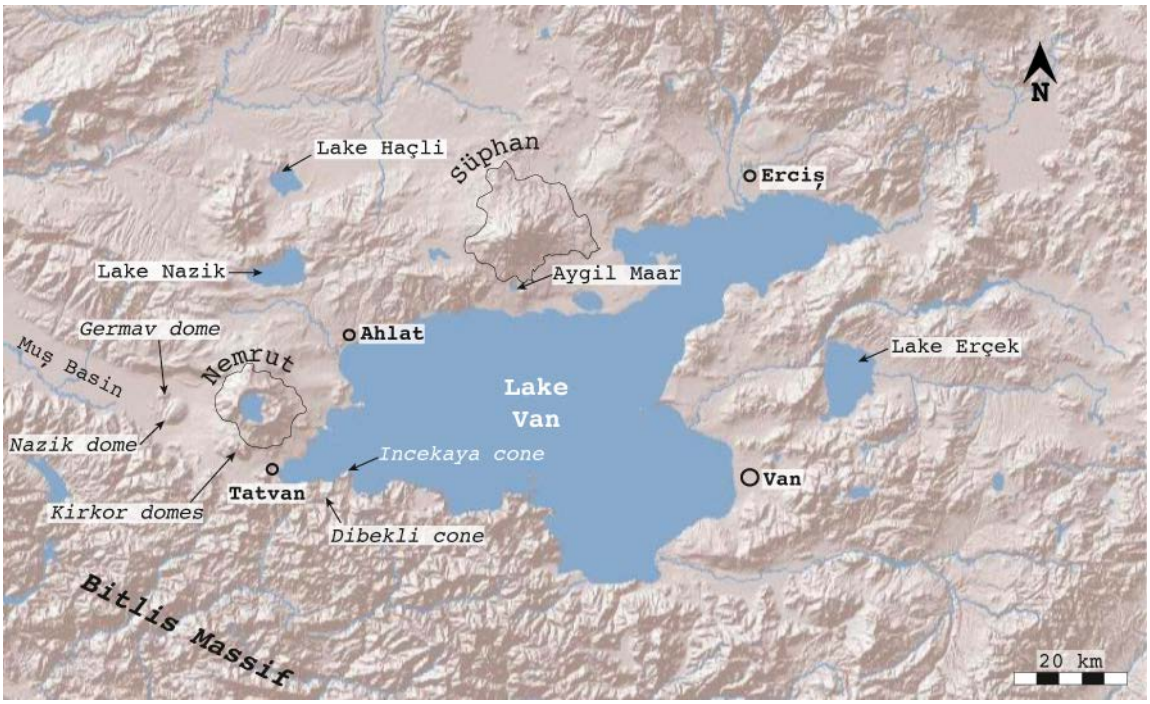

Figure 2.3: Shaded relief map of Lake Van from remote sensing data of the shuttle radar topography mission (SRTM). The map identifies the location of the largest towns with a circle and in bold characters. Arrows identify several lakes, volcanic domes and cones. Steepest slopes of Nemrut and Süphan are outlined with a thin black line.

Lake Van represents the largest soda lake on Earth. The lake water is highly basic (pH >9) and has throughout the entire water column a total alkalinity of > 150 mmol/L (Reimer et al., 2009). Salinity of the lake water is typically around 21.5 ‰. Chemical water stratification is mainly observed for the most upper 50 m. Evaporation processes, hydrothermal activity, chemical weathering of the volcanic rocks and the supply of alkaline tephra into the lake basin, cause the extreme alkalinity of the lake water (Reimer et al., 2009; Litt et al., 2012).

Two large volcanic edifices flank Lake Van: Nemrut and Süphan. The Nemrut stratovolcano represents the most active volcano of Turkey (Sumita and Schmincke, 2013b) and erupted basaltic as well as rhyolitic lava historically. Its last documented eruption is reported in Armenian chronicles and dates back to the year 1692 (Karakhanian et al., 2002). Nemrut's highest summit (2948 m asl) is situated on the rim of a caldera that is about 8 km in diameter (Fig. 2.3). The Nemrut volcano represents a topographic swell that it is situated between two basins: the basin of Lake Van and the Muş Basin. Both basins represent structures that are described as half-grabens (Cukur et al., 2014b) and/or pull-apart graben structures (Dhont and Chorowicz, 2006; Sumita and Schmincke, 2013b). Süphan stratovolcano is located in a distance of 60 km to the Northeast of Nemrut and reaches an elevation of 4058 m. In contrast to Nemrut, Süphan is less explosive, and tends to form domes and subvolcanic intrusions. Accordingly, the summit is capped with a voluminous dome that has an extent of about 1 km in lateral diameter.

2.1.2 Tectonic background of the Lake Van area

Lake Van is situated north of the Bitlis-Zargos-Fold-Belt (BZFB), which is among the seismically most active regions on the planet (Abdulnaby et al., 2014). It is the result of the on-going

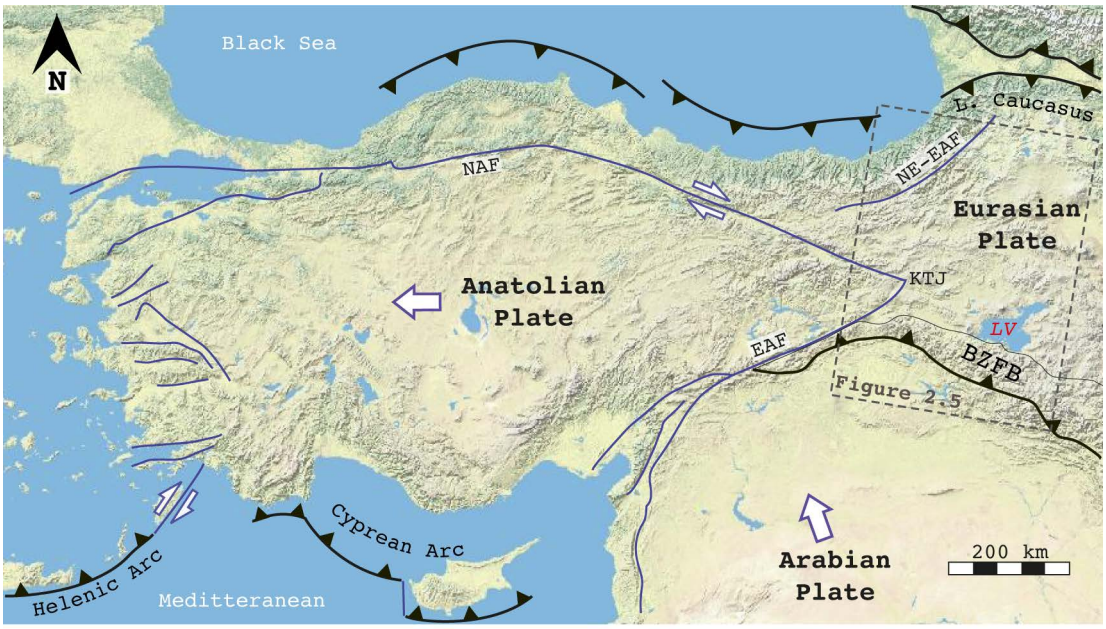

Figure 2.4: Simplified relative plate movements in Anatolia from Reilinger et al. (1997). Major thrust faulting is indicated with thick black lines and with triangles on the overriding block. Major transform and normal faults are given in thin blue lines. A dashed box represents the extent of the tectonic map in Fig. 2.5. The Lower Caucasus and the BZFB represent the northern and the southern border of the East Anatolian Plateau, respectively. Abbreviations are NAF: North Anatolian Fault Zone; EAF: East Anatolian Fault Zone; NE-EAF: Northeast Anatolian Fault Zone; KTJ: Karilova triple junction; LV: Lake Van; BZFB: Bitlis-Zargos Fold Belt. Physical map was provided by the U.S. National Park Services and © esri.

convergence between the Arabian and the Eurasian continental plates. The northwest-ward motion of the Arabian plate is a major force that causes a westward drift of the Anatolian plate, which is illustrated in Fig. 2.4 (McKenzie, 1970; Reilinger et al., 1997). Furthermore, it causes earthquake activity, whose most recent devastation was the Van-Erçis earthquake in autumn 2011, which had a magnitude of M7.2 (Erdik et al., 2012). The Anatolian plate is flanked by two major transform faults: the East Anatolian Fault and the North Anatolian Fault. They merge in the Karilova triple junction, which is located ca. 140 km northwest of Lake Van (Fig. 2.4). The tectonically active region of the East Anatolian Plateau can be differentiated into five tectonic blocks: (i) the eastern part of the Rhodope-Pontide Fragment; (ii) the Northwest Iranian Fragment, (iii) the Eastern Anatolian Accretionary Complex; (iv) the Bitlis Massif, (v) the Arabian Foreland (Keskin, 2007). Fig. 2.5 represents a map that illustrates the central position of Lake Van on two of these tectonic blocks. The southern shoreline of Lake Vans exposes units of the Bitlis Massif that are locally overlain by Quaternary volcaniclastics (Sanver, 1968; Sumita and Schmincke, 2013c). The crystalline Bitlis Massif consists mainly of Precambrian to Cretaceous metamorphic rocks that are covered by tertiary sediments (Oberhänsli et al., 2012).

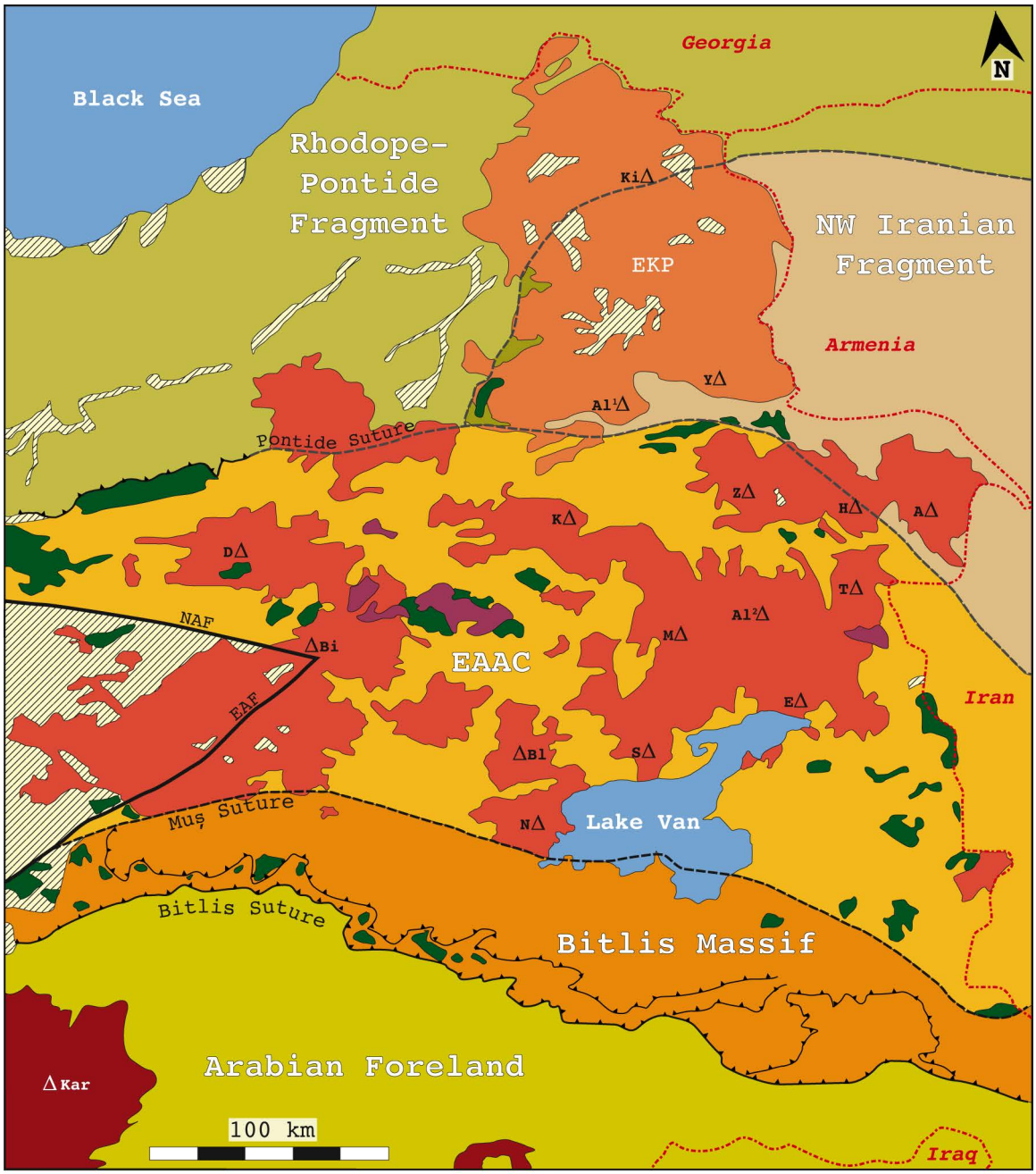

Explanations

- Undifferentiated units of the *Arabian Foreland*
- Medium to high metamorphic sediments and igneous units of the *Bitlis Massif*
- Mélange and flysch units of the *East Anatolian Accretionay Complex (EAAC)*
- Plagiogranitic and phyllitic basement of the *Northwest Iranian Fragment*
- Metamorphic basement and volcano-sedimentary cover of the *Rhodope-Pontide Fragment*
- Northern collision-related volcanics
- Metamorphic blocks within the EAAC
- Ophiolites related to the formation of the EAAC
- Southern collision-related volcanics
- Undifferentiated units
- Thrust faults
- Strike-slip faults
- Suture
- National border
- Δ Volcanic structures

Figure 2.5: (previous page) Simplified tectonic map of Eastern Anatolia after Şengör et al. (2003) and Keskin (2007). Abbreviations of volcanic structures (from N to S) are stated in the following. Ki: Mt. Kisirdağ; Y: Mt. Yaglicadağ; Al^1: Northern Mt. Aladağ; Z: Mt. Ziyaretdağ; H: Mt. Hamadağ; A: Mt. Ağri (a. k. a. Mt. Ararat); K: Mt. Kisirdağ; D: Mt. Dumanlidağ; T: Mt. Tendürek; Al^2: Southern Mt. Aladağ; M: Mt. Meydangdağ; Bi: Mt. Bingöl; E: Mt. Etrüsk; S: Mt. Süphan; Bl: Mt. Bilicandağı; N: Mt. Nemrut; Kar: Karacalidağ.

Its palaeo-geographic and tectonic evolution is matter of debate and might represent either a part of the Anatolian plate or an individual continental block (Şengör and Yilmaz, 1981; Göncüoğlu and Turhan, 1997; Oberhänsli et al., 2012; Oberhänsli et al., 2014). The Muş suture represents the northern contact of the Bitlis Massif to the Eastern Anatolian Accretionary Complex (EAAC) and crosses the southern part of the Lake Van basin. From the Late Cretaceous to the Oligocene the EAAC formed within a northward dipping subduction zone between the Rhodope-Pontide micro-continent and the Bitlis Massif (Keskin, 2007). The EAAC consists of two contrasting groups of rock units: ophiolithic mélanges of Cretaceous age and Palaeocene to Oligocene flysch sequences (Şengör et al., 2003; Keskin, 2007). Shallow marine deposits that are Oligocene to Middle Miocene in age, locally cover both tectonic blocks that surround Lake Van. Furthermore, collision-related volcaniclastics and igneous rocks unconformably overlie sedimentary cover and basements of all five tectonic blocks over great distances (Fig. 2.5).

A more detailed geological map is provided in Fig. 2.6. The diversified range of geological units is connected to Lake Van's location on the Muş Suture and thus covering two different tectonic blocks. Fig. 2.6 illustrates that the geological units that surround Lake Van can be summarized in three different geological divisions along the shores. (i) Metamorphic rocks that are associated with the tectonic block of the Bitlis Massif dominate the south. (ii) Volcaniclastic and effusive rocks dominate the lake's eastern and northern shores. These units are associated with the volcanic activity of Nemrut, Süphan and Bilicandağı volcanoes. The north east reveals a slightly higher abundance of andesites that are older than Quternary ages. To the east Lake Van borders mostly (iii) sedimentary units of Tertiary and Quaternary ages.

The collision-related volcanics can be subdivided into those occurring either south or north of the tectonically active Bitlis Suture. The southern volcanics are mainly described by investigating volcanic rocks of the Karacalidağ shield volcano (Pearce et al., 1990; Notsu et al., 1995; Keskin, 2007). These consist predominantly of porphyritic basalts that erupted from fissures, which trend in a N-S direction. Intermediate and acidic rocks are rare within this unit. According radiometric ages range dominantly from 1.04 Ma to 0.88 Ma (Sanver, 1968; Pearce et al., 1990). Notsu et al. (1995) presented K-Ar ages that are significantly younger than 880 ka. Their youngest age is 100 ± 10 ka. However, the oldest collision-related volcanic rocks of the Eastern-Anatolian Plateau are located north of the Bitlis Suture and date back into the Late Miocene. Volcanics north of the Bitlis Suture have higher fractions of highly silicic, evolved rocks. The most comprehensive chemical analyses of volcanics south and north of the Bitlis Suture zone were conducted by Pearce et al. (1990) and by Notsu et al. (1995). These works and the study of Keskin (2007) provide the background for the information presented in the following section about the collision-related volcanics on the Eastern Anatolian Plateau.

2.1.3 Collision-related volcanics

Collision-related lavas of Eastern Anatolia vary in their petrographic assemblages across the region (Pearce et al., 1990; Notsu et al., 1995; Keskin, 2007). Pearce et al. (1990) and Keskin

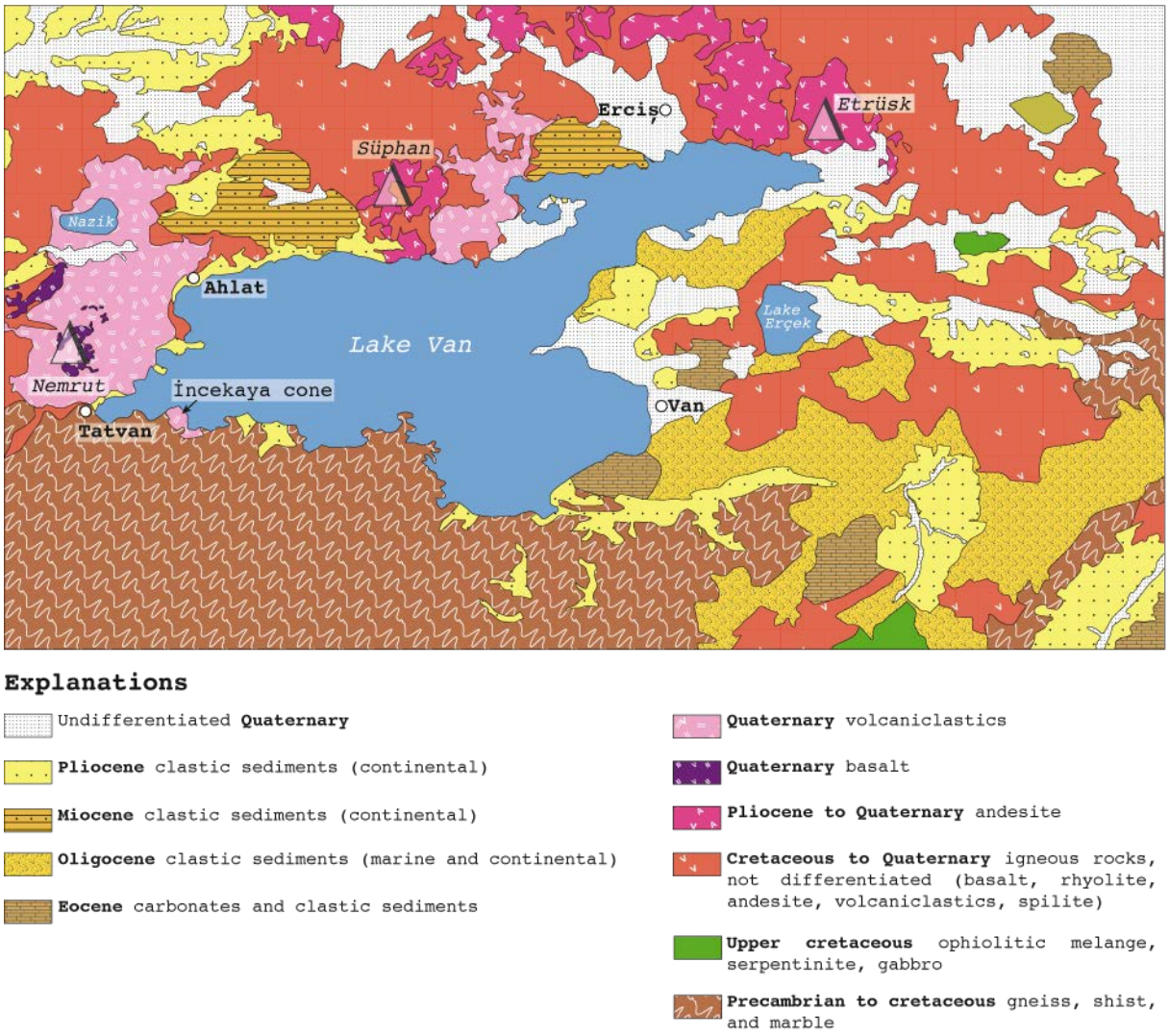

Figure 2.6: Geological map of the area surrounding Lake. The map represents data from Müdür et al. (2011) and has been simplified following Selcuk et al. (2010).

(2007) stated that the northern part of the plateau contains anhydrous and hydrous minerals, whereas volcanics in the southern part of the plateau contain little volumes of hydrous minerals. In contrast to this observation Sumita and Schmincke (2013b) reported that biotites (and to a lesser degree amphiboles) are a petrographic characteristic of volcaniclastics from Süphan volcano. The collision-related volcanic activity on the East Anatolian Plateau migrated from the Late Miocene to historic times along a NNW-SSE trend (Fig. 2.7a). Whereas volcanics from the northern Erzurum-Kars Plateau (EKP) are dominantly calcalkaline, most southern volcanics reveal alkaline compositions (Figs. 2.7b, 2.7c, 2.7d, 2.7e). Normalized multi-element patterns in spider diagrams show that volcanics from Ararat volcano and from the EKP have slightly different Ta and Nb concentrations (Fig. 2.7f and 2.7g) in comparison to the southern volcanics (Nemrut, Tendürek, Muş-Varto). Ta and Nb have the lowermost ratio of atomic numbers relative to the ionic radii and are thus of exceptional (aqueous) immobility (Rollinson, 1993). It is common practice to interpret a sharp decrease (or valleys) of normalised Th, Ta and Nb fractions (normalised to the normal-type mid ocean ridge basalt, N-MORB) to be typical for a distinctive subduction signature. Trends that do not show a decrease in these elements

are interpreted to represent a within-plate signature. Keskin (2003) and Keskin (2007) thus interpreted comprehensive trace element and isotopic data from the EKP and Ararat volcano to reflect a subduction signature and an enriched mantle as a magmatic source.

The mantle signature diminishes in chemical data from the volcanic centres of the Muş-Varto depression, from the Nemrut volcano, and from the Tendürek volcano. Rocks from these volcanic structures are dominantly of alkaline character and an interpretation of their trace elements and Sr isotopes suggests intra-plate magmatic sources (Pearce et al., 1990; Keskin, 2007). Pearce et al. (1990), Notsu et al. (1995), and Keskin (2007) have focused furthermore on relative Ta, Th and Y concentrations and argued that mantle metasomatism is considerably more pronounced in rocks from Tendürek, Nemrut and Muş-Varto volcanoes. From comparisons to petrological modelling it has been inferred that magmatism on the southern rim of the East Anatolian Plateau is devoid of any chemical subduction signature and has dominantly evolved from an enriched mantle through combined assimilation and fractional crystallisation processes (Pearce et al., 1990). Combining Ta/Th ratios with MgO concentrations supported the detected trends from multi-element data and outlined a distinct difference in the trace element compositions of the EKP and Ararat volcanics versus the Nemrut, Tendürek and Muş-Varto volcanics (Keskin, 2007). However, it needs to be stated that the majority of available element signatures are not unequivocally supporting the above-mentioned trends. A sharp N-S directed chemical change is only visible in the geochemical data from a minority of available samples, which is attributed to the predominance of highly evolved and silica-rich volcanic rocks (>65 wt% SiO2). The high degrees of fractional crystallisation may camouflage the mantle sources in trace element patterns. Additionally, sparse radiometric ages from the northern volcanic suites may bias interpretations of the tectono-magmatic evolution as well (Keskin, 2007). Analysing and dating volcaniclastics from Lake Van drill cores faces this matter of debate and the data generated in this study contributes to the knowledge about the collision-related volcanism in the South of the East Anatolian Plateau.

2.1.4 Local tectonics

Ca. 1500 km of multi-channel seismic reflection profiles were recorded offshore Lake Van previous to the drilling of the PALEOVAN campaign (Cukur et al., 2014a). These profiles aimed the detection of predominantly NE-SW and E-W trending faults that are sub-parallel to the lineament of the Bitlis Suture (Fig. 2.8). Whereas southern, eastern and northern shores are dominated by strike-slip faulting, the western area of Lake Van reveals thrust faults that can be linked to the Muş Suture and the southern border of the Muş Basin. Lake Van is situated on a tectonic depression that is a part of an active faulting system, whose occurrence is connected to the seismic, volcanic and hydrothermal activity of the region (Degens et al., 1984; Kipfer, 1994; Keskin, 2003; Şengör et al., 2003; Litt et al., 2009).

The seismic site surveys were carried out in 2004 and 2012 (Litt et al., 2009; Cukur et al., 2014a). These revealed the continuation of the thrust-fault in the south of the Muş Basin into the Lake Van subsurface. Cukur et al. (2014a) defined an 'acoustic basement' and 19 seismic units (SU) that represent the seismic stratigraphy of Lake Van. The acoustic basement was defined as anything underlying earliest deltaic and fluvial mass transport deposits that are related to the subsidence of the Lake Van basin. Slightly atypical for pull-apart basins and

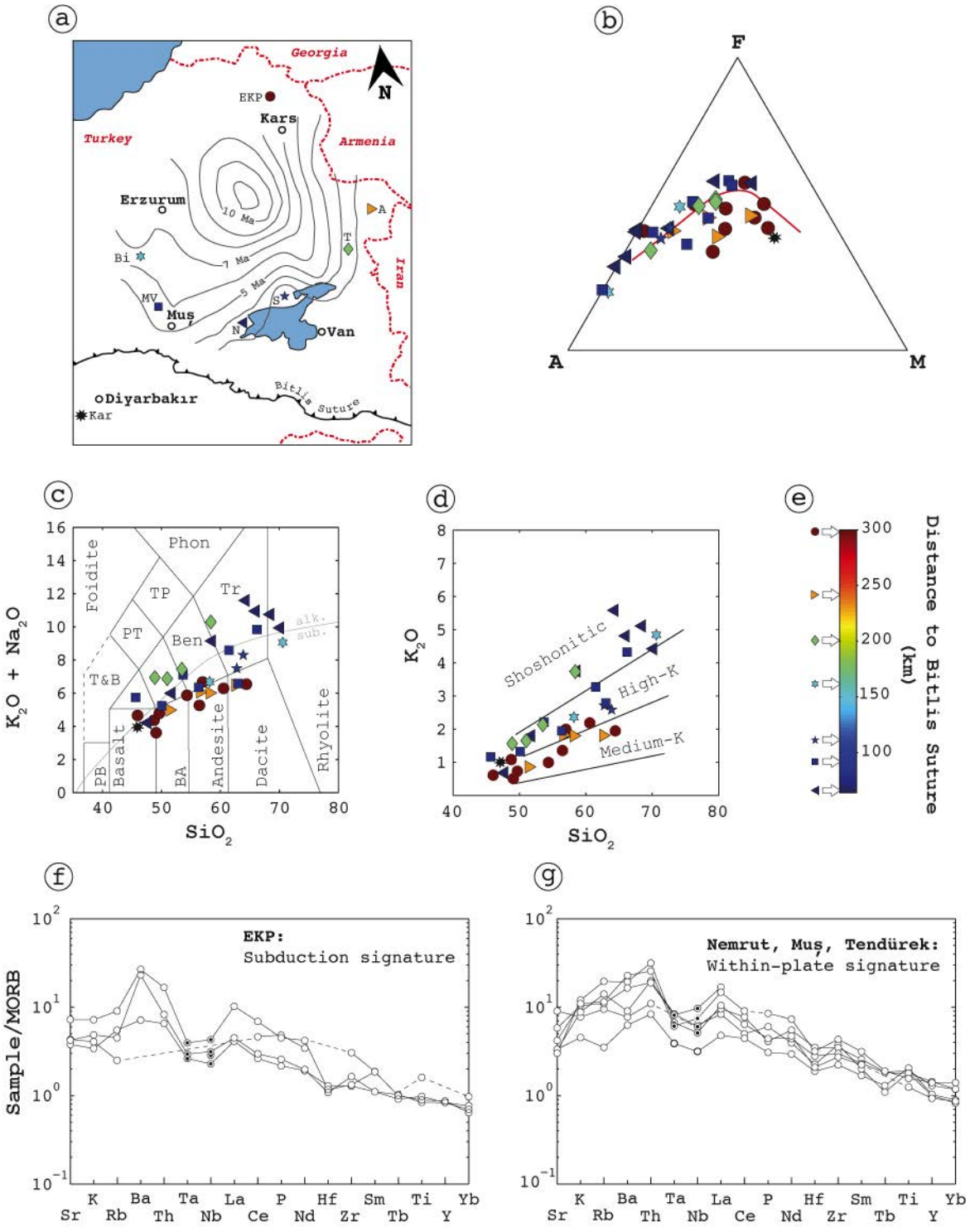

Figure 2.7: (previous page) Summary of representative geochemical data for selected collision-related volcanic units north of the Bitlis Suture from the literature (Pearce et al., 1990; Notsu et al., 1995; Buket and Temel, 1998; Keskin et al., 1998; Şen et al., 2004; Özdemir et al., 2006; Keskin, 2007). (a) Isolines representing oldest available radiometric ages of volcanic rocks north of the Bitlis Suture. Volcanic units become younger following a NNW – SSE trend. (b) AFM diagram indicating a weak tendency of southern volcanic rocks to follow tholeiitic trends. Red line divides tholeiitic from calcalkaline rocks after Irvine and Baragar (1971). (c) Total alkali versus silica diagram after Lebas et al. (1986). The discrimination of alkaline and subalkaline rocks follows Irvine and Baragar (1971). (d) Discrimination in a SiO_2 versus K_2O diagram after Peccerillo and Taylor (1976). (e) Colour coding of symbols with respect to the N-S distances of sampled locations to the Bitlis Suture. (f) Relative trace element distribution in a spider diagram of low-silica rocks (<50 wt%) from the EKP. (g) Trace elements of low-silica rocks from Muş, Nemrut and Tendürek volcanoes. Selected elements follow an order that separates H_2O mobile and H_2O immobile elements and was suggested in Pearce et al. (1984). Normalisation is conducted relative to a MORB composition from Pearce (1983); Pearce et al. (1984) and Bevins et al. (1984). Marked elements represent concentrations of Ta and Nb. Except for MV (volcanic rocks in the Muş-Varto depression) all abbreviations are explained in caption of Fig.2.5.

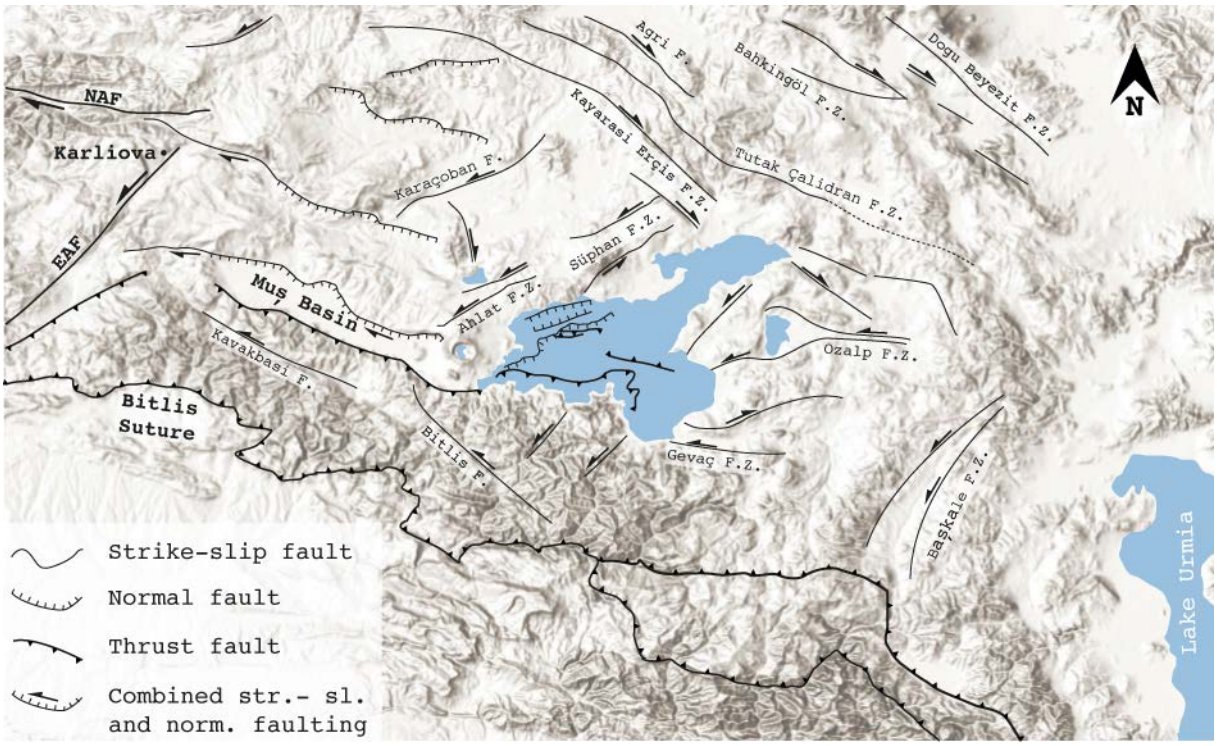

Figure 2.8: Major faults and fault zones in the surrounding area of Lake Van. Faults are adapted from Selcuk et al. (2010) and Cukur et al. (2014a). The hill-shade topography model is based on SRTM data and was provided by © esri ArcGIS Online 2017.

half graben structures is the thrusting component in the south of Muş and Lake Van basins. Cukur et al. (2014a) detected a consistent acoustic basement only in the subsurface of the Tatvan Basin and mapped it for its relative depth underneath the lake floor (Fig. 2.9a). The seismic signal dominantly reveals an angular unconformity. Diminishing of the detectability is potentially attributed to volcanic extrusion and intrusions. However, the acoustic basement is clearly bound to NE-trending faults that suggest a NE-SW to E-W directed extension. The southern border of the Tatvan basin is interpreted by Dhont and Chorowicz (2006) and Cukur et al. (2014a) to be characterised by reverse-faulting mechanisms with southern units overriding the Muş and the Tatvan basins. Nomenclature from Cukur et al. (2017) labels this fault as South Boundary Fault (SBF). The proposed reverse-faulting mechanism is not typical for pull-apart basins and is at odds with interpretations by Selcuk et al. (2010). A rather normal-faulting character is suggested by interpretations of seismic cross-sections (Fig. 2.9b, 2.5c) from Cukur et al. (2014a). The actual faulting mechanisms in the south of Lake Van are thus not unequivocal and a potential matter of current and future research. Dhont and Chorowicz (2006) labelled the neighbouring Muş Basin to be a half-ramp basin and it appears likely that the Lake Van Basin is formed accordingly. The normal-fault as interpreted in the seismic cross-section by Cukur et al. (2014a) could be derived from more progressive faulting and/or in connection to a not identified thrusting further south or in greater depths (indicated in Fig. 2.9c). Half-ramp basins are typical for intraplate thrust belts. The according scenario is potentially adequate to explain the thrust faulting of the SBF and the uplift of the AR (Voigt et al., 2008). However, half-ramps remain undiscussed for the tectonic setting of the Lake Van subsurface.

The AR formed between 340 and 290 ka (Cukur et al., 2014a). It represented subsequently

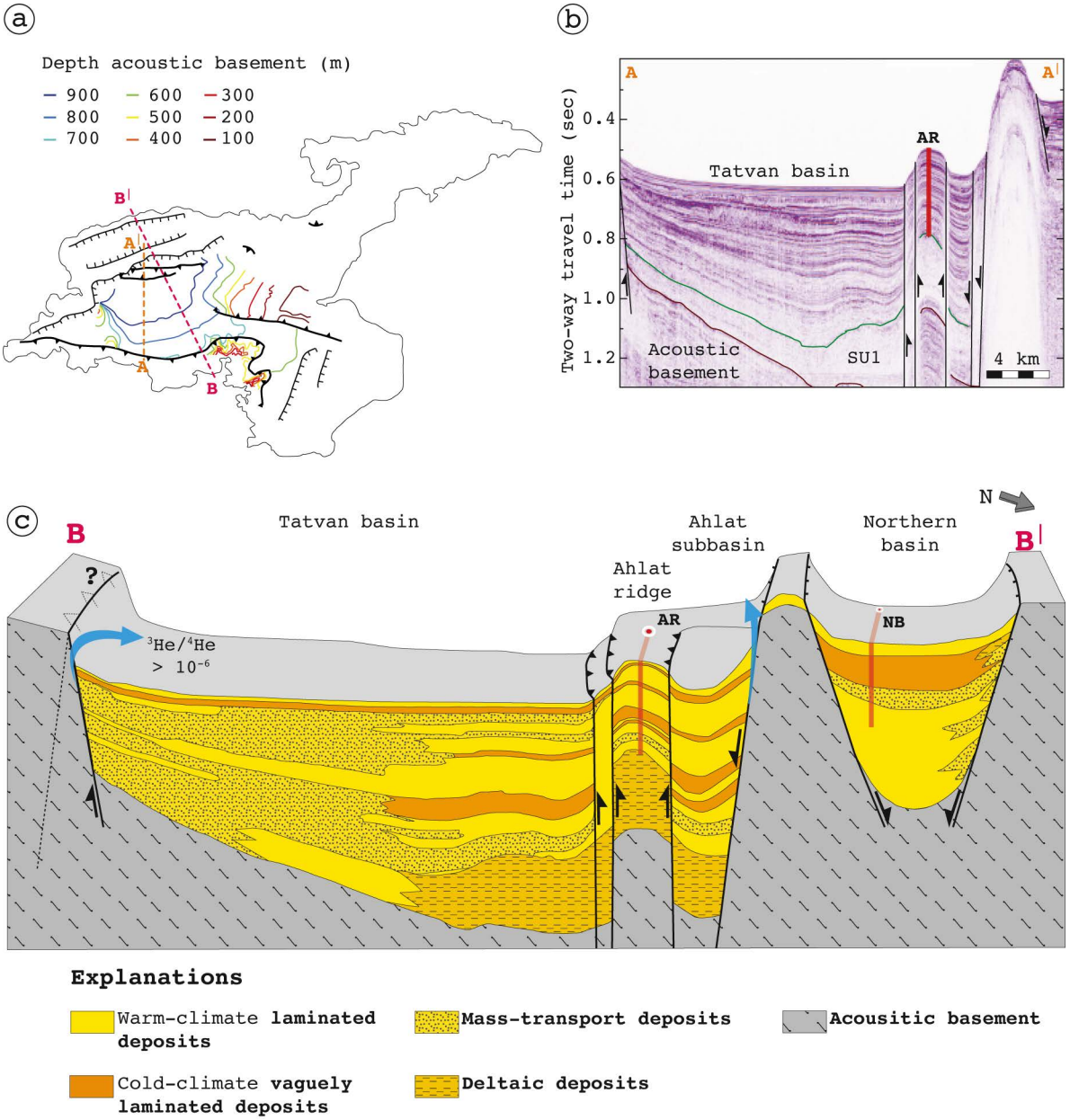

Figure 2.9: (a) Major faults and depth structure of the acoustic basement. The depth is given in meters of sediment cover. The map is drawn after Dhont and Chorowicz (2006), Cukur et al. (2014a), and Cukur et al. (2017). (b) N-S directed seismic profile (A-A'). Seismic unit 1 (SU1) represents mostly deltaic and mass transport units. It is interpreted to reflect basal fluvial facies that precede the lacustrine history of Lake Van (Cukur et al., 2014a; Cukur et al., 2014b). (c) Schematic cross-section (B-B') simplifying and summarising the sediment fill of the Lake Van basin. Sketch is drawn and modified after Cukur et al. (2014a). The dashed line and open triangles represent an inferred thrusting mechanism. Helium isotope anomalies suggest hydrothermal pathways to be connected with the major faults bordering the Tatvan basin (Tomonaga et al., 2014) and are indicated with blue arrows.

a topographic swell and was protected from the deposition of mass-transport deposits. Consequently, AR was ascribed to represent the key-site for drilling the complete lacustrine history of Lake Van. Omnipresent active faulting throughout the lake's history triggered margin-wide slope failures and the majority of vast mass-transport deposits. The overall tectonic activity of the major faults decreased significantly between 30 ka and present (Cukur et al., 2014a). A very different setting was detected for the NB. A local graben structure is flanked by two parallel normal faults. The sedimentation rate in the NB is significantly higher, which is attributed to an increased abundance of volcaniclastic mass transport from the lake's shores.

2.1.5 Recovered sediments in ICDP PALEOVAN cores

The recovered material was derived from seven and four parallel-drilled cores at AR and NB sites, respectively. Stockhecke et al. (2014b) and Çağatay et al. (2014) compiled composite records from the multiple cores (Fig. 2.10). The total recoveries of the composite records reach a length of 219 m (AR) and 145 m (NB). It is the common convention to indicate stratigraphic positions of samples from the composite records with the unit 'meters of composite below lake floor' (mcblf). Average recoveries of 86 % (AR) and 91 % (NB) provided almost complete sediment records, with only a few instances of hiatus.

Correlations of characteristic laminated clayey silt layers and volcaniclastic layers between the composite records of AR and NB suggest that the NB record accumulated significantly more event-related clastic material (mass-transports and volcaniclastics). These hamper the interpretation of the lacustrine evolution, which is higher resolved and less disturbed at the AR (Fig. 2.11). The two composite records furthermore show differences in the style of background sedimentation, which supported the identification of some lake-wide trends in changing lake-levels (Çağatay et al., 2014; Cukur et al., 2014a; Cukur et al., 2014b; Stockhecke et al., 2014b). About 17 % of all recovered material from AR represents volcaniclastic material (Stockhecke et al., 2014a; Stockhecke et al., 2014b). Volcaniclastic layers are identified with the letter V and a consecutive number (e.g. V-236 for layer No. 236). The counting procedure is organized from top downwards. Stockhecke et al. (2014b) identified 300 volcaniclastic layers and provided a drilling-campaign-internal register of their stratigraphic positions and thicknesses. This thesis adopts their nomenclature for layer identification of volcaniclastic material. North-eastward-directed winds dominated the southern part of the East Anatolian Plateau in the Pleistocene (Sumita and Schmincke, 2013c) and most volcaniclastic material that was recovered from Ahlat Ridge and the Nothern Basin drilling locations (Fig. 2.2) is presumably connected to the explosive volcanism of Nemrut. To a minor degree, drilled volcaniclastics can also be linked to Süphan Stratovolcano (Schmincke et al., 2014). One volcanic layer (V-80) has been correlated to pumice from the eruptive centre of the hyaloclastic İncekaya cone (Fig. 2.3). The vast majority of volcaniclastics deposited in ICDP PALEOVAN cores is of a fallout type. Syn-ingimbritic turbidites and reworked material are less abundant (Schmincke et al., 2014; Stockhecke et al., 2014b).

The overall lithostratigraphic framework of Lake Van is dominated by carbonaceous clayey silt. This lacustrine material was found to represent about 76 % of the recovered material in ICDP PALEOVAN cores and can be subdivided into six lithotypes (Stockhecke et al., 2014b): (i) graded beds that are frequently intercalated with varved clays, (ii) varved clays silts, (iii)

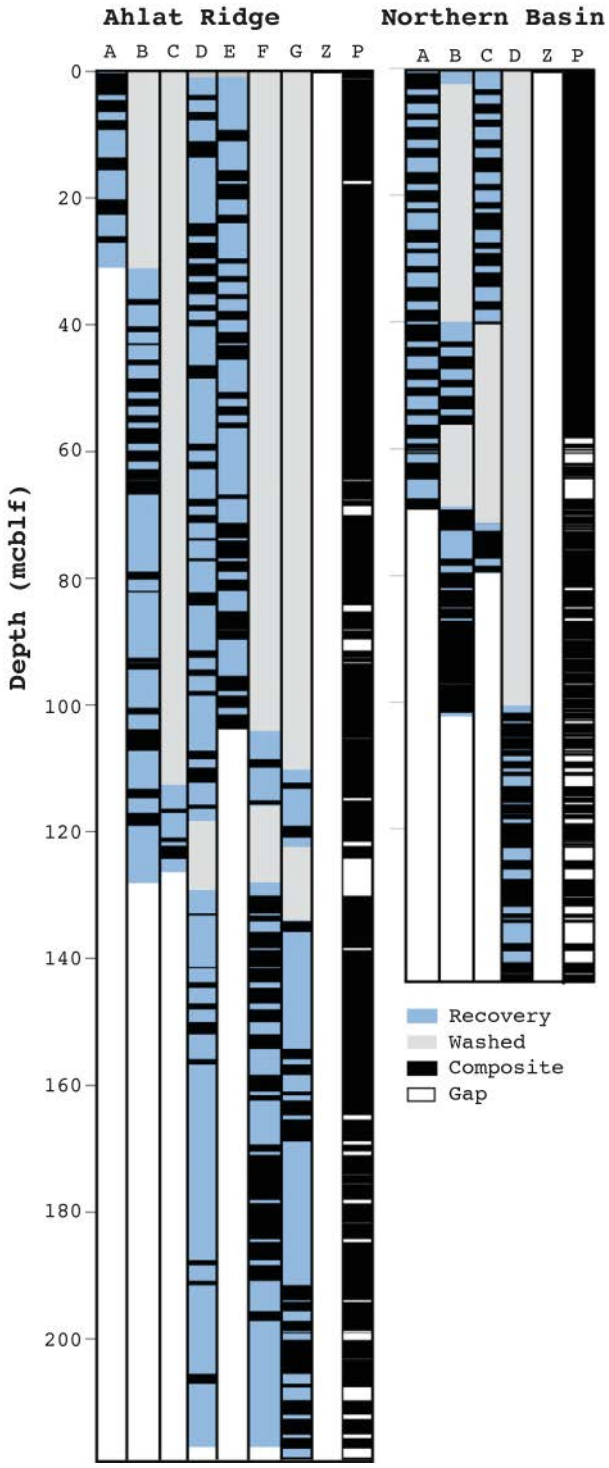

Figure 2.10: Compilation of the PALEOVAN drilling recovery from Stockhecke et al. (2014b). Compiling composite records (P) from multiple parallel records achieved almost complete records. Short cores recovering the shallowest deposits are identified with Z. The other labels accord to the campaign's borehole identifiers. Washed sections were drilled but the borehole cuts were not recovered. The depth scale is 'meters composite below lake floor' (mcblf).

$CaCO_3$-rich banded sediments, (iv) $CaCO_3$-poor banded and mottled clayey silt, (v) diatomaceous mud, and (vi) fluvial sands and gravels. Fluvial deposits represent only 2 % of the total drilling record and dominate the base of the drilled materials from AR that indicate the initial flooding of the Lake Van basin. Table 2.1 lists the major lithotypes that are presented in Stockhecke et al. (2014b). Furthermore, Stockhecke et al. (2014b) offers concise descriptions and interpretations of the lacustrine lithostratigraphy and subdivides the AR record into 25 lithostratigraphic units. The first five lithostratigraphic units of the AR record can be correlated to the NB record. A complete description of these units exceeds the aim of this study. However, the units represent a convenient organisation of the AR strata and will be used for approximating stratigraphic positions in this thesis. Two units from the AR record differ from all other deposits of background and event-related sedimentation. The mottled unit (MU) is characterized by mottled, dominantly brown, faintly laminated lithologies that reveal micro-deformations (Stockhecke et al., 2014b). It is known from seismic imaging that the MU onlaps on a prograding sequence that represents extreme lake level low stands. The prograding sequence itself is not recovered in the composite core but would require a lake level low stand of ca. 506 meters below present lake level. Such a scenario would cause an erosional unconformity in the AR record, which has not been detected (Stockhecke et al., 2014b).

A prominent 20-m-thick unit reveals disturbed sediment successions and is stratigraphically overturned (Stockhecke et al., 2014b). This unit is characterised by disrupted, folded and deformed lacustrine lithologies that are capped by a turbidite. The whole unit has been interpreted to represent a giant mass movement deposit (MMD) and is named the deformed unit (DU). The lateral extent of the DU is well-detectable in seismic profiles throughout Tatvan Basin as an acoustically chaotic layer (Cukur et al., 2014a; Stockhecke et al., 2014b). The wide lateral extent of the DU and the thickness of the turbidite (> 5 m) that caps the DU, suggest that overturning, folding, and disrupting occurred in situ, whereas the turbidite represents the actual MMD. Stockhecke et al. (2014b) assume that a seismic mega-event triggered the event that is connected with the deformation of the DU.

Table 2.1: List of major lithotypes in AR composite core after Stockhecke et al. (2014b). The total stratigraphic thickness represents a cumulative value from the AR composite record.

Abbreviation	Lithotype	Total thickness (m)
Li	Laminated clayey silt	20.9
LiLb	Intercalating laminated and banded clayey silt	2.1
LiLf	Intercalating laminated silt and faint laminated clayey silt	2.3
LiLmoLg	Intercalating laminated, mottled clayey silt and graded beds	1.6
LiLg	Laminated clayey silt intercalated by graded beds	15.1
Lf	Faint laminated clayey silt	7.8
LfLb	Intercalating faint laminated and banded clayey silt	1.2
LfLmo	Intercalating faint laminated and mottled clayey silt	0.8
LfLg	Faint laminated clayey silt intercalated by graded beds	1.9
Lmo	Mottled clayey silt	9.0
LmoLg	Mottled clayey silt intercalated by graded beds	1.6
LmoLb	Intercalated mottled and banded clayey silt	13.4
Lb	Banded clayey silt	54.4
LbLg	Banded clayey silt intercalated by graded beds	2.8
Lm	Massive clayey silt	23.3
Fms	Fluvial muddy sands	4.6
Fgv	Fluvial gravel	0.3
Lg	Graded beds	6.7
V	Volcaniclastics	36.6

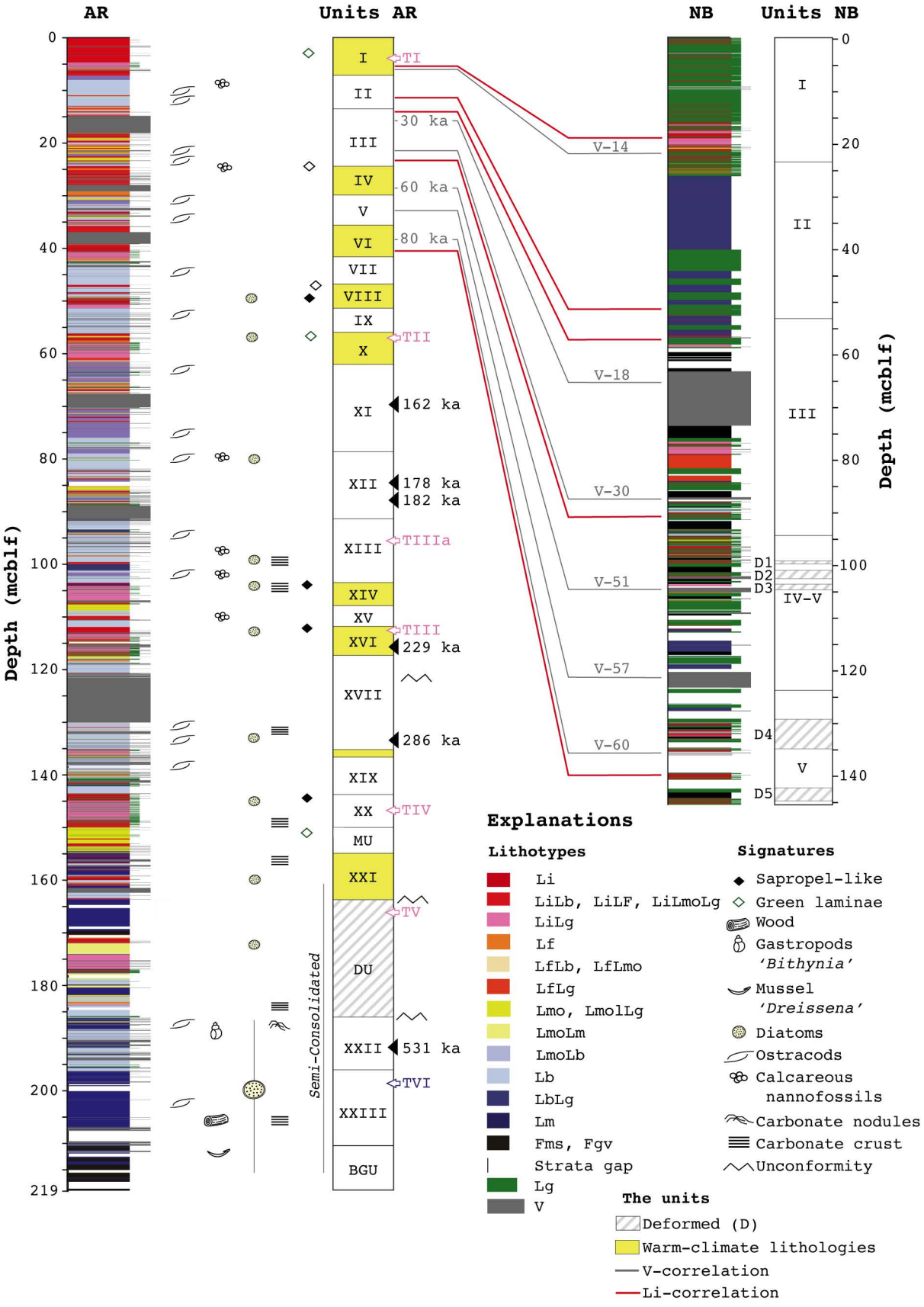
AR
Units AR
NB
Units NB
Depth (mcblf)
I
II
III
IV
V
VI
VII
VIII
IX
X
XI
XII
XIII
XIV
XV
XVI
XVII
XIX
XX
MU
XXI
DU
XXII
XXIII
BGU
TI
TII
TIIIa
TIII
TIV
TV
TVI
30 ka
60 ka
80 ka
162 ka
178 ka
182 ka
229 ka
286 ka
531 ka
Semi-Consolidated
V-14
V-18
V-30
V-51
V-57
V-60
D1
D2
D3
IV-V
D4
D5
Explanations
Lithotypes
Li
LiLb, LiLF, LiLmoLg
LiLg
Lf
LfLb, LfLmo
LfLg
Lmo, LmolLg
LmoLm
LmoLb
Lb
LbLg
Lm
Fms, Fgv
Strata gap
Lg
V
Signatures
Sapropel-like
Green laminae
Wood
Gastropods
'Bithynia'
Mussel
'Dreissena'
Diatoms
Ostracods
Calcareous nannofossils
Carbonate nodules
Carbonate crust
Unconformity
The units
Deformed (D)
Warm-climate lithologies
V-correlation
Li-correlation

Figure 2.11: (previous page) Lithologies of AR and NB composite drilling records from Stockhecke et al. (2014b). The most prominent isochronous deposits that correlate between NB and AR are displayed in grey (volcaniclastics) and in red (laminated lacustrine layers, Li). Ages from tephrostratigraphy are stated in grey and $^{40}Ar/^{39}Ar$ ages from Stockhecke et al. (2014b) are given in black. Major climatic terminations are indicted as TI to TVI. Lithotype abbreviations are identified in Table 2.1. DU abbreviates the Deformed Unit, MU the Mottled Unit, and BGU the Basal Gravel Unit.

The sum of background sedimentation and event sedimentation is about three times higher at the NB drill site (1.6 m ka^{-1}) than at the AR drill location (0.5 m ka^{-1}) (Stockhecke et al., 2014a; Stockhecke et al., 2014b). The different style of background sedimentation and the high abundance of event deposits in the NB hinder ideal proxy records such as total organic carbon (TOC) or the relative $CaCO_3$ content. The 145-meters-long NB composite core correlates with the upper 40 mcblf of the AR composite core and thus covers only the youngest lacustrine history of Lake Van. As the NB composite record is limited to the younger age range, it was no particular sampling target for radioisotopic dating of the lacustrine history.

The following section (2.2) provides an introduction into a climate-stratigraphic age model for the composite record from AR. Timing the lake's history with this model represents a key-aspect in discussing $^{40}Ar/^{39}Ar$ data that is presented later in this thesis. Furthermore, sampling targets are assigned and the potential of $^{40}Ar/^{39}Ar$ geochronology on the AR composite record is outlined.

2.2 $^{40}Ar/^{39}Ar$ geochronology of Ahlat Ridge strata

The wealth of available chemical and lithological data in the strata of the AR composite core allowed aligning proxy data to Quaternary climatostratigraphic timescales (Fig. 2.12). The alignment resulted in a neat chronostratigraphy, which had been established previous to the commencement of this study and, thus, previous to establishing a petrologically corroborated and statistically robust $^{40}Ar/^{39}Ar$ geochronology for the AR composite record (Stockhecke et al., 2014b). Interpolation of distinct climatostratigraphic markers allowed composing an age model for the AR composite record (Stockhecke et al., 2014a; Stockhecke et al., 2016). Validation and/or modification of the model by considering results from $^{40}Ar/^{39}Ar$ geochronology is a major aim of this thesis and requires outlining of the limits and potentials of the age model. This chapter reviews in the following the age model of the AR composite core, outlines a sampling strategy, and finally illustrates the goals and the potentials in establishing $^{40}Ar/^{39}Ar$ geochronology on volcaniclastics from the AR drill cores.

2.2.1 The age model

The chronostratigraphy of the AR composite core is predominantly based on a detailed lithostratigraphic framework that compiles various age constraints (Stockhecke et al., 2014a; Stockhecke et al., 2014b). In order to review the establishment of a climatostratigraphic chronology sufficiently, the following section will first focus on the methodology of climate-proxy-tuning of AR strata. Subsequently all other relative chronometers that helped establishing an age versus depth relationship are summarised.

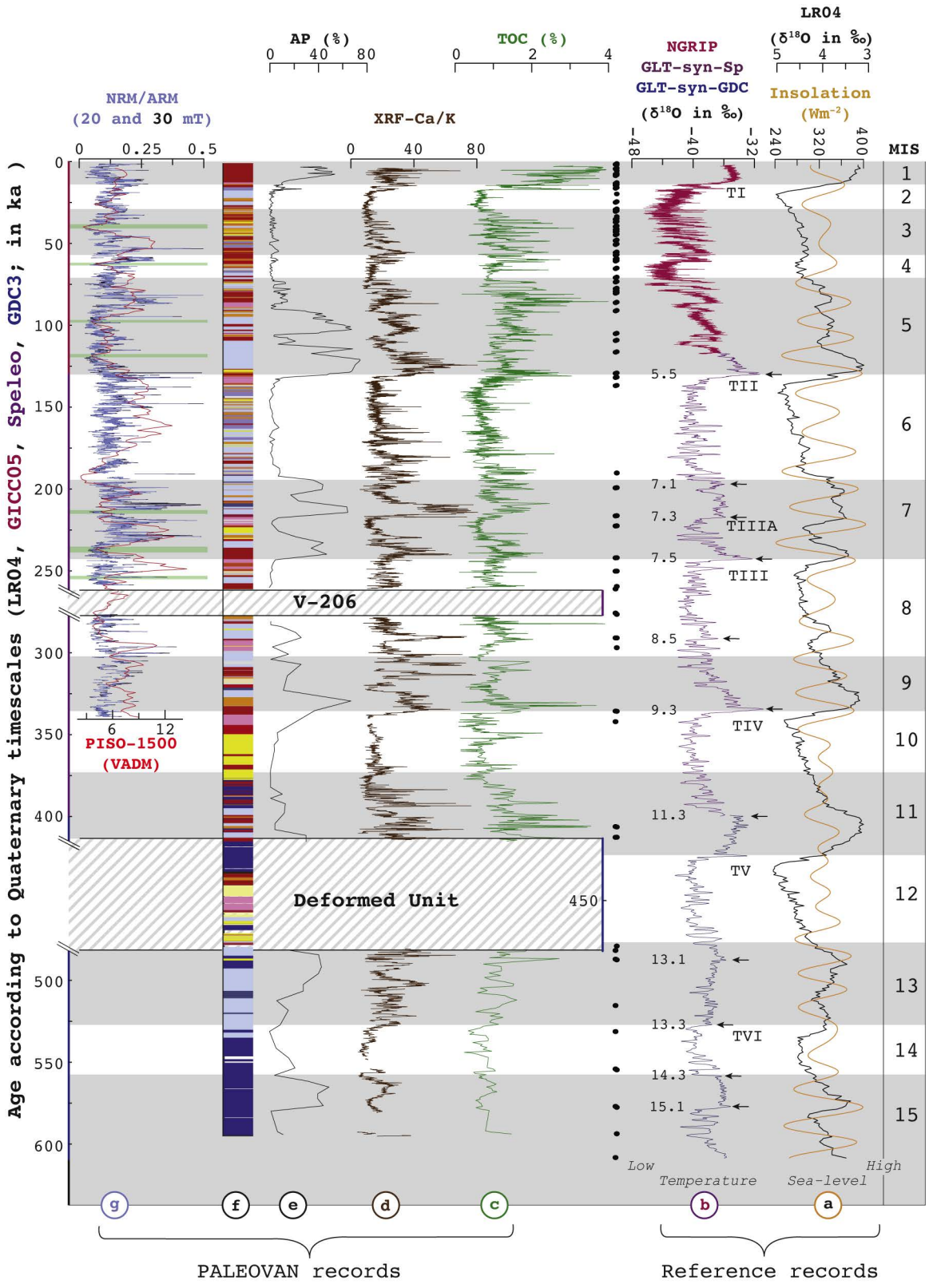
LR04
(δ18O in ‰)
AP (%)
TOC (%)
NGRIP
GLT-syn-Sp
GLT-syn-GDC
(δ18O in ‰)
Insolation
(Wm-2)
NRM/ARM
(20 and 30 mT)
XRF-Ca/K
MIS
Age according to Quaternary timescales (LR04, GICC05, Speleo, GDC3; in ka)
TI
TII
TIIIA
TIII
TIV
TV
TVI
5.5
7.1
7.3
7.5
8.5
9.3
11.3
13.1
13.3
14.3
15.1
V-206
Deformed Unit
450
PISO-1500
(VADM)
Low
Temperature
High
Sea-level
PALEOVAN records
Reference records

Figure 2.12: (previous page) Marine-, ice core-, and synthetic isotope chronologies aligned to the Lake Van paleoclimate records after Stockhecke et al. (2014a). Black dots represent age control points between reference records and the proxy data. MIS abbreviates marine isotope stages. (a) The difference between June and December insolation after Laskar et al. (2004) reflects seasonality (yellow graph). The black graph reflects the LR04 δ^{18}O record relative to Vienna Pee Dee Belemnite (VPDB) after Lisiecki and Raymo (2005). (b) Three different ice-core isotope records (NGRIP, GLT-syn Speleo, GLT-syn GDC3) relative to Vienne Standard Mean Ocean Water (VSMOW). Nomenclature of the MIS sub-stages (marked with arrows) follows Jouzel et al. (2007). (c) AR composite core TOC record (Stockhecke et al., 2014b). (d) Ca/K ratio of the AR composite core (Kwiecien et al., 2014). (e) Arboreal Pollen abundance in AR cores (Litt et al., 2014). (f) Tuned non-event stratigraphy of AR composite cores. Colour coding is identical to Fig. 2.11. (g) Natural remanent magnetization (NRM) normalized by anhysteric remanence (ARM) for 20 and 30 mT. Prominent minima agree with PISO-1500 stack reference record (Channell et al., 2009) and are highlighted in green. Stockhecke et al. (2016) refined the chronology shown here by adding the AICC 2012 isotope stratotype (Veres et al., 2013) between 100 and 113 ka and by involving sediment colour reflectance as a proxy.

Climatostratigraphic chronology

Proxy records from TOC, Ca/K ratios, and arboreal pollen abundance were compiled for an event-free modification of the AR composite record (Stockhecke et al., 2014a). Fluvial and volcaniclastic deposits were therefore substracted from the composite record. Another unit was assigned to this modified record: mcblf-nE (nE abbreviates no event). The event-free proxy records were then visually tuned in order to mimic common Quaternary isotope stratotypes (Fig. 2.12). These are the records from the North Greenland Ice Core Project (NGRIP) and the synthetic record of Greenland Temperature variability (GLT). Stockhecke et al. (2016) furthermore aligned a small interval of proxy records to the Antartic Ice Core Chronology (AICC). The alignment of the AR strata to the isotope stratotypes resulted in defining age control points that anchor temporal signals from the established Quaternary timescales. The reference timescales used were GICC05 (Svensson et al., 2008; Blockley et al., 2012), GICC05_modeltext (Wolff et al., 2010), AICC2012 (Veres et al., 2013), GLT-syn SpeleoAge, and GLT-syn GDC3Age (Barker et al., 2011). Integrating these different reference timescales (instead of one continuous timescale) had the goal to mimic the Lake Van proxy record with timescales of similar resolutions. A record of sediment colour served as an additional proxy to the illustrated proxies in Fig. 2.12 (Stockhecke et al., 2014a; Stockhecke et al., 2016). The climate sensitivity in the AR proxy record is likely replicating the Greenland isotope stratotypes. One linkage between the records is the meteoric water budget in the Lake Van area. Greenland temperature variations are transmitted to precipitation in Eastern Anatolia due to atmospheric circulation changes (Stockhecke et al., 2014a). High lake level stands of Lake Van are representing warm interstadial/interglacial stages and low lake level stands represent cold stadial/interstadial stages. Precipitation and lake-level stands are reflected in the TOC record (Stockhecke et al., 2014b) and in the Ca/K record (Çağatay et al., 2014; Kwiecien et al., 2014; Stockhecke et al., 2014b). The interstadial onsets are reported to be very consistent patterns in climate records from globally diverse locations (Wang et al., 2001; Cheng et al., 2009; Deplazes et al., 2013). These onsets are also identified in the ratio of TOC to sediment colour reflectance (which is labeled with b^*) and in the Ca/K ratio (Stockhecke et al., 2014a).

Interstadial onsets hence align the Lake Van proxy record. These alignments worked as anchors on a chronology that 'squeezed and stretched' the event-corrected strata among the anchors. The abundance of arboreal pollen (AP) similarly identifies climatic events as the Ca/K and TOC/b^* proxies. A slight lag of the AP record to the other proxies is reported but difficult to assess due to different resolutions in sampling strategy (Stockhecke et al., 2014a). The AR

proxy records have been sufficiently tuned by aligning the interstadial onsets, which implies that a very consistent sedimentation rate existed between the control points (Stockhecke et al., 2014a). Control points are derived by tuning either the TOC, the Ca/K or the AP records to the reference ^{18}O records. Onsets of Greenland Interstadial phases and peaks of Marine Isotope Stages (MIS) (e.g. Capron et al., 2010) allocate ages to the control points and therefore define 'age control points'.

The proxy records are significantly interrupted in two stratigraphic positions: by the DU and by the ca. 10-m-thick volcaniclastic layer V-206. Other volcaniclastic layers than V-206 represent a sudden event type (air falls and flow currents) and do not cover significant time spans by hampering background deposition. The age model by Stockhecke et al. (2014a) suggests a temporal gap for the stratigraphic extent of V-206 that lasts 17 ka. Stockhecke et al. (2014b) speculated that deposition of V-206 eroded material from background sedimentation. The DU offers background sedimentation providing proxy data (Fig.2.12). Lacustrine lithologies underneath a turbidite that caps the DU show micro-deformations that are connected to the early marine isotope stage (MIS) 11. Accordingly, deformation and deposition must have occurred at that time. Varved sediments are intercalated with event deposits in the upper DU and indicate a warm/wet climate similar to present day conditions. Additionally, the DU shows stratigraphically downwards cold/dry climate lithologies and less event deposits. Thus, the transition from MIS 11 to MIS 12 and the glaciation termination V (labelled as TV in Fig. 2.12) is recorded. Nevertheless, no climatostratigraphic age control points can be anchored in this position as the continuous sediment record cannot be reconstructed. The DU covers a temporal gap in the AR record of ca. 67 ka. Excluding these two major temporal gaps, the tuned and event-corrected AR record provides a continuous sedimentation for a timespan that covers 517 ka in total. Oldest sediments reveal lithologies that deposited during the MIS 15 and are thus as old as 600 ka (Stockhecke et al., 2014a; Stockhecke et al., 2014b). The latest update of the AR proxy record alignment from Stockhecke et al. (2016) provides a total of 78 paleoclimatic (tuning-based) age control points. Another four temporal 'tie points' limit the two major gaps in the proxy records (V-206 and the DU) by extrapolating an assumed linear sedimentation rate (Fig. 2.13).

Additional chronometers

Besides the age control points from tuning the event-corrected AR strata, temporal tie points and dates were derived from other chronometers that refined the lacustrine age model. A total of four markers were assigned with ages from varve chronology in the uppermost meters of the AR and NB records. The varve ages were taken from Landmann et al. (1996), Lemcke (1996), and Lemcke and Sturm (1997).

The volcaniclastic layers V-18, V-51 and V-60 served for a tephrostratigraphic correlation to three units that have been described by Sumita and Schmincke (2013b). These are the Nemrut Formation (NF), the Halepkalesi Pumice-10 (HP-10), and the İncekaya-Dibekli tephra. Sumita and Schmincke (2013c) reported three weighted mean $^{40}Ar/^{39}Ar$ ages from anorthoclase phenocrysts of the NF that are 29 ± 3 ka, 30 ± 4, and 34 ± 11 ka (1σ uncertainties to all ages from this study). The latter age (34 ± 11 ka) is derived from sampling an ignimbrite that represents the Middle NF. The former two ages (29 ka, and 30 ka) represent an underlying plinian fallout sheet of the Lower NF. As all ages agree within uncertainties the median of the three results is

expected to represent the age of V-18. Sumita and Schmincke (2013c) dated also the HP-10 via $^{40}Ar/^{39}Ar$ to be 75 ± 5 ka ka in age. In contrast to this age, Sumita and Schmincke (2013c) refer to an unpublished dating approach of HP-10 samples from NB and AR cores that is 62 ± 3 ka in age. Although, no discussion is presented that faces this discrepancy, the latter age has been accepted in designing the chronostratigraphy of the AR record (Stockhecke et al., 2014a; Stockhecke et al., 2014b). The İncekaya-Dibekli tephra consists dominantly of hyaloclastite and fallout scoria (Sumita and Schmincke, 2013c). Whereas the hyaloclastite is sourced in the İncekaya cone, the tachyliltic scoria is sourced in the Dibekli scoria cone. Notsu et al. (1995) dated basalt ground-masses from the latter cone by the K-Ar method and reported an age of 80 ± 20 ka.

Stockhecke et al. (2014b) presented six preliminary $^{40}Ar/^{39}Ar$ ages of volcaniclastics layers V-114, V-137, V-144, V-184, V-210, and V-279. $^{40}Ar/^{39}Ar$ ages from this study remained uncommented upon methodology, analysed phases, and statistics. Uncertainties were also not presented. Thus, it remains impossible discussing their potential agreement with results from the other chronometers. The study presented here reassesses two of these volcaniclastic samples (Chapter 4).

Acceleration mass spectrometry radiocarbon ages were established for terrestrial remains in six turbidite deposits from the NB record (Çağatay et al., 2014). Three of them could be correlated to the AR record (Stockhecke et al., 2014a). They date materials in stratigraphic positions of 0.36 mcblf, 2.29 mcblf, and 8.9 mcblf to be 0.61 ± 0.05 ka, 4.33 ± 0.08 ka, and 18.59 ± 0.07 ka in age, respectively (1σ uncertainty).

The paleomagnetic record of the relative paleointensity (RPI) variations provides furthermore temporal tie-points to the AR strata (Vigliotti et al., 2014). RPI are considered to be a globally occurring phenomena and to be devoid of any local environmental influences (Singer, 2014a). The methodology is briefly outlined by describing the detection of the RPI minimum that is associated with the Laschamp geomagnetic excursion (Guillou et al., 2004; Cassata et al., 2008; Singer, 2014a). Natural remanent magnetisations with negative inclinations represent the directional expression of the excursion and were detected in the AR record. The Laschamp excursion is well dated by agreeing ages from several locations and studies via astrochronology and $^{40}Ar/^{39}Ar$ dating (summary given in Singer, 2014a). Normalised natural remanent magnetizations (NRM) records exist for the uppermost 110 mcblf of the AR record. The normalisation employed 20 mT and 30 mT anhysteric remanence and likely approximates the RPI of the Earth's magnetic field (Vigliotti et al., 2014). Temporal tie points represent the extent on a temporal reference template that is the PISO-1500 stack (Channell et al., 2009). This template is anchored by a wealth of $^{40}Ar/^{39}Ar$ ages that are summarized in Singer (2014a). Other directional excursions than that of the Lashamp could not have been identified in the AR record. Nevertheless, six more RPI minima correspond to global geomagnetic minima of the virtual axial dipole momentum (VADM). They provide temporal tie points that match constraints from climatostratigraphic tuning (Fig. 2.13). Table 2.2 offers an overview of the stratigraphic positions and associated ages for the seven RPI minima that are detected in the AR record. The table also compares expected ages from the age model of Stockhecke et al. (2014a) with ages associated with RPI minima.

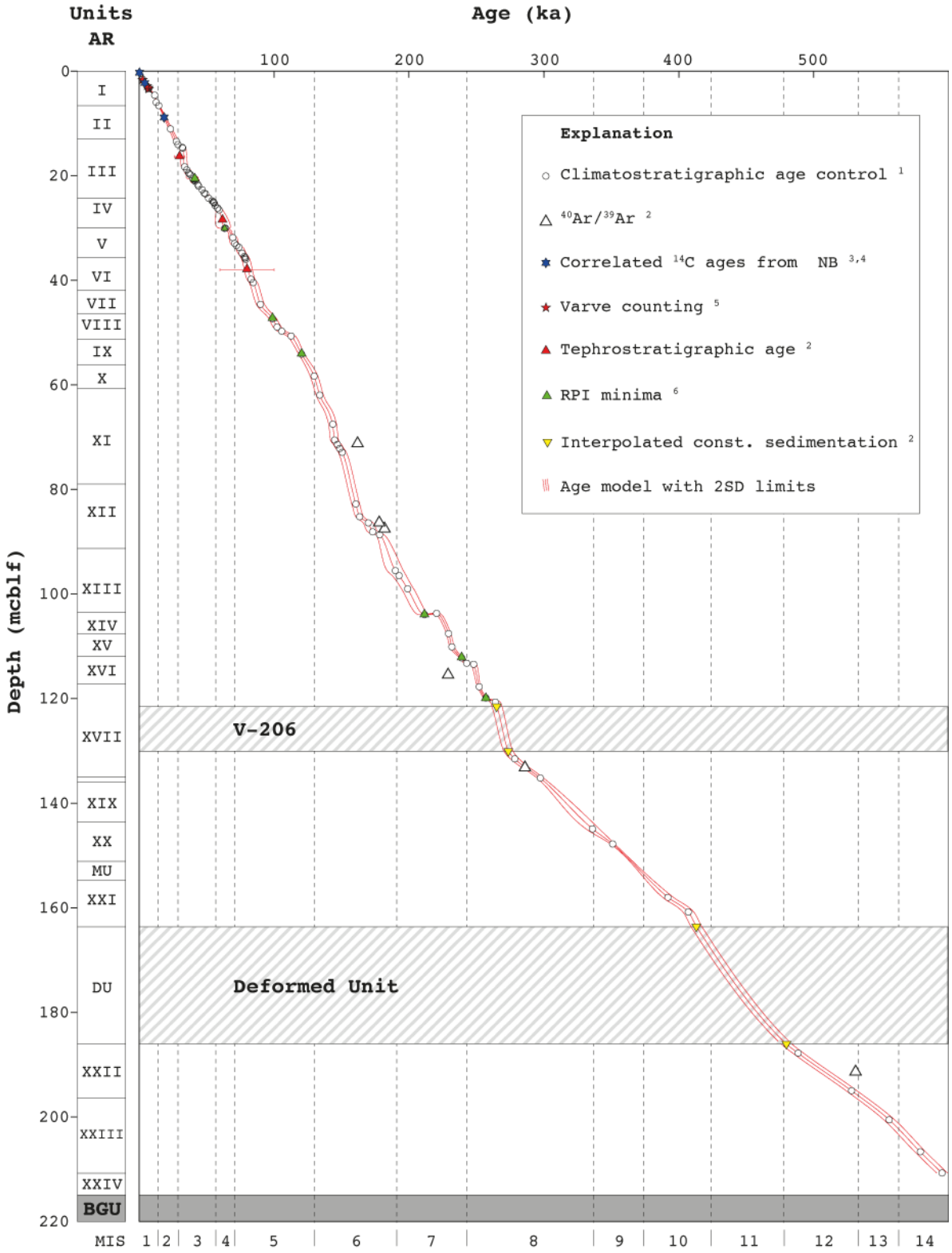

Figure 2.13: Age model for the AR composite core strata. Age control points from climatostratigraphic tuning are summarized in Stockhecke et al. (2016)[1]. Preliminary $^{40}Ar/^{39}Ar$ dates, tephrostratigraphic ages, and control points from interpolating an assumed constant sedimentation are published in Stockhecke et al. (2014b)[2]. Ages from correlating lacustrine sediments to ^{14}C ages in the NB record are from Stockhecke et al. (2014a)[3] and Çağatay et al. (2014)[4]. Age control points from varve counting were taken from Landmann et al. (1996)[5]. Relative paleointensity (RPI) minima of the earth magnetic field were presented in Vigliotti et al. (2014)[6]. The model was calculated using all age control points, except the preliminary $^{40}Ar/^{39}Ar$ dates and applied a piecewise cubic hermite interpolating polynomial (pchip) (Fritsch and Carlson, 1980; Kahaner et al., 1989). This type of interpolation is a matter of a more detailed discussion in Chapter 6. Error bars represent one standard deviation and are visible if uncertainties are provided by the quoted source and if the uncertainty exceeds the relative marker size.

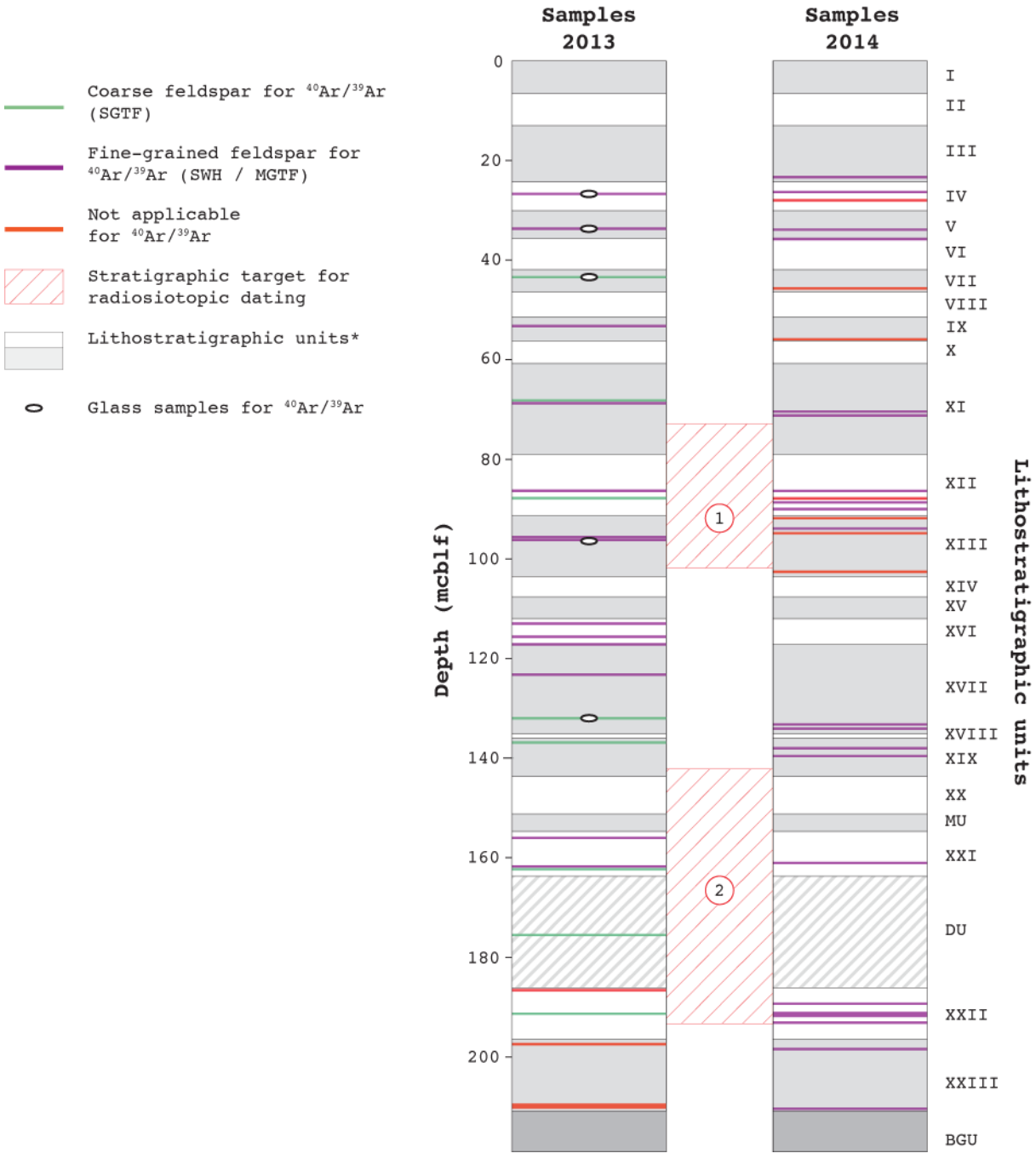

Figure 2.14: Lithostratigraphy of the AR record after Stockhecke et al. (2014b) and stratigraphic positions of volcaniclastic samples taken in the present study. The alternating grey and white units outline the lithostratigraphic units. Coloured lines represent the positions of samples and indicate the potential to date either anorthoclase or sanidine via single grain total fusion (SGTF) or multi grain methods such as total fusion (MGTF) and stepwise heating (SWH) methods. Thicknesses of the samples are not proportional to the thickness of the volcaniclastics. Sample positions that appear thick indicate several samples in similar stratigraphic positions. Extend of stratigraphic targets are highlighted with dashed red boxes and discussed in the text.

Table 2.2: Stratigraphic positions and ages of seven RPI minima identified by Vigliotti et al. (2014). Expected ages from the climatostratigraphic age model of Stockhecke et al. (2014a) are compared to the ages published elsewhere (pub. ages). Channell et al. (2009) presents the PISO-1500 reference.

Depth(mcblf)		Age (ka)		Pub. Age (ka)		Reference
Top	Base	From	To	From	To	
20.09	20.16	38.8	39.0	38.4	42.4	(Guillou et al., 2004)
29.94	30.19	64	65	63	64	(Channell et al., 2009)
46.41	48.21	97	103	97	101	(Channell et al., 2009)
51.89	55.36	115	123	119	122	(Channell et al., 2009)
103.46	104.45	214	217	210	213	(Channell et al., 2009)
111.81	112.58	237	240	238	240	(Channell et al., 2009)
119.51	120.33	257	259	256	258	(Channell et al., 2009)

2.2.2 Sampling targets

Sampling targets for $^{40}Ar/^{39}Ar$ geochronology followed two main strategies. (i) The selected samples should cover an even distribution over the entire AR record. (ii) Samples should be in stratigraphic positions of poorly constructed chronostratigraphy and potentially reassess samples that had been dated from Stockhecke et al. (2014b). In August 2013 twenty-five well-distributed samples were obtained from AR cores. Main criteria to gain a sample from a chosen ash layer were: (1) the visible abundance of transparent feldspars and/or hardly altered glass shards, (2) stratigraphic features indicating a volcaniclastic origin, minimizing the potential risk of a detrital contamination. The samples were divided into four aliquots and subsequently prepared for sanidine and/or glass separation, for whole-lapilli XRF analyses and for grain mounts that are cut and polished to thin-sections. One aliquot is kept for potential additional instrumental approaches, such as Raman Spectroscopy or LA-ICP-MS studies. In June 2014 a second set of samples was collected, that was based on the previous sampling and first analyses using scanning electron microscopy (SEM) and energy dispersive X-ray spectroscopy (EDX). Volcaniclastic layers were chosen by considering the stratigraphic positions of promising samples for $^{40}Ar/^{39}Ar$ dating from the first set of samples. Fig. 2.14 provides an overview of the stratigraphic positions of the samples taken in 2013 and 2014. Two stratigraphic positions were of particular interest for $^{40}Ar/^{39}Ar$ dating: (i) the stratigraphic range from unit XI to unit XIII and (ii) upper and lower limits of the deformed unit (Fig. 2.14). The first target was chosen in order to strengthen the transition from MIS 6 to MIS 7, which relied by the time of the commencing project on one age-control point only (Fig. 2.12). Additionally, this stratigraphic range showed deviations of the preliminary $^{40}Ar/^{39}Ar$ data to the obtained climatostratigraphic temporal marker from Stockhecke et al. (2014b) (Fig. 2.13). The stratigraphically lower target had the main goal to add ages to the units XX to XXII. The section lacked age control points for the MIS 9, MIS 10 and the transition from MIS 11 to MIS 12, which is hampered by the presence of the DU.

2.2.3 Tasks and potentials

This section briefly describes the tasks that are associated with the application of $^{40}Ar/^{39}Ar$ dating of volcaniclastics from the AR record and outlines their potentials. Main tasks which this study has to accomplish are:

- to select volcaniclastic samples that are suitable for $^{40}Ar/^{39}Ar$ studies and located in the stratigraphic positions of interest.
- to search for potential discrepancies between results from $^{40}Ar/^{39}Ar$ dating and various

other chronometers.

- to analyse various grain size fractions of feldspar and discuss tendencies in resulting $^{40}Ar/^{39}Ar$ ages with respect to mineral texture, morphology and composition.

- to apply $^{40}Ar/^{39}Ar$ on volcanic glass that is visibly free of vesicles and was sampled from stratigraphic positions of different pore water conditions.

Stratigraphic divisions that contain sparse age control points from climate tuning or other chronometers have been identified above in Fig. 2.14 and represent the major task in this thesis. However, an even distribution of samples over the full length of the AR record is also required. In order to find suitable but well distributed samples, the description of cm-scale stratigraphic features depicted another task. Additionally, XRF analyses from aliquots were needed to provide geochemical data that help characterising and provenancing samples. Providing the according data and offer interpretations rise a potential for further studies on the volcaniclastics in the Lake Van area.

Designing the $^{40}Ar/^{39}Ar$ experiments made clear that multi grain total fusion (MGTF) analysis are inevitable as available feldspar phenocrysts are not big and/or K-rich enough for single grain total fusion. The comparison of SGTF and MGTF approaches provided a promising approach for some samples. MGTF approaches are rare as this method may involve contamination of older material without being resolvable in isochron diagrams (e.g. Morgan et al., 2012). SWH is rather preferred for multi-grain approaches as contaminations are expected to be more visible in plateau age calculations and according isochrons. Calculations of minimum amounts suggest 20 mg of inclusion-free feldspar for stepwise heating (SWH) analyses. It remained difficult to gather this minimum amount of feldspar from aliquots that represented one fourth of 15 to 5 cm^3 sample material. In order to carefully analyse most promising crystal fractions, combined SGTF and MGTF studies represented the dominant type of $^{40}Ar/^{39}Ar$ analyses. The chance to compare both approaches has the potential to monitor the influence of inherited and excess ^{40}Ar to MGTF methods. The combined SGTF and MGTF analyses have the potential to be tested as a tool for analysing young and K-poor feldspars from small sample volumes.

Exact and appropriate error discussions and statistics are used to compare results from $^{40}Ar/^{39}Ar$ dating presented in this thesis with temporal constraints from other chronometer. This comparison has the potential to improve and strengthen the age model for the AR record and vice versa. In combination with the combined MGTF and SGTF approach the age model for the AR record has the potential to reveal small age deviations and the according Ar systematics.

Several samples provided feldspars of different grain size fractions that also revealed differences in chemical and textural characteristics. The comparison of $^{40}Ar/^{39}Ar$ data from differently textured feldspar fractions potentially provides information about the radiogenic ^{40}Ar budget of young and K-poor feldspar that experienced different magmatic and eruptive processes.

The AR age model allows recalculating the age of the used $^{40}Ar/^{39}Ar$ mineral standard with using ages from the climatostratigraphic age model as an input parameter. This approach has the potential to test the synchronicity of radioisotopic and climate forcing chronometers.

The AR record further revealed a stratified pore water chemistry of low-mobility (Litt et al., 2012; Tomonaga et al., 2014). The pore water chemistry of the AR record develops from fresh

water of a neutral pH at the base to basic (pH of ca. 9.5) and saline water in the uppermost units. Low pore water mobility likely conserves the composition of co-deposited lake water (Litt et al., 2012). Volcanic glass has the disadvantage to be challenged with the loss of radiogenic ^{40}Ar due to fast hydration, and devitrification. Furthermore, excess ^{40}Ar is also frequently observed and related to fast quenching (Noble and Naughton, 1968; Dalrymple and Lanphere, 1969; Kaneoka, 1972; Walker and Mcdougall, 1982; Foland et al., 1993; Morgan et al., 2009). Dating volcanic glass from the AR record provides a potential to compare radiometric ages from glass samples that had been exposed to highly saline pore water compositions with data from samples that had been exposed to less saline pore water. Glass samples from different stratigraphic positions may furthermore show an influence from contrasting pore water compositions on the Ar isotope budget. Samples that are suitable for feldspar ^{40}Ar/^{39}Ar analyses and volcanic glass ^{40}Ar/^{39}Ar analyses offer a comparison of the Ar-isotope results from the glass phase with the data from the co-genetic feldspar phase. Ar-isotope data from both phases have the potential to investigate the effect of excess ^{40}Ar from melt-inclusions in feldspars.

3 Instrumental Methods

3.1 $^{40}Ar/^{39}Ar$ Geochronology

The $^{40}Ar/^{39}Ar$ method potentially represents the most versatile radiometric chronometer that is available for dating rocks. As a variant of the K-Ar method it is applicable to K-bearing minerals, bulk rocks and glasses, which are fairly common in nature. K is the 8^{th} most abundant element in the earth's crust (Taylor and MacLennan, 1985) and is present in a diversified range of minerals as major and minor element. The radioactive (mother-) nuclide ^{40}K has a half-life of ca. 1.25 Ga (Burch, 1953; Beckinsale and Gale, 1969), which is about a fourth of the age of the earth and thus an ideal clock generator in rocks and minerals of any conceivable age. Given adequate phases, the $^{40}Ar/^{39}Ar$ technique allows dating of Archean samples (Wijbrans and Mcdougall, 1987) just like samples of historic age (Renne et al., 1997).

The methodology is fivefold and contains: (i) a simplified theoretical background, (ii) the role of the mineral standard and decays constants in this study, (iii) the instrumental set up at the University of Potsdam, (iv) sample preparation, and (v) the methodology in data presentation and age calculation.

3.1.1 $^{40}Ar/^{39}Ar$ Geochronology in theory

The $^{40}Ar/^{39}Ar$ method is an extension of the K-Ar method (Merrihue and Turner, 1966). Before entering the theory about the $^{40}Ar/^{39}Ar$ method, a brief introduction to the K-Ar method is described here. Potassium has three natural isotopes: ^{39}K (93.2581 $\pm$ 0.0029 %), ^{40}K (0.01167 $\pm$ 0.00004 %), and ^{41}K (6.7302 $\pm$ 0.0029 %) (Garner et al., 1975). The radioactive ^{40}K decays by positron decay (decay constant described with $\lambda_{\beta+}$) and two different kinds of electron capture modes (λ_e and λ_e') to the stable ^{40}Ar and by electron emission ($\lambda_{\beta-}$) to the stable ^{40}Ca (Beckinsale and Gale, 1969). As $\lambda_{\beta+}$ represents a minor proportion of the total ^{40}K decay (λ) of ca. 0.001%, it is commonly neglected and considered in the uncertainty of the other decay constants (Beckinsale and Gale, 1969). If the quantities of the parent and the daughter nuclides at present time are given and if the decay constants are known, the calculation of the age of a geologic sample since the diffusive closure (temperature dependent) of the relevant isotopes is practicable. As potassium is a solid and Ar a noble gas at room temperature, the K-Ar method requires different instrumental analyses of K and Ar (commonly flame photometry for K and gas mass spectrometry for Ar) from sample splits (Dalrymple and Lanphere, 1969). Instead, the $^{40}Ar/^{39}Ar$ method relies on gas mass spectrometry only and, thus, only one sample fraction is required. Consequently $^{40}Ar/^{39}Ar$ works for smaller sample sizes and avoids the systematic error that is derived from the different types of analyses in the K-Ar method. The determination of Ar isotope ratios suffice to conduct the $^{40}Ar/^{39}Ar$ method. Therefore, an analytical improvement is the absence of problems that derive from sample heterogeneity and sample splitting. Following the advent of the $^{40}Ar/^{39}Ar$ method (Merrihue and Turner, 1966), techniques like the stepwise heating (SWH) and laser heating initiated at a later date. The latter methodological achievement provided insights about the distribution of radiogenic ^{40}Ar

and of inferred ^{39}K within coarse single crystals (e.g. Wartho et al., 1999; Flude et al., 2014). The disadvantages of the ^{40}Ar/^{39}Ar method are connected to the need for an activation of the sample with fast neutrons in a nuclear reactor (Merrihue and Turner, 1966). Subsequently, laboratory facilities have to deal with radioactive materials and furthermore need to determine an extra set of isotopic measurements in order to quantify the effectiveness of the activation during neutron irradiation. Neutron irradiation causes a transformation of ^{39}K to ^{39}Ar by neutron capture. Assuming that ^{40}K/^{39}K is constant in terrestrial samples (Crasty and Mitchell, 1966), the production of ^{39}Ar is in direct dependence of the ^{40}K content, the decay constant, and the elapsed time since closure of the system. Due to slight local variations in the neutron flux within a reactor, monitoring of the neutron flux is required. With respect to the target nuclide ^{39}K, the number of $^{39}Ar_K$ nuclides that were produced by the nuclear reaction ^{39}K(n,p)^{39}Ar, is described with the following equation.

$$^{39}Ar_K = ^{39}K \times \Delta t \times \int_{E=E_T}^{\infty} \phi(E) \times \varphi(E) \times dE \tag{3.1}$$

The duration of the irradiation is expressed in Δt, the neutron flux during irradiation (at energy E) in $\phi(E)$, and the neutron capture cross section against the energy flux (at energy E) with $\varphi(E)$. The integral is over the interval of $[E_T, \infty]$, where E_T represents the threshold energy to start the neutron capture. The natural decay of ^{40}K that produced radiogenic ^{40}Ar* since the diffusive closure of the isotopic mobility is given by

$$^{40}Ar^* = \frac{\lambda_e + \lambda'_e}{\lambda} \times ^{40}K \times \left(e^{\lambda t} - 1\right) \tag{3.2}$$

where ^{40}Ar that has been produced in situ from K decay ($^{40}Ar^*$) distinguishes from ^{40}Ar that is derived from equilibration with the atmosphere ($^{40}Ar_{atm}$) or other sources (e.g. inherited ^{40}Ar or excess ^{40}Ar) with an asterisk (McDougall and Harrison, 1999). These identifiers will be applied throughout this thesis. However, combining Eq. 3.1 and Eq. 3.2 it follows that for an irradiated sample the following equation establishes.

$$\frac{^{40}Ar^*}{^{39}Ar_K} = \frac{^{40}K}{^{39}K} \times \frac{\lambda_e + \lambda'_e}{\lambda} \times \frac{1}{\Delta t} \times \frac{\left(e^{\lambda t} - 1\right)}{\int_{E=E_T}^{\infty} \phi(E) \times \varphi(E) \times dE} \tag{3.3}$$

Following Crasty and Mitchell (1966) data treatment is most convenient by applying the dimensionless J-value, which is represented as follows.

$$J = \frac{^{39}K}{^{40}K} \times \frac{\lambda_e + \lambda'_e}{\lambda} \times \Delta t \times \int_{E=E_T}^{\infty} \phi(E) \times \varphi(E) \times dE \tag{3.4}$$

The substitution of Eq. 3.7 into Eq. 3.3 results in

$$\frac{^{40}Ar^*}{^{39}Ar_K} = \frac{\left(e^{\lambda t} - 1\right)}{J} \tag{3.5}$$

and the rearrangement of Eq. 3.5 allows the calculation of the age of a sample.

$$t = \frac{1}{\lambda} \times \ln\left(1 + J \times \frac{^{40}Ar^*}{^{39}Ar_K}\right) \tag{3.6}$$

Hence, once the irradiation parameter J is known, the measurement of radiogenic $^{40}Ar^*$ in relation to potassium derived $^{39}Ar_K$ suffices to calculate the age of the (cooling) event of a geological sample. In order to monitor the irradiation dose, unknown samples are irradiated together with minerals with precisely known K-Ar ages (Merrihue and Turner, 1966). A simple rearrangement of Eq. 3.5 yields a convenient determination of the J-Value.

$$J = \frac{\left(e^{\lambda t} - 1\right)}{^{40}Ar^*/^{39}Ar_K} \tag{3.7}$$

In theory, geochronologists work with these relationships. It needs to be stressed that some assumptions must be satisfied for the K-Ar and $^{40}Ar/^{39}Ar$ techniques in order to yield geologically meaningful ages. These assumptions are summarised in McDougall and Harrison (1999) and in McDougall (2014). The assumptions are listed in the following.

- The analysed phase (e.g. minerals, glass, groundmass, whole rock) was completely degassed for any pre-existing $^{40}Ar^*$ at the time of the radiometric resetting. In other words, no $^{40}Ar^*$ was trapped in the analysed phase at the time of crystallisation or solidification.
- $^{40}Ar^*$ that accumulated since crystallisation or solidification of the analysed phase has been fully retained (e.g. > 99 % of $^{40}Ar^*$ since t). This assumption is particularly not met in slowly cooled igneous and in metamorphic rocks. Such samples require careful assessment of the meaning of the age in a geologic and petrologic context.
- Subsequent to crystallisation or solidification no change in K concentration has occurred (apart of the minute but negligible change that is caused by the ^{40}K decay).
- Due to the involvement of the K-Ar method as the primary radiometric system, the $^{40}K/K$ ratio is assumed to be constant in terrestrial materials at any given time.
- The atmospheric $^{40}Ar/^{36}Ar$ composition and the decay constants involved in the ^{40}K decay are known accurately and with appropriate precision.

The above given theory represents only a basis for discussions presented in this thesis. A more detailed background about the $^{40}Ar/^{39}Ar$ method is provided in McDougall and Harrison (1999) and in Dickin (2008).

3.1.2 Mineral standard, decay constant, atmospheric air

The potential absolute error in an age derived by the $^{40}Ar/^{39}Ar$ method consists of uncertainties and assumptions in the decay constants, the uncertainty of the irradiation parameter J and the $^{40}Ar^*/^{39}Ar$ ratio gained from the unknown sample. Most approaches to improve the accuracy of the $^{40}Ar/^{39}Ar$ method have concentrated on dating standard minerals (e.g. Renne et al., 1998; Lanphere and Baadsgaard, 2001) or determining decay constants (e.g. Min et al., 2000; Dazé et al., 2003; Spell and McDougall, 2003; Renne et al., 2010).

Standard minerals for flux monitoring

The J-value is originally attributed with the uncertainty of the absolute age (from K-Ar dating) of the mineral standard. Sine the 1990ies $^{40}Ar/^{39}Ar$ dating of mineral standards has become more established (e.g. Renne et al., 1998; Nomade et al., 2005; Jourdan and Renne, 2007). These 'secondary' standard ages are intercalibrated to mineral standards that are dated by the K-Ar method and offer higher precision due to the analytical advantages of the $^{40}Ar/^{39}Ar$ method and due to a high number of analytical measurements that have excellent reproduction in calculated ages (e.g. Renne et al., 1998; Nomade et al., 2005; Jourdan and Renne, 2007).

Before explaining the concept of secondary mineral standards, a simple and helpful form of the $^{40}Ar^*/^{39}Ar$ ratio from unknown samples or secondary mineral standards needs to be stated. This identifier is the widely used F.

$$F = \frac{^{40}Ar^*}{^{39}Ar} \tag{3.8}$$

The essential parameter for the intercalibration of mineral standards was the advent of the R-value (Karner and Renne, 1998; Renne et al., 1998). R is defined as the ratio of two F values obtained from two different standards.

$$R_0^1 \equiv \frac{F_1}{F_0} \equiv \frac{\left(\frac{^{40}Ar^*}{^{39}Ar_K}\right)_{secondary}}{\left(\frac{^{40}Ar^*}{^{39}Ar_K}\right)_{primary}} = \frac{\left(e^{\lambda t_{sec}} - 1\right)}{\left(e^{\lambda t_{prim}} - 1\right)} \tag{3.9}$$

The R-value enables an endless combination of secondary standard ages to be calibrated relative to a primary standard age by applying the following relationships (Karner and Renne, 1998).

$$t_{unknown} = \frac{1}{\lambda} \ln \left[\left(\frac{\lambda}{\lambda_e + \lambda'_e} \right) K \prod_{i=1}^{n} R_{i-1}^i + 1 \right] \tag{3.10}$$

The variable K in Eq. 3.10 represents the K-Ar age that is assigned to a primary standard which is addressed in the standard intercalibration.

$$K \equiv \left(\frac{^{40}Ar^*}{^{40}K} \right)_{primary} \tag{3.11}$$

The comprehensive listings of intra-laboratory R-values (Renne et al., 1998; Spell and McDougall, 2003; Jourdan and Renne, 2007) hence allow fast recalculation of ages obtained by secondary mineral standards to a primary K-Ar standard. A detailed error propagation for the intercalibration process was provided by Renne et al. (1998). Their study is recommended for more details about the methodology in standard intercalibration. Although intra-laboratory intercalibration is capable of resulting in excellent reproducibility of <0.2% (Renne et al., 1998; Jourdan and Renne, 2007), R-values from inter-laboratory intercalibrations may vary more than 1% (Spell and McDougall, 2003).

The Fish Canyon sanidine mineral standard (FCs) represents the most commonly used neutron flux monitor in $^{40}Ar/^{39}Ar$ geochronology and has a central role in several intercalibration approaches of the past (Renne et al., 1998; Spell and McDougall, 2003; Jourdan and Renne, 2007). The age of the sanidine crystals from the Fish Canyon tuff (FCT) in the San Juan

Mountains, Colorado, caused a decade-lasting and still vibrant discussion about standard improvement in $^{40}Ar/^{39}Ar$ geochronology. Following a compilation given in McDougall (2014) the age of the FCs has ranged from ca. 27.8 Ma (Steven, 1969), to 27.99 ± 0.27 Ma (Hurford and Hammerschmidt, 1985), to 27.5–27.7 Ma (Lanphere and Baadsgaard, 2001), to 28.02 ± 0.16 Ma (Renne et al., 1998), to 28.03 ± 0.08 Ma (Jourdan and Renne, 2007), and to 28.10 ± 0.04 Ma (Spell and McDougall, 2003). These ages were either determined by direct K-Ar dating or by intercalibration of secondary and primary dating approaches. Renne et al. (2010) and Renne et al. (2011) optimized various parameters in the ^{40}K decay scheme by intercalibration to ages obtained from zircon U-Pb geochronology and arrived finally at a new value for FCs of 28.294 ± 0.036 Ma (details provided later in this chapter).

Another approach which has been conducted to date and calibrate mineral standards bases on the orbital parameters of the Earth. Some cyclostratigraphic signals in various sedimentary sequences can be connected to the Earth's precession. Highly resolved timescales (potentially of millennial resolution), which describe the variation in solar radiation due to the Earth's orbital precession (e.g. Laskar et al., 2004; Laskar et al., 2011) have the potential to link sedimentary proxies to geologic timescales. Renne et al. (1994) compared and connected astronomical and radioisotopic chronometers for the first time in order to improve the FCs age. These authors compared seven formerly published $^{40}Ar/^{39}Ar$ ages with predicted ages from an astronomically calibrated geomagnetic polarity timescale (Shackleton et al., 1990; Hilgen, 1991a; Hilgen, 1991b). As the age determinations were most consistent, Renne et al. (1994) recalculated the age of the monitor mineral by changing the role of the standard minerals with the role of the unknown materials. The formerly unknown samples were assigned in Renne et al. (1994) with ages from the astronomically calibrated timescale and a new age of 27.95 ± 0.18 Ma was recommended for the FCs. Renne et al. (1994) furthermore showed that astronomical calibration of mineral standards improve the comparison of results from $^{40}Ar/^{39}Ar$ dating with results from U-Pb dating.

The cyclostratigraphic interpretations of dark-coloured sapropels in light-coloured marine carbonates have resulted in precise astronomic chronologies of Tertiary records in sequences that are exposed in the Mediterranean (Hilgen, 1991a; Lourens et al., 1996). Tephras that are interlayered in some of the sequences became of particular interest for $^{40}Ar/^{39}Ar$ geochronologists in order to compare their astronomical and radiometric eruption ages (Hilgen et al., 1997). Kuiper et al. (2008) adopted the methodology from Renne et al. (1994) and provided an astronomical age for the FCs of 28.201 ± 0.023 Ma. This age also represents an inter-laboratory calibration of $^{40}Ar^*/^{39}Ar_K$ measurements (involving laboratories from the Berkley Geochronology Center and the Vrije Universiteit Amsterdam) from sanidine crystals that were embedded in tephras of the astronomically tuned Messâdit sequence in Morocco. Rivera et al. (2011) revisited this methodology by $^{40}Ar^*/^{39}Ar_K$ measurements on sanidine of the A1 tephra at the base of an astronomically tuned sapropel layer of the Faneromeni sequence on the island Crete, Greece. The resulting age of 28.172 ± 0.009 Ma is indistinguishable from the age obtained by Kuiper et al. (2008). The two astronomically calibrated results are widely accepted in the community of $^{40}Ar/^{39}Ar$ geochronologists and have led to a frequent use of the age recommended by Kuiper et al. (2008) when irradiating samples with FCs as flux monitors. Furthermore, the two studies have outlined problems with the currently used ^{40}K decay constants, which are expected to con-

tribute to differing FCs ages from K-Ar and $^{40}Ar/^{39}Ar$ methods (McDougall, 2014). However, the debate about the age of the FCs has not yet finished and reached to questioning of the suitability of FCs as a mineral standard in $^{40}Ar/^{39}Ar$ geochronology (Phillips and Matchan, 2013; Jicha et al., 2016). It remains the geochronologist's decision whether $^{40}Ar/^{39}Ar$ dating should be applied relative to a standard age that is intercalibrated with ages from U-Pb geochronology, from primary K-Ar geochronology, or from an astronomical timescale (McDougall, 2014).

The cored lacustrine sediments from ICDP PALEOVAN were assigned with a chronostratigraphic age model that is tuned to astronomic forcing of climate variations. Therefore, the thesis given here dates volcaniclastics from the astronomically tuned record with a mineral standard that is tied to astronomical ages. The given study monitored irradiations with the widely used Alder Creek sanidine (ACs-2) mineral standard. ACs-2 minerals are separated from the transitionally magnetized Alder Creek rhyolite (Turrin et al., 1994; Nomade et al., 2005; Singer, 2014a). The age of the ACs-2 is therefore tied to the temporal extent of the paleomagnetic Cobb Mountain Subchron (CMS). The CMS and ACs-2 are Pleistocene in age and thus comparably close to the age of the unknown samples from the Lake Van sediments. $^{40}Ar/^{39}Ar$ ages are basically functions of the R-value (Eq. 3.10), which is the ratio of F from the unknown to F from the standard. If a standard and an unknown differ significantly in age, the accuracy and the precision of the measured F values might be limited by Ar isotope abundance sensitivity and detector linearity. The dynamic range of F is minimized using ACs-2 rather than FCs or even older standards for $^{40}Ar/^{39}Ar$ dating of unknown samples that are expected to be Quaternary in age (Nomade et al., 2005).

The disadvantage of using the ACs-2 is a controversy about the temporal extend of the CMS. This controversy concerned two studies of different marine sediment records that reveal the CMS in signals of remanent magnetisation. Both studies established astronomical age models from $\delta^{18}O$ signals. Whereas Channell et al. (2002) bracketed the CMS from 1215 ka to 1190 ka, Horng et al. (2002) dated the extent of the CMS from 1185 to 1173 ka. Recently, Channell (2017) presented a new astronomical age model that brackets the CMS from 1215 to 1178 ka. With respect to this controversy $^{40}Ar/^{39}Ar$ geochronologists have also been discussing ACs-2 ages. Some studies published $^{40}Ar/^{39}Ar$ ages that support the interpretations of Channell et al. (2002). These $^{40}Ar/^{39}Ar$ ages range from 1189 to 1205 ka (Mankinen et al., 1978; Turrin et al., 1994; Nomade et al., 2005; Singer, 2014a). Other studies could also agree with the timing of the CMS that has been suggested by Horng et al. (2002). These ACs-2 ages range from 1181 to 1185 ka (Phillips and Matchan, 2013; Rivera et al., 2013; Jicha et al., 2016; Niespolo et al., 2017; Phillips et al., 2017). Ages presented in Rivera et al. (2013), Niespolo et al. (2017), and Phillips et al. (2017) rely on $^{40}Ar/^{39}Ar$ dating relative to astronomically calibrated ages of feldspars from the A1 and Messâdit tephras. $^{40}Ar/^{39}Ar$ dating in Jicha et al. (2016) was relative to the astronomical FCs age of Kuiper et al. (2008). Ages from Phillips and Matchan (2013) were obtained relative to FCs with an age that is intercalibrated with a primary K-Ar standard (Renne et al., 1998). Rivera et al. (2013) interpreted their results to date the begin of the CMS as suggested by Horng et al. (2002). Singer (2014a) argued that the ACs-2 just closed its radioisotope system right at the end (or stratigraphically at the top) of the CMS. This interpretation is supported by the PISO-1500 stack from Channell et al. (2009), which is based on 14 different stratigraphic records that reveal paleomagnetic and $\delta^{18}O$ data and suggests that

the CMS is associated with a 30 kyr period of exceptionally low intensity from 1215 to 1185 ka. Accordingly, Jicha et al. (2016) concluded that their ACs-2 age represents the younger reversal of the CMS. Furthermore, recent developments in instrumental analytics need to be considered in the discussion about the ACs-2 age. Ages that range from 1181 to 1185 ka had been measured with a new generation of multi-collector noble gas mass spectrometers (Noblesse by Nu Instruments and Argus VI by ThermoFisher). The reproducibility of $^{40}Ar/^{36}Ar$ measurements in repeated air standards by these instruments are commonly measured with a ca. 5 times smaller scatter than measurements that are typical for single-detector mass spectrometers in a peak jumping mode (Mark et al., 2009). Multi-collection benefits from the rapid and simultaneous collection of beam intensities and improves the measurement of ^{36}Ar peak intensities that is particularly important for correcting the trapped atmospheric $^{40}Ar_{atm}$ component.

Saxton (2015) presented a tuned mode in a Nu Noblesse mass spectrometer that reaches a considerably high mass resolution power (abbreviates as MRP and is described in Ireland, 2013) of ∼4000. This tuning allowed for the first time to measure ^{36}Ar on shoulder peaks of the m/e 36 mass without potential isobaric interference from $H^{35}Cl$ and $^{12}C_3$ masses (Fig. 3.1a). The $^{40}Ar/^{39}Ar$ laboratory at the University of Potsdam is equipped with a mass spectrometer that offers the resolution of the ^{36}Ar + $H^{35}Cl$ shoulder from a ^{36}Ar + $H^{35}Cl$ + $^{12}C_3$ peak with a single electron multiplier detector (Fig. 3.1b). ^{36}Ar measurements presented in the given thesis were conducted on the lower-mass shoulder of the peak and are potentially devoid of $^{12}C_3$. For dating ACs-2 Jicha et al. (2016) also used a Nu Noblesse multi-colletcor mass spectrometer that provides a high MRP (∼3000) and resolved isobaric interference of the $^{12}C_3$ masses in blank analyses (Fig. 3.1c). These authors furthermore applied advanced ion beam detection using four ion-counting electron multipliers. Jicha et al. (2016) highlighted the importance of precise measurements of ^{36}Ar and the application of improved ion counting statistics for secondary dating of mineral standards.

The thesis presented here is the first to deliberately choose ACs-2 as a monitor flux for $^{40}Ar/^{39}Ar$ dating at the $^{40}Ar/^{39}Ar$ laboratory of the University of Potsdam. The background information about the recent development on standard ages mentioned above, offers a documentation of the considerations that have been involved in choosing an adequate age for the ACs-2 mineral standard. Most of the studies dating the ACs-2 standard were published during the progress of this thesis. After working with ACs-2 ages from Nomade et al. (2005) and Rivera et al. (2013) all $^{40}Ar/^{39}Ar$ ages in the given thesis were calculated using an age of 1186.5 ± 0.3 ka from Jicha et al. (2016).

Constants and correction factors

The determination of the $^{40}Ar^*/^{39}Ar_K$ ratio is the essential goal of the $^{40}Ar/^{39}Ar$ dating technique. This ratio needs to be derived from several Ar isotope ratios of the extracted gas from the geological sample, from an age standard, from K and Ca salts and from atmospheric gas. An overview of the most common corrections and constants that are involved in the determination of the $^{40}Ar^*/^{39}Ar_K$ ratio is presented in the following. The equation to isolate the $^{40}Ar^*/^{39}Ar_K$ ratio from analysed Ar isotope ratios can be found in several technical papers describing the

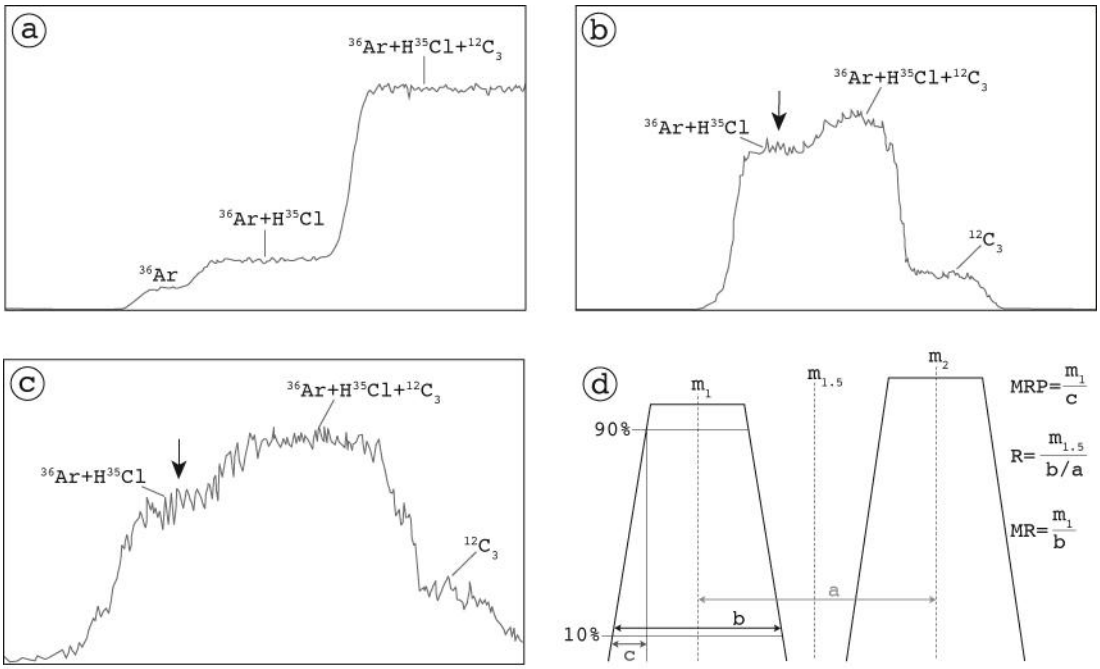

Figure 3.1: (a) A resolved ^{36}Ar shoulder in a m/e 36 scan of air analyses from the study of Saxton (2015) (Noblesse, Nu Instruments Ltd.). (b) Typical scan of m/e 36 during mass calibration with an air pipette in the study given here (MM5400, University of Potsdam). The black arrow represents the position for ^{36}Ar measurements. (c) Resolving isobaric interferences in blank analyses in the study from Jicha et al. (2016) (Noblesse, University of Wisconsin-Madison). (d) Difference of mass resolution (R or MR) and mass resolution power (MRP) illustrated after Ireland (2013). Peak width b and slope width c are defined by the peak heights of 90 % and 10 %. The results of the mass resolution from valley definition (R) and the peak-width definition (MR) are almost identical for the resolution of two Ar isotopes. Note, that the definition of MRP is interchangeable in other disciplines of mass spectrometry (Ireland, 2013).

^{40}Ar/^{39}Ar method (e.g. Uto et al., 1997; McDougall and Harrison, 1999; McDougall, 2014).

$$\frac{^{40}Ar*}{^{39}Ar_K} = \frac{\left(\frac{^{40}Ar}{^{39}Ar}\right)_m - \left(\frac{^{40}Ar}{^{36}Ar}\right)_{Atm} \times \left(\frac{^{36}Ar}{^{39}Ar}\right)_m + \left(\frac{^{40}Ar}{^{36}Ar}\right)_{Atm} \times \left(\frac{^{36}Ar}{^{37}Ar}\right)_{Ca} \left(\frac{^{37}Ar}{^{39}Ar}\right)_m}{1 - \left(\frac{^{39}Ar}{^{37}Ar}\right)_{Ca} \times \left(\frac{^{37}Ar}{^{39}Ar}\right)_m} - \left(\frac{^{40}Ar}{^{39}Ar}\right)_K \tag{3.12}$$

The subscript m refers to measured isotopic ratios. Atmospheric ratios of ^{40}Ar/^{36}Ar are subscripted with the term Atm and are treated as a constant, which is commented later in detail. The subscript Ca refers to correction factors that determine production ratios of ^{39}Ar and ^{36}Ar relative to ^{37}Ar. Calcium correction addresses ^{37}Ar, ^{36}Ar and ^{39}Ar isotopes that are produced whilst irradiation (Brereton, 1970; Turner, 1971). As ^{37}Ar is only produced from irradiation of calcium, measuring ^{37}Ar represents a good reference that allows correcting for Ca-produced ^{36}Ar and ^{39}Ar. The short half-life of ^{37}Ar of 34.95 ± 0.08 days (Renne and Norman, 2001) requires prompt analyses following on irradiation of the samples. The production ratios on pure calcium salts are usually very similar to one another independent of the reactor used and typical correction factors are $(^{36}\text{Ar}/\ ^{37}\text{Ar})_{Ca} = (2.65 \pm 0.41) \times 10^{-4}$ and $(^{39}\text{Ar}/^{37}\text{Ar})_{Ca} = (7.7 \pm 1.6) \times 10^{-4}$ (McDougall and Harrison, 1999). The $^{40}Ar^*/^{39}Ar$ ratio that is subscripted with K corrects for ^{40}Ar production from ^{40}K in the nuclear reactor relative to $^{39}\text{Ar}_K$. Ca and K corrections are achieved by the co-irradiation of K- and Ca-salts. Cadmium shielded irradiation is often applied to absorb thermal neutrons and typically results in very low correction factors for

$(^{40}Ar/^{39}Ar)_K$ that are $< 20 \times 10^{-4}$ (McDougall, 2014). Calcium and potassium salts were co-irradiated in Cd-shielded irradiations in this study. The resulting correction factors were within the range of the above expected values. Obtained values are presented in the supplementary materials to the given thesis (Appendix D).

The atmospheric value of $^{40}Ar/^{36}Ar$ has long been accepted to be 295.5 (Steiger and Jäger, 1977) and was derived from measurements by Nier (1950) who actually determined the ratio to be 296.0 ± 0.5. Steiger and Jäger (1977) calculated the value of 295.5 using the ratio of rounded percentages of relative isotope abundance published by Nier (1950). It has been common practice using the IUGS recommendation from (Steiger and Jäger, 1977) without propagating the uncertainty that was potentially associated to the ratio (McDougall and Harrison, 1999). Lee et al. (2006) prepared highly pure (>99.5%) spikes of ^{36}Ar and ^{40}Ar and measured on a dynamically operated mass spectrometer the $^{40}Ar/^{36}Ar$ ratio of air samples from La Jolla, California and Vostok Station, Antartica. This advanced instrumental method improved the precision of the calibration gas mixtures (meeting the requirements of the international organisation for standardisation [ISO] in 2001) and eliminated uncertainty factors that existed in the instrumental set up of Nier (1950) (e.g. the use of vacuum grease in stopcocks that is expected to provide hydrogen and nitrogen impurities). New ^{40}Ar : ^{38}Ar : ^{36}Ar proportions from Lee et al. (2006) were supported by Mark et al. (2011), who analysed 5 different sources of atmospheric air. Calculations by Renne et al. (2009) show that very young (i.e. Quaternary), K-poor and/or Ca-rich samples are adjusted with 0.6 to 1.2 % in age if using the atmospheric Ar isotope proportions suggested by Lee et al. (2006). These studies suggest that the revised value from Lee et al. (2006) should now enter common routines in $^{40}Ar/^{39}Ar$ geochronology. The new $^{40}Ar/^{36}Ar$ ratio determined by Lee et al. (2006) is 298.56 ± 0.31. As this thesis calculates in a later chapter $^{40}Ar/^{39}Ar$ ages with minimum estimates of full external errors, the ratio determined by Lee et al. (2006) was preferred over the value of 295.5 due to its error assignment. Nevertheless, the values recommended by Steiger and Jäger (1977) are still recommended by the Sub-Commission on Geochronology of the International Union of Geo Sciences (IUGS). Despite exceptional cases modelled in Renne et al. (2009) age dating should not be affected by the choice of the atmospheric $^{40}Ar/^{36}Ar$ ratio. It is emphasized that all Ar isotope ratios must be consequently corrected with the same atmospheric Ar ratios (via Eq. 3.12) that were used for the determination of the mass discrimination of the mass spectrometer: blank, fluence monitor standard, and unknown. Following this emphasis the final age of a geological sample is hardly effected by the choice of the atmospheric Ar composition. The given thesis represents the first work that applied the new ratio from Lee et al. (2006) on measurements at the $^{40}Ar/^{39}Ar$ laboratory at the University of Potsdam.

The difficulty of determining the decay constants of the K-Ar system is in connection to the vibrant discussion about the ages of irradiation flux monitors (see above). Min et al. (2000) summarised that partial decay constants, which have been presented in different studies, show standard deviations being >1% (considering data from Beckinsale and Gale, 1969; Endt and Van der Leun, 1973; Audi et al., 1997). Beckinsale and Gale (1969) presented counting statistics of the ^{40}K decay to the stable ^{40}Ca that allowed calculating the decay to ^{40}Ar by proposed electron capture modes (λ_e and λ'_e). The resulting decay constants were recommended by Steiger and Jäger (1977) for the K-Ar and $^{40}Ar/^{39}Ar$ dating techniques (Table 3.1).

Table 3.1: Summary of ^{40}K decay constant and abundance recommendations. Pairs of ^{238}U-^{206}Pb and ^{40}Ar/^{39}Ar data from a diversified range of rocks were used as inputs for statistical optimisation of ^{40}K activity data and (partial) decay constants in Renne et al. (2010) and Renne et al. (2011)†.

Constant	Steiger and Jäger (1977)	Min et al. (2000)	Renne et al. (2011)
$\lambda_{\beta+}$	4.962×10^{-10} (a^{-1})	$4.88 \pm 0.05 \times 10^{-10}$ (a^{-1})	$4.955 \pm 0.014 \times 10^{-10}$ (a^{-1})
$\lambda_e + \lambda'_e$	0.581×10^{-10} (a^{-1})	$0.580 \pm 0.007 \times 10^{-10}$ (a^{-1})	$0.5757 \pm 0.0016 \times 10^{-10}$ (a^{-1})
λ	5.543×10^{-10} (a^{-1})	$5.5 \pm 0.1 \times 10^{-10}$ (a^{-1})	$5.531 \pm 0.014 \times 10^{-10}$ (a^{-1})
^{40}K/K	1.167×10^{-4}	$1.17 \pm 0.01 \times 10^{-4}$	$1.167 \pm 0.002 \times 10^{-4}$
Source λ	Beckinsale and Gale (1969)	Endt and Van der Leun (1973)	Paired ^{40}Ar/^{39}Ar and U-Pb†
Source ^{40}K/K	Garner et al. (1975)	Audi et al. (1997)	Garner et al. (1975)

In Min et al. (2000) all available values for the decay constants were reviewed. These authors criticised that the activity data that underlie decay constants recommended in Steiger and Jäger (1977) were more dispersed than acknowledged in common practice. Furthermore, this study showed that discrepancies in results from U-Pb and ^{40}Ar/^{39}Ar dating techniques on the same sample (Mesoproterozoic rhyolite) are considerably less pronounced by computing ^{40}Ar/^{39}Ar ages based on a set of counting statistics from Endt and Van der Leun (1973) and a different ^{40}K/K ratio from Audi et al. (1997).

Subsequently, Grau Malonda and Grau Carles (2002) and also Kossert and Günther (2004) provided new liquid scintillation counting (LSC) studies of the total ^{40}K decay. Renne et al. (2010) compiled these studies and optimized paired ^{40}Ar/^{39}Ar and ^{238}U-^{206}Pb data (both methods applied on identical rock units) in order to calculate a set of decay constants that show an improvement in precision. Their study assumed that the different chronometers result in identical ages if the ^{40}K decay is adjusted to the ^{238}U decay. However, Schwarz et al. (2011) criticised that different LSC studies by Grau Malonda and Grau Carles (2002) and Kossert and Günther (2004) were only in agreement due to different branching ratios ($\lambda_{\beta-}$/ $\lambda_e + \lambda'_e$). They highlighted that an independent determination of branching ratios is required before comparing geochronological and physical data. Schwarz et al. (2011) furthermore showed that the widely accepted branching ratio from Beckinsale and Gale (1969) should be taken into account. The resulting total ^{40}K decay constants that consider this branching ratio do not agree to the constraints from the paired intercalibration presented in Renne et al. (2010). Facing these and other critics, Renne et al. (2011) responded with ^{40}K decay constants that were derived from the optimization of paired ^{40}Ar/^{39}Ar and U-Pb data only (without consideration of the LSC measurements). McDougall (2014) recalculated branched decay activities by taking the adjusted values from Renne et al. (2011). The disintegrations per gram of potassium were calculated using the formula from Beckinsale and Gale (1969), an updated Avogadro constant of 6.0221413 $\times$ 10^{23} mol^{-1}, an atomic weight for potassium of 39.09830 $\pm$ 0.0003 (Garner et al., 1975), and 3.1556925 $\times$ 10^7 seconds for the duration of a solar year (Holden et al., 2011). McDougall (2014) stated that the recalculation of the γ activity is indistinguishable to those derived by Beckinsale and Gale (1969) and Endt and Van der Leun (1973), and that the β activity is closest to that of Beckinsale and Gale (1969) but deviates to that of Endt and Van der Leun (1973) and Audi et al. (1997) by ca. 1 %. However, an independent verification of the constants presented by Renne et al. (2011) is still absent and an acceptance by an international community has also not been recorded, yet (McDougall, 2014).

An important fact in the discussion about optimizing decay constants is that Min et al. (2000) revised rather $\lambda_{\beta+}$ than $\lambda_e + \lambda'_e$ to smaller values. Together with the ^{40}K/K ratio from

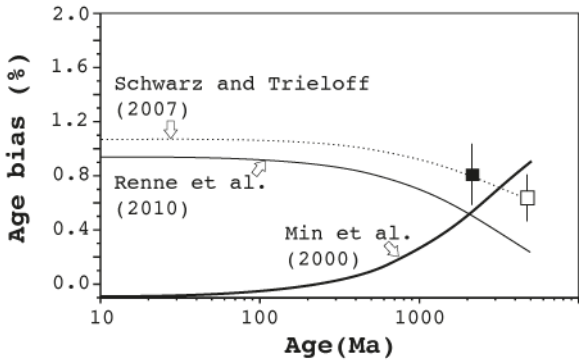

Figure 3.2: Summary of the potential age bias of $^{40}Ar/^{39}Ar$ and U-Pb ages from Schwarz et al. (2011). The correlation lines were calculated by Schwarz et al. (2011) and represent different sets of partial decay constants $\lambda_{\beta+}$ and $\lambda_e + \lambda'_e$ that are described in the text and shown in Table 3.1; except for the dashed line by Schwarz and Trieloff (2007). The open box represents $^{40}Ar/^{39}Ar$ and U-Pb data from the H chondrite and the filled box from impact rocks of the Vredefort complex, South Africa. The $^{40}Ar/^{39}Ar$ and U-Pb ages that were used for the according K decay constants are listed in Schwarz and Trieloff (2007) and Schwarz et al. (2011).

Audi et al. (1997) this revision causes that age biases between U-Pb and $^{40}Ar/^{39}Ar$ methods rise with the age of the sample target (Fig. 3.2). According calculations from Schwarz et al. (2011) show that U/Pb and $^{40}Ar/^{39}Ar$ ages have a minimum bias for samples younger than Mesozoic ages, if using decay constants presented in Min et al. (2000). Aside the fact that the given thesis discusses samples that are significantly younger than the Mesozoic, three other reasons support the use of the decay constants presented in Min et al. (2000).

- The most relevant astronomical age calibrations of FCs used decay constants presented in Min et al. (2000) (e.g. Kuiper et al., 2008).
- Age determinations of ACs-2 were mostly obtained relative to FCs and used decays constants from Min et al. (2000) (Chapter 6 provides more details).
- To date, the uncertainties stated in Min et al. (2000) represent the most realistic approach for a full external error calculation relative to primary standards.

3.1.3 Instrumental set-up at the University of Potsdam

Analyses at the University of Potsdam were conducted with a sector-type noble gas mass spectrometers: Micromass 5400. This instrument (Fig. 3.3) is a high-sensitivity and low background Nier-type mass spectrometer and is used in single ion beam detection mode with either a faraday cup or an electron multiplier. A New Wave Research DualWave laser system comprises a CO_2 continuous and a UV pulsed laser. The given thesis applied exclusively the continuous CO_2 system that has a maximum power of 50W. The actual laser energy used on a sample is properly selected for sample type (single grain, multigrain) and analyses type (stepwise heating, total fusion). As the CO_2 laser is not guaranteeing the uniform heat within the spotted beam size, a widely defocused beam was used and the beam moved across the sample during heating. The applied beam size varied between 1.5 and 3 mm in this study. The actual sample heating is conducted in holes of a copper sample tray. These holes are 4 mm in depth and either 1.5 mm (total fusion analyses) or 3 mm (stepwise heating) in diameter. Double layered ZnS viewport MPF (Manufacturing Precision Feedthrough Products Inc.) guarantee ultra high

Figure 3.3: Instrumental set-up for noble gas analyses at the University of Potsdam. The areas of labels A, B, and G consists of the noble gas extraction line. Boxes labeled with C to F represent components belonging to the Micromass 5400 mass spectrometer. A: New Wave Research DualWave laser; B: purification line; C: ion source box; D: magnet; E: control panels for ion beam optics (system analyser, acquisition unit and power supply as well as magnet power supply units); F: control panel for pneumatic valves; G: vacuum control units. Computer in front of the set-up are responsible for raw data collection and operation of the laser system. The photo was provided courtesy by Dr. Masafumi Sudo.

vacuum (UHV) conditions (usually $\sim 1 \times 10^{-10}$ torr) during CO_2 laser beam heating in the sample chamber (Fig. 3.4).

A pre-vacuum (down to 5×10^{-7} torr) guarantees the stability of the ZnS viewport by providing a stepwise pressure gradient to the atmosphere. The purification line (also named Ar extraction line, Fig. 3.5) has been designed by Dr. Masafumi Sudo under consideration of the $^{40}Ar/^{39}Ar$ laboratory of the Geological Survey of Japan. It consists mainly of two ZrAl alloy getters manufactured by SAES (Società Apparecchi Elettrici e Scientifici) getters. These pumps remove chemically active gases such as O_2, N_2, CO_2, H_2, and hydrocarbon species. One getter works at room temperature, the other one is heated constantly with an electric current of 0.4 A (400° C). In advance to starting analyses of a sample set both getters are cleaned by baking up to 0.75 A (750° C).

A removable cold trap extracts condensable gases (especially H_2O) by cooling ethanol to ca. -90° C. In the given study, the cold trap was not applied for the analyses of feldspars, but for analyses of volcanic glass shards. For correction of the mass discrimination, the aliquot from an atmospheric air standard reservoir is extracted into the purification line by manually operating a Dörflinger pipette valve.

The purification line is pumped with a Varian (nowadays manufactured by Agilent) SH-100 or -110 dry scroll pump and a Varian MacroTorr V70 LP turbo-molecular pump. A similar set-up pumps the pre-vacuum in the viewport (Agilent SH-100 or -110 scroll pump and Varian MacroTorr V70 turbo-molecular pump). High vacuum pressures are monitored with an Agilent

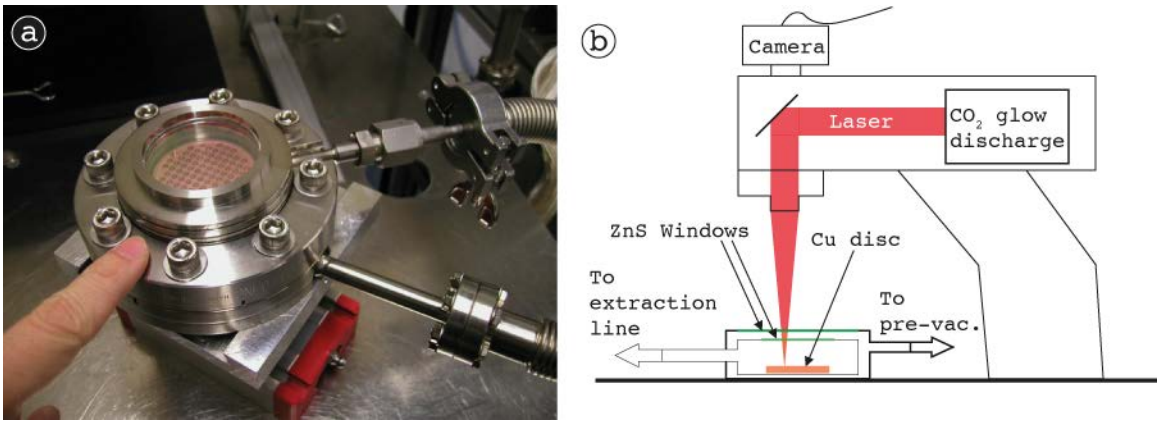

Figure 3.4: (a) Sample chamber consisting of the MPF viewport and the copper disk tray. Lower connection provides viewport vacuum. The upper connection is the sample gas outlet to the Ar extraction line. (b) Simplified schematic sketch of the laser gas extraction system. This sketch is drawn and modified after Kelley (1995). Image in (a) was provided courtesy of Dr. Masafumi Sudo.

UHV-24 ion gauge and an Agilent Eysys Mini B/A ion gauge for the purification and the pre-vacuum lines, respectively. Agilent ConvecTorr gauge tubes monitor the lower vacuum pressures gained by the scroll pumps. Isolating the purification line whilst sample gas cleaning from the pumps is achieved by using a pneumatic VAT (Series 57) valve. Sample inlet into the Micromass 5400 also uses the identical valve. The Micromass 5400 (MM5400) is a 90° sector instrument and has a 27 cm radius magnet with an effective flight radius of 54 cm. The flight tube is constructed of laser-cut stainless steel that minimizes ion scattering effects on its walls. A combination of a Varian SH-110 scroll pump, a Varian V-81 turbo pump and a Varian ion pump (identical to the instrument in the purification line) pump the MM5400 and provide UHV in the source housing and in the flight tube. An ion gauge monitors the vacuum in the source housing and in the flight tube and a Pirani gauge monitors the vacuum between turbo and scroll pump.

3.1.4 Sample preparation and irradiation

The unconsolidated volcaniclastics were grounded softly with mortar and pestle and washed in 10 % acetic acid and 3 % hydrogen peroxide. After sieving with three normed grid sizes (#20 $\equiv >$ 1 mm; #30 $\equiv >$ 500 μm; #45 $\equiv >$ 375 μm) the samples underwent heavy-liquid density separation in a centrifuge with sodium polytungstate (STP) solutions. One centrifuge run was applied to two to four sample test tubes (Fig. 3.6a). In order to separate plagioclases from alkali feldspars, the SPT solution was adjusted to 2.61 g/cm^3 (Campbell et al., 1978). The SPT underwent density control for every centrifuge run. All samples were centrifuged for 15 minutes. Test tube tips were then dipped in liquid nitrogen that instantly froze and fixated the sink (Fig. 3.6b). The samples float was finally decanted, rinsed and filtered.

Four to ten grains of float feldspars and glass shards (picked without density separation) underwent qualitative testing of the chemical composition with energy-dispersive element detection in a scanning electron microscope (SEM) at the University of Potsdam. The minimal masses of required material for ^{40}Ar/^{39}Ar were calculated from the rough estimates of the K content and the assumed ages of the samples. Final fractions were picked in reflecting light microscopy two times and avoided inclusion-bearing shards or crystals. Sample packing for the nuclear irradiation and their neutron activation was organized in commercial-grade Al foil sleeves and 99.999

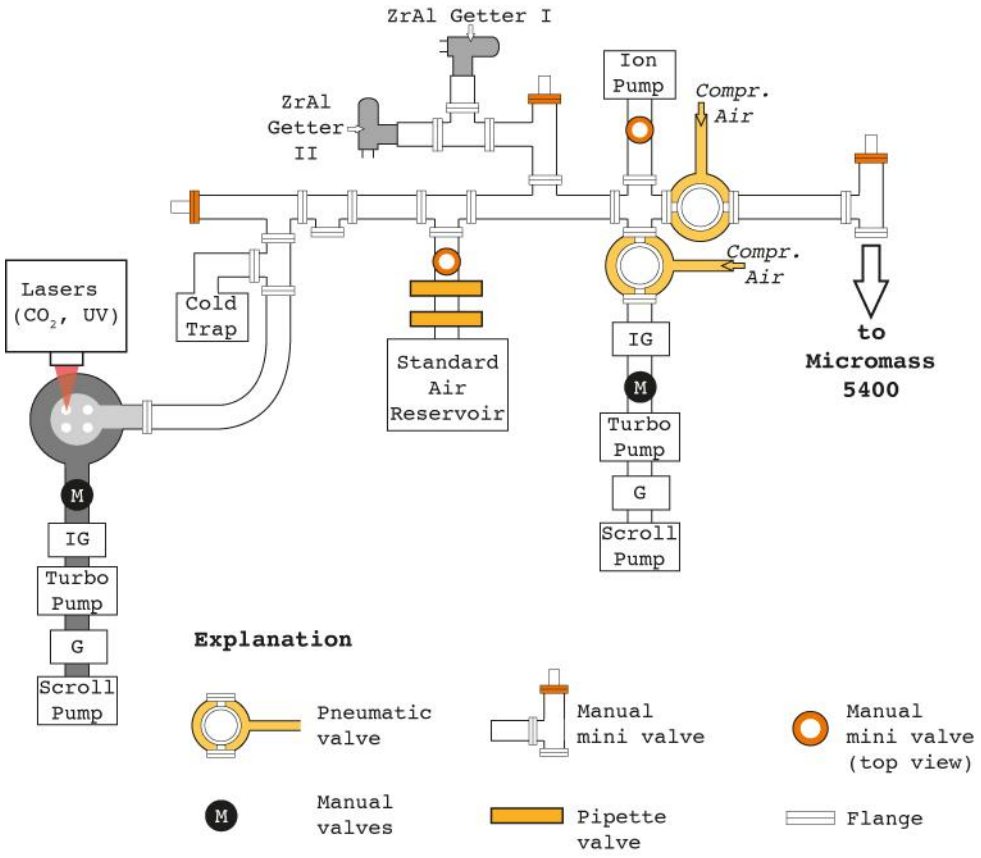

Figure 3.5: Schematic set-up of the purification line. The sketch is drawn after an in-house sketch by Dr. Masafumi Sudo, who constructed the line following a set-up of the $^{40}Ar/^{39}Ar$ laboratory of the Geological Survey of Japan. IG abbreviates 'ion gauge', and G abbreviates a conventional 'gauge' tube. Pneumatic valves can be opened and closed by toggle switches on the panel 'F ' in Fig. 3.3.

% pure Al containers (Fig. 3.7). Samples were wrapped in Al-foil and stacked in the sleeves. Four sleeves were packed in one container. A tabular overview about irradiation position can be found in the supplementary materials (Appendix D). Irradiation monitors were loaded in the sleeves at the top, the bottom, and among the samples in each sleeve. The packing guaranteed that every third sample in the sleeves represents monitor minerals. ACs-2 predominantly served as monitor minerals. FCs was additionally packed in one sleeve. The irradiation was conducted at the Cd-lined in-core irradiation tube (CLICIT) facility in the TRIGA reactor at the Oregon State University (OSTR). The pool-type reactor is particularly designed for scientific purposes such as training, research, isotopes studies and general atomistic studies (TRIGA).

Two different batches of Lake Van sample material were irradiated in two irradiations in June and December 2014. The samples were loaded in containers CGJ-PO-2 (Lake Van samples only), C-S-PO-2, and CG2-PO-3. Both irradiations lasted for four hours. The neutron energies inside CLICIT are usually between 2 to 3 MeV (Renne et al., 2005). The reactor has a common annual power generation of about 1 MWh (Reese, 2005). Temperatures in CLICIT potentially reach up to 93° C (Hughes, 1989).

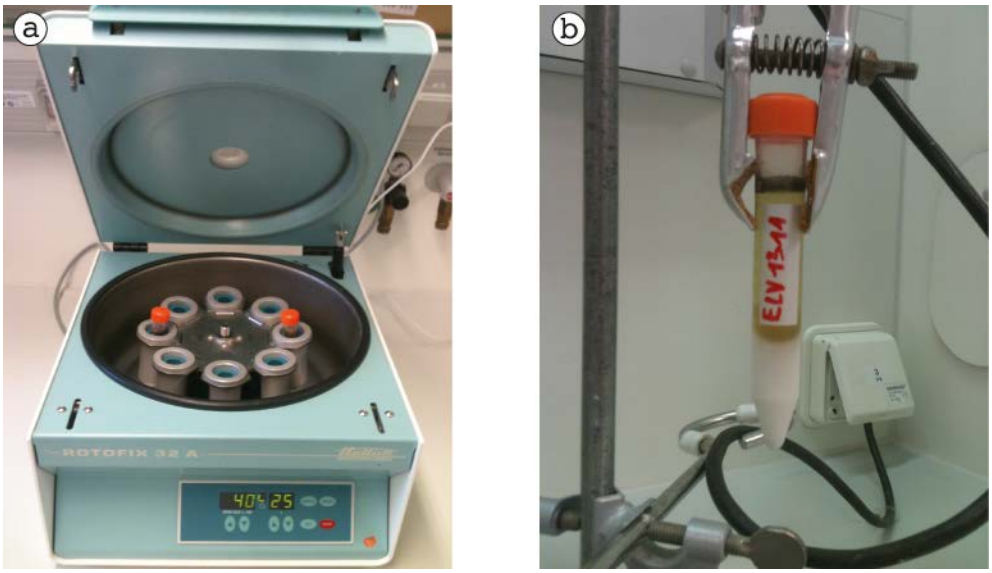

Figure 3.6: (a) Hettichlab Rotofix 32 A centrifuge. (b) Test tube tip after dipping in liquid nitrogen in order to freeze the centrifuged sink.

3.1.5 Calculation of ages and uncertainties

The discussion of radiometric ages that are presented later in this thesis requires a description of age calculations and the according error propagation. Raw isotope data reduction as well as all following calculations were achieved using the software ArArCALC (Koppers, 2002). In order to provide the actual age calculations conducted with ArArCALC a brief summary of the calculations presented in Koppers (2002) and in Kuiper (2003) will be presented in the following. This part begins with discussing the variance of the most crucial value in age calculation, which is the $^{40}Ar^*/^{39}Ar_K$ ratio (F-value). In a later stage this chapter describes the actual age calculations in ArArCALC that were applied for all age calculations in the given thesis. Finally, the independent numerical method for error propagation in ^{40}Ar/^{39}Ar geochronology by Scaillet (2000) will be briefly described.

Data reduction and F-value calculations in ArArCalc

The majority of algorithms that are utilized by the ArArCALC software are described in the book of McDougall and Harrison (1999) and in a number of previous papers (e.g. York, 1968; Dalrymple et al., 1981; Uto et al., 1997; Karner and Renne, 1998; Renne et al., 1998; Min et al., 2000). The error propagation in ArArCALC applies a linearised error expansion approach. This approach considers that each parameter that contributes to the F-value in Eq. 3.12 $(X1, X2, , Xn)$ comes with a variance $(\sigma X1, \sigma X2, , \sigma Xn)$. The contribution to the variance of the F-value is weighted by the squared partial derivative $((\partial F/\partial X_1)^2, (\partial F/\partial X_2)^2$,..., $(\partial F/\partial X_n)^2)$ of each parameter of the F-equation (Eq. 3.12). The same approach is applied for the contributions to the age equation (Eq. 3.6 and Eq. 3.10). Finally, the total variance is the sum of all weighted variances.

$$\sigma_F^2 = \sum_{i=1}^{n} \left(\frac{\delta F}{\delta X_i} \right) \times \sigma_{x_i}^2 \tag{3.13}$$

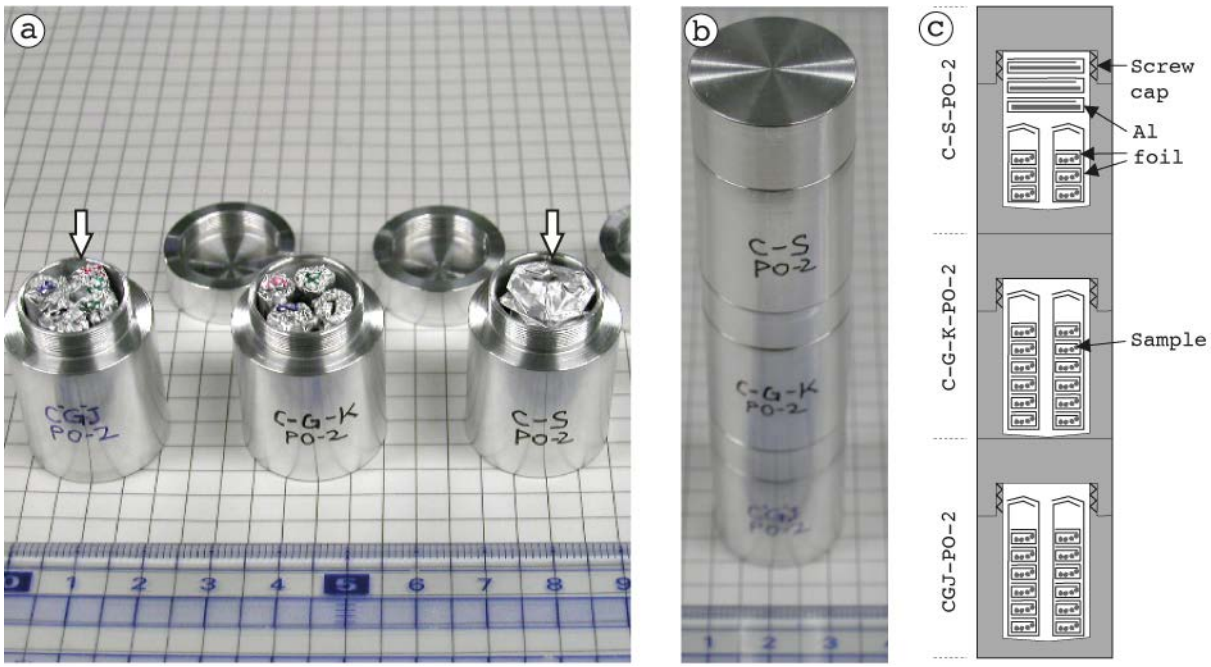

Figure 3.7: (a) Preparation of containers for irradiation 14-064 (ID from OSTR). CGJ PO-2 and C-S PO-2 (arrows) contained samples that have been analysed in the given thesis. (b) Fully stacked container set-up. (c) Schematic cross-section of packed containers showing samples being wrapped in Al foil that were stacked in Al foil sleeves. C-S-PO-2 also contained thick-section samples from different studies. These were packed on top of the Lake Van samples. Photos in (a) and (b) were provided courtesy by Dr. Masafumi Sudo.

Numerical solutions offer an alternative error propagation. Roddick (1987) provided an extension to Eq. 3.13 that is described as follows.

$$\sigma_F^2 = \sum_{i=1}^{n} \left(\frac{\delta F}{\delta X_i} \right) \times \sigma_{x_i}^2 + 2 \times \sum_{i=1}^{n} \sum_{\substack{i=1 \\ i \neq j}}^{n} \left(\frac{\delta F}{\delta X_i} \right) \times \sigma_{x_i}^2 \times \left(\frac{\delta F}{\delta X_i} \right) \times \sigma_{x_j}^2 \times \sigma_{x_i x_j} \tag{3.14}$$

This equation incorporates the possible covariance between two variables (X_i, X_j) in the function of F. The numerical approach weights the respective variance of each input datum by its functional influence on the equation (Scaillet, 2000). Assuming that F represents indeed a linear equation, Eq. 3.13 provides an error calculation that is exact. As the unknown age of a sample is determined by a nonlinear relationship of different variables, linearized methods assume that non-linearity effects are negligible (Scaillet, 2000; Koppers, 2002). The potential of an application of numerical error analysis to $^{40}Ar/^{39}Ar$ geochronology (Scaillet, 2000) will be described later in more detail.

The ArArCALC software offers different regression modes for isotope intensity raw data. The operator can choose between exponential, linear, parabolic and averaging methods. Exponential fits were chosen for fitting ^{40}Ar and ^{39}Ar in samples, blanks, and air measurements. The goodness of the fitting (or Pearson's squared correlation coefficient r^2) usually justifies exponential fitting with values being > 0.97. The residual isotopes (^{38}Ar, ^{37}Ar, ^{36}Ar) are fitted linearly. The scatter of the intensities of these isotopes was usually too large to justify curve-fitting approaches. ArArCALC is an add-in for Microsoft Excel and realises the regression with least squared methods by applying the LINEST function (Koppers, 2002). The exponential fit

bases on

$$Y_i = aZ_i + b \tag{3.15}$$

with

$$Z_i = e^{ct_i}. \tag{3.16}$$

Y_i represents the measurements (in V) and t_i the exceeded time between the sample gas inlet and the actual measurement. Coefficients a, b, and c are iteratively derived by using the LINEST function in Excel. The iteration seeks the highest r^2 values and the lowest subtraction values for two r^2 values from consecutive iterations (convergence level). The minimum convergence level is set by the operator and was 0.01 % in the given study. The standard error of the intercept value at zero time is consequently realized with the following equation.

$$SE = SE_{YX} \sqrt{\frac{\left(\sum_n^{i=1} X_i^2\right)}{\left(n \times \sum_n^{i=1} X_i^2 - \left[\sum_n^{i=1} X_i\right]\right)}} \tag{3.17}$$

This equation is based on the number of analytical cycles (n) in the static mode and on the standard error of the interpolated isotope intensity (SE_{YX}). ArArCALC uses the STEXY function in Excel for calculating SE_{YX}.

The raw data reduction is followed by corrections for blanks, mass discrimination and nuclear interferences (see also Section 3.1.2). A more detailed summary on correcting nuclear interferences is provided in McDougall and Harrison (1999). The correction of the radioactive decay of isotopes produced during the irradiation follows an algorithm from Wijbrans and Mcdougall (1987) and Wijbrans (1985). The error on the time that has elapsed between irradiation and measurement is assumed to be zero. The propagation of the uncertainties from the decay constants is achieved by using Eq. 3.13 (Koppers, 2002). Considering all corrections mentioned above, an extension of Eq. 3.12 is needed and results in the following definition of F.

$$\begin{aligned} F = \Bigg(& \frac{(40_m - 40_b)}{(39_m - 39_b) \times \left(\frac{C\lambda_{39^e}{}^{\lambda_{39}t_B}}{1-e^{-\lambda_{39}t_C}}\right) \times \frac{1}{D}} - A \\ & \times \frac{(36_m - 36_b) \times \left(\frac{4}{D} - 3\right)}{(39_m - 39_b) \times \left(\frac{C\lambda_{39^e}{}^{\lambda_{39}t_B}}{1-e^{-\lambda_{39}t_C}}\right) \times \frac{1}{D}} - AZ_{Ca} \\ & \times \frac{(37_m - 37_b) \times \left(\frac{C\lambda_{37^e}{}^{\lambda_{37}t_B}}{1-e^{-\lambda_{37}t_C}}\right) \times \left(\frac{3}{D} - 2\right)}{(39_m - 39_b) \times \left(\frac{C\lambda_{39^e}{}^{\lambda_{39}t_B}}{1-e^{-\lambda_{39}t_C}}\right) \times \frac{1}{D}} \Bigg) \\ & \Big/ 1 - Y_{Ca} \times \frac{(37_m - 37_b) \times \left(\frac{C\lambda_{37^e}{}^{\lambda_{37}t_B}}{1-e^{-\lambda_{37}t_C}}\right) \times \left(\frac{3}{D} - 2\right)}{(39_m - 39_b) \times \left(\frac{C\lambda_{39^e}{}^{\lambda_{39}t_B}}{1-e^{-\lambda_{39}t_C}}\right) \times \frac{1}{D}} - X_K \end{aligned} \tag{3.18}$$

Intensities of isotope masses measured from unknown are labelled with the subscript m. Those that were obtained from analysing procedural blanks are labelled with the subscript b. A is the atmospheric ratio of 298.56 (Section 3.1.2). The mass discrimination factor is represented

in D. Y_{Ca} is the $(^{39}Ar/^{37}Ar)_{Ca}$ correction factor, Z_{Ca} is the $(^{36}Ar/^{37}Ar)_{Ca}$ correction factor, and X_K is the $(^{40}Ar/^{39}Ar)_K$ correction factor. The duration of the irradiation is given in C, whereas B represents the time elapsed between measurement and irradiation. Decay constants are denoted as λ and the subscript refers to the respective mass. Following Eq.3.13, the according variance is:

$$\begin{aligned}\sigma_F^2 = &\left(\frac{\delta F}{\delta M}\right)^2 \delta_M^2 + \left(\frac{\delta F}{\delta N}\right)^2 \delta_N^2 + \left(\frac{\delta F}{\delta O}\right)^2 \delta_O^2 + \left(\frac{\delta F}{\delta P}\right)^2 \delta_P^2 + \left(\frac{\delta F}{\delta Q}\right)^2 \delta_Q^2 + \left(\frac{\delta F}{\delta R}\right)^2 \delta_R^2 \\ &+ \left(\frac{\delta F}{\delta S}\right)^2 \delta_S^2 + \left(\frac{\delta F}{\delta T}\right)^2 \delta_T^2 + \left(\frac{\delta F}{\delta A}\right)^2 \delta_A^2 + \left(\frac{\delta F}{\delta D}\right)^2 \delta_D^2 + \left(\frac{\delta F}{\delta Y_{Ca}}\right)^2 \delta_{Y_{Ca}}^2 + \left(\frac{\delta F}{\delta Z_{Ca}}\right)^2 \delta_{Z_{Ca}}^2 \\ &+ \left(\frac{\delta F}{\delta X_K}\right)^2 \delta_{X_K}^2 + \left(\frac{\delta F}{\delta \lambda_{39}}\right)^2 \delta_{\lambda_{39}}^2 + \left(\frac{\delta F}{\delta \lambda_{37}}\right)^2 \delta_{\lambda_{37}}^2 + \left(\frac{\delta F}{\delta B}\right)^2 \delta_B^2 + \left(\frac{\delta F}{\delta C}\right)^2 \delta_C^2\end{aligned} \tag{3.19}$$

The variables M to$P$ refer to Ar isotope measurements of masses, 40, 39, 37, and 36. Variables Q to T represent the blank analyses of these masses. B and C are assumed to be determined without any uncertainty (elapsed time from irradiation to measurement and during irradiation, respectively). Thus, these terms are treated as zero and omitted.

Age calculations in ArArCalc

$^{40}Ar/^{39}Ar$ ages are routinely calculated from replicate analyses of extracted gas from stepwise heating or repeated crystal fusion from the unknown material. If subsequent analyses of F are statistically indistinguishable, an average of F and a standard error of the average are calculated. Statistical homogeneity between two analyses is proven if the subsequent analyses fall within a range of a confidence envelope (C_E), which is defined by Dalrymple and Lanphere (1969) and bases on the uncertainty of an analysis (σ_a) together with the uncertainty of the subsequent measurement (σ_b).

$$C_E = 1.96 \times \sqrt{\sigma_a^2 + \sigma_b^2} \tag{3.20}$$

A weighting factor E_i is represented by $1/\sigma^2$ of the F-value of each degassing step. The average and its standard error from several measurements are calculated with the following equations.

$$F_{mean} = \frac{\sum_{i=1}^{n} E_i \times F_i}{\sum_{i=1}^{n} E_i} \tag{3.21}$$

$$SE_F = \sqrt{\frac{1}{\sum_{i=1}^{n} E_i}} \tag{3.22}$$

Plateau ages from incremental heating steps are also combined and weighed in this way. Plateaux need to cover minimum of three concordant incremental heating steps that represent minimum 50 % of the total released $^{39}Ar_K$ (Fleck et al., 1977; Lanphere and Dalrymple, 1978; Pringle, 1993). Assuming that a single degassing step from incremental heating contains perfectly retained radiogenic Ar and that the only initial Ar is of an atmospheric composition, the calculation of an age is meaningful without repeated measurements of the same material or further increments.

These ages are frequently referred to as "apparent ages" (McDougall and Harrison, 1999). This thesis adapts the term for ages that were calculated from single incremental heating steps and those calculated from single total fusion experiments.

Isochron calculation in ArArCALC base on least square fitting of a straight line (York, 1968). The fitting considers the correlated errors in the common denominator regression. A normal isochron regression uses ^{36}Ar as the common denominator. The inverse isochron applies the regression with the same isotope intensities but uses ^{40}Ar as the common denominator. An inverse isochron does not represent an isochron per se, because the age of the sample is not related to the slope of the regression. However, treating the inverse isochron as a common denominator mixing-line, has important benefits to $^{40}Ar/^{39}Ar$ geochronology. A radiogenic and an atmospheric end-member are defined by the intersection of the regression with the ordinates. This approach is particularly helpful for checking the initial $^{40}Ar/^{36}Ar$ composition. The initial value of the $^{39}Ar/^{40}Ar$ composition (intersection of the mixing line with the abscissa in a typical inverse isochron diagram) is used to calculate the inverse isochron age using Eq. 3.6. If more than two isotopically different Ar components (e.g. radiogenic and atmospheric) are present, Ar isotope ratios would not reveal a linear relationship in an inverse isochron diagram.

The linear regression calculations are commonly tested by the calculation of the mean squared weighted deviation (MSWD) of the linear regression (Wendt and Carl, 1991). ArArCALC provides this statistical test also to assess the validity of plateau ages and weighted mean ages. If the analytical errors account perfectly for the observed scatter of the data, the MSWD results in a value of 1. A scatter that cannot be explained by the analytical errors, results in MSWD values that exceed 1. Analytical errors that overestimate the observed scatter are < 1. ArArCALC calculates MSWD values as suggested by York (1968) and Roddick (1978). Depending on the number of analyses and a pre-determined confidence level, ArArCALC compares the MSWD to distributions from an f-test (isochrons) or a t-test (weighted mean ages, plateau ages). Using these tests ArArCALC defines an upper limit for the MSWD following Wendt and Carl (1991) and Pringle (1993). If data exceeds this limit the software reports ages to be either "errorchrons" or "error weighted means". The statistical distributions are calculated in ArArCALC using FINV and TINV functions of Microsoft Excel (Koppers, 2002).

ArArCALC assigns errors that follow the partial differentiation of Eq.3.6 as exemplarily shown in Eq 3.13. The resulting formula is stated in the following.

$$\sigma_t^2 = \left[\frac{J}{C\lambda}\right]^2 \times \sigma_F^2 + \left[\frac{F}{C\lambda}\right]^2 \times \sigma_J^2 + \left[\frac{-lnC}{\lambda^2}\right]^2 \times \sigma_\lambda^2 \tag{3.23}$$

The variable C represents the last term in Eq.3.6 (which is $C = 1 + J \times F$). So-called internal errors (Koppers, 2002) are represented by the first two terms that combine analytical errors with the error of the J-value. The complete error equation in Eq. 3.23 also includes the systematic error on the total decay constant λ in the last term. The standard age equation (Eq.3.6) doesn't allow the calculation of the full external error which should include the relevant error of the individual λ_β and $\lambda_e + \lambda'_e$ decay constants, the measurements of the primary K-Ar standards and all intercalibration factors of involved secondary $^{40}Ar/^{39}Ar$ standards (Renne et al., 1998; Min et al., 2000). Instead Eq. 3.23 represents the combination of the analytical error, the error of the J-value, and the error in the total decay constant. Therefore, the external error

provided in Eq. 3.23 is the minimum estimate for the absolute error on the $^{40}Ar/^{39}Ar$ ages. Nevertheless, equations of Karner and Renne (1998), Renne et al. (1998), and Min et al. (2000) are also implemented to ArArCALC and offer a tool that is capable of (re-)calculating $^{40}Ar/^{39}Ar$ ages relative to primary K-Ar standards. This thesis offers recalculations relative to primary K-Ar standards (Appendix G) and a short explanation of the according age equation appears inevitable. The approach bases on Eq. 3.10 that intercalibrates ages of unknowns to primary and other secondary standards involved. In order to group some variables for a later description of the error treatment, Eq. 3.10 can be rewritten as shown in the following equations.

$$t_{unknown} = M \ln \left[NK \prod_{i=1}^{n} R_{i-1}^{i} + 1 \right] = M \times \ln[X] \tag{3.24}$$

This version of Eq. 3.10 contains the placeholders M N and K that are substituted with differently connected formulas, which are dependent from the type of age (re-)calculation. Subscripts of these placeholders indicate the possible combinations in the following list of equations.

$$M_1 = \frac{f \times N_0}{(A_\varepsilon + A_\beta)\, WS} \leftrightarrow M_2 = \frac{1}{\lambda_\varepsilon + \lambda_\beta} \tag{3.25}$$

$$N_1 = \frac{A_\varepsilon + A_\beta}{A_\beta} \leftrightarrow N_2 = \frac{\lambda_\varepsilon + \lambda_\beta}{\lambda_\varepsilon} \leftrightarrow N_3 = 1 \tag{3.26}$$

$$K_1 = \frac{^{40}Ar_P^*}{K_P f} \leftrightarrow K_2 = \frac{^{40}Ar_P^*}{K_P} \leftrightarrow K_3 = \exp\left[(\lambda_\varepsilon + \lambda_\beta)\, T_0\right] - 1 \tag{3.27}$$

The $^{40}K/K$ ratio of a primary standard is represented by f, the Avogardo constant by N_0, and the nuclear activity of potassium by A. The subscript ε combines the two electron capture decay modes ($\lambda_\varepsilon = \lambda_e + \lambda'_e$). W is the atomic weight of potassium and S represents the duration of a solar year in seconds (e.g. Holden et al., 2011). $^{40}Ar_P^*$ and K_P represent the concentrations of radiogenic ^{40}Ar and K in the primary standard. T_0 is the age of the primary standard. X summarizes a part of Eq. 3.24.

$$X = \left[NK \prod_{i=1}^{n} R_{i-1}^{i} + 1 \right] \tag{3.28}$$

Using the expressions M, N, and K, Koppers (2002) highlighted that the input data may be changed quickly depending on the data availability for the age (re-)calculation. The combination of M_1 and N_1 works for a (re-)calculation with nuclear activity constants. M_2 and N_2 apply the (re-)calculation with the decay constants. K_3 and N_3 work together in order to (re-)calculate the unknown age against the age of the primary standard. The partial differentiation of Eq. 3.25 results in the linearized error propagation of all relevant uncertainties with the following

equation.

$$
\begin{aligned}
\sigma^2_{t\,uknown} = & \left[\left(\frac{Z\ln X}{f}\right) + \left(\frac{-ZBK\prod R^i_{i-1}}{fX}\right)\right]^2 \times \sigma^2_f \\
& + \sum_{i=1}^{n}\left[\sum_{j=1}^{n}\left(\frac{ZBK\prod R^i_{i-1}}{R_jX}\right)\right]^2 \times \sigma^2_{R^i_{i-1}} \\
& + \left[\left(\frac{-Z\ln X}{A_\varepsilon + A_\beta}\right) + \left(\frac{-A_\beta ZK\prod R^i_{i-1}}{A^2_\varepsilon X}\right)\right]^2 \times \sigma^2_{A_\varepsilon} \\
& + \left[\left(\frac{-Z\ln X}{A_\varepsilon + A_\beta}\right) + \left(\frac{ZK\prod R^i_{i-1}}{A_\varepsilon X}\right)\right]^2 \times \sigma^2_{A_\beta} \\
& + \left[\left(\frac{ZB\prod R^i_{i-1}}{K_P fX}\right)\right]^2 \times \sigma^2_{Ar^*_P} \\
& + \left[\left(\frac{-ZBK\prod R^i_{i-1}}{K_P X}\right)\right]^2 \times \sigma^2_{K_P} \\
& + \left[\left(\frac{Z\ln X}{N_0}\right)\right]^2 \times \sigma^2_{N_0} + \left[\left(\frac{-Z\ln X}{W}\right)\right]^2 \times \sigma^2_W
\end{aligned}
\tag{3.29}
$$

Numerical error analyses

Due to the existence of error correlations among the variables of Eq. 3.14 the use of a numerical error analysis (NEA) is the only way to address exact errors to $^{40}Ar/^{39}Ar$ ages. A numerical model proposed by Roddick (1987) tested the effects of non-linearity first. Scaillet (2000) described a more detailed application of the NEA in $^{40}Ar/^{39}Ar$ geochronology. Although the non-linearity in the common error propagation (Eq. 3.19) was outlined in this paper, a close agreement between linearised and numerical error propagation was found. This agreement justified the usual linearised approach for the most types of $^{40}Ar/^{39}Ar$ analyses. Nevertheless, Scaillet (2000) warned that numerical error analyses should be applied in situations involving few (<10) input variables (i.e. when stating analytical errors only). An additional warning was stated for situations where input parameters significantly exceed 10 % in uncertainty. Another outcome of the study by Scaillet (2000) is the illustration of the contribution of each variable to the total variance of the age. Deriving the same information from the linearised approach is complex, as the total variance equation needs to be fully derived for every single variable in Eq. 3.19. Scaillet (2000) offered complete error analyses from three different samples. These exemplarily NEA were conducted on data from a Jurassic biotite, a Paleoproterozoic amphibole, and a Neogene igneous muscovite. Fig. 3.8 illustrates all major contributions to the total variances from Ar analytics of the Neogene igneous muscovite. The NEA in Scaillet (2000) included the full external error age calculations relative to a primary standard (Fig. 3.8a). Kuiper (2003) recalculated the variance contributions for the F-value by using the linearised approach that is shown in Eq. 3.19 (Fig. 3.8b). Comparing the two variance compositions with respect to the F-value parameters only (without pie slice in Fig. 3.8a) highlights that the impact of the different error analysis is minimal and potentially negligible. Furthermore, the additional

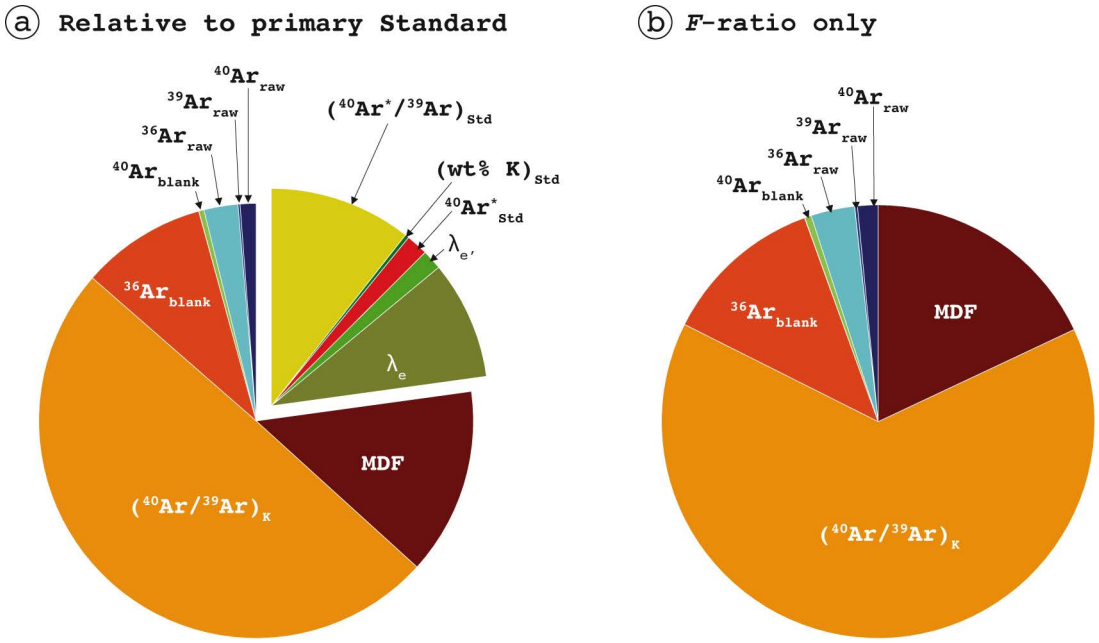

Figure 3.8: (a) Pie chart illustrating the variance contribution of the age uncertainty that considers full external errors and involves uncertainties that are derived from a primary standard. (b) Pie chart showing the variance contribution to calculations of the F-ratio following a linear error propagation. The highlighted pie slice in (a) shows the contribution of parameters that are derived from the (primary) standards and decay constants. The pie charts display the variance contribution from analyses of a Neogene muscovite by Scaillet (2000). The recalculation of the data using Eq. 3.19 resulted in the data shown in (b) and has been taken from Kuiper (2003). MDF abbreviates mass discrimination fractionation.

proportion of the variance that is derived from age calculation relative to a primary standard, which includes decay constant uncertainties from analyses of unknown and standard, is outlined (pie slice in Fig. 3.8a). The mass-discrimination factor (MDF), the analyses of ^{36}Ar in the blank samples, and the $(^{40}\mathrm{Ar}/^{39}\mathrm{Ar})_K$ nucleogenic interference correction represent by far the biggest contributions to the variances of the age and the F-value.

The variance composition in Fig. 3.8 represents data from the youngest sample in the study by Scaillet (2000). Additionally, this sample was irradiated for an overly long time. Thus the data exaggerates the proportion of the nucleogenic interference correction factor. Nevertheless, this uncertainty contribution is expected to be also high for young ($<$ 1 Ma) and/or K-poor (K $\leq$ Ca) samples. The example from Scaillet (2000) showed that NEA is capable of dropping the exact amount of error contribution from the interference corrections and the age of the example would result in 18.32 $\pm$ 0.23 Ma instead of 18.32 $\pm$ 0.44 Ma. As the Pleistocene samples from the here presented study are young and comparably K-poor, the correction of the $(^{40}\mathrm{Ar}/^{39}\mathrm{Ar})_K$ variance contribution in a numerical error analysis shows the potential to significantly improve the precision in future studies. However, more extensive determinations of the $(^{40}\mathrm{Ar}/^{39}\mathrm{Ar})_K$ correction factor would have been required to benefit from NEA in the given study. The potential benefit from implying NEA to common practice in age dating of Quaternary samples is the improved control about effects from non-ideal irradiation (i.e. overly long durations or the presence of ^{39}Ar recoil from irradiating small effective grain sizes) and the isolation of these imprecise contributions. A QuickBasic NEA code provided by Scaillet (2000) uses a rigorous central finite difference method and can be requested by the author directly. However, several authors stated that the common linearised error propagation sufficiently agrees to the numerical method (Min et al., 2000; Scaillet, 2000; Koppers, 2002; Kuiper, 2003). The

here presented thesis represents the first time operation of ArArCALC for data reduction of Ar isotope data from the $^{40}Ar/^{39}Ar$ laboratory at the University of Potsdam. Further implementing an additional NEA would have been beyond the aim of this thesis. This study assumes that the linearised error propagation in ArArCALC sufficiently describes all errors in their correct proportions. Nevertheless, a future treatment involving NEA is recommended.

3.2 Electron microprobe analyses

Chemical characterisation of minerals and glasses presented in the given thesis base on analyses from an electron microprobe analyser (EMPA) on polished surfaces. Interaction of the analysed solid with an electron beam results in x-ray spectra that are interpreted via wave-length dispersive spectroscopy (WDS). The EMPA is a micro-beam instrument that provides non-destructive chemical analyses of solid, inorganic materials. It has many similarities to the scanning electron microscopy (SEM). The methodological description about EMPA given in the following suffices to cover also the instrumental theory of SEM. An advantage of the EMPA is the chemical in-situ analyses of solids. EMPA allow to detect chemical variations within a single feldspar crystal and volcanic glass shard, which has been a major aim in this study. This chapter offers a brief background in EMPA theory that will be followed by the specific application on different phases. As the given thesis cannot provide a full comprehensive introduction to electron beam and X-ray analytics, the textbooks by Skoog and Leary (1992) and Reed (2005) are recommended for further reading. These books represent the basis for the following theory.

3.2.1 EMPA in theory

Electron optics are of a much higher resolution than visible-light optics. Thus, the scanning electron microscopy was designed primarily for imaging of small-scale structures (tens of nm) in the late 1930s (Burton et al., 1939). The magnification is achieved by scanning the electron beam over a sample surface and by displaying the resulting signal on a screen. Depending on the detection mode, the operator is able to focus on a topographic or on a compositional contrast. The range of detector types can be extended to also involve the detection of light emission or the detection of cathodoluminescence. EMPA can be regarded as an enhancement of the SEM. It offers the same magnification as SEM, but furthermore provides the operator the opportunity to conduct analyses in positions where the focused electron beam excited X-rays within the sample. In order to briefly outline the functionality of the EMPA it is inevitable to describe the electron-specimen interactions during an analysis and the detection of the resulting X-rays.

Electron-specimen interaction

During electron microprobe analyses accelerated electrons impinge and enter a solid surface of interest. Electrons will either slow down due to inelastic interaction with the outer atomic electrons or receive elastic deflections by atomic nuclei. Due to the impact of primary electrons from the source, secondary electrons are released from the first few nanometers of the sample surface. These have energies of a few eV and can be detected with an Everhart-Thornley detector (Everhart and Thornley, 1960). Some primary electrons leave the sample target again, having been deflected through an angle of >90°. Secondary and backscattered electrons can be used to

image the sample. The interaction of the primary electrons with the atomic nuclei of the sample matter excites the emission of X-ray photons with any spectrum up to the primary energy of the impacting electron (E_0). The resulting energy spectrum is called 'continous X-ray spectrum' or just 'continuum'. Characteristic X-rays are produced from electron transitions in the atomic shells of the nuclei of the target material. These characteristic X-rays are caused by vacancies of inner shell electrons and can be used for analysing the chemical composition of a solid material. The primary (or bombarding) electrons have commonly energies that range from 5 to 30 keV. In the case of inelastic scattering these primary energies dissipate with bound electrons and lattice coordination. This mechanism causes a smoothing of the primary energy. Elastic interactions result in large deflections that can be described mathematically following

$$\tan\left(\frac{\gamma}{2}\right) = \frac{Z}{1.4 \times p \times E} \tag{3.30}$$

where p is the minimum distance between the undeflected electron path and the colliding nucleus, γ is the angle between the electron pathway and the final deflection around the positively charged nucleus and E is the energy at the time of deflection. One can conclude that the degree of deflection is highest for atoms of highest atomic number (Z) and low electron energies. This effect relates to the contrast that can be seen in backscattered electron (BSE) images. If the average atomic number in different regions of the sampled phase is in strong contrast, the BSE image will show high contrasts as well. Eq. 3.30 indicates that high common atomic numbers will reflect more electrons and the BSE image appears bright. Monte Carlo simulations are helpful in order to model the spatial distribution of electrons in the target. The simulations divide the total electron path into short tracks and use random numbers to model the deflection angle (Joy, 1995). Figure 3.9 provides an example of an according simulation. Here, the value for Z was averaged by stating the chemical composition of the analysed material as an input parameter (Drouin et al., 2007).

The bombardment by electrons produces X-rays in two different ways. A smooth 'continuous' spectrum is caused from electrons that interact with different atomic nuclei. Instead, the 'characteristic' spectra are a result from electron transitions between energy levels that are specific to a distinct element (Fig. 3.10). The continuum (or in German: 'Bremsstrahlung') limits the detectability of the characteristic lines that are present in low concentrations. It is released from the electrons as they jump to lower states whilst passing through the electric fields of atomic nuclei. The intensity of the continuum can be represented by a law that was formulated by Kramers (1923) and is simplified here in Eq. 3.31.

$$I = C \times Z \times \frac{E_0 - E}{E} \tag{3.31}$$

C represents a chemical constant and E the actual X-ray photon energy. The Intensity is proportional to the common atomic number (Z) of a compound. It falls to zero at the 'Duane-Hunt' limit. According to Eq. 3.31 the shape of the continuum is always the same and independent of the bombarded material.

The characteristic X-rays are produced differently by the transition of electrons between bound electron orbits. Energies required for these transitions are in principal dominated by the quantum number (n). The inner orbits form closed shells that are commonly labelled as K

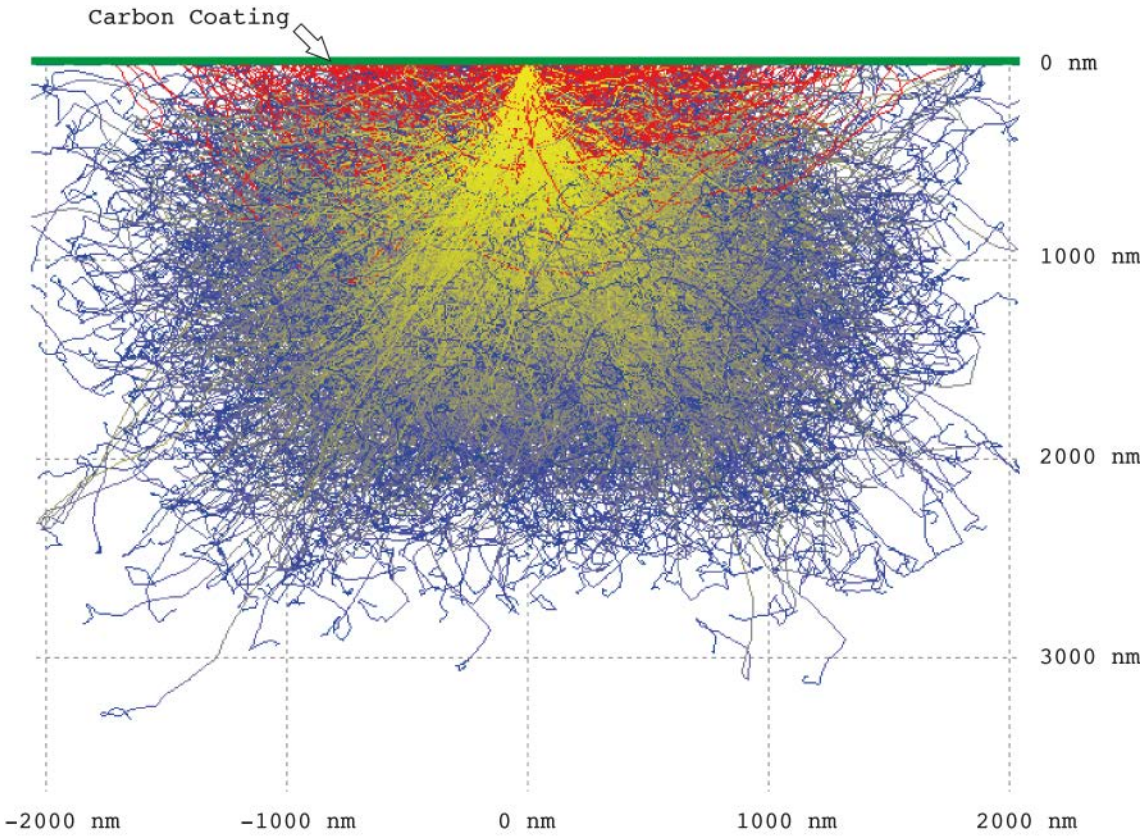

Figure 3.9: Modelled electron trajectories in anorthoclase feldspar. Beam size is 100 nm in diameter. Red trajectories represent pathways of backscattered electrons. Blue trajectories show elastic scattering of absorbed electrons and yellow pathways represent high-energy inelastic electrons. Modelling was conducted for 10,000 electrons with an acceleration voltage of 10 kV via the CASINO software (Drouin et al., 2007).

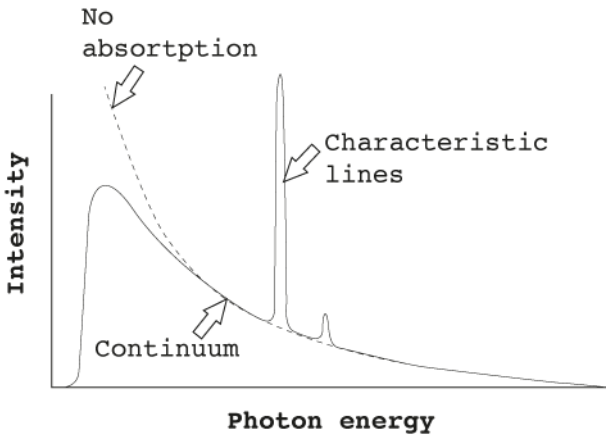

Figure 3.10: X-ray spectrum showing characteristic lines that are superimposed on the continuum. Sketch was drawn after Reed (2005).

(n=1), L (n=2), and M (n=3), and so forth (Fig. 3.11). These inner shells are typically filled completely (except for atoms of low atomic numbers). Electrons being associated with the shells are determined by other quantum numbers that relate to the angular momentum. The K-shell contains a maximum of 2 electrons, the L-shell 8, the M-shell 18, and so forth. The L- and the M-shell (as well as higher shells) have three and five subshells, respectively. These have different quantum energies.

The production of the characteristic X-ray photon is caused by the removal of an inner-shell electron. This removal leaves the atom in an ionized state. The emission of a characteristic X-ray line requires that an incident electron has a primary energy (E_0) that exceeds a critical excitation energy (E_c). The probability for an ionisation is expressed as a cross-section (Q). This probability rises strongly from E_c to ca. $2E_c$ and then falls quickly (Fig. 3.12). Thus, E_0 must be substantial above E_c for an intense characteristic X-ray emission. The resulting X-ray photon energy is the difference between the energies of the initial and the final energy levels of the electron transition.

Transitions that follow the rules of quantum mechanics are allowed. The most significant transitions are illustrated in Fig. 3.13 and labelled with respect to their initial vacancy (K, L, M, etc.). The transitions that are most intense within a shell are labelled α. Next most intense transitions are labelled β. These subgroups are again sorted with respect to the order of decreasing intensity. The energies of the transitions and the resulting wavelengths of the X-rays have a relationship as shown in Fig. 3.14. Most frequent used lines are commonly $K\alpha$ (for

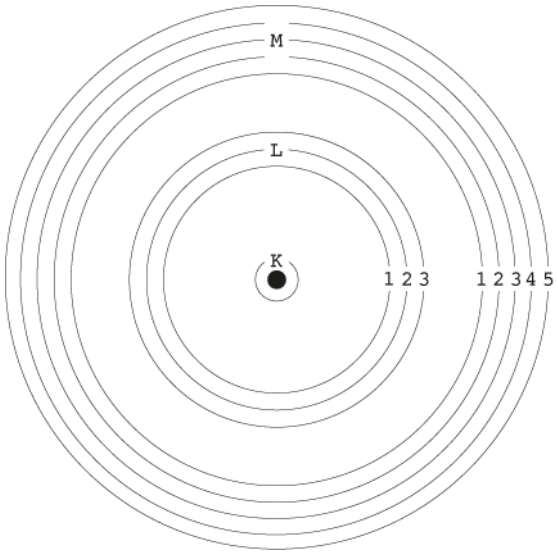

Figure 3.11: The schematic structure of inner atomic electron shells. The sketch follows Reed (2005).

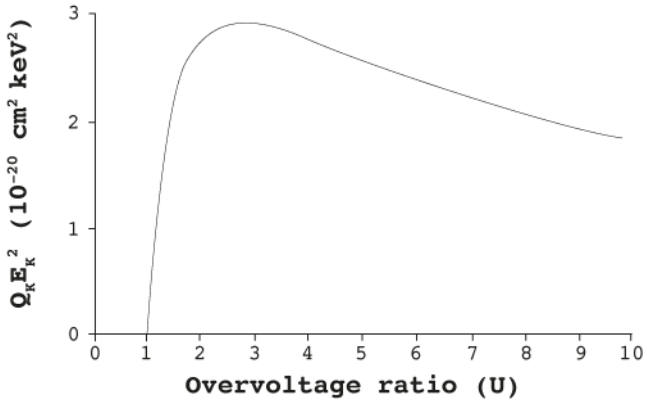

Figure 3.12: Ionization cross-section of the K-shell (Q_K). The ionization is expressed as $Q_K E_K^2$ (with E_K being the excitation energy of the K-Shells). The overvoltage ratio is expressed as $U = E_0/E_K$, with E_0 representing the primary incident energy. Q_K is the probability of the ejection of an electron from the K-shell. The diagram is drawn after Reed (2005).

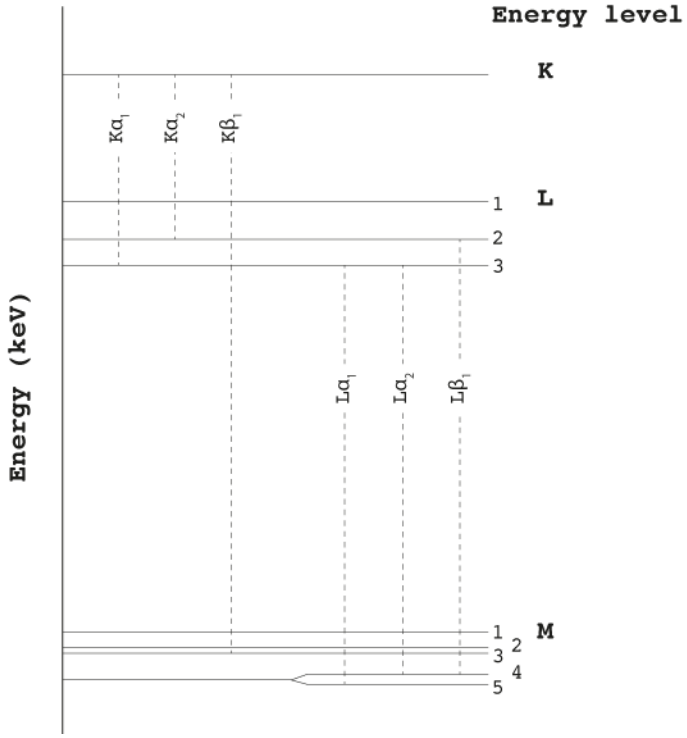

Figure 3.13: Typical energy-level diagram. Characteristic X-ray photon energy is the difference between the two levels involved in the transition and illustrated here in dashed lines for transition in the K and L shells. This sketch follows Reed (2005)

elements up to an atomic number of 30) and deal with X-ray energies of ca. 10 keV. Elements of higher atomic numbers interpret $L\alpha$ lines. Relative intensities and positions are typically very similar for X-ray lines of different elements, but are shifted with respect to the particular atomic number. The intensity of the observed X-ray lines may be affected by significant absorption of X-ray lines in the sample itself. Absorption is also modelled in CASINO and follows an equation that describes this effect in a thin layer.

$$I = I_0 \exp(-\mu\rho x) \tag{3.32}$$

Equation 3.32 combines the initial intensity (I_0), the intensity after absorption (I), the mass absorption coefficient (μ), the density (ρ), and the path length (x). Figure 3.15 illustrates modelled X-ray absorption with respect to X-ray lines generated from Na and Ba in anorthoclase feldspar using the CASINO software. The absorption coefficient mostly depends on the type of X-ray line (compare Figs. 3.15c and 3.15d) and on the atomic number (compare Ba and Na in Figure 3.15). Absorption is mainly caused by the ejection of inner shell electrons. Plotting μ versus the X-ray energy allows the detection of very sharp discontinuities (so called absorption edges). The energies at the discontinuities correspond to the critical excitation energy of the given electron transition.

Produced X-rays can be finally interpreted with two kinds of spectrometer: (i) an energy-dispersive X-ray spectrometer (EDX) and (ii) a wavelength-dispersive X-ray spectrometer (WDX). The EDX uses a detector that produces pulses that are proportional in height to the photon energy recorded. Instead, the WDX employs the Bragg reflection of a crystal. These spectrometers

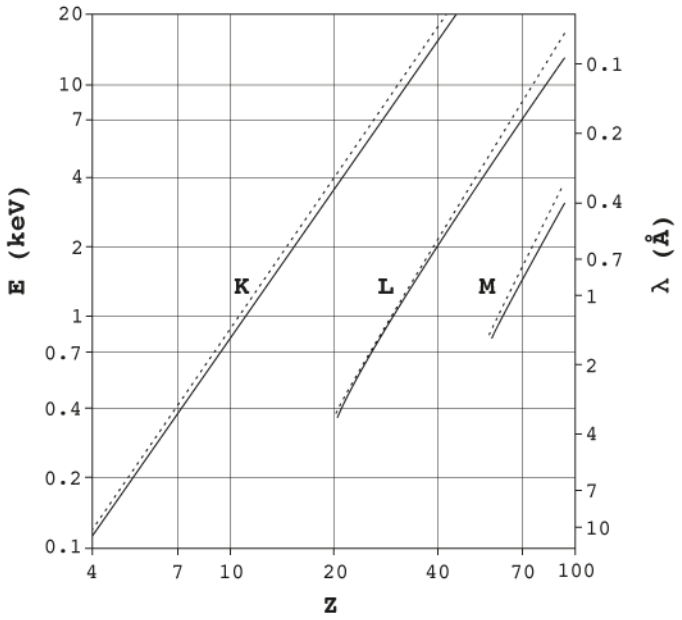

Figure 3.14: Resulting energy (E) and wavelength (λ) of $K\alpha$, $L\alpha$, $M\alpha$ lines (solid lines) relative to the atomic number (Z). Required excitation energies are shown in dashed lines. This diagram follows Reed (2005).

(usually there are several adjusted to one electron source in EMPA) are tuned to one wavelength at a time and operate in a serial mode. In a common EMPA several crystals of inter-planar latitude spacing are available that cover the required wavelength range. Therefore, WDX offers a significantly higher spectral resolution than EDX but is more time consuming and requires frequent peak scans for spectrometer calibration. The EMPA at the University of Potsdam is equipped with 5 WDX spectrometers that are adjustable with different analyzing-crystals. Some analyses were conducted at the German Research Center for Geosciences (German abbreviation: GFZ) in Potsdam. The EMPA there is similarly equipped, although the electron source is of a different type (field emission electron gun) and offers a higher resolution in imaging and in chemical analyses.

X-ray detection

The detection in EDX spectrometer is achieved with semiconductor materials that have fully occupied valence bands (usually silicon or germanium). These valence bands are separated by energy gaps, which in turn cause a very low conductivity at room temperatures (e.g. 1.1 eV for a gap in Si). Absorption of an X-ray photon generates Auger-Meitner electrons and photo-electrons in the EDX semiconductor. Electrons dissipate their energy by raising valence electrons to the conduction band. As a bias-voltage is applied to the semiconducting material, incoming X-ray photons create a pulse of current caused by pairs of electrons and 'holes'. The semiconductor front is usually covered by a thin layer of Au, which serves as a contact for the biasing voltage. A field effect transistor is attached to the semiconductor's back that serves as a pre-amplifier to the signal. The transistor requires constant cooling, which can be achieved with liquid nitrogen or electric refrigeration (depending on the type of semiconductor used). The entire set-up is adjusted in a high vacuum chamber that is equipped with a beryllium window, which allows the inlet of X-ray photons. EDX detection in the given study was used

for instant identification of phases and for checking the purity of separates for $^{40}Ar/^{39}Ar$ dating. Furthermore, EDX detection helped to roughly estimate the K-content in these phases. EDX and WDX are usually complementary in working with EMPA. However, the vast majority of EMPA measurements presented in the given thesis applied WDX detection. The according spectrometer employs a scattering of the incoming X-rays with respect to their wavelength. In dependence of the direction of the incoming X-rays, the intensity can be enhanced using evenly distributed atomic layers of an analyser crystal. Fig. 3.16 illustrates that scattered waves are in phase, where the difference between points A, B, C and A', B', C' is equal to an integral multiple of the incoming wavelength. The particular condition results in the reflection of X-rays of a certain wavelength by the atomic planes that have an interplanar spacing d. The certain angle of the incidence (θ) allows to establish a relationship that is widely known as Bragg's law (Bragg, 1913) and given in Eq. 3.33.

$$n \times \lambda = 2 \times d \times \sin\theta \tag{3.33}$$

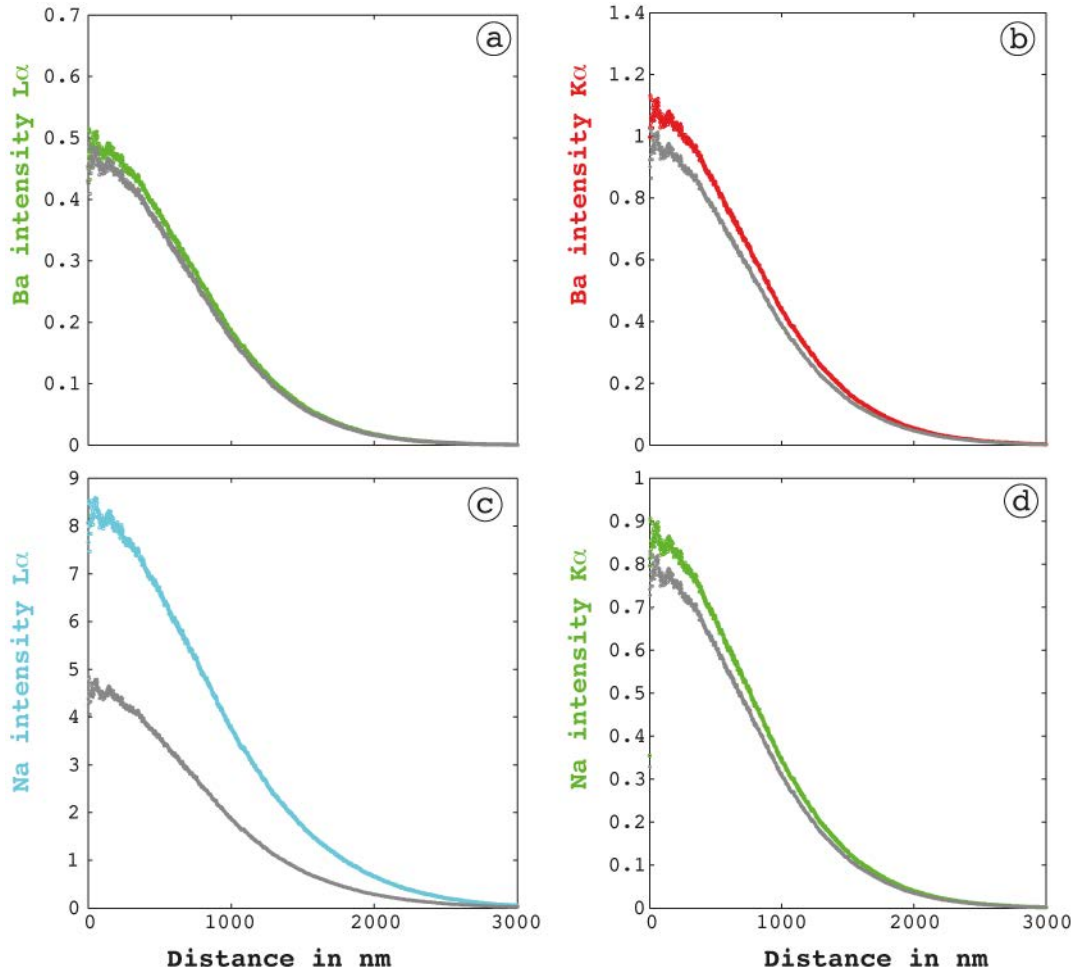

Figure 3.15: Generation of $L\alpha$ and $K\alpha$ intensities from Ba and Na depending on the lateral position within an anorthoclase crystal. The distance in the x-axis is radial from the beam centre (beam size: 2000 nm diameter). The total intensity produced by the incidental electron beam is given in colours, the absorbed intensity in grey. Modelling was conducted using the CASINO software from Drouin et al. (2007) and applied trajectories for 10,000 electrons with an acceleration voltage of 10 kV.

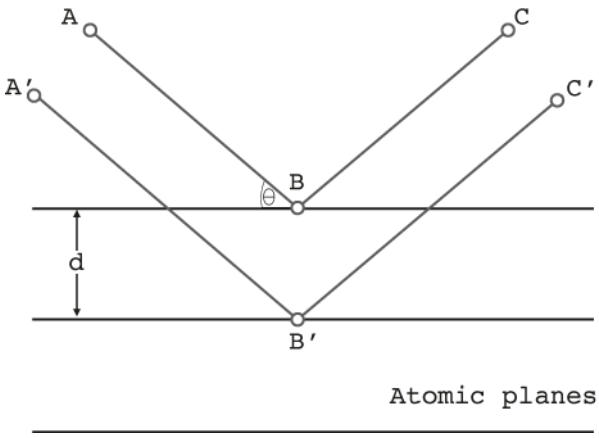

Figure 3.16: Simplified systematics of Bragg's reflection. The diffracted X-rays are in phase to each other if the distance A'B'C' differs from the distance ABC by an integral number of the incoming wavelength.

Bragg's law described the occurrence of constructive interference of scattered (or partly reflected) waves from a crystal lattice with respect to the angle of the incoming wave. The variable n is an integer and represents the order of the deflection. Most intense reflections are of first order and WDX spectrometers make usually a use of it (n=1). The range of wavelengths is limited for a given value of $2d$. Therefore, it is common practice to cover the full range of wavelengths of interest with several different crystals. The widely used crystals are lithium fluoride (LIF), thallium acid phthalate (TAP), and pentaerythritol (PET). As the ranges of accessible wavelengths by the different crystals overlap (Fig. 3.17), the EMPA operator needs to configure the available crystals. If two crystals cover a certain wavelength, the crystal that offers the smaller lattice spacing (d) is usually preferred (Fig. 3.18). Eq. 3.33 shows that smaller lattice spacing improves the resolution of the wavelength significantly. Crystals with lattice spacing larger than TAP are not available (Reed, 2005). This problem can be overcome by using artificially layered materials ('pseudo-crystals') that allow the detection of K-lines down to the atomic number of 4 (the element Be). These artificial 'layered dispersive element' (LDE) crystals are employing different components that are produced by evaporating alternate materials.

The detecting devices of WDX spectra are proportional counter (Skoog and Leary, 1992). They consist of gas-filled tubes that contain a coaxial wire, which is held with a positive potential. X-rays entering the gas through a window of the detector chamber cause an ionisation of some gas atoms that in turn generate free electrons and positive ions. The detector chamber walls function as an anode and the coaxial wire as a cathode. Thus, electrons and ions are attracted to the anode wire and to the body of the counter, respectively. The accelerated electrons cause an avalanche by further ionisation of gas atoms. This avalanche is recordable as pulse of an electrical charge appearing on the anode wire. The size of the pulse depends on the amount of ionized gas atoms, which in turn is proportional to the energy of the absorbed X-ray photon. Proportional counters are usually filled with Ar or Xe and have methane as an additive. Longer wavelengths need very thin inlet Be windows in order to minimize absorption whilst X-ray invasion. The large-wavelengths proportional counters are thus not completely sealing the counter body and a steady supply of gas must be guaranteed. Devices of these types are called 'flow counter'. The interpretation of shorter wavelengths, however, is employed with completely sealed counters. Common EMPA is usually equipped with both types of WDX detection and guarantees that

EMPA is capable of analysing the vast majority of characteristic wavelengths.

3.2.2 EMPA on feldspar

The vast majority of EMPA measurements presented in the given thesis were conducted on feldspar. Sample preparation was of a twofold character: (i) mounted sample aliquots of volcaniclastics were prepared as thin-sections and (ii) picked crystals that underwent separation procedure for $^{40}Ar/^{39}Ar$ analyses were mounted in epoxy. Whereas the samples in (i) gave an overview over the range of available feldspar compositions, the samples in (ii) showed the compositions of the picked crystals only and were embedded in the resin parallel to cleaved surfaces. Sample polishing was achieved with various steps using different grain sizes of silica carbide and diamond paste. Final polishing for EMPA analyses were 1 μm diamond sprays. Mounted samples and thin-sections were coated with a ca. 25-nm-thick layer of carbon in high vacuum (ca. 0.0002 torr) that is equipped with a carbon evaporation source. Thickness control was achieved by applying a fixed current and evaporation time that were optimized to the used evaporation source (carbon rods). All analyses on feldspar were conducted at the University of Potsdam using a JEOL JXA-8200 electron microprobe. The following section presents the instrumental set-up and adjustments for analysing feldspar. Furthermore, the methodology of modelling electron trajectories, excitation volume and energy distribution with the CASINO software (Drouin et al., 2007) is also presented.

JEOL JXA-8200 at the University of Potsdam

A thermal tungsten filament represents the electron gun in the EMPA at the University of Potsdam. Alternatively the probe can also be equipped with LaB6 filaments (JEOL, 2001). A high-precision sample stage (0.5 μm reproducibility) and a sub-μm beam focus allow resolving nm features in BSE and SEM imaging and sub-μm features in element mapping. The source is held at a negative potential of typically 10 to 25 kV. The maximum obtainable beam current is dependent to the electron source and the beam size. Whilst operating with a sub-μm-scaled beam for imaging in BSE and SEM modes, the current is usually about 0.1 to 1 nA. Widening the beam for WDX spot analyses also allows higher currents and thus more effective excitation of the sampled spot. Filament saturation was checked during operations on a daily basis in

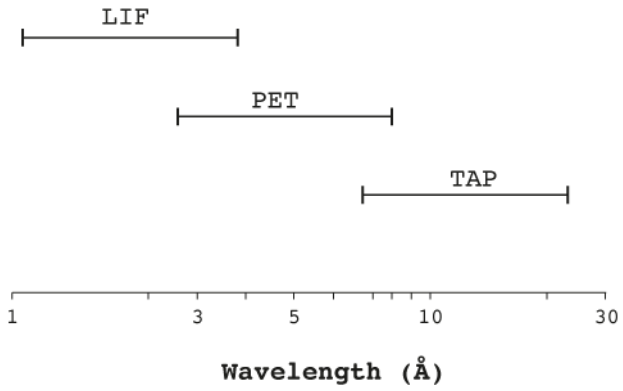

Figure 3.17: Coverage of wavelength using three different crystals in the WDX spectrometer.

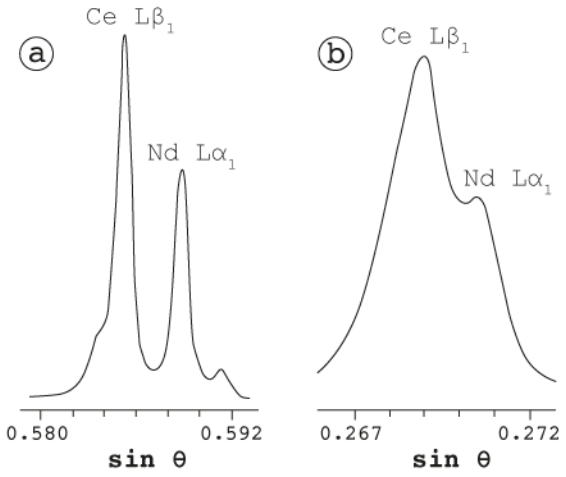

Figure 3.18: Wavelength-dispersive spectra resolving the Ca $L\beta_1$ and Nd $L\alpha_1$ X-ray lines with an LIF (a) and a PET (b) crystal. The diagram was taken from Reed (2005).

order to guarantee small beam sizes for imaging and insensitivity in variations of temperature. Furthermore, the occurrence of defocussing effects such as spherical aberrations and astigmatism were also checked on a daily basis. A stigmator is capable of adjusting the latter effect by observing the change in shape of the beam on cathodoluminescent benitoite (Ben163) as the lens is swept through the focus. The JXA-8200 is capable of working fully automated and conducting pre-programmed analyses and mappings without any staff- or operator-control. A point-logger system furthermore allows to define and to save spots that are of analytical interest by using another peripheral optical microscope. It allows observing samples in both reflecting and transmitting light. Recorded coordinates can than be recalled for analyses with the probe.

Most images were recorded in BSE modes. However, applying a cathodoluminescnce (CL) detector offered grey-scale images that represented light emission from the crystals from 200 to 1200 nm wavelengths (Ginibre et al., 2004). The grey-scaled CL images had the advantage of the ultimate comparison to WDX and EDX analyses. The probe is equipped with five WDX spectrometers that work with the following analyzer crystals: (i) LDE1, (ii) TAP, (iii) PETJ, (iv) PETH, (v) LIF, and (vi) LIFH. PETH, PETJ and LIFH crystals are modified versions of the PET and LIF crystals and are available products by JEOL. They are particularly useful in guaranteeing a high mid-range collection efficiency of these crystals (JEOL, 2001; Jercinovic et al., 2008). Elements above an atomic number of 11 are commonly recorded using TAP, PET, LIF crystals. The LDE1 crystal in the JXA-8200 can cover atomic numbers down to 5 (which is B). As the feldspars were expected to have Na as the lightest element, the set-up in Table 3.2 has been chosen for analyses of the chemical composition. The JXA-8200 at the University of Potsdam is equipped with an Oxford instruments silicon drift EDX detector. EDX detection was mainly used for instant phase identification and for estimating element composition.

Analyses were conducted with a defocused beam of 2000 nm width. The beam was generated with an accelerating voltage of 15 kV and had beam current of 10 nA. Counting times were 5 seconds for Na, Si, and K. All other elements were counted for 20 s. This adjustment allowed sensitive measurements of the elements Na, Si, and K, which behave fugacious under electron bombardment. Standards for quantitative analyses were throughout natural crystals of proven sample homogeneity (on a μm-scale) and assured purity. Standards have an in-house reference

Table 3.2: WDX spectrometer set-up for feldspar analyses in the given study. Sr has been measured in two different settings*. The $K\alpha$ line was measured during two settings in 2015. All other measurements interpreted $L\alpha$ lines.

Channel	CH1	CH2	CH3	CH4	CH5
Crystal	TAP	TAP	PETJ	LIFH	PETH
Element 1	Na $K\alpha$	Mg $K\alpha$	Ti $K\alpha$	Fe $K\alpha$	K $K\alpha$
Element 2	Si $K\alpha$	Al $K\alpha$	Sr $K\alpha$*	Mn $K\alpha$	Ca $K\alpha$
Element 3	Sr $L\alpha$*			Ba $L\alpha$	

Table 3.3: Typically used standards for analysing feldspar compositions in this study. Mineral abbreviations follow Whitney and Evans (2010).

Element	Na	Mg	Ti	Fe	K	Si	Al	Sr	Mn	Ca	Ba
Std. ID	37	117	115	117	109	108	108	162	123	106	163
Std. Min.	Alb	Hyp	Hbl	Hyp	Mc	Ano	Ano	Str	Fa	Pl	Ben

number that relates the standard to the supplier and to the mounted position on the respective standard mount (Table 3.3). The standards used for analyses represented similar purities and followed recommendations for standards of Jarosewich et al. (1979). Reference materials illustrated in Table 3.4 are dominantly official Smithsonian microbeam standards (Jarosewich, 2002). Standard selection in off-line corrections depended on the actual feldspar's composition. In order to represent the most similar element concentration Na was either referenced to albite (Ab37) or anorthoclase (An108). Furthermore K, Si, and Al were occasionally referenced to an in-house sanidine standard from the German Eifel. Table 3.4 offers furthermore identification codes of the Smithsonian United States Natural Museum (USNM-ID).

The obtained chemical compositions were corrected using the standard *Sun Microsystems* workstation software. The common ZAF corrections provide optimization for biasing effects from inadequately estimated mean atomic numbers, the amount of absorbed X-rays, and the co-excitement of characteristic X-rays that have similar critical excitation energies. The latter effect is overcome with applying a correction from characteristic fluorescence (F-correction) that corrects the effect of unwanted characteristic X-ray lines. For X-rays that are produced at depth within a sample the factor by which the intensity is reduced due to absorption is: $exp(-\xi\rho d)$. Where ξ is a parameter that combines the particular mass absorption coefficient (μ in Eq. 3.32) and the X-ray emission angle, ρ the sample's density, and d the depth of the X-ray source relative to the bombarded surface. The range of depths that host X-ray production can be described with a function $f(\rho d)$. Integration of both functions allows to determine an overall factor by which the intensity of X-rays are reduced due to absorption (A-correction). The efficiency with which characteristic samples are exited in the unknown sample is dependent to its average atomic number. X-ray intensities are dependent on the mass penetrated and increase with increasing Z. On the other hand, the correction for the loss of X-ray intensities is related to the occurrence of backscattered electrons that also increases with increasing Z. Thus, the two effects almost completely counterbalance each other (slight domination of the backscattering effect). However, samples that have a higher average atomic number than the standard need an upward directed correction according to the difference in Z (Z-correction).

Final data was exported as wt% and recalculated as atoms per formula unit of feldspar (apfu). An exemplary recalculation that involves a full error propagation is presented in the electronic supplementary materials of Engelhardt et al. (2017).

Table 3.4: List of mineral standards used to measure chemical compositions with JXA-8200 at the University of Potsdam. Mineral standards marked with an asterisk are not referenced in Jarosewich et al. (1979) and in Jarosewich (2002). All other standards are referenced in these publications. The pyrite represents an in-house standard from the University of Bern. Detailed determination of the chemical compositions of the gem-quality Volkesfeld sanidine is presented in Weitz (1972) and in Hofmeister and Rossman (1984). An albite in-house standard was rarely used for analysing anorthoclase with highest Na concentrations.

Mineral	Stdandard-ID	In-house ID
Albite*	none	37
Bytownite	USNM 11590	106
Anorthoclase	USNM 133868	108
Microcline	USNM 1143966	109
Hornblende	USNM 143965	115
Augite	USNM 164905	116
Hypersthene	USNM 746	117
Forsterite (Fo_{82})	USNM 2566	118
Forsterite (Fo_{90})	USNM 111312	119
Fayalite	USNM 85276	123
Pyrite*	C/011 - Bern	137
Siderite	USNM R2460	161
Strontianite	USNM R10065	162
Benitoite	USNM 86539	163
Sanidine*	Volkesfeld Sanidine	none

CASINO modelling

Chapter 8 deals with interpretations of data from step scanning across a compositional or a trace-element zoning of feldspars. In order to find optimum step sizes for step scanning analysis, preliminary results from EMPA measurements were modelled in the CASINO software (Drouin et al., 2007). Therefore, instrumental settings (acceleration voltage, beam size, etc.) were recorded and entered in CASINO with respective sample composition. Modelling approaches were conducted with 8000 to 15.000 electrons and with 10 to 15 kV acceleration voltage. In order to calculate an adequate estimate for the average atomic number (Z in Eq. 3.30), the chemical composition of the feldspars was normalized to atomic fractions of the elements of Na, Al, Ti, Fe, K, Si, Ca, Ba, and O. Facing compositionally zoned feldspars from V-45 and V-221a, modelling was conducted for each of the different compositions. Furthermore, a carbon coating of 25 nm was considered in the simulations. Knowing the lateral extend of the excited area for several analytical conditions also allowed applying deconvolution calculations for those steps that contained data from a mixed phase in compositionally zoned feldspar (Ganguly et al., 1988). The approach in the given study was to use the 'energy by position' distribution in CASINO (Drouin et al., 2007). This feature interprets the simulated data in a three-dimensional array that is defined by the operator in terms of resolution and extent. The 'energy by position' parameter is the amount of energy lost by electrons along their trajectories. Resulting data can be exported as raw data sets. A Matlab code was used to import, sort and organize the simulations from CASINO. Following this approach the extent of the excited volume in feldspar was treated as a Gaussian intensity distribution, which has a radial symmetry. Cross-section contours were derived from projecting the cumulative data on a two-dimensional surface that shows a depth versus lateral extend plot (Figs. 3.19a and 3.19c). Projecting the data cumulatively in one dimension revealed the Gaussian distribution of the energy distributions (Fig. 3.19b and 3.19d) and allowed the calculation of the standard deviation (σ) of the maximum energy location underneath the centre of the electron beam. Fig. 3.19 reveals that anticorrelated Ca and K contents cause slightly different excited volumes with σ-values of 777 nm and 862 nm. Besides interpreting the data in cross-sections, contour plots of the energy distribution in a two-dimensional top-view (Fig. 3.19e) are also available from CASINO simulations.

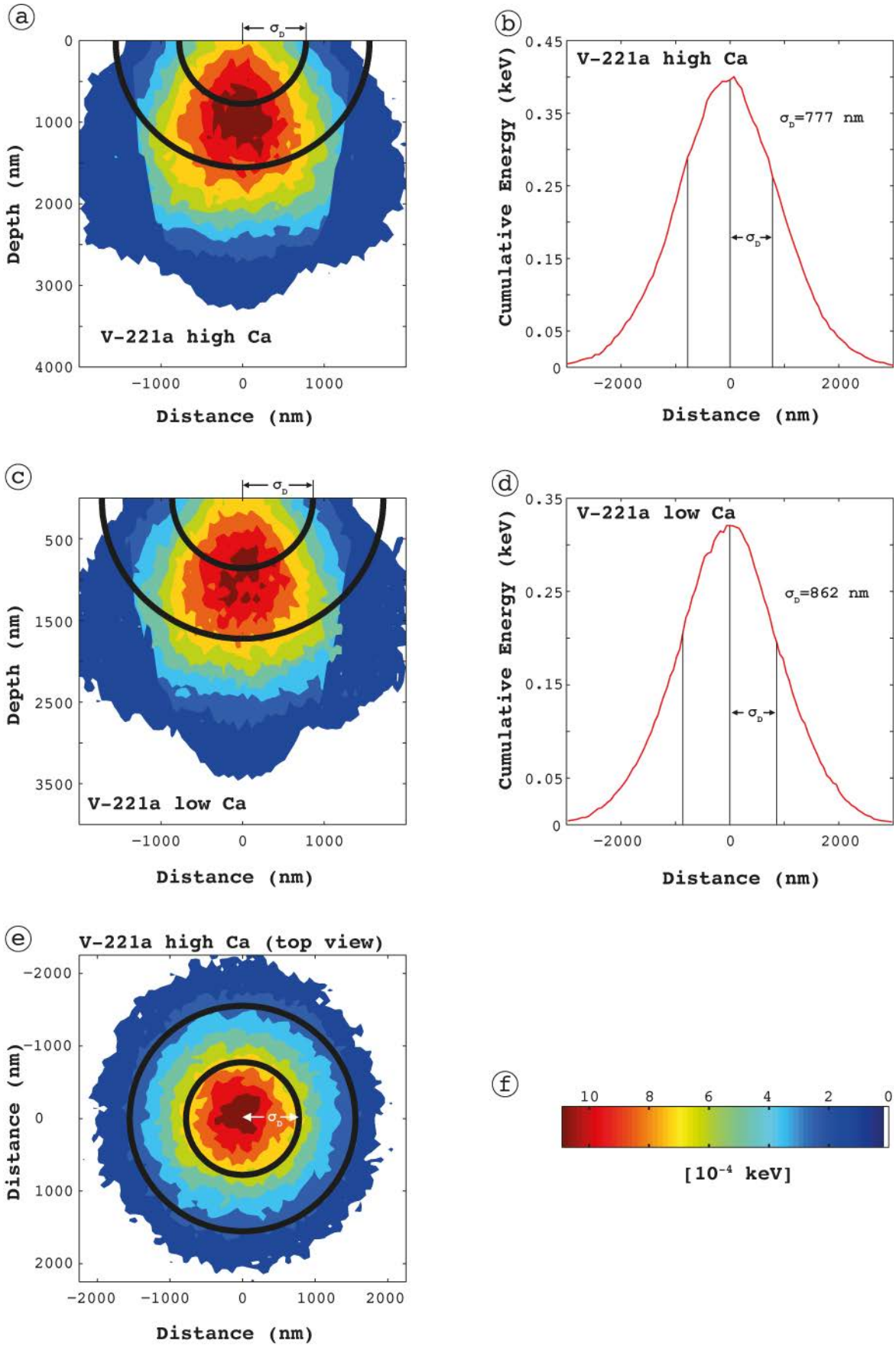
a
σD
Depth (nm)
V-221a high Ca
Distance (nm)
b
V-221a high Ca
σD=777 nm
Cumulative Energy (keV)
Distance (nm)
c
σD
Depth (nm)
V-221a low Ca
Distance (nm)
d
V-221a low Ca
σD=862 nm
Cumulative Energy (keV)
Distance (nm)
e
V-221a high Ca (top view)
Distance (nm)
f
[10-4 keV]

Figure 3.19: (previous page) CASINO simulation of the energy distribution in anorthoclase feldspar from sample V-221a. The sample has two compositionally contrasting domains. Results from simulations with the composition from a Ca-rich domain (> 0.1 apfu) are shown in (a), (b) and (e). Simulations representing excitation in a Ca-poor domain (< 0.05 apfu) are shown in (c) and (d). Illustrating the excitation in the Ca-rich domain in a top view is shown (e). The other two energy distributions are cross-sections. Colour-coding of the contour plots is illustrated (f).

3.2.3 EMPA on volcanic glass

A small number of measurements of volcanic glass were conducted at the University of Potsdam using the settings described in Section 3.2.4. These measurements, however, were semi-quantitative estimations of the chemical composition. The dominant amount of EMPA measurements on volcanic glass was conducted with a JEOL hyperprobe JXA-8500F at the GFZ Potsdam. The according analytical set-up and procedures are presented in the following briefly. The main advantage of the JXA-8500 is the electron gun. The development of the thermal field-emission gun (TFEG) allowed electron beams to be significantly brighter and smaller than tungsten filament guns. The advent of TFEG to microprobe analysers has dramatically improved the spatial resolution of electron beam analytics (Armstrong et al., 2013). In TFEG, electrons are drawn from a tungsten tip by strong electric fields. The TFEG of the JXA-8500 is a 'Shottky' type emitter, which has a tungsten tip that is usually coated with ZrO around its stem in order to enhance electron emission. Beam adjustment and correction methods of X-ray intensities are widely identical to the procedures described in chapter 3.2.2 as the probe is similarly operated with *Sun Microsystems* software. WDX analyses were conducted with a widely defocused electron beam of 10 μm in diameter. By using 15 keV energy and 2 nA beam current, a comparably low current density (of 0.025 nA/μm^2) was achieved (the settings for analysing feldspar resulted in a current density of 3.183 nA/μm^2). The low current density was envisaged in order to avoid sodium migration, which is a major obstacle in analysing rhyolitic glasses (Morgan and London, 1996; Morgan and London, 2005). Acquisition times varied between 10 seconds (K, Na, and Si) and 20 seconds (Ca, Fe, Al, Ti, Cl, Mn, F, P, Ba, S, Zn, and Mg). The acquisition time to collect the background level on either side of characteristic X-ray lines of the corresponding peak was half the time of peak acquisition. WDX analyses employed the following standards: tugtupite for for Si, Al, Na and Cl; orthoclase for K; fluorite for F; diopside for Mg and Ca; rutile for Ti; rhodonite for Mn; apatite for P and Ba; sphalerite for Zn and S. Spectrometer and crystal adjustment are summarized in Table 3.5.

ZAF-corrected data is summarized in this study as wt% oxides. However, the calculation of molar oxide fractions was needed for the calculation of alteration indices and followed a calculation procedure suggested by Price and Velbel (2003).

Table 3.5: WDX spectrometer set-up for glass analyses in the given study.

Channel	CH1	CH2	CH3	CH4	CH5
Crystal	TAP/LDE1	PETJ	PETJ/LIF	TAP	LIFH
Element 1	Si Kα (TAP)	K Kα	Ca Kα (PETJ)	Na Kα	Fe Kα
Element 2	Al Kα (TAP)	Ti Kα	Cl Kα* (PETJ)	Mg Kα	Mn Kα
Element 3	F Kα (LDE1)	P Kα	Ba Lα (PETJ)		
Element 4		S Kα	Zn Lα (LIFH)		

Table 3.6: WDX spectrometer set-up for analyses of various phases in the given study.

Channel	CH1	CH2	CH3	CH4	CH5
Crystal	TAP	TAP	PETJ	LIFH	PETH
Element 1	Na Kα	Al Kα	Mn Kα	Fe Kα	K Kα
Element 2	Si Kα	Mg Kα	Ti Kα	Cr Kα	Ba Kα
Element 3			S Kα	Caα	Sr Kα

Table 3.7: Standard setting for analyses of plagioclase and pyroxene. Plagioclase did not receive an off-line correction. Aluminium concentrations were off-line corrected for the analyses of pyroxenes with using standard No. 113 (augite)*. Depending on the amount of iron in pyroxenes, Fe concentrations were off-line corrected with standard No. 117 (hypersthene with 15.2 wt% FeO)**.

Element	Na	Al*	Mn	Fe**	K	Si	Mg	Cr	Ba	S	Ca	Sr
Std. ID	106	106*	161	115**	109	106	115	116	163	137	106	162
Std. Min.	Pl	Pl*	Sd	Hbl**	Mc	Pl	Hbl	Aug	Ben	Py	Pl	Str

3.2.4 EMPA on various phases

Some approaches of EMPA presented in this study had phase identification as a main target. A precise mineral composition was not necessary for such a purpose. Clinopyroxenes (CPX) were among the most frequently investigated phases and thus settings were optimized to analyse these phases with sufficient precision. Other phases were regarded as measurements in non-optimum analytical set-ups and were dominantly: plagioclase, olivine (fayalite), quartz, Fe-Ti oxides, glass shards, apatite and amphibole. Table 3.6 presents the instrumental set-up for measurements of the various phases. Standards for the analyses of CPX, plagioclase and olivine are presented in Table 3.7. Measurements on other phases received post-analytical off-line corrections in order to gain higher precision in determination of the mineral composition.

The varying element content in analysing CPX and plagioclase is most significant for measuring Al. Thus, Al was off-line corrected for data from pyroxenes. Fe-rich hedenbergite and ferrohedenbergite were offline-corrected with a hypersthene standard for the determination of FeO. Other than these off-line corrections, the standardisation for element characterisation of pyroxenes and plagioclase was identical. Besides CPX, plagioclase and volcanic glass, olivine was frequently analysed. The according standard setting is similar to the setting presented for plagioclases above. However, off-line corrections were made for Si, Mg, and Fe. The final standard setting for the calculation of olivine composition is presented in Table 3.8. All standards involved in calculating chemical compositions of the various phases used the list of standards that is given in Table 3.4.

3.3 X-ray fluorescence spectrometry

Major elements and selected trace elements from bulk lapilli or bulk ash aliquots were determined using x-ray fluorescence spectrometry (XRF) on fused lithium tetra borate discs. 49 out of 51 samples were analysed using XRF. The following section provides the theoretical background to XRF analyses and to analytical procedures for analyses in the given study. Most information presented about the theory are taken from Skoog and Leary (1992), Beckhoff et al. (2005) and Haschke (2014).

Table 3.8: Full standard setting after off-line correction for calculation of the fayalite mineral compositions. Elements that were off-line corrected are marked with an asterisk.

Element	Na	Al	Mn	Fe*	K	Si*	Mg*	Cr	Ba	S	Ca	Sr
Std. ID	106	106	161	119	109	123	119	116	163	137	106	162
Std. Min.	Pl	Pl	Sd	Ol	Mc	Fa	Ol	Aug	Ben	Py	Pl	Str

3.3.1 XRF in theory

XRF is in its methodology partly analogue to X-ray dispersive spectrometry described in Section 3.2. The major differences is that the sampled material is not excited with an electron beam but with short wavelength of either X-rays or Gamma-rays. Similarly to analyses in EMPA, the excited sample dislodges inner orbital electrons and ionizes partly. Vacancies in lower orbitals open up and electrons from higher energy potentials fall into the lower order vacancies. The refill of electron vacancies to lower energy levels releases a characteristic secondary radiation: fluorescent X-rays (Fig. 3.20). The fluorescent radiation is basically a flux of photons. These photons are released as electrons move to lower orbitals in order to stabilize the excited atom. As the binding energy in the low orbital is less than in the one of a higher order, the surplus in energy releases the fluorescent photons. The released energy is roughly equal to the difference in the binding energy of the electron orbitals that are involved. The secondary radiation is characteristic to the element that got excited by the primary X-ray. Similar to the wavelength-dispersive spectrometry of X-rays in EMPA, fluorescent radiation is reflected using analyzing crystals. Following relations shown in Bragg's equation (Eq. 3.33), the resolution of the wavelength of a characteristic fluorescence can be significantly increased and allows an almost 'isolated' detection. This isolated detection employs a specific combination of analyzing crystals and angels for each element. The nomenclature on characteristic X-ray lines that was introduced for the EMPA (Section 3.2) is equivalent to the interpretation of the spectra gained in XRF. However, a difference needs to be outlined in describing the beam-sample interaction and thus also in the conducted matrix-corrections. Contrasting to the characteristic X-rays detected in EMPA, XRF analyses require an absorption correction that considers the primary radiation intensity. Here, the absorption depends on the mass attenuation coefficient (μm), the density of the sample (ρ), the primary intensity (I_0), and the thickness of the absorbing material (t). It

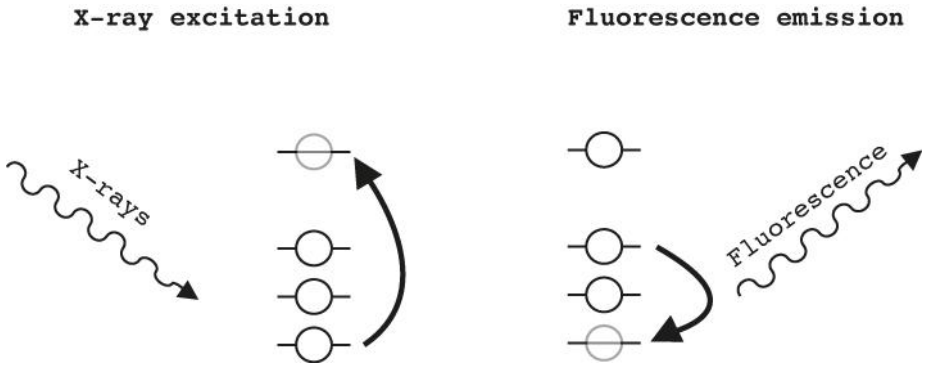

Figure 3.20: Simplified illustration of X-ray excitation and fluorescent X-ray emission.

can be described by the Lambert-Beer-law.

$$I = I_0 \times \exp^{-(\mu m \times \rho \times t)} \tag{3.34}$$

The mass attenuation coefficient depends on the mass absorption coefficient of the particular elements involved in the unknown and their mass fraction. Measured X-ray intensities of an element depend not only on instrumental conditions and the weight fraction of the element itself. The gained intensities have furthermore to consider the potential influence of all other elements in the sample. The Sherman-equation corrects for the matrix effects on a first order basis. In the dependence of the accuracy needed, corrections of third order and second order can be considered. The following equation represents the 'fundamental-parameter-approach' after Sherman (1954).

$$I_i = G \times \int_E \frac{w_i \tau_i(E) \frac{S-1}{S} p_i \omega_i}{\frac{\mu(E)}{\sin \Psi_{ein}} + \frac{\mu(E)}{\sin \Psi_{aus}}} I_0(E) \times dE \tag{3.35}$$

In Eq. 3.35 the intensity of the element i (I_i) is described with the following parameters:

- G - geometry factor
- τ - linear absorption coefficient
- $(S-1)/S$ - jump ratio
- p - transition probability
- ω - fluorescence yield
- w - weight fraction
- μ - linear mass absorption coefficient
- E - energy
- Ψ - incident and take-off angles
- $I_0(E)$ - excitation spectrum

This equation describes the intensity of an element as a function of excitation, geometry, and weight fractions of the element. The latter is actually the unknown. In an analytical situation the situation is vice versa: the intensities are measured and the element weight fractions need to be calculated. A relationshipt would be required like

$$w_i = f(I_i, M) \tag{3.36}$$

that describes the weight fractions with a functional relationship (f) of the intensity (I_i) and a description of all relevant matrix interactions (M). Unfortunately, this relation is impossible and approximations to this relationship are used. An element of interest is therefore corrected with a functional relationship to the measured intensity and the weight fraction of all other expected elements.

$$w_i = f(I_i, w_j) \tag{3.37}$$

In Eq. 3.37 the subscript i refers to the element of interest, the subscript j to all other elements. Concentration correction models that apply iterative solutions, overcome the problem that the weight fractions of all other elements are still unknown. In practice, linear and exponential fitting is used to estimate the influence of the matrix elements.

$$w_j = a \times I_i \tag{3.38}$$

The factor a in Eq. 3.38 represents the sensitivity and replaces all kinds of variables that are needed to define a linear or an exponential equation. Eq. 3.38 can be changed to the following relationship.

$$w_i = f(I_i, I_i) \tag{3.39}$$

This functional relationship offers parameters that can be calculated from the measured spectrum and allows an iterative solution for the intensity correction. Several iterative models are described in greater detail elsewhere (e.g. Lucas-Tooth and Price, 1961). A detailed description of the theories exceeds the aim of this theoretical explanation. However, main input factors in these models are the instrument's sensitivity and factors describing potential element overlapping. Both factors require a calibration procedure, which is achieved by measuring samples of precisely known weight fractions. Certified materials and reference samples are therefore usually approved by inter-laboratory analyses. Finally, measured intensities from these reference materials are correlated with the known standard weight fractions, apply a suitable quantification model, and result in a calibration curve. The correlation allows the determination of the correction coefficient, which is applied for the quantification of the elements in the unknown samples (Fig. 3.21). Before calibration curves are applied an adequate intensity determination of the peak is required. Therefore, total counts are calculated by defining a peak area that is separated from the background and corrected for escape peaks and separated from overlapping peaks. Additionally, corrections for the sensitivity of the detector, for the absorption of the detector's window, for geometric effects and for the excitation spectrum are considered as well. XRF spectra evaluation requires in summary the following procedure: (i) peak identification, (ii) calculation of the peak area, and (iii) calculation of quantitative results by using calibration curves (Haschke, 2014). Together with frequent standard analyses, these steps are usually software automatized and common practise in modern XRF spectrometers.

3.3.2 XRF on bulk samples from PALEOVAN cores

A number of 49 bulk-rock samples were grinded to homogenous powders < 62 μm in vibrating agate-disc-mills. Sample aliquots were processed as fused discs for XRF analyses, as tin capsules for combustion analyses of volatiles, and as chemical digestions for determination of the Fe^{2+} content. Each process will be described separately in the following.

H_2O^+ and CO_2 analyses

The weight fractions of crystal water (H_2O^+) and CO_2 were determined by oxidative combustion of sample powder in tin capsules (Zn). Combustion was achieved explosively in an O_2-enriched He-atmosphere. The combustion transferred C, H, N, and S gases into N_2, CO_2, H_2O, NO, NO_2, and SO_2. Oxides of nitrogen were reduced via Cu to N_2. A thermodiode analysed the gasses in a

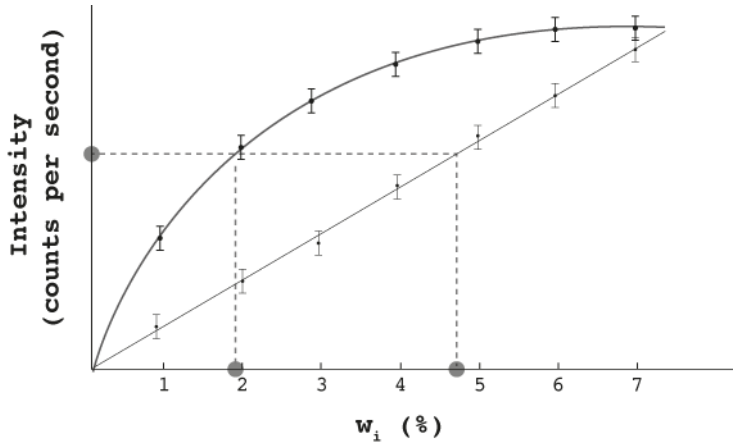

Figure 3.21: Two schematic empirical calibrations of standards of known concentration. The empirical calibration will be fitted with a linear regression if there are hardly any influences from co-existing elements and matrix. Dashed lines show the difference between a strongly and a hardly corrected measurement of an element fraction. Diagram was plotted following Haschke (2014).

thermal conductivity cell. The diode, however, is not specific for the particular gases and has to separate the mix of He, N_2, CO_2, H_2O, and SO_2 prior to actual analysis. Therefore, the sample gas had to pass a chromatographic column first. The gasses were separated with respect to their molecular size and were measured in the following order: N_2, CO_2, H_2O, and SO_2. A EuroVector EA 3000 element analyser analysed the extracted gasses. This unit is particularly optimized for methods that use He as a carrier gas (Eksperiandova et al., 2011). The EA 3000 is a double chamber element analyser that detected the thermal conductivity (TCD) of sample gases in a constant flux of He carrier gas in one and the TCD of the carrier gas only in a reference unit. The TCD is measured with a filament in the unit. Whenever an analyte elutes, the TCD of the column effluent is reduced and the filament heats up and changes its electrical resistance. Thus, an electric potential between the two filaments is proportional to the amount of sample gas. The cell's signal is recorded with respect to the temporal duration of the signal relative to the flux. A software recording all parameters allows the quick calculation of the weight fraction of the analysed gasses. Prior to every measurement procedural blanks are analysed and their results are used for corrections of the analyses. Detection calibrations were conducted on a daily basis. Gas measurements were conducted prior to XRF measurements and their results considered as %LOI (the loss of ignition), which occurs during preparation of the sample material to fused analysis discs.

Fused discs analyses

Masses of 6.0000 ± 0.0001 g Fluxana FX-X 65 (66 % lithium tetraborate [$Li_2B_4O_7$] and 34 % lithium metaborate [$LiBO_2$]) were homogenously mixed with 1.0000 ± 0.0001 g of sample material and 0.5000 ± 0.0001 g ammonium nitrate (NH_4NO_3). The powder mixes were vitrified using five heating torches with temperatures of ca. 400°C, 500°C, 600°C, 1050°C, and 1150°C. Analyses were conducted using a PANanalytical AXIOS Advanced spectrometer at the GFZ Potsdam that employs six analyser crystals (LIF, PX1, PX8, PX10, Ge111 and PE002). Two sets of collimators narrowed fluorescent X-rays that either range from 150 to 330 to 700 μm (primary collimator) or from 6 to 10 to 20 to 27 to 30 to 37 μm (secondary mask collimator).

Detection was achieved with Ar-flow proportional counters as well sealed Xe-detectors. The X-ray source was produced with a 50 kV acceleration voltage and a 45 mA beam current.

Titration of Fe^{2+}

The approach of oxidation of ammonium metavanadate (NH_4VO_3) was used for discriminating the amount of Fe^{2+} in the sample (Wilson, 1955). The according procedure applies the chemical digestion with hydrofluoric acid and first employs the following reaction.

$$(V^{V}O^{+})_2 + Fe^{2+} + 2H^{+} -> V^{IV}O^{2+} + H_2O + Fe^{3+} \tag{3.40}$$

In a second step the vanadium excess is reduced via adding a defined amount of ammonium iron sulphate solution (containing Fe^{2+}) to the chemically digested sample. The surplus of Fe^{2+} is finally titrated back with adding potassium dichromate ($K_2Cr_2O_7$). The titrated amount is determined potentiometrically.

$$(Cr_2O^{2-})_7 + 6Fe^{2+} + 14H^{+} -> 2Cr^{3+} + 6Fe^{3+} + 7H_2O \tag{3.41}$$

The workflow requires dry sample materials. Samples are accordingly dried in an oven at 105°C for minimum two hours. Cooling to standard conditions is achieved by keeping the samples in a desiccator. Weighing the sample is then conducted in the polyethylene (PE) wide neck bottles that already represent the vessels for the later chemical digestion. In dependence to the (expected) weight fraction of FeO in the samples, the aliquots were weighted to 0.1 g (5 to 12 wt%), or 0.2 g (< 5 wt%). Two aliquots per sample were chemically digested and titrated together with two procedural blanks and one standard of known FeO. The aliquots were mixed thoroughly with 2 ml of 40 % HF and 1 ml of 0.2 molar NH_4VO_3 solution. Subsequently, the samples were rested overnight in order to guarantee an effective performance of the reaction in Eq 3.40. The samples rested another two hours after adding 50 ml of 4.8 % H_2BO_3 solution. Just prior to titration 10 ml of 96 % H_2SO_4 and 10 ml of 0.1 molar $(NH_4)_2Fe(SO_4)_2$ solutions were added. The solutions were then stirred with a magnetic stirrer. An electrode was dipped into the solution in order to record the electric potential. Titration is conducted with 0.025 molar $K_2Cr_2O_7$ solution and the equivalence point was recorded in observing the strongest increase in conductivity. Finally the wt% fractions of FeO were calculated using the following formula.

$$FeO(wt\%) = \frac{(Uptake_{Sample}\,[ml] - Uptake_{Reference}\,[ml]) \times 0.025\,[mol/l] \times 71.846\,[g/mol]}{m_{Sample}\,[g] \times 10} \tag{3.42}$$

In this equation the variable "Uptake" represents the amount of titrated $K_2Cr_2O_7$ and m the mass of the sample. Units are presented in square brackets. The weight fraction of Fe_2O_3 was corrected with Eq. 3.43.

$$Fe_2O_3(wt\%) = (Fe_2O_3)_{total} - 1.1 \times FeO_{titration} \tag{3.43}$$

$(Fe_2O_3)_{total}$ refers to the total iron measurement in the XRF spectrometer. Equation 3.43 follows a suggestion of Rollinson (1993).

4 Feldspar $^{40}Ar/^{39}Ar$ Dating of ICDP PALEOVAN Cores

This chapter represents a quotation of a publication by Jonathan Franz Engelhardt, Masafumi Sudo, Mona Stockhecke, and Roland Oberhänsli in Geochimica et Cosmochimica Acta. Except for formatting the layout, the following chapter is identical to the publication. All rights of this chapter remain reserved to Elsevier Ltd.

4.1 Abstract

Volcaniclastic fall deposits in ICDP drilling cores from Lake Van, Turkey, contain sodium-rich sanidine and calcium-rich anorthoclase, which both comprise a variety of textural zoning and inclusions. An age model records the lake's history and is based on climate-stratigraphic correlations, tephrostratigraphy, paleomagnetics, and earlier $^{40}Ar/^{39}Ar$ analyses (Stockhecke et al., 2014a). Results from total fusion and stepwise heating $^{40}Ar/^{39}Ar$ analyses presented in this study allow for the comparison of radiometric constraints from texturally diverse feldspar and the multi-proxy age model and vice versa. This study has investigated several grain-size fractions of feldspar from 13 volcaniclastic units. The feldspars show textural features that are visible in cathodoluminescence (CL) or back-scattered electron (BSE) images and can be subdivided into three dominant zoning-types: (1) compositional zoning, (2) round pseudo-oscillatory zoning and (3) resorbed and patchy zoning (Ginibre et al., 2004). Round pseudo-oscillatory zoning records a sensitive alternation of Fe and Ca that also reflects resorption processes. This is only visible in CL images. Compositional zoning reflects anti-correlated anorthite and orthoclase contents and is visible in BSE. Eleven inverse isochron ages from total fusion and three from stepwise heating analyses agree with the age model. Four experiments resulted in older inverse isochron ages that do not concur with the model within 2σ uncertainties and that deviate from 1 ka to 17 ka minimum. C- and R-type zoning are interpreted as representing growth in magma chamber cupolas, as wall mushes, or in narrow conduits. Persistent compositions of PO-type crystals and abundant surfaces recording dissolution features correspond to formation within a magma chamber. C-type zoning and R-type zoning have revealed an irregular incorporation of melt and fluid-inclusions. These two types of zoning in feldspar are interpreted as preferentially contributing either heterogeneously distributed excess ^{40}Ar or inherited ^{40}Ar to the deviating $^{40}Ar/^{39}Ar$ ages that are discussed in this study.

4.2 Introduction

$^{40}Ar/^{39}Ar$ analyses of alkali feldspar phenocrysts commonly date late stage cooling processes in Quaternary volcanics with <5% precision (Hu et al., 1994; Bogaard, 1995; Chen et al., 1996; Smith et al., 1996; Mark et al., 2014, and literature herein). Studies on extraneous radiogenic ^{40}Ar from disaggregated cognate crystals (antecrysts) from earlier magmatic pulses (Chen et al., 1996; Gansecki et al., 1996; Rivera et al., 2016), from mixed phases (Kelley, 2002), and from

complex heterogeneous growth histories (Ginibre et al., 2004; Renne et al., 2012) challenge the interpretation of quaternary $^{40}Ar/^{39}Ar$ ages from ternary feldspar. Air fall volcaniclastics in lacustrine ICDP drill cores from Lake Van, Turkey, bear sodium rich sanidine and calcium-rich anorthoclase combining the features mentioned. Stockhecke et al. (2014a), Stockhecke et al. (2014b), and Stockhecke et al. (2016) established an age model for Lake Van's history that is based on climate-stratigraphic correlations, paleomagnetics, tephrostratigraphy, varve counting, and ^{14}C and $^{40}Ar/^{39}Ar$ analyses of the sedimentary record from ICDP PALEOVAN (Litt et al., 2014). Recovering material from seven adjacent boreholes at the Ahlat Ridge (AR) resulted in a 219-m-long composite record that contains lacustrine and volcaniclastic material and presumably records the complete, ca. 600-ka-long history of Lake Van (Stockhecke et al., 2014a; Stockhecke et al., 2014b; Stockhecke et al., 2016). A second composite record from the Northern Basin (NB) is rich in detrital material and covers a ca. 90-ka-long history that correlates to the upper record from AR (Çağatay et al., 2014). The volcanic edifices of Nemrut and Süphan dominate the eastern and northern shore's landscape (Fig. 4.1). They have periodically (Nemrut) and episodically (Süphan) supplied abundant volcaniclastic material throughout the lake's lacustrine history (Çubukçu et al., 2012; Özdemir and Güleç, 2013; Sumita and Schmincke, 2013b; Sumita and Schmincke, 2013c; Schmincke et al., 2014; Macdonald et al., 2015). Anorthoclase crystals reflecting texturally and chemically complex growth histories are ubiquitous in the cored air fall volcaniclastics. Applying laser heating $^{40}Ar/^{39}Ar$ analyses of these samples allows for the comparison of textural observations with resulting isotopic signatures as well as the temporal constraints from either radiometric or cyclo- and climate- stratigraphic methods. Final $^{40}Ar/^{39}Ar$ dates have been tested for concordance with the existing age model and vice versa. This work further discusses results from applying the $^{40}Ar/^{39}Ar$ total fusion and stepwise heating methods to zoned, K-poor feldspar with respect to detected zoning types and melt (as well as fluid) inclusions.

4.3 Materials and methods

4.3.1 Sample properties

Three hundred volcaniclastic layers have been identified and serially numbered in the AR record (Stockhecke et al., 2014b). Feldspars from 13 tephras were processed for irradiation prior to $^{40}Ar/^{39}Ar$ analytics. Syn-ignimbrite turbidites and reworked fallouts potentially bear epiclastic components that affect radiometric dating approaches. Thus, with respect to the application of the $^{40}Ar/^{39}Ar$ method, pumice falls were preferably sampled. Aqueous deposition of fallout material results in variations of pyroclast and phenocryst abundance, relative to stratigraphic positions within a tephra horizon (Chesterman, 1956). The clasts' different densities and buoyancies result in different settling behaviour, impeding a typical interpretation of volcano-stratigraphic features (Hansen et al., 1963; White et al., 2009). Material was sampled from tephra with thicknesses from 3 to 90 cm. Prerequisites for sampling were sharp basal and diffuse upper contacts, the absence of non-volcanic debris, grading features related to the density of the pyrogenic components, and angular pyroclast morphology. The samples' granulometric classification mostly ranges from coarse ash to lapillis (often as inverse grading within one tephra layer, Fig. 4.2b and 4.2d). Sample V-111 represents a fine-grained ash layer. This ash bears abundant

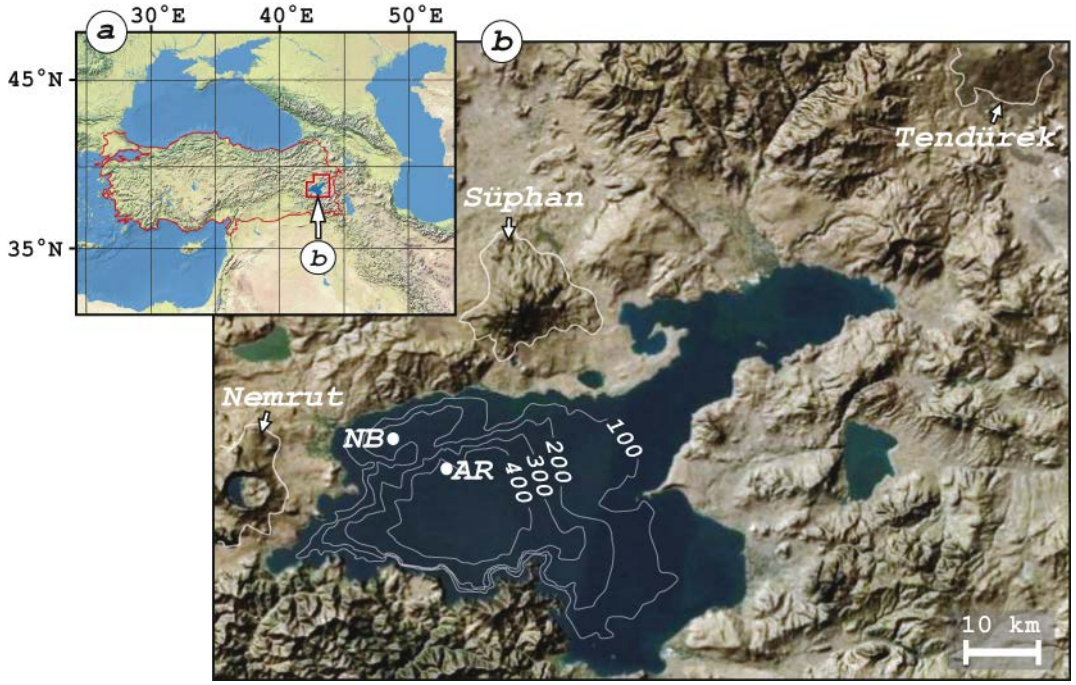

Figure 4.1: Location of Lake Van, Turkey (a) and local ICDP drill site (b). NB: Northern Basin; AR: Ahlat Ridge. Lines without labelling frame the steepest slopes of three volcanic edifices. Labelled contour lines indicate water depth after Stockhecke et al. (2014b). The thin red line in the topographic map (a) represents the spatial extent of Turkey. The digital elevation model for the hill shade map is from NASA, powered by USGS and ESRI, 2015.

feldspar and fine-grained glass shards (< 300 μm) in a cryptocrystalline ground-mass. Sparse pumice abundance is related to sub-cm stratigraphic variations (Fig. 4.2c). Samples V-111 A and V-111(B) are from the same deposit and have been used to test the sampling method. The petrographic inventory of the coarser samples varies. Material from V-184 and V-299 has a mineral composition that is characterised by plagioclase, augite, fayalite, hedenbergite and hypersthene. Plagioclase is corroded, oscillatory zoned and oligoclase to andesine in composition (An_{13}-An_{32}). Less abundant lithic fragments show vitric ground-masses and varying contents of microlites (mostly plagioclase). Ophitic and glomerocrystic lapilli of plagioclase together with clinopyroxene rarely exist. Iron-titanium oxides occur as inclusions in olivine, in pyroxene, in feldspars (Fig. 4.2h), and as single crystals.

All other samples show significantly higher proportions of vitric components. Pumice commonly represents the majority of the vitric particles (Fig. 4.2e and 4.2f). Glass shards also frequently occur (Fig. 4.2g). Vitrophyric lapillis are rare. Lithic fragments can be microcrystalline felsitic andesites, rhyolites, or trachytes (Fig. 4.3b). Microlitic lapillis are less frequently observed. Feldspars and pyroxenes are the most abundant phenocrysts. Pyroxenes are hedenbergite and (ferro-) augite in composition and feldspars are mostly anorthoclase (rarely Na-sanidine). Plagioclases are compositionally andesine or oligoclase. Olivine and quartz occur as accessories. In addition to the phenocrysts, xenocrystic clinopyroxene and xenocrystic feldspar is observed. The feldspar nomenclature is dependent on the instrumental type of magnification and on information about crystallographic structure (Parsons et al., 2015). We used transmitting light as well as electron-beam techniques that detect exsolution patterns to a limited size (μm-scales) and only along distinct crystallographic orientations. Crystals from samples of interest were embedded in resin parallel to one of their well-developed cleavage planes. We

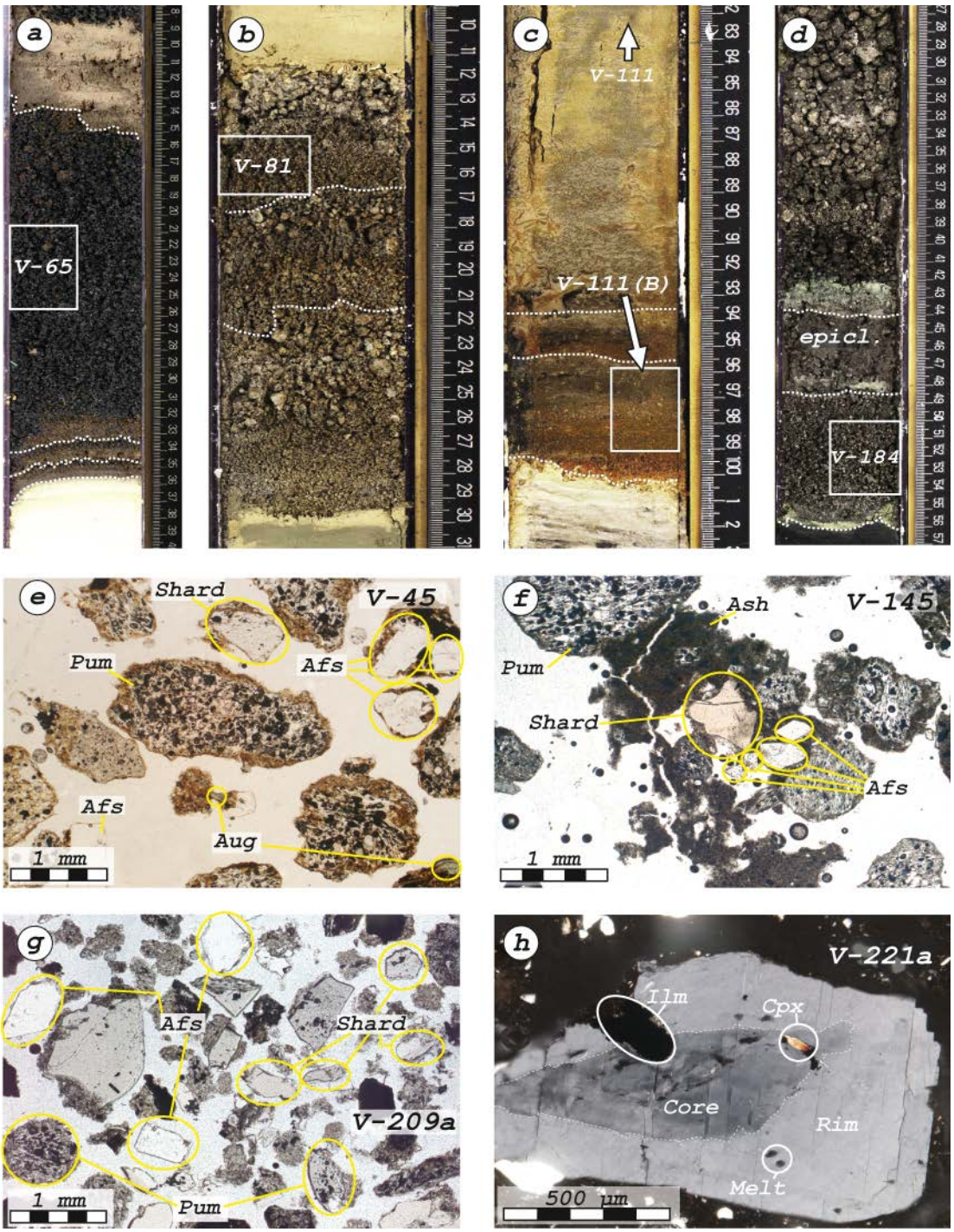

Figure 4.2: (a) Thin beds of inverse graded material at the base of coarse ash. (b) Three pulses of fallout deposition varying from ash to lapilli in grain size. (c) Two cm-thick and compositionally sorted ash deposits underneath 80-cm-thick fine ash. (d) Tephra particle size distribution ranging from fine ash to lapilli. Another fine-grained and possibly epiclastic subunit interrupts an inverse grading succession. (e) Photomicrograph of V-45 in transmitting light. (f) Transmitting light photomicrograph of V-145. (g) Photomicrograph of V-209a. (h) Photomicrograph of ternary feldspar from V-221a in crossed nicols. Abbreviations are as follows: Shard: glass shard; Fsp: feldspar; Ilm: Ilmenite; Pum: Pumice; Aug: augite; Cpx: clinopyroxene (not more closely defined).

applied a nomenclature according to Parsons (2010). Most feldspar types are defined chemically in this nomenclature, except for anorthoclase. Anorthoclase is defined as triclinic feldspar at room temperature and inverts instantaneously and reversibly to monoclinic symmetries with increasing temperature. This study simplifies this definition and calls compositions between Or_{10} and Or_{37} with Or > An anorthoclase.

Anorthoclase and sanidine phenocrysts can be subdivided into four groups of crystal zoning, following a modified classification of Ginibre et al. (2004). Compositional zoning (C-type) can be detected in transmitted light microscopy (Fig. 4.2h). We classified textures to be C-type that vary by 7 mol% or more in one of the feldspars' main components. Pseudo-oscillatory zoning texture (PO-type) is visible only in cathodoluminescence (CL) images (Fig. 4.4b). Concentric zoning (CC-type) is also exclusively detectable with CL imaging and the only type of zoning not described in Ginibre et al. (2004). Resorbed and patchy zoning (R- type) occurs as a chaotic variation of PO-type and C–type textures with abundant resorption embayments and is best visible in CL imaging modes. Normal zoned andesine from sample V-299 was estimated to be old and K-rich enough to undergo the dating procedure in order to analyse the less-differentiated tephra that dominates the base of the composite core.

4.3.2 Sample preparation for $^{40}Ar/^{39}Ar$ analyses

Aliquots for $^{40}Ar/^{39}Ar$ analyses were softly ground with a mortar and pestle and washed in 10% acetic acid and 3% hydrogen peroxide. The material was sieved with normed grid sizes of #20 (> 1 mm), #30 (> 500 μm), and #45 (> 375 μm). In order to isolate plagioclases from the alkali feldspars, sieved fractions underwent heavy-liquid density separation in a centrifuge with sodium polytungstate at 2.61 g/cm^3. Float material (except for V-299) was hand-picked three times for transparent to slightly blurry and euhedral feldspars. The fractions picked underwent cleaning with 5% HF and sonic cleaning with acetone as well as distilled water several times. A minimum of four grains from the final fractions underwent qualitative testing of the feldspars' composition with energy-dispersive element detection in a scanning electron microscope at the University of Potsdam. Minimal masses of required material were calculated with estimates for K-content and age. The final fractions avoided corroded and inclusion-bearing crystals and concentrated on samples offering euhedral and transparent feldspar (Fig. 4.3a, 4.3c, and 4.3e). Out of 51 samples, 13 contained feldspar phenocrysts that were visibly free of inclusions in reflected-light microscopy and that were most promising for a successful application of the $^{40}Ar/^{39}Ar$ method.

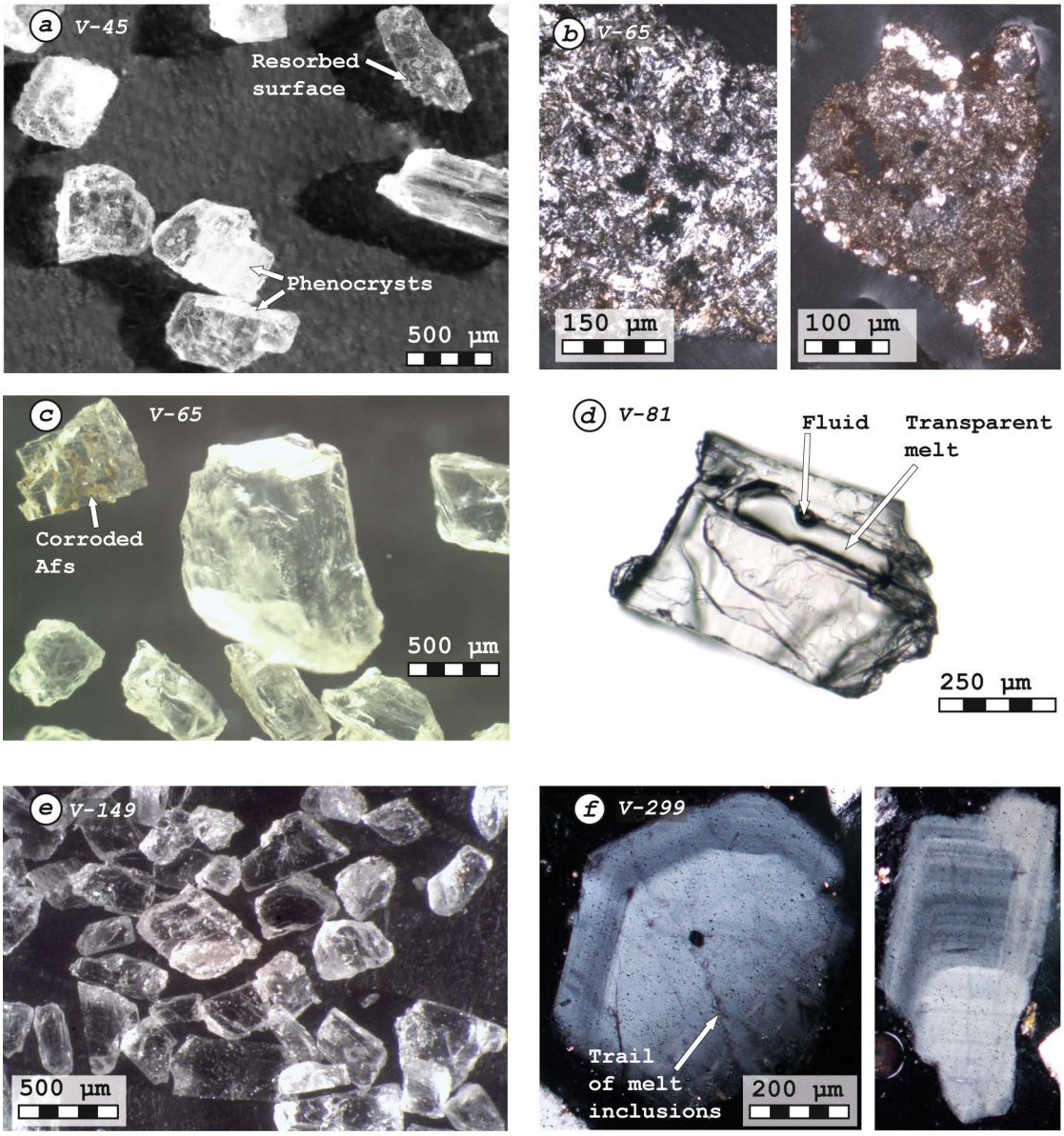

Figure 4.3: Photomicrographs of feldspar grains in reflected (a, c, d, e) and transmitted light (b and f). Two photomicrographs in (f) are of equivalent scaling. Corroded felsitic lithics are displayed in different scaling in (b).

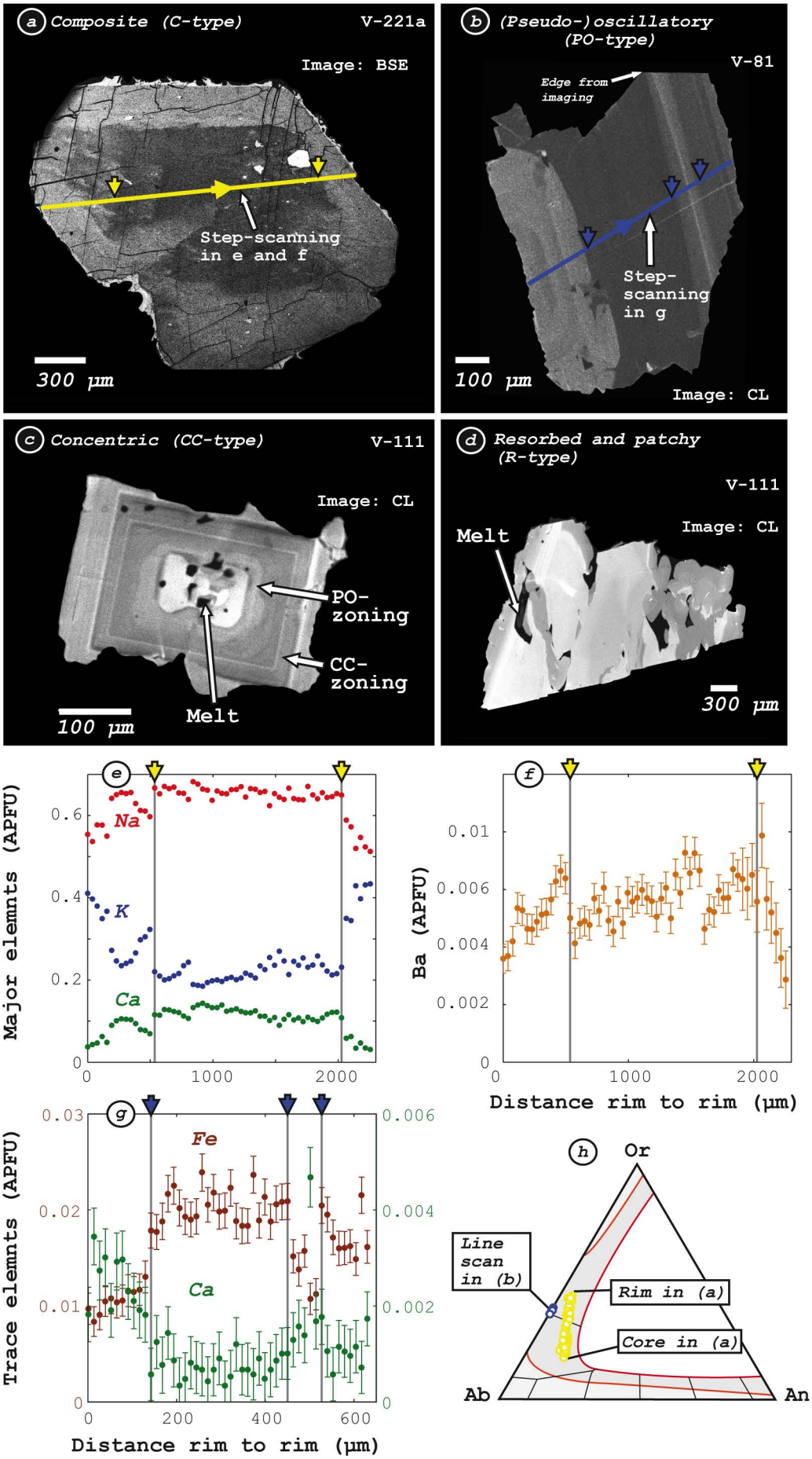
a Composite (C-type)
V-221a
Image: BSE
Step-scanning in e and f
300 µm
b (Pseudo-)oscillatory (PO-type)
V-81
Edge from imaging
Step-scanning in g
100 µm
Image: CL
c Concentric (CC-type)
V-111
Image: CL
PO-zoning
CC-zoning
Melt
100 µm
d Resorbed and patchy (R-type)
V-111
Image: CL
Melt
300 µm
e
Na
K
Ca
Major elemnts (APFU)
f
Ba (APFU)
Distance rim to rim (µm)
g
Fe
Ca
Trace elemnts (APFU)
Distance rim to rim (µm)
h
Or
Ab
An
Line scan in (b)
Rim in (a)
Core in (a)

Figure 4.4: (previous page) (a to d) Four categories of feldspars modified after Ginibre et al. (2004). Coloured lines and arrowheads mark pathways and directions for EMPA scans. (e) Relative Na, K, and Ca concentrations vary along step scanning in feldspar from V-221 in 4.4a. (f) Ba concentration from step scanning along the yellow line in 4.4a. (g) Scanned Ca and Fe concentrations from feldspar in V-81 along the blue line in 4.4b. (h) A ternary diagram for feldspar classification illustrates the chemical heterogeneity of the crystal shown in 4.4a with yellow points and the homogeneity of the crystal shown in 4.4b with blue circles.

4.3.3 Irradiation and $^{40}Ar/^{39}Ar$ analyses

Separated feldspars were irradiated for four hours at the Cd-lined in-core irradiation tube (CLICIT) facility in the TRIGA reactor of Oregon State University (OSTR) in June and December 2014. Samples were wrapped in Al foil and stacked in Al sleeves. Stacks were loaded with irradiation monitors at the bottom, at the top, and in alternating positions within the sleeve (every third sample being a monitor). The sleeves were distributed over two containers (99.999 % pure Al) and irradiated for four hours each. Alder Creek sanidine (ACs-2) monitored neutron flux during irradiation. J-Values were calculated relative to the age of 1.1864 ± 0.0012 Ma (Jicha et al., 2016). The accuracy of the system was checked by co-irradiation of Fish Canyon Tuff (FC3) sanidines prepared by the Geological Survey of Japan (Uto et al., 1997; Ishizuka, 1998). A weighted average of 14 apparent ages from 16 single-grain total fusion analyses resulted in 28.06 ± 0.56 Ma. Our result agrees with an astronomically calibrated age of 28.201 ± 0.046 Ma (Kuiper et al., 2008), which was used to calibrate the $^{40}Ar/^{39}Ar$ age of ACs-2 (Jicha et al., 2016) and suggests internal consistency among the monitor minerals. As the age model from (Stockhecke et al., 2014a) similarly uses astronomical constraints, we directly compare the $^{40}Ar/^{39}Ar$ ages from this study to the model's temporal markers. Crystals of K_2SO_4 and CaF_2 were co-irradiated for common corrections of the flux' reaction with K and Ca. Samples were analysed at the University of Potsdam with a Micromass 5400 high-sensitivity, low-background, sector-type mass spectrometer and a New Wave Research 50W CO_2 continuous laser. Extracted gas lasted for ten minutes in an ultra-high vacuum metal purification line that included two SAES ZrAl alloy getters. An electron multiplier pulse-counting system detected ion-beam intensities in a 15-minute-long data acquisition with eight cycles of peak-jumping mass detections. Procedural blanks were analysed in every fourth measurement. Isotopic ratios were corrected for blank measurements, mass discrimination, interferences of K- and Ca-derived argon, and decayed ^{37}Ar and ^{39}Ar. The corrections, isochron ages, and weighted averages of apparent ages were calculated using ArArCalc, following Koppers (2002). This study compares radiometric ages with an age model and hence states all results at the 2σ-level. Uncertainties include a minimum estimate of absolute errors due to the incorporation of the systematic error on the total decay constant λ_{40K} (Koppers, 2002).

4.3.4 Electron microprobe analyses (EMPA)

Wavelength-dispersive x-ray diffraction analyses were conducted using a JEOL JXA 8200 electron microprobe (EMP) at the University of Potsdam. Carbon-coated and polished thin-sections as well as grain mounts were analysed with a beam current of 10 nA, a defocused beam with a diameter of 2 μm, and accelerating voltages of 15 kV. Elemental content was acquired using an analysing crystal LIF for Fe kα. PET crystals analysed for Ti kα, Ca kα, K kα, Ba kα, Sr kα, and TAP for Al kα, Na kα, Si kα, and Mg kα. Counting times varied between 5 s (Na, Si and K) and 20 s (all other elements). A CL detector within the EMP was used. Grey-scale images

of cathodoluminescence represent the light emission from 200 to 1200 nm and have the advantage of ultimate comparisons to backscatter electron images and WDX spot analyses. Element concentrations are stated in atoms per formula unit of feldspar (APFU) and typically sum up totals ranging from 4.98 to 5.02 APFU. Uncertainties were propagated in calculating atoms per formula units with two standard deviations of the instrumental intensities.

4.4 Results

4.4.1 Feldspar compositions and textures

The feldspars compositional zoning represents anti-correlations of anorthite to orthoclase or albite to orthoclase components. Discernibility in BSE images is caused by contrasting K (and Ca) contents and is attenuated by varying Ba contents due to its high atomic number (Fig. 4.4e and 4.4f). Samples V-45, V-65, and V-221a show C-type textures in feldspar phenocrysts as the dominant feldspar species. Contrastingly, C-type textures were only detected as accessories in V-254 and V-279. Most samples show C-type zoning as an enrichment of an orthoclase component towards the rim (Fig. 4.4e).

Feldspars characterised by PO-type are predominant in samples V-81, V-111, V-149, V-254, and V-279. A few crystals showing PO-type zoning exist in V-65. Feldspar crystals with PO-type zoning are almost anorthite free. CL imaging unravels the PO-type textures and step-scanning electron microprobe analyses document anti-correlated Fe and Ca contents to be the reason for visibility (Figs. 4.4b and 4.4g). Finch and Klein (1999) showed that red luminescence is typically an effect of Fe^{3+} and blue luminescence typically an effect of Ti^{4+}. Ginibre et al. (2004) described a threshold of blue to red luminescence in sanidine (Or_{60}) from the German Eifel as Fe/Ti dependent. We recorded low Ti concentrations relative to the alternating Fe contents but treat our results for Ti with care, as (i) most of them overlap the analytical detection limits within their standard deviation and as (ii) we did not analyse the actual spectral wavelength of the zones. CC-type zoning is rarely observed. Similarly to PO type zoning, the Fe/Ti ratio and Ca contents vary perpendicularly across the zoning texture. An important distinction is that PO-type zoning records wavy, rounded, or embayed resorption surfaces and displays processes other than the kinetic effects of magmatic crystal growth. The indication of periodic destabilisation has led to labelling of these textures as pseudo-oscillatory (Ginibre et al., 2004). This visual contrast between PO- and CC-type zoning is easily detectable in crystals from V-111 (Fig. 4.4c). R-type zoning is detected in a small number of feldspars from V-65, V-111, V-149, V-254, and V-279. In contrast, crystals from V-209a show mainly R-type zoning. Step scanning EMPA across patches revealed changes in feldspar compositions similar to C-type zoning. Compositional variations often relate to C-type sub-domains within the patchy zoning (Fig. 4.5e). Other patches correlate to varying Fe, Ti or Ca contents. Observing similar textures and chemical evidence, Ginibre et al. (2004) classified the patchy zoning of red CL cores from sanidine to be derived from resorbed cores of the feldspars' earliest growth stages.

4.4.2 $^{40}Ar/^{39}Ar$ – Total fusion analyses

Total fusion analyses (TF) were conducted on multi grain separates (MG) for fractions < 1 mm. Single grain (SG) total fusion analyses would have been preferred but a limited amount of

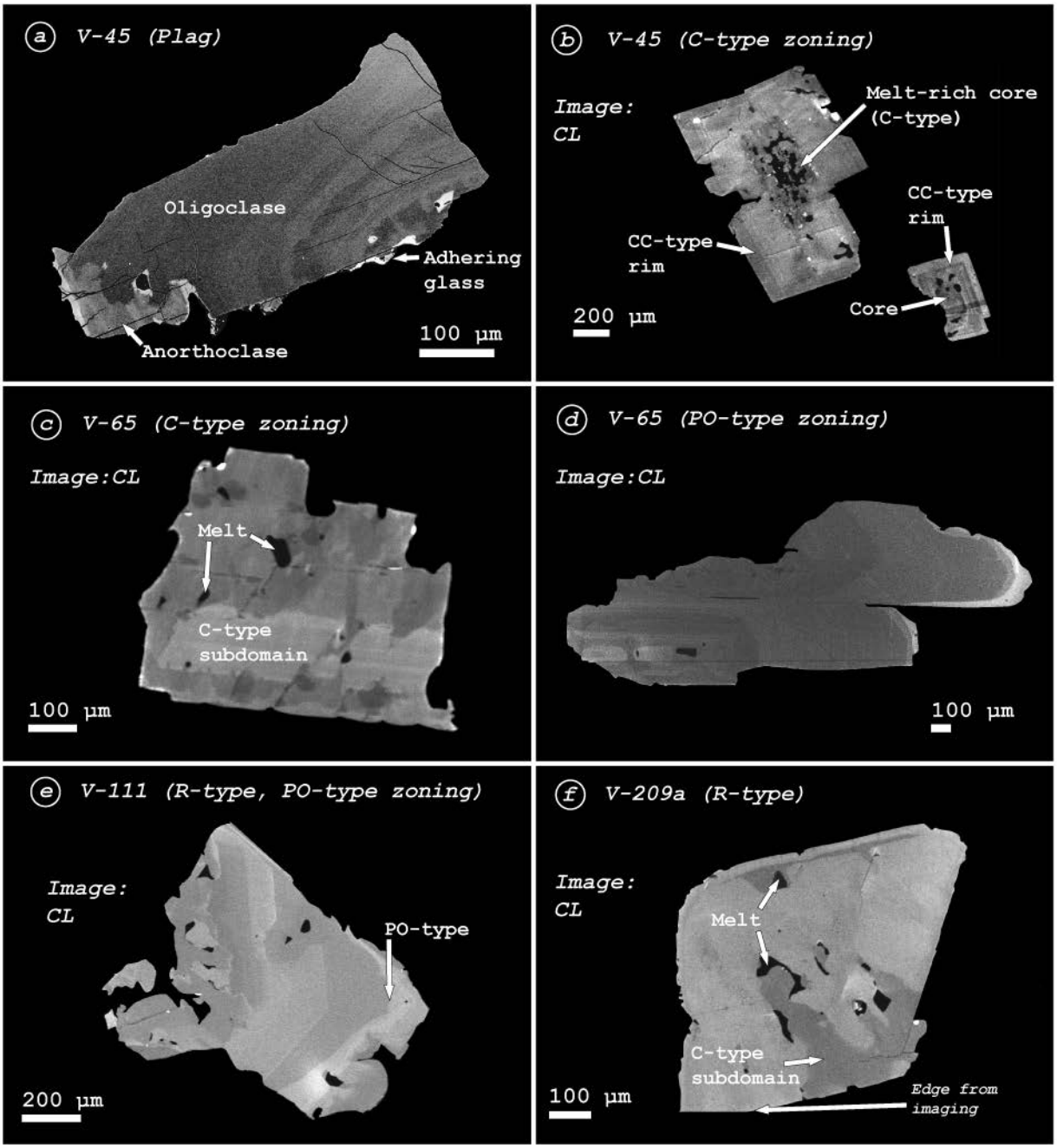

Figure 4.5: Predominant feldspar-types classified after Ginibre et al. (2004).

sample material required additional analyses of smaller fractions. Conducting SGTF in addition to MGTF allows for monitoring the possible presence of xenocrysts in the separates. Weighted mean apparent ages were calculated for each sampled volcanic unit (Fig. 4.6) by combining data from the same sample but from different experiments (different grain-size fractions). The number of MGTF analyses from V-81 #30 (n = 3), V-111 #20 (n=2), V-111(B) #20 (n=2), V-111(B) #45 (n=2) and V-145 #45 (n = 1) are insufficient to constitute an isochron regression. The resulting apparent ages of these MGTF analyses were integrated into the weighted mean age calculations for the particular tephra. Ages from MGTF analyses hinder the detection of potential single xenocrysts and thus represent maximum ages.

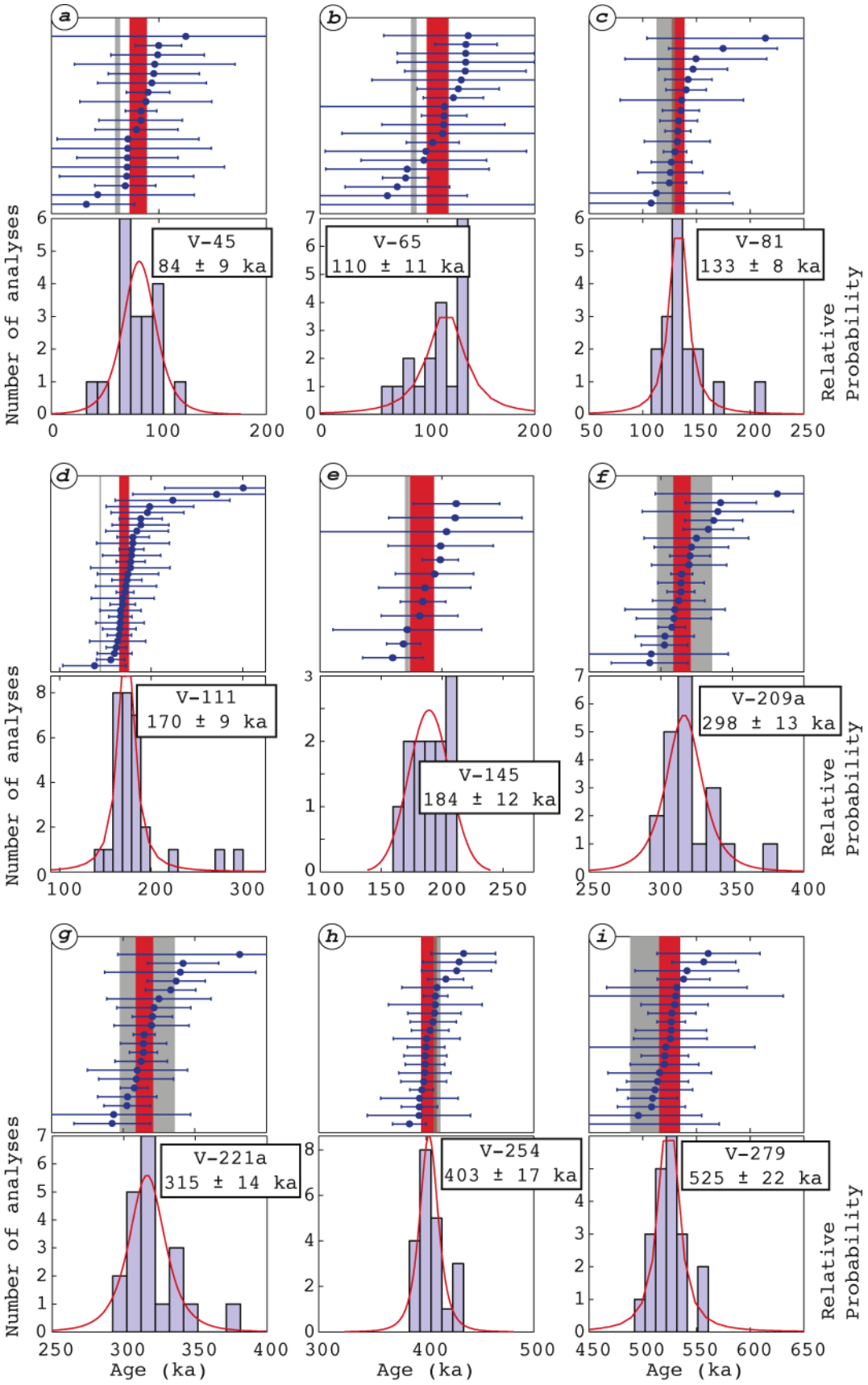

Figure 4.6: Age-probability distribution spectra from TF analyses. Grey bars represent the age range suggested from the next over- and underlying age control points (ACPs) from Stockhecke et al. (2016). Red bars display the 2σ range of the weighted average ages.

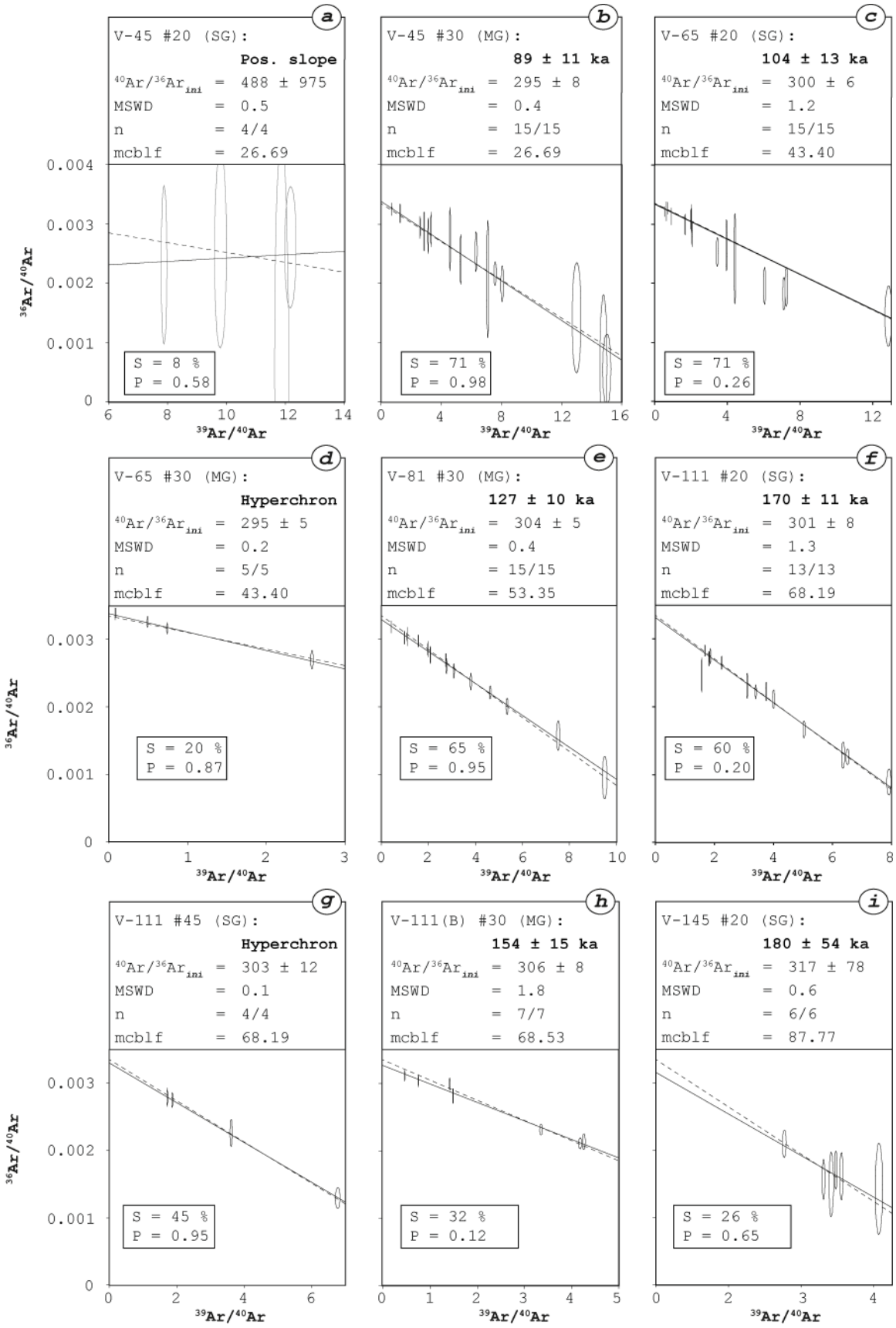

Figure 4.7: Three-isotope correlation diagrams of samples from 26.7 to 87.8 meters composite-core below lake floor (mcblf). P represents the probability from χ^2 testing and S the spreading factor of ellipses along the isochron (Jourdan et al., 2009). Dashed lines depict the line between the weighted-mean age intercept and the atmospheric $^{40}Ar/^{36}Ar$ intercept. Atmospheric Ar was corrected with 298.6 for $^{40}Ar/^{36}Ar$ (Lee et al., 2006). All ellipses and uncertainties represent two standard deviations.

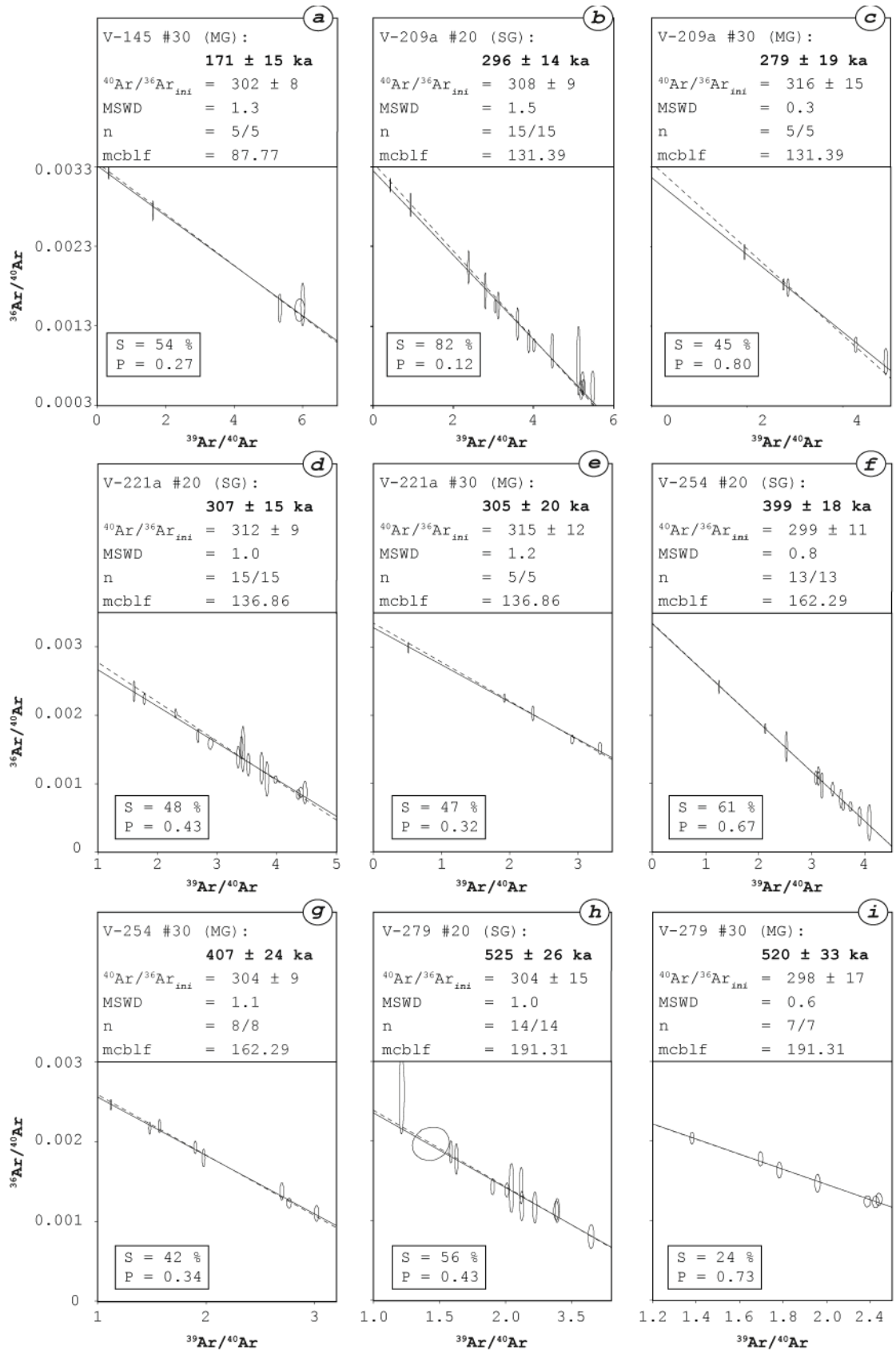

Figure 4.8: Three-isotope correlation diagrams that allow inverse isochron calculations of samples from 87.8 to 191.3 mcblf.

A number of inverse isochrons show an initial $^{40}Ar/^{36}Ar$ component that exceeds the ratio for the atmosphere of 298.6 (Lee et al., 2006) and indicates an extraneous component of ^{40}Ar (Figs. 4.7 and 4.8). Facing evidence of extraneous ^{40}Ar components isochron age calculations were preferably used. Some of the inverse isochrons resulted in MSWD values being < 1 (Figs. 4.7 and 4.8). MSWD values less than 1 suggest a scatter along the isochron that is smaller than the statistical expectation from the errors of the individual analyses. Isochrons that were calculated for V-65 #30 and V-111 #45 resulted in a MSWD < 0.3. These regressions are derived from analyses whose analytical uncertainty has been considerably overestimated and require more exact isotope determination to apply statistical testing with MSWD (Wendt et al., 1991; Ludwig, 2012). Hence, inverse isochron ages of the V-65 #30 and V-111 #45 samples are not presented, and their regressions are labelled with the term 'hyperchron'. The apparent ages of the samples contribute to weighted mean calculations for the particular volcanic unit (Fig. 4.6). Other than the two cases mentioned, MSWD values fulfil the criterion of Wendt et al. (1991) and the according regressions can be regarded as isochrones. Four analyses from V-45 #30 show very similar $^{39}Ar/^{40}Ar$ ratios. The least-squares method resulted in an inverse isochron calculation that has a positive slope, and, accordingly, no isochron age has been stated for this sample. Inverse isochrons of analyses of V-145 (Fig. 4.7i and 4.8a) are of a sensitive character as the number of available analyses is small. Most $^{39}Ar/^{40}Ar$ ratios from V-145 #20 resulted in a comparably narrow range. The sample's inverse isochron calculation thus has high uncertainties in the initial $^{40}Ar/^{36}Ar$ ratio and the age. Nevertheless, the resulting inverse isochron ages from a finer grain-size fraction of V-145 (#30) agrees within two standard deviations with the result of the coarser sample. Intra-sample concordance was observed for all other samples that underwent an application of the $^{40}Ar/^{39}Ar$ method on two or three different grain-size fractions (Figs. 4.6 to 4.8). The combined calculation of a weighted mean age from V-209a resulted in an erroneous mean with a probability of fit of 0.02. Combined weighted mean ages from all other volcanic units are statistically robust.

4.4.3 Stepwise heating analyses

Three out of four stepwise heating (SWH) analyses resulted in statistically robust, conventional plateau ages. Isochron calculations resulted in ages that agree with the conventional plateau ages (Fig. 4.9). We prefer isochron ages due to elevated initial $^{40}Ar/^{36}Ar$ ratios that indicate the presence of extraneous ^{40}Ar. Except for the first two degassing steps from V-36, filtering was neither applied to plateau nor to isochron age calculations. Fig. 4.10 displays the absence of isotopic equilibrium in andesine from V-299.

4.5 Discussion

4.5.1 Age model constraints

This geochronological study has the potential to compare $^{40}Ar/^{39}Ar$ ages (Fig. 4.11) to an age model for the lacustrine record (Stockhecke et al., 2014a; Stockhecke et al., 2014b; Stockhecke et al., 2016). The age model consists of homogeneous results from various age control points (i.e., climate-stratigraphic correlations, varve counting, limnologic correlation of ^{14}C ages). Tephro-stratigraphic correlations with three onshore tephra units (Sumita and Schmincke, 2013c), six

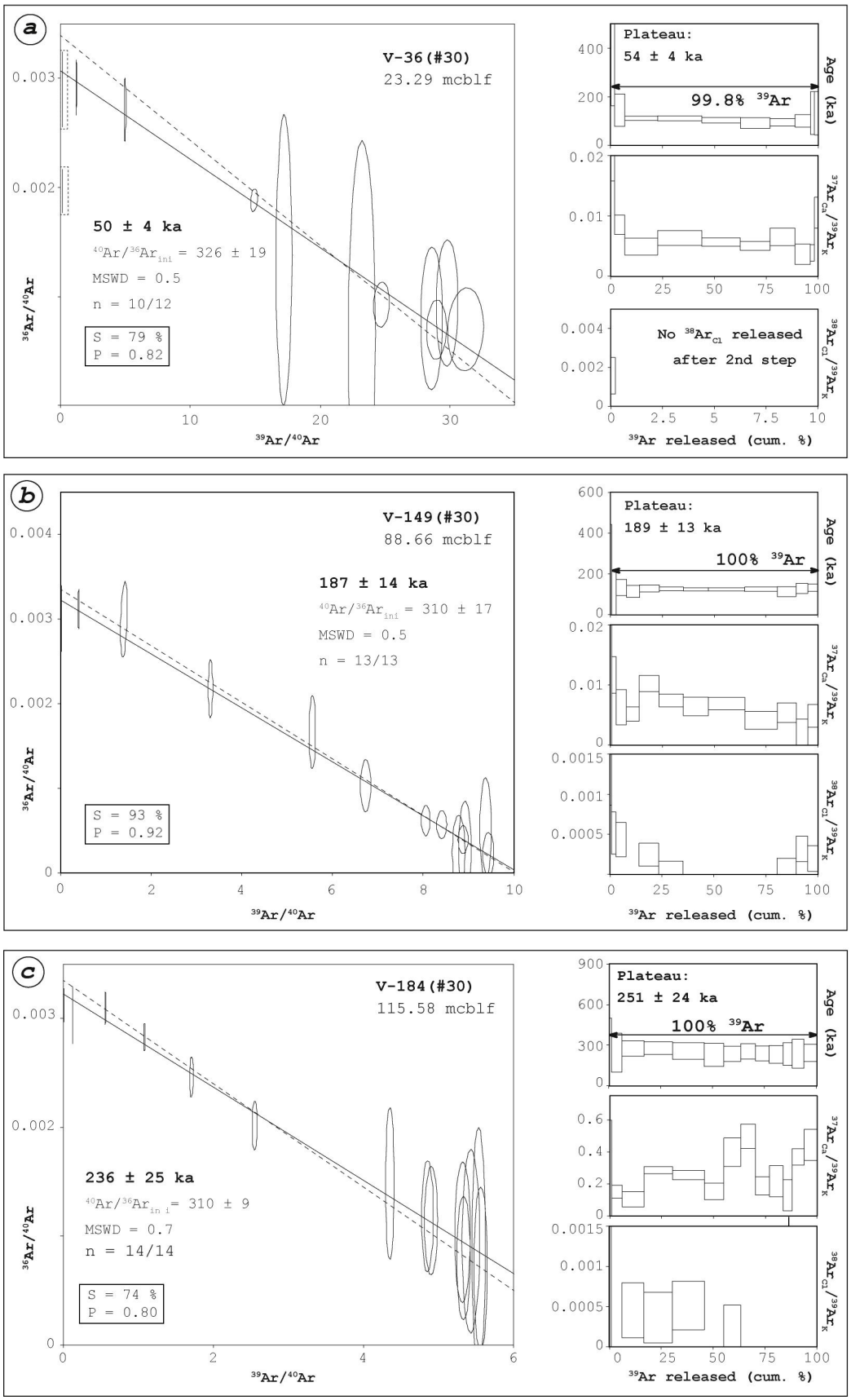

Figure 4.9: Stepwise heating results combining 3-isotope correlation diagrams together with common plateau age calculation and ratios of degassing $^{37}Ar_{Ca}$ and $^{38}Ar_{Cl}$ relative to $^{39}Ar_K$. Isotopic ratios from degassing steps that were not considered are displayed with dashed frames. Ellipses and boxes display results at the 2σ level.

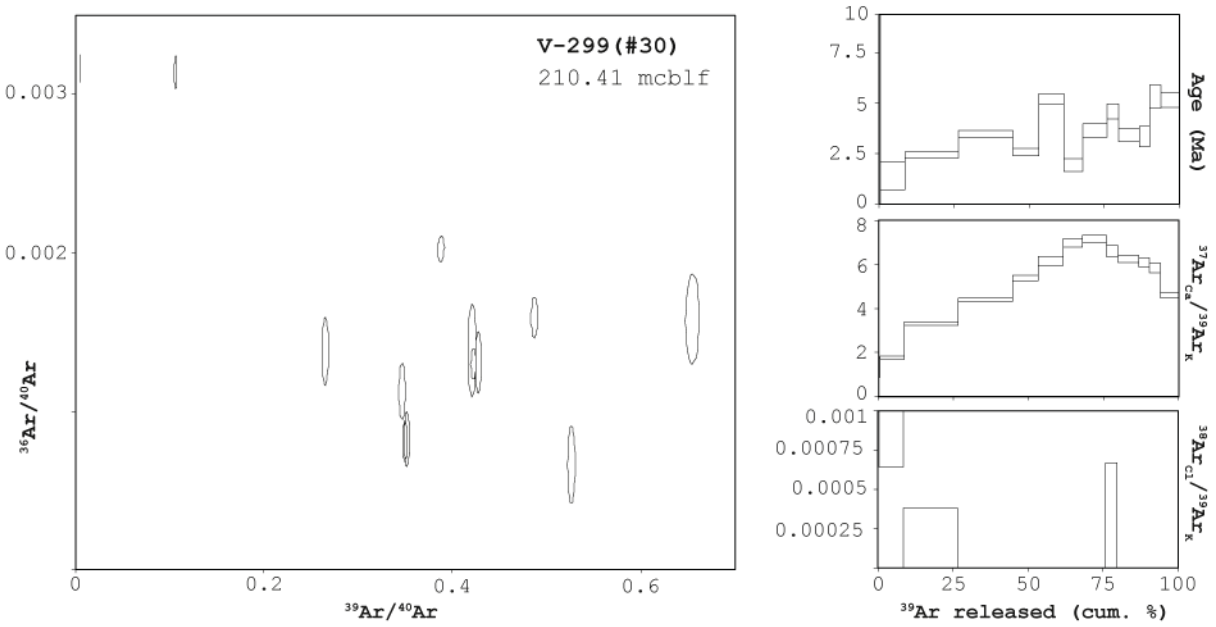

Figure 4.10: Stepwise heating results of sample V-299 are presented in the same way as in Fig. 4.9. Neither an inverse isochron nor a common plateau could be derived from the data. $^{37}Ar_{Ca}$ variations indicate normal zoning in the plagioclases.

$^{40}Ar/^{39}Ar$ dates (Stockhecke et al., 2014b), seven relative paleo-intensity (RPI) minima from remanent/anhysteric magnetisations (Vigliotti et al., 2014), and an increased cosmogenic nuclide (^{10}Be) flux peak (Stockhecke et al., 2014a) agree with the temporal record from the age control points (ACP). The agreement allows for a robust age-depth relation down to a stratigraphic depth of ca. 164 m of composite core below lake floor (mcblf) (Stockhecke et al., 2014b) but considers the lowest constraints of the composite core as preliminary. Stockhecke et al. (2016) refined the ACPs by synchronising lacustrine sediment colour reflectance data (i.e., from measuring the blue-yellow chromaticity) to the $\delta^{18}O$ NGRIP record. Sedimentation rates from Stockhecke et al. (2016) refer to a linear interpolation of the ACPs using a no-event depth scale (mcblf-nE) that assumes continuous lacustrine sedimentation and that excludes tephras and turbidites.

4.5.2 Schema in comparing $^{40}Ar/^{39}Ar$ ages to age model constraints

We have compared our results in three ways: (i) The first comparison relates the inverse isochron ages to the next over- and underlying age control points (ACP) from Stockhecke et al. (2014a) and Stockhecke et al. (2016). (ii) The second, more sophisticated comparison was to project the stratigraphic position of the samples on the mcblf-nE depth and to assume linear sedimentation rates (LSR) between the next upper and lower ACP. The event-corrected stratigraphic distance between the ACPs and the sample's position was converted to a modelled age for each sampled volcanic unit. The modelled ages were then compared to the inverse isochron ages from this study. Table 4.1 lists a comparison to the ACPs and to the modelled lacustrine ages of the samples. (iii) The third comparison used two t-tests with apparent $^{40}Ar/^{39}Ar$ ages and either the closest ACPs (two-sample t-test) or the modelled age from the mcblf-nE depth scale (one-sample t-test). The two-sample t-test collected all available ACPs within a distance of 5

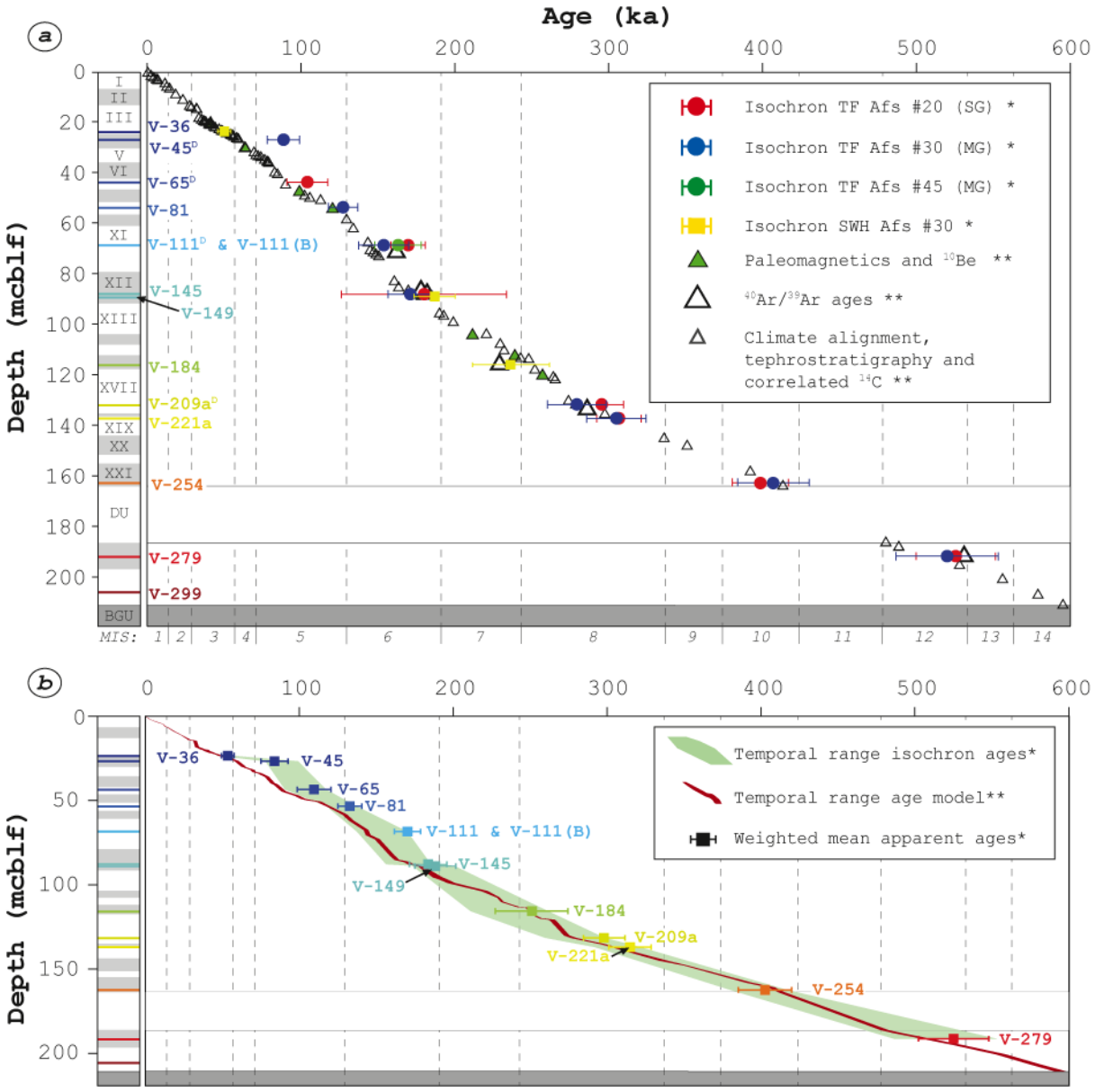

Figure 4.11: Compiled age constraints for the Ahlat Ridge sediment record. Alternating grey and white units in stratigraphic sketches indicate lacustrine units defined by Stockhecke et al. (2014b) and Stockhecke et al. (2016). These two publications summarise all temporal markers that are labelled with two asterisks in the legends. Data points from the given study are marked with one asterisk in the legends. Colours in stratigraphic sketches are distinctive for the corresponding sample's position throughout this study. (a) Age-versus-depth-plot comparing inverse isochron calculations relative to the temporal markers from the age model. Filled circles and squares display the method applied. Colours indicate the grain-size fraction. The superscript *D* labels samples showing deviation of an inverse isochron age to the age model. (b) Age-versus-depth-plots comparing ages from weighted averages of apparent $^{40}Ar/^{39}Ar$ ages with constraints from isochrones, as covered in the discussion (section 4.5). The temporal range from the age model represents inter- and extrapolated minimum uncertainties from Stockhecke et al. (2016). MIS abbreviates marine isotope stages, BGU the basal gravel unit, MU the mottled unit, and DU the deformed unit. MG: multi grain; SG: single grain; TF: total fusion; SWH: stepwise heating; # mark grain size range following classification described in the methods.

m stratigraphically up- and downward, except for when the next available ACP exceeded this distance. The t-tests applied a significance level of 0.05. Fourteen inverse isochron ages from 10 tephras are consistent with the age model in the first and in the second means of comparison. Inverse isochron ages for V-45 #30, V-65 #20, V-111 #20 and V-209a #20 do not agree with the next underlying ACP and deviate from the model following the first and second comparisons. All deviations have revealed inverse isochron ages that are significantly older than the temporal constraints from the age model. Both the one- and two-sample t-tests resulted in non- significant deviations for distributions of apparent ages for V-36, V-149, V-184, V-221a, V-254, and V-279. The one-sample t-tests of model ages with age distributions for V-65, V-81, V-145, and V-209a revealed significant deviations, whereas the two-sample tests did not. V-45 and V-111 significantly deviated from the age model in both t-tests. Probabilities are listed in Table 4.2.

4.5.3 Comparison of $^{40}Ar/^{39}Ar$ ages to age model constraints

V-36 in comparison to the age model

Sample V-36 shows a plateau age of 54 ± 4 ka, which is a minimum of 1 ka older than the next underlying ACP. The plateau-related incremental heating steps resulted in an inverse isochron age that agrees with the temporal marker. This age of 50 ± 4 ka overlaps the modelled age from the mcblf-nE scale projection as well. As the initial $^{40}Ar/^{36}Ar$ does exceed an atmospheric composition, we assign 50 ± 4 ka to be the age of V-36.

V-45 in comparison to the age model

An inverse isochron age of 89 ± 11 ka from MGTF analyses of V-45 deviates from the next lower ACP by ca. 17 ka and the modelled age by ca. 19 ka. T-testing the distribution of combined apparent ages from V-45 #30 and V-45 #20 has revealed a significant deviation from age model constraints. Thus, a weighted mean age of 84 ± 9 ka also deviates from the next lower ACP by a minimum of 14 ka. The sample's stratigraphic location is situated in an intermediate position between two recorded paleomagnetic time markers. Vigliotti et al. (2014) identified the directional excursion of the Laschamp event as about 7 mcblf above V-45. Additionally a pronounced ^{10}Be flux peak was revealed in sediments from the corresponding stratigraphic position (Stockhecke et al., 2014b). The flux agrees with an expected increase by a factor of two and particularly strengthens the stratigraphic alignment with the record of the North Green- land Ice Core Project (NGRIP) (Stockhecke et al., 2014a). The Laschamp excursion is dated radiometrically at 41.3 ± 0.6 ka (Singer et al., 2009) and agrees with age constraints from astrochronology (Laj and Channell, 2007). At about 3 mcblf stratigraphically underneath V-45, Vigliotti et al. (2014) identified a RPI minimum that is correlated with the PISO-1500 stack (Channell et al., 2009). The correlation has revealed an age range of 63–64 ka (Channell et al., 2009). Furthermore, 1.83 m below V-45, another temporal marker is represented due to tephrostratigraphic indications from V-51 that allow a correlation with the onshore tephra unit Halepkalesi Pumice-10 (Sumita and Schmincke, 2013c; Stockhecke et al., 2014b). Sumita and Schmincke (2013c) dated this pumice with SGTF analyses of 8 feldspar crystals and presented a weighted mean from apparent $^{40}Ar/^{39}Ar$ ages of 75.1 ± 4.5 ka. All the aforementioned temporal markers are robust and mark consistency with the dense abundance of ACPs from

Table 4.1: Comparison of $^{40}Ar/^{39}Ar$ data from this study[1] to age control points (ACP) from Stockhecke et al. (2014a)[2] and Stockhecke et al. (2016)[3]. Minimal age deviations are expressed relative to the next underlying ACP and to projections of the samples' stratigraphic position on the mcblf-nE depth scale.

Sample	Analysis	Age next upper ACP[2,3] (ka)	Age next lower ACP[2,3] (ka)	Modeled n-E Age[2,3] (ka)	Inverse isochron age[1] (ka)	Min. Deviation to next lower ACP (ka)	Min Deviation to mcblf-nE Model[3] (ka)
V-36	SWH #30	46 ± 1	48 ± 1	48.5	50 ± 4	0	0
V-45	SGTF #20	58.5 ± 1.3	59.4 ± 1.3	59	Pos. slope	-	-
V-45	MGTF #30	58.5 ± 1.3	59.4 ± 1.3	59	89 ± 11	17.3	19
V-65	SGTF #20	85 ± n. s.	90 ± n. s.	88	104 ± 13	1	3
V-65	MGTF #30	85 ± n. s.	90 ± n. s.	88	Hyper-chron	-	-
V-81	MGTF #30	112 ± n. s.	129.7 ± 1.4	121	127 ± 10	0	0
V-111	SGTF #20	143.5 ± 1.5	144.9 ± 1.5	144	170 ± 11	12.6	15
V-111	MGTF #45	143.5 ± 1.5	144.9 ± 1.5	144	Hyper-chron	-	-
V-111B	MGTF #30	143.5 ± 1.5	144.9 ± 1.5	144	154 ± 16	0	0
V-145	SGTF #20	169.8 ± 1.9	173.2 ± 1.9	172	180 ± 54	0	0
V-145	MGTF #30	169.8 ± 1.9	173.2 ± 1.9	172	171 ± 15	0	0
V-149	SWH #30	178.3 ± 1.6	190 ± 3	178	187 ± 14	0	0
V-184	SWH #30	248 ± 1	252.0 ± 0.6	250	236 ± 25	0	0
V-209a	SGTF #20	273.8 ± 1.7	278.5 ± 1.6	279	296 ± 14	1.9	3
V-209a	MGTF #30	273.8 ± 1.7	278.5 ± 1.6	279	279 ± 19	0	0
V-221a	SGTF #20	297.5 ± 1.2	336.0 ± 2.5	304	307 ± 15	0	0
V-221a	MGTF #30	297.5 ± 1.2	336.0 ± 2.5	304	305 ± 20	0	0
V-254	SGTF #20	407 ± n. s.	413 ± n. s.	409	399 ± 18	0	0
V-254	MGTF #30	407 ± n. s.	413 ± n. s.	409	407 ± 24	0	0
V-279	SGTF #20	489 ± n. s.	528 ± n. s.	508	525 ± 26	0	0
V-279	MGTF #30	489 ± n. s.	528 ± n. s.	508	520 ± 33	0	0
V-299	SWH #30	579 ± n. s.	595 ± n. s.	593	None	-	-

Table 4.2: Statistical comparison of distributions from apparent $^{40}Ar/^{39}Ar$ ages and temporal markers of the age model. Probability, MSWD, and the result of weighted mean age calculations are also reported in Figs. 4.6 and 4.9.

Volcanic unit	n	Wt.mean age (ka)	Probability mean age	MSWD mean age	Probability two-sample t-test	Probability one-sample t-test
V-36	10/12	54 ± 4	0.11	1.6	0.19	0.34
V-45	19/19	84 ± 9	0.85	0.66	< 0.01	< 0.01
V-65	20/20	110 ± 11	0.26	1.19	0.08	< 0.01
V-81	17/17	133 ± 8	0.86	0.64	0.05	< 0.01
V-111	30/30	170 ± 9	0.06	1.43	0.02	< 0.01
V-145	12/12	184 ± 12	0.1	1.58	0.06	< 0.01
V-149	13/13	189 ± 13	0.85	0.59	0.59	0.33
V-184	14/14	251 ± 24	0.26	1.21	0.59	0.31
V-209a	20/20	298 ± 13	0.02	1.76	0.15	< 0.01
V-221a	20/20	315 ± 14	0.08	1.49	0.24	0.52
V-254	21/21	403 ± 17	0.22	1.23	0.62	0.11
V-279	21/21	525 ± 22	0.66	0.85	0.78	0.35
V-299	0/14	none	none	none	none	none

correlation with the NGRIP record. We have thus interpreted $^{40}Ar/^{39}Ar$ ages from V-45 as being erroneously old.

V-65 in comparison to the age model

SGTF analyses from V-65 #20 resulted in an isochron age that slightly deviates from the next underlying ACP by 1 ka and the sample's modelled age by 3 ka. Combining the SGTF with five MGTF analyses of V-65 #30 resulted in a weighted mean age that deviates from the two temporal markers by 9 ka and 11 ka, respectively. V-65 is situated about 3 m above a recorded onset of a RPI minimum that extends from 46.41 to 48.42 mcblf. The RPI minimum can be correlated with an age range of 96.6 ka to 103.1 ka (Channell et al., 2009) and agrees with $^{40}Ar/^{39}Ar$ ages for V-65. Thus, the $^{40}Ar/^{39}Ar$ ages of V-65 deviate from one ACP aligned with the NGRIP GICC05modelext time scale (Wolff et al., 2010; Stockhecke et al., 2014a). This ACP is located 1 m underneath V-65 and marks the onset of the Greenland interstadial GI-22. Proxies that allow for a correlation are total organic carbon content (TOC), sediment reflectance, and relative signals from x-ray-fluorescence core scanning (Ca/K). Lead and lag compensation between the different proxies is difficult to assess, as these are derived from different stratigraphic resolutions. A corresponding compensation could shift the onset stratigraphically upwards, although such a shift would be expected to be minute. Subsequently downward from this ACP, proxies are correlated with the record of the Antarctic Ice Core Chronology 2012 (AICC2012) (Veres et al., 2013; Stockhecke et al., 2016) instead of the NGRIP GICC05modelext. Differences in timing the onset of GI- 22 between AICC2012 and GICC05modelext are reported to be about 0.3 ka maximum (Veres et al., 2013). However, this shift dates the onset of GI-22 at an even younger age and increases the deviation to the $^{40}Ar/^{39}Ar$ age from V-65. We suggest the inverse isochron age of 104 ± 13 ka as the maximum age assigned to V-65, but we caution against the 1ka deviation. A discussion regarding the feldspars' mineralogy and its' potential isotopic character appears appropriate (see below).

V-81 in comparison to the age model

The inverse isochron age of V-81 is concordant with both next underlying ACP and the modelled age. The weighted mean age deviates from the latter by 6 ka. A RPI minimum identified in lacustrine material above and below V-81 (Vigliotti et al., 2014) furthermore agrees with the inverse isochron age. The initial $^{40}Ar/^{36}Ar$ ratio indicates an extraneous ^{40}Ar component, and we prefer assigning the inverse isochron age. The MGTF analyses resulted in a maximum age of 127 ± 10 ka for V-81.

V-111 in comparison to the age model

V-111(B) #30 resulted in an inverse isochron age that agrees with a modelled age from the local age-depth relation and with an ACP located 2.22 m stratigraphically downwards. In contrast, the inverse isochron age of V-111 #20 deviates from the age model by ca. 13 to 15 ka (Table 4.1). The distribution of all apparent ages from V-111 deviate significantly from the modelled age and nearest ACPs (Table 4.1). Within a stratigraphic distance of ± 10 m to V-111, the age model is based on 7 ACPs. They represent correlation of the colour reflectance record with the synthetic Greenland record of the Speleo age scale (Barker et al., 2011). Furthermore, Stockhecke et al. (2014b) presented a preliminary $^{40}Ar/^{39}Ar$ age of ca. 162 ka for tephra V-114. This tephra is located about 3 m stratigraphically underneath V-111. $^{40}Ar/^{39}Ar$ ages from their study remain uncommented upon, and uncertainties are not presented. The age indication of V-114 agrees with the two inverse isochron ages from V-111 as well as putatively with the sample's weighted mean age. The three inverse isochron calculations for V-111, however, resulted in slightly elevated initial $^{40}Ar/^{36}Ar$ ratios that hamper the interpretation of the weighted mean age. Preliminarily, we suggest an inverse isochron age of 155 ± 15 ka for V-111, as it agrees with both climate-stratigraphic alignment and calculated $^{40}Ar/^{39}Ar$ ages. A detailed discussion of age constraints for V-114 has the potential to provide clarification if systematically deviating age constraints exist. A conflict between radiometric and stratigraphic constraints, hence, cannot be excluded in the record of the late marine isotope stage (MIS) 6 and requires a mineralogical discussion of the crystals analysed (see below).

V-145 in comparison to the age model

For the reasons mentioned above, V-145 #20 resulted in an inverse isochron age of low precision that accurately matches data from the age model. Another implication of the regression's poorly defined interception with the axis of the diagram is the imprecision of the initial $^{40}Ar/^{36}Ar$. The initial $^{40}Ar/^{36}Ar$ is significantly higher than that of the atmosphere and restrains the use of the respective apparent ages in a weighted mean calculation for V-145. A problem similar to that of discussing the results from dating V-111 is the comparison of V-145 to the $^{40}Ar/^{39}Ar$ ages from V-137 and V-144 (Stockhecke et al., 2014b), which roughly correspond with both the ages presented here and the ACPs. The inverse isochron age of V-145 #30 agrees with the constraints from the age model, points to less pronounced extraneous ^{40}Ar content, and is more precise than the result for V-145 #20. We therefore assign 171 ± 15 ka as the maximum age of V-145.

V-149 in comparison to the age model

Another indication of an increased initial $^{40}Ar/^{36}Ar$ ratio is suggested by the inverse isochron calculation of analyses of sample V-149. Again, using the inverse isochron age is preferred, although the plateau age calculation does not deviate from the age model constraints. An age of 187 ± 14 ka is suggested to be most representative of V-149.

V-184 in comparison to the age model

V-184 was one of the two tephras sampled for $^{40}Ar/^{39}Ar$ dating by Stockhecke et al. (2014b) and in this study. The age of ca. 229 ka fits our results from the SWH analyses. The inverse isochron age from our study is close to this value and also agrees with the age model constraints. V-184 is situated between two identified RPI minima. Within 4 m stratigraphically upwards, the upper minimum is correlated with a time span from 237 to 240 ka. Another minimum ties the lacustrine deposition from 257 to 260 ka, ca. 5 m below V-184 (Channell et al., 2009; Vigliotti et al., 2014). The paleomagnetic constraints match the constraints from the ACPs. Although the initial $^{40}Ar/^{36}Ar$ ratio exceeds atmospheric conditions, we recommend a plateau age of 251 ± 24 ka for V-184. As the increased initial $^{40}Ar/^{36}Ar$ ratio is derived from the earliest degassing steps, the plateau age calculation is robust. Isolating the first two degassing steps (<1% of cumulative ^{39}Ar) result in a lower initial $^{40}Ar/^{36}Ar$ ratio of 303 ± 11.

V-209a in comparison to the age model

SGTF analyses of V-209 #20 resulted in an inverse isochron age that deviates from the age model constraints by 2 to 3 ka. Similarly, the weighted mean age of all available apparent ages deviates from the age model by 5 to 6 ka. As inverse isochron calculations from both V-209 #20 and V-209 #30 indicate increased initial $^{40}Ar/^{36}Ar$ ratios, the weighted mean age is neglected. The nearest ACP is located 0.22 m above V-209a. It has been interpreted as marking the onset of the Dansgaard-Oeschger event LV-C4 in MIS 8 (Barker et al., 2011; Stockhecke et al., 2016). V-210, which is situated 1.43 m stratigraphically underneath V-209a, has been assigned to an $^{40}Ar/^{39}Ar$ age of ca. 286 ka (Stockhecke et al., 2014b). This age fits the model's age constraints. Stratigraphically upwards, the nearest ACP is positioned at 1.31 m distance to V-209a. This ACP represents an age estimate at the base of a ca. 10-m-thick tephra (V-206) (Stockhecke et al., 2014b). By applying a cubic-spline extrapolation for an estimated lacustrine sedimentation of 0.3 mm/yr (Stockhecke et al., 2016), this ACP indicates an age of about 274 ka. V-209a is located in the lower part of the lithostratigraphic unit XVII. As the transition from lithostratigraphic units XVII to XIX records a change in mass accumulation rates (Stockhecke et al., 2014b), a detailed comparison of V-209a to the modelled age from extrapolation of a LSR is not ideal. Nevertheless, the LSR of about 0.3 mm/yr appears to be roughly continuous from V-209a upwards and agrees with the majority of temporal constraints stratigraphically above V-206. The inverse isochron age of sample V-209a #30 (279 ± 19 ka) agrees with the model's constraints and is thus recommended. Potential reasons for the deviation from V-209a #20 are discussed below in greater detail.

V-221a in comparison to the age model

Both inverse isochron calculations for V-221 have an initial $^{40}Ar/^{36}Ar$ signal that exceeds that of the atmosphere. The weighted mean age is accordingly older than the inverse isochron ages, although the distribution of apparent ages does not significantly deviate from the nearest ACPs (Table 4.2). Stratigraphically upwards, the next ACP is defined by a correlation of TOC and Ca/K contents with a minimum just before the onset of MIS 8.5 (0.71 m distance to V-221a) and ties the lacustrine deposition to an age of 297 ± 1 ka. At a distance of 8.03 m underneath V-221a, the underlying ACP marks the onset of MIS 9.3 (Barker et al., 2011; Stockhecke et al., 2014a). This ACP is not helpful for constraining the expected age range for V-221a. However, SGTF analyses have resulted in a statistically robust regression and their inverse isochron age corresponds with the next highest ACP. We therefore assign the corresponding isochron age of 307 ± 15 ka to V-221a.

V-254 in comparison to the age model

All available age calculations from analyses of V-254 fit the age model constraints. V-254 #30 shows an elevated initial $^{40}Ar/^{36}Ar$ ratio. The inverse isochron of V-254 #20 has revealed an initial $^{40}Ar/^{36}Ar$ ratio that is indistinguishable from that of the atmosphere. An influence of extraneous ^{40}Ar from the MGTF analyses to the weighted mean age appears negligible, and we assign the age of 407 ± 24 ka to the emplacement of V-254.

V-279 in comparison to the age model

Stockhecke et al. (2014a) provided an approximate $^{40}Ar/^{39}Ar$ age of ca. 531 ka for V-279. $^{40}Ar/^{39}Ar$ ages for V-279 presented in this study agree with that age. The inverse isochron calculation for V-279 #20 hints at an extraneous ^{40}Ar component, although its imprecise initial $^{40}Ar/^{36}Ar$ overlaps that of the atmosphere. About 3.5 m above V-279, an ACP was derived from correlation with a peak in MIS 13.1 of the speleothem-based synthetic Greenland record GLT_syn (Barker et al., 2011) and ties the lacustrine deposition to an age of about 488ka (Stockhecke et al., 2014a). At a distance of about 4 m stratigraphically below V-279, an ACP was derived from the same timescale, refers to the onset of MIS 13.3, and ties the deposition to an age of about 528 ka (Barker et al., 2011; Stockhecke et al., 2014a). This age is almost identical to results from the $^{40}Ar/^{39}Ar$ dating of V-279. The deformed unit (DU) has been characterised by several over-turned as well as over-thrusted sections (Stockhecke et al., 2014b) and is located ca. 5 m above V-279. The ACP marking the base of the DU has been derived by extrapolating about 22 m of stratigraphy with an average LSR of 0.18 mm/yr. The low resolution of proxy data underneath the DU has the potential of an erroneous match between synthetic ice-core chronology and proxy records (Stockhecke et al., 2014a). We assign the inverse isochron age of 525 ± 26 ka to V-279.

V-299 in comparison to the age model

Plagioclase from V-299 is a compositionally zoned andesine (Fig. 4.3f) that has resulted in varying $^{37}Ar_{Ca}/^{39}Ar_K$ contents (Fig. 4.10) typical of a pure separate of crystals, showing a normal zoning patterns (Foland et al., 1993). The grains show no indications of rounding or

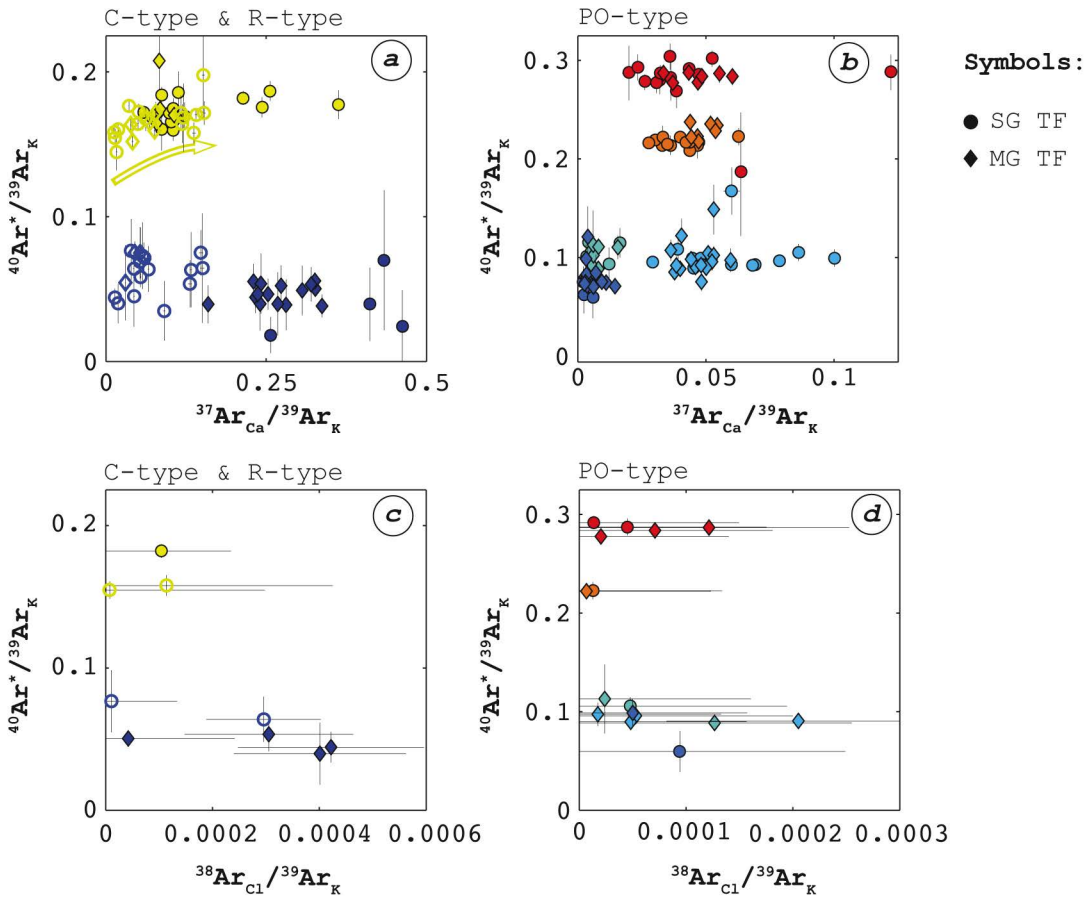

Figure 4.12: Common-denominator diagrams of $^{37}Ar_{Ca}/^{39}Ar_K$ (a, b) and $^{38}Ar_{Cl}/^{39}Ar_K$ (c, d) versus putative radiogenic $^{40}Ar^*/^{39}Ar_K$. The colour explanation of the corresponding sample is given in Fig. 4.13d. The symbol's shapes represent analysed fusion type. All uncertainties are presented with two standard deviations. Data with negative $^{38}Ar_{Cl}$ have not been plotted.

resorption. Possible mineralogical obstacles are melt and apatite inclusions. The scatter in obtained $^{39}Ar/^{40}Ar$ ratios illustrates the absence of isotopic equilibrium. Well-sorted epiclastic plagioclase explains this scatter best. All apparent ages exceed largely the earliest stage of the formation of Lake Van (Sumita and Schmincke, 2013c; Stockhecke et al., 2014a). The youngest apparent ages of V-299 cover the earliest ages of volcanic rocks assigned to Nemrut (Innocenti et al., 1976; Ercan et al., 1990; Notsu et al., 1995; Çubukçu et al., 2012). In close proximity to Lake Van's north-eastern shore, Lebedev et al. (2010) dated trachytes, rhyolites and andesites from the Etrüsk Caldera with ages ranging from 3.7 to 4.2 Ma, which coincide with the oldest apparent ages for V-299. However, these dates are of no significance to the lacustrine history of Lake Van.

4.5.4 Feldspar zoning and deviating $^{40}Ar/^{39}Ar$ ages

Correcting ^{38}Ar intensities by subtracting blank, atmospheric, and K-derived contributions resulted in intensities that can be interpreted as being chlorine-derived. Similarly, blank- and decay-corrected ^{37}Ar intensities display variations in the sample's Ca-contents (McDougall and Harrison, 1999). Both values are useful tools in discussing results from $^{40}Ar/^{39}Ar$ dating (Har-

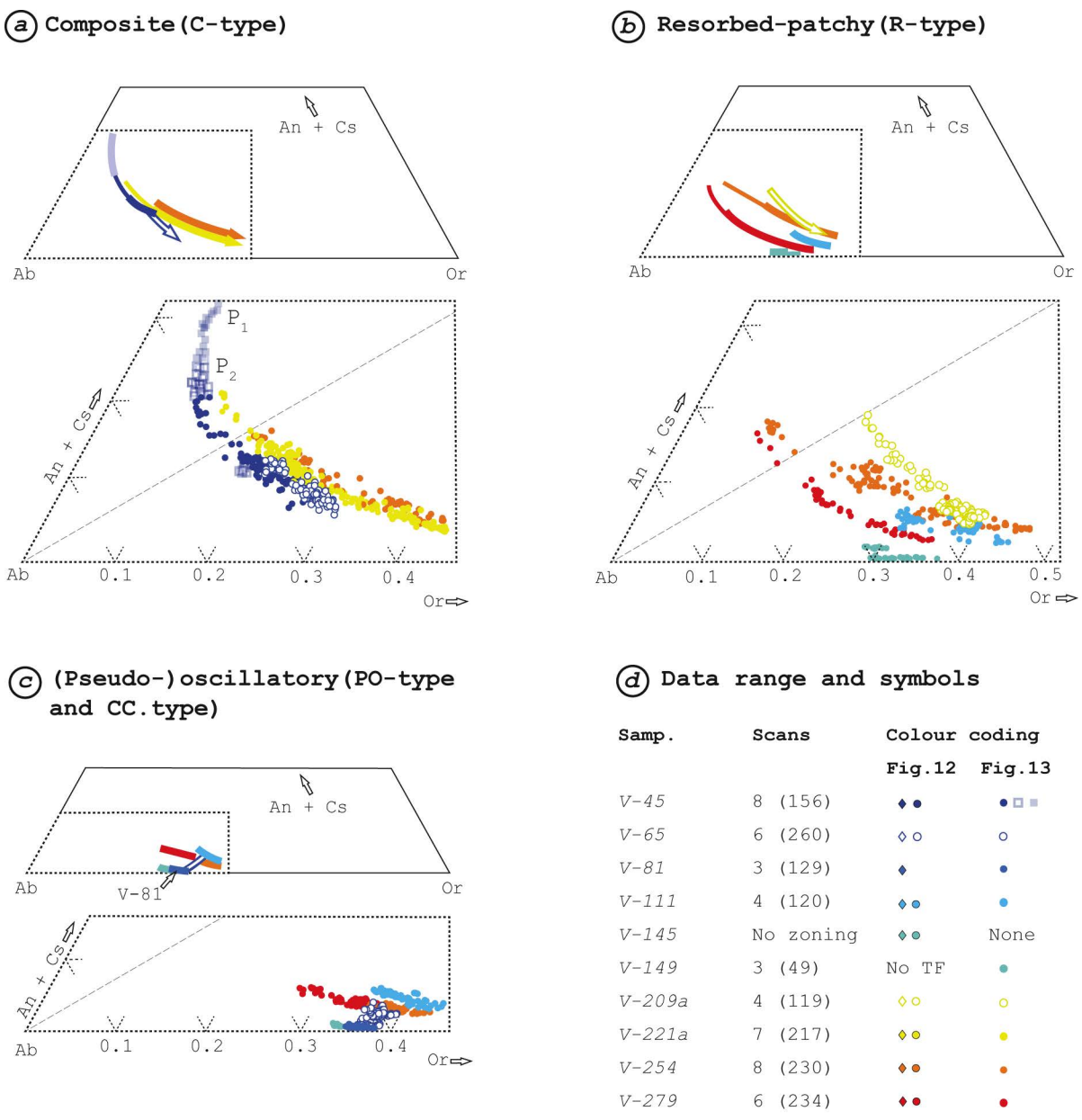

Figure 4.13: Discrimination of feldspar compositions from EMP analyses in step scans across feldspar grains that reveal textural zoning. (a) Represents step scans across compositional zoning. Arrows in (a) indicate a dominant compositional trend from core to rim across the interface of C-type zoning. Transparent blue boxes present plagioclase compositions in V-45. (b) Compositional variations across patchy zoning. (c) Compositional variations across (pseudo-)oscillatory zoning. (d) Table explaining colour coding and filling as well as data range. Scans always reflect consecutive steps from core to rim across zoning features and represent different crystals. The total number of analyses per sample is listed in brackets. Long dashed lines represents a ratio of An = Or for convenience, but do not represent a crystallographic boundary between plagioclase and alkali feldspar.

rison et al., 1994; Singer et al., 1998; Kelley, 2002). Common-denominator Ar isotope diagrams potentially allow for identification of heterochemical components (Villa, 2006). Data from TF analyses are presented in Fig. 4.12. Analysing the incremental release of $^{38}Ar_{Cl}$ and $^{37}Ar_{Ca}$ (relative to $^{39}Ar_K$) allows for discussion of analyses from SHW in a similar way (Figs. 4.9 and 4.10). Most of the $^{38}Ar_{Cl}$ values are negative and indicate either the absence of chlorine-derived ^{38}Ar or the determination of sample and blank analyses of ^{36}Ar and ^{39}Ar with low precision due to low intensities. The small signals of $^{38}Ar_{Cl}$ are surprising, as BSE imaging has revealed melt inclusions that are commonly potential hosts for $^{38}Ar_{Cl}$ (Kelley, 2002) in some of the feldspars picked. Below, we discuss feldspar zoning and melt inclusions with respect to their possible relation to deviating ^{40}Ar/^{39}Ar ages. We are aware of the possibly masked influence of mixed phases that could not be resolved with monitoring $^{38}Ar_{Cl}$.

Feldspar zoning in V-45

MGTF analyses of V-45 #30 were conducted on 10 grains per fusion. Investigating picked anorthoclase revealed the sporadic occurrence of resorption embayments. Compositional zoning with melt-rich cores is frequent in these grains (Fig. 4.5b). Some anorthoclase crystals in V-45 indicated resorbed crystal surfaces and were not picked (Fig. 4.3a). The most extreme variations in An-content revealed cores that are characterised by An > Or and that show an Or-rich overgrowth. TF analyses of V-45 show, accordingly, the highest contents of $^{37}Ar_{Ca}$ relative to $^{39}Ar_K$ (Fig. 4.12a). Contamination of the dated separates by plagioclase cannot be excluded. Euhedral plagioclase crystals in V-45 ranging from An_{38} to An_{25} (P1 in Fig. 4.13a) are similar in size to anorthoclase crystals and show oscillatory zoning. A second fraction of plagioclase (P2 in Fig. 4.13a) is also texturally similar but more depleted in An (<An_{25}) towards the rim and shows an overgrowth of anorthoclase compositions (Or > An). This overgrowth indicates dissolution surfaces (Fig. 4.5a). The low An-rims and the anorthoclase overgrowth (about $Ab_{70}Or_{20}An_{10}$) are chemically identical to C-type domains in anorthoclase crystals that have been separated for radiometric dating. Ba concentrations do not follow systematic enrichment with respect to texture (Fig. 4.14b), but span a wide range of concentrations from 600 to 2000 ppm, and correlate to Or. This observation contradicts to a partitioning of Ba between feldspar and peralkaline trachytic melt. The according partitioning coefficient decreases relative to increasing Or (Mahood and Stimac, 1990). Or contents in anorthoclase cease at Or_{30}. The growth of anorthoclase over plagioclase and the coupled increase in Ba and Or concentrations argue against a sequential as well as against a simultaneous two-feldspar crystallisation path (Brown and Parsons, 1994) for crystals from V-45. A peritectic one-plagioclase crystallisation path is thus the most suitable for these feldspars. The high-An plagioclase suggests a slightly different magmatic growth, as it does not show anorthoclase overgrowth and ended by crystallising An_{25}. However, the overall similar chemical compositions of the different plagioclase suggest a common magmatic source but slightly different magmatic compositions. As all feldspar in V-45 either occurs as incorporated in pumice or adheres to pumice, we assume that the different feldspars were incorporated in the same melt prior to eruption. Thus, the deviation in age potentially represents an influence of inherited cognate material.

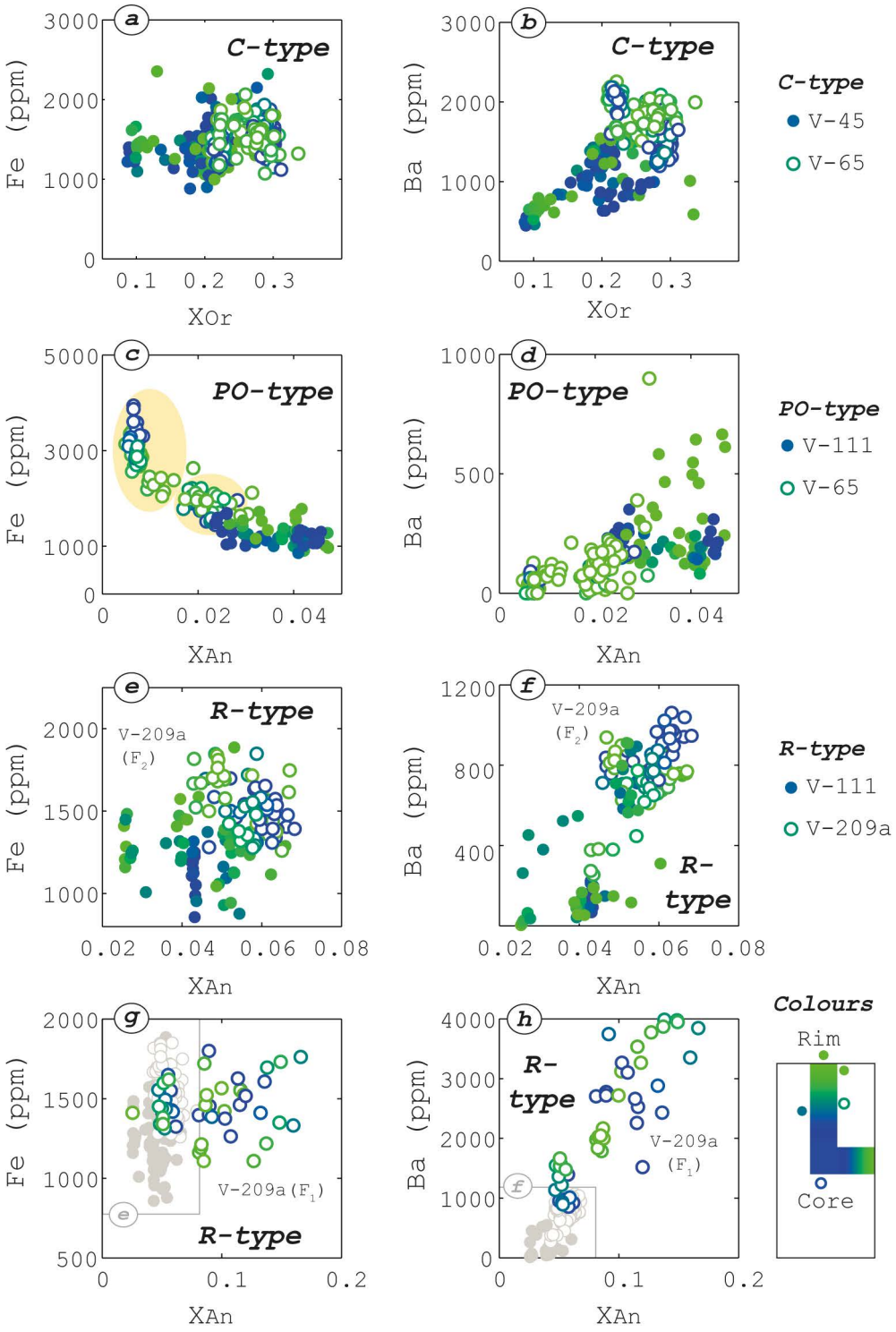

Figure 4.14: Concentrations of Fe and Ba in feldspar relative to Or and An components. C-type crystals are shown in (a) and (b). Data from PO- type crystals are represented in (c) and (d). R-type crystals of different compositions are illustrated in (e–h). Explanations for the signature are given underneath titles. Colour coding represents the position and is exemplified with a sketch next to (h).

Feldspar zoning in V-65

Some anorthoclase crystals from V-65 show stained surfaces that commonly originate from corrosion (Fig. 4.3c). These grains were not picked, but they point to the presence of a second fraction of feldspar in V-65. Non-corroded C- type zoned crystals show feldspar compositions identical to corroded crystals. C-type zoned crystals also reveal faint patchy patterns in CL images (Fig. 4.5c). The less abundant PO-type zoned crystals (Fig. 4.5d) document a second type of 'non-corroded' anorthoclase. PO-type crystals contain significantly less Ba (Fig. 4.14d). Two groups of PO-type zoned crystals can be distinguished by Fe contents (i. e., yellow patches in Fig. 4.14c). The Fe-rich group shows depletion of their Fe content towards the rims. Fe in PO-type zoning thus suggests heterogeneity among crystals, revealing PO- zoning. C-type crystals from V-65 contain less An than C-type crystals from V-45. This difference in feldspar composition is more distinct in $^{37}Ar_{Ca}$ relative to $^{39}Ar_K$ (Fig. 4.12a). The lowest ratios of $^{37}Ar_{Ca}$ are possibly due to the analyses of PO-type crystals. The compositional constraints suggest that PO-type crystals are formed at lower temperatures and increased P_{H_20} conditions (Brown and Parsons, 1994; Nekvasil, 1994; Ginibre et al., 2004). Their occurrence does not correspond to the expected magmatic conditions for the coexisting (and partly corroded) C-type crystals. We suggest that the C-type crystals precipitated prior to the formation of PO-type crystals and/or in a different magmatic environment. As no intergrowth of PO-type and C-type crystals (or zoning features) has been observed, a sequential crystallization path (Brown and Parsons, 1994) in a dry trachytic melt explains their co-occurrence best. Following this argumentation, C-type crystals can be suspected to represent disaggregated crystals from peripheral positions of a magmatic reservoir or a conduit. Corroded felsitic and devitrified lithics exist in V-65 and support this scenario (Fig. 4.3b).

Feldspar zoning in V-111

Anorthoclase crystals from V-111 are dominated by R-type and PO-type zoning textures (Fig. 4.4d and 4.5e). R-type zoning dominates coarse crystals and shows a maximum Ca/K of 0.21. Regarding the production ratio of $^{37}Ar_{Ca}$ and the spatial proportion of high An-domains in R-type crystals, this value matches the highest $^{37}Ar_{Ca}/^{39}Ar_K$ ratios from SGTF data, which show a maximum of ca. 0.1 (Fig. 4.12b). Ca, Ba and Fe contents in R-type crystals are comparable to those from PO-type analyses (Figs. 4.14c–f, and 4.13b). Embayed core-rim interfaces in PO-zoned crystals (Fig. 4.4c) indicate multiple phases of feldspar destabilisation. R-type zoned crystals can also reveal PO-type zoning towards the rims (Fig. 4.5e). The strong chemical and textural similarity of R-type crystal rims to PO-type crystals suggests that both types have experienced the same magmatic history. R-type crystals dominate the coarse #20 fraction in V-111 and V-111B. This fraction deviates from the age model by at least 12 ka. PO-type crystals dominate fine fractions. Combining the textural observation with the inverse isochron ages suggests that R-type crystals are hosts of an extraneous ^{40}Ar component. MGTF analyses are apparently less affected by this isotopic component. If R-type crystal fragments are mixed in MGTF analyses with predominant PO-type crystals, the extraneous ^{40}Ar component appears to be less dominant and goes unnoticed in the inverse isochron age of V-111B #30. These observations indicate a heterogeneous contribution of non-radiogenic excess ^{40}Ar (Fig. fig:isosketcha) to the inverse isochron of V-111 #20.

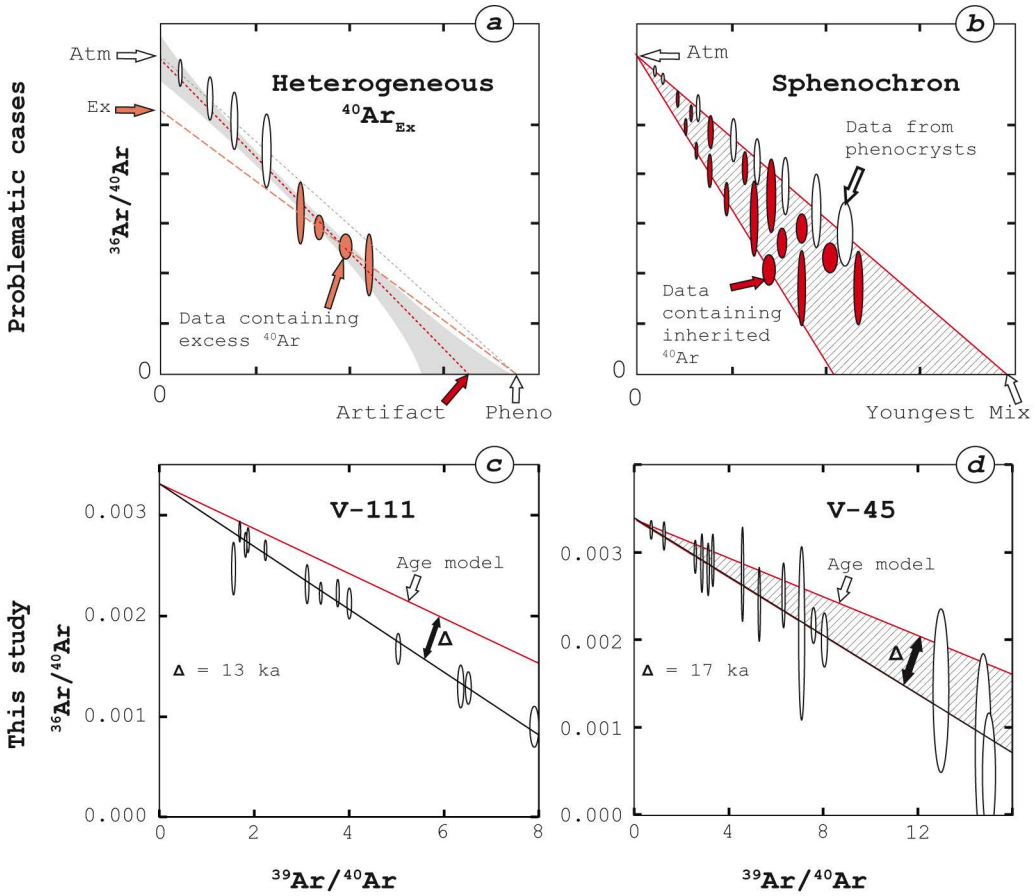

Figure 4.15: (a) A heterogeneous distribution of non-radiogenic excess ^{40}Ar impacting an inverse isochron is sketched after (Kuiper, 2002). (b) A sketch showing the impact of inherited radiogenic ^{40}Ar from antecrystic or xenocrystic crystals and creating a sphenochron (Chen et al., 1996). (c) Age contrast between inverse isochron calculation for V-111 #20 (black line) and the tephra's modelled maximum age (red line). (d) Comparison of inverse isochron for V-45 #20 (black line) with the tephra's modelled maximum age (red line). The idealised isochrons in red assume common initial ^{40}Ar/^{36}Ar and J-values. Age deviations are expressed with Δ. Pheno: age of phenocryts; Artifact: disturbed artifact age; Youngest mix: youngest possible mix age.

Feldspar zoning in V-209a

A small number of crystals show patchy R-type zoning covering a compositional range > 5 mol% An or Or (Fig. 4.13b). Fig. 4.14h displays varying Ba concentrations from such crystals (labelled F1). Other than these, most crystals have clustering Ba concentrations (F2 in Fig. 4.14f) and vary less in feldspar composition. The two types of patchy zoning contain similar concentrations of Fe (Fig. 4.14g). Some fragments of patchy anorthoclase have revealed that an An-rich rim grew during the last stage of crystallisation (Fig. 4.5f). Other crystals exhibit hardly any zoning and are compositionally similar to the An-poor patches of R-type crystals. The occurrence of the R-type crystals is not restricted to a single grain-size fraction. Average $^{40}Ar^*/^{39}Ar_K$ ratios from V-209a increase with higher ratios of $^{37}Ar_{Ca}/^{39}Ar_K$ (Fig. 4.12a). Anorthoclase crystals from V-209a #20 and V-209a #30 fractions have both revealed a non-radiogenic excess of ^{40}Ar in their initial ^{40}Ar/^{36}Ar data (Fig. 4.8). The calcium-related increases in $^{40}Ar^*/^{39}Ar_K$ hence hints an abundance of An-rich R-type crystals contributing to higher 'apparently radiogenic' ^{40}Ar and potentially include an extraneous component of ^{40}Ar. Emphasising the instrumental limitation in detecting $^{38}Ar_{Cl}$ mentioned above, this trend is interpreted with caution.

4.6 Interpretation of magmatic processes

Ginibre et al. (2004) were able to detect distinct magmatic environments from trace element pattern in sanidine zoning. This conclusion was based on the existing compositional stratification of the magma chamber that is displayed in the stratification of the sampled tephra. Their work further linked C-type zoning feldspars to cumulate xenoliths, and they deduced processes within a crystal wall mush as a potential source of the formation of C- and R-type zoning in sanidine. Another process was proposed by Troll and Schmincke (2002), who investigated feldspars that compositionally resembled anorthoclase and oligoclase from V-45. Ternary feldspars from their study were sampled from trachytic and rhyolitic ignimbrites. Interpreting compositional and trace element data, they proposed a step-cycle process that involved the mechanical movement of feldspars across the interfaces of small-scale immiscible magma batches. Compositional variations described by Troll and Schmincke (2002) occurred across small growth bands, interrupting normal or reverse zoning, and not as a pattern similar to R- or C-type zoning from this study. A comparison to patterns from their study thus lacks textural similarity. Processes recorded in PO-type crystals were characterised by Ginibre et al. (2004) by comparing Ba, Sr, and Ti relative to Ca. Sr is low in Nemruth and Süphan volcanics and only rarely exceeds 300 ppm in bulk rock samples (Özdemir et al., 2006; Çubukçu et al., 2012; Özdemir and Güleç, 2013; Sumita and Schmincke, 2013b). Accordingly, Sr was hardly detected in anorthoclase. Systematic trends in concentrations of Ti from anorthoclase with the different zoning types are absent (data provided in the electronic supplementary materials of the published study). Therefore, the given study has to rely on anticorrelation of Ca and Fe occurring across resorption surfaces (Fig. 4.4) in PO-type crystals. This anti-correlation across zoning patterns points to growth from a kinetically controlled, disequilibrium crystal-melt boundary layer (Shore and Fowler, 1996; Mollo et al., 2011). The overall consistent main composition of PO-type crystals shows that compositional changes in the magmatic environment are not involved in the formation of the zoning feature. Decompression, varying water contents, and/or temperatures are thus favourable processes recorded in PO-type surfaces that indicate dissolution (Nekvasil, 1994; Ginibre et al., 2004). Possible mechanisms are either magmatic ascent in a conduit or crystal migration in a residing reservoir (Ginibre et al., 2004). PO-crystals hence monitor an evolution that is located in the interior of a reservoir rather than in boundary layers or cupolas of a magma chamber. In comparison to C-type zoned crystals, resorption surfaces appear often plain and correspond with considerably less abundant melt inclusions. Combining the style of the resorption surfaces and the potential magmatic environment represented in PO-type zoned crystals indicates such crystals to be promising candidates for $^{40}Ar/^{39}Ar$ geochronology. We emphasise that inverse isochron ages from V-81 and V-111B #30 have been derived by analysing predominantly PO-type crystals that recorded the timing of the eruption concordantly to constraints from the age model.

4.7 Inherited ^{40}Ar or excess ^{40}Ar?

In describing extraneous ^{40}Ar a distinction can be made between inherited and excess ^{40}Ar. A radiogenic ^{40}Ar component that is produced within minerals via the decay of ^{40}K before the event dated (physical contamination of older material) is termed inherited ^{40}Ar. Incorporation

of ^{40}Ar via processes other than in-situ radioactive decay of ^{40}K is described with the term excess ^{40}Ar (McDougall and Harrison, 1999). In the following, we discuss both types of extraneous ^{40}Ar and their possible impact on ages presented in this study. Irrespective of the particular magmatic mechanism discussed above, the expected temperature that is required to resorb and re-precipitate hypersolvus anorthoclase would quickly degas inherited crystals. Spell et al. (2001) modelled Ar degassing from sanidine that is probably more retentive than anorthoclase, as it does not undergo a displacive transformation from monoclinic to triclinic symmetries during cooling, producing fine-scale twinning of Albite and Pericline laws (Parsons et al., 2015). Modelling the degassing behaviour of an antecrystic sanidine, which is entrained into a shallow and pre-eruptive silicic magma at temperatures that partially dissolve the crystal (e.g., ca. 800 °C for a P_{H_2O} of 3 kbar), revealed that a 1-mm-sized spherical sanidine (i.e., several ka older than syneruptive phenocrysts) degasses > 99% within days (Spell et al., 2001). We thus expect subdomains in C-type and R-type zoning in feldspars from V-45 and V-65 to be unlikely to account for any inherited ^{40}Ar.

An entrainment of material from the magma chamber walls (or conduit walls) would result in a mix of juvenile and disaggregated cognate material from an earlier magmatic pulse. If these antecrysts experienced a fast (duration of days) pre-eruptive combination of entrainment, dispersion, and eruption, they potentially impact on a distribution of apparent ^{40}Ar/^{39}Ar ages (Gansecki, 1998; Spell et al., 2001; Rivera et al., 2016). This scenario suggests the presence of abundant xenolithic fragments. V-65 shows corroded microcrystalline felsitic lithics. Another mechanism resulting in statistically robust inverse isochrons and overestimated ages is that of heterogeneously-distributed excess ^{40}Ar (Kuiper, 2002; Flude and Storey, 2016). This scenario (Fig. 4.14a) assumes a distribution of excess 4.14Ar that is derived from mixing three reservoirs: atmospheric, radiogenic, and non- radiogenic excess ^{40}Ar. Data points not affected by excess ^{40}Ar define a near-atmospheric end-member in an inverse isochron calculation. Data points that are affected increase the slope of the inverse isochron and result in an erroneously old age. By comparing stepwise and total fusion data from different aliquots in the same sample, Flude and Storey (2016) collected evidence for the existence of such a heterogeneous appearance of excess ^{40}Ar in feldspars from miarolitic granophyres. Applying a combined filtering and deconvolution approach to apparent ^{40}Ar/^{39}Ar ages Flude and Storey (2016) successfully isolated an age population that was likely unaffected by an excess of ^{40}Ar and matched other chronometers. The deconvolution assumes a Gaussian distribution of both contaminated and uncontaminated crystals. As substantially older apparent ages do not fulfil a Gaussian distribution, filtering the most deviating ages is required before applying an unmixing algorithm (Sambridge and Compston, 1994) such as the unmixing function in isoplot software (Ludwig, 2012). Except for data from V-65, an application of the algorithm did not unmix age populations younger than the deviating ages. As V-65 shows evidence for the coexistence of entrained crystallisates, it remains unclear whether the isolated population of apparent ages is derived from inherited or excess ^{40}Ar or both. However, the untangled younger population resulted in an age of 84 ± 23 ka for V-65 (Appendix 4.C).

Investigations of water geochemistry from the Nemrut crater lake and from Lake Van have detected a mean excess of $^{3}He/^{4}He$ and an incorporation of mantle helium components (Kipfer, 1994). ^{40}Ar/^{36}Ar ratios in mantle-derived Ar reaches values up to 40,000 (Graham, 2002), and

a heterogenic occurrence of fluid inclusions containing mantle-derived Ar in TF analysis could explain deviations from the age model. Ellis et al. (2017) argued that excess ^{40}Ar from mantle-derived Ar potentially explains the age deviations that have been discussed as being derived by analysing antecrystic feldspar elsewhere (Gansecki et al., 1996; Rivera et al., 2016). This scenario fits data from the here presented study with the observations that age deviations occur mainly in the youngest samples and only in TF experiments. The irregularly distributed fluid inclusions in combination with melt inclusions (Fig. 4.3d) point to an importance of excess ^{40}Ar for this study. We have interpreted the deviating ^{40}Ar/^{39}Ar dates to represent either a mix of antecrystic feldspar and syneruptive phenocrysts, or heterogeneously distributed excess ^{40}Ar (Fig. 4.14a) due to the variable abundance of melt and fluid inclusions in C-type and R-type crystals.

4.7.1 Inverse isochron calculations based on low ^{36}Ar signals

Smaller uncertainties in ^{36}Ar would potentially indicate extraneous ^{40}Ar components by resolving either trends in $^{38}Ar_{Cl}$ or deviations in inverse isochrons. Slightly scattering ^{36}Ar intensities from 11 cycles (this study) of peak-jumping ion-beam detection can generally be derived from collector noise, ion beam fluctuations (Mark et al., 2009), and interferences with isobaric hydrochlorine and hydrocarbon species (McDougall and Harrison, 1999). Simultaneous multi-collection of several masses, an increased mass resolving power, and reference gases represent approaches that improve the detection of ^{36}Ar (Mark et al., 2009; Saxton, 2015; Jicha et al., 2016). Working with data from a single detector instrument, we have recorded variations in the precision of the detection of ^{36}Ar. Significant variations in the precision of ^{40}Ar/^{36}Ar ratios call for caution when calculating inverse isochrons. This imprecision hinders the detection of sphenochrons, as suggested by (Chen et al., 1996) (Fig. 4.15b). Drawing an isochron for V-45 by connecting the maximum age model constraint with the same initial ^{40}Ar/^{36}Ar ratio from V-45 #30 results in a wedge that envelopes the upper limit of most data ellipses (Fig. 4.15d). The example of V-45 shows that low MSWD values (mostly due to low ^{36}Ar intensities) caution against the interpretation of the according inverse isochron age. The low value of 0.4 practically requires more precise ^{40}Ar/^{36}Ar data before the MSWD can be used as a statistical test (Wendt et al., 1991). The deviating age from the inverse isochron calculation for V-45 also illustrates the potential problem of calculating youngest mix ages in interpreting sphenochrons. Dating tephra from ICDP PALEOVAN cores shows the importance of carefully interpreting these ages in the light of age constraints from other chronometers.

4.8 Conclusions

This work presents radiometric ^{40}Ar/^{39}Ar ages from tephra in the composite core of the ICDP PALEOVAN drilling record. A multi-proxy age model from lacustrine sediments has been used to test statistically and stratigraphically radiometric ages and vice versa. Facing different ways to calculate and to interpret results from ^{40}Ar/^{39}Ar analyses, this work offers radiometric age assignments. Evidence for the presence of extraneous ^{40}Ar is given for most of the samples, and accordingly weighted average calculations from apparent ^{40}Ar/^{39}Ar age spectra predominantly deviate from the model. Fourteen inverse isochron ages have revealed concordance with the age

model and support particularly the lower part of the PALEOVAN record. Four inverse isochron ages are discordant with the age model. Reviewing the feldspar compositions, as well as over- and underlying age control points, indicates extraneous ^{40}Ar contributing to the deviation. The majority of the dated feldspars show zoning patterns that are subdivided into three main types. Feldspars from samples that provided deviating ages show either a compositional zoning type (C-type zoning), a minor element zoning type (PO-type zoning), or a heterogonous-patchy zoning pattern (R-type-zoning). Compositional variations from C-type and most of the R-type crystals are interpreted as representing crystallisation in magma chamber cupolas, as wall mushes, or in narrow conduits. The consistent compositions of PO-type crystals and the number of surfaces recording dissolution argue for growth from a more differentiated melt and in a central location of a magma reservoir. As PO-type crystals also incorporate a lesser degree of melt inclusions, they are the most promising crystals for $^{40}Ar/^{39}Ar$ dating of tephras that provide a variety of feldspar compositions and textures within a small sample size. It is inferred that C-type and R-type crystals contribute preferentially to inverse isochron age calculations that deviate the climate-stratigraphic age model.

Acknowledgements

We are grateful to T. Litt and N. Pickarski, who joined the sampling at the Bremen core repository at MARUM. J. Engelhardt gives thanks to two anonymous reviewers and Fred Jourdan for commenting on an earlier version of this manuscript. We thank C. Günther, who operated some EMP analytics and M. Müller, who assisted in sample preparation and argon analytics. This work has been funded by the International Continental Scientific Drilling Program (ICDP) and the Deutsche Forschungsgemeinschaft (DFG) [OB80/48-1].

Appendix 4.A: Electronic supplementary material

Supplementary data associated with this article can be found, in the online version, at http://dx.doi.org/10.1016/j.gca.2017.07.039.

Appendix 4.B: $^{40}Ar/^{39}Ar$ methods

A value of (5.463 ± 0.0214) 10^{-10} as the total ^{40}K decay constant λ (Min et al., 2000) was used for age calculations in this article. K_2SO_4 and CaF_2 were co-irradiated in the first irradiation (PO-2). Samples from irradiation PO-3 were corrected with the same interference corrections as samples from PO-2. J values were derived by 4 TF analyses of the monitor mineral. Production rates of ^{37}Ar from Ca were calculated by using a factor of 1.84 (Onstott et al., 1995).

Appendix 4.C: Deconvolution of V-65

The unmix algorithm from Ludwig (2012) was used to detect a population that resulted in an age of 83 ± 23 ka. This population represents a fraction of 0.28 from the entire distribution. The relative misfit parameter (Sambridge and Compston, 1994) represents an inverse logarithmic likelihood as a function of the suggested age populations. This calculation assumed two populations and resulted in a relative misfit of 0.975. As this deconvolution faces the absence

of a Gaussian distribution, the age of 83 ± 23 ka is only suited for a qualitative exploration of data from V-65.

5 $^{40}Ar/^{39}Ar$ Dating of Volcanic Glass from ICDP Lake Van Cores

5.1 Introduction

Engelhardt et al. (2017) applied three different $^{40}Ar/^{39}Ar$ dating approaches on feldspars from volcaniclastic air falls and strengthened the validity of the age model with dominantly agreeing $^{40}Ar/^{39}Ar$ ages. Outliers from three samples were significantly older than constraints from the age model. The heterogeneous incorporation of excess ^{40}Ar (by heterogeneously distributed melt and fluid-inclusions) and the inheritance of ^{40}Ar from epiclastic or shallow magmatic contamination are potential reasons for deviations in age. In order to re-assess the deviating samples, co-genetic volcanic glass was analysed by the $^{40}Ar/^{39}Ar$ method using stepwise laserprobe heating (SWH). Discussing Ar isotopes from volcanic glass may provide information on the potential involvement of excess ^{40}Ar in melt-inclusions that could have affected $^{40}Ar/^{39}Ar$ dating of feldspars and thus caused deviating ages. As volcanic glass is prone to rapid hydration, Ar isotope data from volcanic glass will furthermore be screened for potential analogous in noble gas isotope analyses from pore waters that had been sampled from similar depth underneath the lake floor. Tomonaga et al. (2014) investigated pore water from core material from AR by noble gas isotope analyses of Ne, Ar, and He and deduced fluid migration in sediments. The on-site pore water analyses (Fig. 5.1) document a hydrochemical trend from freshwaters to waters having increased pH and salinity (Litt et al., 2012; Litt et al., 2014). This chapter thus screens Ar isotope ratios from volcanic glass for similarities to noble gas data from pore water (Tomonaga et al., 2014) and takes chemical indices of glass alteration from electron microprobe analysis (EMPA) into account.

5.2 Materials and methods

5.2.1 Samples

Four sampled tephra layers (V-45, V-65, V-57b, V-209a) show a sorted abundance of pyroclasts and phenocrysts within the layer. Grading features relative to the density and buoyancy of the pyrogenic components are observed as well. An additional sample (V-165) shows no grading and no sorting. V-45, V-65, V-57b, and V-209a vary from coarse ash to lapillis. Besides pumice and low vesicular glass shards the petrography includes anorthoclase, oligoclase, augite, and fragments of fayalite and hedenbergite. V-165 is a thin (< 3cm), highly vitric, and homogenous lapilli tephra containing very fresh glass shards. Sampled glass shards range from 250 to 750 μm in grain size and show hydrated rims that are visible in transmitting light (Fig. 5.2a) and in back scattered electron (BSE) images (Fig. 5.2b). Rim thickness reaches a maximum of 200 micrometres. No systematic relation between age and rim thickness was observed as would be expected for obsidian hydration dating (Pierce and Friedman, 2000). Shards from V-65 and V-209a have abundant microphenocrysts of apatite (Fig. 5.2c). Shards from V-45 reveal

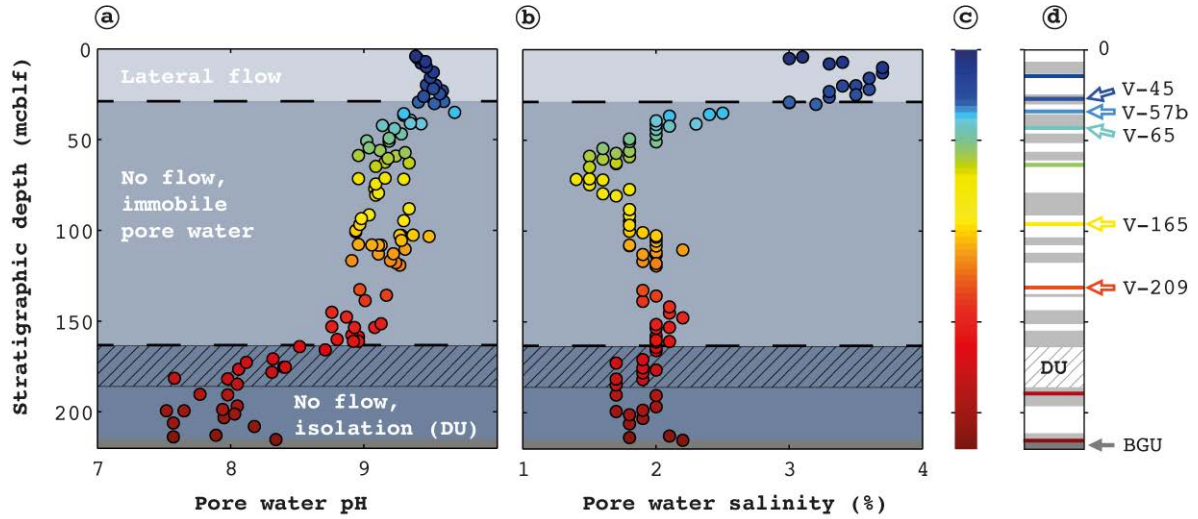

Figure 5.1: Pore water chemistry from Lake Van drill cores at Ahlat Ridge drilling site. (a) On site pH measurements versus stratigraphic depth in meter composite core below lake floor (mcblf). (b) Salinity in % versus depth. (c) Colour indicates sample depth. (d) Lithostratigraphic sketch after Stockhecke et al. (2014b) indicating sample positions (arrows indicate samples that underwent $^{40}Ar/^{39}Ar$ dating, locations of samples analysed by the XRD method are simply represented by colours). The colour coding for the sample position in the vertical axis is analogue for all figures. Pore water data was provided by the PAELOVAN scientific drilling team (Litt et al., 2012). Interpretation of three pore water regimes is illustrated in three grey scales and dashed lines. The interpretation was adopted from Tomonaga et al. (2014).

entrapped gas that shows a characteristic corona in transmitting light and that is separated from a second phase by a thin meniscus (Fig. 5.2d). Whether the second phase represents a fluid requires confirmation by microthermometry. The glasses are trachytic to rhyolitic in composition (Fig. 5.3a). Glasses from V-65 and V-45 show vesicles containing two phases.

V-43, V-114, V-269 and V-299 represent four additional samples that have been selected for XRD analyses. The XRD analyses were conducted in order to check whether the presence of alteration products of volcanic glass are a result of contrasting pore water regimes. V-43 represents a dark, vitric coarse ash. Grey to rusty coarse and pumice-rich lapillis were found in V-114. V-269 represents a dark and coarse ash and is made of well-sorted scoria. The sampled material from V-299 is fine lapillis of dominantly plagioclase, mafic minerals and dark vitreous lithic fragments. All four samples contain glassy components but are expected to have resided in highly contrasting pore water regimes since their deposition (Tomonaga et al., 2014).

5.2.2 Methods

Electron microprobe analyses were conducted at the GFZ Potsdam. Chemical analyses of mounted glass shards were obtained using a Jeol Hyperprobe JXA-8500F with a wavelength-dispersive detector. The energy of the 10 μm-wide electron beam was 15 keV and the beam current was 2 nA resulting in a current density of 0.025 nA/mm^2 to avoid sodium migration (Morgan and London, 2005). Standards and procedures are presented in the methodoloy in greater detail (Chapter 3). The EMPA data are used to calculate three alteration indices for the sampled volcanic glass. Molar proportions of element oxides of Na, K, Ca, Mg, and Al are used for calculating the weathering index of Parker (1970) (WIP), the chemical index of alteration (CIA) following Nesbitt and Young (1982), and the chemical index of weathering of Harnois (1988) (CIW). For the application of the $^{40}Ar/^{39}Ar$ method shards were handpicked

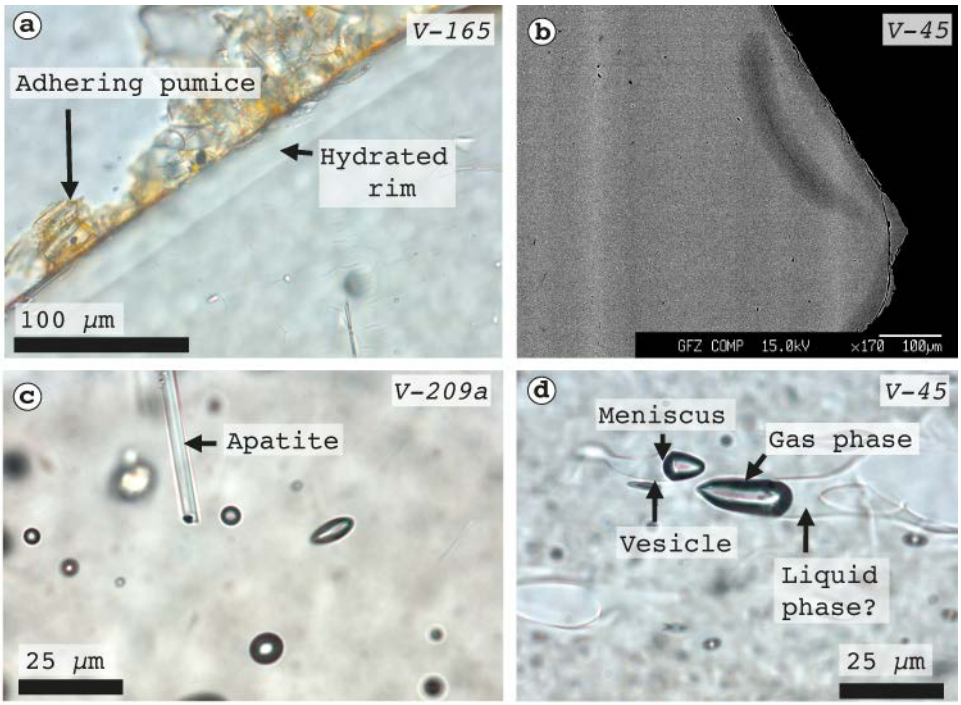

Figure 5.2: Photomicrographs of exemplary glass shards from three different samples. (a) Altered pumice adhering to a hydrated rim from V-165 in transmitting plane-polarized light (ppl). (b) Glass from V-45 in a backscattered electron image shows a darker edge that indicates the lower common atomic number in the hydrated rim. (c) Vesicles and an apatite crystal in pristine glass from V-209a in ppl. (d) Vesicles from V-45 showing the existence of two trapped phases separated by a meniscus in ppl.

two times. Separated material underwent a cleaning procedure that involved bathing in 0.001 M HCl, acetone and in distilled H_2O. As bathing in HCl is critical for discussing Ar isotope data with respect to ^{38}Ar, ultra sonic bathing in H_2O was repeated four times.

Irradiation of the shards took four hours at the Cd-lined in-core irradiation tube (CLICIT) facility in the TRIGA reactor of the Oregon State University. Alder Creek sanidine (ACs-2) monitored neutron flux during the irradiation and J-values were calculated relative to the age of 1.1864 ± 0.0003 Ma (Jicha et al., 2016). An electron multiplier pulse-counting system detected ion-beam intensities during 11 cycles of peak-jumping mass analysis. Isotopic corrections, statistical tests and age calculations were conducted using ArArCalc (Koppers, 2002). Uncertainties include an estimate of absolute errors by incorporation of the systematic error on the total decay constant λ_{40K} (Koppers, 2002). High fractions of atmospheric ^{40}Ar (> 97 %) resulted in imprecise determination of the radiogenic components. Therefore, all stated uncertainties will be represented on the one standard deviation level. High atmospheric ^{40}Ar fractions also required frequent measuring of air samples in order to monitor changing mass discrimination factors. A total of 13 measurements of air (Appendix D) have been conducted before and during analyses of glass. The instrumental equipment and the applied constants as well as the procedures are presented in Chapter 3. The methodology and analytical procedure of the XRD measurements are presented in Appendix A.

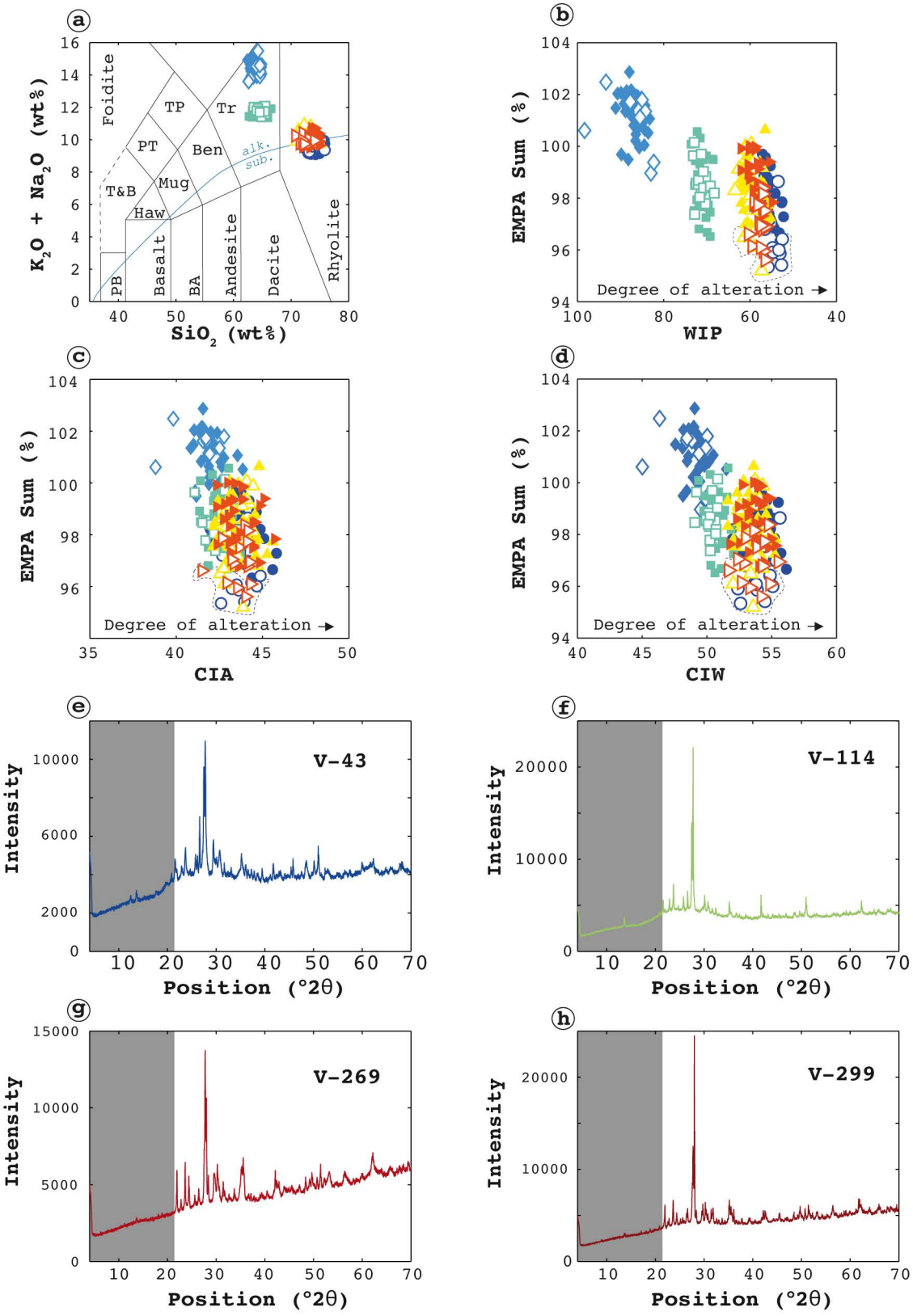

Figure 5.3: (a) Total alkali versus silica diagram after Lebas et al. (1986). (b) to (d) Different weathering indices versus Cl- and F- corrected totals from EMP analyses. Measurements of hydrated rims are displayed as open symbols. Measurements of the pristine interior are displayed as filled symbols. Dashed lines in (b) to (d) envelope data of hydrated rims only. (e) to (h) XRD 2θ-scans for four samples from different pore water regimes. Grey bars indicate the 2θ range that is expected to identify peaks for typical clay minerals from glass alteration. Colour-coding is given in 5.1d for XRF and XRD data.

5.3 Results

Calculated weathering indices, of CIA and CIW, classify volcanic glass as fairly fresh (Table 5.1). Instead, the WIP records a slight trend (Fig. 5.3b) that identifies the stratigraphically uppermost (V-45) as well as the two lowermost samples (V-165, V-209a) as more strongly altered than V-65 and V-57b. Price and Velbel (2003) concluded that the WIP is most suitable for screening the degree of alteration of felsic igneous rocks. CIW and CIA do not allow Al mobility and differ from each other in considering K leaching (CIA considers K loss).

XRD-scans from four vitreous volcaniclastics that resided in different pore water-regimes hardly show peaks in 2θ positions $< 22°$ (Fig. 5.3e to 5.3h). The low-angle range is expected to typically reveal significant peaks from weathering products of silicic volcanic glass such as kaolinite, smectites (montmorillonites and bidellites), illites, zeolithes, halloysite, allophan and gibbsite (Kirkman and McHardy, 1980; Nesbitt and Young, 1984; Quantin et al., 1988). The overall low degree of alteration is surprising for samples that resided tens of thousands of years in basic pore water and indicates pore water immobility and rapid equilibration of the water rock interaction.

The mass discrimination factor (MDF) has been obtained twice during the measuring campaign (Fig. 5.4a) and both values were statistically indistinguishable. The high fractions of atmospheric ^{40}Ar causes high uncertainties of the calculated radiogenic Ar proportion (Fig. 5.4b). This effect is known to limit the precision and applicability of the ^{40}Ar/^{39}Ar method (see Fig. 3 in McDougall, 2014). Blank measurements during the campaign were fairly constant. Outliers are displayed best by screening ^{36}Ar intensities (Fig. 5.4c) and were documented during analyses of V-165 and V-57b. V-45, V-165 and V-57b show that highest blank intensities are connected to late degassing steps. Early degassing steps from V-65 show an opposite trend as the last two blanks showed the lowest intensities.

The plateau ages (Fig. 5.5) and the stratigraphically closest temporal markers (Fig. 5.6) from the paleoclimatic age control model (Stockhecke et al., 2014b; Stockhecke et al., 2016) suggests that the ^{40}Ar/^{39}Ar chronometer is intact in the volcanic glass samples. Table 5.2 presents an overview of the selected results relative to next underlying and overlying temporal markers from the age model (Stockhecke et al., 2014a; Stockhecke et al., 2016).

Corrected ^{38}Ar intensities (for contributions from blank-, atmosphere- and K-derived ^{38}Ar) may represent the abundance of chlorine due to neutron capture of ^{37}Cl during the neutron irradiation (McDougall and Harrison, 1999). V-65 and V-165 show that the release of $^{38}Ar_{Cl}$ resembles the release of potential radiogenic $^{40}Ar^*$ (Fig. 5.7) and indicate the existence of chlorine-rich phases that contribute to the Ar budgets of the samples. V-57b and V-65 reveal a correlation of $^{40}Ar^*$ and $^{38}Ar_{Cl}$ having $^{39}Ar_K$ as a common denominator (Table 5.3). V-45 and V-209a show no correlations of $^{38}Ar_{Cl}$ to the other Ar isotopes. The first two degassing steps from V-57b contain very low $^{39}Ar_K$ (each less 1% of all released $^{39}Ar_K$) and are isolated from a discussion about the potential relation of $^{38}Ar_{Cl}$ to $^{40}Ar^*$. All samples construct fairly well defined planes in mix diagrams (Fig. 5.3) following Kelley et al. (1986), Turner (1988), and Villa (2001).

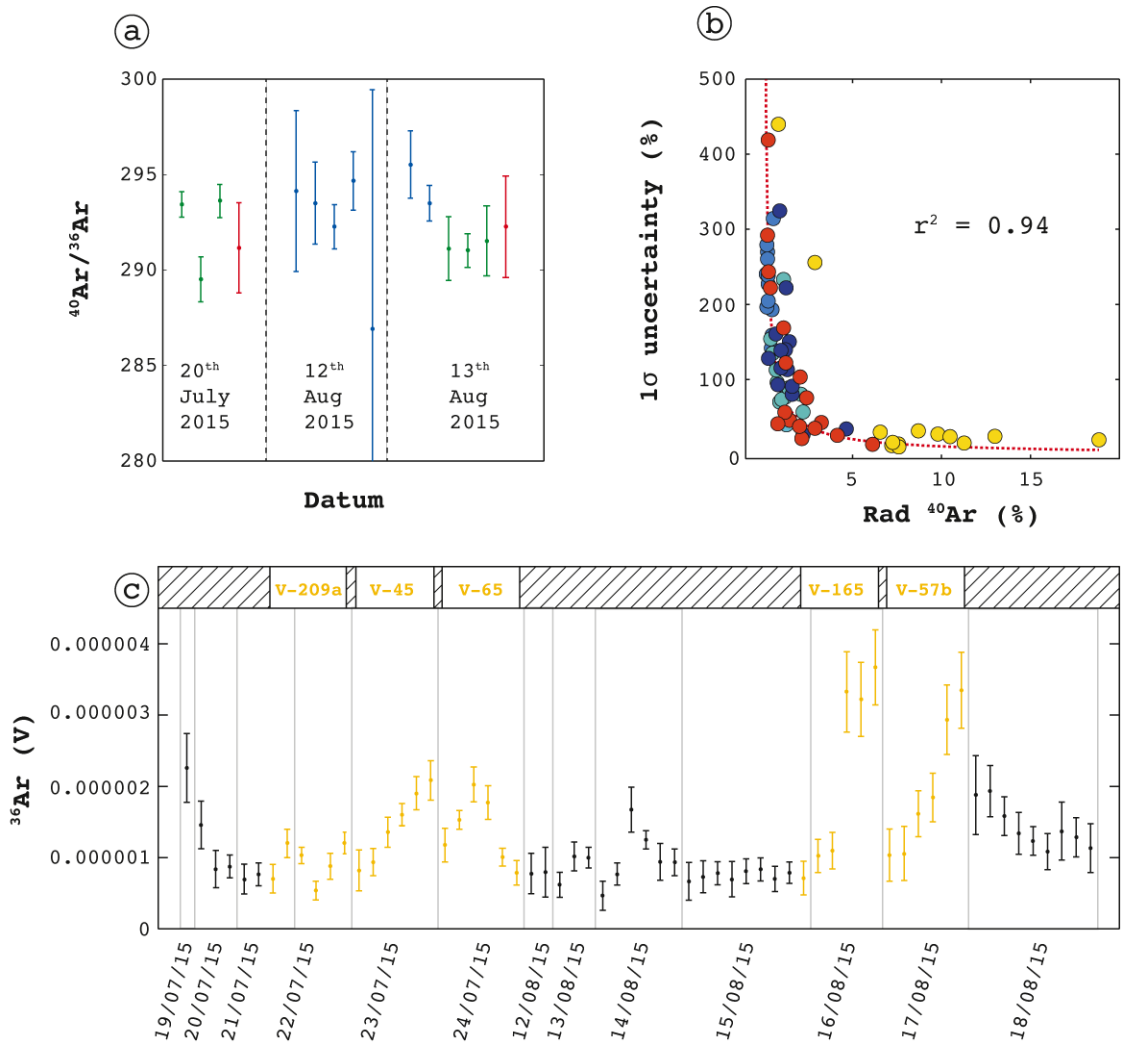

Figure 5.4: (a) $^{40}Ar/^{36}Ar$ from measurements of atmospheric air. Green ratios served for calculating a weighted average that is shown in in red. These weighted averages represent the inverse of the mass discrimination factor. Dashed lines separate the dates of the analyses. (b) Relation of the uncertainty in apparent age and the fraction of radiogenic ^{40}Ar. Symbol colours indicate samples as presented in Fig. 5.1d. (c) ^{36}Ar intensities from blank measurements during analyses in summer 2015. All measurements of volcanic glass have been taken between 19^{th} of July and 18^{th} of August 2015. Those analyses that correct measurements on sample gas are shown in yellow.

Table 5.1: Summary of average EMPA data. The standard deviation of the mean of all measurements is presented underneath of each row of average values. The number of analyses is given as n. The ranges of possible alteration indices are provided underneath EMPA data.

Sample	n	SiO_2	TiO_2	Al_2O_3	FeO	MnO	MgO	CaO	Na_2O	K_2O	BaO	ZnO	F	Cl	P_2O_5	SO_3	Total	WIP	CIW	CIA
V-45 (core)	32	74.60	0.15	10.60	2.55	0.02	0.010	0.15	5.30	4.37	0.127	0.07	0.03	0.03	0.05	0.03	98.09	55.6	54.1	43.8
SD		0.79	0.07	0.15	0.10	0.03	0.012	0.07	0.19	0.22	0.125	0.09	0.06	0.03	0.09	0.04	0.94	1.7	1.0	0.9
V-45 (rim)	15	73.70	0.14	10.39	2.54	0.02	0.013	0.13	5.22	4.33	0.104	0.06	0.03	0.04	0.02	0.04	96.78	54.9	54.1	43.6
SD		1.01	0.06	0.16	0.09	0.03	0.021	0.08	0.19	0.21	0.110	0.08	0.05	0.03	0.04	0.05	1.03	1.6	1.0	0.7
V-57b (core)	34	63.91	0.38	15.86	5.44	0.02	0.025	0.80	9.08	5.32	0.127	0.06	0.10	0.04	0.07	0.04	101.27	87.0	49.2	41.9
SD		0.64	0.08	0.21	0.15	0.03	0.023	0.08	0.24	0.20	0.157	0.08	0.11	0.04	0.10	0.05	0.80	2.0	0.7	0.7
V-57b (rim)	10	63.78	0.37	15.76	5.38	0.01	0.029	0.77	9.31	5.18	0.204	0.08	0.09	0.03	0.08	0.04	101.11	87.5	48.6	41.6
SD		1.06	0.06	0.19	0.14	0.03	0.015	0.08	0.72	0.15	0.177	0.07	0.10	0.03	0.05	0.05	1.10	4.9	1.7	1.3
V-65 (core)	29	64.45	0.50	13.84	6.25	0.02	0.015	1.35	6.70	5.03	0.149	0.08	0.01	0.04	0.07	0.05	98.55	71.2	50.7	42.5
SD		1.00	0.07	0.31	0.22	0.02	0.016	0.10	0.16	0.21	0.165	0.10	0.03	0.03	0.07	0.06	1.11	1.4	0.8	0.6
V-65 (rim)	15	64.67	0.50	13.64	6.24	0.02	0.007	1.32	6.75	5.04	0.179	0.05	0.01	0.04	0.16	0.04	98.66	71.3	50.2	42.3
SD		0.63	0.08	0.48	0.15	0.02	0.012	0.14	0.17	0.16	0.160	0.06	0.03	0.04	0.15	0.04	0.74	1.4	0.5	0.7
V-165 (core)	40	72.97	0.20	11.31	3.05	0.01	0.009	0.25	5.72	4.55	0.123	0.07	0.04	0.03	0.03	0.02	98.39	59.5	53.4	43.5
SD		0.81	0.06	0.16	0.15	0.03	0.011	0.07	0.18	0.24	0.133	0.10	0.08	0.03	0.05	0.04	0.91	1.8	0.9	0.9
V-165 (rim)	19	72.64	0.19	11.32	2.93	0.02	0.007	0.23	5.74	4.56	0.120	0.05	0.02	0.03	0.06	0.03	97.95	59.7	53.4	43.6
SD		1.02	0.07	0.27	0.14	0.02	0.012	0.05	0.23	0.26	0.160	0.07	0.05	0.03	0.08	0.04	1.37	1.7	0.7	0.7
V-209a (core)	30	73.69	0.19	11.11	2.86	0.02	0.007	0.23	5.57	4.55	0.107	0.08	0.01	0.04	0.06	0.04	98.56	58.5	53.7	43.6
SD		0.79	0.08	0.16	0.13	0.02	0.012	0.06	0.17	0.21	0.122	0.07	0.02	0.03	0.06	0.05	0.96	1.8	0.8	0.9
V-209a (rim)	14	72.44	0.20	10.98	2.84	0.01	0.012	0.25	5.49	4.47	0.113	0.05	0.03	0.04	0.04	0.03	97.00	57.7	53.7	43.6
SD		0.91	0.05	0.18	0.13	0.02	0.014	0.08	0.15	0.15	0.145	0.09	0.08	0.03	0.05	0.06	0.87	1.2	1.1	0.8

Indices Scaling	WIP	CIW	CIA
Optimum fresh	$\geq$100	$\leq$50	$\leq$50
Optimum weathered	0	100	100
Al mobility allowed?	Yes	No	No

Table 5.2: Summary of SWH $^{40}Ar/^{39}Ar$ results. Probability (p) is derived from statistical f-tests (isochrons) and t-tests (plateaus). Initial $^{40}Ar/^{36}Ar$ from air is assumed to be 298.56 ± 0.31 (Lee et al., 2006). Next lower and upper temporal markers from relative dating are presented in detail in Stockhecke et al. (2014a)[1] and Stockhecke et al. (2016)[2]. Those that are displayed with $\pm n.s.$ have no specified uncertainty in the cited reference. $^{40}Ar/^{39}Ar$ age recommendations are displayed in bold numbers.

Sample	n	Depth (mcblf)	Plateau age (ka)	Plateau MSWD	Plateau p (%)	Inverse isochron age (ka)	Inverse isochron MSWD	Inverse isochron p (%)	Initial $^{40}Ar/^{36}Ar$	Next upper temporal marker[1,2] (ka)	Next lower temporal marker[1,2] (ka)
V-45	14 (14)	26.69	87 ± 20	0.9	56	**63 ± 17**	0.9	53	300 ± 1	58.5± 1.3	59.4 ± 1.3
V-57b	14 (14)	33.81	**71 ± 55**	0.1	100	9 ± 12	0.1	100	299 ± 1	74 ± n.s.	76 ± n.s.
V-65	13 (13)	43.41	129 ± 30	0.2	100	**105 ± 44**	0.2	100	299 ± 1	85 ± n.s.	90 ± n.s.
V-165	9 (14)	99.32	**194 ± 12**	0.1	100	216 ± 53	0.1	100	296 ± 7	199 ± 2	220 ± 2
V-209a	18 (18)	131.38	**268 ± 25**	0.4	99	279± 34	0.4	98	298 ± 1	274 ± 2	279 ± 2

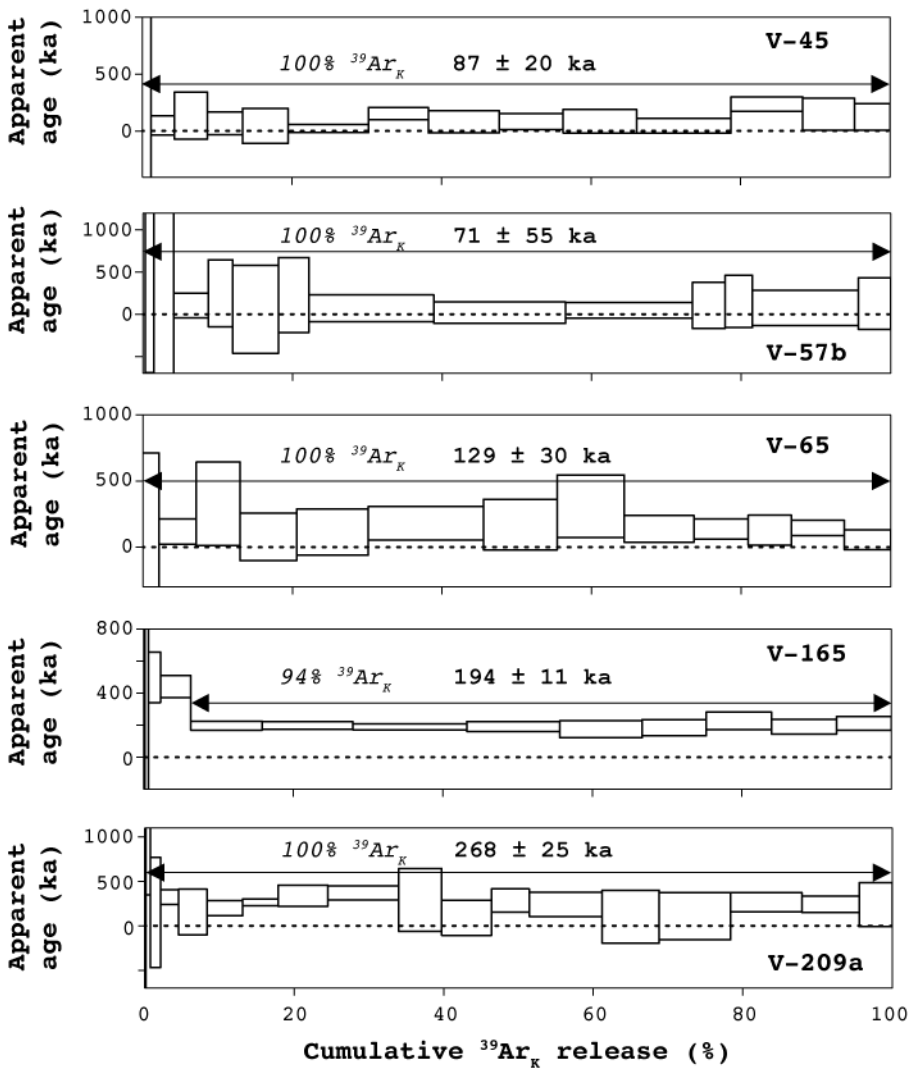

Figure 5.5: Distribution of apparent ages vs. the cumulative degassing of K-derived ^{39}Ar. Plateau forming degassing steps are presented by the span of a double-sided arrow.

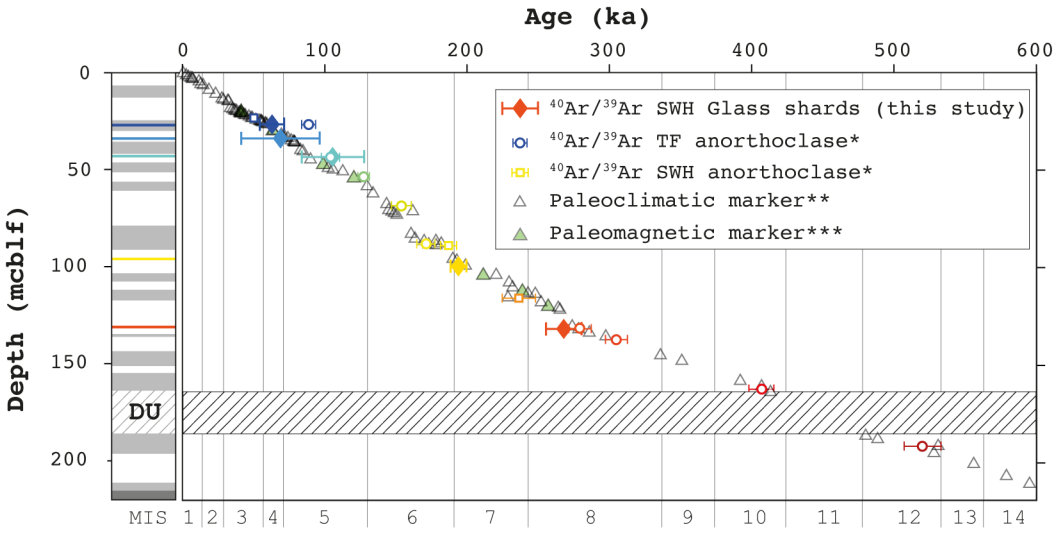

Figure 5.6: Ages versus stratigraphic depth. Selected results from total fusion (TF) and stepwise heating (SWH) ^{40}Ar/^{39}Ar dating of anorthoclase are presented in (Engelhardt et al., 2017)*. Various temporal markers (tephrostratigraphy, climate tuning, varve counting) are summarised in (Stockhecke et al., 2014b)**. Paleomagnetic data are presented in detail in Vigliotti et al. (2014)***. MIS abbreviates marine isotope stages. All uncertainties represent one standard deviation.

5.4 Discussion

5.4.1 Glass ages from V-45, V-65 and V-209a

Glass shards from all three samples reveal inverse isochron ages that overlap the age model. Plateau ages from glass of V-45 and V-65 deviate the next underlying modelled temporal marker (Table 5.2) by being 6 ka and 9 ka older, respectively. The deviation of these plateau ages and the low radiogenic ^{40}Ar proportions (commonly $< 2\%$ in all degassing steps) suggest that a small excess ^{40}Ar component is potentially camouflaged by the predominance of atmospheric ^{40}Ar but affects the plateau age calculations. Accordingly, isochron ages were preferentially assigned for dating the emplacement of V-45 and V-65. V-65 reveals a multi-linear correlation of ^{40}Ar to $^{38}Ar_{Cl}$ in a CAKE mix diagram and indicates the involvement of excess ^{40}Ar in a Cl-rich Ar source of the glass (Fig. 5.8). This line of argument implies that the deviating age from co-genetic anorthoclase (Engelhardt et al., 2017) is a result of camouflaged excess ^{40}Ar. The feldspar inverse isochron age, that is slightly older than the the suggestion of the age model, can thus be explained by an irregular contamination of melt- (and potentially appendant fluid-) inclusions. Such an irregular contamination has been described by described by Kuiper (2002) and Flude and Storey (2016) and its effect on inverse isochron calculations is illustrated in Fig. 4.14.

5.4.2 A Cl-rich end member in the Ar budget of V-57b and V-65

V-57 and V-65 allow the determination of point M (Figs. 5.8a to 5.8b, statistical parameters are given in Table 5.3), that represents the ratio of excess ^{40}Ar to atmospheric ^{40}Ar in a hypothetical Cl-rich Ar end member (Kelley et al., 1986). This ratio was used to calculate an alternative initial ^{40}Ar/^{36}Ar ratio in point M ($^{40}Ar_M/^{36}Ar_M$) that unravels the potential excess of ^{40}Ar from a chlorine-bearing end member. The $^{40}Ar_M/^{36}Ar_M$ ratio from V-65 reveals an outlier from atmospheric values (Fig. 5.9a). Similarly ^{40}Ar/^{36}Ar ratios from over and underlying pore

water samples (Tomonaga et al., 2014) point to a surplus of ^{40}Ar, but overlap atmospheric compositions due to high uncertainties. Tomonaga et al. (2014) suggest that excursions, which show an enrichment of the heavier isotopes (^{22}Ne and ^{40}Ar) in the pore water, are related to one of two potential fractionation processes: (i) the formation of a free gas phase (e.g., methane production) in the pore space and (ii) diffusion controlled degassing. Assuming that the ratio of the volume of the free gas phase relative to the volume of the fluid phase is $<< 1$, process (i) would strip the lighter isotope from the pore water (Ballentine et al., 2002). As the fractionation of Ne by process (i) is greater than the fractionation of Ar (Ballentine et al., 2002) process (i) seems more eligible to explain the qualitative excursions from air saturated water (ASW) in the pore waters between 30 and 55 mcblf (Fig. 5.9a and 5.9b). Cukur et al. (2013) collected evidence from high-resolution seismic data that document the existence of free gas phases in lacustrine sediments of the Ahlat Ridge. Tephra deposits are preferential host for the free gas phases (Cukur et al., 2013).

The Cl-related $^{40}Ar_M/^{36}Ar_M$ ratio from V-65 raises the question whether mechanical and chemical comminution of volcanic glass is a mechanism that links noble gas signatures in the pore water of the lake sediments to magmatic volatiles from vitric volcaniclastics. Sub-atmospheric ^{20}Ne/^{22}Ne in pore waters (Tomonaga et al., 2014) co-occurs with ^{40}Ar/^{36}Ar values that qualitatively exceed the atmospheric ratio of 298.56 ± 0.31 (Lee et al., 2006) (Fig. 5.9). Low and sub-atmospheric ^{20}Ne/^{22}Ne ratios ($\leq$ 9.8) are neither derived from terrigenic nor from atmospheric reservoirs and favour fractionation processes mentioned above. The in-situ gas release from vitric volcaniclastics thus seems to play no role in the noble gas geochemistry of pore waters from the upper AR record.

5.4.3 Problems and potentials in detecting the Cl-rich Ar end member

As V-57 and V-65 have high fractions of atmospheric ^{40}Ar (> 97.5% in all degassing steps) it remains possible that the plane fitting in the CAKE mix diagram represents an artefact of clustering atmospheric values. Furthermore, the petrography offers three potential Cl-bearing phases in the shards: hydrated rims, microphenocrystic apatite and volatiles trapped in vesicles. As the largest $^{38}Ar_{Cl}$ release is not restricted to earliest degassing steps (Fig. 5.7), it appears unlikely that hydrated rims are the host of a Cl-rich Ar end member that contributes to the Ar release of the samples. This observation is in accordance with the virtual absence of alteration in the samples in the alteration indices and the lack alteration products. Irradiation and extraction

Table 5.3: Statistics and results of calculating an alternative initial $^{40}Ar_M/^{36}Ar_M$ ratio of a chlorine-rich end member contributing to the Ar budget of the samples. Goodness of fit (r^2) and slope (m) of linear regressions are presented for two different common denominator plots (specified in grey bars above). The goodness of fit from multi-linear regression in a CAKE mix diagram is listed in the column "r^2 plane".

	$^{40}Ar^*/^{39}Ar_K$ vs. $^{38}Ar_{Cl}/^{39}Ar_K$		$^{36}Ar/^{40}Ar$ vs. $^{38}Ar_{Cl}/^{40}Ar$					
Sample	r^2	m	r^2	m	r^2 plane	$\frac{^{40}Ar_M}{^{36}Ar_M}$	±	Remark
V-45	0.32	-53	0.17	-0.04	0.60	-	-	No (positive) correlation of $^{38}Ar_{Cl}$ to $^{40}Ar^*$
V-57b	0.60	28	0.26	-0.04	0.47	301	7	Filtering first two degassing steps
V-65	0.70	141	0.68	-0.21	0.81	306	3	None
V-165	0.03	-56	0.71	-0.12	0.98	-	-	No positive correlation of $^{38}Ar_{Cl}$ to $^{40}Ar^*$
V-209a	0.10	591	0.18	-0.67	0.78	-	-	No correlation of $^{38}Ar_{Cl}$ to $^{40}Ar^*$

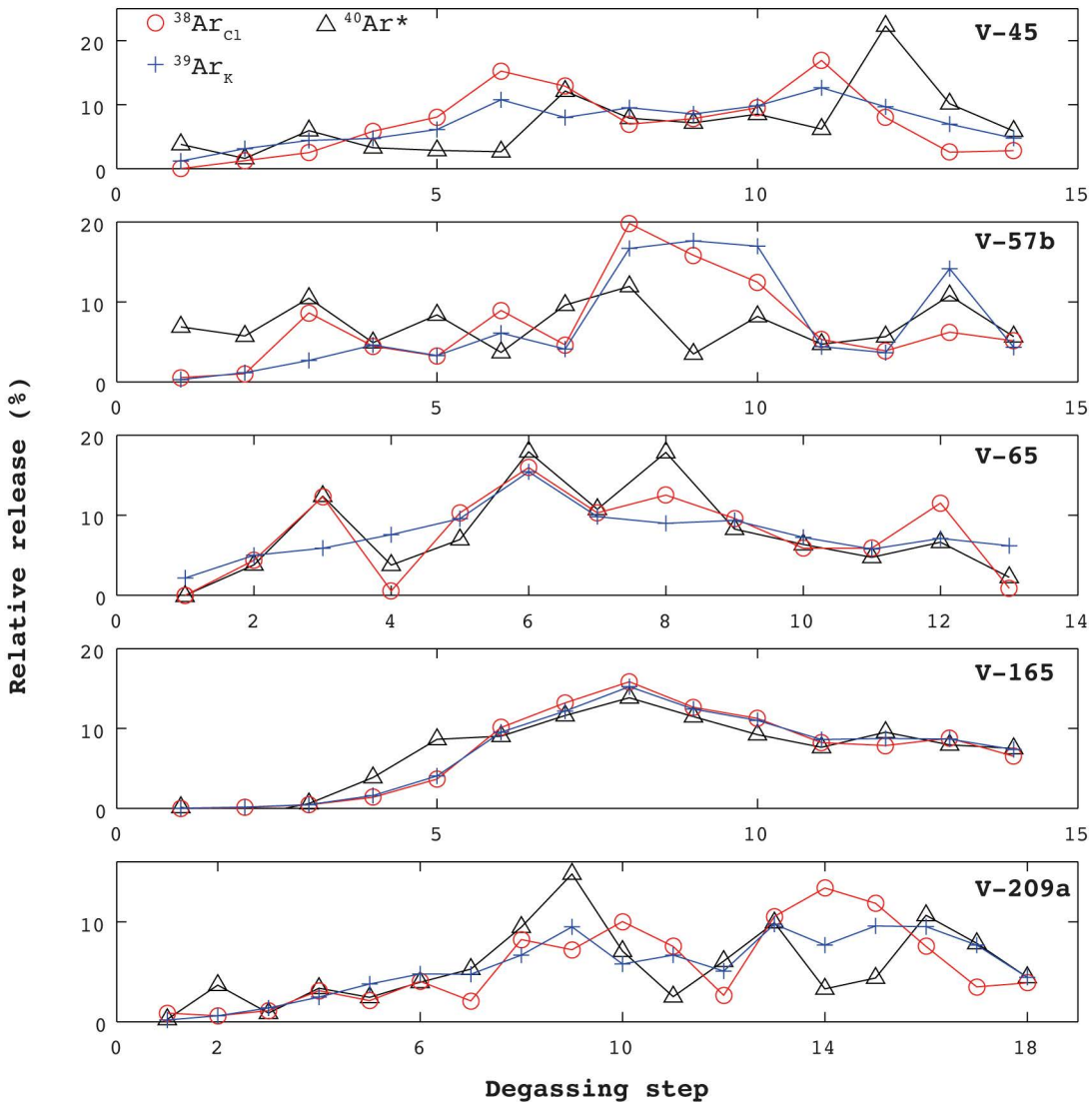

Figure 5.7: Relative release of $^{38}Ar_{Cl}$,$^{39}Ar_K$ and $^{40}Ar^*$ during stepwise degassing of the volcanic glass samples.

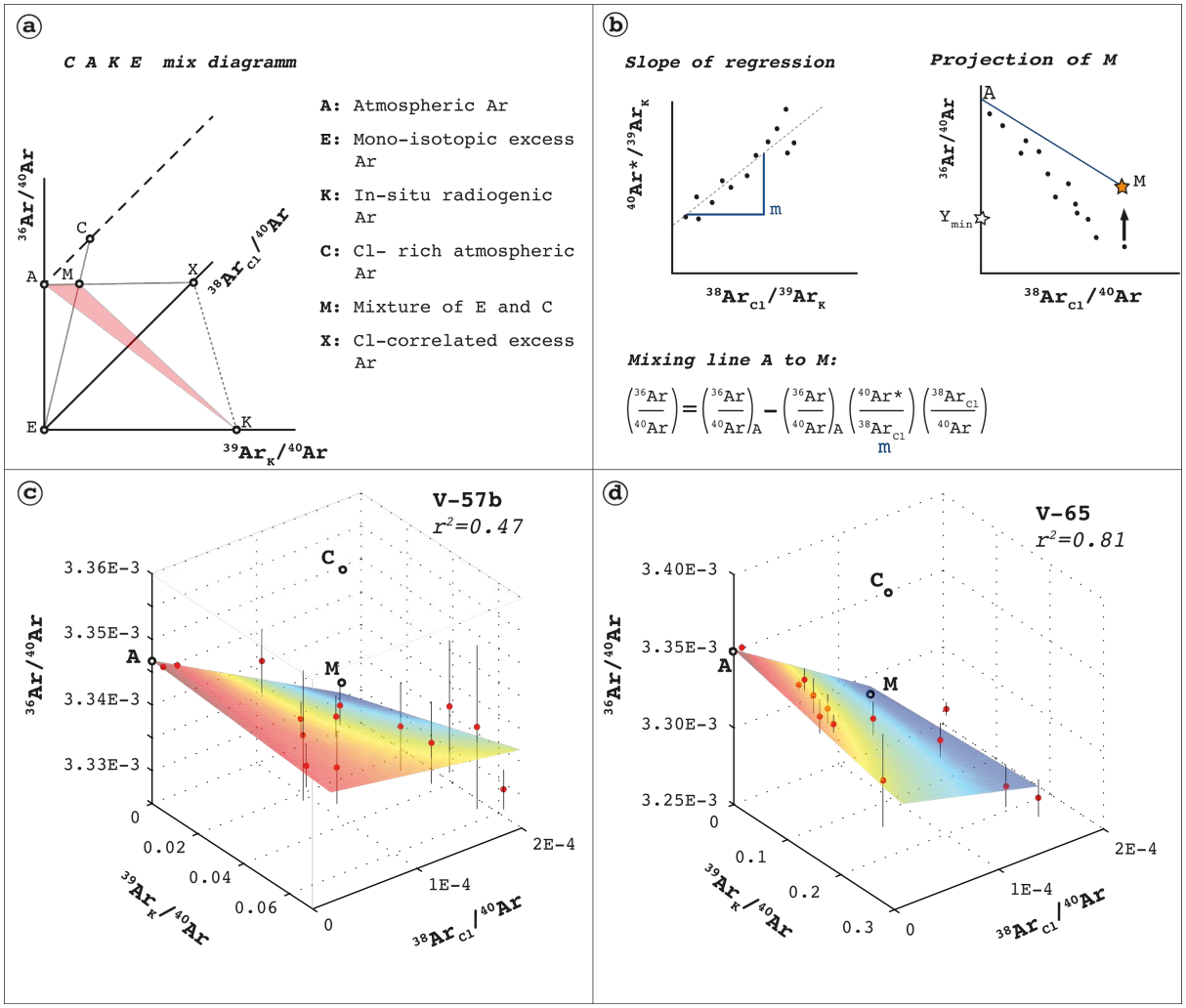

Figure 5.8: (a) Positions of Ar source end members in a hypothetical and three-dimensional CAKE mix diagram (Kelley et al., 1986; Turner, 1988). (b) Determination of the point M that represents a mix of mono-isotopic excess ^{40}Ar (point E) and atmospheric ^{40}Ar in a hypothetical Cl-rich phase (point C). (c) CAKE diagram presentation of data from sample V-57. (d) CAKE diagram presentation of data from sample V-65. Colour coding of the fitted plane is scaled relative to the vertical extend of the data set (that is the $^{36}Ar/^{40}Ar$ ratio).

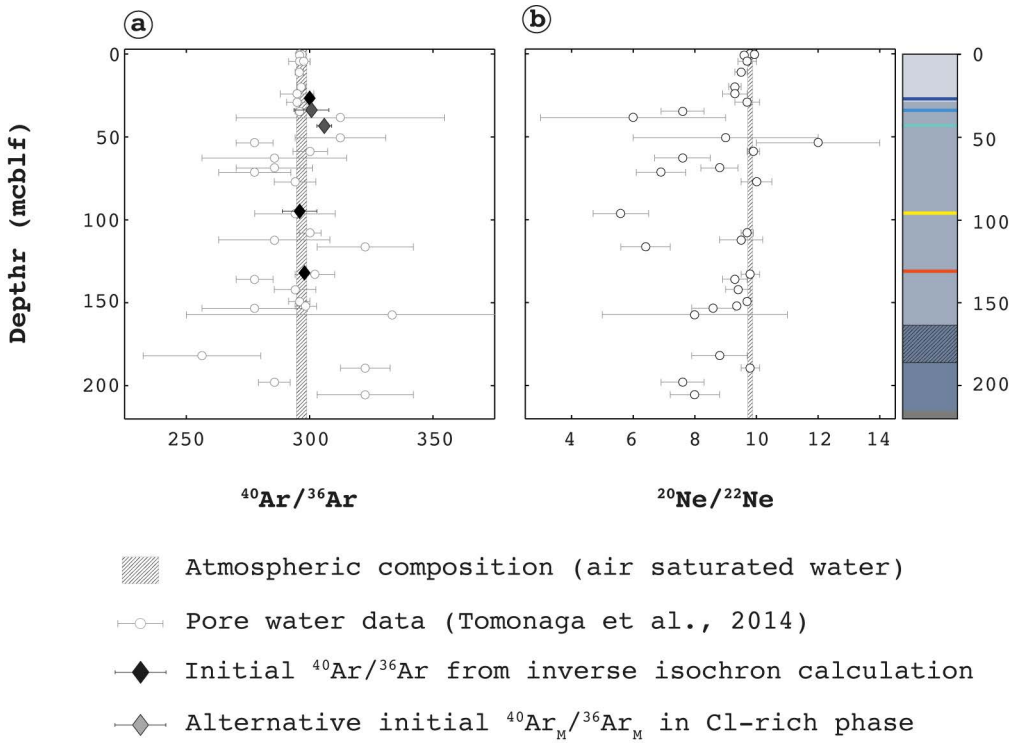

Figure 5.9: Noble gas ratios from sediment pore water from Tomonaga et al. (2014). (a) $^{40}Ar/^{36}Ar$ from pore water, measured initial $^{40}Ar/^{36}Ar$ ratios from volcanic glass and calculated alternative initial $^{40}Ar_M/^{36}Ar_M$ from a chlorine-rich end member in volcanic glass. (b) $^{22}Ne/^{20}Ne$ ratios of pore water. Grey bars represent the extend of atmospheric $^{22}Ne/^{20}Ne$ (Porcelli et al., 2002) and $^{40}Ar/^{36}Ar$ ratios. The latter ranges from a minimum value of Steiger and Jäger (1977) to a maximum value of Lee et al. (2006).

methods used in this study are not designed to analyse $^{38}Ar_{Cl}$ in detail due to the absence of thermal neutron irradiation and in-vacuo crushing methods (Turner, 1988). However, pyroclastic material represents ca. 17 % of the recovered material from the AR composite core (Stockhecke et al., 2014a). Faulting and alteration of the abundant vitric volcaniclastics may release magmatic volatiles that contribute to the noble gas signatures in pore water regimes. Accordingly, highest He concentrations from pore water in shallow lake sediments (Tomonaga et al., 2011) were measured in locations close to faults flanking the Tatvan Basin (Fig. 2.9c) . In-vacuo crushing analyses of volcanic glass from tephra in ICDP PALEOVAN cores remain to be done have the potential to mimic the noble gas release from faulted tephra into pore water regimes of the Lake Van basin.

5.5 Conclusions

This chapter presents five $^{40}Ar/^{39}Ar$ ages from glass shards of trachytic and rhyolitic pumice falls from the ICDP Lake Van drill cores. Assigned ages from volcanic glass are imprecise due to a surplus of atmospheric Ar. Nevertheless, $^{40}Ar/^{39}Ar$ ages overlap a climate-stratigraphic age model. Whereas anorthoclase $^{40}Ar/^{39}Ar$ ages from two samples deviated the age model, co-genetic volcanic glass resulted in inverse isochron ages that roughly overlap with the model. Chemical alteration indices show that the degree of alteration of glass shards is small for samples that resided tens of thousands of years in basic pore water.

Two samples unravelled correlations between chlorine-derived $^{38}Ar_{Cl}$ and $^{40}Ar^*$ and allowed

the calculation of an alternative initial $^{40}Ar_M/^{36}Ar_M$ compositions. These ratios represent the influence of a hypothetical Cl-rich phase in the volcanic glass and indicate a small contribution of excess ^{40}Ar. One of the $^{40}Ar_M/^{36}Ar_M$ ratios is stratigraphically coincident with outliers from ^{40}Ar/^{36}Ar measurements of pore waters. As an excursion of low ^{22}Ne/^{20}Ne is also observed in the particular pore water sample, it appears unlikely that pore water and volatiles from volcanic glass are connected. The multi-linear regression of the three isotope ratios remains imprecise due to high atmospheric fractions of ^{40}Ar. It is speculated that a chlorine-rich source provided an Ar-reservoir that is capable of affecting feldspar ^{40}Ar/^{39}Ar dating of V-65 by irregularly distributed melt- (and possibly fluid-) inclusion.

6 Recalculation of an $^{40}Ar/^{39}Ar$ Standard Validates Chronostratigraphy in ICDP Lake Van Record

6.1 Introduction

Orbital tuning of well-recorded cyclic stratigraphy has the potential to accurately model emplacement ages of volcaniclastics (Kuiper et al., 2008; Meyers et al., 2012). In application together with radioisotopic dating procedures, cyclostratigraphic age modelling has the potential to reveal misinterpretations and vice versa (Engelhardt et al., 2017). Most notably, the benefit of combining both methods has resulted in astronomical calibrations of feldspar mineral standards that are widely used in radiometric $^{40}Ar/^{39}Ar$ geochronology (Kuiper et al., 2005; Kuiper et al., 2008; Rivera et al., 2011). Aligned climate proxies from the AR record are in precise synchronicity to climate reference curves (Stockhecke et al., 2014a). The AR composite record thus allows reference to astronomical cyclicity and in parts to Dansgaard-Oeschger events (Litt et al., 2014; Stockhecke et al., 2014a; Stockhecke et al., 2014b). This study presents a calculation of a piecewise cubic hermite interpolating polynominal (pchip) (Fritsch and Carlson, 1980; Kahaner et al., 1989) that models a straightforward age to depth relationship. $^{40}Ar/^{39}Ar$ ages that date the emplacement of volcaniclastic layers (Engelhardt et al., 2017) are transformed into $^{40}Ar/^{39}Ar$ irradiation monitor values (J-values) that are usually obtained by analyzing mineral standards. Thus, the analytical and the geological setup from Engelhardt et al. (2017) allows treating the Alder Creek Sanidine mineral standard (e. g. Turrin et al., 1994; Nomade et al., 2005; Jicha et al., 2016; Niespolo et al., 2017) as an unknown sample. An exemplary recalculation of the reference age will hence be possible. This unprecedented climatostratigraphic calibration of an $^{40}Ar/^{39}Ar$ (or any radioisotopic) mineral standard tests the lacustrine age to depth model.

6.2 Age-depth relationship

A hypothetical lacustrine composite record was compiled that discards all volcaniclastic and fluvial deposits from the composite core (Stockhecke et al., 2014a; Stockhecke et al., 2014b; Stockhecke et al., 2016). Thus, an event-corrected composite record offered the construction of an age model by correlating signals from sediment color reflectance, elemental Ca/K ratios, total organic carbon content, and arboreal pollen statistics to Quaternary time scales (Kwiecien et al., 2014; Litt et al., 2014; Stockhecke et al., 2014a; Stockhecke et al., 2014b; Stockhecke et al., 2016). Stockhecke et al. (2016) presented a refinement of the event-free chronology that assigned temporal marker to the lacustrine record from proxy alignment to 5 Quaternary time scales (Table 6.1). Additionally five temporal markers were assigned to the age model by extrapolating the lacustrine sedimentation. The chronological model was largely approved by agreeing data from relative paleointensity of the earth's magnetic field (Vigliotti et al., 2014), by varve counting, tephrostratigraphy and cosmogenic nuclides (Stockhecke et al., 2016) and radiometric

$^{40}Ar/^{39}Ar$ dating (Stockhecke et al., 2014a; Engelhardt et al., 2017). A more thorough review of the age-depth model constructed by Stockhecke et al. (2014a) and Stockhecke et al. (2016) is provided in Chapter 2.

6.2.1 Details about methods and calculations

Instrumental $^{40}Ar/^{39}Ar$ analytics are sufficiently described in detail in Engelhardt et al. (2017) and in Chapter 3. Furthermore, Ar isotope intensities can be found in Appendix C. Calculations of irradiation monitoring of the volcaniclastic PALEOVAN minerals and of single crystal ACs-2 ages were achieved by using the ArArCALC software (Koppers, 2002). Apparent ages were exported from ArArCALC and a weighted mean was calculated using the 2σ analytical uncertainty as a weighing factor. The weighted average, the standard deviation and the weighted error of the mean were computed in MATLAB and followed calculations stated in Samson and Alexander (1987), Deino and Potts (1992), and Taylor (1997). ArArCALC provides a J-value normalization that enables the calculation of an inverse isochron from differently irradiated aliquots of the same sample. An inverse isochron of the 38 analyses that were interpreted in the given study resulted in an age of 1193 ± 12 ka. The common statistical parameters are as follows: p-value (f-test statistics) = 1; MSWD = 0.4. Ar isotope intensities, according J-values and inverse isochron data (Fig. D.1) are available in Appendix D.

Monitor ages all based on an interpolation of the age to depth relationship obtained in the composite core from the Ahlat Ridge drill site. The interpolated age to depth relationship used temporal markers from climatostratigraphic tuning presented in Stockhecke et al. (2016), variations of the earth magnetic field presented in Vigliotti et al. (2014), and varve counting as well as extrapolated sedimentation from Stockhecke et al. (2014a). The interpolation is constructed with 22,000 modeled data points. Accordingly, the model has a resolution of about one modeled age per cm of stratigraphy. The pchip calculation was achieved by the 'pchip' command in the software MATLAB. Additionally, 5^{th} degree polynomial and the spline interpolation were achieved by the 'spline' and 'polyfit' commands, respectively, using the same software.

As the Lashamp event was detected in two different signals (paleomagnetics and ^{10}Be flux peak) the pchip interpolation bases on an averaged stratigraphic (the signals overlap stratigraphically) position for the identical age. 66 of total 99 temporal marker from climate tuning provide assigned uncertainties. Those having no assigned uncertainties were either interpolated with a least squares approach or extrapolated linearly (lowest nine marker). The modelled values were assigned with uncertainties in the same way, unless they are the stratigraphically closest value to a temporal marker and assigned with its uncertainty. All uncertainties of the markers in the climate-stratigraphic model were treated as the representation of one standard deviation. As some errors assigned to temporal markers in climatic time scales represent absolute errors, an overrepresentation exists and was propagated to the age calculation of the ACs-2 age. These overestimations represent a minimal effect on J-value uncertainty and they are regarded to be negligible for the purpose of this chapter.

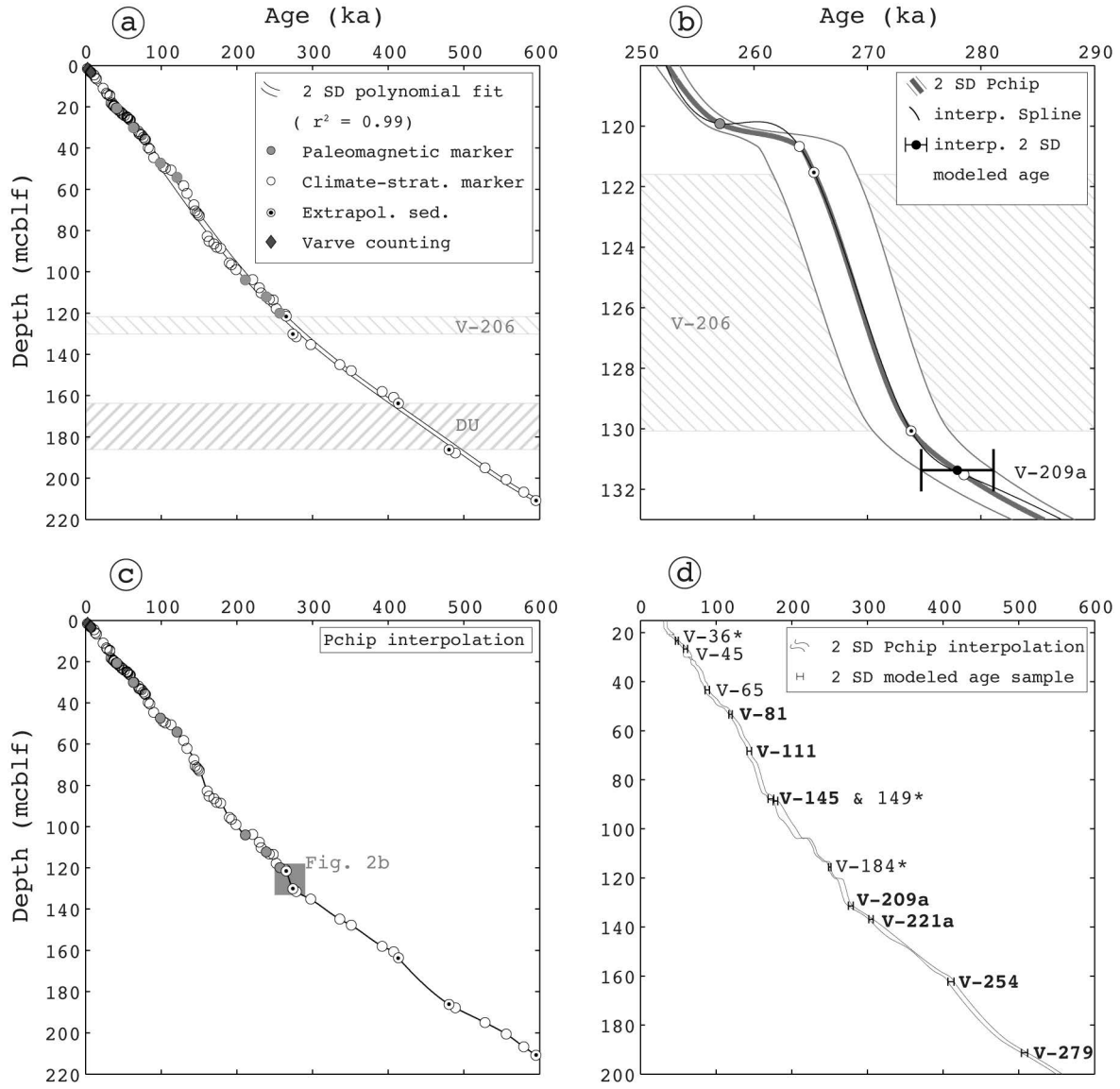

Figure 6.1: Age versus depth plots. (a) Various temporal marker being interpolated with a 5^{th} degree polynomial. (b) Close-up of age to depth relationship for V-206 comparing spline to pchip modelling at higher resolution. (c) Modelling the age to depth relationship using the pchip interpolation and highlighting the extend of the close-up in Fig. 6.1b. (d) Extent of the pchip interpolation and its two standard deviation together with age assignments for the selected volcaniclastics. Bold numbers in (d) label sample IDs that contribute minerals to the here presented ACs-2 recalculation. Sample IDs with an asterisk were irradiated differently and do not appear in this chapter at all.

Table 6.1: Timescales contributing to the age model from Stockhecke et al. (2014b). GLT_syn_SA* and GLT_syn_GDC** abbreviate the GLT_syn SpeleoAge and the GLT_GDC3Age timescales, respectively.

Timescale	Number of markers	Stratigraphic Range (mcblf)	Temporal range (ka)	References
NGRIP GICC05	30	5 - 27	12 - 60	Rasmussen et al. (2006), Andersen et al. (2004)
GICC05modeltext	13	30 - 45	64 - 90	Wolff et al. (2010)
AICC2012	3	49 - 51	102 - 113	Veres et al. (2013)
GLT_syn_SA*	27	58 - 151	130 - 392	Barker et al. (2011)
GLT_syn_GDC**	5	161 - 207	489 -579	Barker et al. (2011)

6.3 Modelling ages for volcaniclastics

Engelhardt et al. (2017) presented feldspar $^{40}Ar/^{39}Ar$ ages that agree with temporal marker from the climatostratigraphic age model between 53 and 191mcblf of the AR record. Two samples taken from the upper 53 mcblf deviated next underlying temporal markers from the model. By dating cogenetic volcanic glass this thesis showed in Chapter 5 that deviating anorthoclase $^{40}Ar/^{39}Ar$ ages are a result of a heterogeneous contamination of excess ^{40}Ar from irregularly occurring melt- or fluid-inclusions as proposed by Esser et al. (1997) and Kuiper (2002). Stratigraphically below 53 mcblf feldspar $^{40}Ar/^{39}Ar$ ages are in good agreement to the climate-stratigraphic age model. Simple polynomial fitting of the age to depth relationship including all event-related layers succeeds with covering >99 % of the variance of the climatostratigraphic, limnologic and paleomagnetic marker (Fig. 6.1a). The cubic spline interpolations homogenize the second derivative (De Boor, 1978) and do not guarantee a detailed preservation of the shape of the modeled chronology. Although pchip interpolations are considerably less smooth than spline interpolations, they are less oscillatory at high resolutions and interpolate slow and/or absent sedimentation more confidently (Fig. 6.1b). Interpolating the temporal evolution for thick 'event-deposits' (e.g. volcaniclastic layer V-206 in Fig. 6.1b) gained identical results from both type of interpolations. The pchip interpolation (Fig. 6.1c) has been chosen for the assignment of interpolated climate-stratigraphic model ages to the volcaniclastic samples (Fig. 6.1d). A complete list of age assignments from this model is provided in Appendix B for all 300 volcaniclastic layers that have been identified by Stockhecke et al. (2014a).

The samples have been irradiated with fast neutrons in a 99.99 % pure Al container (Fig. 6.2). Packing the samples with respect to their stratigraphic positions allowed isolating deviating samples for recalculating the standard's age (column 1 in Fig. 6.2). As all samples in columns 2, 3, and 4 resulted in $^{40}Ar/^{39}Ar$ ages that are in agreement with the climatostratigraphic temporal markers, they are suitable to monitor the neutron irradiation with ages modelled from the pchip interpolation presented in this chapter.

6.4 Recalculation of the age of ACs-2

Packing several fractions per sample resulted in a set of 18 J-values (irradiation parameters). Samples of identical ages in neighbouring positions guaranteed good control on vertical J-Value gradients. The recalculated apparent $^{40}Ar/^{39}Ar$ ages of the ACs-2 standard crystals are normal distributed (Fig. 6.3a). Isolating two outlying data points is authorized by a Chauvenet's criterion being << 0.5 (Taylor, 1997). The outliers' old ages (> 1.5 Ma) do not suggest contamination from Lake Van sample material and points to xenocrystic feldspars within the population of the ACs-2 aliquot.

The climate-stratigraphic calibration of ACs-2 resulted in a weighted average of 1189 ± 8 ka (two standard deviations analytical uncertainty, Fig. 6.3c). This result agrees with $^{40}Ar/^{39}Ar$ ages and age intercalibrations for ACs-2 from other studies (Table 6.2). The agreement suggests that the proxy alignment to Quaternary climate curves successfully constructed the chronology of the stratigraphy of the AR composite record. As this chapter recycles unknown samples from an earlier study to become irradiation monitors and as the precision of the ACs-2 age presented here is instrumentally and statistically limited, a detailed discussion of the ACs-2 age

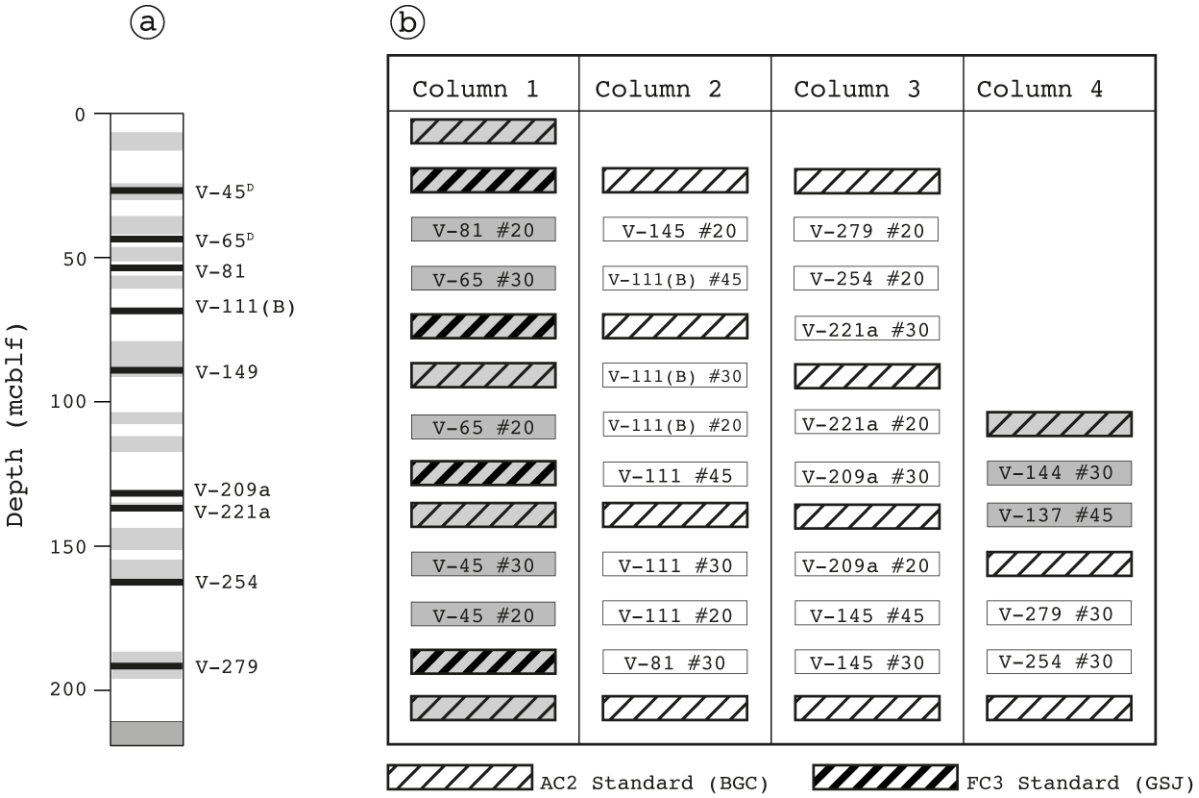

Figure 6.2: (a) Stratigraphic position of samples serving as monitor minerals in the presented study. Sample IDs labelled with superscripted D were discussed in Engelhardt et al. (2017) to deviate the age model of Stockhecke et al. (2014b) and thus do not contribute to the recalibration of ACs-2. (b) Packing of the PO2CGJ2 container for irradiation. Sample and monitor positions are shown for four columns. This sketch uses a simplified two-dimensional representation of the actual packing (Fig. 3.7). Material not contributing to the here presented recalculation of the ACs-2 age is presented in grey.

is inappropriate. Due to the mineralogical and instrumental limitations mentioned in Engelhardt et al. (2017) the usage of the here presented age in future $^{40}Ar/^{39}Ar$ age calculations is clearly discouraged.

ACs-2 were separated from the transitionally magnetized Alder Creek rhyolite (Turrin et al., 1994; Nomade et al., 2005; Singer, 2014b) and thus their age is tied to the extend paleomagnetic Cobb Mountain Subchron (CMS) (Laj and Channell, 2007; Channell et al., 2009; Singer, 2014b). Recently, Channell (2017) bracketed the Cobb Mountain Subchron between 1215 and 1178 ka astronomically. Accordingly, the ACs-2 age from the Lake Van climatostratigraphic recalculation accords to both, $^{40}Ar/^{39}Ar$ and astrochronologic age constraints.

6.5 Conclusions

6.5.1 Validation of climate-chronology

Lake Van feldspars that had been irradited in column 2 (Fig. 6.2) represent the most confident astronomical age assignments but only represent irradiation monitors for about 20% of the calculated apparent ages. Accordingly, the older monitor minerals in column 3 and 4 make the majority in irradiation monitoring but were sampled in stratigraphic positions of sparse temporal marker density. Nevertheless, irradiation monitoring from these samples resulted in apparent ACs-2 ages that are very homogenous. As the samples from below 50 mcblf were

Table 6.2: ACs-2 age determinations since 2005 and taken from a summary provided by Jicha et al. (2016). All ages represent 2σ analytical uncertainties. Some of the listed ages were recalculated in order to be relative to an age of the Fish Canyon sanidine (FCs) of 28.201 Ma[1]. Ages labeled with FCs* did not need to be recalculated. Rivera et al. (2011) used an astronomically intercalibrated FCs age of 27.172 Ma (FCs**). FC*** used an age for FCs of 28.02 Ma (Renne et al., 1998). FC****used an FCs of 28.1 Ma (Spell and McDougall, 2003)

Reference	Irradiation Monitors	Age (ka)	Signature
Phillips et al. (2017)	Astronom. calibration	1184.0 ± 0.7	A
Phillips and Matchan (2013)	40Ar/39Ar relative to FCs***	1184.7 ± 0.6	B
Niespolo et al. (2017)	Astronom.- and Intercalibration rel. to FCs*	1184.8 ± 0.6	C
Jicha et al. (2016)	40Ar/39Ar relative to FCs*	1186.4 ± 0.3	D
Rivera et al. (2011)	Astronom.- and Intercalibration rel. to FCs**	1186.4 ± 0.6	E
Coble et al. (2011)	40Ar/39Ar relative to FCs***	1187.7 ± 6.8	F
Singer (2014b)	40Ar/39Ar relative to FCs*	1189.2 ± 1.7	G
McDougall et al. (2012)	40Ar/39Ar relative to FCs****	1189.8 ± 4.3	H
Nomade et al. (2005)	40Ar/39Ar relative to FCs***	1200.6 ± 0.7	I

recalculated as irradiation monitors in this study, the chronostratigraphy of the PAELOVAN composite core has been validated. The validated chronostratigraphy in depths between 50 and 191 mcblf involves the alignment of proxy data to three different Quaternary timescales (AICC2012, GLT_syn_SA* and GLT_syn_GDC). Age control points that are referenced to these timescales appear to represent synchronous chronometers. This chapter showed an unprecedented approach of validating a chronostratigraphy by recalculating a radioisotopic mineral standard using Quaternary paleoclimate data.

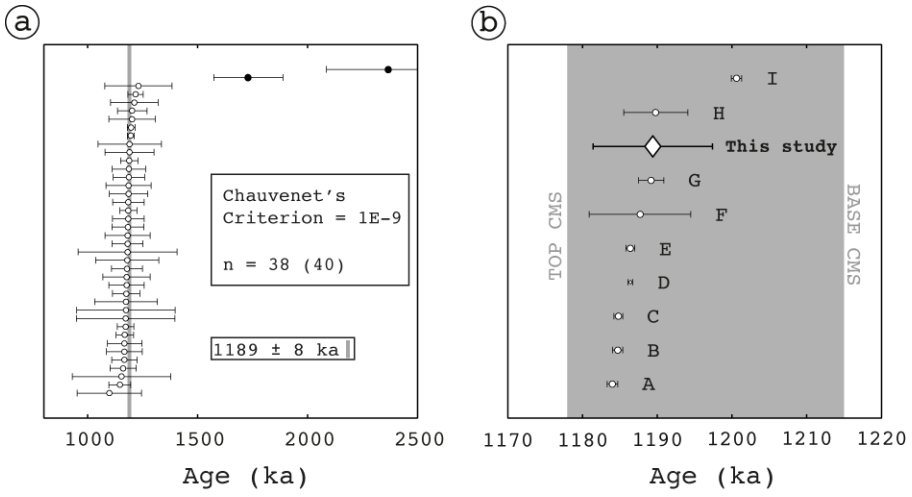

Figure 6.3: Apparent ACs-2 ages obtained in this study. The Chauvenet Criterion gives confidence in isolation of two measurements that are displayed in filled circles. (d) Summary of ACs-2 ages listed in Table 6.2. All ages represent 2σ analytical uncertainties

6.5.2 $^{40}Ar/^{39}Ar$ chronostratigrapy testing

The successful recalculation of the ACs-2 age emphasizes the high and accurate temporal resolution of the AR composite record. Testing the synchronicity of chronologic constraints from different relative dating methods is an important benefit of the $^{40}Ar/^{39}Ar$ geochronology method. As the $^{40}Ar/^{39}Ar$ method offers astronomical calibration calculations, it remains the only radioisotopic dating method that is easily capable of proofing chronostratigraphic constraints from

long lasting (> 0.5 Ma) Quarternary records as exemplified here. A high number of recalculated $^{40}Ar/^{39}Ar$ mineral standard ages has the potential to contribute in the long term to laboratory as well as standard mineral intercalibrations. This chapter represents a simple blueprint for recalculations and outlines the plausibility of using the $^{40}Ar/^{39}Ar$ method as a validation tool for chronostratigraphic models.

7 Tephra Provenance

7.1 Introduction to the volcano-stratigraphic framework of Nemrut and Süphan volcanoes

In order to discuss the potential provenance of selected volcaniclastic layers, this chapter requires a brief review of previous studies on Nemrut and Süphan ejecta. The following summary of previous works focuses on a review section in the extensive works on volcaniclastic deposits by Sumita and Schmincke (2013a), Sumita and Schmincke (2013b), and Sumita and Schmincke (2013c). The development of Süphan explosives focused dominantly on the study by Özdemir and Güleç (2013). Two dormant volcanoes to the Northeast (Tendürek, Ararat) have potentially contributed to volcaniclastic sedimentation in the Lake Van basin (Gülen, 1980; Pearce et al., 1990). Ararat's moderately alkaline and Tendürek's calc-alkaline characters resemble those of Nemrut and Süphan, respectively (Gülen, 1980; Gülen, 1984; Yilmaz et al., 1998; Kheirkhah et al., 2009). However, due to their eastern distal position (> 180 km to the AR drill location) and due to stable WSW to WNW major wind directions during the last 400 ka (Sumita and Schmincke, 2013b), both volcanic edifices are not further considered as potential provenances.

7.1.1 Nemrut

Yilmaz et al. (1998) provided geochemical data and geological field observations for four volcanic edifices: Nemrut, Süphan, Tendürek, Arrarat. These authors postulated five evolutionary phases for the Nemrut and Süphan stratovolcanos that are represented by (i) a pre-volcanic phase, (ii) a cone building phase, (iii) a climactic phase, (iv), a late stage, (v), and a latest eruptive phase. Oldest ejecta ascribed to Nemrut were dated by Pearce et al. (1990) via K-Ar geochronology of basaltic groundmass with an age of 1.18 ± 0.23 Ma. Sumita and Schmincke (2013a) and Sumita and Schmincke (2013c) argued that this age had been obtained from historic lavas that were erupted in 1441 AD and that the age is an artefact due to the presence of excess ^{40}Ar. This interpretation has also been suggested by Pearce et al. (1990). Other authors agree to oldest Nemrut ejecta being about 1 Ma in age (Aydar et al., 2003; Ulusoy et al., 2012). Ercan et al. (1990) postulated oldest rocks related to Nemrut to be fissure basalts in the Bitlis Valley (45 km south of Nemrut) and dated them by K-Ar dating to be about 2.5 Ma in age. Ulusoy et al. (2012) quoted unpublished data of the equivalent basalts to be 0.75 Ma in age. Despite this conflict in radiometric ages, Ercan et al. (1990) and Çubukçu (2008) suggested that the according basalts should not be regarded as products of the Nemrut volcanic system. Sumita and Schmincke (2013c) provided the oldest known tephra age in the eastern area of Lake Van. An isochron age of 404.6 ± 1.8 ka (1σ uncertainty) from SGTF feldspar analyses was obtained for the Selviat Tepe Pumice Formation. This age represents the oldest known onshore tephra of the Nemrut stratovolcano.

Several authors proposed different evolutionary scenarios for the Nemrut stratovolcano. Aydar et al. (2003) interpreted morphological analyses and suggested an early collapse of the Nemrut stratovolcano (forming the characteristic caldera) that had occurred around 300 ka ago.

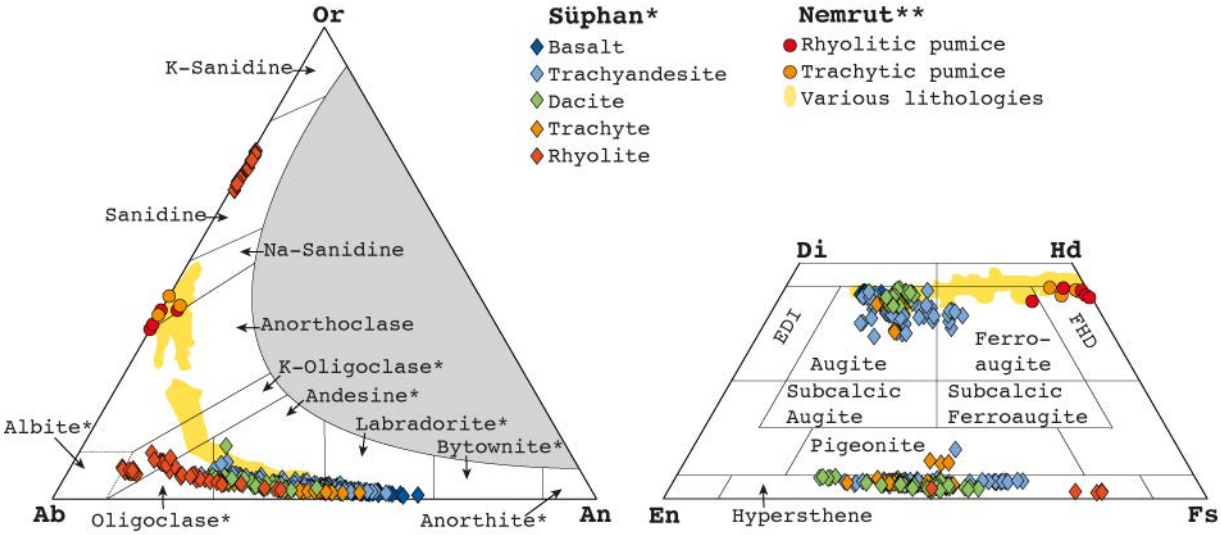

Figure 7.1: Feldspar and pyroxene compositions of Süphan (Özdemir and Güleç, 2013)* and Nemrut (Sumita and Schmincke, 2013b)** volcanic rocks from the literature. Major petrographic contrasts are highlighted by the lack of orthopyroxene crystals in Nemrut-derived volcanics and the absence of anorthoclase and Na-sanidine in Süphan-derived volcanics. Fields discriminating feldspar compositions are adapted from Parsons (2010) at about 1000°C. Note that the boundary between K-oligoclase and anorthoclase is drawn for convenience only along An=Or. Feldspar phases marked with an asterisk are high-temperature modifications and represent unsorted Al-Si arrangements (e.g. high-albite). The pyroxene compositions are adapted from Rock (1990).

Interlayered pumice falls and ignimbrites that are tens of meters in thickness were interpreted to represented an paroxysmal event that accords to the onset of the caldera formation. As these ignimbrites overly the Kirkor dome on the southern flanks of the Nemruth edifice (Figure 2.3) they have been assigned with K-Ar ages from trachytes of the dome that are vaguely constrained to be ca. 300 ka (Ercan et al., 1990). Similarly, Karaoğlu et al. (2005) interpreted the ignimbrites to have deposited during the caldera formation. The nomenclature of the ignimbrite formation varies slightly from 'Nemrut Ignimbrite', to 'Nemruth Depositional Unit' (NDU), and to 'Nemrut Formation'. According to Sumita and Schmincke (2013b) this thesis applies the term Nemrut Formation (NF) for the deposits associated with the caldera-forming eruption. The NF consist of a rhyolitic fallout that is covered by an ignimbrite, welded agglutinates, a surge deposit and a less silicic second fallout (Sumita and Schmincke, 2013b). A main outcome of the study by Sumita and Schmincke (2013b) was the presentation of three, statistically identical $^{40}Ar/^{39}Ar$ ages of the NF from single feldspar phenocrysts. Two of them have a weighted mean age of 30 ± 5 ka and revealed the formation of the Nemrut caldera to be considerably younger than suggested in earlier studies.

Karaoğlu et al. (2005) and Özdemir et al. (2006) suggest three evolutionary stages for Nemruth volcano: (i) pre-caldera stage, (ii) post-caldera stage, and (iii) latest stage and estimated the onset of the post-caldera stage around 0.03 Ma. Ulusoy et al. (2012) subdivided the Nemruth evolution into a pre-caldera phase, a syn-caldera phase, and a post-caldera phase that range from 1 Ma to 80 ka, from 80 ka to 30 ka and from 30 ka to the present, respectively. A petrological study of effusives by Çubukçu et al. (2012) concluded that the Nemrut caldera collapsed between 90 and 30 ka. These authors applied K-Ar on groundmasses of commendites, trachytes and pantellerites and deduced a petrological evolution of Nemrut volcanic rocks. They detected a compositional gap (Daly gap) between 53 wt% and 59 wt% of SiO_2 in whole rock analyses.

This gap is exclusively filled with benmoreitic enclaves in peralkaline rhyolites in the earliest effusive rocks of their pre-caldera stage. Furthermore, the study by Çubukçu et al. (2012) offered calculations that employ the MELTS software and that suggest that the Daly gap likely represents a compositionally stratified magma chamber. In this scenario the missing intermediate compositions form an interface between mafic and felsic melts. Despite the study from Pearce et al. (1990), who investigated several collision-related volcanic edifices in the east of Anatolia, the study by Çubukçu et al. (2012) remains the only petrological investigation of Nemrut lavas and dikes up to date. Sumita and Schmincke (2013a) interpreted several ignimbrite deposits to be caldera-forming and suggest the existence of earlier calderas prior to the currently exposed structure that has formed around 30 ka. Their oldest caldera-forming phase documented by ignimbrite deposition is interpreted to be minimum 264 ± 3 ka in age. Youngest materials are represented by Holocene lava flows, domes and phreatomagmatic deposits in the centre of the caldera.

7.1.2 Süphan

The Süphan stratovolcano is probably the least known Quaternary volcano in Eastern Anatolia. Özdemir and Güleç (2013) provided the most recent study about the volcano-stratigraphy of Süphan and reviewed data from Özdemir et al. (2011). Both works are unique in focusing on Süphan volcanic rocks alone. Earlier studies investigated Süphan volcanic rocks within the volcano-tectonic history of the eastern Anatolian plateau (e.g. Innocenti et al., 1976; Ercan et al., 1990; Pearce et al., 1990; Notsu et al., 1995; Yilmaz et al., 1998; Keskin, 2003; Keskin, 2007). The oldest reported radiometric age from Süphan rocks is 700 ± 140 ka (Innocenti et al., 1976). The age has been obtained from analysing the groundmass of an andesite lava flow via the K-Ar method. Yilmaz et al. (1998) described three major volcanic stages for the Süphan stratovolcano: (i) a pre-cone phase, (ii) a cone-building phase, and (iii) a flank-eruption phase. The first phase has been characterised by thick Plinian felsic fallouts. The initial eruptions that represent the cone building stage are represented by alternating lavas (andesites and basalts) and pyroclastic flow deposits. Subsequently, this succession has been covered by several aprons of hyalo dacite, andesite and basalt lavas. These lavas have poured from the central crater and were covered by thick (> 100 m) pyroclastic fall out deposits. The cone-building phase has no defined end and can be regarded accordingly to the activity of the volcano as dormant. The last stage that was defined by Yilmaz et al. (1998) is characterised by erupting mainly on flanks. These eruptions co-occurred roughly with the formation of the voluminous dome that still plugs the summit of Mount Süphan and likely its major vent. Pyroclastic materials and highly silicic dacite and rhyolite lavas also extruded from fissures and subsiderary domes. Numerous cinder cones and domes were formed in three sub-stages. The first sub-stage formed andesitic domes and cones that aligned along tensional cracks on a NE-SW direction on the eastern flank. Small cinder cones and domes evolved on northern and southern flanks during the second sub-stage. Voluminous basaltic lavas poured from a chain of subsidiary cones that are close to the summit and situated on the northern flank during the third sub-stage. The basalts cover an extensive area and can be traced downslope into the surrounding flatlands over distances > 25 km. To the south of the Süphan edifice the Aygir Maar (also described as Aygirgölü Maar) had developed by phreatomagmatic eruptions in the later part of the flank-eruption stage. The composition

of the predominant fallouts were only described granulometrically by Yilmaz et al. (1998) and lack compositional classifications and chronostratigraphic constraints.

Özdemir and Güleç (2013) presented compositional analyses and petrological modelling together with a slightly modified volcano-stratigraphy. Furthermore, $^{40}Ar/^{39}Ar$ dating was conducted on mineral separates (Pl, Amp, Bt) and groundmasses from effusive rocks, such as trachyandesite, basalt, dacite and rhyolite by Özdemir and Güleç (2013). Based on these radiometric ages, they grouped the emplacement of trachyandesitic and basaltic/trachyandesitic lava flows into early and late stage. Unfortunately, this procedure is slightly incomprehensible as the radiometric ages do not resolve the early and late emplacement stages, due to elevated uncertainties. The stratigraphic descriptions of the pyroclastic deposits by Özdemir and Güleç (2013) are more comprehensive. Various volcaniclastic units were grouped into three phases that are separated by visible paleosol horizons in the field (Özdemir and Güleç, 2013). The first phase is described as a succession of green pumice falls and white pumice falls. Blocks of rhyolite in ash flows mark the beginning of the second major pyroclastic stage. These are covered by a thin plinian ash. The third stage is represented by the deposition of pumice falls that are also rich in lithic fragments.

Trachyte lava flows furthermore cover wide areas on the southern and eastern flanks of the volcano and are interpreted to represent youngest effusives of the major conduit of Süphan volcano. Özdemir and Güleç (2013) report that dome forming effusives represent the latest stage in the evolution of Süphan and thus agree to the evolutionary concept of Yilmaz et al. (1998). Özdemir and Güleç (2013) dated amphiboles from dacite that were sampled from one of the a major subsidiary domes on the northern flank. The according age is 110 ± 30 ka and was obtained via $^{40}Ar/^{39}Ar$ geochronology. The dome that plugs the major Süphan vent is 64 ± 14 ka in age (Özdemir and Güleç, 2013). This age is probably influenced by excess ^{40}Ar. A plateau age that is significantly older than the inverse isochrone age indicates the presence of excess ^{40}Ar in the sample. Nevertheless, these two ages suggest that dome construction at Süphan volcano may preceded the latest caldera formation at Nemrut stratovolcano.

7.2 Petrographic contrasts

The major petrographic characteristics of pyroclastic material from Nemrut and Süphan volcanics have been described by Özdemir et al. (2011), Özdemir and Güleç (2013), and Sumita and Schmincke (2013b). Macdonald et al. (2015) outlined petrographic and petrologic characteristics of Nemrut volcaniclastics from the AR composite record. The following section provides a brief summary of their descriptions.

Süphan pumice falls can be detected visually due to a characteristic small vesicle size and the predominance of white pumice colours. Major petrographic features of Süphan volcanic rocks are either the presence of a cogenetic feldspar pair or the absence of (pseudo-) monoclinic feldspars such as anorthoclase, sanidine or microcline. In contrast, feldspars from Nemrut derived rocks represent complete evolutionary mixing of plagioclase to anorthoclase without showing any alkali feldspars having a composition $>Or_{60}$ (Fig. 7.1). Plagioclase commonly represents the dominant felsic phase in Süphan derived rocks (except for trachytes and rhyolites). Another characteristic in the petrography of Süphan rocks is the potential presence of orthopyroxene (hypersthene),

Table 7.1: Summary of major compositional and petrographic contrasts of Nemrut and Süphan pyroclastic rocks modified after Sumita and Schmincke (2013b). Zr, Nb and Y represent HFSE that have been detected in all samples (disregarding Ti contents). Ba, Sr, Rb mark representative LILE. Mineral abbreviations follow Whitney and Evans (2010).

Potential provenance	Phenocrysts	Lithics	Trace Elements	Glass Composition
Nemrut	Ano, Qz, Fay, Hd, Aug	Trachytic hardly phyric to equicrystalline lapilli, shards highly vesicular	High Zr, Nb, Y	Per-(alkaline)
Süphan	Pl, San, Qz, Cpx, Hyp, Bt, Amp, Ol	Microlites in vitreous lapilli, glomerocrystic and ophititc lithics, rare poikilithic feldspar hosting Cpx, phyric lapilli, fine vesicular white pumice	High Ba, Sr, Rb	Subalkaline, calcalkaline

amphibole and biotite. Orthopyroxene (Opx) have not been reported from petrographic descriptions of Nemrut volcanic rocks (Fig. 7.1) up to date (Çubukçu et al., 2007; Özdemir et al., 2007; Çubukçu, 2008; Sumita and Schmincke, 2013b; Schmincke et al., 2014; Macdonald et al., 2015). Biotite is expected to be restricted to Süphan volcanic rocks by most authors. The abundance of biotite in Nemrut volcanic rocks has been a matter of debate. Özdemir et al. (2006) and Özdemir et al. (2007) proclaim that pre-caldera trachytes and rhyolites show biotite, whereas Çubukçu et al. (2007) state that they could not detect any biotite occurrences in rocks that are derived from Nemrut volcanism. Sumita and Schmincke (2013b) endorse the observation of biotite-free Nemrut volcanics by stating that they did not find any biotite during investigations of 45 Nemrut tephra deposits.

According to Çubukçu et al. (2007) the biotite absence is in agreement with the finding of aenigmatite crystals, which implies that the Nemrut magmatic plumbing system has low pressures (< 100 MPa), reducing pre-eruptive conditions and temperatures of > 700°C. These conditions are not expected to form biotite from peralkaline magmas (Scaillet and Macdonald, 2001). Nevertheless, biotite crystallization can not completely be excluded, because it crystallised from experiments with peralkaline rhyolites under similar conditions (Scaillet and Macdonald, 2003).

Microscopic observations of textures in lithic fragments furthermore help constraining the volcanic provenance of volcaniclastic layers in the AR record. Following Sumita and Schmincke (2013b) corrosion and complex mineral intergrowth of plagioclase and clinopyroxene (glomerocrystic, ophitic, and poikilitic intergrowths) are common in Süphan derived volcanics. Furthermore, glass shards are less vesicular (< 20 % vesicularity), and typically contain equant plagioclase microlites. Özdemir and Güleç (2013) and Sumita and Schmincke (2013b) observed that concentrations of high field strength elements (HFSE) and of Ba and Sr have the potential to outline compositional contrasts between Nemrut and Süphan volcanoes. Table 7.1 provides an overview of petrographic characteristics that are involved in discussing the potential provenance of sampled tephra in this chapter.

7.3 Petrography of sampled volcaniclastic units

The predicted mineral assemblages for Süphan and Nemrut volcaniclastics could be detected in most of the samples. Samples that show a predominance of cryptocrystalline ash with only a minority of phenocrystic minerals needed chemical discrimination of volcanic glass or whole-lapilli aliquots. This petrographic summary describes the granulometric composition of all

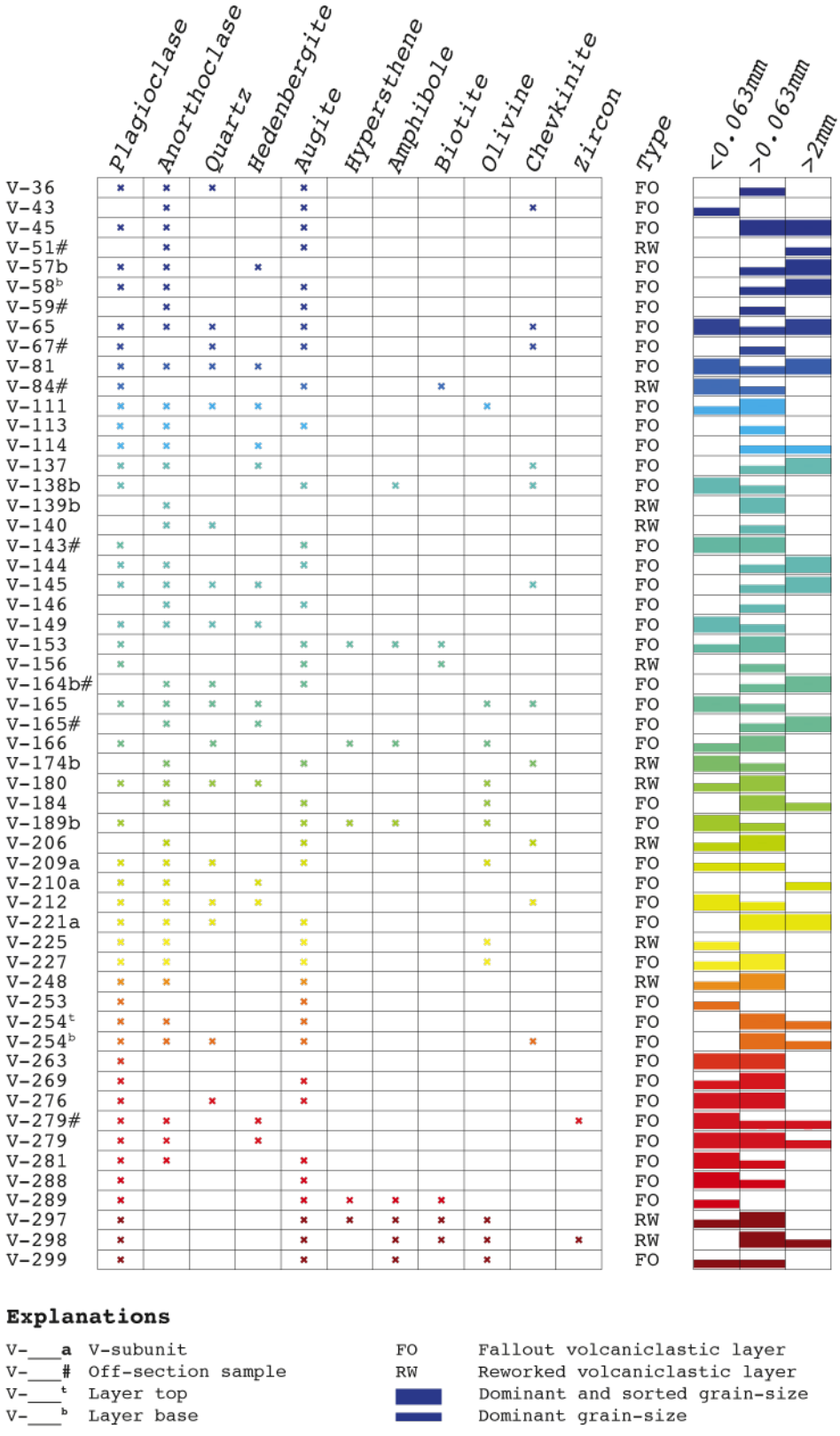

Explanations

V-___a V-subunit
V-___# Off-section sample
V-___t Layer top
V-___b Layer base

FO Fallout volcaniclastic layer
RW Reworked volcaniclastic layer
Dominant and sorted grain-size
Dominant grain-size

Figure 7.2: Petrography and grain size distributions of tephra from AR composite core. Colour coding represents the stratigraphic positions of the samples and has a scaling in Fig. 7.5f.

samples, the observed mineral assemblages and finally the petrochemical data.

7.3.1 Granulometry and mineral assemblage

Coarse ashes dominate the sample inventory (Fig. 7.2). Most of the coarse ashes show inverse or normal grading. Lapilli sizes occur either in poorly sorted samples or (most frequently) as coarsest grain sizes of inversely graded strata. Lapillis mostly represent pumice pyroclasts that show different degrees of phenocryst abundance, which varies approximately between 0.5 and 5 vol%. Pumice and glass shards predominantly represent the coarse ash components. Nevertheless, depending on sample petrography phenocrysts, xenocrysts, and lithic fragments may reach portions up to ca. 25 vol%. Vitric debris, vitric alteration products, and fragments from phenocrysts dominate commonly the fine ash fractions. The calculation of the CIPW normative mineral abundance suggests a trend of rather dry magmatic conditions for the majority of the samples that have been analysed via XRF (Fig. 7.3a). Only a minority of the normative composition suggests wet magmatic conditions at elevated pressures. Alkali feldspar with K-contents $> Or_{60}$ have not been detected in this study at all. This finding, however, does not imply that Süphan samples are absent, because most Süphan lithologies are subalkaline trachyandesites to dacites. Detailed compositional analyses from Özdemir and Güleç (2013) confirm the absence of alkali feldspar in these rocks (Fig. 7.1). Nevertheless, the presence of anorthoclase is an indication for Nemrut as their eruptive volcanic source. Therefore, feldspar EMP analyses indicate the predominance of Nemrut volcaniclastics in the samples (Fig. 7.3b).

The mineral inventory is thus of a twofold character and clearly characterised by the presence and absence of anorthoclase crystals. This Na-rich feldspar is characterized structurally by a triclinic symmetry that is kept in a pseudo-monclinic shape by the development of fine-scale twinning after Pericline and Albite laws (Kroll and Bambauer, 1981; Bambauer, 1988; Parsons et al., 2015). Twining and habitus are characteristic for volcanic anorthoclase in thin-section microscopy (Fig. 7.4a). Feldspars of any composition show melt and appendant fluid inclusions. Other frequent inclusions are apatite and clinopyroxene (Fig. 7.4b). Plagioclase, anorthoclase and Na-sanidine reveal several types of magmatic zoning (Chapter 4).

The vast dominance of analysed and observed pyroxene are clinopyroxene that represent a complete compositional diversity from augite to hedenbergite (Fig. 7.3c). A minority of samples show orthopyroxene crystals (Fig. 7.2). Biotite is rare and occurs mostly in lithic lapillis and rarely as platy flakes (Fig. 7.4c). Olivine crystals mostly occur as small fragments and are Fe-dominant. EMP analyses of idiomorphic olivine (Fig. 7.4d) in two samples from stratigraphic positions between 209 and 210 mcblf show several compositions between Fo_{70} and Fo_{20} that are virtually Mn-free (Fig. 7.3d). These crystals are furthermore rich in apatite inclusions that can reach several tens of μm in size. Amphibole crystals are rare and mostly represented by small (< 150 μm) fragments. The majority of these findings were interpreted by optical microscopy to represent hastingsite crystals. EMP measurements from one sample that shows subhedral amphiboles (Fig. 7.4e) revealed magnesio-hastingsite following the nomenclature after Leake (1978). The same sample, however, shows rare fragments of quartz-muscovite schists and thus reveals detrital material. Another sample reveals shell fragments from freshwater molluscs 'bithynia' (Fig. 7.4f) and indicates potential detritus.

Observed accessories were chevkinite and rare zircon. Chevkinite occurs as subhedral to

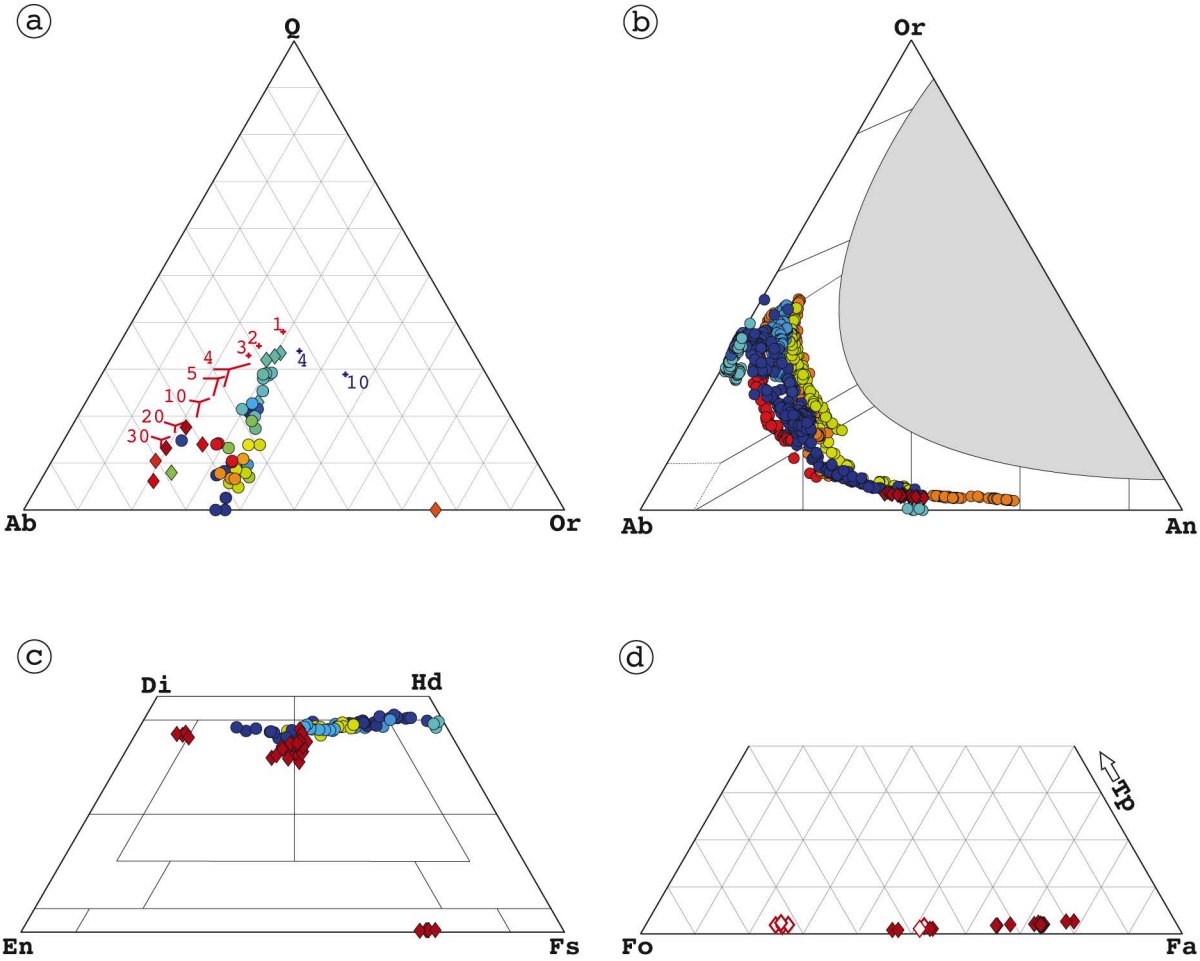

Figure 7.3: (a) CIPW-normative proportions of albite (Ab), orthoclase (Or), and quartz (Q) in a ternary diagram. Red markers represent minima (crosses for 1 to 3 kbar) and eutectics (4 to 30 kbar) in the H_2O-saturated system at different pressures, which are denoted with the labelling numbers in kbar. Blue crosses and numbers represent minima in the dry system. The according experimental data is from Tuttle and Bowen (1958), Luth et al. (1964), Huang and Wyllie (1975), and Steiner et al. (1975). (b) Feldspar compositions from EMP analyses on selected samples. (c) Pyroxene compositions from EMP analyses. (d) Olivine compositions from EMP analyses on two selected samples in a ternary diagram between tephroite (Tp), fayalite (Fa) and forsterite (Fo). Nemrut and Süphan volcaniclastic samples are denoted in circles and diamonds, respectively. Colour coding is analogue to Fig. 7.2 and represents also the stratigraphic position as illustrated in Fig. 7.5f. Listed evidence for the interpretations of the provenances of the samples is provided in Table 7.2.

xenomorphic flakes (mostly < 50 μm). Fe-Ti oxides are ubiquitous components in most samples and occur frequently as inclusions in pyroxenes and feldspars as well as subhedral and idiomorphic crystals that reach grain sizes of about 150 μm maximum. This study did not analyse the Fe^{2+}/Fe^{3+} ratios of the oxides. Semi-quantitative EMP analyses suggest, however, a predominance of ilmenite and ülvospinel and an absence of rutile. This observation accords to oxide compositions from analyses of Nemrut volcanic rocks by Çubukçu et al. (2012) and Macdonald et al. (2015).

Mineral assemblages displayed in Fig. 7.2 are twofold. One group of samples is characterised by the predominance of plagioclase and clinopyroxene. This group occasionally shows amphibole and/or biotite as well as rare orthopyroxene. The provenance of the particular samples is interpreted to be Süphan stratovolcano. This interpretation is in agreement with findings from Özdemir et al. (2011), Çubukçu et al. (2012), and Sumita and Schmincke (2013b). Although detrital reworking of some of these samples has been observed, the absence of anorthoclase suggests that epiclastic mixing with Nemrut pyroclasts is unlikely. The other group is characterised by the predominance of anorthoclase together with plagioclase, and clinopyroxene. Furthermore, the presence of (ferro-) hedenbergite is restricted to this group of samples. This study deduces that the second group accords to material that has been erupted from Nemrut stratovolcano.

7.3.2 Bulk-lapilli XRF analysis

The loss of ignition ranges predominantly from 5 to 1 wt% for most samples. Seven out of 49 results from XRF analyses exceed these values and reach outstanding maxima by loosing extreme amounts of >9 wt% during disc-fusion. Nevertheless, considering trace element analyses, H_2O^+, CO_2 content and SO_3 concentration all samples sum up between 98.7 and 99.6 wt% and indicate that most elemental constituents were detected with sufficient accuracy. An important note is that the sampled amounts hardly ever represent the entire fallout deposit. Subaerial and subaqueous transport and deposition of fallout particles in a non-turbulent water column enhances a compositional sorting. The lacustrine settling of pumice lapilli is the slowest of all pyroclastic particles and usually results in coarse pumice representing the top of inverse graded volcaniclastic strata. Thus, some XRF results presented here may be biased in their main elemental composition. Particularly the crystal-rich sampling targets can result in conflicting main elemental compositions by K- and Na- overestimations and an underestimation of the melt proportion.

Discrimination using chemical compositions

Analysed aliquots are dominantly of trachytic and alkaline compositions (Fig. 7.5a). Three analyses resulted in benmoreitic compositions and another two in mugearitic compositions. These intermediate compositions represent the lowest differentiated rocks in the given study. Another sample of andesitic composition represents an outlying silica-oversaturated composition. All intermediate compositions indicate Süphan volcano as the source of their mineral assemblages. Süphan-interpreted volcaniclastics are subalkaline. Exceptions are the trachytic sample V-189b and the mugearitic sample V-269 (combined observation of Fig. 7.2 and Fig. 7.5a is recommended). The vast majority of Nemrut-derived volcaniclastics is (per-) alkaline in composition, except for the trachytic samples V-145 and V-174a. These two are among those samples that

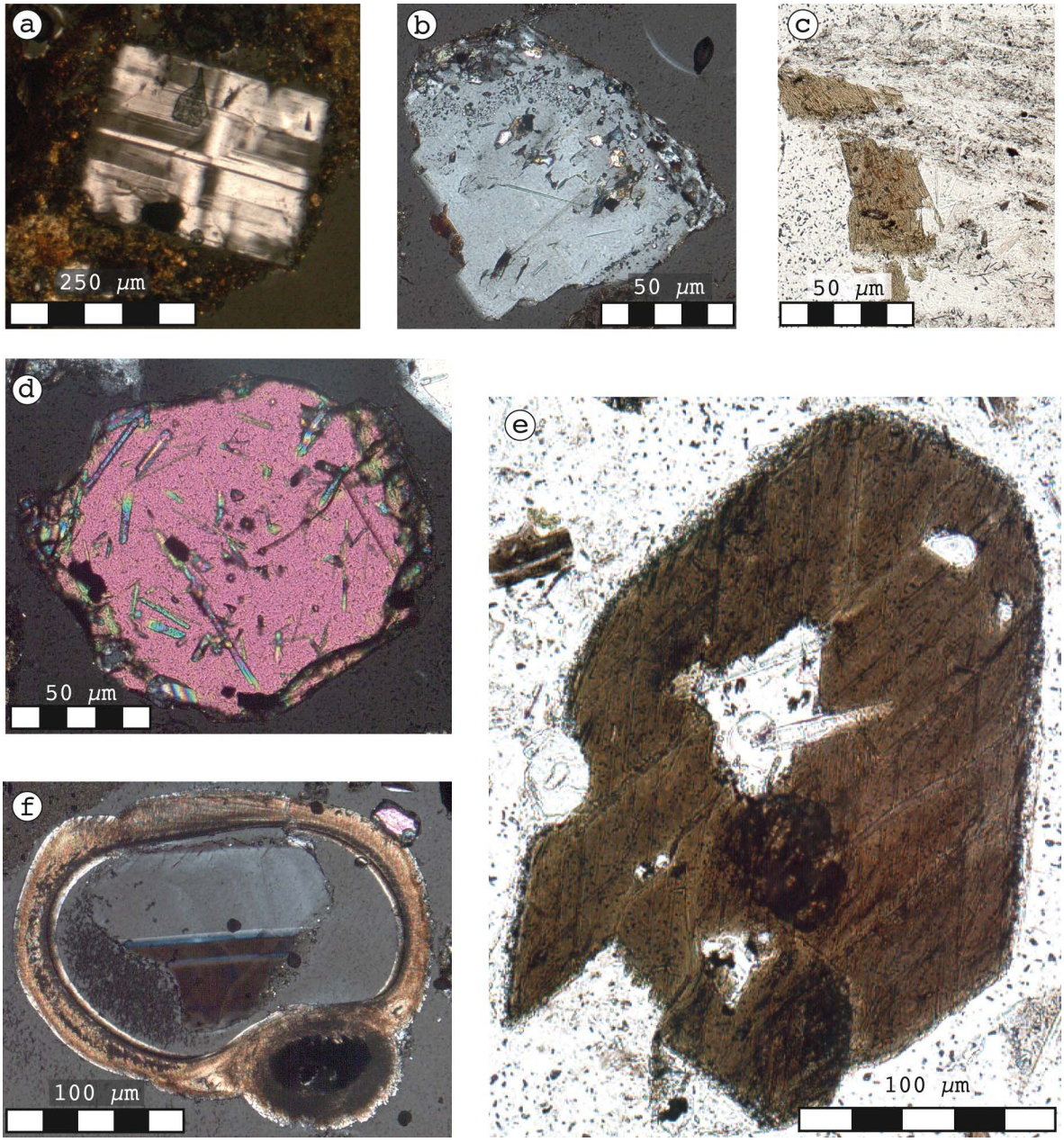

Figure 7.4: Microphotographs in transmitting plane-polarised light (PPL) or cross-polarized light (CPL). (a) Anorthoclase revealing twining after Pericline and Albite laws in CPL. (b) Inclusion-rich oligoclase crystal in CPL. (c) Two biotite flakes in PPL. (d) Idiomorphic, poikilitic olivine that shows apatite needles as chadacrysts in CPL. (e) Magnesio-hastingsite in PPL. (f) Cross cut through a mollusc shell in CPL. The shell envelopes a zoned plagioclase crystal and adheres a zircon crystal in the upper right part of the image.

revealed outstanding high H_2O^+ (4 to 5 wt%) and CO_2 (6 to 12 wt%) abundances. The high water and CO_2 abundances indicate that these samples over-represent a proportion of material that has been rich in fluid-inclusions during the disc-fusion in the laboratory. This interpretation agrees to the observation of melt and appendant fluid-inclusions in phenocrysts and the fluid and gas phases entrapped in vesicles of glass shards.

Highest H_2O contents are detected in the same samples that show most extreme CO_2 concentrations (Fig. 7.6a). Identifying entrapped CO_2 phases and according host material remains to be done and might bear valuable information about either the presence of phreatomagmatic processes or exsolution processes of CO_2 at greater depths.

Findings of rhyolitic and trachytic lapilli fit to the chemical discriminations of the samples in the TAS diagram. Alkaline samples are predominantly of metaluminous to peralkaline compositions (Fig. 7.5b). Acidic, quartz-normative, and peralkaline samples are throughout commenditic and sourced from explosive volcanism at Nemrut stratovolcano (Fig. 7.5c). Tectonic discrimination using trace elements after Pearce et al. (1984) shows that acidic samples accord to within-plate or A-type granitoid magmatism (Figs. 7.5c and 7.5d). Concentrations of Y and Nb correlate linearly and reveal a systematic behaviour of the two HFS elements.

Major and trace element variations

The peralkalinity index (molecular ratio of $(Na_2O+K_2O)/Al_2O_3$) highlights the predominance of peralkaline compositions among the acidic volcaniclastics (Fig. 7.6b). It furthermore indicates a discrimination of most subalkaline samples to be sourced at Süphan stratovolcano. Common oxide-versus-oxide plots poorly reveal compositional magmatic evolutions (Fig. 7.7). Oxides that showed vague compositional trends relative to SiO_2 concentrations are TiO_2, P_2O_5 and K_2O. The potential reasons for the absence of compositional trends are twofold: (i) the mix of samples from two chemically different magmatic provenances and (ii) the lack of a compositional diversity of the samples. The letter reason accounts particularly for those samples that are interpreted to be sourced in Nemrut volcano. A major similarity to more detailed petrological studies on Nemrut volcanism is the inflection of K_2O contents at about 62 to 64 wt% SiO_2 (Çubukçu et al., 2012; Sumita and Schmincke, 2013b; Macdonald et al., 2015). This inflection is also observed in Na_2O and Al_2O_3 contents in data from Çubukçu et al. (2012) and Macdonald et al. (2015). Typically these inflections point to fractional crystallisation being the dominant differentiation mechanism (Macdonald et al., 2015). Such a scenario is consistent with observations in the according mineral assemblages. Modelling fractionation processes using the software MELTS (Ghiorso and Sack, 1995) has been used in the literature to predict the main magmatic processes involved in the compositional evolution of Süphan (Özdemir and Güleç, 2013) and Nemrut (Macdonald et al., 2015) volcanic rocks. Fractional crystallisation, magma mingling and volatile loss are the main processes that control the compositional evolution of H_2O-poor (< 0.25 wt%) Nemruth volcanic rocks (Macdonald et al., 2015). Özdemir et al. (2011) highlighted fractional crystallisation and magma mixing processes to be the predominant processes controlling the chemical differentiation of moderately hydrated Süphan volcanic rocks. Assimilation of upper crustal rocks also contaminate Süphan magmas from 2% to 10% (Özdemir and Güleç, 2013). The major compositional contrast in the magmatic suites from Nemrut and Süphan magmatic systems is thus the H_2O content. This study provides a simple model of the potential evolution of

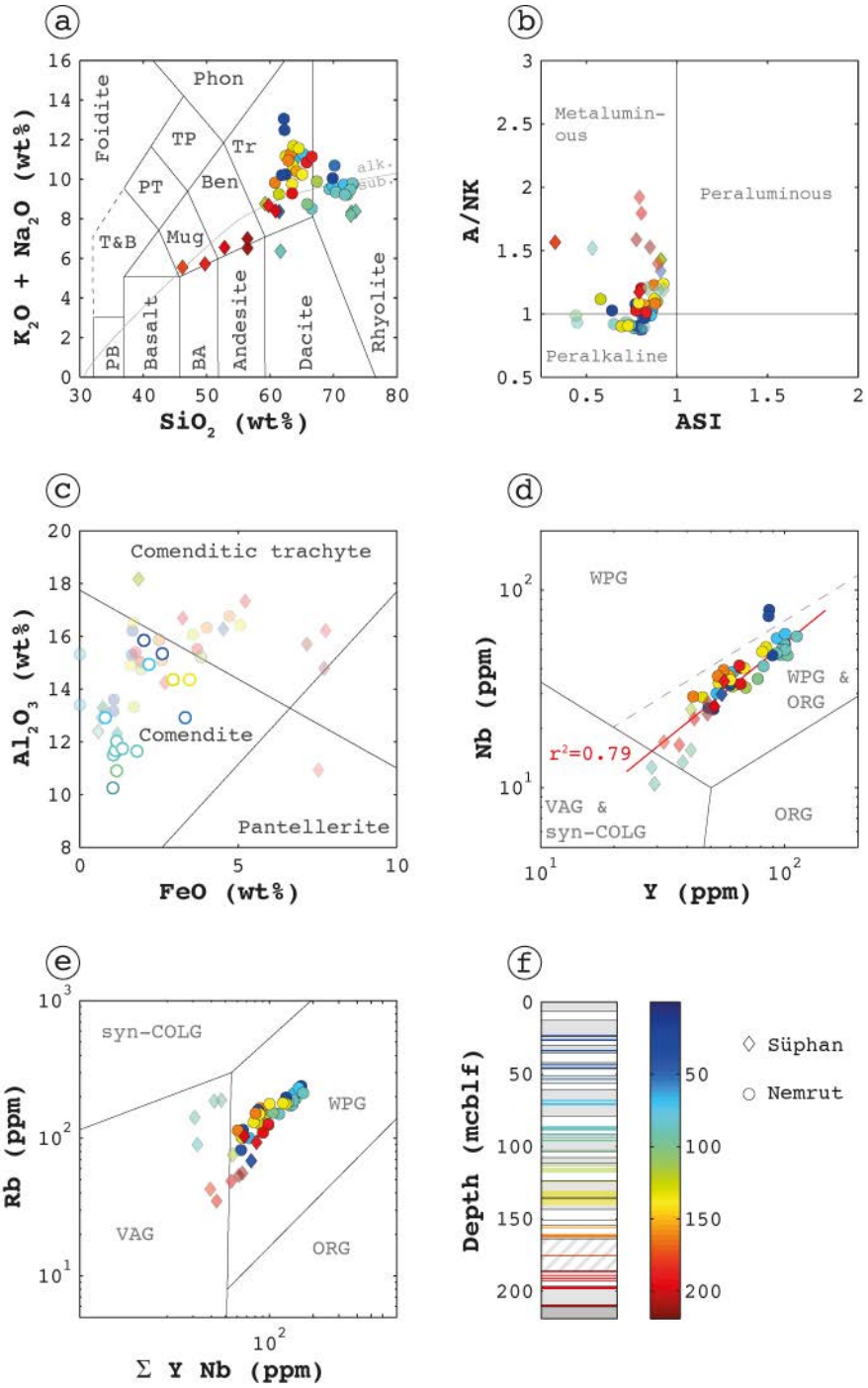

Figure 7.5: (a) Total alkalis vs. silica plot classifies bulk-rock pyroclastic samples in the same way as in Fig. 2.7. (b) Aluminium-silica index (ASI) after Frost and Frost (2008) vs. molecular oxides of aluminium relative to sodium and potassium after Shand (1949). Samples of subalkaline compositions are illustrated in transparent colours. (c) Discrimination of peralkaline and quartz-normative rocks are presented in solid rings after Macdonald (1974). All other samples are plotted in transparent dots and diamonds. (d) Coefficient of correlation (r^2) in concentrations from Y versus Nb for all samples. The tectonic discrimination of granitic rocks is adapted from Pearce et al. (1984). Intermediate samples are presented in transparent colours. VAG & synCOLG: Volcanic arc granitoids and syn−collision granitoids; ORG: ocean-ridge granitoids; WPG: within-plate granitoids. (e) Sample discrimination with (Y+Nb) versus Rb concentrations after Pearce et al. (1984). Intermediate samples are presented in transparent colours. (f) Colour coding follows a colour scale relative to the stratigraphic position in the AR composite core. Interpretation of potential volcanic provenance is highlighted with different marker symbols.

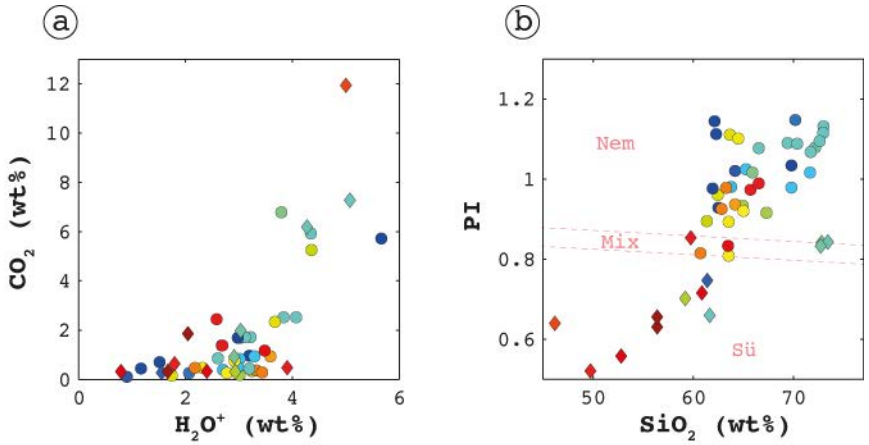

Figure 7.6: (a) CO_2 and H_2O^+ volatiles from whole lapilli analyses. Highest CO_2 weight fractions co-occur with highest H_2O^+ fractions. (b) Peralkalinity index (PI) versus SiO_2 contents.

benmoreites from Süphan and Nemrut volcanoes by crystal fractionation during isobaric cooling between 1200 °C maximum and 750 °C minimum. The model shown in this thesis has the aim to outline the difference in the evolution of alkali abundances in feldspar compositions between Nemrut and Süphan volcanoes.

Starting composition for the Nemruth model has been a benmoreitic whole rock analysis from Çubukçu et al. (2012). The starting composition for the Süphan model is a benmoreitic whole rock composition presented in Özdemir et al. (2011). A LOI of 0.17 wt% was used in the MELTS calculations to be 0.15 wt% H_20 in the Nemrut model (after normalizing all components to 100 %). The Süphan starting material had a LOI of 1.7 %, which was normalised in the model to 2 wt% H_20. Isobaric pressures were assumed to be 2 and 4 kbar for Süphan and 0.5 and 3 kbar for Nemruth magmatic systems.

The results show that the potential evolution from crystal fractionation is capable of roughly mimicking the analysed compositions and highlights several samples that represent outliers (Fig. 7.8). With respect to the inflections in the chemical evolution during cooling (Fig. 7.8a to 7.8d) the difference between a peralkaline evolution of Nemruth and a calcalkaline evolution of Süphan is clearly highlighted by the simple model.

The model that applies an increased pressure on the dry Nemruth sample (3 kbar) indicates the potential of decreasing K_2O contents for most acidic samples from Nemrut. Although this scenario has been described to be unusual for peralkaline suites, it is characteristic for Nemrut magmatism (Macdonald et al., 2015). The modelling in this chapter agree to the modelling by (Macdonald et al., 2015), that also calculated a pressure of 3 kbar to fit the inflection of the alkalis in the compositions from trachytic Nemrut samples best (Fig. 7.8c). However, it is apparent that modelling fractional crystallisation alone is not capable to qualitatively fit the divers trachytic Nemrut compositions. Three samples of (near-) dacitic compositions represent most outlying whole-lapilli compositions that were interpreted to be sourced from Nemrut. These samples also show very high volatile contents and are interpreted to represent misguiding main element concentrations and thus deviating discriminations in TAS classifications. Three rhyolitic samples that are interpreted to have Süphan as a source are far from modelling the differentiation of K_2O (Fig. 7.8d). These samples are either misinterpreted or analysed overrepresented K-rich phases in the sampled aliquot.

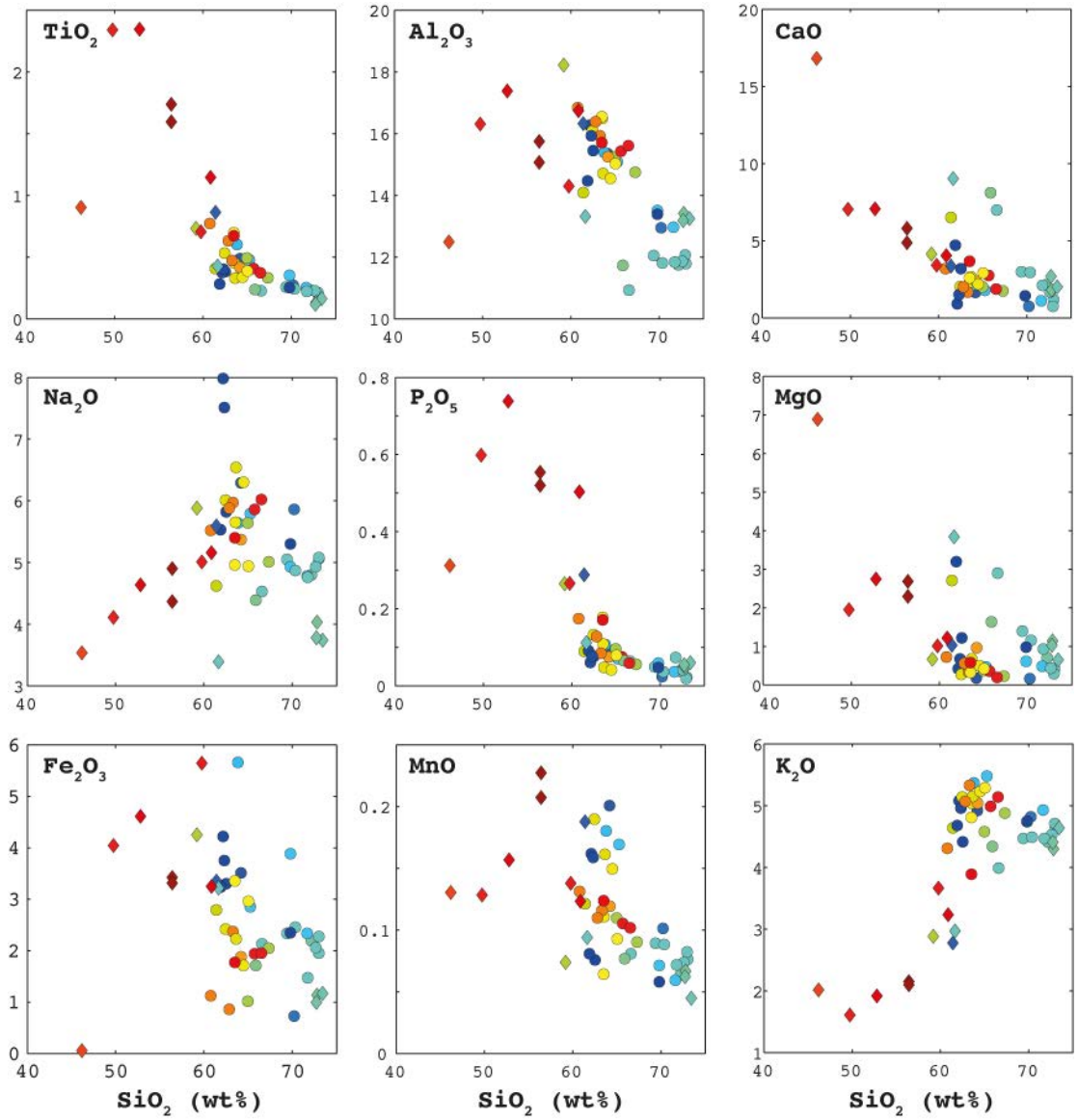

Figure 7.7: Major element concentrations relative to SiO_2 content. Colour coding is presented in Fig. 7.5f. Diamonds represent samples that are interpreted to be volcaniclastics that were sourced from Süphan stratovolcano. Circles identify Nemrut volcaniclastics.

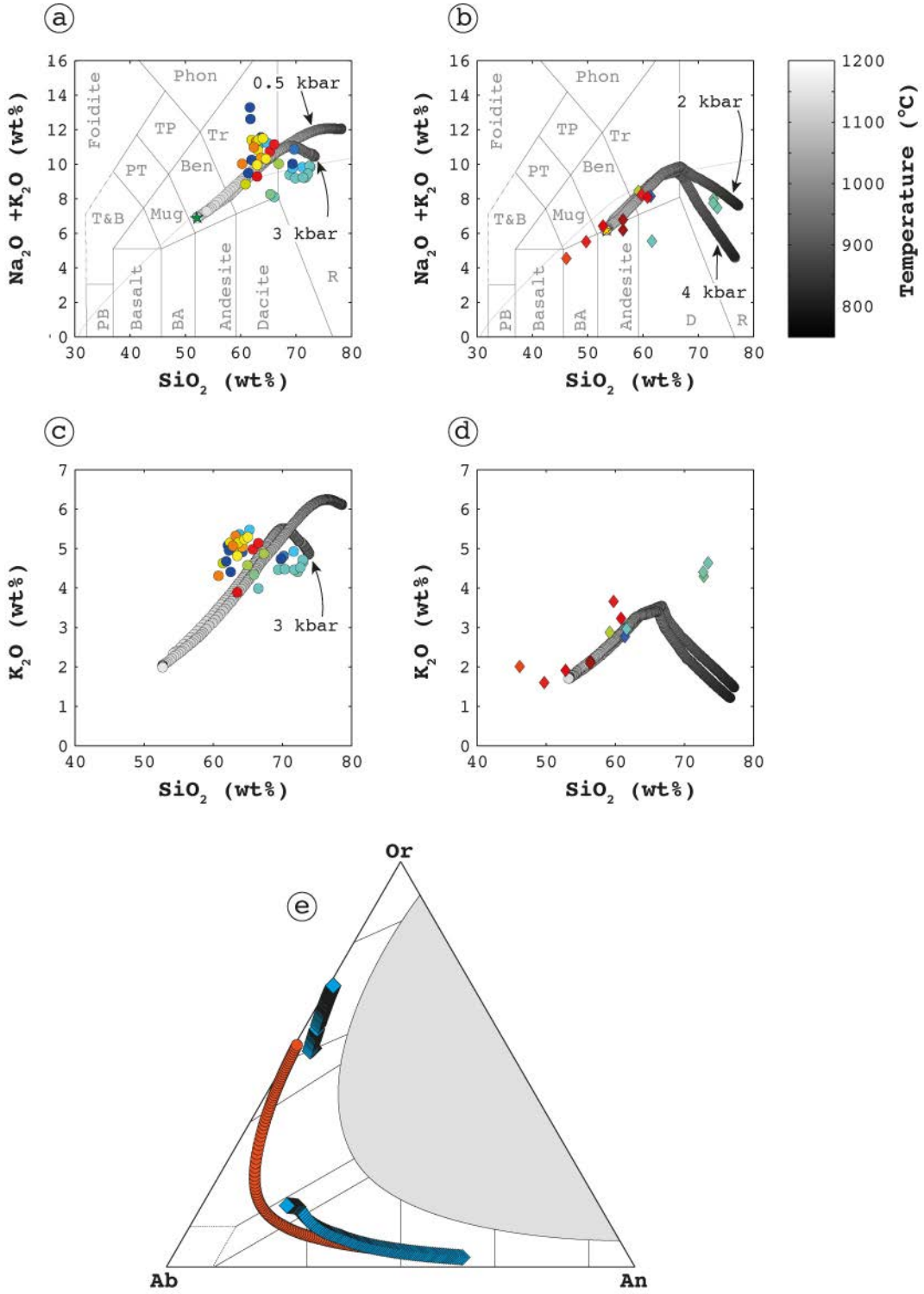

Figure 7.8: (a) Na_2O + K_2O compositions attributed to Nemrut volcaniclastics and fractional crystallisation modelling via MELTS (Ghiorso and Sack, 1995) using an intermediate starting composition from Çubukçu et al. (2012). (b) Na_2O + K_2O compositions attributed to Süphan volcaniclastics and fractional crystallisation modelling using an intermediate starting composition from Özdemir et al. (2011). (c) Modelled and measured K_2O compositions of Nemrut volcaniclastics. (d) Modelled and measured K_2O compositions of Süphan volcaniclastics. (e) Feldspar evolution modelled with MELTS from Nemrut intermediate sample at 0.5 kbar (red dots) and from the Süphan intermediate sample (blue diamonds) at 3 kbar. Models for Nemruth are based for a starting compositions that involved 0.15 wt% H_2O. The modelling for Süphan volcaniclastics used a starting composition that contained 2 wt% H_2O.

The low water activity in the Nemrut model keeps the feldspar crystallisation to be peritectic (odd number of crystallising solids - only one feldspar phase) and results in a single plagioclase crystallisations path (Fig. 7.8e). High water activity in the Süphan model causes that the feldspar liquidus and solidus temperatures decrease and therefore have an increased intersection with the solvus. An increased intersection is more likely to crystallise sanidine (Fig. 7.9).

The precipitation of sanidine is responsible for the more pronounced inflection in the compositional trends of the alkalis that have been modelled for Süphan. Modelled Nemrut feldspar compositions cease at about Or_{55}. This is in contrast to measured compositions from this study and from earlier published studies. The discrepancy is probably derived from inappropriate modelling of the cooling steps. EMP analyses from volcanic glass presented in Chapter 5 and from three further samples partly agree to suggested compositional trends for Nemrut volcanic rocks. Deviations are mainly attributed to highly alkaline trachytic samples (Fig. 7.10a). Macdonald et al. (2015) suggested that high-alkaline trachytes indicate differentiation processes from different initial compositions and point to a multi-lineage of Nemrut volcanics. Modelling the evolution from peraluminous to peralkaline Nemrut compositions has been confirmed by overlapping and correlating data of the aluminium saturation index (ASI) relative to the inverse of the peralkalinity index (Fig. 7.10b). EMPA data from glassy groundmasses of one sample scatter. This sample is interpreted to be sourced from Süphan volcano and its scattering EMP analyses emphasise suspicion about an epiclastic contamination.

Çubukçu et al. (2012) showed that Nemrut volcanic rocks reveal a compositional gap between 53 and 59 wt% SiO_2. This gap (named Daly gap) indicates the presence of a stratified magma chamber in the Nemrut plumbing system. The occurrences of compositionally stratified tephra (Sumita and Schmincke, 2013b) strengthen this interpretation. Benmoreitic enclaves in higher evolved Nemrut lavas represent compositions within the proposed Daly gap. These enclaves evidence mingling and have been interpreted to be characteristic for zoned reservoirs that are capped by trachytic to rhyolitic magmas. In contrast, a stratified reservoir does not agree to a compositional multi-lineage of melt evolutions that are suggested by the variety of alkali-contents in the trachytic rocks (Macdonald et al., 2015). However, the study presented here emphasizes that stratified magmatic reservoirs are ideal to explain the presence of single-plagioclase-path crystallisation and the co-existence of two different zoning types in anorthoclase (Ginibre et al., 2004; Ginibre and Worner, 2007).

Nemrut samples occur with SiO_2 contents between 61 and 73 wt% SiO_2 and are thus not diversified enough for a detailed discussion about a potential compositional trend. A detailed interpretation of magmatic processes is hence impossible. In order to create a substantiated identification of the volcanic provenances selected trace elements are briefly discussed in the following.

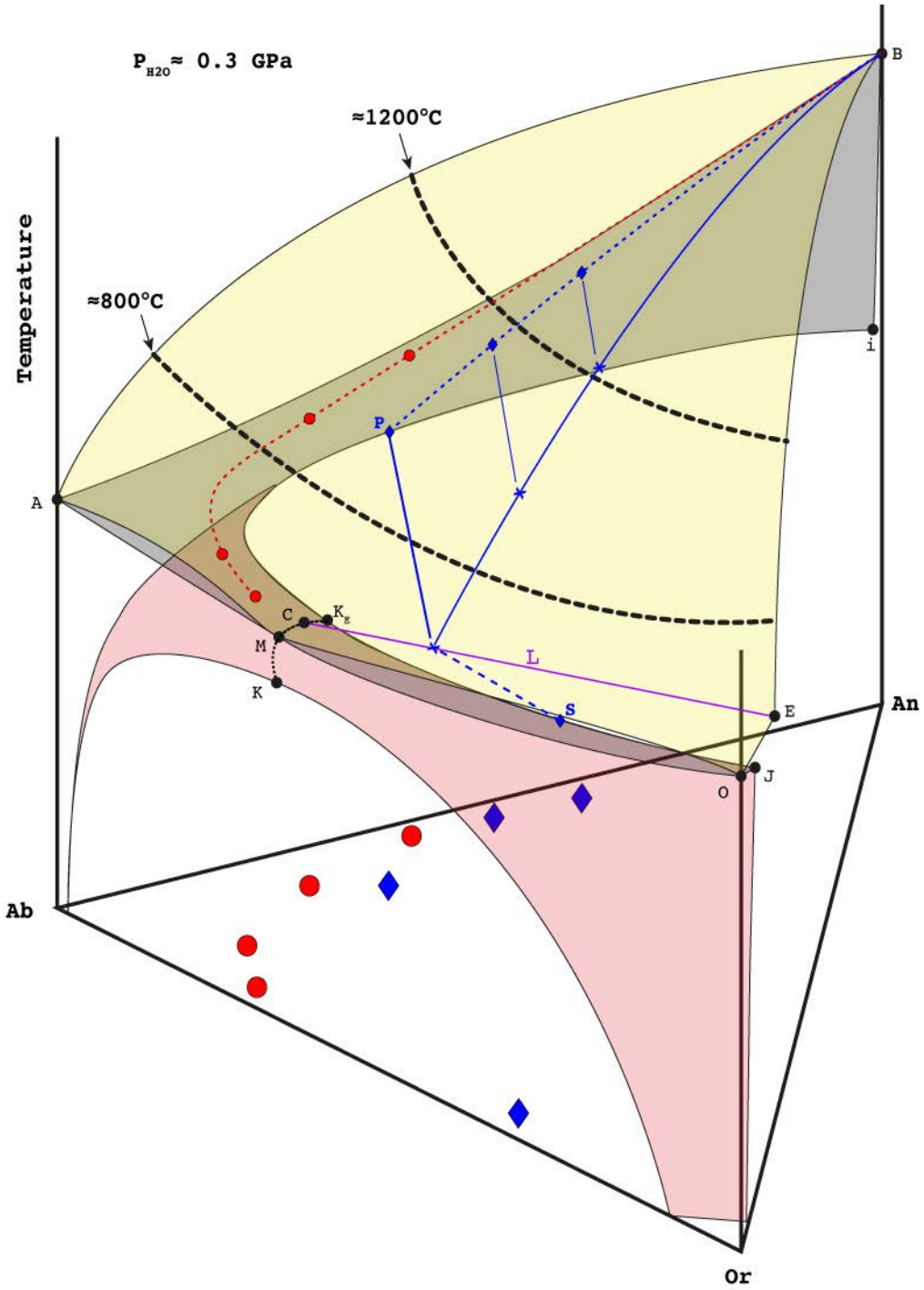

Figure 7.9: Ternary feldspar phase relationships at low H_2O pressure of 0.3 GPa. The plagioclase liquidus is the yellow plane among the **MABE** corner points. The sanidine liquidus spans between **MOE**. The two planes intersect along the two-feldspar 'boundary line' between **E** and **C**. This line ceases in the end point **C** and is close to the Ab-Or join, which crosses the minimum **M**. The two solidi planes are displayed in grey. The plagioclase solidus is among **MABI** and the sanidine solidus among **MOJ**. The solidi intersect with the ternary feldspar solvus along the line **IPK**$_E$**SJ**. A 'critical solution line' exists on the solvus (red plane) along the line **KK**$_E$. This line is metastable at temperatures that exceed the temperature of **K**$_E$. Liquids on the liquidi planes coexist with one feldspar phase on the corresponding solidi. The blue line shows such a scenario by three blue crosses and according plagioclase compositions. Liquids on the boundary line (**L**) coexist with two feldspars. The lowest blue cross highlights this scenario. The according feldspar compositions are **P** and **S**. A liquidus evolution starting close to An could meet the boundary line **L** or the minimum **M**. The latter scenario is indicated with a series of potential plagioclase compositions in red dots. Increasing pressure and water activity lower the temperatures of the liquidi and solidi and cause a larger intersection of the solvus with the solidus (**IPK**$_E$**SJ**). The diagram has been modified after Brown (1993) and Brown and Parsons (1994).

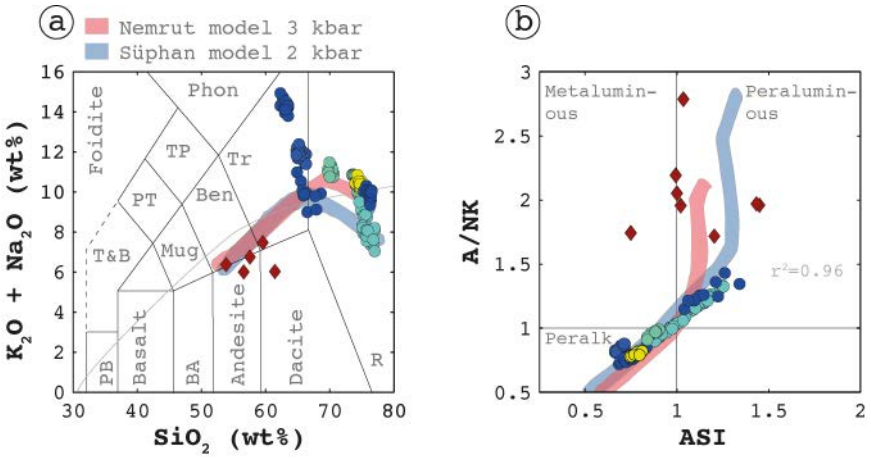

Figure 7.10: (a) Discrimination of results from EMP analyses on volcanic glass from selected samples in a total alkali versus silica diagram. (b) Discrimination of glass compositions after Frost and Frost (2008). The blue (Süphan) and red (Nemrut) fields represent modelled compositions. The coefficient of determination (r^2) represents all data points except for the scattering red diamonds. Colour coding for the symbols is presented in Fig. 7.5f.

Ba, Sr and Rb are large-ion lithophile elements (LILE) that have been detected in all analyses. These trace elements do not correlate in any of the possible comparisons. Plotting Sr versus Ba suggests that volcaniclastics from Süphan are predominantly Sr-rich (Fig. 7.11a). However, no systematic trend is detected between Ba and Sr. Sumita and Schmincke (2013b) state that Süphan pyroclastic rocks are typically more rich in Ba and Sr than Nemrut pyroclastic rocks of similar SiO_2 contents. The here presented study lacks samples of comparable major element compositions from the two volcanoes and a potential discrimination of the samples using Ba and Sr is thus impossible. Detected high-field-strength elements (HFSE) in this study were Nb, Zr, Y and Ti. Ti represents a major element that is dramatically enriched by the presence of Fe/Ti oxides. Investigating the relative HFSE content by comparison of Nb, Zr and Y is therefore more appropriate.

The approach is validated by positive correlation coefficients of 0.79 and 0.89 for relations between Zr and Nb and Y and Nb (Figs. 7.5d and 7.11b), respectively. Samples summing Nb, Zr and Y $>$ 900 ppm are considered as revealing high HFSE contents. Medium HFSE contents are between 650 to 900 ppm and low HFSE contents $<$ 650 ppm. Together with the peralkalinity index the sum of HFSE might represent a useful tool to distinguish Süphan from Nemrut volcaniclastics (Fig. 7.11c). Samples that are attributed to Süphan are dominated by low HFSE contents and low PI. An according discrimination in the plot has only one Nemrut sample in the field that is dominated by Süphan samples. Plotting the sum of Rb and Ba versus the PI is also effective in separating the two provenances (Fig. 7.11d). The same discrimination does not work when including Sr to the discrimination. Partition coefficients between high-silica melt and plagioclase are very different for Sr and Ba, whereas Ba and Rb are rather similar (Arth, 1976; Nash and Crecraft, 1985; Blundy and Wood, 1991). This is in contrast to the partioning of Ba, Sr and Rb between trachytic melt and sanidine (Mahood and Stimac, 1990). However, as sanidine crystallises closer to the solidus of trachytic melts and as sanidine is only expected in highly differentiated Süphan rocks, its partitioning has a subordinate role for trace element systematics. This study thus recommends the combined use of Rb and Ba instead of Ba and Sr to differentiate between Nemrut und Süphan tephra in ICDP PAEOVAN

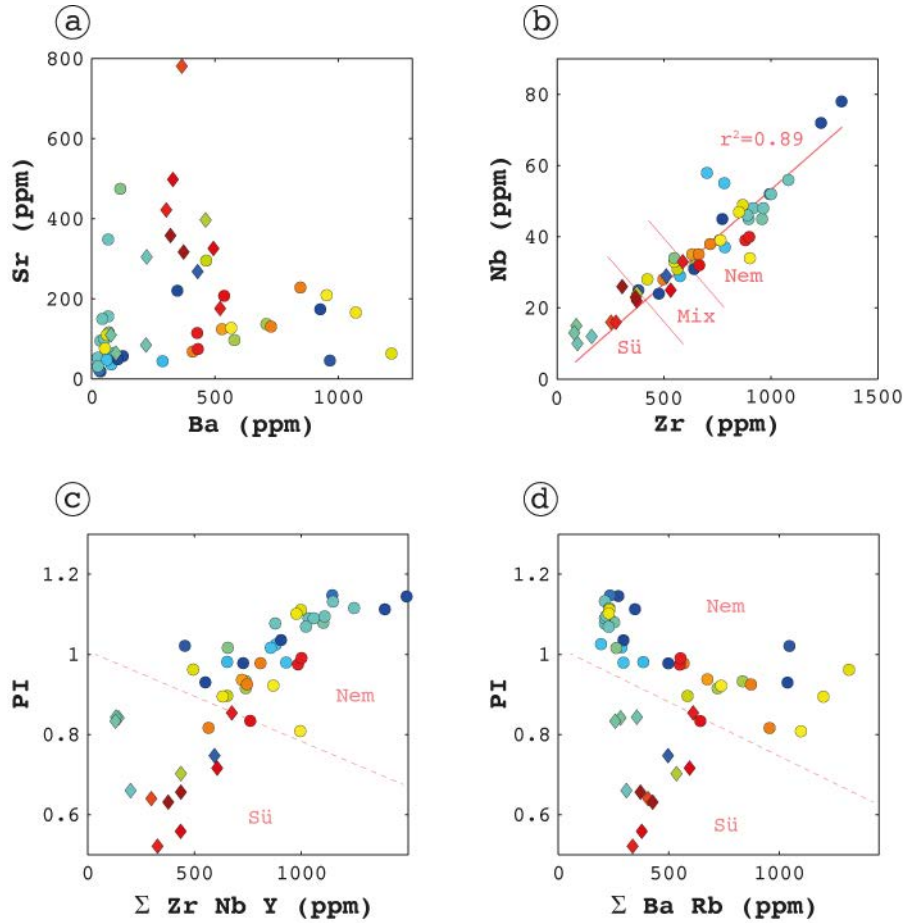

Figure 7.11: (a) Whole lapilli concentrations of Sr versus concentrations of Ba. (b) Trace element contents of Nb vs. Zr having a high coefficient of correlation (r^2). Lowest concentrations indicate Süphan as a potential source and accord to observations from Sumita and Schmincke (2013b). (c) Sum of representative HFSE (Zr, Nb, Y) detected in all whole lapilli samples from XRF analyses versus peralkalinity index (PI). A dashed line highlights the contrast of samples that are interpreted to be derived from Nemrut and Süphan. (d) Sum of Ba and Rb versus PI. Colour coding is presented in Fig. 7.5.

drill core material. Petrographic features that are reported to be typical for Süphan volcanics (Table 7.1) agree to the expected discrimination using the PI, selected HFSE as well as Ba and Rb. The petrographic and the compositional features typical for Nemrut and Süphan facilitate the attribution of volcanic provenances of the sampled material, which is listed in the following section. It is emphasised that this attribution is possible due to the findings from earlier published studies on Süphan and Nemrut volcanoes (such as Pearce et al., 1990; Notsu et al., 1995; Yilmaz et al., 1998; Özdemir et al., 2006; Özdemir et al., 2011; Çubukçu et al., 2012; Özdemir and Güleç, 2013; Sumita and Schmincke, 2013b; Sumita and Schmincke, 2013c; Macdonald et al., 2015).

7.3.3 Provenances

Table 7.2 provides characteristic petrographic and chemical evidences that justify the identification of the potential provenance of each sample in this study. Some evidences are equivocal and need to be briefly described. Unequivocal attribution of a provenance is provided when petrographic observations agree to compositional data of a sample. An unequivocal example is

V-58. XRF analyses from two samples of this layer show almost identical compositions that indicate Nemrut as a volcanic source (highly alkaline, high HFSE, peralkalinity >1). Furthermore, the sample shows anorthoclase and equicrystalline trachytic lapilli. It thus provides agreeing petrographic and chemical indications for Nemrut being the sample's provenance. V-297 is an example for a volcaniclastic layer that is unequivocally sourced at Süphan. It shows the presence of hydrous minerals, the absence of anorthoclase, low concentrations of selected HFSE, a low peralkalinity index and is thus confidently attributed to Süphan volcano according to both: petrographic and chemical indications. The existence of equivocal provenance interpretations is derived from the lack of detecting decisive phenocrysts (anorthoclase, hydrous minerals) in combination with three potential cases.

1. The sample did not undergo compositional analytics and relies on results from transparent light microscopy.
2. The sample provides conflicting chemical compositions.
3. Detrital reworking has contaminated the sample.

Preliminary provenance attributions that require additional investigations (e.g. EMPA on volcanic glass) are marked in Table 7.2 with an asterisk. The list further provides analytical methods and major evidences that justify the provenance attribution. Another uncertainty is derived from the potential sorting of volcaniclastic air falls that deposits in a lake. The absence of biotite doesn't proof that biotite was not associated to the mineral assemblage of a sample. The lamellar morphology of the crystals is expected to behave differently during transport and deposition. Thus biotite was possibly not deposited although ejected. The cautious sampling of the recovered volcaniclastics rarely allowed to sample the fully graded extent of a volcaniclastic layer and potentially hampers the detection of all phenocrysts. It is emphasised that the given study does not interpret the appearance of zoned plagioclase phenocrysts as an indication for a magmatic origin at Süphan as suggested by Sumita and Schmincke (2013b). This thesis shows in Chapter 4 that compositional zoning of anorthoclase crystals involves zones of plagioclase compositions. The presence of these phenocrysts in samples that have a magmatic origin in the Nemrut magmatic system disqualifies the term 'zoned plagioclase' as a characteristic feature for Süphan samples. Nevertheless, zoned plagioclase that is An-rich andesine or labradorite in composition is potentially decisive for attributing tephra to Süphan. The attribution of the provenance can be combined with either the radiometric ages from the given study or with ages from the age model. Age, composition and provenance thus may allow correlation to tephra that has been described in greater detail onshore. Major onshore Nemrut tephra has been dated by feldspar $^{40}Ar/^{39}Ar$ geochronology (Sumita and Schmincke, 2013c).

Table 7.2: Interpretations of potential provenances of the volcanic layers investigated in the given study. EMP analyses are either on phenocrysts (PC) or volcanic glass (G). The samples that have been analysed with XRF are labelled with Y. Those lacking XRF data are labelled with N. The trace elements Zr, Y, Nb represent characteristic HFSE. Mineral abbreviations follow Whitney and Evans (2010). Equivocal provenances are labelled with an asterisk.

Sample	Top (mcblf)	Base (mcblf)	EMPA	XRF	Characteristic Evidence	Provenance
V-36	23.28	23.31	None	Y	Equicrystalline lapilli | high HFSE & PI	Nemrut
V-43	26.24	26.27	None	Y	Hardly phyric | no corrosion	Nemrut*
V-45	26.26	27.62	PC | G	Y	Ano | equicrystalline trachytic lapilli	Nemrut
V-51#	27.92	28.52	None	N	Hardly phenocrysts	Nemrut*
V-58t	33.71	33.90	G	Y	Ano | hardly phyric | high HFSE & PI	Nemrut
V-58b	33.71	33.90	PC | G	Y	Ano | hardly phyric | high HFSE & PI	Nemrut
V-59#	35.78	35.81	None	N	Hardly phyric | no corrosion | coarse vesicles	Nemrut*
V-65	43.18	43.52	PC | G	Y	Ano | equicrystalline lapilli	Nemrut
V-67#	45.24	45.26	None	Y	Low HFSE & PI | fine vesicles | pale pumice	Süphan
V-81	53.30	53.48	PC	Y	Ano | equicrystalline lapilli | high HFSE	Nemrut
V-84#	54.66	54.72	None	N	Bt | fine vesicles	Süphan*
V-111	67.68	68.55	PC	Y	Ano | high HFSE	Nemrut
V-113	70.38	70.46	None	Y	High HFSE | equicrystalline lapilli	Nemrut
V-114	71.08	71.18	PC	Y	Ano | hardly phyric lapilli	Nemrut
V-137	86.24	86.26	None	Y	Hardly phyric lapilli | high HFSE	Nemrut*
V-138b	86.42	86.44	None	Y	Amp | low HFSE | pale grey pumice	Süphan
V-139b	86.99	87.04	None	Y	High HFSE | sorted epiclastic lapilli	Nemrut*
V-140	87.08	87.10	None	Y	High HFSE | hardly vitric | epiclastic lapilli	Nemrut*
V-143#	87.39	87.49	None	N	Pale pumice | small vesicles	Süphan*
V-144	87.56	87.62	G	Y	Equicrystalline lapilli | high HFSE & PI	Nemrut
V-145	87.76	87.78	PC	Y	Ano | equicrystalline lapilli	Nemrut
V-146	87.91	87.93	PC | G	Y	Ano | high HFSE & PI	Nemrut
V-149	88.64	88.66	PC	Y	High HFSE | Ano | equicrystalline lapilli	Nemrut
V-153	91.70	91.78	None	Y	Low HFSE | Bt | Amp	Süphan
V-156	93.90	93.95	None	Y	Low HFSE | Bt | white pumice lapilli	Süphan
V-164b#	95.71	95.76	G	N	Alkaline glass	Nemrut
V-165	95.77	95.81	G	Y	High HFSE | equicrystalline lapilli	Nemrut
V-165#	95.81	95.98	None	N	Aphyric | cryptocrystalline | altered	Nemrut*
V-166	95.94	96.13	G	Y	Amp | fine vesicles | low HFSE	Süphan*
V-174a	102.66	102.68	None	Y	Hardly phyric | cryptocrystalline ash	Nemrut*
V-180	112.96	113.13	None	Y	Trachytic equicrystalline lapilli | coarse vesicles	Nemrut*
V-184	115.25	115.72	None	Y	Ano | coarse vesicles	Nemrut
V-189b	116.45	116.48	None	Y	Low HFSE | Amp | glomerocrystic lapilli	Süphan
V-206	121.62	130.07	None	Y	Epiclastic lapilli | silt	Nemrut*
V-209a	131.74	132.22	PC | G	Y	Ano	Nemrut
V-210a	133.17	133.23	None	Y	High HFSE & PI | coarse vesicles	Nemrut
V-212	134.06	134.12	None	Y	High HFSE | dark pumice	Nemrut
V-221a	136.83	136.88	PC	Y	Ano	Nemrut*
V-225	137.83	138.10	None	Y	Trachytic equicrystalline lapilli	Nemrut*
V-227	139.53	139.64	None	Y	High HFSE | coarse vesicles	Nemrut
V-248	156.08	156.16	None	Y	Aphyric | cryptocrystalline | altered	Nemrut*
V-253	160.97	161.03	None	Y	Alkaline whole lapilli	Nemrut*
V-254t	161.52	162.42	PC	Y	Ano | equicrystalline lapilli	Nemrut
V-254b	161.52	162.42	PC	Y	Equicrystalline lapilli	Nemrut
V-263	175.42	175.47	None	Y	Low HFSE & PI | microlitic lapilli	Süphan
V-269	186.63	186.65	None	Y	Low HFSE & PI | microlitic and vitrophyric lapilli	Süphan
V-276	189.21	189.25	None	Y	Cryptocrystalline | fine vesicles	Süphan*
V-279#	191.27	191.52	PC	N	High HFSE | equicrystalline lapilli	Nemrut*
V-279	191.27	191.52	PC	Y	High HFSE | equicrystalline lapilli	Nemrut*
V-281	192.95	193.07	None	Y	Ano	Nemrut*
V-288	197.42	197.45	None	Y	Low HFSE & PI | highly vitric | vesicle-free	Süphan*
V-289	198.32	198.46	None	Y	Low HFSE & PI | Bt | Amp	Süphan
V-297	209.71	209.72	PC | G	Y	Low HFSE & PI | Bt | Amp	Süphan
V-298	209.75	210.07	PC | G	N	Bt | Amp | mollusc shell	Süphan*
V-299	210.20	210.51	PC	Y	Low HFSE | Amp | angular vitrophyric lapilli	Süphan

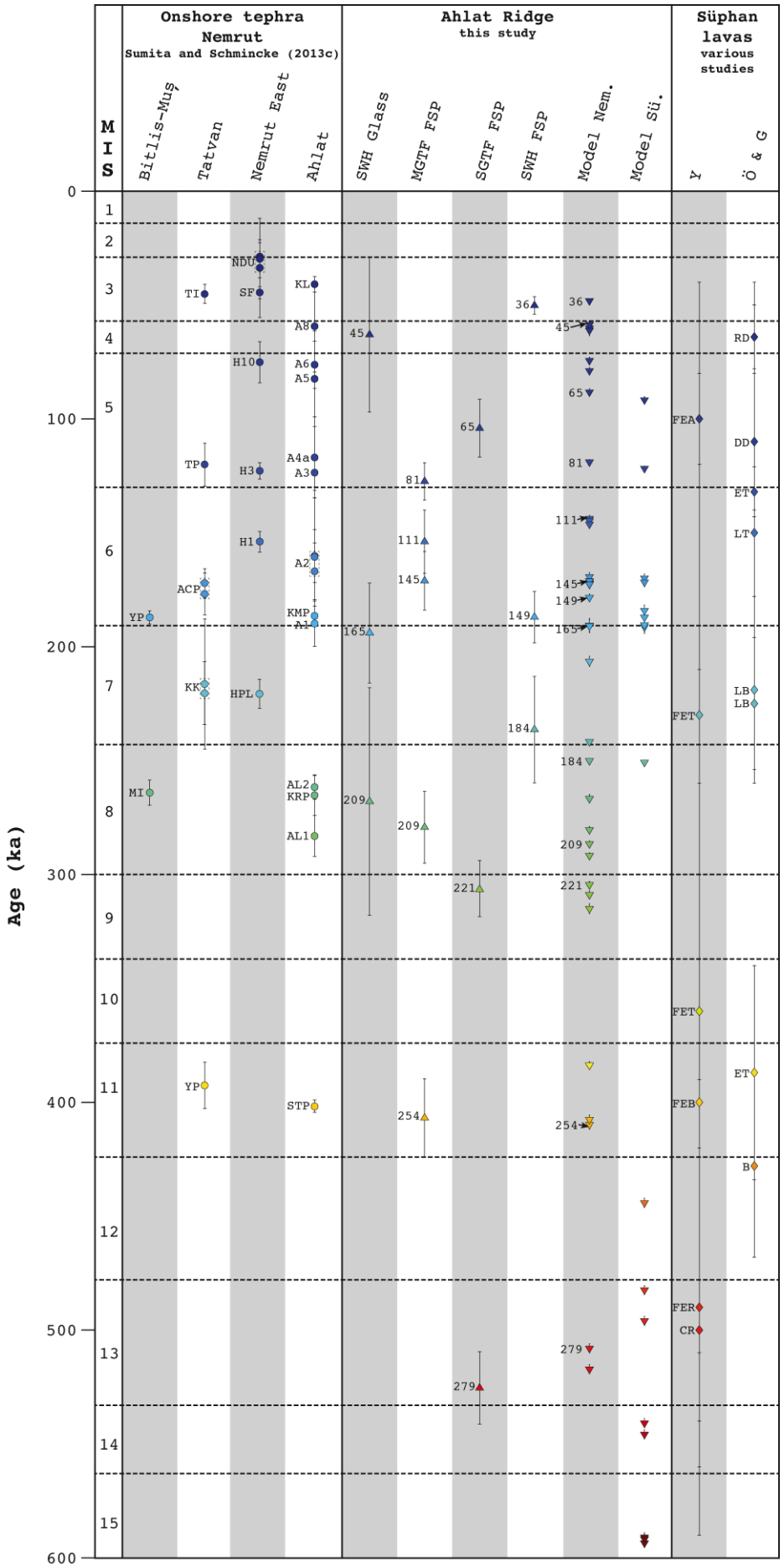
Onshore tephra
Nemrut
Sumita and Schmincke (2013c)
Ahlat Ridge
this study
Süphan lavas
various studies
MIS
Bitlis-Muş
Tatvan
Nemrut East
Ahlat
SWH Glass
MGTF FSP
SGTF FSP
SWH FSP
Model Nem.
Model Sü.
Y
Ö & G
Age (ka)
0
100
200
300
400
500
600
1
2
3
4
5
6
7
8
9
10
11
12
13
14
15
NDU
SF
TI
KL
A8
H10
A6
A5
A4a
A3
H3
TP
H1
A2
ACP
KMP
A1
YP
KK
HPL
AL2
KRP
AL1
MI
STP
YP
45
81
111
145
165
209
254
279
36
65
149
184
221
RD
FEA
DD
ET
LT
LB
LB
FET
FET
ET
FEB
B
FER
CR

Figure 7.12: (previous page): Comparison of onshore and offshore ages. Summary of radiometric ages obtained from onshore Nemrut tephra were adopted from Sumita and Schmincke (2013b). Radiometric ages obtained from volcaniclastic from Ahlat Ridge drill cores are presented in this thesis. The modelled climate-stratigraphic ages are presented separately for volcaniclastic layers that have been attributed in this study to Süphan or Nemrut. Radiometric ages of Süphan lavas were either compiled by Yilmaz et al. (1998) or obtained by Özdemir and Güleç (2013). The nomenclature of onshore locations for major Nemrut tephra deposits has been modified as listed in the following. Tatvan: Tatvan-Köprücek; Nemrut East: compiles locations of Cekmece, Haplepkalesi, and Serinbayir; Ahlat: Ahlat-Nazik. Table 7.3 offers an overview of all abbreviations for dated onshore units from the literature. All AR numbers represent sample numbers excluding the letter "V". All uncertainties represent two standard deviations, except for the ages of the Süphan lavas. Ages from Süphan rocks are displayed with one standard deviation, as the uncertainties would exceed the dimensions of the diagram.

A wealth of K-Ar age data from Nemrut lavas is furthermore present (Ercan et al., 1990; Pearce et al., 1990; Notsu et al., 1995; Yilmaz et al., 1998; Çubukçu, 2008; Çubukçu et al., 2012). The correlation of volcaniclastics from the AR requires the explosive volcano-stratigraphic framework. Thus, radiometric ages from effusives are neglected for potential correlations. The timing of phases of Süphan activity has been presented in a compilation of radiometric ages by Yilmaz et al. (1998). Furthermore, Özdemir and Güleç (2013) obtained $^{40}Ar/^{39}Ar$ dating on groundmasses, amphiboles and plagioclases from several Süphan lavas. However, all these radiometric ages did not analyse onshore tephra from Süphan volcano and do not allow a correlation to distinct units. An illustration of available Süphan lava ages together with radiometric ages from volcaniclastics from the AR and from onshore Nemrut is given in Fig. 7.12. It highlights the future need for additional substantiate radiometric dating of Süphan volcanic rocks as most ages are statistically indistinguishable from each other and do not reveal a detailed temporal evolution of Süphan volcano.

This section provides a discussion about potential correlations of volcaniclastics from AR to the explosive volcano-stratigraphic framework from Nemrut. The successful calibration of the Alder Creek mineral standard with modelled climate-stratigraphic ages between 50 and 190 mcblf of AR composite stratigraphy (Chapter 6) suggests that modelled tephra ages allow the correlation to onshore tephra. The following discussion exclusively treats samples that have been dated by the $^{40}Ar/^{39}Ar$ method in the given thesis. All of these samples suggest Nemrut as their mutual provenance. Correlations of samples that were assigned only with modelled ages exceed the aim of the given thesis. This thesis furthermore provides a list of modelled ages for all volcaniclastic layers identified in the AR composite record including interpolated uncertainties from stratigraphically nearest temporal tie points (Appendix B). A petrologic investigation of drilled volcaniclastics by Macdonald et al. (2015) involved samples V-16, V-70, V-89, V-111, V-144, V-215 and V-279. These samples were furthermore assigned with age estimates from the climatostratigraphic age model in the study by Macdonald et al. (2015). Unfortunately, no information about the underlying age model and no uncertainties were presented to these ages. An example is the attribution of an age of ca. 530 ka to volcaniclastic layer V-279 (Macdonald et al., 2015). This age estimate is in general agreement with the SGTF age for V-279 presented in this thesis (525 ± 26 ka). However, the modelled age for V-279 is 508 ± 2 ka and considerably younger than ca. 530 ka. The list of the modelled ages in Appendix B has the potential to avoid imprecise estimates and is recommended for future studies on volcaniclastics from the AR drilling cores.

The following correlations rely on compositions, granulometric descriptions and $^{40}Ar/^{39}Ar$ ages (assigned with two standard deviations) presented in Sumita and Schmincke (2013c) and

Table 7.3: List of abbreviations in Fig. 7.12. Some of the dated Süphan lavas were compiled in Yilmaz et al. (1998). Their initial references are: Nagao et al. (1989)[1], Pearce et al. (1990)[2], Sanver (1968)[3], and Innocenti et al. (1976)[4]. $^{40}Ar/^{39}Ar$ ages of further Süphan lavas have been provided by Özdemir and Güleç (2013)[5]. All Nemrut onshore tephra units name in the list are taken from Sumita and Schmincke (2013c).

Onshore Nemrut		Onshore Süphan	
YP	Yolgözler Pumice	FEA	Flank eruption andesite[1]
MI	Muş Ignimbrite	FET	Flank eruption trachyte[2]
TI	Tatvan Ignimbrite	FEB	Flank eruption basalt[3]
TP	Tatvan Pumice	FER	Flank eruption rhyolite[4]
ACP	Alacabük Pumice	CR	Climatic rhyolite[4]
KK	Kücüksu Ignimbrite	RD	Dome rhyolite[5]
YP	Yelkenli Pumice	DD	Dome dacite[5]
NDU	Nemrut Depositional Unit (or NF)	ET	Early trachyandesite[5]
SF	Sentepe Formation	LT	Late trachyandesite[5]
H10, H3, H1	Halepkalesi Pumice + ID	LB	Late basaltic trachyandesite[5]
HPL	Halepkalesi Fallout (lacustrine)	B	Basalt[5]
KL	Upper Kınalıkoç Ignimbrite		
A8, A6, A5,..	Ahlat Pumice + ID		
KMP	Karmis Pumice		
KRP	Karak River Pumice		
AL1, AL2	Ahlat Lower Pumice + ID		

in the given thesis.

V-36

V-36 agrees in age within uncertainties to the Tatvan Ignimbrite, the Sentepe Formation and the Ahlat Pumice 8b. The chemical composition of V-36 suggests a correlation to the Tatvan Ignimbrite due to almost identical major element contents. Sumita and Schmincke (2013c) highlighted that the Tatvan Ignimbrite, the Ahlat Pumice 8b (or Ahlat Ignimbrite) and the Upper Kınalıkoç Ignimbrite are potentially correlated. They also pointed out that the according eruptions may have happened at slightly different times and that a correlation might be misleading. Any of the three potential correlations would link V-36 to an ignimbrite onshore.

V-45

The imprecise age from dating glass shards does not allow a correlation to onshore deposits. As the MGTF age from feldspars has been interpreted to be erroneously old (see Chapter 4), only the modelled age of 60 ± 2 ka serves for a potential correlation. The $^{40}Ar/^{39}Ar$ age of the Ahlat Pumice 8b (or Ahlat Ignimbrite) by Sumita and Schmincke (2013c) agrees to this age. A compositional contrast of V-45 to whole-rock analyses of the fallout suggests that a correlation between Ahlat Pumice 8 and V-45 is unlikely (the samples differ by ca. 10 wt% in SiO_2, and disagree in trace element contents). Thus, V-45 remains uncorrelated.

V-65

The MGTF age of V-65 has to be treated with care. A two-sample t-test with ages from climate-stratigraphy and the apparent MGTF ages of V-65 show a low probability of 0.08. However, V-65 agrees to the Ahlat Pumice 5, Ahlat Pumice 4a, Ahlat Pumice 3, Tatvan Pumice, and the Halepkalesi Pumice 3 in age. Chemical compositions of the Halepkalesi Pumice 3 and the Ahlat Pumice 3 have not been published and cannot be correlated. However, a correlation to these deposits seems unlikely as the modelled age for V-65 is 88 ± 2 ka and thus significantly younger.

The alkali content, some of the trace element concentrations, the CaO concentration and the timing agree with data from the Ahlat Pumice 5. SiO_2 concentrations differ by > 4.5 wt%. Sumita and Schmincke (2013c) furthermore noted that Ahlat Pumice 5 appears as a bipartite tephra north of the village of Ahlat that is < 50 cm in thickness. The ca. 40 cm thickness of V-65 at AR and the succession of three inverse graded beds do not accord to the description of Ahlat Pumice 5 and V-65 remains uncorrelated.

V-81

The result from MGTF dating of V-81 agrees within uncertainties with ages from Ahlat Pumice 4a, Tatvan Pumice, Halepkalesi Pumice 3, Ahlat Pumice 3, and the Ahlat Pumice 2. V-81 is compositionally similar to the Tatvan Pumice and to the Ahlat Pumice 4a. Sumita and Schmincke (2013c) stated that Ahlat Pumice 4a has an outstanding high peralkalinity (PI of 1.34). The peralkalinity of V-81 is considerably lower (1.10) but also slightly higher than the peralkalinity of the Tatvan Pumice (1.01). A correlation to the Tatvan Pumice is hampered by a significant discrepancy between the $^{40}Ar/^{39}Ar$ isochron age and the weighted mean of $^{40}Ar/^{39}Ar$ apparent ages of presented in Sumita and Schmincke (2013c). The lack of information about the initial $^{40}Ar/^{36}Ar$ composition and the filtering systematics of TF analyses amplify this problem. Mouralis et al. (2010) applied $^{40}Ar/^{39}Ar$ dating on feldspars from Nemrut fallout tephra which has been attributed by Sumita and Schmincke (2013c) to correspond to the Tatvan Pumice. The age of 117 ± 5 (1σ) agrees well to ages from $^{40}Ar/^{39}Ar$ dating and age modelling of V-81 in this thesis. The Tatvan Pumice offers a potential correlation to V-81.

V-111

The MGTF age of V-111 agrees within uncertainties to ages from the Halepkalesi Pumice 1, Ahlat Pumice 2, and the Alacabük Pumice. Chemical compositions of the Halepkalesi Pumice 1 and the Alacabük Pumice have not been obtained. Contrasting major element compositions and highly contrasting Zr/Nb ratios exclude a correlation to Ahlat Pumice 2. A correlation is impossible and requires further compositional and petrographic data.

V-149

The SWH age of V-149 overlaps radiometric ages presented for the Ahlat Pumice 2, the Alacabük Pumice, the Karmis Pumice, the Yolgözler Pumice, the Ahlat Pumice 1 and the Kücüksu Ignimbrite. Ahlat Pumice 2 can be excluded for a correlation to V-149 due to highly contrasting Zr/Nb ratios. The Kücüksu Ignimbrite agrees in age due to elevated uncertainties. The age of the underlying Kücüksu Pumice is significantly older than V-149 and suggests that there is no correlation between V-149 and the Kücüksu units. Yolgözler Pumice slightly differs in SiO_2 content and the Karmis Pumice in Zr/Nb ratio. Nevertheless, the later two are compositionally close to V-149. The Yolgözler Pumice is compositionally and stratigraphically also correlative to Ahlat Pumice 1 (Sumita and Schmincke, 2013b). The lack of compositional data from Alacabük Pumice and Ahlat Pumice 1 hamper a more detailed correlation to onshore Nemrut tephra.

V-165

The age of V-165 agrees within uncertainties to a number of onshore Nemrut tephra formations: Ahlat Pumice 2, the Alacabük Pumice, the Karmis Pumice, the Yolgözler Pumice, the Ahlat Pumice 1, the Kücüksu Ignimbrite, the Kücüksu Pumice, and to a fallout tephra that is embedded in lacustrine sediments at the Halepkalesi peninsula (HPL). The overlap in age to the Kücüksu units and to HPL is probably caused by the elevated uncertainties that are derived from the extreme corrections of atmospheric ^{40}Ar in the sample gas from V-165. The sample V-165 is compositionally similar to the Yolgözler Pumice and the Karmis Pumice. Nevertheless, the comparisons lack an unequivocal identification and a correlation remains vague. A potential correlation also requires further compositional data of Ahlat Pumice 1.

V-184

SWH analyses on V-184 resulted in an age that agrees within uncertainties to the two Kücüksu units, to the HPL, to the Ahlat Lower Pumice 2, to the Muş Ignimbrite, and to the Karak River Pumice. The modelled age of V-184 suggests that V-184 does not represent a correlative unit to the Kücüksu units and to the HPL. The Ahlat Lower Pumice 2, the Muş Ignimbrite, and the Karak River Pumice have a trachytic composition that is similar to the one from V-184. The Karak River Pumice has furthermore a trace element composition that is similar to the one from V-184, but deviates >2.5 wt% in SiO_2 content. A correlation to the Ahlat Lower Pumice 2 and to the Muş Ignimbrite is unlikely due to differing trace element compositions. The lack of compositions to other contemporaneous onshore units leaves V-184 uncorrelated.

V-209a

The MGTF age from V-209a is in agreement with the ages obtained for the Ahlat Lower Pumice 2, the Karak River Pumice, Ahlat Lower Pumice 1 and the Muş Ignimbrite. The Ahlat Lower Pumice 2 and the Muş Ignimbrite differ slightly in major element compositions to V-209a. Ahlat Lower Pumice 1 and Karak River Pumice agree vaguely to the major element composition of V-209a but show contrasting trace element compositions. No unequivocal correlation could be established for V-209a.

V-221a

The radiometric age of V-221 agrees within uncertainties with the Ahlat Lower Pumice 1. Although these units have similar trachytic compositions, they differ significantly in several trace element concentrations. The good agreement of the SGTF age for V-221 with the modelled age suggests that the V-221 is significantly older than the Ahlat Lower Pumice 1.

V-254

The MGTF age of V-254 is in agreement with the age obtained for the Selaviat Tepe Pumice and the Yelkeni Pumice. Thorough glass alteration did not allow obtaining the chemical composition of the Yelkeni Pumice (Sumita and Schmincke, 2013b). Trace and major compositions of the Selaviat Tepe Pumice agree well to the composition of V-254 and reveal a potential for correlation. The Selaviat Tepe Pumice is the oldest onshore Nemrut tephra known.

7.3.4 Conclusion on tephra correlation

Three samples (V-36, V-81 and V-254) show indications for a possible correlation to onshore Nemrut tephra. Nevertheless, the outlined compositional similarities are not decisive and detailed comparisons of glass compositions from these three samples are recommended for future studies. The majority of the discussed samples probably lack compositional onshore equivalents due to erosion. Moderately sized eruptions are prone to transport tephra to the location of the AR (Sumita and Schmincke, 2013c). On the other hand, this type of eruption does not particularly deposit tephra in onshore proximity of the Nemrut caldera. Medium to strong westward-directed winds (medium wind speed of 4 m/s in January) are a characteristic for the southern and western slopes of Nemrut (Öztopal et al., 2000; Sensoy et al., 2008). Most samples from AR discussed in this thesis have been taken from volcaniclastic layers that have thicknesses of a few centimetres. It seems legit to assume that the majority of the samples may have no contemporaneous onshore equivalent due to aeolian erosion.

8 Modelling Retention of Inherited ^{40}Ar in Volcaniclastic Anorthoclase

8.1 Introduction to assessing potential inherited ^{40}Ar

Xenocrystic feldspar have been suspected to retain radiogenic $^{40}Ar^*$ if the timing of magmatic entrainment, dispersion and ejection is fast and has a duration of days (Singer et al., 1998; Spell et al., 2001; Renne et al., 2012). Engelhardt et al. (2017) applied feldspar $^{40}Ar/^{39}Ar$ geochronology on volcaniclastic layers that are embedded in a lacustrine record from Lake Van, Turkey. These ages dominantly agree to a detailed climatostratigraphic age model (Stockhecke et al., 2014a; Stockhecke et al., 2014b; Stockhecke et al., 2016). Outliers resulting in deviating old ages indicated to be either obtained from assimilated minerals that contain inherited $^{40}Ar^*$ or from heterogeneous distributed melt inclusions and appendant excess ^{40}Ar (Esser et al., 1997; Kuiper, 2002; Flude and Storey, 2016). Analysing cogenetic volcanic glass shows that the latter process camouflaged a significant impact of chlorine-derived excess ^{40}Ar to one of the deviating samples (Chapter 5). In order to test the potential of inherited $^{40}Ar^*$ in xenocrysts from the most deviating sample (V-45), this chapter analyses Ba diffusion couples and models the degree of degassing of any previously accumulated $^{40}Ar^*$. Compositionally zoned phenocrysts from a sample that resulted in stratigraphically assured $^{40}Ar/^{39}Ar$ ages (V-221a) were additionally investigated in order to illustrate the successful degassing of coarse (> 500 μm) feldspar subdomains.

8.2 Material and methods

8.2.1 Samples and selected crystals

Both samples analysed in this chapter are from thin (< 10 cm) lapilli falls (Fig. 8.1). A slightly pronounced inverse grading from predominant pumice <1 mm to pumice >1.5 mm is observed in both samples. V-221a is capped by sand sized ash and its top was probably smeared during coring. The eruption age for V-221a is 307 ± 15 ka (Engelhardt et al., 2017) and agrees to temporal constraints from the chronostratigraphic age model by Stockhecke et al. (2014a) and Stockhecke et al. (2016). Multigrain separates of anorthoclase from V-45 resulted in an age of 89 ± 11 ka (all ages stated with 2σ full external error) that deviate from the age model constraints by being minimum 17 ka older. Cogenetic volcanic glass gave an age of of very low precision (63 ± 34 ka) that widely overlaps the temporal constraints suggested by the age model (Fig. 8.2).

The whole rock lapilli composition from both samples is trachytic. Electron microprobe analyses (EMPA) of melt reveal more subalkaline and rhyolitic compositions (Fig. 8.3a). Classification after Frost et al. (2001) suggests ambiguity in terms of Al saturation for V-221a (Fig. 8.3b). As none of the two samples contain hornblende, diopside, or biotite the Al saturation in sample V-221a is surprising. Compositional sorting of these phases during transport potentially may explain the absence of these minerals. Feldspar and clinopyroxene represent the dominant phenocrysts in the petrographic inventory of both tephra layers. Furthermore Fe-Ti oxides are

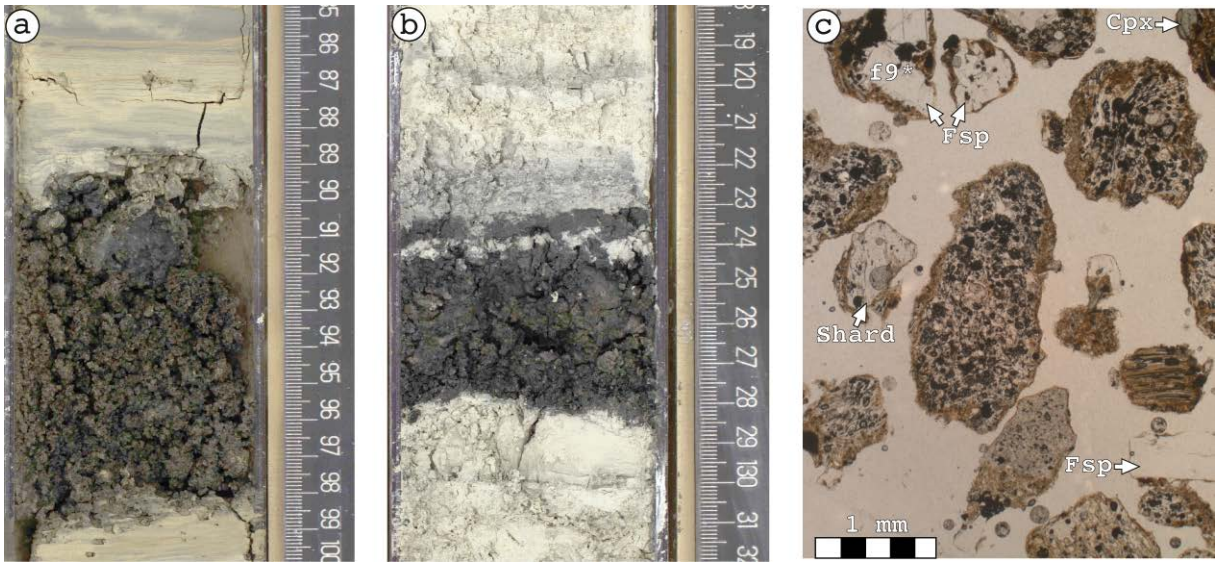

Figure 8.1: (a) Recovered pumice fall V-45. (b) Angular pumice V-221a. (c) Photomicrograph of a mounted strewn aliquot of V-45 in transmitting linear polarized light. Anorthoclase is labelled FSP, Clinopyroxene is labelled Cpx. Subhedral feldspar f9 is labelled and discussed later in detail. Unlabelled particles are dominantly pumice of different vesicularities.

frequent in both samples and fragments of fayalite occur in V-221a. Clinopyroxenes are dominantly ferroaugite in composition. V-45 bears rare augite and ferrohedenbergite (Fig. 8.3c). Feldspars are compositionally zoned and reach from andesine over oligoclase and anorthoclase to sanidine (Fig. 8.3d). Alkali feldspar and plagioclase differ optically in transmitting microscopy. Whereas plagioclase shows oscillatory normal zoning, anorthoclase and Na-sanidine have a compositional zoning with a core to rim relationship (Engelhardt et al., 2017). Rare plagioclase crystals from V-45 are irregularly overgrown by anorthoclase and reveal dissolution surfaces in backscattered electron BSE images and in CL images (Chapter 4).

C-type crystals dominate feldspars from both samples. Crystals from V-221a show mainly anorthoclase cores and Na-sanidine rims (Fig. 8.4a and Fig. 8.4b). Some feldspar crystals show oligoclase zones and extreme patchy zoning in Na-sanidine domains (Fig. 8.4e). Anorthoclase from V-45 has melt-rich anorthoclase cores that are mantled by thin oligoclase domains (Fig. 8.4c). The oligoclase-anorthoclase zoning also appears as patchy structures (Fig. 8.4d). The nomenclature in this study uses an identifier that organizes the sample-ID and the crystal-ID in the following way: $V\text{-}xFy$. Sample number and crystal number are presented by x and y, respectively. The ID of the EMPA line-scan extends this nomenclature. EMPA line scans are D, L, S or O. The IDs D, L, and S represent scans that were conducted perpendicular to the C-type zoning interface, whereas O measured oblique traverses.

8.2.2 Methodology

Electron backscatter diffraction (EBSD) analyses have been applied to 2 crystals from V-45 in order to verify the potential existence of misorientations in the C-type anorthoclase crystals. Higher degrees of misorientation potentially bias Ba diffusion couples (Cherniak, 2002) and give rise to investigate C-type zoning via EBSD on one of the two samples. EBSD will be briefly described in this section. A more detailed methodology on EBSD is provided in Appendix A. This section will furthermore review briefly the strategy in obtaining EMPA data at the zoning

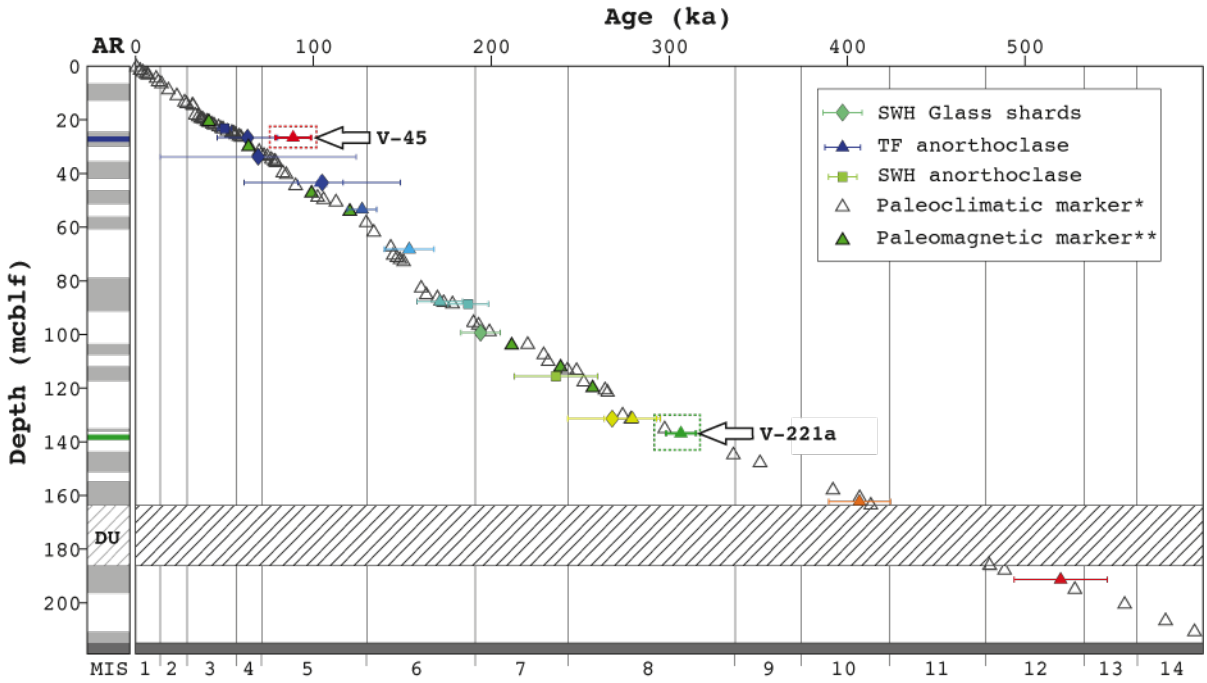

Figure 8.2: Compilation of various temporal marker for the composite record from Ahlat Ridge (AR) in an age to depth diagram. Results from feldspar dating of the two samples V-45 and V-221a are highlighted in green and red boxes. Paleoclimatic temporal marker are from Stockhecke et al. (2016)* and paleomagnetic marker from Vigliotti et al. (2014)**. MIS abbreviates marine isotope stages and DU the deformed unit. All uncertainties represent two standard deviations.

interfaces and describes an inherent optimization of the diffusion couple data. Furthermore the applied two-feldspar thermometry (Putirka, 2008) will be summarized. A more detailed methodology and the exact setup of EMPA is provided in Chapter 3. That chapter also provides a detailed methodology of modelling the spatial extent of the excited volume during EMPA, which provided the basis for a considerate decision of the step size in EMPA line-scans across compositional feldspar interfaces.

EMPA step scanning

The contrast in Ba-concentration between the different C-type zones in anorthoclase crystals is most evident in BSE imaging. The contrast in major elements is furthermore evident in transmitting light microscopy (Engelhardt et al., 2017). Transmitting microscopy therefore served to determining suitable interfaces between anorthoclase overgrowth and anorthoclase core. A straight shape of the Becke line during racking the focus of a petrographic microscope indicates a near vertical interfaces within a few hundred μm (Renne et al., 2012). The straight Becke line potentially serves as a prerequisite in the selection of suitable crystals for EMPA analyses and thus for calculation of Ba diffusion couples. Compositional contrasts of the C-type domains in this study are considerably weaker than the typical contrast between perthite and antiperthite domains of exsolved feldspars. Interfaces that are sub-parallel to a well-developed crystal surface and perpendicular to a cleavage plane are expected to offer vertical interfaces and were primary targets for the diffusion couple measurements. Element mapping was conducted subsequently to collecting step scan data and enhances the evidence for near vertical interfaces due to strong contrasts along the sharp interfaces. This approach identified unequivocal straight

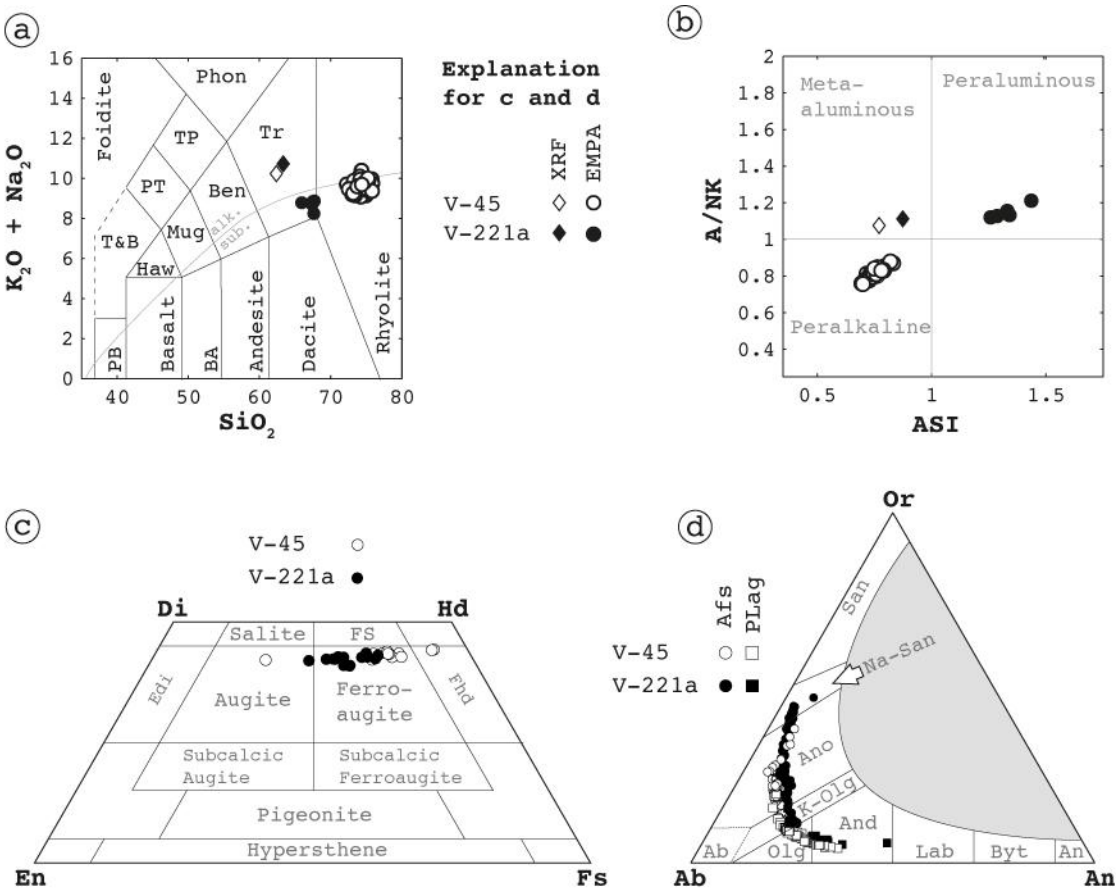

Figure 8.3: (a) TAS discrimination of glass and whole lapilli via XRF after Lebas et al. (1986).(b) Discrimination of melt and whole lapilli chemistry after Frost et al. (2001). (c) Chemical CPX discrimination after Rock (1990). (d) Composition of monocline feldspar at 1000° C or higher. The discrimination is taken from Parsons (2010) and the boundary between feldspar and plagioclase is drawn for convenience as An = Or. Abbreviations are explained in the following. Edi: Endiopside, Fhd: Ferrohedenbergite, Olg: Oligoclase, And: Andesine, Lab: Labradorite, Byt: Bywtonite, Anor: Anorthoclase, San: Sanidine.

interfaces in two crystals from V-221a (Fig. 8.4a and Fig. 8.4b). Suitable interfaces in crystals from V-45 were difficult to detect but underwent the same systematic selection. These crystals show a combination of R-type and C-type zoning and the EMPA line scans were conducted on one type of zoning each (Fig. 8.4c and Fig. 8.4d). The crystal V-45F9 showed zoning in a BSE image that was interpreted to reveal C-type zoning (Fig. 8.5a). Step scanning and element mapping revealed R-type zoning that involved patchy C-type domains (Fig. 8.4d). Nevertheless, V-45F9 revealed a step in Ba concentrations and the data has been processed for applying a Ba diffusion couple.

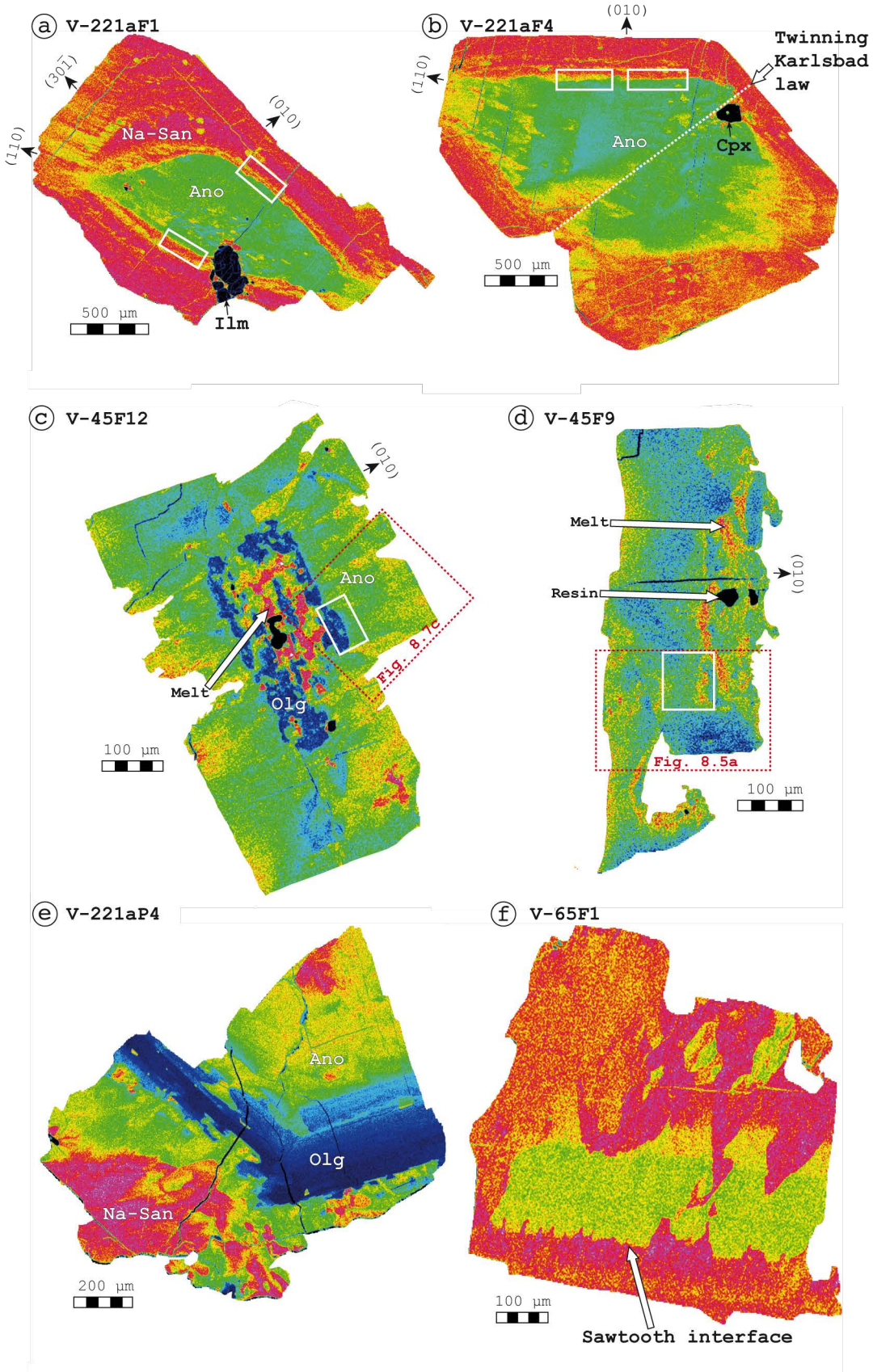
ⓐ V-221aF1
(301)
(010)
(110)
Na-San
Ano
500 µm
Ilm
ⓑ V-221aF4
(010)
(110)
Twinning
Karlsbad
law
Ano
Cpx
500 µm
ⓒ V-45F12
(010)
Ano
Fig. 8.7c
Melt
Olg
100 µm
ⓓ V-45F9
Melt
Resin
(010)
Fig. 8.5a
100 µm
ⓔ V-221aP4
Ano
Olg
Na-San
200 µm
ⓕ V-65F1
100 µm
Sawtooth interface
high
low
Relative K content

Figure 8.4: (previous page): EMPA element mapping of C-type crystals. (a) Subhedral feldspar from V-221a. (b) Euhedral feldspar from V-221a showing twinning after the Karlsbad law. (c) Resorbed subhedral feldspar showing a zone of oligoclase that mantels a melt-inclusion-rich anorthoclase core from V-45. (d) Strongly resorbed feldspar showing patchy zoning of varying major compositions from V-45. Dashed red boxes highlight the extent of images presented in Figs. 8.5a and 8.7c. (d) C-type and R-type zoning of a crystal from V-221a. (e) Patchy feldspar zoning at the interface to a C-type subdomain. Zones highlighted by white boxes have been investigated by EMPA step scanning prior to element mapping. Highest relative K contents represent about 250 counts in a dwell time of 25 μs. Lowest relative K contents represent 0 counts.

C-type zoning that revealed saw-tooth or comb-like interfaces (Fig. 8.4f) were rejected, as they would result in mixed EMPA analyses close to the interface. The majority of EMPA step scans across C-type interfaces applied a perpendicular line-scans across the interface. Some line scans have been oriented in oblique traverses and followed an approach that had been presented in Renne et al. (2012). These traverses had an angle of 59.1° to the normal interface. Data obtained from this set up has been projected on the normal by multiplying the traverse distance by the cosine of the angle between normal and traverse (Fig. 8.5b).

Table 8.1: Radial intensity distributions of excitation volumes from CASINO modelling.

Sample	Crystal	1σ high K-domain (nm)	1σ 1ow K-domain (nm)
V-45	F9	796	761
V-45	F12	852	784
V-221a	F1	862	777
V-221a	F4	789	759

Processing of EMPA step scan data

The procession of EMPA data was twofold. It involved i) a deconvolution of potential excitation volume effects and ii) the determination of the potential timing of the Ba mobility using an optimization procedure. X-ray emission is stimulated in the analysed feldspars within a finite volume that is dependent on feldspar composition, feldspar density, and electron beam energy. EMP analyses close to the compositional interface represent an averaged concentration that is commonly corrected by assuming that the excitation volume has an intensity distribution that is radially symmetric (Ganguly et al., 1988). Therefore, modelling the radial intensity distribution preceded any data processing and was conducted by the CASINO software (Drouin et al., 2007). Excitation volume modelling has been conducted with feldspar compositions of each crystal discussed in this chapter. Furthermore, modelling has been obtained for compositions on each side of the interface (Table 8.1). The deconvolution procedure has been developed by Guillemoteau (2018) and is currently in preparation for publication elsewhere. It treats the measured concentrations as spatially weighted averages and follows an approach by Ganguly et al. (1988). The deconvolution of apparent concentration data allows the determination of a more realistic lateral distribution of concentrations and a shaper gradient in changing concentrations. It is performed in the spatial domain by using a deterministic optimization procedure with spatial constraints (Menke, 2012). With such an approach, it is possible to propagate the standard deviation of the data (Tarantola and Valette, 1982). The resulting lateral distribution of concentrations is then interpreted by using a one-dimensional biphasic model of diffusion as given by Crank (1975) and Ganguly et al. (1988):

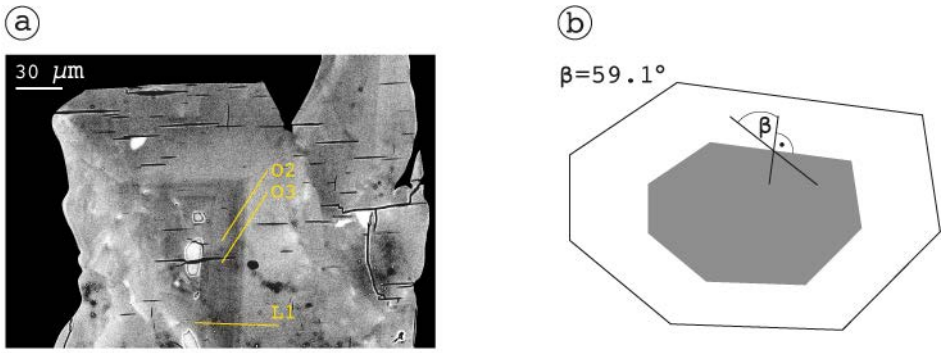

Figure 8.5: (a) BSE image of step scan traverses in V-45F9. (b) Sketch showing the systematic set up for analysing EMPA step scans on an oblique traverse with an angle of 59.1° between normal and traverse.

$$C(x) = C_1 + \frac{C_2 - C_1}{2}\left[1 + erf\left(\frac{x - x_C}{2\sqrt{Dt}}\right)\right] \tag{8.1}$$

Here, the position x_C is the position of the interface, C_1 and C_2 the corrected concentrations on each side of the diffusion couple, D the diffusivity, which is assumed to be independent from the varying composition, and t the time (Crank, 1975; Zhang, 2010). A linearisation of this formula results in in equation 8.2.

$$C = C_0 + J[m - m_0] \tag{8.2}$$

The initial parameters $\{C_1, C_2, t, \Delta x, D\}$ are represented by m_0. C_0 represents the concentration distribution that is associated to the initial set of parameters. The set of parameters that evaluates the concentration distribution is given in C. J is a Jacobian matrix that contains the local derivative with respect to each parameter and that has a dimension of Nm times (5).

$$J = \begin{vmatrix} \frac{\partial C(x_1)}{\partial C_1} & \frac{\partial C(x_1)}{\partial C_2} & \frac{\partial C(x_1)}{\partial t} & \frac{\partial C(x_1)}{\partial \Delta x} & \frac{\partial C(x_1)}{\partial D} \\ \vdots & \vdots & \vdots & \vdots & \vdots \\ \frac{\partial C(x_i)}{\partial C_1} & \frac{\partial C(x_i)}{\partial C_2} & \frac{\partial C(x_i)}{\partial t} & \frac{\partial C(x_i)}{\partial \Delta x} & \frac{\partial C(x_1)}{\partial D} \\ \vdots & \vdots & \vdots & \vdots & \vdots \\ \frac{\partial C(x_{Nm})}{\partial C_1} & \frac{\partial C(x_{Nm})}{\partial C_2} & \frac{\partial C(x_{Nm})}{\partial t} & \frac{\partial C(x_{Nm})}{\partial \Delta x} & \frac{\partial C(x_{Nm})}{\partial D} \end{vmatrix} \tag{8.3}$$

Each column of this matrix will be evaluated in an analytical derivation of formula 8.1.

$$\frac{\partial C(x)}{\partial C_1} = 0.5 \times \left[1 - erf\left(\frac{x - x_C}{2\sqrt{Dt}}\right)\right] \tag{8.4}$$

$$\frac{\partial C(x)}{\partial C_2} = 0.5 \times \left[1 - erf\left(\frac{x - x_C}{2\sqrt{Dt}}\right)\right] \tag{8.5}$$

$$\frac{\partial C(x)}{\partial t} = \frac{(C_1 - C_2)(x - x_C)}{4\sqrt{\pi D t^{1.5}}} \exp\left(-\frac{(x - x_C)^2}{4\sqrt{Dt}}\right) \tag{8.6}$$

$$\frac{\partial C(x)}{\partial \Delta x} = \frac{C_1 - C_2}{2\sqrt{\pi D t}} \exp\left(-\frac{x - x_C}{4\sqrt{\pi D t}}\right) \tag{8.7}$$

$$\frac{\partial C(x)}{\partial D} = \frac{(C_1 - C_2)(x - x_C)}{4\sqrt{\pi D t^{1.5}}} \exp\left(-\frac{(x - x_C)^2}{4\sqrt{\pi D t}}\right) \tag{8.8}$$

The set of parameters $\{C_1, C_2, t, \Delta x, D\}$ is also determined by deterministic optimization/inversion procedure. However, for the latter case, all derivatives depend on a parameter for which they are evaluated. It follows that the inverse problem is non-linear and must be solved by using an iterative process with a starting model $mp = 0$. With such a process, the model is subsequently updated in order to reduce the data misfit $||C - C(mp)||$, as described in the following equation.

$$m^{p+1} = m^p + G^{-g}[C - C(m^p)] \tag{8.9}$$

The according generalized inverse is represented by the following equation.

$$G^{-g} = [J^T W_d J + W_m] + J^T W_d \tag{8.10}$$

W_d represents the covariance of the data vector C, whose diagonal elements contain the posterior errors of $C(x)$ that have been obtained from the deconvolution procedure.

$$Wd, ii = \frac{1}{\sigma^2_{C,i}} \tag{8.11}$$

W_m represents a 5 times 5 prior covariance of the model parameter. Its diagonal elements are the inverse of the predefined uncertainties (standard deviations of the individual measurements and values from the literature) that characterize the degree of freedom of each parameter as illustrated in the following.

$$J = \begin{vmatrix} \sigma_{C_1}^{-2} & 0 & 0 & 0 & 0 \\ 0 & \sigma_{C_2}^{-2} & 0 & 0 & 0 \\ 0 & 0 & \sigma_t^{-2} & 0 & 0 \\ 0 & 0 & 0 & \sigma_{x_C}^{-2} & 0 \\ 0 & 0 & 0 & 0 & \sigma_D^{-2} \end{vmatrix} \tag{8.12}$$

Prior variances of C_1, C_2 and t are comparably large since they constitute the principal unknowns of the problem. The variance of the position of the interface x_C can be set according to the positioning precision of the measurement. Temperature in diffusion couple modelling is another primary input parameter and its relationship to the diffusivity D is given by

$$D = D_0 \times \exp\left(-\frac{E}{RT}\right) \tag{8.13}$$

where E is the activation energy, R the gas constant, T the temperature (in K) and D_0 the value of D at infinite temperatures. Thus, the temperature controls the prior variance of D and the prior variance of D is small in comparison to C_1, C_2, and t. In order to propagate the uncertainty due to the temperature we use:

$$\sigma_D = \sigma_T \partial D \partial T \tag{8.14}$$

where the according derivative is evaluated analytically via the following formula.

$$\frac{\partial D}{\partial T} = D_0 \frac{E}{RT^2} \exp\left(\frac{E}{RT}\right) \tag{8.15}$$

This approach incorporates the uncertainty of the temperature as an effect on the diffusivity. An approximation of all posterior errors contributing to equation 8.8 is presented by Menke (2012) and is

$$\sigma_m = \sqrt{diag[G^{-g} \times {W_d}^{-1} \times G^{-g^T} + N \times W_m^{-1} \times N^T]} \tag{8.16}$$

N is given by the following the relationship.

$$N = I - G{-}g \times J \tag{8.17}$$

Here, the variable I represents the identity of the matrix. The error distribution resulting from this non-linear problem is non-Gaussian. Therefore, the expression in Eq. 8.15 should be regarded as an approximation of the posterior errors. Nevertheless, testing the entire approach (deconvolution of the apparent concentration and the optimization) with synthetic data provided reliable outcomes (Guillemoteau, 2018). Limiting factors are small diffusion durations as the selected EMPA sampling steps are of low resolution (predominantly $\Delta x_d = 4\mu m$). All calculations were conducted with a Ba diffusivity for sanidine (Or_{60}) from Cherniak (2002). The composition of the sanidine in this experimental study is closest to the anorthoclase in the study given here. However, V-45F12 involves oligoclase, which has a considerably slower diffusivity Cherniak (2002). Therefore, diffusion couples from V-45F12 have been calculated a second time with the higher diffusivity of Ba in oligoclase.

FSP thermometers

The temperature has been obtained by applying a two-feldspar-thermometer for pressures between 1.5 and 3 kbar. Pressures of 2.5 to 3.5 kbar served for multiple calculations and followed (Macdonald et al., 2015), who suggested a pressure of 3 kbar from modelling the compositional variations of Nemrut explosives. The given study furthermore estimated the pressure based on a geothermal gradient of ca. 30° C/km and a maximum temperature of ca. 300 °C. Xenocrysts situated in wall rocks of higher temperatures are neither expected to accumulate nor retain any significant amounts of radiogenic $^{40}Ar^*$ (Renne et al., 2012). The gradient is based on a heat flux of 46 mW/m^2 for Nemrut (Akin et al., 2014) and on averaged heat conductivities for sandstone, limestone, rhyolite, mafic effusive and a rhyolitic volcaniclastic deposit (Robertson, 1988). Two-feldspar-thermometry has been applied by using equation № 27 in Putirka (2008), which is

$$T(C) = \frac{-442 - 3.72 \times P(kbar)}{-0.11 + 0.1 \ln\left(\frac{X_{Ab}^{AF}}{X_{Ab}^{PL}}\right) - 3.27(X_{An}^{AF}) + 0.098 \ln(X_{An}^{AF}) + 0.52(X_{An}^{PL} \times X_{Ab}^{PL})} \tag{8.18}$$

Where X^{AF} represents albite (or anorthite) fractions (in cations per formula) of the alkali feldspar and X^{PL} the compositions of the plagioclase counterpart. Feldspar compositions that

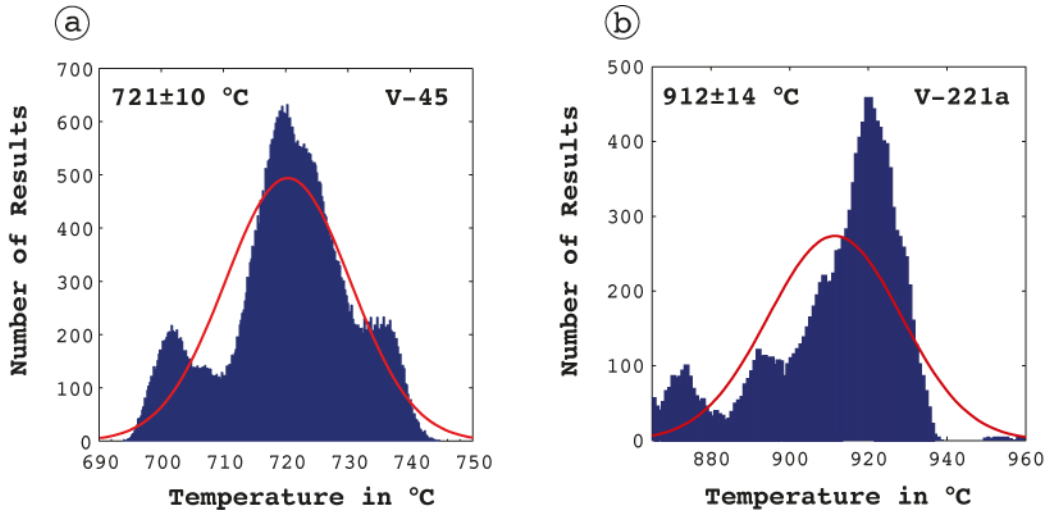

Figure 8.6: Distribution of calculated temperatures in histograms with according distribution curves. Resulting temperatures represent weighted averages with one standard deviation. Temperature distribution shown for V-221a isolated temperatures < 860 °C.

served for thermometry were analysed in the K-rich rim of the compositionally zoned C-type crystals. Temperature calculations were conducted with the complete series of available plagioclase compositions and pressures ranging between 2.5 and 3.5 kbar in 0.1 kbar steps.

V-45 resulted in several overlapping peaks between 690 and 740 °C (Fig. 8.6a). A weighted average of the entire distribution results in a temperature of 721 ± 10 °C. This temperature agrees to the considerably higher liquidus temperatures predicted by MELTS (Ghiorso and Sack, 1995) of 1151 °C at 2.5 kbar and 999°C at 3.5 kbar. Modelling via MELTS used whole lapilli XRF data and fO_2 values at the FMQ buffer (Macdonald et al., 2015). Another testing was conducted by calculation of a plagioclase-liquid-thermometer using equation 23 of Putirka (2008). This test resulted in a low precision with a temperature of 750 ± 65 °C. It is assumed that the predicted one-plagioclase crystallisation path discussed in Chapter 4 does not hamper the two feldspar thermometer and illustrates the temperature at which oligoclase became mantled by anorthoclase compositions. This temperature is subsequently regarded as maximum temperature that enabled diffusion across the investigated steps in the Ba concentration.

V-221a resulted in temperature distributions that show four different peaks. The given study used the peak representing the highest temperatures in order to model the maximum possible diffusion speed and thus the possibly shortest magmatic residence time of the coarse phenocrysts in V-221a. The scattering temperatures are a result of varying compositions in the K-rich rim of C-type feldspars in V-221a (Figure 8.4e). A filter isolated temperatures < 690 °C. The weighted mean of this distribution of temperatures is 912 ± 14 °C. This value agrees to liquidus modelling in MELTS, which resulted in 1153 °C at 2.5 kbar and in 1131°C at 3.5 kbar.

EBSD

The orientation of the two idiomorphic crystals from V-221a is inferred from twinning and the columnar anorthoclase habitus. Orientations of the crystals from V-45 have been investigated for potential misorientations along traverses that are parallel to the normal of the investigated interface. Crystallographic orientations from EBSD analysis showed that both V-45F12 and

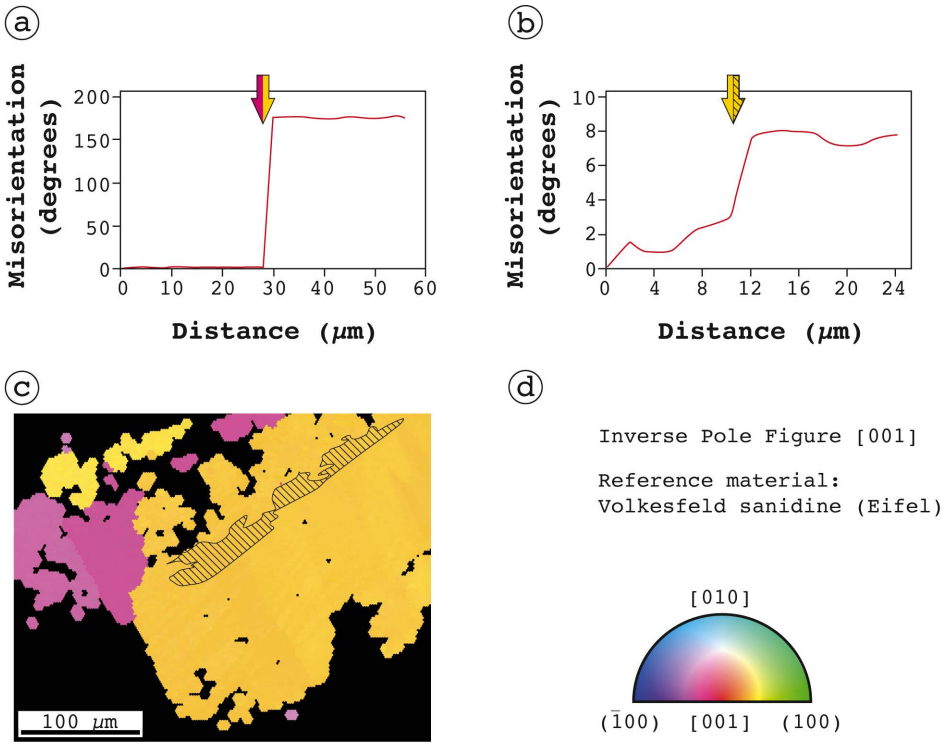

Figure 8.7: (a) Line scanning of relative misorientation due to twining in V-45F12. The arrow indicates the inferred position of the twin plane. (b) Line scanning of relative misorientation due to compositional zoning. The interface is highlighted with an arrow. (c) Colour coded inverse pole figure map of V-45F12 with respect to the normal of the [001] direction. Dashed area represents domains of oligoclase compositions. (d) Explanation of the colour coding.

V-45F9 are twinned feldspars with sharp misorientations of 180° (Fig. 8.7). The twin interface, however, does not intersect the investigated zoning interfaces. Polished surfaces from both crystals are (sub-) perpendicular to the [001] direction.

Scanning misorientations along a normal to the interface of C-type zoning reveals a maximum misorientation of about 5° between oligoclase and anorthoclase domains in C-type crystals. The EBSD analytics suggest that different C-type domains can be regarded as epitactic. Interfaces from C-type zoning hence do not indicate to serve as a diffusion boundary or diffusion acceleration lane.

Modelling retention of inherited $^{40}Ar^{*}$

The given study models a potential retention analogue to modelling presented by Renne et al. (2012). *Dt* values were obtained from Ba diffusion across the observed compositional interfaces in crystals V-45F12, V-221aF4, V-221aF1 and the sharp variation in Ba concentration from V-45F9. By taking the available Ba diffusion data (Cherniak, 2002) the *Dt* values can be displayed as square-pulse time-temperature histories. This approach has the advantage of a direct comparison of the diffusion couple with square-pulse time-temperature degassing of $^{40}Ar^{*}$ (Renne et al., 2012). The exact knowledge of the parameters that dictate Ar diffusion in feldspars can not be determined analytically and approximations from modelling Ar-diffusion with laboratory degassing experiments is a thorny issue (Foland and Xu, 1190; Foland, 1974; Arnaud and Kelley, 1997; Parsons et al., 1999; Wartho et al., 1999; McLaren and Reddy, 2008; Cassata and Renne, 2013; Harrison and Lovera, 2014; Villa, 2014). However, this study modelled of Ar-loss by taking

activation energies (E_a) and pre-exponential factors D_0 from Cassata and Renne (2013), who provide diffusion parameters that are derived from degassing experiments of the 'Easy Chair Crater Anorthoclase'. These anorthoclase crystals are compositionally similar to the C-type anorthoclase crystals discussed here. Consequently, the given study modelled $^{40}Ar^*$ retention by using a value of 286 ± 12 kj/mol and 0.8 ± 1.7 m^2/s for E_a and $\ln(D_0)$, respectively (Cassata and Renne, 2013). Ar loss models in the given study represent calculations that assume one-dimensional plane sheet geometries. The lengthscales of whole xenocrysts and phenocrysts serve as the diffusive dimension for Ar loss. Therefore, fractional loss of Ar has been calculated with the half-width of the crystals' average grain size. The equations for the approximate fractional loss are taken from McDougall and Harrison (1999) and are

$$f \approx 1 - \left(\frac{8}{\pi^2}\right) \exp\left(\frac{-\pi^2 Dt}{4r^2}\right) \tag{8.19}$$

for $0.45 \leq f \leq 1$ and

$$f \approx 1 - \left(\frac{8}{\pi^2}\right) \exp\left(\frac{-\pi^2 Dt}{4r^2}\right) \tag{8.20}$$

for $0 \leq f \leq 0.6$. The variable f represents the fractional loss and r the half-width of the plane sheet.

8.3 Results diffusion couple modelling

Step scans across C-type zoning interfaces reveal K concentrations that are anticorrelated to Na and Ca (Fig. 8.8a). The transitions are smooth and indicate diffusive behaviour of the major elements. Ba concentrations show similarly diffusive transitions at the interface (Fig. 8.8b). The Ba concentration typically decreases within the core towards the compositional interface. The rim reveals an analogue of that pattern with a decrease in Ba concentration further to the crystal's surface.

Results from diffusion couple modelling are listed in Table 8.2. Five different line scans from V221aF1 resulted in diffusive durations of magmatic heating from 11 to 21 years. These scans reveal very sharp steps in Ba concentrations that lack evidence of intermediate compositions close or at the compositional interface (Fig. 8.8c). However, these scans also show strong Ba heterogeneities parallel to the zoning interface. The heterogeneities potentially hamper the definition of plateaus of constant Ba concentrations on either side of the interface in the data from scans S1 and O3. Consequently, these scans have not been processed in diffusion couple calculations. The sharp steps in Ba concentrations are attributed to the comparably wide steps from EMPA line scanning. Scans S2, S5, S8, S9 resulted in step-scanning profiles that reveal significant higher durations of magmatic heating. These profiles do not show sharp changes in Ba concentrations. Intermediate compositions in S2, S5, S8, S9 may represent mixed analyses that were not sufficiently deconvolved. An overestimation of the temporal duration of relaxation in Ba concentrations would be the according consequence. One line-scan from V-221aF4 illustrates the same effect best. The scan S1 offers an intermediate composition and potentially overestimates the distance between the two plateaus in Ba concentration (Fig. 8.8d). This line-scan results in a temporal duration that does not agree within uncertainties with results S2 and S3 (Table

8.2) that show sharp contrasts in Ba concentrations and thus shorter distances in maximum relaxation profiles.

The two crystals from V-45 showed more homogenous results. Two scans (V-45F9O2 and V-45F12O3) revealed heterogeneities in Ba concentration and hampered the definition of constant Ba plateaus. Nevertheless, all scans show similar shapes and intermediate Ba concentrations. The resulting durations from Ba diffusion couple modelling agree to each other within uncertainties.

Table 8.2: Results from Ba diffusion modelling. The calculated diffusion duration is given in years. Scans from V-45F12 involve oligoclase and have thus been recalculated using the Ba diffusivity for oligoclase (D_O) from Cherniak (2002).

Traverse	t	±	Data quality	Traverse	t	±	Data quality
V-221aF4S1	84	47	processable	V-45F9L1	536	312	processable
V-221aF4S2	22	12	processable	V-45F9O2	None		bad
V-221aF4S3	19	10	processable	V-45F9O3	454	257	processable
V-221aF1S1	None		bad	V-45F12L1	314	175	good
V-221aF1S2	51	28	processable	V-45F12O2	235	130	good
V-221aF1S3	11	6	processable	V-45F12O3	None		bad
V-221aF1S4	19	11	processable	V-45F12D2	472	264	processable
V-221aF1S5	48	26	processable				
V-221aF1S6	None		bad				
V-221aF1S7	21	12	processable	V-45F12L1 (D_O)	5.2	1.9	good
V-221aF1S8	66	36	processable	V-45F12O2 (D_O)	4.1	1.52	good
V-221aF1S9	48	27	processable	V-45F12O3 (D_O)	None		bad
V-221aF1L1	14	8	processable	V-45F12D2 (D_O)	8.6	3.2	processable
V-221aF1O2	16	9	processable				
V-221aF1O3	None		bad				

The different time-temperature scenarios from both crystals of sample V-221a agree to each other within propagated uncertainties (Figs. 8.9a and 8.9b). Estimations of maximum time spans that govern relaxation of the contrasting Ba concentrations can therefore be interpreted to be legit. Nevertheless, the diffusion couples from sharp steps in Ba concentrations are clearly highlighted to represent maximum durations for the potential relaxation of Ba concentrations. Although the investigated zoning types are different in V-45F12 (C-type domains) and V-45F9 (contrasting Ba concentrations) an almost identical result has been obtained in predicting a time-temperature scenario for these crystals (Figs. 8.9c and 8.9d).

This similarity suggests that Ba-diffusion is almost unaffected by the compositional zoning. Modelling the same diffusion couple under the assumption that the slow Ba diffusivity in oligoclase governs the Ba relaxation across the interface reveals considerably shorter magmatic residence times (intersection of dashed bar with red band in Fig. 8.9c). Ar-loss models assume the most retentive behaviour of Ar in anorthoclase as suggested by Cassata and Renne (2013). These parameters are 298 kj/mol and -1.1 m2/s for E_a and D_0, respectively. Calculating Ar loss with least retentive parameters (E_a = 274 kj/mol and D_0=2.5 m^2/s) shows that temperature-time predictions for coarsest and smallest crystals would result in complete Ar degassing (Figs. 8.9e and 8.9f).

8.4 Discussion

The calculation of Ba diffusion couples from selected crystals in the given study shows that $^{40}Ar^*$ inheritance is unlikely. None of the predicted time-temperature scenarios indicate incomplete degassing of C-type subdomains (Fig. 8.9a and 8.9b) or xenocrysts (Figs. 8.9c and 8.9d). Con-

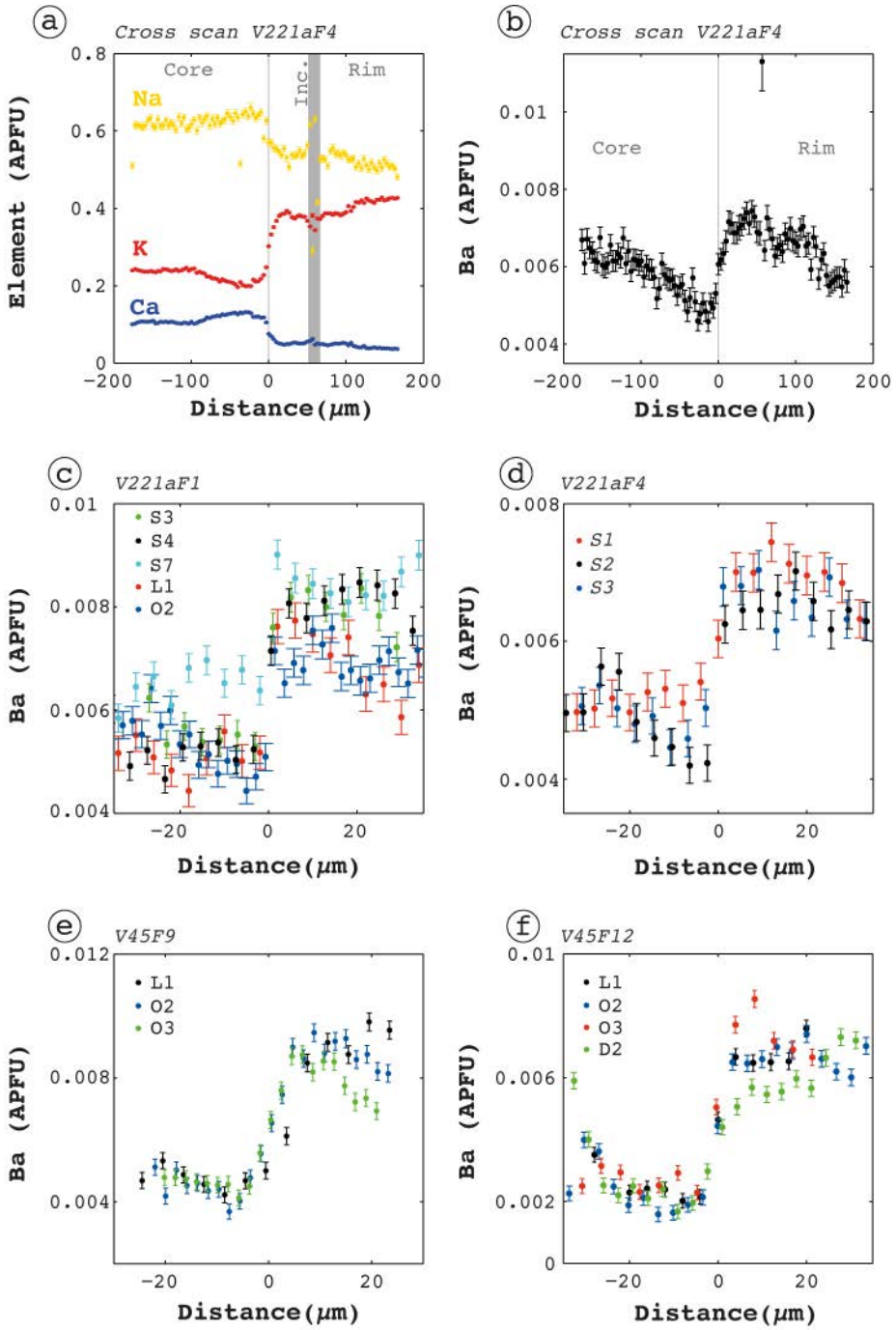

Figure 8.8: (a) Alkaline and earth alkaline metal distributions in V221aF4 across the compositional zoning interface. Grey bar represents analyses that are derived from mixed composition with melt inclusions. (b) Ba distribution in V221aF4 across the compositional zoning interface. (c) Ba distributions in proximity to the zoning interface from selected step scans in V221aF1. (d) Ba concentrations from EMPA step scans in V221aF4. (e) Ba concentrations from EMPA step scans in V45F9. (f) Ba concentrations from EMPA step scans in V45F12. All uncertainties represent one standard deviation. Concentrations are provided in atoms per formula unit (apfu) feldspar.

sidering the extent of the uncertainties, the scans S2 and S3 from V-221aF4 allows a potential incomplete degassing that is capable of retaining ca. 30 % of earlier accumulated Ar maximum. However, none of the two $^{40}Ar/^{39}Ar$ ages obtained from feldspars of V-221a suggest significant proportions of inherited $^{40}Ar^*$. The time-temperature scenario thus either underestimates Ba relaxation, overestimates Ar retention or indicates that subdomains never accumulated radiogenic Ar prior to the K-rich mantling. The smaller grain size of V-221aF1 results in a less-retentive model and does not indicate any Ar inheritance. Time-temperature scenarios from the two crystals of V-45 do not indicate any inheritance of $^{40}Ar^*$. An exception is the calculation of the diffusion couple that bases on the slow Ba diffusivity in oligoclase. This scenario allows the inheritance of almost 50% of any previously accumulated radiogenic Ar^*. Nevertheless, within the uncertainty of the according time-temperature scenario this inheritance has a minimal probability. Furthermore, the similarity in results from diffusion couples from V-45F9 and V-45F12 based on Ba diffusivity in sanidine suggest that the relaxation of Ba is governed by the fast diffusivity of Ba in sanidine and not by the slow diffusivity of Ba in oligoclase. Considering that all Ar loss models base on the assumption that crystals behaved most retentive, it is unlikely that any of the analysed crystals bear significant amounts of inherited $^{40}Ar^*$. Therefore, the age deviation between dating V-45 and temporal constraints from the climatostratigraphic age model (Engelhardt et al., 2017) is most likely attributed to the irregular incorporation of excess ^{40}Ar from melt and fluid inclusions alone (Chapter 4). Nevertheless, several aspects on the insights from Ba diffusion couple modelling presented here have the potential to question the time-temperature scenarios and are thus discussed briefly in the following.

8.4.1 Sharp contrasts in Ba concentrations

Sharp contrasts in Ba concentrations from V-221aF1 (Fig. 8.8c) clearly indicate short diffusion timescales. This observation underlines the need of deconvolution of potentially mixed analyses from point measurements close to the inferred interface (Ganguly et al., 1988; Morgan et al., 2004; Costa and Morgan, 2010; Bradshaw and Kent, 2017). Line-scans that show intermediate compositions resulted in larger durations for relaxation of the different Ba concentrations. Bradshaw and Kent (2017) discussed synthetic diffusion data sets and showed that higher spatial analytical resolution gives access to shorter timescales. Thus, each analytical resolution has a minimum threshold timescale. Applying a method although the minimum threshold is exceeded, significantly overestimates the true timescales. An approximation is that diffusion modelling becomes accurate when the width of a diffusive gradient between two constant concentrations is minimum two times the spot size of the analytical method Bradshaw and Kent (2017).

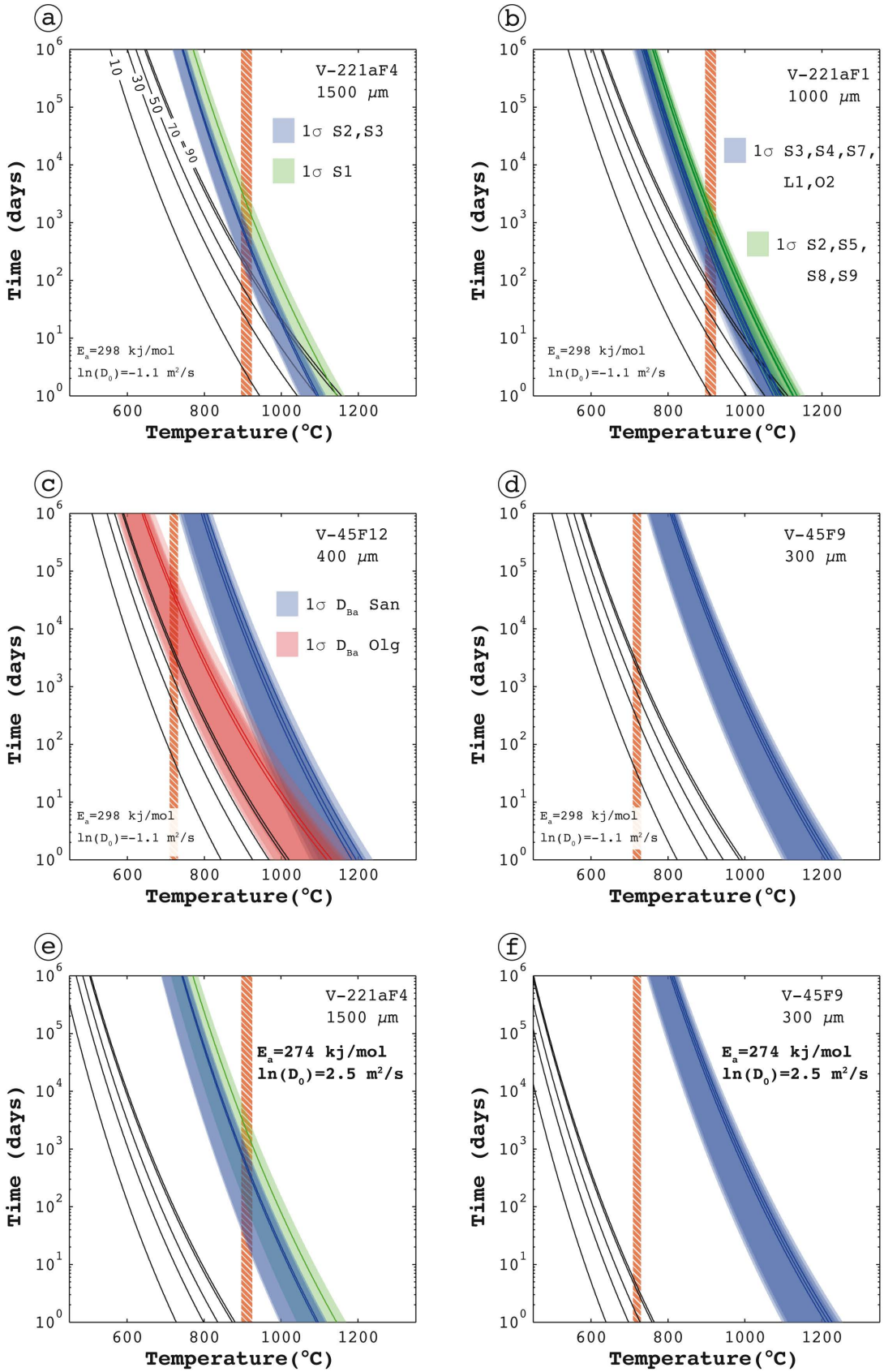
a
V-221aF4
1500 μm
1σ S2,S3
1σ S1
10
30
50
70
90
Ea=298 kj/mol
ln(D0)=-1.1 m2/s
b
V-221aF1
1000 μm
1σ S3,S4,S7,
L1,O2
1σ S2,S5,
S8,S9
c
V-45F12
400 μm
1σ DBa San
1σ DBa Olg
d
V-45F9
300 μm
e
V-221aF4
1500 μm
Ea=274 kj/mol
ln(D0)=2.5 m2/s
f
V-45F9
300 μm
Time (days)
Temperature(°C)

Figure 8.9: Time-temperature square-pulse heating scenarios deduced from Ba diffusion couples. (a) Prediction of the Ba diffusion profile in V-221aF4 (blue and green lines indicate different scans) in comparison with the time-temperature $^{40}Ar^*$ loss model in black lines (values in %). The according magma temperature is represented by the width of the dashed vertical orange bar. The potential magmatic residence time is illustrated in the intersection of the heating scenario (green and blue lines) and the temperature range (bar). (b) Heating and degassing scenario for V-221aF4. (c) Heating and degassing scenario for V-45aF12 using a Ba diffusivity for oligoclase (red) and sanidine (blue). All other scenarios were calculated using the Ba diffusivity for sanidine only. (d) Heating and degassing scenario for V-45aF9. (e) Least retentive $^{40}Ar^*$ degassing scenario of the coarsest crystal investigated in this study. (f) Least retentive $^{40}Ar^*$ degassing of the smallest crystal investigated in this study. The widths of the coloured bands represent a 1σ uncertainty range.

Diffusive Ba gradients have been determined only poorly (a maximum of 3 analyses) or not at all (e.g. V-221aF1) in this study. Considering the modelled radial intensity distributions (Table 8.1), the ratio of the diffusive gradient width to the effective spot size is close to or rather $<$ 2. Bradshaw and Kent (2017) suggested the following simple equation for estimating the lower temporal limit for a timescale accuracy of 20%.

$$t_{20\%} = (0.24 \times x_s^2) \times D^{-1} \tag{8.21}$$

The minimum diffusive relaxation time that reaches an accuracy of 20% is given in t_{20}%. The spatial resolution is represented in x_s (m) and the diffusivity in D (m^2/s). According to this equation, line-scans from V-221a would meet the threshold criteria, whereas line-scans from V-45 would not. As the spatial resolution is identical to both samples the difference is explained by the change of the Ba diffusivity at higher temperatures (Table 8.3). Thus, the limited spatial resolution in EMPA hampers interpretations from Ba diffusion couple modelling in the given study. It is evident that time scales for relaxation of Ba concentrations were too short to be detected in EMP analyses and that diffusion couple modelling overestimates the true timescales. Higher spatial resolutions by secondary ion mass spectrometry (SIMS) or field-emission EMPA are required to rule out this potential of an overestimation.

8.4.2 Gradients in Ba concentrations

This study assumed that the constant decrease of Ba concentration from the core to the interface and from the interface to the outer rim (Fig. 8.8b) is reasoned by (diffusive) exploitation of the feldspar-compatible Ba in the surrounding melt during crystal growth. The straightforward calculations conducted in the given study averaged Ba concentrations on both sides of the diffusion gradient and applied the according diffusion couple models. If the gradients in Ba concentrations are derived from long-range diffusion during crystal growth (Mollo et al., 2011) this approach defines legit distances of the diffusion gradient width. The Ba partition coefficient decreases as a function of increasing orthoclase component in the feldspar (Mahood and Stimac, 1990). Whereas a feldspar composition of Or_{20} partitions Ba from the melt with a feldspar/melt

Table 8.3: Lower limits of diffusion timescale accuracy at 20% after Bradshaw and Kent (2017).

Temperature (°C)	Step size (μm)	$t_{20\%}$ (ka)
720	4.0	559
910	4.0	0.08
720	1.5	178
910	1.5	0.02

coefficient of > 5, a composition of Or_{40} has a coefficient of < 2. An instant change in peralkalinity potentially also explains the rapid increase in Ba concentration at the investigated interfaces and would allow the set-up of a Ba diffusion couple. Till et al. (2015) illustrated that increasing Ba gradients during initial growth of the rim severely impacts Ba diffusion profiles and misleads to overestimation in final time-temperature scenarios. This chapter might similarly overestimate the width of the diffusion gradient due to averaging decreasing trends on either side of the of the relaxation profile. The study by Till et al. (2015) showed that these problems can be treated by high-resolution analytics (spatially and analytically) using SIMS. Their approach investigated trace element diffusion of Ba, Sr and Mg. Sr and Mg in the investigated crystals from V-221a and V-45 are predominantly below the detection of EMPA and the Ba diffusion couples lack comparison to other diffusing trace elements. Analyses using SIMS are required to further investigation of Ba diffusion couples in feldspars from V-221a and V-45.

8.4.3 Uphill diffusion and effective binary diffusion

The Ba concentration pattern illustrated in Fig. 8.8b is similar to patterns that formed by uphill diffusion. Uphill diffusion describes diffusion against the concentration gradient and predominantly occurs in binary systems that formed under spinodal decomposition (Zhang, 2010; Kohn and Penniston-Dorland, 2017). This counterintuitive process is also a consequence of cross-linkages among other diffusive species. For example, isothermal models of diffusive interaction in plagioclase across a step function in anorthite content (Costa et al., 2003) would predict uphill diffusion of Mg. The variation in anorthite content influences the activity component of Mg in plagioclase (Costa et al., 2003; Kohn and Penniston-Dorland, 2017). Uphill diffusion of Mg^{2+} is caused by a simple exchange with Ca^{2+}.

In anorthoclase the cross-linkage could be given to the major elements and in particular to Ca that prefers identical valences to Ba. However, such a scenario would require a normal correlation of Ba and Ca in the anorthoclase zoning (Costa et al., 2003). The crystals discussed in this study show an anticorrelation of these elements. Up to date uphill diffusion of Ba in anorthoclase remains not described in detail and comparisons to other studies lack similarity in concentration patterns shown here.

The major elements (Na, K, and Ca) show patterns that resemble diffusive behaviour across the C-type interface. However, the involvement of mobile Ca^{2+} cations would require a simultaneous transport of Al^{3+} and Si^{4+}, which is known to be comparably slow (Parsons et al., 2015). As the width of the diffusive gradient of Ca covers less than 50 μm (Fig. 8.8a) it seems unrealistic that diffusion of major elements is involved in feldspars from V-221a and V-45. The anticorrelated compositional gradients are thus more likely to be derived from compositional variations during crystal growth alone.

The major element gradients in the C-type feldspars from V-221a and V-45 could also be treated as effective binary diffusion (EBD) between two different phases (Zhang, 2010). Such an approach would require detailed knowledge of Ba diffusivity in anorthoclase and in Na-sanidine, which remains unreported up to date. Therefore this study treated Ba diffusivity as trace element diffusion by using diffusivities of Ba from either oligoclase or sanidine. Diffusion couples from V-45F12 would allow a recalculation with an EBD approach. However, it is assumed that the result would be an intermediate time-temperature scenario between the two approaches shown in

Fig. 8.9c. As the computation of an EBD mechanism is not expected to offer new insights to the question whether the xenocrystic feldspars from V-45 were potentially incompletely degassed, it has not been conducted.

8.5 Conclusions

In order to test a potential incomplete $^{40}Ar^*$-degassing of feldspar xenocrysts, time-temperature scenarios were established on modelling trace element diffusion in selected feldspars. The relaxation of contrasting Ba concentrations shown in EMPA line scans has been modelled via diffusion couples. Extracting time-temperature scenarios from these EMPA line scans resulted in overlapping results for each of the two analysed crystals in both samples. Furthermore, Ar degassing of anorthoclase was modelled and offers a direct comparison to the time-temperature scenarios deduced for the selected crystals. $^{40}Ar^*$-inheritance is not evidenced by any of the time-temperature scenarios established in this chapter. The deviation of the $^{40}Ar/^{39}Ar$ age of V-45 to data from a climatostratigraphic age model (deviation of 17 ka) is best explained by the irregular incorporation of excess ^{40}Ar. Spatial and analytical resolutions represent major hurdles that might have led to overestimation of the presented time-temperature scenarios. The limit of minimum spatial resolution is partly exceeded and an overestimation of the suggested magmatic residence times can not be excluded. Ba diffusion couples presented in this chapter preliminary rule out the involvement of any inherited ^{40}Ar in feldspars dated in Engelhardt et al. (2017), but would require confirmation by analytics of higher spatial resolution.

9 Overall Discussion

This chapter provides a brief discussion about the merits and the problems of $^{40}Ar/^{39}Ar$ dating on the Pleistocene volcaniclastics. Additionally, this chapter names potential improvements and outlooks on Quaternary $^{40}Ar/^{39}Ar$ dating of the AR composite core.

9.1 ^{36}Ar in Quaternary $^{40}Ar/^{39}Ar$ dating

The mass 36 is important for the application of the $^{40}Ar/^{39}Ar$ technique because it corrects the total measured ^{40}Ar for the trapped atmospheric ^{40}Ar. Trapped air correction is thus particularly important for samples of a small sample size, of a very low K-content, or of a young geologic age (e.g. < 1 Ma). This study had to deal with hurdles from the latter two issues and the precision in the detection of ^{36}Ar influenced the precision of the isotope ratios in inverse isochron diagrams and the precision of apparent ages. The measurement of ^{36}Ar is therefore crucial for detecitng Ar isotope data that are typical for irregularly distributed extraneous ^{40}Ar components or for the presence of xenocrystals. Measured intensities from repeated cycles of peak-jumping ion-beam detection may further be influenced by collector noise, ion beam fluctuations (Mark et al., 2009), and interferences with isobaric hydrochlorine and hydrocarbon species (McDougall and Harrison, 1999).

Dating feldspars from V-45 and V-65 (Chapter 4) resulted in a comparably small MSWD values in the inverse isochron calculation. These samples offered radiogenic ^{40}Ar proportions of mainly $< 3\%$ from the total measured ^{40}Ar. Most other feldspar samples provided radiogenic ^{40}Ar proportions $> 5\%$ (Appendix C). This set of samples also shows higher MSWD values in inverse isochron calculations, which suggest that the according regression calculations have no overestimated uncertainties. Their inverse isochrons thus display more condfidently a linear trend between a radiogenic and an atmospheric end-members in the Ar budget of a sample. Overestimated uncertainties in data from V-45 and V-65 indicate that the given testing (via f-testing and t-testing, see Chapter 3) does not suffice proofing a linear relationship between the end-members as the error of the individual analyses is too big.

Whereas intensities for all masses have dominantly $< 2\%$ standard deviations, intensities of ^{36}Ar have standard deviations that range from 5% to 11%. Figure 3.8 shows that the $^{36}Ar_{blank}$ intensity, the mass discrimination factor and the $(^{40}Ar/^{39}Ar)_K$ correction factor dominantly contribute to the error of apparent ages. As blank ^{36}Ar measurements also contribute to calculating the uncertainty of the $(^{40}Ar/^{39}Ar)_K$ correction factors, all of these factors would benefit from a precise detection of ^{36}Ar. The proportion of radiogenic ^{40}Ar is particularly small for geologically young samples. Uncertainty contributions from isotope raw intensities become marginal and hardly contribute to the error variances of the final radiometric age at all (Scaillet, 2000). A precise measurement of mass 36 is thus the key to keep theses contributions from $^{36}Ar_{blank}$ intensity, the mass discrimination factor and the $(^{40}Ar/^{39}Ar)_K$ correction factor as small as possible. The improvement of ^{36}Ar detection can be achieved by simultaneous multi-collection of several masses, an increased mass resolving power, and detector calibrations by using reference

gases (Mark et al., 2009; Saxton, 2015; Jicha et al., 2016).

An instrumental hurdle is the stability of the mass 36 background. The measurements in the given thesis assume that the isobaric $H^{35}Cl$ and $^{12}C_3$ signals are constant and measuring the mass 36 on a peak shoulder suffices to correct for any isobaric overlaps, as long as the blank is measured in the identical peak position. If $H^{35}Cl$ and $^{12}C_3$ signals were released from the sample (e.g. by problematic sample preparation as discussed in Chapter 5), the trapped air correction will be overestimated and resulting ages are expected to be erroneously young. This is not the case in analysing volcanic glass in chapter 5 and the assumption of constant isobaric interferences seems legit. However, Saxton (2015) claims that $^{12}C_3$ is unstable during step-heating experiments and removing the isobaric overlap is beneficial to the $^{40}Ar/^{39}Ar$ method. The future in $^{40}Ar/^{39}Ar$ dating of Quaternary samples will therefore involve simultaneous multi-collection of several masses and detailed corrections for isobaric overlaps as presented in Saxton (2015). Such an application would also have supported $^{40}Ar/^{39}Ar$ geochronology of PALEOVAN samples, but is, however, inapplicable to instrumental methods that have been applied in the given study.

9.2 Single ion-beam detection: an antiquated methodology?

The question arises whether total fusion analyses on feldspars from V-45 would have been revealed as problematic, if an improved ^{36}Ar detection would have been applied. A re-investigation of this sample appears legit, but is problematic as sample material is rare. Two studies are briefly reviewed in the following in order to present material from the German Eifel, which provided datasets that are similar to the Ar-isotope data from V-45.

Similar to the approach in this thesis, Bogaard (1995) analysed feldspars of diversified magmatic textures from the Laacher See Tephra by single beam ion detection and single grain laser fusion. The high K-content of these feldspars, however, supported the identification of outliers having a xenocrystic heritage or an irregular excess ^{40}Ar contribution. A frequently cited age from this work is the age of the Lower Lacher See Tephra (LLST), which is 12.9 ± 0.56 ka (Bogaard, 1995). The according inverse isochron evidences the presence of either xenocrysts or irregularly distributed excess ^{40}Ar, which is underlined by an elevated MSWD of 2.4. In fact, this MSWD labels the inverse isochron as an errochron following Wendt and Carl (1991). However, no reported geological inconsistencies are reported and the age for the LLST is still reasonably cited when mentioning the earliest eruption age of the Lacher See Tephra (e.g. Schmitt, 2006; Schmitt et al., 2010).

Furthermore, Bogaard et al. (1989) analysed anorthoclase crystals from the Hüttenberg tephra by laser fusions that presumably had potentially been affected by xenocrystic contaminations (most analyses resulted in sphenochrons).

A re-investigation of the LLST and the Hüttenberg tephra with state of the art multi-collector and detector calibration methods would proof whether mixing of irregularly distributed excess ^{40}Ar or a xenocrystic population has been successfully avoided in these two milestone studies of laser heating $^{40}Ar/^{39}Ar$ dating of Quaternary minerals. Such a study would furthermore define a limit for the applicability of single mass-collection methods on young (Pleistocene), K-poor and texturally diversified feldspar.

A simple study that determines the limits of the applicability of single ion-beam mass hopping analyses with respect of the K-content, and fraction of $^{40}Ar^{*}$ would be beneficial for $^{40}Ar/^{39}Ar$ dating strategies.

However, as the majority of the radiometric dates in this thesis supported the climate-straigraphic age model (and vice versa) it has to be summarized that conventional single ion-beam detection has not become an antiquated method. Instead, the limits of the applicability of the $^{40}Ar/^{39}Ar$ routine in the laboratory of the University of Potsdam were found, which are represented by the youngest ages for anorthoclase crystals (ca. $<$ 65 ka) and volcanic glass (ca. $<$ 95 ka).

9.3 Standard age calibration with tephra from PALEOVAN cores

The recalculation of the ACs-2 age in chapter 6 revealed the accurate temporal resolution of the age model for the AR composite record. Chapter 6 tests the synchronicity of chronologic constraints from different relative dating methods. Therefore, the question remains whether there is a benefit in recommending monitor ages from a recalibration with PALEOVAN volcaniclastics. Any recalibration involving tephra from PALEOVAN cores cannot compete in precision with model ages from Kuiper et al. (2008). The variation of the insulation from modelling the earth's precession is in tune with the climate-stratigraphic alignment (Chapter 3, Fig. 2.12). Thus modelling the prescession is a chronologic element in both the astronomical calibration in Kuiper et al. (2008) as well as in the calibration presented in chapter 6. The uncertainties in the astronomical ages of tephra layers have been drescribed briefly in Kuiper et al. (2008) and depend on (i) the astronomical solutions (that considers the tidal dissipation and the dynamical ellipticity); (ii) the interpolation of the age-depth-relationship (that assumes constant sedimentation rate between astronomically tuned calibration points; and (iii) the lag between the orbital forcing and sedimentary expression. Assuming that the errors from (ii) and (iii) are comparable for sections of high temporal resolution the temporal variation of the modelled earth's precession has a constant uncertainty. Thus the precision in astronomical ages is higher for sequences of older ages. The Quaternary PALEOVAN sequences will therefore be less precise in astronomical standard calibration than the Neogene marl and limestone sequences that have served for several astronomical calibrations of monitor minerals (Kuiper, 2003; Kuiper et al., 2005; Kuiper et al., 2008; Rivera et al., 2011; Niespolo et al., 2017; Phillips et al., 2017). A Quaternary astronomical calibration is hence of no benefit in gaining higher precision on monitor mineral ages.

9.4 PALEOVAN cores: a natural $^{40}Ar/^{39}Ar$ laboratory?

With a focus on the potential of inherited ^{40}Ar, the author of this thesis gave presentations, which concluded that the PALEOVAN drill record potentially serves as a natural laboratory for $^{40}Ar/^{39}Ar$ geochronology (Engelhardt et al., 2015). That conclusions involves the confident age vs. depth model of the AR composite core, which bears a potential for future work in $^{40}Ar/^{39}Ar$ geochronology on feldspars and volcanic glasses. The following two paragraphs discuss the potentials for investigations of both phases in greater detail.

9.4.1 Is anorthoclase prone to inherited ^{40}Ar?

Gansecki (1998), Spell et al. (2001), and Renne et al. (2012) propose that a fast scenario of assimilation, dispersion and ejection of antecrystals or xenocystals has the potential to eject magmatic feldspars that are not fully degassed of previously accumulated radiogenic ^{40}Ar. Modelling shows that such a scenario has to be limited to a duration of days (Spell et al., 2001). Renne et al. (2012) offered unambiguous in-situ data that showed cores from C-type sanidine containing an inherited ^{40}Ar component. Their study provided Ba diffusion couples that indicate durations of tens of years for the processes of assimilation, crystal dissolution, feldspar overgrowth and ejection. Parameter that determine the Ar-diffusivity such as the activation energy and the pre-exponential factors were the most retentive setting from Lovera et al. (1997). Whether or not these parameters are adequately depicting Ar release of feldspars is debated (e.g. Harrison and Lovera, 2014; Villa, 2014).

In order to briefly describe this debate it is necessary to mention that the laboratory release of $^{39}Ar_K$ is long known to be non-linear in Arrhenius plots (Mussett, 1969; Foland, 1974; Berger and York, 1981; Harrison and McDougall, 1982; Zeitler, 1987, and literature herein). The upward-concave shaped Ar release patterns in Arrhenius diagrams are explained by a discrete distribution of various diffusion length scales in feldspar (Foland, 1974; Zeitler, 1987; Lovera et al., 1989; Lovera et al., 1993). This explanation is widely accepted in the $^{40}Ar/^{39}Ar$ community (McDougall and Harrison, 1999). Lovera et al. (1997) provided a model that fit the Ar release data in Arrhenius plots with a multi-diffusion domain (MDD) behaviour. However, as the distributions of small diffusion domains are smaller than domains observable from ^{39}Ar recoil redistribution experiments (Villa, 1997) and as microtextures that are expected to operate as diffusion domains are reported to be metastable during laboratory step heating experiments (Parsons et al., 1999; Cassata and Renne, 2013), the MDD faces some severe mistrust in the $^{40}Ar/^{39}Ar$ community.

The relevant microstructures are formed by compositional exsolution and structural Si and Al ordering that occur when feldspar crystals reside at temperatures less than the strain-dependent solvus temperature (Parsons and Lee, 2000). Feldspars from volcanic rocks experience rapid cooling and either have no microstructures or are cryptoperthites, which are difficult to detect with ordinary electron beam imaging methods (Parsons, 2010).

The compositions of Na-sanidine and anorthoclase crystals from tephra in PALEOVAN drill cores suggest that some of these crystals potentially underwent solvus temperatures (e.g. V-45 in chapter 8). Another microstructure frequently seen in feldspars from the PALEOVAN cores is the combination of Pericline and Albite twinning features. This structure represents a shearing transformation from monoclinic to triclinic symmetries and it is characteristic for anorthoclase (Kroll and Bambauer, 1981). Cassata and Renne (2013) investigated ^{39}Ar release from anorthoclase and oligoclase crystals that also show the combined twinning features. They were able to mimic the symmetry transformation during heating experiments by an anomalous Ar degassing rate and extrapolated a linear Arrhenius low-temperature degassing that allowed defining diffusion coefficients (which have been applied in chapter 8). The study by Cassata and Renne (2013) clearly showed that Na-rich feldspars are the most retentive of all feldspar minerals. Thus, the question arises whether Quaternary anorthoclase crystals are particularly prone to be contaminated by xenocrystals that did not fully reset during the processes of assimilation,

crystal dissolution, and ejection.

Modelling the degree of Ar degassing in potential xenocrystals in this study (chapter 8) reached analytical limitations and suggests that the crystals from sample V-45 were fully degassed before they had become ejected. However, a systematic testing of $^{40}Ar/^{39}Ar$ ages from PALEOVAN sanidine and anorthoclase crystals against the climate-stratigraphic age model provides a way to address the question, whether anorthoclase is particularly prone Ar inheritance. During preparation of the sample material in this study, corroded feldspars that likely represent xenocrystals were frequently detected. As either C-type or PO-type zoning features are almost omnipresent in volcaniclastic feldspars from PALEOVAN cores, the calculation of diffusion couples would be possible (either by analysing Mg, Ba or Sr concentrations that are expected to vary across interfaces, if the analytical method is able to resolve the differences in concentrations). Given the required improvements that are stated in chapter 8 (e.g. using secondary ion mass spectrometry for trace element analysis with small step size), diffusion-thermo-speedometry could test whether the retentive diffusion parameters from Cassata and Renne (2013) explain xenocrystic data obtained in SGTF analyses.

Such an investigation would require a higher precision in the detection of ^{36}Ar in order to identify xenocrystals in SG TF analyses. A hurdle in distinguishing excess and inherited ^{40}Ar would be the high abundances of small (e.g. tens of μm) melt-inclusions. The latter hurdle is particularly relevant as Nemrut is known to have isotopic $^{3}He/^{4}$ He signatures that are characteristic for mantle signatures. Mantle-derived Ar signatures from melt- or fluid inclusions could easily be mistaken as too old xenocrysts, if they are not forming a linear excess trend. Compositionally zoned anorthoclase and sanidine that represent polybaric and/or polythermal histories are frequent in many volcanic suites (e.g. Nakano, 1992; Nekvasil et al., 2000). The unique advantage that the tephra material from PLAEOVAN cores offers, is the accurate age control model as well as the stratigraphic description and the sample inventory from this and earlier studies (Schmincke et al., 2014; Stockhecke et al., 2014a; Stockhecke et al., 2014b; Macdonald et al., 2015).

9.4.2 Glass $^{40}Ar/^{39}Ar$ ages and noble gas geochemistry

The great potential of analysing volcanic glass from ICDP PALEOVAN core material is the investigation of the degree and the type of alteration of volcanic glass in comparison with the varying pore water chemistry. Furthermore, the age model provides a precise timing. Given this potential, the question arises whether the degree of alteration and/or hydrolysis is linked to the $^{40}Ar/^{39}Ar$ systematics of the shards. Volcanic glass is known to be challenged with the loss of radiogenic ^{40}Ar due to fast hydration, and devitrification (e.g. Kaneoka, 1972). On the other hand, excess ^{40}Ar is a hurdle in dating glass. Excess ^{40}Ar is typically related to fast quenching processes (Noble and Naughton, 1968; Dalrymple and Lanphere, 1969; Kaneoka, 1972; Walker and Mcdougall, 1982; Foland et al., 1993; Clay et al., 2011) and a very slow diffusive loss of excess ^{40}Ar in glass (Clay et al., 2011). The study by Clay et al. (2011) presents a systematic approach to investigate the mechanisms that cause high excess ^{40}Ar proportions in volcanic glass of phonolitic volcaniclastics. Their work analysed cogenetic feldspar and volcanic glass samples from a volcaniclastic unit of a known age. By detecting a correlation between excess ^{40}Ar and atmospheric ^{36}Ar in glass, Clay et al. (2011) suggested a mechanism of incorporation

of atmospheric and excess Ar prior to eruption. Furthermore, Clay et al. (2011) showed that excess ^{40}Ar is more retentive in feldspars than in glass and that a low partition coefficient K_D of 10^{-3} ($K_D = {}^{40}Ar_{excessfeldspar}/{}^{40}Ar_{excessglass}$) explains the problems with extreme excess ^{40}Ar in volcanic glass.

A similar approach could be combined with a re-assessment of the attempt presented in chapter 5. However, testing correlations between atmospheric ^{36}Ar and excess ^{40}Ar would require the instrumental advantages suggested in paragraph 9.2 (above). Whether or not a correlation between atmospheric ^{36}Ar and excess ^{40}Ar exists (and thus an incorporation of atmospheric and excess Ar prior to eruption) could be then discussed under consideration of the composition, the degree of vesiculation and the degree of alteration of the volcanic glass.

As five samples investigated in this study were throughout surprisingly fresh, pore water mobility and local equilibration seem to dominate the processes that have led to alteration of vitric pyroclasts in the AR record. A systematic comparison of compositional data from volcanic glass with the available pore water chemistry from the AR record could identify mobile and immobile pore water regimes. Having samples identified that reveal a varying degree of alteration, ^{40}Ar/^{39}Ar dating of vitric tephra material from the different regimes allows to quantify the effect of the degree of alteration on ^{40}Ar/^{39}Ar ages and to investigate potential limits for the applicability of the method.

A systematic investigation of atmospheric ^{36}Ar, excess ^{40}Ar and degree of alteration from volcanic glass over a well characterised stratigraphic unit that provides a confident age control model has not been established ever before to the author's knowledge.

9.5 Noble gas geochemistry mafic minerals

In order to explain the potential of noble gas studies on PALEOVAN core material, a brief introduction into regional tectonics is necessary: Lake Van is situated about 50 km north of the Bitlis Suture Zone that represents the southern margin of the East Anatolian Plateau and also marks the convergent boundary between the Arabian Platform to the south and an Eurasian collage of continental fragments, islands arcs and ophiolithic mélanges to the north (Şengör and Yilmaz, 1981). The East Anatolian Plateau exhibits active N-S shortening and has a common elevation of some 2000 meters above sea level. Teleseismic recordings by Zor et al. (2003) revealed an unexpectedly thin crustal thickness underneath the East Anatolian Plateau of about 45 km and implied that crustal thickening is not explaining the uplift of the Eastern Anatolian Plateau. A widely accepted interpretation is that a central part of the Eastern Anatolian Plateau is devoid of the lithospheric mantle (Şengör et al., 2003). The absence of the lithospheric mantle is ascribed to a breakoff of the northward subducted slab (Şengör et al., 2003; Cosentino et al., 2012). Proposed areas of no mantle lithosphere coincide widely with the extent of the East Anatolian Accretionary Complex (EACC, see chapter 2), which is a subduction-accretionary complex of late Cretaceous to Oligocene age (Şengör et al., 2003). The EACC is further characterized by the widespread volcanism. The volcanic activity initiated North of the EACC with calc-alkaline magmatism and migrated to the Southeast of the EACC by developing a more alkaline type magmatism and represents the most recent volcanic activity in East Anatolia.

Lake Van is located among the most recent volcanic edifices and archived intermediate to highly silicic volcaniclastics from Nemrut and Süphan volcanoes (Sumita and Schmincke, 2013b; Engelhardt et al., 2017). Least evolved volcaniclastics buried in the deepest basin of Lake Van represent reworked tephra and air fall deposits of mugearitic compositions (Fig. 7.5). Olivines ($Fo_{25}Fa_{75}$) have been identified in these particular units (up to max. 3 vol%) and contain apatite-, melt- and fluid- inclusions. Clinopyroxenes of (ferro-) augitic compositions contain inclusions of apatite, melts and fluids as well. Analysing $^3He/^4He$ isotope ratios of olivine and clinopyroxenes from the particular samples of Lake Van drill cores offer a unique opportunity to validate the absence of a subducted component (Van Soest et al., 1998; Dunai and Porcelli, 2002) in the most recent volcanic rocks of the Eastern Anatolian Plateau. As crustal assimilation processes affect the integrity of $^3He/^4He$ analyses on coexisting mafic phases (Hilton et al., 2002), testing homogeneity of the sampling media is desired. The coexistence of melt- and fluid- bearing clinopyroxene and olivines can provide such testing. Lake water from Lake Van and from the crater lake of Nemrut volcano were investigated by measurements of He, Ne and Tritium (Kipfer, 1994). Water from the Nemrut crater lake contains a mantle helium component similar to signatures typical for MORB ($^3He/^4He \approx 10^{-5}$). Furthermore, mantle helium also accounts for an excess of helium in water samples from Lake Van (Kipfer, 1994). Pore waters from core catcher materials of the PALEOVAN drilling campaign in 2010 have been analysed for their noble gas content in a resolution of about 6 meters (Tomonaga et al., 2014).

Analysing $^3He/^4He$ from mafic minerals or vitrophyric lapillis in drilled volcaniclastics will potentially monitor the evolution of the magmatic noble gas signatures during the lacustrine history of Lake Van and provide comparisons to published analyses from pore waters. An according data set would potentially contribute to the discussion about the absence or presence of a lithospheric mantle underneath the EACC.

10 Conclusions

Rhyolitic and trachytic tephra layers from the AR record of the PALEOVAN campaign were dated by the $^{40}Ar/^{39}Ar$ method. Resulting ages were tested statistically for their concordance with a climate-stratigraphic age model. The dated phases had also been analysed for their chemical composition in order to evaluate their suitability as target materials for the $^{40}Ar/^{39}Ar$ method.

Feldspar $^{40}Ar/^{39}Ar$ ages from two samples deviated statistically from the age model. All other feldspar samples resulted in identical ages. The deviations displayed older ages than those obtained from the age model. t-Tests compared radiometric ages with available age control points from various proxies and from the relative paleointensity of the earth magnetic field within a stratigraphic range of $\pm$ 10 m. Concordant age control from different relative chronometers indicated that deviations are a result of erroneous $^{40}Ar/^{39}Ar$ ages. This thesis identified two potential reasons for these ages: (1) the irregular appearance of excess ^{40}Ar from rare melt- and fluid- inclusions and (2) the contamination of the samples with older xenocrystals due to a rapid combination of assimilation and ejection. The latter process cannot be excluded, but seems unlikely due to normally distributed apparent ages and ubiquitous melt and fluid inclusions.

This thesis observed the predominance of different types of magmatic zoning in the feldspar samples. The zoning types are compositional zoning (C-type zoning), pseudo-oscillatory zoning of trace element concentrations (PO-type zoning), chaotic and patchy zoning of major and trace element concentrations (R-type zoning) and concentric zoning of trace elements (CC-type zoning). Samples that deviated in $^{40}Ar/^{39}Ar$ ages showed C-type zoning and R-type zoning (V-45) or a mix of C-type and PO-type zoning (V-65). Feldspars showing PO-type zoning typically represent smaller grain size fractions in samples that show various zoning types. The constant major element compositions of these crystals are typical for the late stages in the compositional evolution of magmatic feldspars in peralkaline melt. PO-type crystals contain less melt-inclusions than other zoning types and are rarely corroded. This thesis concludes that feldspars that show PO-type zoning are most promising chronometers for the $^{40}Ar/^{39}Ar$ method. Particularly, if samples provide mixed zoning types of Quarternary anorthoclase feldspars.

Another five samples were dated by applying the $^{40}Ar/^{39}Ar$ method to volcanic glass. Extreme contents of atmospheric Ar (typically $> 98\%$) significantly hampered the precision of the $^{40}Ar/^{39}Ar$ ages and result in rough age estimates that widely overlap ages from the age model. Ar isotopes indicate that the glasses bore a non-radiogenic, non-atmospheric and chorine-rich Ar-source. This indication strengthens assumption that irregularly distributed melt-inclusions and thus irregular distributed excess ^{40}Ar influenced the problematic feldspar $^{40}Ar/^{39}Ar$ ages.

This thesis offers a new age model, which is similarly based on the interpolation of the temporal tie points from geophysical and climate-stratigraphic data. Whereas an older, existing age model used a spline-interpolation, a PCHIP-interpolation was calculated in this study and allows the presentation of ages for all volcaniclastic layers in the AR composite record. The modelled ages allowed a recalculation of the Alder Creek sanidine mineral standard by swapping the role of unknowns and standards. This climate-stratigraphic calibration of an $^{40}Ar/^{39}Ar$ mineral standard proved that the age versus depth interpolations from PAELOVAN drilling

cores were accurate, and that every chronometer involved recorded the temporal evolution of Lake Van synchronously.

Petrochemical discrimination of the sampled volcaniclastic material is furthermore given in this thesis. 41 from 57 sampled volcaniclastic layers have Nemrut as their provenance. The sampled volcaniclastics usually have a thickness of < 40 cm and thus have been ejected by small to medium sized eruptions. Onshore deposits from these types of eruptions are difficult to identify or potentially eroded due to predominant strong winds on Nemrut and Süphan slopes. An exact correlation with the data presented here is therefore equivocal or not possible at all.

In order to test, whether inherited ^{40}Ar affected the deviating ages from V-45, diffusion couples of Ba were investigated in compositionally zoned feldspar crystals. The diffusive behaviour of Ba in feldspar is known. Gradients in Ba concentration across zoning interfaces allowed for the calculation of the duration of the crystal's magmatic development since the formation of the interface. Degassing scenarios, which model the Ar-loss during assimilation and subsequent ejection of the xenocrystals were compared with timing from the Ba diffusion couples. The Ar loss models do not show any indication of an involvement of inherited ^{40}Ar in the deviating sample V-45. Therefore, the irregular incorporation of excess ^{40}Ar by melt- and fluid inclusions potentially represents the critical problem that needs to be overcome in dating youngest volcaniclastic feldspars from the PALEOVAN drill cores. However, the spatial resolution for analysing the diffusion gradients represents the lower limit. It cannot be discounted that the low resolution causes an overestimation of the maximum duration of the magmatic history.

The AR record from the ICDP PALEOVAN campaign is a key archive for reconstructing climate evolution in the eastern Mediterranean and in the Near East. It provides a climate-stratigraphic age model with a remarkable accuracy and resolution. This thesis provides the complete theoretical and analytical background that is required in generating, presenting and discussing ^{40}Ar/^{39}Ar ages for the AR composite record.

References

Abdulnaby, W., H. Mahdi, N. M. S. Numan, and H. Al-Shukri (2014). Seismotectonics of the Bitlis-Zagros Fold and Thrust Belt in Northern Iraq and Surrounding Regions from Moment Tensor Analysis. *Pure and Applied Geophysics* 171.7, pp. 1237–1250.

Akçar, N. and C. Schlüchter (2005). Paleoglaciations in Anatolia: – A Schematic Review and First Results –. *Eiszeitalter und Gegenwart* 55, pp. 102–121.

Akin, U., E. U. Ulugergerli, and S. Kutlu (2014). The Assessment of Geothermal Potential of Turkey by Means of Heat Estimation. *Bulletin of the Mineral Research and Exploration* 149, pp. 201–210.

Andersen, K. K., N. Azuma, J. M. Barnola, M. Bigler, P. Biscaye, N. Caillon, J. Chappellaz, H. B. Clausen, D. DahlJensen, H. Fischer, J. Fluckiger, D. Fritzsche, Y. Fujii, K. Goto-Azuma, K. Gronvold, N. S. Gundestrup, M. Hansson, C. Huber, C. S. Hvidberg, S. J. Johnsen, U. Jonsell, J. Jouzel, S. Kipfstuhl, A. Landais, M. Leuenberger, R. Lorrain, V. Masson-Delmotte, H. Miller, H. Motoyama, H. Narita, T. Popp, S. O. Rasmussen, D. Raynaud, R. Rothlisberger, U. Ruth, D. Samyn, J. Schwander, H. Shoji, M. L. Siggard-Andersen, J. P. Steffensen, T. Stocker, A. E. Sveinbjornsdottir, A. Svensson, M. Takata, J. L. Tison, T. Thorsteinsson, O. Watanabe, F. Wilhelms, J. W. C. White, and N. G. I. C. Project (2004). High-resolution record of Northern Hemisphere climate extending into the last interglacial period. *Nature* 431.7005, pp. 147–151.

Armstrong, J. T., P. McSwiggen, and C. Nielsen (2013). A thermal field-emission electron probe microanalyzer for improved analytical spatial resolution. *Microscopy and Analysis* 27, pp. 18–22.

Arnaud, N. O. and S. P. Kelley (1997). Argon behaviour in gem-quality orthoclase from Madagascar: Experiments and some consequences for 40Ar39Ar geochronology. *Geochimica et Cosmochimica Acta* 61.15, pp. 3227–3255.

Arth, J. G. (1976). *Behavior of Trace Elements During Magmatic Processes—A Summary of Theoretical Models and their Applications.*

Audi, G., O. Bersillon, J. Blachot, and A. H. Wapstra (1997). The NUBASE evaluation of nuclear and decay properties. *Nuclear Physics A* 624.1, pp. 1–124.

Aydar, E., A. Gourgaud, I. Ulusoy, F. Digonnet, P. Labazuy, E. Sen, H. Bayhan, T. Kurttas, and A. U. Tolluoglu (2003). Morphological analysis of active Mount Nemrut stratovolcano, eastern Turkey: Evidences and possible impact areas of future eruption. *Journal of Volcanology and Geothermal Research* 123.3-4, pp. 301–312.

Ballentine, C. J., R. Burgess, and B. Marty (2002). Tracing fluid origin, transport and interaction in the crust. In: *Reviews in mineralogy and geochemistry.* Ed. by D. Porcelli, C. J. Ballentine, and R. Wieler. Vol. 47. Mineralogical Society of America, pp. 539–614.

Bambauer, H. U. (1988). Feldspäte - ein Abriß. *Neues Jahrbuch Mineralogische Abhandlungen* 158.2, p. 21.

Barker, S., G. Knorr, R. L. Edwards, F. Parrenin, A. E. Putnam, L. C. Skinner, E. Wolff, and M. Ziegler (2011). 800000 Years of Abrupt Climate Variability. *Science* 334.6054, pp. 347–351.

Bar-Matthews, M., A. Ayalon, M. Gilmour, A. Matthews, and C. J. Hawkesworth (2003). Sea - land oxygen isotopic relationships from planktonic foraminifera and speleothems in the Eastern Mediterranean region and their implication for paleorainfall during interglacial intervals. *Geochimica et Cosmochimica Acta* 67.17, pp. 3181–3199.

Beckhoff, B., B. Kanngießer, N. Langhoff, R. Wedell, and H. Wolff (2005). Handbook of Practical X-Ray Fluorescence Analysis. Berlin: Springer-.

Beckinsale, R. D. and N. H. Gale (1969). A Reappraisal of Decay Constants and Branching Ratio of 40k. *Earth and Planetary Science Letters* 6.4, p. 289.

Berger, G. W. and D. York (1981). Geothermometry from 40Ar/39Ar dating experiments. *Geochimica et Cosmochimica Acta* 45.6, pp. 795–811.

Bevins, R. E., P. B. Kokelaar, and P. N. Dunkley (1984). Transition, Petrology and geochemistry of lower to middle Ordovician igneous rocks in Wales: a volcanic arc to marginal basin. *Proceedings of the Geological Association* 95, pp. 337–347.

Blockley, S. P. E., C. S. Lane, M. Hardiman, S. O. Rasmussen, I. K. Seierstad, J. P. Steffensen, A. Svensson, A. F. Lotter, C. S. M. Turney, and C. B. Ramsey (2012). Synchronisation of palaeoenvironmental records over the last 60,000 years, and an extended INTIMATE event stratigraphy to 48,000 b2k. *Quaternary Science Reviews* 36, pp. 2–10.

Blundy, J. D. and B. J. Wood (1991). Crystal-chemical controls on the partitioning of Sr and Ba between plagioclase feldspar, silicate melts, and hydrothermal solutions. *Geochimica et Cosmochimica Acta* 55.1, pp. 193–209.

Bogaard, P. v. d. (1995). 40Ar/39Ar ages of sanidine phenocrysts from Laacher See Tephra (12,900 yr BP): Chronostratigraphic and petrological significance. *Earthand Planetary Science Letters* 133, pp. 163–174.

Bogaard, P. v. d., C. M. Hall, H. U. Schmincke, and D. York (1989). Precise Single-Grain Ar-40/Ar-39 Dating of a Cold to Warm Climate Transition in Central-Europe. *Nature* 342.6249, pp. 523–525.

Bradshaw, R. W. and A. J. Kent (2017). The analytical limits of modeling short diffusion timescales. *Chemical Geology* 466, pp. 667–677.

Bragg, W. L. (1913). The structure of some crystals as indicated by their diffraction of x-rays. *Proceedings of the Royal Society of London* 89.610, pp. 248–277.

Brentano, J. (1924). Focussing method of crystal powder analysis by x-rays. *Proceedings of the Physical Society of London* 37.1, pp. 184–193.

Brereton, N. R. (1970). Corrections for Interfering Isotopes in 40ar/39ar Dating Method. *Earth and Planetary Science Letters* 8.6, pp. 427–&.

Brown, W. L. (1993). Fractional crystallization and zoning in igneous feldspars: ideal water-buffered liquid fractionation lines and feldspar zoning paths. *Contributions to Mineralogy and Petrology* 113.1, pp. 115–125.

Brown, W. L. and I. Parsons (1994). Feldspars in igneous rocks. In: *Feldspars and their reactions*. Ed. by I. Parsons. Proceeding. Springer Science and Business Media Dordrecht, pp. 449–499.

Buket, E. and A. Temel (1998). Major-element, trace-element, and Sr-Nd isotopic geochemistry and genesis of Varto (Mus) volcanic rocks, Eastern Turkey. *Journal of Volcanology and Geothermal Research* 85.1-4, pp. 405–422.

Bunge, H. J. (1981). Fabric Analysis by Orientation Distribution-Functions. *Tectonophysics* 78.1-4, pp. 1–21.

Burch, P. R. J. (1953). Specific Gamma-Activity, the Branching Ratio and Half-Life of Potassium-40. *Nature* 172.4373, pp. 361–362.

Burton, E. F., J. Hillier, and A. Prebus (1939). A report on the development of the electron supermicroscope at Toronto. *Physical Review* 56.11, pp. 1171–1172.

Çağatay, M. N., N. Öğretmen, E. Damcı, M. Stockhecke, U. Sancar, K. K. Eriş, and S. Özeren (2014). Lake level and climate records of the last 90 ka from the Northern Basin of Lake Van, eastern Turkey. *Quaternary Science Reviews* 104, pp. 97–116.

Campbell, I. H., P. L. Roeder, and J. M. Dixon (1978). Plagioclase Buoyancy in Basaltic Liquids as Determined with a Centrifuge Furnace. *Contributions to Mineralogy and Petrology* 67.4, pp. 369–377.

Capron, E., A. Landais, J. Chappellaz, A. Schilt, D. Buiron, D. Dahl-Jensen, S. J. Johnsen, J. Jouzel, B. Lemieux-Dudon, and L. Loulergue (2010). Millennial and sub-millennial scale climatic variations recorded in polar ice cores over the last glacial period. *Climate of the Past* 6.3, pp. 345–365.

Cassata, W. S. and P. R. Renne (2013). Kinetics of argon diffusion in calcite. *Chemie Der Erde-Geochemistry* 73.1, pp. 113–115.

Cassata, W. S., P. R. Renne, and D. L. Shuster (2008). Ar-39 and Ar-37 diffusion in plagioclase. *Geochimica Et Cosmochimica Acta* 72.12, A142–A142.

Channell, J. E. T. (2017). Cobb Mountain Subchron recorded at IODP Site U1306 (Eirik Drift, off SE Greenland). *Geophysical Journal International* 209.3, pp. 1389–1397.

Channell, J. E. T., A. Mazaud, P. Sullivan, S. Turner, and M. E. Raymo (2002). Geomagnetic excursions and paleointensities in the Matuyama Chron at Ocean Drilling Program Sites 983 and 984 (Iceland Basin). *Journal of Geophysical Research-Solid Earth* 107.B6.

Channell, J. E. T., C. Xuan, and D. A. Hodell (2009). Stacking paleointensity and oxygen isotope data for the last 1.5 Myr (PISO-1500). *Earth and Planetary Science Letters* 283.1-4, pp. 14–23.

Chen, Y. S., P. E. Smith, N. M. Evensen, D. York, and K. R. Lajoie (1996). The edge of time: Dating young volcanic ash layers with the Ar-40-Ar-39 laser probe. *Science* 274.5290, pp. 1176–1178.

Cheng, H., R. L. Edwards, W. S. Broecker, G. H. Denton, X. Kong, Y. Wang, R. Zhang, and X. Wang (2009). Ice age terminations. *science* 326.5950, pp. 248–252.

Cherniak, D. J. (2002). Ba diffusion in feldspar. *Geochimica et Cosmochimica Acta* 66.9, pp. 1641–1650.

Chesterman, C. W. (1956). Pumice, Pumicite, and Volcanic Cinders in California. San Francisco: California Department of Natural Resources, Division of Mines, p. 97.

Clay, P. L., S. P. Kelley, S. C. Sherlock, and T. L. Barry (2011). Partitioning of excess argon between alkali feldspars and glass in a young volcanic system. *Chemical Geology* 289.1-2, pp. 12–30.

Coble, M. A., M. Grove, and A. T. Calvert (2011). Calibration of Nu-Instruments Noblesse multicollector mass spectrometers for argon isotopic measurements using a newly developed reference gas. *Chemical Geology* 290.1-2, pp. 75–87.

Cosentino, D., T. F. Schildgen, P. Cipollari, C. Faranda, E. Gliozzi, N. Hudáčková, S. Lucifora, and M. R. Strecker (2012). Late Miocene surface uplift of the southern margin of the Central Anatolian Plateau, Central Taurides, Turkey. *Geological Society of America Bulletin* 124.1-2, pp. 133–145.

Costa, F., S. Chakraborty, and R. Dohmen (2003). Diffusion coupling between trace and major elements and a model for calculation of magma residence times using plagioclase. *Geochimica et Cosmochimica Acta* 67.12, pp. 2189–2200.

Costa, F. and D. Morgan (2010). Time Constraints from Chemical Equilibration in Magmatic Crystals. In: *Timescales of Magmatic Processes: From Core to Atmosphere*. Ed. by A. Dosseto, S. P. Turner, and J. A. Van Orman, pp. 125–159.

Crank, J. (1975). The mathematics of diffusion. Oxford: Clarendon Press, p. 414.

Crasty, R. L. and J. G. Mitchell (1966). Single sample potassium-argon ages using the omegatron. *Earth and Planetary Science Letters* 1.3, pp. 121–122.

Çubukçu, H. (2008). "Petrologic evolution of Nemrut Stratovolcano (Turkiye): Peralkaline magmatism in a collisional domain." PhD Thesis. Université Clermont- Ferrand II & Hacettepe Üniversitesi, p. 223.

Çubukçu, H., E. Aydar, and A. Gourgaud (2007). Volcano stratigraphy and petrogenesis of the Nemrut stratovolcano (East Anatolian high Plateau): The most recent post-collisional volcanism in Turkey. *Chemical Geology* 245.1-2, pp. 120–129.

Çubukçu, H., I. Ulusoy, E. Aydar, O. Ersoy, E. Sen, A. Gourgaud, and H. Guillou (2012). Mt. Nemrut volcano (Eastern Turkey): Temporal petrological evolution. *Journal of Volcanology and Geothermal Research* 209, pp. 33–60.

Cukur, D., S. Krastel, F. Demirel-Schlüter, E. Demirbağ, C. Imren, F. Niessen, and M. Toker (2013). Sedimentary evolution of Lake Van (Eastern Turkey) reconstructed from high-resolution seismic investigations. *International Journal of Earth Sciences* 102.2, pp. 571–585.

Cukur, D., S. Krastel, H.-U. Schmincke, M. Sumita, M. N. Çağatay, A. F. Meydan, E. Damcı, and M. Stockhecke (2014a). Seismic stratigraphy of Lake Van, eastern Turkey. *Quaternary Science Reviews* 104, pp. 63–84.

Cukur, D., S. Krastel, H.-U. Schmincke, M. Sumita, Y. Tomonaga, and M. N. Çağatay (2014b). Water level changes in Lake Van, Turkey, during the past ca. 600 ka: climatic, volcanic and tectonic controls. *Journal of Paleolimnology* 52.3, pp. 201–214.

Cukur, D., S. Krastel, Y. Tomonaga, H. U. Schmincke, M. Sumita, A. F. Meydan, M. N. Çağatay, M. Toker, S. P. Kim, G. S. Kong, and S. Horozal (2017). Structural characteristics of the Lake Van Basin, eastern Turkey, from high-resolution seismic reflection profiles and multibeam echosounder data: geologic and tectonic implications. *International Journal of Earth Sciences* 106.1, pp. 239–253.

Dalrymple, G. B., E. C. Alexander, M. A. Lanphere, and G. P. Kraker (1981). *Irradiation of samples fo 40Ar/39Ar dating using the Geological Survey TRIGA reactor*. Ed. by U. S. G. Survey. US Goverment Printing Office NV - 1176.

Dalrymple, G. B. and M. A. Lanphere (1969). Potassium-argon dating: principles, techniques and applications to geochronology. San Francisco, California: Freeman, p. 258.

Day, A. (1993). "Developments in the EBSP Technique and their Application to Grain Imaging". PhD thesis. Bristol, p. 156.

Dazé, A., J. K. W. Lee, and M. Villeneuve (2003). An intercalibration study of the Fish Canyon sanidine and biotite 40Ar/39Ar standards and some comments on the age of the Fish Canyon Tuff. *Chemical Geology* 199.1-2, pp. 111–127.

De Boor, C. (1978). A practical guide to splines. Vol. 27. New York: Springer-Verlag, p. 348.

Debye, P. and P. Scherrer (1916). Interferenzen an regellos orientierten Teilchen im Röntgenlicht. I. *Nachrichten von der Gesellschaft der Wissenschaften zu Göttingen, Mathematisch-Physikalische Klasse* 1916, pp. 1–15.

Deer, W. A., R. A. Howie, and J. Zussman (2013). *An Introduction to the Rock-Forming Minerals*.

Degens, E. T., H. K. Wong, S. Kempe, and F. Kurtman (1984). A geological study of lake van, Eastern Turkey. *Geologische Rundschau* 73.2, pp. 701–734.

Deino, A. and R. Potts (1992). Age-probability spectra for examination of single-crystal 40Ar39Ar dating results: Examples from Olorgesailie, southern Kenya Rift. *Quaternary International* 13, pp. 47–53.

Deplazes, G., A. Lückge, L. C. Peterson, A. Timmermann, Y. Hamann, K. A. Hughen, U. Röhl, C. Laj, M. A. Cane, D. M. Sigman, and G. H. Haug (2013). Links between tropical rainfall and North Atlantic climate during the last glacial period. *Nature Geoscience* 6.3, pp. 213–217.

Dhont, D. and J. Chorowicz (2006). Review of the neotectonics of the Eastern Turkish-Armenian Plateau by geomorphic analysis of digital elevation model imagery. *International Journal of Earth Sciences* 95.1, pp. 34–49.

Dickin, A. (2008). Radiogenic isotope geology. Repr., 2. Cambridge: Cambridge University Press, p. 490.

Drouin, D., A. R. Couture, D. Joly, X. Tastet, V. Aimez, and R. Gauvin (2007). CASINO V2.42—A Fast and Easy-to-use Modeling Tool for Scanning Electron Microscopy and Microanalysis Users. *Scanning* 29, pp. 92–101.

Dunai, T. J. and D. Porcelli (2002). Storage and transport of noble gases in the subcontinental lithosphere. In: *Reviews in mineralogy and geochemistry*. Ed. by D. Porcelli, C. J. Ballentine, and R. Wieler. Vol. 47. Mineralogical Society of America, pp. 371–409.

Eksperiandova, L. P., O. I. Fedorov, and N. A. Stepanenko (2011). Estimation of metrological characteristics of the element analyzer EuroVector EA-3000 and its potential in the single-reactor CHNS mode. *Microchemical journal* 99.2, pp. 235–238.

Ellis, B. S., D. F. Mark, J. Troch, O. Bachmann, M. Guillong, A. J. R. Kent, and A. von Quadt (2017). Split-grain Ar-40/Ar-39 dating: Integrating temporal and geochemical data from crystal cargoes. *Chemical Geology* 457, pp. 15–23.

Endt, P. M. and C. Van der Leun (1973). Energy levels of 21 to 44 nuclei. *Nuclear Physics A* 214, pp. 1–625.

Engelhardt, J. F., M. Sudo, M. Stockhecke, and R. Oberhänsli (2017). Feldspar 40Ar/39Ar dating of ICDP PALEOVAN cores. *Geochimica et Cosmochimica Acta* 217, pp. 144–170.

Engelhardt, J., M. Sudo, and R. Oberhänsli (2015). "A natural laboratory for 40Ar/39Ar geochronology: ICDP cores from Lake Van, Turkey". In: *EGU General Assembly Conference Abstracts*. Vol. 17.

Ercan, T., T. Fujitami, J.-l. Madsuda, K. Notsu, and T. Ui (1990). Doğu ve Güneydoğu Anadolu Neojen-Kuvaterner volkanitlerine ilişkin yeni jeokjmyasal, radyometrik ve izotopik verilerin yorumu. *Maden Tetkik ve Arama Dergisi* 110.110, pp. 143–164.

Erdik, M., Y. Kamer, M. Demircioğlu, and K. Şeşetyan (2012). 23 October 2011 Van (Turkey) earthquake. *Natural Hazards* 64.1, pp. 651–665.

Esser, R. P., W. C. McIntosh, M. T. Heizler, and P. R. Kyle (1997). Excess argon in melt inclusions in zero-age anorthoclase feldspar from Mt. Erebus, Antarctica, as revealed by the Ar-40/Ar-39 method. *Geochimica Et Cosmochimica Acta* 61.18, pp. 3789–3801.

Everhart, T. E. and R. F. M. Thornley (1960). Wide-Band Detector for Micro-Microampere Low-Energy Electron Currents. *Journal of Scientific Instruments* 37.7, pp. 246–248.

Ewald, P. (1913). Zur Theorie der Interferenzen in Kristallen. *Physikalische Zeitschrift* 14, pp. 465–472.

Finch, A. A. and J. Klein (1999). The causes and petrological significance of cathodoluminescence emissions from alkali feldspars. *Contributions to Mineralogy and Petrology* 135.2-3, pp. 234–243.

Fleck, R. J., J. F. Sutter, and D. H. Elliot (1977). Interpretation of discordant 40Ar/39Ar age-spectra of Mesozoic tholeiites from Antarctica. *Geochimica et Cosmochimica Acta* 41.1, pp. 15–32.

Fleitmann, D. (2003). Holocene Forcing of the Indian Monsoon Recorded in a Stalagmite from Southern Oman. *Science* 300.5626, pp. 1737–1739.

Fliervoet, T. F., S. H. White, and M. R. Drury (1997). Evidence for dominant grain-boundary sliding deformation in greenschist- and amphibolite-grade polymineralic ultramylonites from the Redbank Deformed Zone, Central Australia. *Journal of Structural Geology* 19.12, pp. 1495–1520.

Fliervoet, T. F., M. R. Drury, and P. N. Chopra (1999). Crystallographic preferred orientations and misorientations in some olivine rocks deformed by diffusion or dislocation creep. *Tectonophysics* 303.1, pp. 1–27.

Flude, S., A. M. Halton, S. P. Kelley, S. C. Sherlock, J. Schwanethal, and C. M. Wilkinson (2014). Observation of centimetre-scale argon diffusion in alkali feldspars: implications for 40Ar/39Ar thermochronology. *Geological Society, London, Special Publications* 378.1, pp. 265–275.

Flude, S. and M. Storey (2016). 40 Ar/39 Ar age of the Rotoiti Breccia and Rotoehu Ash, Okataina Volcanic Complex, New Zealand, and identification of heterogeneously distributed excess 40 Ar in supercooled crystals. *Quaternary Geochronology* 33, pp. 13–23.

Foland, K. A. (1974). Ar-40 Diffusion in Homogeneous Orthoclase and an Interpretation of Ar Diffusion in K-Feldspars. *Geochimica Et Cosmochimica Acta* 38.1, pp. 151–166.

Foland, K. A., T. H. Fleming, A. Heimann, and D. H. Elliot (1993). Potassium Argon Dating of Fine-Grained Basalts with Massive Ar Loss - Application of the 40ar/39ar Technique to Plagioclase and Glass from the Kirkpatrick Basalt, Antarctica. *Chemical Geology* 107.1-2, pp. 173–190.

Foland, K. A. and Y. P. Xu (1190). Diffusion of Ar40 and Ar39 in Irradiated Orthoclase. *Geochimica Et Cosmochimica Acta* 54.11, pp. 3147–3158.

Friedrich, W., P. Knipping, and M. Laue (1913). Interferenzerscheinungen bei roentgenstrahlen. *Annalen der Physik* 346.10, pp. 971–988.

Fritsch, F. N. and R. E. Carlson (1980). Monotone piecewise cubic interpolation. *SIAM Journal on Numerical Analysis* 17.2, pp. 238–246.

Frost, B. R., C. G. Barnes, W. J. Collins, R. J. Arculus, D. J. Ellis, and C. D. Frost (2001). A geochemical classification for granitic rocks. *Journal of Petrology* 42.11, pp. 2033–2048.

Frost, B. R. and C. D. Frost (2008). A Geochemical Classification for Feldspathic Igneous Rocks. *Journal of Petrology* 49.11, pp. 1955–1969.

Fynn, G. W. and W. J. A. Powell (1988). Cutting and polishing optical and electronic materials. Ed. by A. Hilger. Bristol: CRC Press.

Ganguly, J., R. N. Bhattacharya, and S. Chakraborty (1988). Convolution Effect in the Determination of Compositional Profiles and Diffusion-Coefficients by Microprobe Step Scans. *American Mineralogist* 73.7-8, pp. 901–909.

Gansecki, C. A., G. A. Mahood, and M. O. McWilliams (1996). 40Ar39Ar geochronology of rhyolites erupted following collapse of the Yellowstone caldera, Yellowstone Plateau volcanic field: implications for crustal contamination. *Earth and Planetary Science Letters* 142.1-2, pp. 91–107.

Gansecki, C. A. (1998). 40Ar/39Ar geochronology and pre-eruptive geochemistry of the Yellowstone Plateau volcanic field rhyolites.

Garner, E. L., T. J. Murphy, J. W. Gramlich, P. J. Paulsen, and I. L. Barnes (1975). Absolute Isotopic Abundance Ratios and Atomic Weight of a Reference Sample of Potassium. *Journal of Research of the National Bureau of Standards Section a-Physics and Chemistry* 79.6, pp. 713–725.

Ghiorso, M. S. and R. O. Sack (1995). Chemical mass transfer in magmatic processes IV. A revised and internally consistent thermodynamic model for the interpolation and extrapolation of liquid-solid equilibria in magmatic systems at elevated temperatures and pressures. *Contributions to Mineralogy and Petrology* 119.2-3, pp. 197–212.

Ginibre, C. and G. Worner (2007). Variable parent magmas and recharge regimes of the Parinacota magma system (N. Chile) revealed by Fe, Mg and Sr zoning in plagioclase. *Lithos* 98.1-4, pp. 118–140.

Ginibre, C., G. Worner, and A. Kronz (2004). Structure and dynamics of the Laacher See magma chamber (Eifel, Germany) from major and trace element zoning in sanidine: A cathodoluminescence and electron microprobe study. *Journal of Petrology* 45.11, pp. 2197–2223.

Göncüoğlu, M. C. and N. Turhan (1997). Rock units and metamorphism of the basement and Lower Paleozoic cover of the Bitlis Metamorphic Complex, SE Turkey. In: *Lower Paleozoic Evolution in Northwest Gondwana. Turkish Association of Petroleum Geology, Special Publications*. Ed. by M. C. Göncüoğlu and A. S. Derman. Vol. 3. Turkish Association of Petroleum Geology, Special Publications, pp. 75–81.

Graham, D. W. (2002). Noble gas isotope geochemistry of mid-ocean ridge and ocean island basalts: Characterization of mantle source reservoirs. *Reviews in mineralogy and geochemistry* 47.1, pp. 247–317.

Grau Malonda, A. and A. Grau Carles (2002). Half-life determination of 40 K by LSC. *Applied Radiation and Isotopes* 56.1, pp. 153–156.

Guillemoteau, J. (2018). "Processing step-scanning microprobe data for diffusion couples".

Guillou, H., B. S. Singer, C. Laj, C. Kissel, S. Scaillet, and B. R. Jicha (2004). On the age of the Laschamp geomagnetic excursion. *Earth and Planetary Science Letters* 227.3-4, pp. 331–343.

Gülen, L. (1980). Strontium isotope geochemistry of Mount Ararat and Mount Süphan volcanics, Eastern Turkey. *Eos, Trans. Am. Geophys. Union* 61, p. 412.

Gülen, L. (1984). "Sr, Nd, Pb isotope and trace element geochemistry of calc-alkaline and alkaline volcanics, Eastern Turkey". PhD thesis.

Hansen, R., R. W. Lemke, J. M. Cattermole, and A. B. Gibbons (1963). Stratigraphy and structure of the Rainier and USGS Tunnel areas Nevada Test Site. *U.S. Geological Survey Professional Paper* Vol. 382a.3, p. 111.

Harnois, L. (1988). The CIW index: a new chemical index of weathering. *Sedimentary Geology* 55.3-4, pp. 319–322.

Harrison, T. M., M. T. Heizler, O. M. Lovera, W. J. Chen, and M. Grove (1994). A Chlorine Disinfectant for Excess Argon Released from K-Feldspar during Step Heating. *Earth and Planetary Science Letters* 123.1-4, pp. 95–104.

Harrison, T. M. and O. M. Lovera (2014). The multi-diffusion domain model: past, present and future. In: *Advances in 40Ar/39Ar Dating: from Archaeology to Planetary Sciences*. Ed. by F. Jourdan, D. F. Mark, and C. Verati. Special Pu. Vol. 378. London: Geological Society, pp. 91–106.

Harrison, T. M. and I. McDougall (1982). The thermal significance of potassium feldspar K-Ar ages inferred from 40Ar/39Ar age spectrum results. *Geochimica et Cosmochimica Acta* 46.10, pp. 1811–1820.

Haschke, M. (2014). Laboratory Micro-X-Ray Fluorescence Spectroscopy. Vol. 55. Heidelberg: Springer Cham.

Hilgen, F. J. (1991a). Astronomical Calibration of Gauss to Matuyama Sapropels in the Mediterranean and Implication for the Geomagnetic Polarity Time Scale. *Earth and Planetary Science Letters* 104.2-4, pp. 226–244.

— (1991b). Extension of the Astronomically Calibrated (Polarity) Time Scale to the Miocene Pliocene Boundary. *Earth and Planetary Science Letters* 107.2, pp. 349–368.

Hilgen, F. J., W. Krijgsman, and J. R. Wijbrans (1997). Direct comparison of astronomical and Ar-40/Ar-39 ages of ash beds: Potential implications for the age of mineral dating standards. *Geophysical Research Letters* 24.16, pp. 2043–2046.

Hilton, D. R., T. P. Fischer, and B. Marty (2002). Noble gases and volatile recycling at subduction zones. *Reviews in mineralogy and geochemistry* 47.1, pp. 319–370.

Hofmeister, A. M. and G. R. Rossman (1984). Determination of Fe3+ and Fe2+ concentrations in feldspar by optical absorption and EPR spectroscopy. *Physics and Chemistry of Minerals* 11.5, pp. 213–224.

Holden, N. E., M. L. Bonardi, P. De Bièvre, P. R. Renne, and I. M. Villa (2011). IUPAC-IUGS common definition and convention on the use of the year as a derived unit of time (IUPAC Recommendations 2011). *Pure and Applied Chemistry* 83.5.

Horng, C. S., M. Y. Lee, H. Palike, K. Y. Wei, and W. T. Liang (2002). Astronomically calibrated ages for geomagnetic reversals within the Matuyama chron. *Earth Planets and Space* 54.6, pp. 679–690.

Hu, Q., P. E. Smith, N. M. Evensen, and D. York (1994). Lasing in the Holocene - Extending the Ar-40-Ar-39 Laser Probe Method into the C-14 Age Range. *Earth and Planetary Science Letters* 123.1-4, pp. 331–336.

Huang, W.-L. and P. J. Wyllie (1975). Melting reactions in the system NaAlSi3O8 - KAlSi3O8 - SiO2 to 35 kilobars, dry and with excess water. *J. Geol.* 83.6, pp. 737–748.

Hughes, S. S. (1989). *The OSTR Cd-lined epithermal neutron activation facility CLICIT: N-flux gradient, operating temperature and experimental recommendations*. Tech. rep. TRIGA Reactor Operations Committee.

Humphreys, F. J. (2001). Review Grain and subgrain characterisation by electron backscatter diffraction. *Journal of Materials Science* 36.16 LB - Humphreys2001, pp. 3833–3854.

Humphreys, F. J., Y. Huang, I. Brough, and C. Harris (1999). Electron backscatter diffraction of grain and subgrain structures - resolution considerations. *Journal of Microscopy-Oxford* 195, pp. 212–216.

Hurford, A. J. and K. Hammerschmidt (1985). 40Ar/39Ar and K-Ar Dating of the Bishop and Fish Canyon Tuffs - Calibration Ages for Fission-Track Dating Standards. *Chemical Geology* 58.1-2, pp. 23–32.

Innocenti, F., R. Mazzuoli, G. Pasquare, F. R. Di Brozolo, and L. Villari (1976). Evolution of the volcanism in the area of interaction between the Arabian, Anatolian and Iranian plates (Lake Van, Eastern Turkey). *Journal of Volcanology and Geothermal Research* 1.2, pp. 103–112.

Ireland, T. R. (2013). Invited Review Article: Recent developments in isotope-ratio mass spectrometry for geochemistry and cosmochemistry. *Review of Scientific Instruments* 84.1.

Irvine, T. N. and W. R. A. Baragar (1971). Guide to Chemical Classification of Common Volcanic Rocks. *Canadian Journal of Earth Sciences* 8.5, pp. 523–548.

Ishizuka, O. (1998). Vertical and horizontal variations of the fast neutron flux in a single irradiation capsule and their significance in the laser-heating Ar-40/Ar-39 analysis: Case study for the hydraulic rabbit facility of the JMTR reactor, Japan. *Geochemical Journal* 32.4, pp. 243–252.

Jarosewich, E. (2002). Smithsonian Microbeam Standards. *Journal of Research of the National Institute of Standards and Technology* 107.6, pp. 681–685.

Jarosewich, E., J. A. Nelen, and J. A. Norberg (1979). Electron microprobe reference samples for mineral analyses. *Smithsonian contributions to the earth sciences* 22, pp. 68–72.

JEOL (2001). *Operation Digest Electron Probe JXA-8100 / JXA-8200*. Tech. rep. Tokyo, Japan, p. 63.

Jercinovic, M. J., M. L. Williams, and E. D. Lane (2008). In-situ trace element analysis of monazite and other fine-grained accessory minerals by EPMA. *Chemical Geology* 254.3-4, pp. 197–215.

Jicha, B. R., B. S. Singer, and P. Sobol (2016). Re-evaluation of the ages of Ar-40/Ar-39 sanidine standards and supereruptions in the western US using a Noblesse multi-collector mass spectrometer. *Chemical Geology* 431, pp. 54–66.

Jourdan, F., P. R. Renne, and W. U. Reimold (2009). An appraisal of the ages of terrestrial impact structures. *Earth and Planetary Science Letters* 286.1, pp. 1–13.

Jourdan, F. and P. R. Renne (2007). Age calibration of the Fish Canyon sanidine 40Ar/39 Ar dating standard using primary K–Ar standards. *Geochimica et Cosmochimica Acta* 71.2, pp. 387–402.

Jouzel, J., V. Masson-Delmotte, O. Cattani, G. Dreyfus, S. Falourd, G. Hoffmann, B. Minster, J. Nouet, J.-M. Barnola, and J. Chappellaz (2007). Orbital and millennial Antarctic climate variability over the past 800,000 years. *Science* 317.5839, pp. 793–796.

Joy, D. C. (1995). Monte Carlo Modeling for Electron Microscopy and Microanalysis. New York: Oxford University Press.

Kahaner, D., C. Moler, and S. Nash (1989). Numerical methods and software. *Englewood Cliffs: Prentice Hall, 1989*.

Kaneoka, I. (1972). The effect of hydration on the K/Ar ages of volcanic rocks. *Earth and planetary science letters* 14.2, pp. 216–220.

Karakhanian, A., R. Djrbashian, V. Trifonov, H. Philip, S. Arakelian, and A. Avagian (2002). Holocene-historical volcanism and active faults as natural risk factors for Armenia and adjacent countries. *Journal of Volcanology and Geothermal Research* 113.1-2, pp. 319–344.

Karaoğlu, Ö., Y. Özdemir, A. Tolluoğlu, M. Karabiyikoğlu, F. Köse, O., and J. L. Froger (2005). Stratigraphy of the volcanic products around Nemrut caldera: Implications for reconstruction of the caldera formation. *Turkish Journal of Earth Sciences* 14.2, pp. 123–143.

Karner, D. B. and P. R. Renne (1998). 40Ar/39Ar geochronology of Roman volcanic province tephra in the Tiber River valley: Age calibration of middle Pleistocene sea-level changes. *Geological Society of America Bulletin* 110.6, pp. 740–747.

Kelley, S. (1995). Ar-Ar dating by laser microprobe. In: *Microprobe Techniques in the Earth Sciences*. Ed. by P. J. Potts, J. F. W. Bowles, S. J. B. Reed, and M. R. Cave. Vol. 6. Boston, MA: The Mineralogical Society.

— (2002). Excess argon in K-Ar and Ar-Ar geochronology. *Chemical Geology* 188.1-2, pp. 1–22.

Kelley, S., G. Turner, A. Butterfield, and T. J. Shepherd (1986). The source and significance of argon isotopes in fluid inclusions from areas of mineralization. *Earth and Planetary Science Letters* 79.3-4, pp. 303–318.

Keskin, M. (2003). Magma generation by slab steepening and breakoff beneath a subduction-accretion complex: An alternative model for collision-related volcanism in Eastern Anatolia, Turkey. *Geophysical Research Letters* 30.24, pp. 1–4.

Keskin, M., J. A. Pearce, and J. G. Mitchell (1998). Volcano-stratigraphy and geochemistry of collision-related volcanism on the Erzurum-Kars Plateau, northeastern Turkey. *Journal of Volcanology and Geothermal Research* 85.1-4, pp. 355–404.

Keskin, M. (2007). Eastern Anatolia: A hotspot in a collision zone without a mantle plume. In: *Special Paper 430: Plates, Plumes and Planetary Processes*. Ed. by G. Foulger and D. Jurdy. Vol. 430. Geological Society of America, pp. 693–722.

Kheirkhah, M., M. B. Allen, and M. Emami (2009). Quaternary syn-collision magmatism from the Iran/Turkey borderlands. *Journal of Volcanology and Geothermal Research* 182.1-2, pp. 1–12.

Kipfer, R. et al. (1994). < et al .pdf>. *EPSL*.

Kirkman, J. H. and W. J. McHardy (1980). A comparative study of the morphology, chemical composition and weathering of rhyolitic and andesitic glass. *Clay minerals* 15.2, pp. 165–173.

Kohn, M. J. and S. C. Penniston-Dorland (2017). Diffusion: Obstacles and Opportunities in Petrochronology. *Reviews in Mineralogy and Geochemistry* 83.1, pp. 103–152.

Koppers, A. A. P. (2002). ArArCALC—software for 40 Ar/39 Ar age calculations. *Computers & Geosciences* 28.5, pp. 605–619.

Kossert, K. and E. Günther (2004). LSC measurements of the half-life of 40 K. *Applied Radiation and Isotopes* 60.2, pp. 459–464.

Kramers, H. A. (1923). On the theory of X-ray absorption and of the continuous X- ray spectrum. *Philosophical Magazine* 46.275, pp. 836–871.

Kroll, H. and H.-U. Bambauer (1981). Diffusive and displacive transformation in plagioclase and ternary feldspar series. *Am Mineral* 66, pp. 763–769.

Kuiper, K. F., A. Deino, F. J. Hilgen, W. Krijgsman, P. R. Renne, and J. R. Wijbrans (2008). Synchronizing rock clocks of Earth history. *science* 320.5875, pp. 500–504.

Kuiper, K., A. Deino, F. Hilgen, W. Krijgsman, P. Renne, and J. Wijbrans (2005). Intercalibration of astronomical and radioisotopic time. *Geochimica Et Cosmochimica Acta* 69.10, A316–A316.

Kuiper, K. F. (2003). "Direct intercalibration of radio-isotopic and astronomical time in the Mediterranean Neogene ". PhD thesis, p. 223.

Kuiper, Y. D. (2002). The interpretation of inverse isochron diagrams in 40Ar/39Ar geochronology. *Earth and Planetary Science Letters* 203.1, pp. 499–506.

Kwiecien, O., M. Stockhecke, N. Pickarski, G. Heumann, T. Litt, M. Sturm, F. Anselmetti, R. Kipfer, and G. H. Haug (2014). Dynamics of the last four glacial terminations recorded in Lake Van, Turkey. *Quaternary Science Reviews* 104, pp. 42–52.

Laj, C. and J. E. T. Channell (2007). Geomagnetic Excursions-5.10.

Landmann, G., A. Reimer, and S. Kempe (1996). Climatically induced lake level changes at Lake Van, Turkey, during the Pleistocene/Holocene transition. *Global Biogeochemical Cycles* 10.4, pp. 797–808.

Lanphere, M. A. and H. Baadsgaard (2001). Precise K-Ar, 40Ar/39Ar, Rb-Sr and U/Pb mineral ages from the 27.5 Ma Fish Canyon Tuff reference standard. *Chemical Geology* 175.3-4, pp. 653–671.

Lanphere, M. A. and G. B. Dalrymple (1978). *The use of 40Ar/39Ar data in evaluation of disturbed K-Ar systems*. Tech. rep.

Laskar, J., A. Fienga, M. Gastineau, and H. Manche (2011). La2010: a new orbital solution for the long-term motion of the Earth. *Astronomy & Astrophysics* 532.

Laskar, J., P. Robutel, F. Joutel, M. Gastineau, A. C. M. Correia, and B. Levrard (2004). A long-term numerical solution for the insolation quantities of the Earth. *Astronomy & Astrophysics* 428.1, pp. 261–285.

Laue, M. (1912). Zur Theorie des Versuches von Trouton und Noble. *Annalen der Physik* 343.7, pp. 370–384.

Leake, B. E. (1978). Nomenclature of amphiboles. *The Canadian Mineralogist* 16.4, pp. 501–520.

Lebas, M. J., R. W. Lemaitre, A. Streckeisen, and B. Zanettin (1986). A Chemical Classification of Volcanic-Rocks Based on the Total Alkali Silica Diagram. *Journal of Petrology* 27.3, pp. 745–750.

Lebedev, V. A., E. V. Sharkov, M. Keskin, and V. Oyan (2010). Geochronology of Late Cenozoic volcanism in the area of Van Lake, Turkey: An example of development dynamics for magmatic processes. *Doklady Earth Sciences* 433.2, pp. 1031–1037.

Lee, J.-Y., K. Marti, J. P. Severinghaus, K. Kawamura, H.-S. Yoo, J. B. Lee, and J. S. Kim (2006). A redetermination of the isotopic abundances of atmospheric Ar. *Geochimica et Cosmochimica Acta* 70.17, pp. 4507–4512.

Lemcke, G. (1996). "Paläoklimarekonstruktion am Van See (Ostanatolien, Türkei)". PhD thesis. Zürich: Swiss Federal Institute of Technology, X, 182 S.

Lemcke, G. and M. Sturm (1997). δ18O and Trace Element Measurements as Proxy for the Reconstruction of Cimate Change at Lake Van (Turkey): Preliminary Results. *NATO AS1 Series* 149, pp. 653–678.

Lisiecki, L. E. and M. E. Raymo (2005). A Pliocene-Pleistocene stack of 57 globally distributed benthic δ 18O records. *Paleoceanography* 20.1, pp. 1–17.

Litt, T., F. S. Anselmetti, H. Baumgarten, J. Beer, M. N. Cagatay, D. Cukur, E. Damci, C. Glombitza, G. Haug, G. Heumann, J. Kallmeyer, R. Kipfer, S. Krastel, O. Kwiecien, A. F. Meydan, S. Orcen, N. Pickarski, R. M., H. Schmincke, C. J. Schubert, M. Sturm, M. Sumita, M. Stockhecke, Y. Tomonaga, L. Vigliotti, and T. Wonik (2012). 500,000 Years of Environmental History in Eastern Anatolia: The PALEOVAN Drilling Project. *Scientific Drilling* 14.September 2012, p. 25.

Litt, T., S. Krastel, S. Örçen, and M. Karabiyikoglu (2007). "Lake Van Drilling Project: A long continental record in eastern Turkey". In: *Scientific Drilling*. 4, pp. 40–41.

Litt, T., S. Krastel, M. Sturm, R. Kipfer, S. Örcen, G. Heumann, S. O. Franz, U. B. Ülgen, and F. Niessen (2009). 'PALEOVAN', International Continental Scientific Drilling Program (ICDP): site survey results and perspectives. *Quaternary Science Reviews* 28.15-16, pp. 1555–1567.

Litt, T., N. Pickarski, G. Heumann, M. Stockhecke, and P. C. Tzedakis (2014). A 600,000 year long continental pollen record from Lake Van, eastern Anatolia (Turkey). *Quaternary Science Reviews*.

Lourens, L. J., A. Antonarakou, F. J. Hilgen, A. A. M. VanHoof, C. VergnaudGrazzini, and W. J. Zachariasse (1996). Evaluation of the Plio-Pleistocene astronomical timescale. *Paleoceanography* 11.4, pp. 391–413.

Lovera, O. M., M. Grove, T. M. Harrison, and K. I. Mahon (1997). Systematic analysis of K-feldspar Ar-40/Ar-39 step heating results .1. Significance of activation energy determinations. *Geochimica Et Cosmochimica Acta* 61.15, pp. 3171–3192.

Lovera, O. M., M. T. Heizler, and T. M. Harrison (1993). Argon Diffusion Domains in K-Feldspar II: Kinetic-Properties of MH-10. *Contributions to Mineralogy and Petrology* 113.3, pp. 381–393.

Lovera, O. M., F. M. Richter, and T. M. Harrison (1989). The Ar-40 Ar-39 Thermochronometry for Slowly Cooled Samples Having a Distribution of Diffusion Domain Sizes. *Journal of Geophysical Research-Solid Earth and Planets* 94.B12, pp. 17917–17935.

Lucas-Tooth, H. J. and B. J. Price (1961). A mathematical method for investigation of interelement effects in X-ray fluorescent analysis. *Metallurgia* 64.383, pp. 149–161.

Ludwig, K. R. (2012). User's manual for Isoplot 3.75. *Berkeley Geochronology Center Special Publications* 5.

Luth, W. C., R. H. Jahns, and O. F. Tuttle (1964). The granite system at pressures of 4 to 10 kilobars. *Journal of Geophysical Research* 69.4, pp. 759–773.

Macdonald, R. (1974). Nomenclature and Petrochemistry of Peralkaline Oversaturated Extrusive Rocks. *Bulletin Volcanologique* 38.4, p. 18.

Macdonald, R., M. Sumita, H. U. Schmincke, B. Baginski, J. C. White, and S. S. Ilnicki (2015). Peralkaline felsic magmatism at the Nemrut volcano, Turkey: impact of volcanism on the evolution of Lake Van (Anatolia) IV. *Contributions to Mineralogy and Petrology* 169.4, pp. 1–22.

Mahood, G. A. and J. A. Stimac (1990). Trace-Element Partitioning in Pantellerites and Trachytes. *Geochimica Et Cosmochimica Acta* 54.8, pp. 2257–2276.

Mankinen, E. A., J. M. Donnelly, and C. S. Grommé (1978). Geomagnetic polarity event recorded at 1.1 my BP on Cobb Mountain, Clear Lake volcanic field, California. *Geology* 6.11, pp. 653–656.

Mark, D. F., D. Barfod, F. M. Stuart, and J. Imlach (2009). The ARGUS multicollector noble gas mass spectrometer: Performance for Ar-40/Ar-39 geochronology. *Geochemistry Geophysics Geosystems* 10.

Mark, D. F., P. Lindgren, and A. E. Fallick (2014). A high-precision 40Ar/39Ar age for hydrated impact glass from the Dellen impact, Sweden. *Geological Society, London, Special Publications* 378.1, pp. 349–366.

Mark, D. F., F. M. Stuart, and M. de Podesta (2011). New high-precision measurements of the isotopic composition of atmospheric argon. *Geochimica Et Cosmochimica Acta* 75.23, pp. 7494–7501.

Matthijs de Winter, D. A., C. Schneijdenberg, M. N. Lebbink, B. Lich, A. J. Verkleij, M. R. Drury, and B. M. Humbel (2009). Tomography of insulating biological and geological materials using focused ion beam (FIB) sectioning and low-kV BSE imaging. *Journal of microscopy* 233.3, pp. 372–383.

McDougall, I., F. H. Brown, P. M. Vasconcelos, B. E. Cohen, D. S. Thiede, and M. J. Buchanan (2012). New single crystal Ar-40/Ar-39 ages improve time scale for deposition of the Omo Group, Omo-Turkana Basin, East Africa. *Journal of the Geological Society* 169.2, pp. 213–226.

McDougall, I. and T. M. Harrison (1999). Geochronology and Thermochronology by the 40Ar/39Ar Method. 2nd ed. New York, Oxford: Oxford University Press, p. 269.

McDougall, I. (2014). Perspectives on 40Ar/39Ar dating. In: *Advances in 40Ar/39Ar Dating: from Archaeology to Planetary Sciences*. Ed. by F. Jouan, D. F. Mark, and C. Verati. Vol. 378. London: The Geological Society, pp. 9–20.

McKenzie, D. P. (1970). Plate tectonics of the mediterranean region. *Nature* 226.5242, pp. 239–243.

McLaren, S. and S. M. Reddy (2008). Automated mapping of K-feldspar by electron backscatter diffraction and application to Ar-40/Ar-39 dating. *Journal of Structural Geology* 30.10, pp. 1229–1241.

Menke, W. (2012). Geophysical Data Analysis: Discrete Inverse Theory MATLAB edition, p. 136.

Merrihue, C. and G. Turner (1966). Potassium-Argon Dating by Activation with Fast Neutrons. *Journal of Geophysical Research* 71.11, pp. 2852–&.

Meyers, S. R., S. E. Siewert, B. S. Singer, B. B. Sageman, D. J. Condon, J. D. Obradovich, B. R. Jicha, and D. A. Sawyer (2012). Intercalibration of radioisotopic and astrochronologic time scales for the Cenomanian-Turonian boundary interval, Western Interior Basin, USA. *Geology* 40.1, pp. 7–10.

Min, K., R. Mundil, P. R. Renne, and K. R. Ludwig (2000). A test for systematic errors in 40Ar/39Ar geochronology through comparison with U/Pb analysis of a 1.1-Ga rhyolite. *Geochimica et Cosmochimica Acta* 64.1, pp. 73–98.

Mollo, S., K. Putirka, G. Iezzi, P. Del Gaudio, and P. Scarlato (2011). Plagioclase–melt (dis) equilibrium due to cooling dynamics: implications for thermometry, barometry and hygrometry. *Lithos* 125.1, pp. 221–235.

Morgan, D. J., S. Blake, N. W. Rogers, B. DeVivo, G. Rolandi, R. Macdonald, and C. J. Hawkesworth (2004). Time scales of crystal residence and magma chamber volume from modelling of diffusion profiles in phenocrysts: Vesuvius 1944. *Earth and Planetary Science Letters* 222.3-4, pp. 933–946.

Morgan, G. B. and D. London (1996). Optimizing the electron microprobe analysis of hydrous alkali aluminosilicate glasses. *American Mineralogist* 81.9-10, pp. 1176–1185.

Morgan, G. B. and D. London (2005). Effect of current density on the electron microprobe analysis of alkali aluminosilicate glasses. *American Mineralogist* 90.7, pp. 1131–1138.

Morgan, L. E., P. R. Renne, R. E. Taylor, and G. WoldeGabriel (2009). Archaeological age constraints from extrusion ages of obsidian: Examples from the Middle Awash, Ethiopia. *Quaternary Geochronology* 4.3, pp. 193–203.

Morgan, L. E., P. R. Renne, G. Kieffer, M. Piperno, R. Gallotti, and J. P. Raynal (2012). A chronological framework for a long and persistent archaeological record: Melka Kunture, Ethiopia. *Journal of Human Evolution* 62.1, pp. 104–115.

Mouralis, D., C. Kuzucuoglu, E. Akköprü, A. F. Dogu, S. Scaillet, A. Christol, H. Zorer, D. Brunstein, M. Fort, and H. Guillou (2010). Les pyroclastites du sud-ouest du Lac de Van (Anatolie Orientale, Turquie): Implications dans la paléohydrographie régionale. *Quaternaire* 21.4, pp. 425–441.

Müdür, G., B. Akbas, N. Akdeniz, A. Aksay, I. E. Altun, V. Balci, E. Bilgnier, T. Biglic, M. Duru, T. Ercan, I. Gedik, Y. Günay, I. H. Güven, H. Y. Hakyemez, N. Konak, I. Papak, S. Pehlivan, M. Sevin, M. Senel, N. Tarhan, N. Turhan, A. Türkecan, Ü. Ulu, M. F. Uguz, and A. Yurtsever (2011). *Geological Map of Turkey*. Tech. rep. Ankara: Genereal Directorate of Mineral Research and Exploration.

Mussett, A. E. (1969). Diffusion Measurements and the Potassium-Argon Method of Dating. *Geophysical Journal of the Royal Astronomical Society* 18.3, pp. 257–303.

Nagao, K., J. I. Matsuda, I. Kita, and T. Ercan (1989). Noble gas and carbon isotopic composition in Quaternary volcanic area in Turkey. *Jeomorfoloji Dergisi* 17, pp. 101–110.

Nakano, S. (1992). Internal textures and chemical compositions of anti-rapakivi mantled feldspars from Oki-Dogo island, Japan. *Mineralogy and Petrology* 46.2, pp. 123–135.

Nash, W. P. and H. R. Crecraft (1985). Partition coefficients for trace elements in silicic magmas. *Geochimica et Cosmochimica Acta* 49.11, pp. 2309–2322.

Nekvasil, H. (1994). Ternary Feldspar/Melt Equilibria: A Review. In: *Feldspars and their Reactions*. Ed. by I. Parsons. Dordrecht: Springer Netherlands, pp. 195–219.

Nekvasil, H., A. Simon, and D. H. Lindsley (2000). Crystal fractionation and the evolution of intra-plate hy-normative igneous suites: Insights from their feldspars. *Journal of Petrology* 41.12, pp. 1743–1757.

Nesbitt, H. W. and G. M. Young (1984). Prediction of some weathering trends of plutonic and volcanic rocks based on thermodynamic and kinetic considerations. *Geochimica et Cosmochimica Acta* 48.7, pp. 1523–1534.

Nesbitt, H. and G. M. Young (1982). Early Proterozoic climates and plate motions inferred from major element chemistry of lutites. *Nature* 299.5885, pp. 715–717.

Nier, A. O. (1950). A Redetermination of the Relative Abundances of the Isotopes of Carbon, Nitrogen, Oxygen, Argon, and Potassium. *Physical Review* 77.6, pp. 789–793.

Niespolo, E. M., D. Rutte, A. L. Deino, and P. R. Renne (2017). Intercalibration and age of the Alder Creek sanidine Ar-40/Ar-39 standard. *Quaternary Geochronology* 39, pp. 205–213.

Nishikawa, S. and S. Kikuchi (1928). Diffraction of cathode rays by mica. *Nature* 121, pp. 1019–1020.

Noble, C. S. and J. J. Naughton (1968). Deep-Ocean Basalts - Inert Gas Content and Uncertainties in Age Dating. *Science* 162.3850, p. 11.

Nomade, S., P. R. Renne, N. Vogel, A. L. Deino, W. D. Sharp, T. A. Becker, A. R. Jaouni, and R. Mundil (2005). Alder Creek sanidine (ACs-2): A Quaternary 40Ar/39Ar dating standard tied to the Cobb Mountain geomagnetic event. *Chemical Geology* 218.3-4, pp. 315–338.

Notsu, K., T. Fujitani, T. Ui, J. Matsuda, and T. Ercan (1995). Geochemical Features of Collision-Related Volcanic-Rocks in Central and Eastern Anatolia, Turkey. *Journal of Volcanology and Geothermal Research* 64.3-4, pp. 171–191.

Oberhänsli, R., R. Bousquet, O. Candan, and A. Okay (2012). Dating Subduction Events in East Anatolia, Turkey. *Turkish Journal of Earth Sciences* 21, pp. 1–17.

Oberhänsli, R., E. Koralay, O. Candan, A. Pourteau, and R. Bousquet (2014). Late Cretaceous eclogitic high-pressure relics in the Bitlis Massif. *Geodinamica Acta* 26, pp. 175–190.

Onstott, T. C., M. L. Miller, R. C. Ewing, G. W. Arnold, and D. S. Walsh (1995). Recoil refinements: Implications for the 40 Ar/39 Ar dating technique. *Geochimica et Cosmochimica Acta* 59.9, pp. 1821–1834.

Özdemir, Y., J. Blundy, and N. Gulec (2011). The importance of fractional crystallization and magma mixing in controlling chemical differentiation at Suphan stratovolcano, eastern Anatolia, Turkey. *Contributions to Mineralogy and Petrology* 162.3, pp. 573–597.

Özdemir, Y. and N. Güleç (2013). Geological and Geochemical Evolution of the Quaternary Süphan Stratovolcano, Eastern Anatolia, Turkey: Evidence for the Lithosphere–Asthenosphere Interaction in Post-Collisional Volcanism. *Journal of Petrology* 12.12, pp. 1–26.

Özdemir, Y., O. Karaoglu, A. Tolluoglu, and N. Gulec (2007). Reply to discussion by Evren Çubukçu, Erkan Aydar and Alain Gourgaud of "Volcanostratigraphy and petrogenesis of the Nemrut stratovolcano (East Anatolian High Plateau): The most recent post-collisional volcanism in Turkey" by Y. Özdemir, Ö. Karaoğlu, A.Ü. *Chemical Geology* 245.1-2, pp. 130–134.

Özdemir, Y., Ö. Karaoğlu, A. Ü. Tolluoğlu, and N. Güleç (2006). Volcanostratigraphy and petrogenesis of the Nemrut stratovolcano (East Anatolian High Plateau): The most recent post-collisional volcanism in Turkey. *Chemical Geology* 226.3-4, pp. 189–211.

Öztopal, A., A. D. Şahin, N. Akgün, and Z. Şen (2000). On the regional wind energy potential of Turkey. *Energy* 25.2, pp. 189–200.

Panalytical (2009). *Empyrean Alpha-1 Unrivalled data quality from a laboratory XRD system*. Tech. rep. Almelo: © PANalytical, p. 4.

Parker, A. (1970). An index of weathering for silicate rocks. *Geological Magazine* 107.06, pp. 501–504.

Parsons, I. (2010). Feldspars defined and described: a pair of posters published by the Mineralogical Society. Sources and supporting information. *Mineralogical Magazine* 74.3, pp. 529–551.

Parsons, I., W. L. Brown, and J. V. Smith (1999). Ar-40/Ar-39 thermochronology using alkali feldspars: real thermal history or mathematical mirage of microtexture? *Contributions to Mineralogy and Petrology* 136.1-2, pp. 92–110.

Parsons, I., J. D. F. Gerald, and M. R. Lee (2015). Routine characterization and interpretation of complex alkali feldspar intergrowths. *American Mineralogist* 100.5-6, pp. 1277–1303.

Parsons, I. and M. R. Lee (2000). Alkali feldspars as microtextural markers of fluid flow. In: *Hydrogeology of Crystalline rocks*. Springer, pp. 27–50.

Pearce, J. A., J. F. Bender, S. E. Delong, W. S. F. Kidd, P. J. Low, Y. Guner, F. Saroglu, Y. Yilmaz, S. Moorbath, and J. G. Mitchell (1990). Genesis of Collision Volcanism in Eastern Anatolia, Turkey. *Journal of Volcanology and Geothermal Research* 44.1-2, pp. 189–229.

Pearce, J. A., N. B. W. Harris, and A. G. Tindle (1984). Trace-Element Discrimination Diagrams for the Tectonic Interpretation of Granitic-Rocks. *Journal of Petrology* 25.4, pp. 956–983.

Pearce, J. A. (1983). Role of the sub-continental lithosphere in magma genesis at active continental margins. *Continental basalts and mantle xenoliths* January, pp. 230–249.

Peccerillo, A. and S. R. Taylor (1976). Geochemistry of eocene calc-alkaline volcanic rocks from the Kastamonu area, Northern Turkey. *Contributions to Mineralogy and Petrology* 58.1, pp. 63–81.

Petráš, I. and D. Bednárová (2010). Total least squares approach to modeling: a Matlab toolbox. *Acta Montanistica Slovaca* 15.2, p. 158.

Phillips, D. and E. L. Matchan (2013). Ultra-high precision Ar-40/Ar-39 ages for Fish Canyon Tuff and Alder Creek Rhyolite sanidine: New dating standards required? *Geochimica Et Cosmochimica Acta* 121, pp. 229–239.

Phillips, D., E. L. Matchan, M. Honda, and K. F. Kuiper (2017). Astronomical calibration of Ar40/Ar39 reference minerals using high-precision, multi-collector (ARGUSVI) mass spectrometry. *Geochimica Et Cosmochimica Acta* 196, pp. 351–369.

Pierce, K. L. and I. Friedman (2000). Obsidian hydration dating of quaternary events. In: *Quaternary Geochronology: Methods and Applications*. Ed. by J. S. Noller, J. M. Sowers, and W. R. Lettiss. Washington, DC: American Geophysical Union, pp. 223–240.

Porcelli, D., C. J. Ballentine, and R. Wieler (2002). An overview of noble gas geochemistry and cosmochemistry. In: *Reviews in mineralogy and geochemistry*. Ed. by D. Porcelli, C. J. Ballentine, and R. Wieler. Vol. 47. Mineralogical Society of America, pp. 1–19.

Price, J. R. and M. A. Velbel (2003). Chemical weathering indices applied to weathering profiles developed on heterogeneous felsic metamorphic parent rocks. *Chemical Geology* 202.3, pp. 397–416.

Pringle, M. S. (1993). Age progressive volcanism in the Musicians Seamounts: a test of the hot spot hypothesis for the late Cretaceous Pacific. In: *The Mesozoic Pacific: Geology, Tectonics, and Volcanism*. Ed. by M. S. Pringle, W. W. Sager, W. V. Sliter, and S. Stein. Washington: American Geophysical Union.

Prior, D. J., A. P. Boyle, F. Brenker, M. C. Cheadle, A. Day, G. Lopez, L. Peruzzo, G. J. Potts, S. Reddy, R. Spiess, N. E. Timms, P. Trimby, J. Wheeler, and L. Zetterstrom (1999). The application of electron backscatter diffraction and orientation contrast imaging in the SEM to textural problems in rocks. *American Mineralogist* 84.11-12, pp. 1741–1759.

Prior, D. J., P. W. Trimby, U. D. Weber, and D. J. Dingley (1996). Orientation contrast imaging of microstructures in rocks using forescatter detectors in the scanning electron microscope. *Mineralogical Magazine* 60.403, pp. 859–869.

Prior, D. J. and J. Wheeler (1999). Feldspar fabrics in a greenschist facies albite-rich mylonite from electron backscatter diffraction. *Tectonophysics* 303.1-4, pp. 29–49.

Prior, D. J., E. Mariani, and J. Wheeler (2009). EBSD in the earth sciences: applications, common practice, and challenges. In: *Electron Backscatter Diffraction in Materials Science*. Ed. by A. J. Schwartz, M. Kumar, B. L. Adams, and D. P. Field. Springer, pp. 345–360.

Putirka, K. D. (2008). Introduction to Minerals, Inclusions and Volcanic Processes. *Minerals, Inclusions and Volcanic Processes* 69, pp. 1–8.

Quantin, P., J. Gautheyrou, and P. Lorenzoni (1988). Halloysite formation through in situ weathering of volcanic glass from trachytic pumices, Vico's volcano, Italy. *Clay Minerals* 23.4, pp. 423–437.

Randle, V. and M. Caul (1996). Representation of electron backscatter diffraction data. *Materials Science and Technology* 12.10, pp. 844–850.

Rasmussen, S. O., K. K. Andersen, A. M. Svensson, J. P. Steffensen, B. M. Vinther, H. B. Clausen, M. Siggaard-Andersen, S. J. Johnsen, L. B. Larsen, and D. Dahl-Jensen (2006). A new Greenland ice core chronology for the last glacial termination. *Journal of Geophysical Research: Atmospheres* 111.D6.

Reed, S. J. B. (2005). Electron Microprobe Analysis and Scanning Electron Microscopy in Geology. 2nd ed. New York: Cambridge University Press.

Reese, S. R. (2005). *Annual Report of the Oregon State University Radiation Center and TRIGA Reactor*. Tech. rep.

Reilinger, R. E., S. C. McClusky, M. B. Oral, R. W. King, M. N. Toksoz, a. a. Barka, I. Kinik, O. Lenk, and I. Sanli (1997). Global Positioning System measurements of present-day crustal movements in the Arabia-Africa-Eurasia plate collision zone. *Journal of Geophysical Research* 102.B5, p. 9983.

Reimer, A., G. Landmann, and S. Kempe (2009). Lake Van, Eastern Anatolia, hydrochemistry and history. *Aquatic Geochemistry* 15.1-2, pp. 195–222.

Renne, P. R., W. S. Cassata, and L. E. Morgan (2009). The isotopic composition of atmospheric argon and 40Ar/39Ar geochronology: Time for a change? *Quaternary Geochronology* 4.4, pp. 288–298.

Renne, P. R., A. L. Deino, R. C. Walter, B. D. Turrin, C. C. Swisher, T. A. Becker, G. H. Curtis, W. D. Sharp, and A. R. Jaouni (1994). Intercalibration of Astronomical and Radioisotopic Time. *Geology* 22.9, pp. 783–786.

Renne, P. R., K. B. Knight, S. Nomade, K. N. Leung, and T. P. Lou (2005). Application of deuteron-deuteron (D-D) fusion neutrons to 40Ar/39Ar geochronology. *Applied Radiation and Isotopes* 62.1, pp. 25–32.

Renne, P. R., S. R. Mulcahy, W. S. Cassata, L. E. Morgan, S. P. Kelley, L. J. Hlusko, and J. K. Njau (2012). Retention of inherited Ar by alkali feldspar xenocrysts in a magma: Kinetic constraints from Ba zoning profiles. *Geochimica Et Cosmochimica Acta* 93, pp. 129–142.

Renne, P. R., R. Mundil, G. Balco, K. W. Min, and K. R. Ludwig (2010). Joint determination of 40K decay constants and 40Ar*/40K for the Fish Canyon sanidine standard, and improved accuracy for 40Ar/39Ar geochronology. *Geochimica Et Cosmochimica Acta* 74.18, pp. 5349–5367.

Renne, P. R. and E. B. Norman (2001). Determination of the half-life of Ar-37 by mass spectrometry. *Physical Review C* 63.4.

Renne, P. R., W. D. Sharp, A. L. Deino, G. Orsi, and L. Civetta (1997). 40Ar/39Ar dating into the historical realm: Calibration against Pliny the Younger. *Science* 277.5330, pp. 1279–1280.

Renne, P. R., C. C. Swisher, A. L. Deino, D. B. Karner, T. L. Owens, and D. J. DePaolo (1998). Intercalibration of standards, absolute ages and uncertainties in 40Ar/39Ar dating. *Chemical Geology* 145.1-2, pp. 117–152.

Renne, P. R., G. Balco, K. R. Ludwig, R. Mundil, and K. Min (2011). Response to the comment by WH Schwarz et al. on 'Joint determination of 40K decay constants and 40Ar*/40K for the Fish Canyon sanidine standard, and improved accuracy for 40Ar/39Ar geochronology'. *Geochimica et Cosmochimica Acta* 75.17, pp. 5097–5100.

Rietveld, H. M. (1967). Line profiles of neutron powder-diffraction peaks for structure refinement. *Acta Crystallographica* 22.1, pp. 151–152.

Rivera, T. A., M. Storey, M. D. Schmitz, and J. L. Crowley (2013). Age intercalibration of Ar-40/Ar-39 sanidine and chemically distinct U/Pb zircon populations from the Alder Creek Rhyolite Quaternary geochronology standard. *Chemical Geology* 345, pp. 87–98.

Rivera, T. A., M. D. Schmitz, B. R. Jicha, and J. L. Crowley (2016). Zircon Petrochronology and 40Ar/39Ar Sanidine Dates for the Mesa Falls Tuff: Crystal-scale Records of Magmatic Evolution and the Short Lifespan of a Large Yellowstone Magma Chamber. *Journal of Petrology* 57.9, pp. 1677–1704.

Rivera, T. A., M. Storey, C. Zeeden, F. J. Hilgen, and K. Kuiper (2011). A refined astronomically calibrated 40 Ar/39 Ar age for Fish Canyon sanidine. *Earth and Planetary Science Letters* 311.3, pp. 420–426.

Robertson, E. C. (1988). Thermal Properties of Rocks. *US Department of the Interior: Geological Survey*, pp. 88–441.

Rock, N. M. S. (1990). The International Mineralogical Association (IMA/CNMMN) pyroxene nomenclature scheme: Computerization and its consequences. *Mineralogy and Petrology* 43.2, pp. 99–119.

Roddick, J. C. (1978). Application of Isochron Diagrams in 40Ar/39Ar-Dating - Discussion. *Earth and Planetary Science Letters* 41.2, pp. 233–244.

— (1987). Generalized numerical error analysis with applications to geochronology and thermodynamics. *Geochimica Et Cosmochimica Acta* 51.8, pp. 2129–2135.

Rollinson, H. (1993). Using Geochemical Data. New York: Pearson Prentice and Hall, p. 352.

Sambridge, M. S. and W. Compston (1994). Mixture modeling of multi-component data sets with application to ion-probe zircon ages. *Earth and Planetary Science Letters* 128.3-4, pp. 373–390.

Samson, S. D. and E. C. Alexander (1987). Calibration of the interlaboratory 40Ar/39Ar dating standard, MMhb-1. *Chemical Geology: Isotope Geoscience Section* 66.1-2, pp. 27–34.

Sanver, M. (1968). A palaeomagnetic study of Quaternary volcanic rocks from Turkey. *Physics of the Earth and Planetary Interiors* 1.6, pp. 403–421.

Sardela, M. (2014). X-Ray Diffraction and Reflectivity. In: *Practical Materials Characterization*. Ed. by M. Sardela. New York: Springer. Chap. 1, pp. 1–43.

Saxton, J. M. (2015). A method for measurement of 36 Ar without H 35 Cl interference. *Chemical Geology* 409, pp. 112–117.

Scaillet, B. and R. Macdonald (2001). Phase Relations of Peralkaline Silicic Magmas and Petrogenetic Implications. *Journal of Petrology* 42.4, pp. 825–845.

— (2003). Experimental Constraints on the Relationships between Peralkaline Rhyolites of the Kenya Rift Valley. *Journal of Petrology* 44.10, pp. 1867–1894.

Scaillet, S. (2000). Numerical error analysis in 40Ar/39Ar dating. *Chemical Geology* 162, pp. 269–298.

Schmid, R. (1981). Descriptive Nomenclature and Classification of Pyroclastic Deposits and Fragments - Recommendations of the Iugs Subcommission on the Systematics of Igneous Rocks. *Geology* 9.1, pp. 41–43.

Schmidt, N. H. and N. O. Olesen (1989). Computer-Aided Determination of Crystal-Lattice Orientation from Electron-Channeling Patterns in the SEM. *Canadian Mineralogist* 27, pp. 15–22.

Schmincke, H. U., M. Sumita, and P. S. Team (2014). Impact of volcanism on the evolution of Lake Van (eastern Anatolia) III: Periodic (Nemrut) vs. episodic (Suphan) explosive eruptions and climate forcing reflected in a tephra gap between ca. 14 ka and ca. 30 ka. *Journal of Volcanology and Geothermal Research* 285, pp. 195–213.

Schmitt, A. K. (2006). Laacher See revisited: High-spatial-resolution zircon dating indicates rapid formation of a zoned magma chamber. *Geology* 34.7, pp. 597–600.

Schmitt, A. K., F. Wetzel, K. M. Cooper, H. Zou, and G. Wörner (2010). Magmatic longevity of laacher see volcano (Eifel, Germany) indicated by U-Th dating of intrusive carbonatites. *Journal of Petrology* 51.5, pp. 1053–1085.

Schwarz, W. H., K. Kossert, M. Trieloff, and J. Hopp (2011). Comment on the "Joint determination of 40K decay constants and 40Ar*/40K for the Fish Canyon sanidine standard, and improved accuracy for 40Ar/39Ar geochronology" by Paul R. Renne et al. (2010). *Geochimica Et Cosmochimica Acta* 75.17, pp. 5094–5096.

Schwarz, W. H. and M. Trieloff (2007). *Revising the K decay constant*. Tuscon NV - 8.

Selcuk, L., A. S. Selcuk, and T. Beyaz (2010). Probabilistic seismic hazard assessment for Lake Van basin, Turkey. *Natural Hazards* 54.3, pp. 949–965.

Şen, P. A., A. Temel, and A. Gourgaud (2004). Petrogenetic modelling of Quaternary post-collisional volcanism: a case study of central and eastern Anatolia. *Geological Magazine* 141.1, pp. 81–98.

Şengör, A. C. M. and Y. Yilmaz (1981). Tethyan evolution of Turkey: a plate tectonic approach. *Tectonophysics* 75.3-4, pp. 181193203–190199241.

Şengör, A. M. C., S. Özeren, T. Genç, and E. Zor (2003). East Anatolian high plateau as a mantle-supported, north-south shortened domal structure. *Geophysical Research Letters* 30.24.

Sensoy, S., M. Demircan, Y. Ulupinar, and İ. Balta (2008). Climate of Turkey. *Republic of Turkey ministry of environment and forestry Turkish state meteorological service. Retrieved December* 10, p. 2007.

Shackleton, N. J., A. Berger, and W. R. Peltier (1990). An Alternative Astronomical Calibration of the Lower Pleistocene Timescale Based on Odp Site 677. *Transactions of the Royal Society of Edinburgh-Earth Sciences* 81, pp. 251–261.

Shand, S. J. (1949). Rocks of the Mid-Atlantic Ridge. *Journal of Geology* 57.1, pp. 89–92.

Sherman, J. (1954). "The correlation between fluorescent X-ray intensity and chemical composition". In: *Symposium on Fluorescent X-ray Spectrographic Analysis*. ASTM International.

Shore, M. and A. D. Fowler (1996). Oscillatory zoning in minerals; a common phenomenon. *The Canadian Mineralogist* 34.6, pp. 1111–1126.

Singer, B. S., J. R. Wijbrans, S. T. Nelson, M. S. Pringle, T. C. Feeley, and M. A. Dungan (1998). Inherited argon in a Pleistocene andesite lava: (40)Ar/(39)Ar incremental-heating and laser-fusion analyses of plagioclase. *Geology* 26.5, pp. 427–430.

Singer, B. S. (2014a). A Quaternary geomagnetic instability time scale. *Quaternary Geochronology* 21, pp. 29–52.

— (2014b). Quaternary Geochronology special issue: Advances in 40Ar/39Ar Dating of Quaternary Events and Processes. *Quaternary Geochronology* 21, p. 1.

Singer, B. S., H. Guillou, B. R. Jicha, C. Laj, C. Kissel, B. L. Beard, and C. M. Johnson (2009). 40 Ar/39 Ar, K–Ar and 230 Th–238 U dating of the Laschamp excursion: A radioisotopic tie-point for ice core and climate chronologies. *Earth and Planetary Science Letters* 286.1, pp. 80–88.

Skoog, D. A. and J. J. Leary (1992). Principles of instrumental analysis. 4th ed. Orlando, Florida: Saunders College Publishing, p. 1612.

Smith, P. E., D. York, Y. Chen, and N. M. Evensen (1996). Single crystal Ar-40-Ar-39 dating of a late quaternary paroxysm on Kos, Greece: Concordance of terrestrial and marine ages. *Geophysical Research Letters* 23.21, pp. 3047–3050.

Spell, T. L. and I. McDougall (2003). Characterization and calibration of 40Ar/39Ar dating standards. *Chemical Geology* 198.3-4, pp. 189–211.

Spell, T. L., E. I. Smith, A. Sanford, and K. A. Zanetti (2001). Systematics of xenocrystic contamination: preservation of discrete feldspar populations at McCullough Pass Caldera revealed by 40Ar/39Ar dating. *Earth and Planetary Science Letters* 190.3-4, pp. 153–165.

Steiger, R. and E. Jäger (1977). Subcommission on geochronology: convention on the use of decay constants in geo-and cosmochronology. *Earth and planetary science letters* 36.3, pp. 359–362.

Steiner, J. C., R. H. Jahns, and W. C. Luth (1975). Crystallization of Alkali Feldspar and quartz in the haplogranite system NaAlSi3O8 - KAlSi3O8 - SiO2 - H2O at 4 kbar. *Bulletin of the Geological Society of America* 86.1, pp. 83–98.

Steven, T. A. (1969). Possible Relation of Mineralization to Thermal Springs in Creede District, San Juan Mountains, Colorado - a Discussion. *Economic Geology* 64.6, pp. 696–&.

Stockhecke, M., O. Kwiecien, L. Vigliotti, F. S. Anselmetti, J. Beer, M. N. Çağatay, J. E. T. Channell, R. Kipfer, J. Lachner, T. Litt, N. Pickarski, and M. Sturm (2014a). Chronostratigraphy of the 600,000 year old continental record of Lake Van (Turkey). *Quaternary Science Reviews* 104, pp. 8–17.

Stockhecke, M., M. Sturm, I. Brunner, H.-U. Schmincke, M. Sumita, R. Kipfer, D. Cukur, O. Kwiecien, F. S. Anselmetti, and D. Ariztegui (2014b). Sedimentary evolution and environmental history of Lake Van (Turkey) over the past 600 000 years. *Sedimentology* 4.1, pp. 1–32.

Stockhecke, M., A. Timmermann, R. Kipfer, G. H. Haug, O. Kwiecien, T. Friedrich, L. Menviel, T. Litt, N. Pickarski, and F. S. Anselmetti (2016). Millennial to orbital-scale variations of drought intensity in the Eastern Mediterranean. *Quaternary Science Reviews* 133, pp. 77–95.

Sumita, M. and H.-U. Schmincke (2013a). Erratum To "Impact of volcanism on the evolution of Lake Van II: Temporal evolution of explosive volcanism of Nemrut Volcano (eastern Anatolia) during the past ca. 0.4 Ma" [J. Volcanol. Geotherm. Res. 253 (2013), 15–34]. *Journal of Volcanology and Geothermal Research*, p. 3.

— (2013b). Impact of volcanism on the evolution of Lake Van I: evolution of explosive volcanism of Nemrut Volcano (eastern Anatolia) during the past 400,000 years. *Bulletin of Volcanology* 75.5, p. 714.

— (2013c). Impact of volcanism on the evolution of Lake Van II: Temporal evolution of explosive volcanism of Nemrut Volcano (eastern Anatolia) during the past ca. 0.4Ma. *Journal of Volcanology and Geothermal Research* 253, pp. 15–34.

Svensson, A., K. K. Andersen, M. Bigler, H. B. Clausen, D. Dahl-Jensen, S. M. Davies, S. J. Johnsen, R. Muscheler, F. Parrenin, S. O. Rasmussen, R. Roethlisberger, I. Seierstad, J. P. Steffensen, and B. M. Vinther (2008). A 60000 year Greenland stratigraphic ice core chronology. *Climate of the Past* 4.1, pp. 47–57.

Tarantola, A. and B. Valette (1982). *Generalized nonlinear inverse problems solved using the least squares criterion.*

Taylor, J. (1997). Introduction to error analysis, the study of uncertainties in physical measurements.

Taylor, S. R. and S. M. C. N. MacLennan (1985). The continental crust: its composition and evolution: an examination of the geochem. record preserved in sedimentary rocks. Oxford: Blackwell, XV, 312 S. . Ill., graph. Darst.

Till, C. B., J. A. Vazquez, and J. W. Boyce (2015). Months between rejuvenation and volcanic eruption at Yellowstone caldera, Wyoming. *Geology* 43.8, pp. 695–698.

Tomonaga, Y., M. S. Brennwald, and R. Kipfer (2011). Spatial distribution and flux of terrigenic He dissolved in the sediment pore water of Lake Van (Turkey). *Geochimica Et Cosmochimica Acta* 75.10, pp. 2848–2864.

Tomonaga, Y., M. S. Brennwald, A. F. Meydan, and R. Kipfer (2014). Noble gases in the sediments of Lake Van – solute transport and palaeoenvironmental reconstruction. *Quaternary Science Reviews* 104, pp. 117–126.

Troll, V. R. and H. U. Schmincke (2002). Magma mixing and crustal recycling recorded in ternary feldspar from compositionally zoned peralkaline Ignimbrite 'A', Gran Canaria, Canary Islands. *Journal of Petrology* 43.2, pp. 243–270.

Turner, G. (1971). Ar-40-Ar-39 Dating - Optimization of Irradiation Parameters. *Earth and Planetary Science Letters* 10.2, pp. 227–&.

Turner, G. (1988). Hydrothermal fluids and argon isotopes in quartz veins and cherts. *Geochimica et Cosmochimica Acta* 52.6, pp. 1443–1448.

Turrin, B. D., J. M. Donnellynolan, and B. C. Hearn (1994). 40Ar/39Ar Ages from the Rhyolite of Alder-Creek, California - Age of the Cobb-Mountain Normal-Polarity Subchron Revisited. *Geology* 22.3, pp. 251–254.

Tuttle, O. F. and N. L. Bowen (1958). Origin of Granite in the Light of Experimental Studies in the System NaAlSi3O8 - KAlSi3O8 - SiO2 - H2O. In: *Geological Society of America Memoirs*. Vol. 74, pp. 1–146.

Ulusoy, I., H. Çubukçu, E. Aydar, P. Labazuy, O. Ersoy, E. Sen, and A. Gourgaud (2012). Volcanological evolution and caldera forming eruptions of Mt. Nemrut (Eastern Turkey). *Journal of Volcanology and Geothermal Research* 245, pp. 21–39.

Uto, K., O. Ishizuka, A. Matsumoto, H. Kamioka, and S. Togashi (1997). Laser heating 40Ar/39Ar dating system of the Geological Survey of Japan: System Outline and Preliminary Results. *Bulletin-Geological Survey Japan* 48, pp. 23–46.

Van Soest, M. C., D. R. Hilton, and R. Kreulen (1998). Tracing crustal and slab contributions to arc magmatism in the Lesser Antilles island arc using helium and carbon relationships in geothermal fluids. *Geochimica et Cosmochimica Acta* 62.19, pp. 3323–3335.

Veres, D., L. Bazin, A. Landais, H. Toyé Mahamadou Kele, B. Lemieux-Dudon, F. Parrenin, P. Martinerie, E. Blayo, T. Blunier, and E. Capron (2013). The Antarctic ice core chronology AICC2012 an optimized multi-parameter and multi-site dating approach for the last 120 thousand years. *Climate of the Past* 9.4, pp. 1733–1748.

Vigliotti, L., J. E. T. Channell, and M. Stockhecke (2014). Paleomagnetism of Lake Van sediments: chronology and paleoenvironment since 350 ka. *Quaternary Science Reviews* 104, pp. 18–29.

Villa, I. M. (2006). From nanometer to megameter: Isotopes, atomic-scale processes, and continent-scale tectonic models. *Lithos* 87.3-4, pp. 155–173.

Villa, I. M. (1997). Direct determination of 39Ar recoil distance. *Geochimica et Cosmochimica Acta* 61.3, pp. 689–691.

Villa, I. M. (2001). Radiogenic isotopes in fluid inclusions. *Lithos* 55.1, pp. 115–124.

— (2014). Diffusion of Ar in K-feldspar: Present and absent. In: *Advances in 40Ar/39Ar Dating: from Archaeology to Planetary Sciences*. Ed. by F. Jourdan, D. F. Mark, and C. Verati. Special Pu. Vol. 378. London: Geological Society, pp. 107–116.

Voigt, T., K. Reicherter, H. von Eynatten, R. Littke, S. Voigt, and J. Kley (2008). Sedimentation during basin inversion. In: *Dynamics of Complex Intracontinental Basins The Central*

European Basin System. Ed. by R. Littke, U. Bayer, D. Gajewski, and S. Nelskamp, pp. 211–232.

Walker, D. A. and I. Mcdougall (1982). Ar-40-Ar-39 and K-Ar Dating of Altered Glassy Volcanic-Rocks - the Dabi Volcanics, Png. *Geochimica Et Cosmochimica Acta* 46.11, pp. 2181–2190.

Wang, Y. J., H. Cheng, R. L. Edwards, Z. S. An, J. Y. Wu, C. C. Shen, and J. A. Dorale (2001). A high-resolution absolute-dated late pleistocene monsoon record from Hulu Cave, China. *Science* 294.5550, pp. 2345–2348.

Wartho, J.-A., S. P. Kelley, R. A. Brooker, M. R. Carroll, I. M. Villa, and M. R. Lee (1999). Direct measurement of Ar diffusion profiles in a gem-quality Madagascar K-feldspar using the ultra-violet laser ablation microprobe (UVLAMP). *Earth and Planetary Science Letters* 170.1, pp. 141–153.

Weitz, G. (1972). Structure of Sanidine at different degrees of order. *Zeitschrift für Krstallographie* 136.5-6, pp. 418–426.

Wendt, I. and C. Carl (1991). The Statistical Distribution of the Mean Squared Weighted Deviation. *Chemical Geology* 86.4, pp. 275–285.

Wendt, I., C. Carl, K. Habfast, D. Tuttas, and J. I. Wendt (1991). Complete Pb/U Analysis of Unspiked Samples by Measuring Pb Isotopes Only. *Earth and Planetary Science Letters* 107.3-4, pp. 618–624.

White, J. D. L., V. Manville, C. J. N. Wilson, B. F. Houghton, N. R. Riggs, and M. Ort (2009). Settling and deposition of AD 181 Taupo pumice in lacustrine and associated environments. *Volcaniclastic Sedimentation in Lacustrine Settings (Special Publication 30 of the IAS)* 15, pp. 141–150.

Whitney, D. L. and B. W. Evans (2010). Abbreviations for names of rock-forming minerals. *American Mineralogist* 95.1, pp. 185–187.

Wieser, M. E., N. Holden, T. B. Coplen, J. K. Bohlke, M. Berglund, W. A. Brand, P. De Bievre, M. Groning, R. D. Loss, and J. Meija (2013). Atomic weights of the elements 2011 (IUPAC Technical Report). *Pure and Applied Chemistry* 85.5, pp. 1047–1078.

Wigley, T. M. L. and G. Farmer (1982). Climate of the eastern Mediterranean and Near East. In: *Paleoclimates, Paleoenvironments and Human Communities in the Eastern Mediterranean Region in Later Prehistory*. Ed. by J. Bintliff and W. van Zeist. BAR Oxford, pp. 3–37.

Wijbrans, J. R. (1985). "Geochronology of metamorphic terrains by the 40Ar/39Ar age spectrum method". PhD thesis. Canberra, p. 267.

Wijbrans, J. R. and I. Mcdougall (1987). On the Metamorphic History of an Archean Granitoid Greenstone Terrane, East Pilbara, Western Australia, Using the 40Ar/39Ar Age Spectrum Technique. *Earth and Planetary Science Letters* 84.2-3, pp. 226–242.

Wijbrans, J. R., M. S. Pringle, A. A. P. Koppers, and R. Scheveers (1995). "Argon geochronology of small samples using the Vulkaan argon laserprobe". In: *Proceedings of the Royal Netherlands Academy of Arts and Sciences*. Vol. 2. 98, pp. 185–218.

Wilkinson, A. J. and P. B. Hirsch (1997). Electron diffraction based techniques in scanning electron microscopy of bulk materials. *Micron* 28.4, pp. 279–308.

Wilson, A. D. (1955). A new method for the determination of ferrous iron in rocks and minerals. *Bulletin of the Geological Survey of Great Britain* 9, pp. 56–58.

Wolff, E. W., J. Chappellaz, T. Blunier, S. O. Rasmussen, and A. Svensson (2010). Millennial-scale variability during the last glacial: The ice core record. *Quaternary Science Reviews* 29.21-22, pp. 2828–2838.

Yilmaz, Y., Y. Guner, and F. Saroglu (1998). Geology of the quaternary volcanic centres of the east Anatolia. *Journal of Volcanology and Geothermal Research* 85.1-4, pp. 173–210.

York, D. (1968). Least squares fitting of a straight line with correlated errors. *Earth and Planetary Science Letters* 5.Supplement C, pp. 320–324.

Zeitler, P. K. (1987). Argon Diffusion in Partially Outgassed Alkali Feldspars - Insights from Ar-40/Ar-39 Analysis. *Chemical Geology* 65.2, pp. 167–181.

Zhang, Y. (2010). Diffusion in minerals and melts: theoretical background. In: *Diffusion in Minerals and Melts*. Ed. by Y. Zhang and D. J. Cherniak. Reviews in. Vol. 72. 1. Mineralogical Society of America, pp. 5–59.

Zor, E., E. Sandvol, C. Gürbüz, N. Türkelli, D. Seber, and M. Barazangi (2003). The crustal structure of the East Anatolian plateau (Turkey) from receiver functions. *Geophysical Research Letters* 30.24.

Appendices

Appendix A: Further Instrumental Methods

A.1 X-ray diffraction analyses (XRD)

Since its discovery by Laue (1912) and Friedrich et al. (1913) the diffraction of X-rays is a vastly applied method in geological and material sciences. It is dominantly used to either analyse the atomic structure of single crystals or to identify single crystalline materials in polycrystalline solids. Approaches by Debye and Scherrer (1916) and Rietveld (1967) allow the method to even quantify the volumetric fractions of different materials in the solids. This thesis analysed a set of ten volcaniclastic samples in order to identify the presence of clay crystals in fine grained vitric groundmasses (< 5 μm) via powder XRD. Target minerals were the weathering products of volcanic glass. The expected minerals are comprised by kaolinite, smectites (montmorillonites and bidellites), illites, zeolithes, halloysite, allophan and gibbsite (Kirkman and McHardy, 1980; Nesbitt and Young, 1984; Quantin et al., 1988). As this approach does not require a quantitative determination of the involved phases the following theory and application of the method focuses on fast and qualitative XRD analyses. The majority of information presented in this section is derived from textbooks of Skoog and Leary (1992) and Sardela (2014). The latter textbook is recommended for further reading.

A.1.1 XRD in theory

XRD is sensitive for identification of crystalline phases down to 0.1 – 1 wt%. Most XRD instruments apply monochromatic x-ray radiation from Cu, Cr, Mo, or Ag anode sources. Most x-ray sources in geological sciences are equipped with Cu anodes that employ the radiation of Cu Kα-lines. The penetration depth of the X-ray is dependent to primary X-ray energy, the sample material, and the angle of the incident X-ray beam. Other X-ray sources are common for XRD measurements on non-silicates. Non-conventional laboratory XRD equipment is able to provide a much wider variety of wavelengths, energies and beam coherence using synchrotron sources.

Physical concept of diffraction

Bragg's law (Eq. 3.33) is the cornerstone in analysing diffracted X-rays. Similar as to identifying characteristic X-rays in WDX, the concept of XRD is related to spacing between atomic planes of crystalline materials. Recalling Eq. 3.33 states that the interplanar spacing (d in Eq. 3.33) can be determined by measuring the angle of 2θ between the incident and the diffracted directions together with wavelengthλ. The measured angular 2θ position from a distinct diffraction peak thus corresponds to the lattice spacing. Specific sets of the lattice spacing act like distinct fingerprints for the particular phases involved in a polycrystalline solid (accounts also for polymorphs). Fig. A.1 illustrates the basic concept of the diffraction process in two ways: (i) as an actual existing space with an atomic entity (Figs. A.1a and A.1c); (ii) as a reciprocal space with respect to the radiation (Fig. A.1b and A.1d). A schematic representation of ordered atoms in a crystalline structure is given in Fig. A.1a. Fourier transformation relocates the same

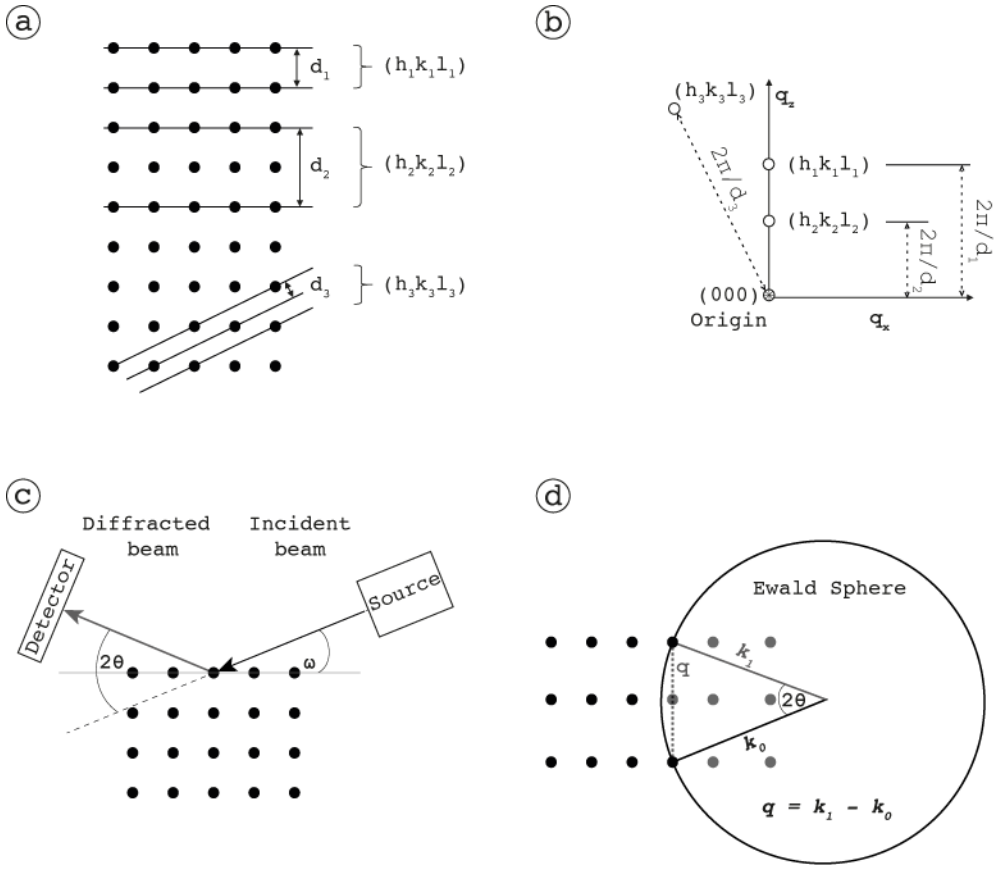

Figure A.1: Sketches illustrating interplanar lattice spacing and orientation in direct and reciprocal spaces. (a) Different planes identified in Miller indices (hkl) and atomic spacing d in real space. (b) The same distance and planes from (a) in a reciprocal space at inverse distances and different orientations. (c) The diffraction process sketched in an actual existing space of atomic spacing of a crystalline material. (d) X-ray diffraction in the reciprocal space of the Ewald sphere. The radius of the sphere is equal to the incident reciprocal wave vector. The figure was drawn after Sardela (2014).

features (crystallographic planes) in a reciprocal space (Fig. A.1b). The diffracted X-ray beam is represented at an angle of 2θ relative to the diffracting lattice parameter in Fig. A.1c. The reciprocal space represents the set of lattice planes as a single point and has a space origin that is represented with a distance of $2\pi/d$ (Fig. A.1d). Diffraction processes are commonly described by using the concept of the Ewald's sphere (Ewald, 1913). This concept represents a vector of a wave that has the same direction as the incident beam (k_0) together with the diffracted wave vector (k_1). The length of k_0 represents the radius of the sphere. During diffractions experiments in the real space, the angles ω and θ vary and the Ewald sphere rotates in the reciprocal space. A diffracted wave vector (k_1) will only occur if the Ewald sphere intercepts reciprocal lattice points. A scattering vector q is defined as (k_1-k_0) and an important quantity in diffraction analyses. It can be derived from the diffraction angle and the incident wavelength via the following relation (Eq. A.1).

$$q = \frac{4\pi}{\lambda} \times \sin\theta \tag{A.1}$$

Exploring the basic concept of reciprocal space representation allows identifying a wide range of material properties. The Ewald sphere shows that only lattice grid points that are smaller than the vector of $|2k_1|$ fulfil the requirement for diffraction by Bragg (1913). It furthermore

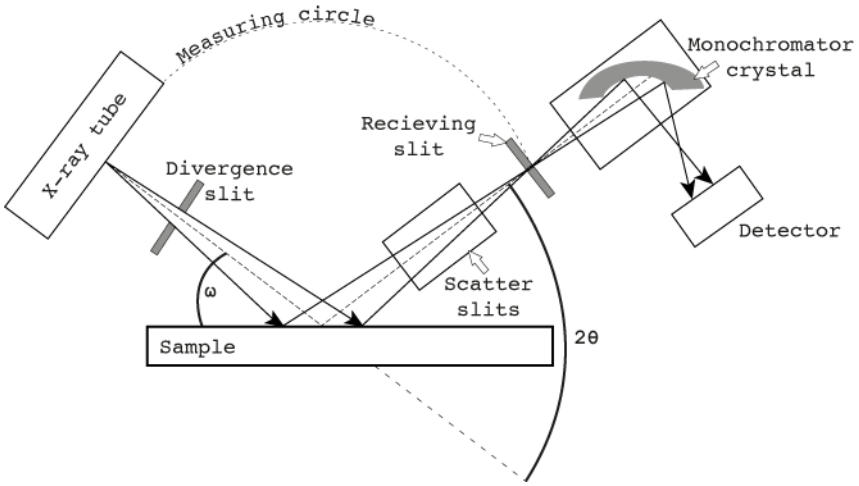

Figure A.2: XRD diffractometer configuration after Sardela (2014). The set-up shown here is the typical Bragg-Brentano configuration. It applies focused x-rays.

illustrates why large wavelength (or small wavenumber k) do not get diffracted by crystal lattices. This concept outlines also that large and broad diffraction peaks correspond to structures with extremely small lattices in real space. Peaks observed at small diffraction angles (small scattering vector q) correspond in contrast to large atomic spacing.

Basic analytical instrumentation

The typically used XRD diffractometer consist of five main parts: (i) the X-ray source, (ii) the primary optics, (iii) the sample stage, (iv) the secondary optics and (v) the detector (Fig. A.2). As described above XRD measurements require the measurement of the 2θ and ω angles and require knowledge about the employed X-rays.

The diffractometer measures the 2θ and ω angles by either rotating detector and X-ray tube or by rotating detector and sample. Sealed ceramic tubes typically serve as X-ray sources. X-rays are generated in vacuum by electrons that are targeted in an anode (most typically Cu). Electron emission is achieved under high voltage potential of a W filament relative to the grounded target. A Be window allows X-ray emission from the tube. The shape of the X-ray beam that targets the sample is dependent of the analytical goal. Conventional XRD measurements (e.g. measurements of thin film thicknesses and phase identification) use a parallel X-ray beam that can be imagined as thin line of X-rays. This line of X-rays has an elongation perpendicular to the diffracting plane. Point focusing of X-rays employs a slightly different set of primary optics. These diffractometers employ beams of an oval or round shape and their set-ups follows the Bragg-Brentano configuration (Brentano, 1924) that is illustrated in Fig. A.2. The Bragg-Brentano method is mostly used for investigating polycrystalline textures in material and in earth sciences. Accordingly, XRD in this thesis applied a diffractometer with a Bragg-Brentano geometry. The primary optics of this configuration consists usually of slits. A sample stage is a simple sample holder of fixed position (in the usual case of tube and detector rotation). Analysing preferred crystal orientations in a solid, single crystalline structures require to design a configuration that involves sample rotation Sardela (2014). Secondary optics are commonly adjusted to the detecting devise and collimate the diffracted beam. Slit configurations and

pinholes are typically employed. Powder diffractometer frequently employ another X-ray mirror focus the beam to the detector. A monochromator is crucial (either as secondary or primary optics) in order to separate a particular wavelength of the the primary radiation. Conventional XRD diffractometers in geological sciences use monochromator crystals that separate the Cu Kα_1 line (λ=0.154056 nm) or an average of the Cu Kα_1 and Cu Kα_2 lines (average λ=0.15418 nm). The final device in a XRD diffractometer is the detector. For common powder analyses point detectors (zero-dimensional) are used. The diffracted and collimated X-rays enter these detector types through a Be window. NaI crystals that scintillate under X-ray radiation record the impacting signal. Proportional counters are also applied as detectors (see section 3.2).

Diffractograms

At any given diffractometer configuration a set of two different angular scans can be performed. The most frequently seen in geological scienes is the $2\theta/\omega$ (or 2theta-omega) scan. This set-up rotates the 2θ and ω simultaneously. In the majority of configurations this set-up is tuned in a way that the rotation measures in synchronized steps, which guarantee 2θ to be the double of ω. These scan types probe a crystallographic orientation perpendicular to the exposed atomic planes. Therefore, this type of scanning is particularly sensitive to variations of atomic positions in polyphase solids. Its sensitivity to interplanar crystallographic spacing makes the $2\theta/\omega$ scans to the key type of measurements that are used for material identification. The resulting diffractograms present the 2θ angle versus intensities of diffracted X-ray intensities (Fig. A.3a). Another way of scanning is the rotation of the incident angle ω only. The resulting scans (also known as 'rocking curves') are usefull for investigating highly orientated samples for lattice deffects or material quality but are of no use for common phase identification.

Fig. A.3a shows a diffractogram that represents a measurement on a dolostone from Sardela (2014). This author also interpreted the diffractogram. This interpretation is partly adapted in order to exemplify the various informations in diffractograms. Three key observations are listed in the following.

- The scan indicates the presence of crystalline materials in the sample powder. A software is able to identfying if the given peaks are from the same family of planes, or from various phases, or various grain orientations (Fig. A.3b). The software indexes the patterns first and applies in a second step the fitting procedure against a database of 'powder diffraction files' (PDF). The PDFs are usually ofered by the International Centre of Diffraction Data (ICDD). Angular position and relative intensity are the parameters for phase identification.

- Relative comparisons of peak areas and peak heights can be used to quantify the fractions of solids and/or their preferred orientations.

- Broad diffraction fetaure (as outlined in Fig. A.3a between 20° and 35°) indicates the presence of amorphous materials. Such non-crystalline materials have an outstandingly short range of ordering (couple of nanometres), which is responsible for the broad diffraction in $2\theta/\omega$ scans.

It needs to be stressed that peaks in $2\theta/\omega$ scans are derived from lattice parameters that are parallel to the sample surface (Fig. A.3b). The analyst therefore needs to ensure that

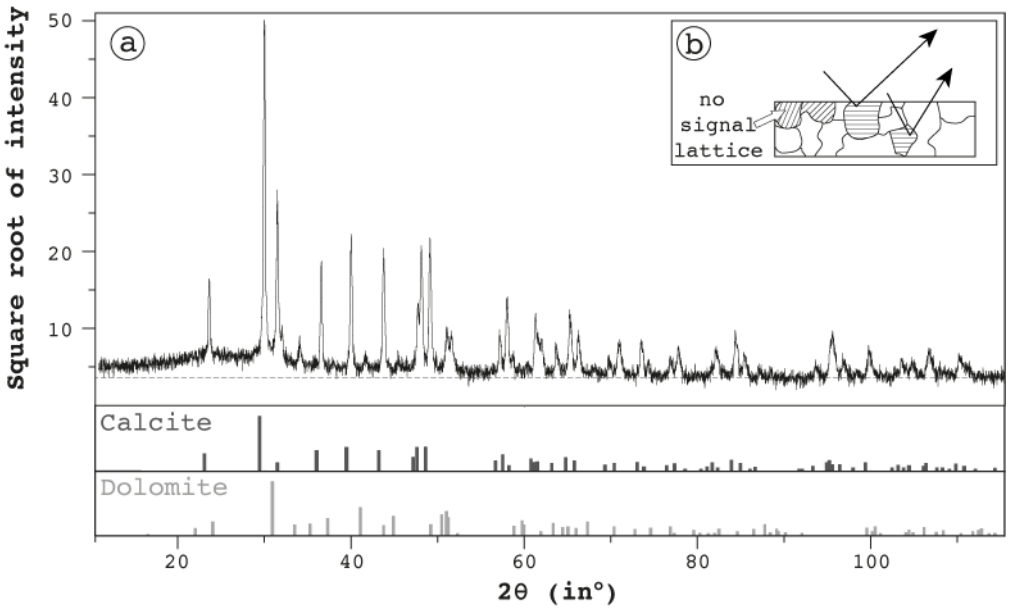

Figure A.3: a) A $2\theta/\omega$ scan of a powder made from a Paleozoic dolostone Sardela (2014). A dashed line reflects an average background intensity for the angular 2θ range of 50° to 110°. The dashed line illustrates the existence of a slight hump between 20° and 35°, which likely represents an amorphous phases. The lower two boxes represent peak identifications of calcite and dolomite. The identification was computed by fitting reference scans from an ICCD PDF database. (b) An additional sketch illustrates lattice orientations that are parallel to the sample surface (e.g. in a powder sample). Only these orientations allow detection in a $2\theta/\omega$ scan. Furthermore, two idealized beam trajectories indicate that the penetration depth and probing volume are dominantly a function of 2θ in a monomineralic sample.

the analysed powder is a well-mixed and a representative aliquot that guarantees a random distribution of crystallographic orientations. Another reason to prepare a random distribution of orientations is that the probing volume is also a function of the 2θ angle. At lower 2θ angles the penetration is small but covers a wide lateral space. The opposite is given at higher 2θ angles (Fig. A.3b).

A.1.2 XRD on selected samples from PALEOVAN cores

Samples were grinded in vibrating agate-disc-mills to homogeneous grain sizes < 65 μm. The powders were carefully brushed on Si sample holders. Two samples were mixed with 0.003% NH3 and centrifuged over night. A pipet load of the sample dispersion was placed on an Si sample holder. Adherent paste was spread evenly over the slide and dried for a couple of hours (minimum two). Measurements were conducted on a Panalalytical Empyran Series 2 at the University of Postdam. The diffractormeter employs a Cu Kα_1 radiation that is separated by a primary monochromator crystal and detected by a scintillation counter. The machine scans in a $2\theta/\omega$ mode with a rotating single sample holder. Data acquisition is available for 0.5° to 140° of 2θ. The first 15° are scanned in an ω scanning mode due to the sample rotation system (Fig. A.4). The HighScore Plus software managed instrument operation and data evaluation. The software employed the ICDD, ICSD, PDF2, and COD databases for mineral phase identification.

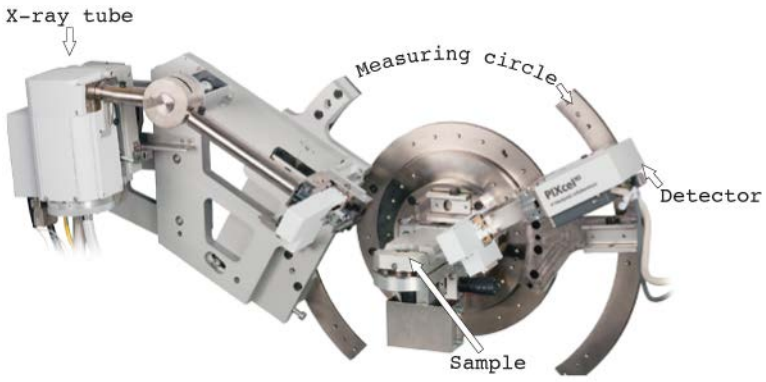

Figure A.4: Instrumental configuration of the Empyrean. The rotating parts are represented by the primary and secondary optics. Photograph taken from Panalytical (2009).

A.2 Electron backscatter diffraction (EBSD)

Electron diffraction provides a way to spatially discriminate measurements of crystallographic orientation. Zoned anorthoclase crystals in the given study were analysed with EMPA line scans across the zoning interfaces. To distinguish between compositional zoning, trace element zoning, and twinning in fractured anorthoclase crystals sporadic EBSD measurements were conducted at the GFZ Potsdam. The calculation of Ba diffusion couples in chapter 8 furthermore requires a verification that observed zoning of Ba content is not a result of changing crystallographic orientation, which are observed in voluminous sub-grains (e.g. 50 % of the host crystal) that typically develop from deformation (Prior et al., 1999; McLaren and Reddy, 2008; Parsons et al., 2015). The following two chapters briefly explain the theory of EBSD using electron beam devices and the application of the method on samples from V-45 at the GFZ Potsdam. The majority of the following theory about the EBSD method bases on and refers to the work of Prior et al. (1999) and Prior et al. (2009).

A.2.1 EBSD in theory

Early literature refers the EBSD technique also as electron backscatter patterns (EBSP) (Day, 1993) or "backscatter kickuchi diffraction". Prior et al. (1999) defined that EBSD refers to the actual diffraction technique and that EBSP refers to individual diffraction patterns. The given thesis adopts these definitions. Diffraction of electrons in EBSD is in theory identical to the diffraction that is employed in transmission electron microscopy (TEM) that first gave rise to the characteristic kikuchi lines (Nishikawa and Kikuchi, 1928). We assume that electrons radiate from a source that represents the incident beam on a tilted sample surface (Fig. A.5a). It is possible to illustrate in two dimensions (Figs. A.5b and A.5c) that the interaction of an incident electron beam with a crystallographic lattice will result in commonly four main trajectories that satisfy Bragg's condition for diffraction on any of the crystals lattice planes (Eq. 3.33).

Treating the electron trajectories that will satisfy the Bragg conditions in three dimensions, highlights that each lattice plane generates two diffraction cones (Fig. A.5a). Detecting the cones on a screen (e.g. phosphor screen) results in a network of bands, which are the so-called kikuchi

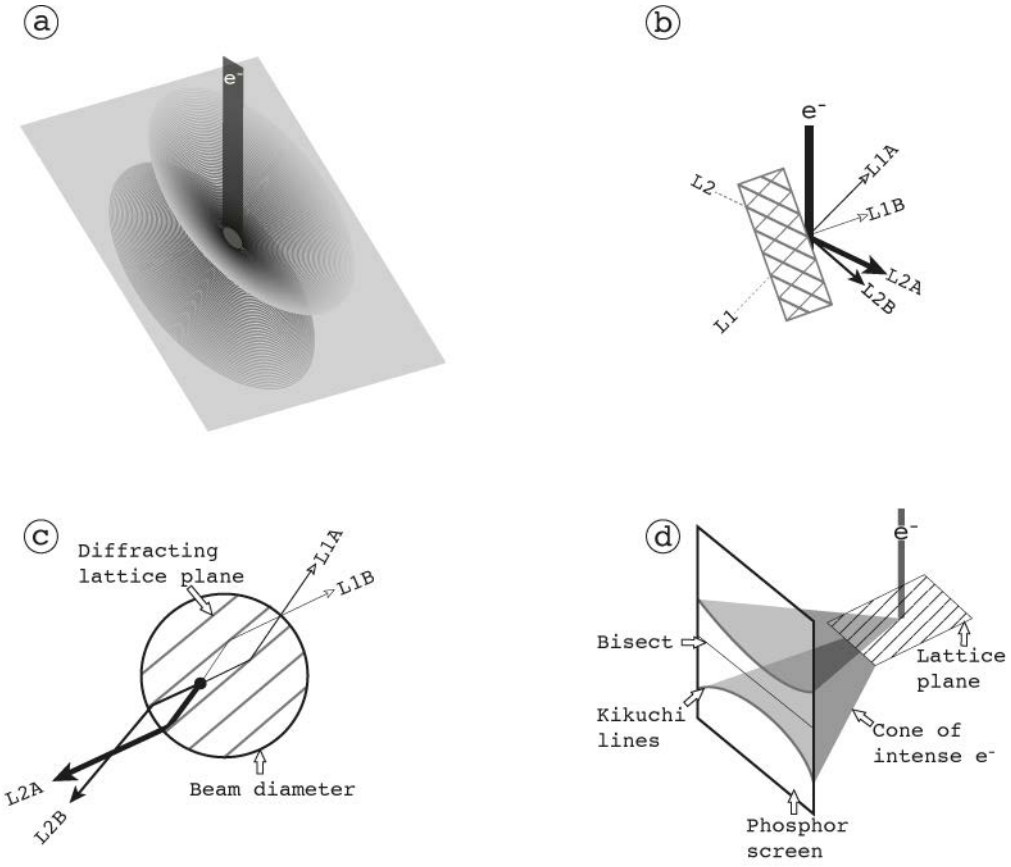

Figure A.5: Sketches illustrating electron beams interacting with a tilted sample surface or lattice planes. (a) Single order diffraction cones radiating from a lattice plane in three dimensions. The grey plane represents a lattice plane. (b) Polished surface of a sample, incident electron beam and cones of intense refraction (L1A, L2A, L2A, L2B) in an idealized two-dimensional view. The example offers two sets of lattice planes. Four trajectories are illustrated that follow Bragg's diffraction condition of $\sin\theta = n\lambda/2d$. Trajectory width is proportional to relative signal intensity and dependent on primary intensity. (c) Two-dimensional top-view of an incident electron-beam on a sample surface. In this example, a single set of lattice planes gives rise to diffraction in a randomly chosen spot within the impacting beam. (d) Idealized segments of single order diffraction cones. The cones can be detected with phosphor screens or typical electron microscope films. The figure is drawn after Prior et al. (1999).

lines. They represent the conic intersection of originally two diffraction cones that are associated with any of the lattice's planes. The bisector of such a pair of cones is identical to a projection of the diffracting lattice plane on to the screen (Fig. A.5d). Diffractions of higher orders (n in Eq. 3.33) will produce multiple bands on a screen (Fig. 2). The bands have width ratios that correspond to the diffraction order. The lowest order diffraction will thus appear brightest and least wide on the screen. Bands interfere positively and high numbers of intersecting bands will produce bright spots in the kikuchi-line-patterns (Fig. A.6). A high number of intersecting bands may cause bright spots, although the individual participating bands are of low intensities and probably hardly visible on a screen (Fig. A.6b). However, the interplay of the bright spots together with the most intense kikuchi lines allows defining symmetry elements from the EBSP. Thus EBSP represent the basis for analyses of crystallographic orientation using EBSD. Reconsideration of the electron beam and sample interactions that are described in chapter 3.2, highlights that backscatter electrons penetrate the sample first before escaping it and appear as a number of elastic scattering events.

The sample-beam interaction affects the final kikuchi-line-patterns in two ways. (i) BSE

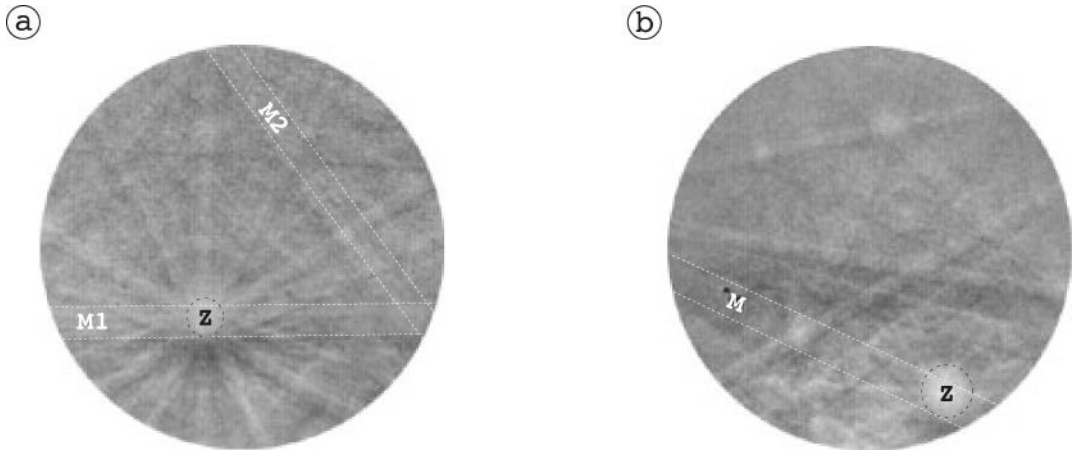

Figure A.6: (a) A background-subtracted EBSP from an albite. In this example a minimum of three lattice planes gave rise to diffraction of orders >1. Diffraction is visible as multiple bands (exemplarily highlighted as M1 and M2). The bright spot that is labeled with 'z' is the intersection of various bands and is the projection of the feldspar's zone axis [001] or the axis of highest crystallographic symmetry. (b) EBSP from garnet. Note that none of the bands crossing the zone axis in 'z' are particularly bright. The mirror plane is represented in M and runs diagonally through the zone axis. Both EBSPs have been taken from Prior et al. (1999).

and SE have a series of energies that range from E_0 (the beam's energy) to zero. Lower energy electrons will contribute to light emission of phosphor and cause a continuous polychromatic source. For any possible spacing of d (lattice distance parameter in the Bragg equation) these polychromatic energy corresponds to a range of Bragg angels and causes an indistinct background signal that needs to be subtracted from finally interpreted pattern. (ii) The excitation volume in the sample is considerably larger than the diameter of the focused beam. Thus the excitation volume blurs the diffraction bands on the screen and limits the spatial volume of the EBSD technique. About 68 % of all BSE are deduced from penetration depths that are < 1 μm, when analyzing with beam settings that are common for EBSD studies on silicates. However, the advent of field emission guns (FEG) to SEM techniques had also a benefit to the EBSD technique. Humphreys et al. (1999) showed for example that different EBSPs could be distinguished that were derived from differently orientated aluminum alloys within 100 nm.

Another way to get qualitative information about the crystallographic orientation is the detection of so-called 'forescatter electrons' and the interpretation of orientation contrast (OC) images. OC imaging is typically realised with usual solid-state detectors, which are also employed for the detection of backscattered electrons in EMPA and SEM (Prior et al., 1996). The difference to the usual BSE detection is their position in a forward-scattering position (Day, 1993) that is in a high angle relative to both the polished sample surface and to the incident electron beam. OC imaging is fairly often co-employed in detecting EBSD patterns and will be reviewed in more detail later. However, the principle in OC imaging indicates that backscattering of electrons potentially provides information about the crystallographic orientation of the solid. The control of the lattice on the intensity of detected BSE is described as the 'channelling' effect (Wilkinson and Hirsch, 1997). It describes the orientation of the strongest diffracting lattice planes, which define BSE trajectories within the sample by channelling-in and channelling-out mechanisms of the incident electrons. The OC signal is an order of magnitude less dominant than the contrast in average atomic number. OC imaging is thus rather applicable to monomineralic samples. Contrasts that are observed in polyphase materials cannot be untangled from

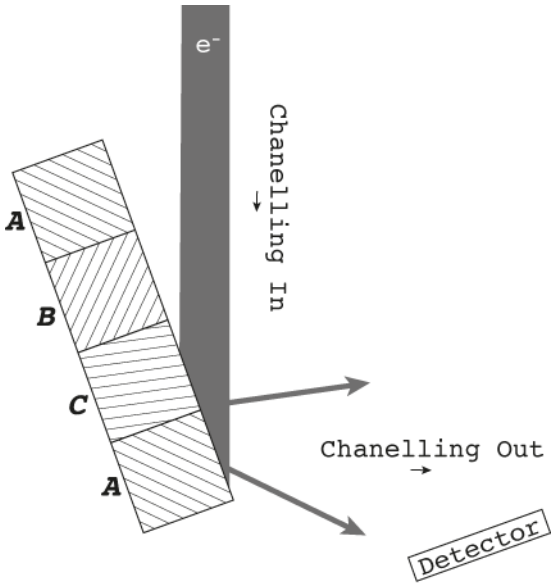

Figure A.7: Sketch showing an electron beam (e^-) in interaction with a tilted specimen. The specimen is made of three crystallographic domains (A, B, C). The lines within the domains indicate a two-dimensional orientation of dominantly diffracting lattice planes. Those lattice planes that would intersect in continuation with the solid-state detector will appear brighter in an OC image (domain A) than those not intersecting (domain B and C). Actual physical processes are more complex and the concept of 'channelling' remains descriptive. The figure is drawn after Prior et al. (1999).

contrasts that are derived from OC within a single phase. Fig. A.7 illustrates the simple concept of the channelling. However, it need to be stated that the actual physical processes are more complex than illustrated in this theory. The approximate concept of the channelling effect can be understood by careful OC-imaging in three ways: (i) spatially distinct domains with different orientation might have identical signal intensities; (ii) spatially distinct domains with identical orientation might have different signal intensities; (iii) differently orientated domains might be invisible in OC imaging.

A typical design of a sample chamber in a SEM is sketched in Fig. 4. The illustration highlights the importance of the distance between phosphor screen and sample surface (DD in Fig. A.8). The hardware set-up is usually in a spatial competition with forescatter detectors. However, the closer the phosphor screen is positioned to the sample and the incident electron beam, the larger is the angular range of the EBSP and the better is the detection of the actual crystallographic orientation. Operators need to balance these analytical advantages with the risk of sample and screen colliding, distortion of the EBSP, and larger angular errors (Prior et al., 1996; Randle and Caul, 1996; Prior et al., 1999). As mentioned above, EBSPs come with a polychromatic background component that varies in dependence to the BSE intensities that are in turn dependent to the dominant scatter angle of the electrons. There are two common modes to correct for the background component: (i) each pixel is subtracted by the average signal of all surrounding pixels; (ii) averaging the signal from a larger number of domains (or crystals) with widened beams or beams in a scanning mode. The first approach mentioned is commonly preferred as it allows estimating the background for each particular EBSP. Background correction improves significantly the resolution of the EBSP and is a sensitive and important proceeding in interpreting EBSD from natural silicates (Prior et al., 1999). Another important factor in the practical use of EBSD is the calculation of the solid angles between the planes involved in projecting kikuchi bands on the phosphor screen. Therefore the position of the source point needs

to be determined relative to the position on the screen. This is achieved by adjusting a pattern centre (PC in Fig. A.8) and the detection distance (DD in Fig. A.8). The common calibration method is to calculate the ideal PC and DD by collecting EBSPs from a known material in a known orientation (in this study is has been polished Fe alloys, but also cleaved Si is frequently used). Several calibration steps follow a first initial calibration. Each calibration uses a different material. This approach considers that an exact repetition of the standard and sample source points is technically impossible. Multiple calibrations of PC and DD are usually averaged and re-calibrating is conducted in reasonable intervals. Calculating the crystallographic orientation of a source point is usually achieved by indexing EBSP of known materials with a known crystallographic orientation. The positions and orientation of kikuchi lines of the unknown are then measured relative to the PC. Algorithms finally calculate the possible orientations of the analysed crystal, by iteratively matching observed planes to a set of lattice planes of the expected material (Schmidt and Olesen, 1989). The bandwidths provide furthermore an information about the distances between lattice planes involved. The actual indexing of the crystallographic orientation thus requires the following information: (i) unit-cell lattice parameters; (ii) the crystal symmetry, (iii) a list of lattice planes that give rise to reflection and thus to visible bands in an EBSP. The first two requirements are available for virtually all known minerals. The third one is more problematic. Any crystal structure will come up with a very large number of potential reflectors. Processing all or the most of the available reflectors will slow down the indexing process (sensitive step for orientation mapping) and overestimates errors. In contrast, a small number of reflectors could be a hurdle in finding the correct or any solution at all. Therefore, the EBSD operator chooses from a list of available reflectors that is presented in an order of decreasing intensity. After experimentation with different intensity cut-offs the precision and the speed of the orientation indexing can be optimized to the analytical needs. Kinematic models dominantly represent the expected reflector list (Schmidt and Olesen, 1989). These base on atomic scattering factors and site-occupancy data. Some minerals, such as albite, lack ideal reflector characterization files that are derived from kinematic modelling. Empirical approaches were needed to develop reflector characterization (Prior and Wheeler, 1999). The quality in the indexing of the patterns is usually achieved by comparing modelled (or empirically determined) patterns with observed patterns and by calculating a goodness of fit. The ideal goodness of fit (=1) would indicate that all modelled bands also occur in the observed EBSP. A more detailed discussion for error source and errors estimation exceeds the aim of the given study and can be found in Prior et al. (1999) and Prior et al. (2009).

EBSD data is usually obtained on a predetermined grid of points, on a line transect of points, or on a wide range of points that cover specific domains that were detected in OC imaging. Applying these systematic EBSD measurements allows examining the orientation relative to observed microstructures, statistical distribution of orientations, and the misorientation between individual EBSD measurements. In summary, the type of the finally gained EBSD data is threefold: (i) distribution of crystallographic orientation in distinct spots; (ii) the distribution of the misorientation; (iii) geometry of phase and grain boundaries. The following section briefly describes these data types but focuses on data type (i) and type (ii) that are relevant information presented in this thesis. The actual orientation measurement is usually termed the 'crystallographic preferred orientation' (CPO). This term clearly treats the orientation measurement as

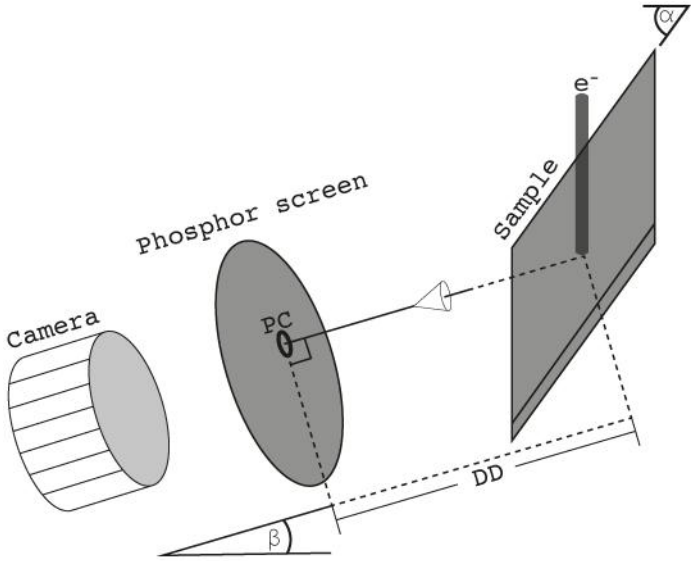

Figure A.8: Instrumental set-up in an EBSD-capable SEM. Specimen inclination (α) and camera inclination (β) are in fixed positions for most hardware configurations. The EBSD calibration requires the deduction of the source point by screening the particular kikuchi pattern center (PC) and adjusting the detector distance. The figure is drawn after Prior et al. (1999).

a to be interpreted in a macroscopic and petrographic context. These CPOs are displayed in pole figures, in which the poles of the lattice planes are plotted on a stereonet relative to reference orientations. An alternative representation type of CPOs is the inverse pole figure, which combines the CPOs with a crystallographic reference axis and uses the symmetrical units of the concerned mineral. Orientation distribution functions allow the representation of individual CPOs as single points in various forms (e.g. Bunge, 1981; Schmid, 1981; Randle and Caul, 1996). Examples are points of distinct orientaions in three-dimensional box diagrams or contour plots of the orientation distribution in pole figures or two-dimensional planes. Spatial variations of the orientations are often colour coded and correspond to Euler angles or predetermined ideal orientations. The term 'misorientation' represents the required rotation of one CPO to match the CPO of another, differently orientated domain or crystal. It is conventional that the misorientation refers to an angle, which accords to a particular axis (Prior et al., 1999; Humphreys, 2001). The theoretically possible amount of angle-axis misorientations that can be calculated from two indexed EBSPs are dependent to the mineral symmetry. Whereas triclinic symmetries have only one solution for misorientation, trigonal crystals offer six solutions, and cubic crystals even 24 solutions. The misorientation angle-axis pairs are often presented relative to their position from line scans. Furthermore the mismatch between a measurement and every other measurement or as randomly selected neighbouring pairs is frequently used. These types of misorientation are called uncorrelated misorientation distributions and represent a measurement of misorientation as a function of CPOs (Fliervoet et al., 1999; Humphreys, 2001). Another and more common way to interpret misorientation data are the correlated distributions. As the data in the given thesis treats a small number of EBSD measurements, correlated distributions were of no use and more detailed literature as in Fliervoet et al. (1997) is recommended for an introduction to the several methods. The bulk physical properties of a monomineralic polycrystalline material are dependent to the boundary network of the individual crystals (Prior et al., 1999). Thus 'selected area electron channelling patterns' are common tools to identify the geometry of grain-

or even phase boundaries in material science. Combined EBSD orientation mapping and OC imaging are tools to support the finding of the traces of boundaries (Prior et al., 1999). Together with three-dimensional focused-ion beam sectioning these techniques offer a wealth of spatial crystallographic information (Matthijs de Winter et al., 2009).

A.2.2 EBSD on anorthoclase from PALEOVAN cores

EBSD samples were feldspars from sample aliquots that were prepared in thin-sections. The thin-sections were polished in several steps with diamond pastes and diamond sprays down to 1 μm of polishing grain size for five to ten minutes. Following immediately after the final polishing step, the samples were rinsed in hot water to avoid adherence of polishing material. The final polishing was achieved with a soft cloth and an alkaline solution of colloidal silica (Fynn and Powell, 1988) for two hours. EBSD data was collected at the GFZ Potsdam using an FEI-Quanta 3-D SEM that is equipped with a field emission gun. An EDAX-TSL Digiview IV EBSD detector recorded the EBSPs that were interpreted using the TSL OIM 5.31 software. Uncoated samples were analysed with a 15 kV accelerating voltage and a 8 nA beam current. The working or detector distance was set to be 12 mm and the sample tilt was adjusted to be 70°. EBSP were indexed as triclinic albite, which is the crystallographically closest reference to the analysed anorthoclase (Parsons, 2010). Confidence indices that exceeded a value of 0.2 were treated as valid measurements. Measurements of lower indices were discarded. Phase identification and sample orientation was achieved with previously collected EMPA and BSE as well as transmitting light images.

Appendix B: Age model from PCHIP interpolation

This appendix offers interpolated ages for all volcanic ashes labelled with consecutive numbers in the AR composite core.The interpolation applied the PCHIP algorithm from the program Matlab 2013a. It bases on 94 age control points that have been taken from Stockhecke et al. (2014b) and Stockhecke et al. (2016). All age control points are either derived from climate stratigraphic alignment or from the alignment of minima in the record relative paleointensity of the Earth's magnetic field. Uncertainties presented in Stockhecke et al. (2014b) and Stockhecke et al. (2016) have been assumed to represent one standard deviation. Uncertainties given in this thesis represent two standard deviations and are derived from linear interpolation of the uncertainties of the next lower and the next upper available age control point. Age control points that are stratigraphically lower than 147 mcblf have not been assigned with uncertainties in Stockhecke et al. (2014b) and Stockhecke et al. (2016). These age control points have been assigned with uncertainties by extrapolating uncertainties linearly.

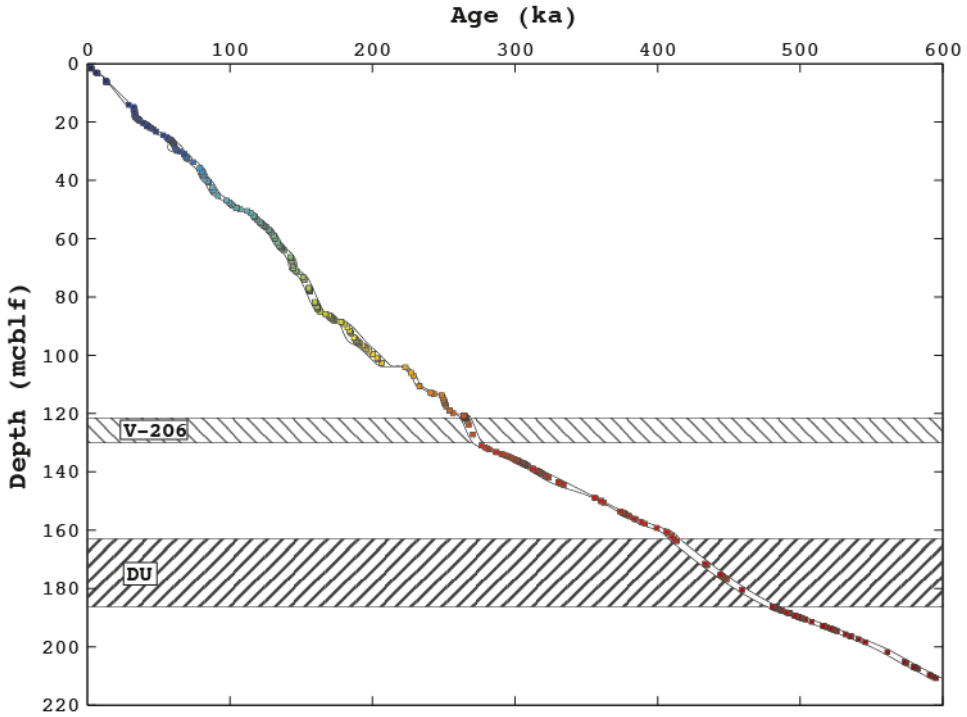

Figure B.1: Age versus depth plot showing modelled ages of volcaniclastic layers in the AR composite core.

Table B.1: Model ages for all volcaniclastic layers in the AR composite core from PHCHIP interpolation. Rounding is systematic and follows the recommendation from Taylor (1997).

Tephra ID (V−№)	Top depth (mcblf)	Bottom depth (mcblf)	Age (ka)	± Age (ka)	Tephra ID (V−№)	Top depth (mcblf)	Bottom depth (mcblf)	Age (ka)	± Age (ka)	Tephra ID (V−№)	Top depth (mcblf)	Bottom depth (mcblf)	Age (ka)	± Age (ka)
2	1.393	1.395	2.19	0.04	44	26.314	26.339	58.8	2.5	86	54.840	54.850	122.2	2.2
3a	1.583	1.653	2.76	0.05	45	26.624	26.719	59.6	2.7	87	55.055	55.060	122.7	2.2
3b	1.726	1.742	3.06	0.06	46	26.866	26.880	59.8	2.9	88	55.400	55.401	123.5	2.3
4	2.903	2.915	6.01	0.12	47	26.944	26.979	60.0	3.0	88	55.401	55.406	123.5	2.3
5	3.255	3.260	6.90	0.14	48	27.128	27.148	60.1	3.3	89	55.781	55.786	124.5	2.4
6	3.345	3.350	7.20	0.14	49	27.548	27.558	60.6	3.8	90a	56.046	56.056	125.1	2.4
8	5.848	5.850	12.72	0.27	50	27.638	27.658	60.6	3.9	90b	56.141	56.151	125.4	2.5
9	5.933	5.939	12.83	0.27	51	27.918	28.518	61.1	4.7	91	56.965	56.970	127.2	2.7
10	5.988	6.023	12.96	0.28	51	28.518	29.115	61.7	5.2	91	56.970	57.017	127.3	2.7
11	6.120	6.123	13.2	0.3	52a	29.612	29.627	62.5	5.2	92	57.327	57.337	127.9	2.7
12	6.138	6.139	13.3	0.3	52b	29.915	29.922	62.9	4.6	93	57.859	57.869	128.9	2.8
13	6.148	6.149	13.3	0.3	53	30.102	30.142	65.4	1.5	94	59.100	59.108	130.7	2.8
14	6.160	6.173	13.3	0.3	54	30.892	30.909	67.7	0.3	95	59.113	59.120	130.8	2.8
15	6.195	6.196	13.4	0.3	55	30.929	30.939	67.8	0.5	96	59.918	59.921	131.7	2.8
16	6.420	6.422	14.2	0.3	56	31.894	31.909	70	3	97	59.923	59.928	131.7	2.8
17	14.071	14.103	29.0	1.8	57a	32.274	32.284	70	3	98	61.564	61.569	133.5	2.7
18a	14.788	14.893	32.5	2.3	57b	32.345	32.717	70	3	99	62.100	62.106	134.2	2.7
18a	14.893	15.635	32.7	2.3	58	33.708	33.903	74	3	100	62.470	62.505	134.8	2.7
18a	15.635	16.243	32.9	2.3	59	35.775	35.855	79	3	101	62.700	62.745	135.2	2.7
18a	16.243	17.360	33.1	2.4	60	36.896	36.923	80	3	102	62.763	62.773	135.3	2.7
18a	17.360	17.790	33.4	2.4	60	36.923	36.961	80	3	103	63.197	63.202	136.2	2.7
18a	17.790	17.837	33.4	2.4	60	36.961	37.824	81	3	104	63.290	63.302	136.4	2.7
18a	17.837	17.967	33.5	2.4	60	37.824	38.196	81	3	105	63.312	63.322	136.4	2.7
18b	17.997	18.017	33.5	2.4	60	38.196	39.103	82	3	106	63.592	63.643	137.1	2.7
19	18.087	18.095	33.6	2.4	61	39.638	39.648	83	3	107	64.065	64.090	138.2	2.8
20	18.132	18.157	33.6	2.4	62	40.316	40.322	84	3	108	66.322	66.405	142.3	2.9
21	18.289	18.291	33.7	2.4	63a	40.497	40.504	85	3	109	66.482	66.522	142.5	2.9
22	18.582	18.597	34.4	2.5	63b	40.536	40.537	85	3	110	66.752	66.778	142.8	2.9
23	18.958	18.971	35.7	2.7	64	42.403	42.638	87	3	110	66.778	66.793	142.8	2.9
24	18.987	18.990	35.7	2.7	65	43.175	43.522	88	3	111	67.618	67.678	143.6	3.0
25	19.232	19.237	36.2	2.7	66	44.012	44.022	89	3	111	67.678	68.548	143.8	3.0
26	19.449	19.477	36.7	2.8	67	45.237	45.257	92	3	111	68.548	68.649	144.0	3.0
27	20.248	20.260	39	4	68	46.896	46.916	97.8	2.8	111	68.649	69.989	144.3	3.0
28	20.411	20.448	40	4	69	47.596	47.614	99.7	2.9	111	69.989	70.047	144.5	3.0
29	21.298	21.308	41.8	3.0	70	48.281	48.341	101.0	2.9	112	70.047	70.067	144.6	3.0
30	21.328	21.343	41.9	2.9	71	48.667	48.702	102	3	112	70.067	70.159	144.6	3.0
30	21.343	21.410	42.0	2.8	72	49.432	49.472	104	3	113	70.383	70.458	144.8	2.9
31	21.430	21.440	42.2	2.6	73	49.534	49.564	105	3	114	71.078	71.178	146.2	2.9
32	21.563	21.570	42.9	2.0	74	49.919	49.969	107	3	115	71.462	71.482	147.2	2.9
33	21.930	21.940	44.1	1.7	75	50.484	50.599	112	3	116a	73.199	73.204	151.2	2.9
34	22.072	22.075	44.6	1.8	76	51.311	51.321	114.8	2.8	116b	73.264	73.274	151.3	2.9
35	22.452	22.455	46.1	1.9	77	52.150	52.175	116.6	2.5	117a	73.955	73.957	152.3	2.9
36	23.276	23.306	48.1	2.0	78	52.455	52.475	117.2	2.4	117b	74.132	74.147	152.5	2.9
37	24.569	24.573	53.2	2.2	79	52.585	52.590	117.5	2.4	118	76.931	76.941	155.3	3.0
38	25.143	25.153	55.6	2.4	80	52.785	52.843	117.9	2.3	119	76.956	76.981	155.3	3.0
39	25.618	25.633	56.4	2.4	81	53.297	53.482	119.0	2.2	120	77.381	77.399	155.7	3.0
40	25.760	25.762	56.7	2.4	82	53.642	53.662	119.5	2.2	121	77.404	77.434	155.7	3.0
41	25.928	25.933	57.2	2.5	83	54.212	54.268	120.8	2.1	122	77.694	77.774	156.0	3.0
42	26.120	26.128	57.9	2.5	84	54.655	54.715	121.8	2.1	123	77.874	77.964	156.1	3.0
43	26.236	26.269	58.6	2.5	85	54.760	54.800	122.0	2.1	124	77.994	78.034	156.2	3.0

Table B.2: Model ages for all volcaniclastic layers in the AR composite core from PHCHIP interpolation. Rounding is systematic and follows the recommendation from Taylor (1997).

Tephra ID (V−№)	Top depth (mcblf)	Bottom depth (mcblf)	Age (ka)	± Age (ka)	Tephra ID (V−№)	Top depth (mcblf)	Bottom depth (mcblf)	Age (ka)	± Age (ka)	Tephra ID (V−№)	Top depth (mcblf)	Bottom depth (mcblf)	Age (ka)	± Age (ka)
125	78.134	78.144	156.3	3.0	164b	95.705	95.755	190	6	201c	121.169	121.219	265	4
126	81.762	81.772	159.6	2.9	165	95.775	95.805	191	6	201d	121.234	121.239	265	4
127	81.987	81.992	159.8	2.9	166	95.935	96.130	191	6	202a	121.249	121.329	265	4
127	81.992	82.001	159.8	2.9	167a	96.574	96.724	193	5	202b	121.354	121.376	265	4
128	82.223	82.448	160.1	2.9	167b	96.792	96.798	194	5	203	121.389	121.479	265	4
129	83.243	83.288	161.1	2.9	168	97.224	97.234	195	5	204a	121.529	121.539	265	4
129	83.288	83.305	161.2	2.9	169	97.767	97.811	196	5	204b	121.539	121.574	265	4
130	83.415	83.445	161.3	2.9	170	98.486	98.498	198	5	205a	121.574	121.589	265	4
131	83.730	83.740	161.6	2.9	171	99.553	99.563	200	4	205b	121.589	121.623	265	4
132	83.795	83.815	161.7	2.9	171	99.563	99.580	200	4	206	121.623	122.213	266	4
133	83.900	83.905	161.7	2.9	172a	101.038	101.043	203	4	206	122.213	123.422	267	4
134	84.053	84.055	161.9	2.9	172b	101.477	101.498	204	4	206	123.422	124.292	268	4
135	84.109	84.111	162.0	2.9	172b	101.498	101.508	204	4	206	124.292	130.072	270	3
136a	85.204	85.239	163.6	2.9	173	102.625	102.640	206	4	207	130.962	130.975	276	3
136b	85.851	85.853	167	3	174a	102.655	102.675	206	4	208	131.582	131.592	279	3
136c	86.014	86.020	168	3	174b	104.140	104.153	223.1	1.8	209a	131.742	132.217	280	3
137	86.244	86.294	169	4	175	105.960	105.980	227.0	1.6	209b	132.308	132.315	282	3
138a	86.324	86.344	170	4	176	106.870	107.220	228.7	1.6	210a	133.172	133.232	286.6	2.7
138b	86.419	86.444	170	4	177	110.549	110.579	233.0	1.6	210b	133.271	133.286	287.0	2.7
138c	86.584	86.604	170	4	178	110.614	110.654	233.1	1.6	211	133.886	133.916	290.6	2.5
139a	86.879	86.914	171	4	179	112.686	112.707	240.6	1.5	212	134.036	134.121	291.6	2.4
139b	86.994	87.044	171	4	180	112.961	113.126	241.8	1.6	213	134.401	134.411	293.4	2.4
140	87.084	87.104	171	4	181	113.222	113.282	243.2	1.7	214	134.571	134.591	294.4	2.4
141	87.184	87.199	171	4	182	113.662	113.682	248.5	2.0	215	134.651	134.671	294.8	2.4
142	87.314	87.329	172	4	183a	114.428	114.463	249.3	1.8	216	134.886	134.908	296.0	2.4
143	87.394	87.404	172	4	183b	115.251	115.253	250.0	1.6	217a	135.213	135.243	297.6	2.4
144	87.564	87.619	172	4	184	115.253	115.716	250.1	1.6	217b	135.657	135.662	299.5	2.5
145	87.764	87.784	172	4	185	115.853	115.873	250.4	1.5	217c	135.748	135.778	300.0	2.5
146	87.909	87.934	173	4	186	116.293	116.333	250.7	1.4	217b	135.980	135.983	300.9	2.6
147	88.094	88.108	173	4	187	116.445	116.475	250.8	1.4	217c	136.130	136.136	301.6	2.7
147	88.108	88.178	173	4	189a	116.970	117.000	251.2	1.3	217d	136.145	136.148	301.6	2.7
148	88.556	88.576	178	3	189b	117.626	117.636	251.8	1.2	217e	136.318	136.323	302.4	2.7
149	88.636	88.656	178	3	189c	118.831	118.833	253.9	0.9	218	136.338	136.373	302.5	2.8
150	88.876	89.666	180	3	189d	118.848	118.850	253.9	0.9	218b	136.413	136.423	302.8	2.8
150	89.666	91.372	182	4	190	118.883	118.898	254.0	0.9	219	136.438	136.461	302.9	2.8
151	91.476	91.626	184	5	191a	118.943	118.963	254.1	1.0	220	136.628	136.758	303.9	2.9
152	91.646	91.676	184	5	191b	119.010	119.012	254.3	1.0	221a	136.828	136.878	304.6	3.0
153	91.701	91.776	184	5	192	119.058	119.086	254.4	1.0	221b	136.925	136.928	305	3
154a	91.851	91.876	184	5	193	119.819	119.824	256.5	1.3	221c	137.081	137.098	305	3
154b	92.146	92.176	185	5	194	120.709	120.714	264	4	221d	137.145	137.150	306	3
155	92.446	92.466	185	5	195	120.734	120.744	264	4	221e	137.165	137.168	306	3
156	93.900	93.950	187	6	196	120.816	120.827	264	4	222a	137.255	137.275	306	3
157	94.000	94.010	187	6	197	120.844	120.856	264	4	222b	137.427	137.435	307	3
158	94.219	94.314	188	6	198	120.899	120.927	265	4	223	137.530	137.605	307	3
159	94.810	94.830	188	6	199a	120.932	120.957	265	4	224	137.615	137.795	308	3
160	94.850	94.860	189	6	199b	120.979	121.009	265	4	225	137.825	138.100	309	4
161	94.915	94.925	189	6	200a	121.049	121.064	265	4	226	138.942	138.962	313	4
162	95.025	95.035	189	6	200b	121.095	121.102	265	4	226	138.962	138.982	313	4
163	95.295	95.305	189	6	201a	121.121	121.139	265	4	227	139.532	139.592	315	4
164a	95.427	95.430	190	6	201b	121.157	121.163	265	4	227	139.592	139.642	315	4

Table B.3: Model ages for all volcaniclastic layers in the AR composite core from PHCHIP interpolation. Rounding is systematic and follows the recommendation from Taylor (1997).

Tephra ID (V−№)	Top depth (mcblf)	Bottom depth (mcblf)	Age (ka)	± Age (ka)	Tephra ID (V−№)	Top depth (mcblf)	Bottom depth (mcblf)	Age (ka)	± Age (ka)
228	139.832	139.902	316	4	269c	186.427	186.437	482	4
229	140.117	140.147	317	5	269d	186.502	186.512	482	4
230a	140.159	140.189	317	5	269e	186.582	186.587	482	4
230b	140.316	140.319	318	5	269	186.629	186.649	482	4
231a	140.479	140.504	318	5	270	186.812	186.837	483	4
231b	140.548	140.551	319	5	271a	186.912	186.922	484	4
232	141.054	141.354	321	5	271b	186.965	186.970	484	4
232	141.354	141.494	322	5	272a	187.053	187.064	485	4
233	141.908	141.968	324	5	272b	187.410	187.430	486	4
234	143.533	143.560	330	5	272c	187.447	187.450	487	4
235	143.643	143.668	331	5	272d	187.577	187.593	487	4
236	144.084	144.089	332	5	273	188.157	188.167	490	4
237	144.499	144.549	334	5	274	188.465	188.470	492	4
238	148.847	148.873	355.71	1.10	275a	188.515	188.520	492	4
239	149.080	149.090	356.66	1.04	275b	188.590	188.600	493	4
240	150.002	150.009	360.39	0.95	275c	188.640	188.645	493	4
240a	150.009	150.016	360.42	0.95	275d	188.677	188.684	493	4
240b	150.506	150.511	362.34	0.99	276	189.210	189.240	496	4
241	153.553	153.563	373.87	2.00	277a	189.415	189.440	497	4
242a	153.623	153.643	374.1	2.0	277b	189.729	189.742	499	4
242b	153.925	153.933	375.2	2.2	277c	189.765	189.770	499	4
242c	154.118	154.137	376.0	2.3	277d	189.934	189.942	500	4
243	154.215	154.225	376.4	2.3	277e	190.144	190.147	501	4
244	154.295	154.305	376.7	2.4	277f	190.209	190.222	501	4
245	154.522	154.527	377.5	2.5	278	190.432	190.839	504	4
246	154.557	154.567	377.7	2.5	279	191.269	191.521	508	4
247a	154.877	154.887	378.9	2.7	280	192.753	192.808	516	4
247b	155.247	155.267	380.3	2.8	281	192.948	193.073	517	4
248	156.082	156.164	384	3	282	193.208	193.338	519	4
248	156.164	156.494	385	3	283	193.733	193.834	521	4
249	157.194	157.444	389	4	283	193.834	193.929	522	4
250	157.834	157.859	391	4	283	193.929	194.179	523	4
251	159.231	159.276	399	4	283	194.179	194.281	524	4
252	160.526	160.556	406	4	284	194.536	194.541	526	4
253	160.974	161.031	408	4	285	195.661	195.779	532	4
254	161.524	162.417	410	4	286	196.308	196.358	535	4
255	162.944	162.964	412	4	287	196.468	196.498	536	4
256	163.644	163.664	413	4	288	197.423	197.453	541	4
257	163.684	163.694	413	4	289	198.324	198.464	546	4
258	171.481	171.501	433	4	290	201.830	201.880	561	4
259	171.691	171.716	434	4	291	205.148	205.163	573	4
260	171.826	171.846	434	4	292	205.508	205.533	575	4
261	172.022	172.032	435	4	293	206.865	206.880	580	4
262	175.294	175.349	444	4	294	207.010	207.025	580	4
263	175.424	175.469	444	4	295	207.090	207.100	581	4
264	175.793	175.823	445	4	295	207.100	207.460	581	4
265	176.093	176.128	446	4	296	207.540	207.667	583	4
266	176.478	176.508	447	4	297	209.707	209.717	591	4
267	176.893	176.923	448	4	298	209.752	210.067	592	4
268	180.429	180.459	459	4	299	210.197	210.507	594	4
269a	186.197	186.202	480	4	300	211.506	211.696	595	4
269b	186.277	186.287	481	4					

Appendix C: Ar Isotope Data: Lake Van Samples

The following appendix provides relative Ar isotope abundances of all total fusion and stepwise measurements on sample material of unknown age. Raw intensities were interpolated as described in chapter 3 using the ArArCALC software (e.g. Fig. C.1). The data shown here is blank- and decay corrected and from ArArCALC output files called 'relative isotope abundances'. Inverse isochron raw data is also presented together with apparent $^{40}Ar/^{39}Ar$ ages and J-values.

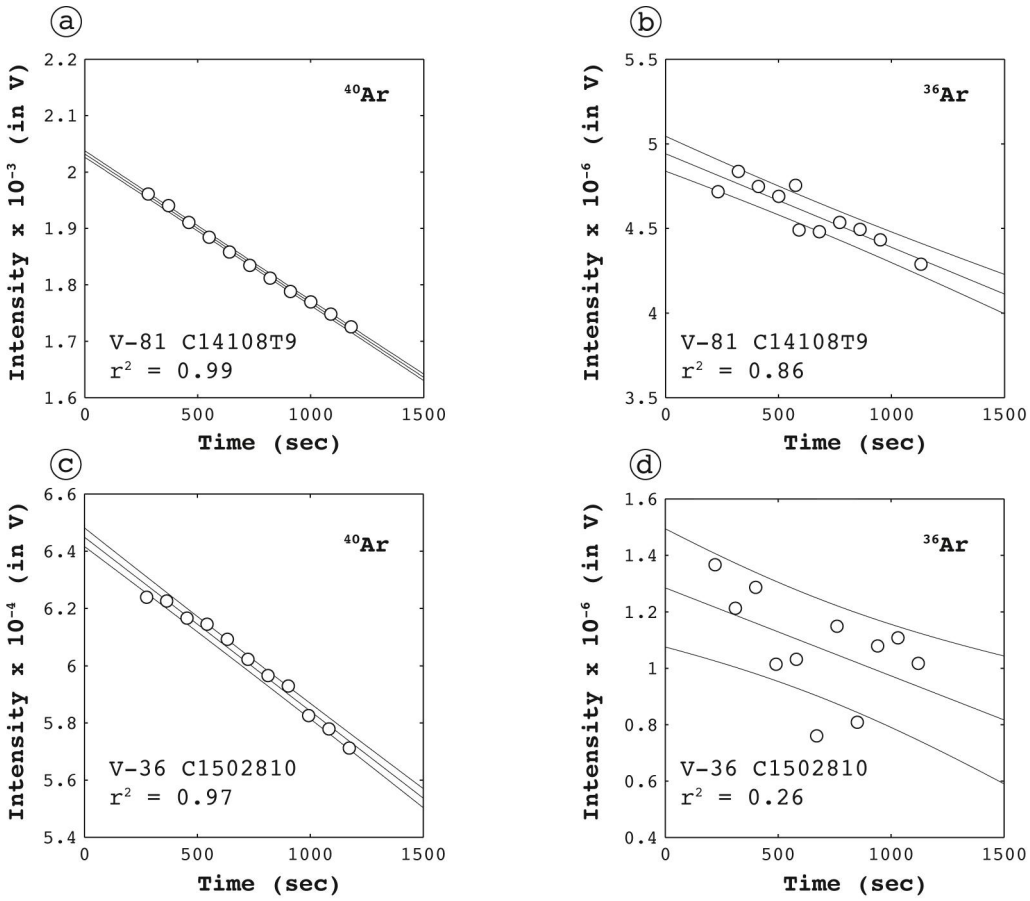

Figure C.1: Exemplaric ^{40}Ar and ^{36}Ar isotope raw intensities and linear regressions for calculations of intercept values (initial intensities at time = 0). a) High-intensity ^{40}Ar signal from MGTF analyses. b) High-intensity ^{36}Ar signal from MGTF analyses. c) Low-intensity ^{40}Ar signal from MGTF analyses. d) Low-intensity ^{36}Ar signal from MGTF analyses. Central lines represent linear regressions, outer lines error envelopes.

Table C.1: Ion beam intensities (in V) from **feldspar total fusion** of V-45 and V-65.

Measurement	^{36}Ar	$\pm$ ^{36}Ar	^{37}Ar	$\pm$ ^{37}Ar	^{38}Ar	$\pm$ ^{38}Ar	^{39}Ar	$\pm$ ^{39}Ar	^{40}Ar	$\pm$ ^{40}Ar	$^{40}Ar^*/^{39}Ar_K$	$\pm^{40}Ar^*/^{39}Ar_K$	$\%^{40}Ar^*$
V-45 #20													
C14113T1	3.28E-07	7.21E-08	3.97E-04	5.62E-06	9.83E-06	1.79E-07	8.58E-04	2.81E-06	8.81E-05	8.18E-07	2.41E-02	1.21E-05	2.35E+01
C14113T2	2.72E-07	4.05E-08	2.48E-04	4.10E-06	1.08E-05	1.73E-07	9.64E-04	3.27E-06	7.98E-05	4.09E-07	1.83E-02	4.60E-06	2.21E+01
C14113T3	1.34E-07	1.34E-07	3.59E-04	7.34E-06	9.54E-06	1.49E-07	8.26E-04	2.67E-06	7.02E-05	5.66E-07	7.00E-02	6.76E-05	8.24E+01
C14113T4	7.60E-07	1.61E-07	7.80E-04	1.35E-05	2.24E-05	2.68E-07	1.90E-03	7.99E-06	2.42E-04	7.02E-07	3.95E-02	2.00E-05	3.10E+01
V-45 #30													
C1411210	1.17E-06	6.49E-08	1.15E-03	1.31E-05	4.27E-05	6.71E-07	3.51E-03	1.21E-05	4.38E-04	1.25E-06	5.03E-02	5.61E-06	4.03E+01
C1411211	2.55E-06	1.25E-07	7.20E-04	1.15E-05	3.15E-05	4.41E-07	2.64E-03	8.99E-06	8.44E-04	1.77E-06	5.23E-02	1.48E-05	1.64E+01
C1411212	2.96E-07	1.18E-07	6.68E-04	9.22E-06	3.47E-05	3.32E-07	2.90E-03	1.05E-05	1.98E-04	6.56E-07	5.52E-02	1.34E-05	8.09E+01
C1411213	4.50E-06	2.16E-07	7.84E-04	1.22E-05	5.98E-05	5.99E-07	4.92E-03	1.60E-05	1.48E-03	2.64E-06	3.95E-02	1.04E-05	1.31E+01
C1411214	2.02E-06	1.08E-07	1.39E-03	1.92E-05	4.98E-05	3.87E-07	4.12E-03	1.54E-05	6.54E-04	1.22E-06	3.84E-02	6.06E-06	2.42E+01
C1411215	7.29E-07	1.53E-07	9.96E-04	1.60E-05	5.34E-05	6.63E-07	4.27E-03	2.41E-05	3.31E-04	2.75E-06	4.43E-02	9.51E-06	5.71E+01
C14112T1	1.01E-05	2.43E-07	9.51E-04	1.10E-05	4.78E-05	5.70E-07	3.95E-03	1.21E-05	3.11E-03	3.48E-06	3.99E-02	1.47E-05	5.06E+00
C14112T2	5.30E-06	1.59E-07	1.11E-03	1.46E-05	5.33E-05	6.33E-07	4.40E-03	1.52E-05	1.70E-03	2.16E-06	4.65E-02	1.00E-05	1.20E+01
C14112T3	2.64E-07	4.26E-08	7.03E-04	1.08E-05	2.51E-05	2.51E-07	2.16E-03	7.99E-06	1.45E-04	8.60E-07	5.57E-02	6.64E-06	8.28E+01
C14112T4	3.88E-06	2.05E-07	1.09E-03	1.53E-05	4.35E-05	5.86E-07	3.58E-03	1.36E-05	1.25E-03	1.99E-06	4.91E-02	1.68E-05	1.40E+01
C14112T5	2.36E-06	2.05E-07	9.83E-04	1.31E-05	4.17E-05	4.01E-07	3.50E-03	1.29E-05	7.66E-04	1.50E-06	3.91E-02	1.37E-05	1.79E+01
C14112T6	1.64E-05	2.52E-07	9.57E-04	1.18E-05	4.76E-05	5.19E-07	3.57E-03	1.63E-05	4.97E-03	1.85E-05	3.98E-02	1.73E-05	2.86E+00
C14112T7	7.64E-07	1.50E-07	5.20E-04	8.89E-06	2.60E-05	2.85E-07	2.15E-03	8.68E-06	3.04E-04	9.91E-07	5.38E-02	2.24E-05	3.80E+01
C14112T8	1.50E-06	5.75E-08	1.02E-03	1.23E-05	5.13E-05	5.15E-07	4.33E-03	1.60E-05	5.73E-04	1.72E-06	4.67E-02	3.77E-06	3.52E+01
C14112T9	1.43E-06	1.05E-07	8.49E-04	9.65E-06	3.31E-05	3.92E-07	2.65E-03	8.67E-06	5.03E-04	1.25E-06	5.33E-02	1.26E-05	2.81E+01
V-65 #20													
C1411110	3.85E-06	1.80E-07	3.05E-04	3.41E-06	6.26E-05	5.48E-07	5.13E-03	2.71E-05	1.50E-03	7.66E-06	7.15E-02	1.52E-05	2.45E+01
C1411111	1.18E-05	5.54E-07	3.43E-04	7.45E-06	9.61E-05	7.60E-07	7.84E-03	2.43E-05	3.86E-03	2.86E-06	4.52E-02	1.91E-05	9.18E+00
C1411112	4.65E-06	1.72E-07	4.88E-04	1.01E-05	3.98E-05	4.54E-07	3.29E-03	1.15E-05	1.60E-03	3.50E-06	7.51E-02	2.35E-05	1.55E+01
C1411113	2.21E-05	3.28E-07	4.35E-04	6.22E-06	6.08E-05	5.43E-07	4.78E-03	1.55E-05	6.74E-03	5.96E-06	3.50E-02	1.44E-05	2.48E+00
C1411114	2.05E-05	4.54E-07	3.35E-04	7.05E-06	7.37E-05	7.16E-07	5.88E-03	1.94E-05	6.52E-03	6.27E-06	7.30E-02	3.37E-05	6.59E+00
C1411115	1.39E-06	1.13E-07	2.65E-04	4.56E-06	5.82E-05	5.08E-07	4.92E-03	1.76E-05	6.83E-04	1.62E-06	5.83E-02	8.01E-06	4.20E+01
C14111T1	1.54E-06	2.30E-07	3.50E-04	4.58E-06	3.11E-05	4.26E-07	2.64E-03	9.38E-06	6.02E-04	1.61E-06	6.33E-02	3.29E-05	2.78E+01
C14111T2	1.24E-06	9.06E-08	2.01E-04	4.08E-06	5.48E-05	6.01E-07	4.63E-03	1.59E-05	6.55E-04	1.46E-06	6.42E-02	7.54E-06	4.54E+01
C14111T3	1.91E-06	1.48E-07	3.57E-04	7.49E-06	3.22E-05	2.98E-07	2.72E-03	9.00E-06	6.91E-04	1.83E-06	5.37E-02	1.74E-05	2.11E+01
C14111T4	9.91E-06	2.45E-07	2.91E-04	6.24E-06	2.43E-05	3.30E-07	1.94E-03	6.15E-06	3.06E-03	4.43E-06	6.45E-02	4.87E-05	4.08E+00
C14111T5	4.24E-05	5.27E-07	2.85E-04	5.71E-06	9.58E-05	7.93E-07	7.27E-03	2.46E-05	1.32E-02	1.42E-05	7.66E-02	3.34E-05	4.22E+00
C14111T6	1.43E-05	4.17E-07	5.25E-04	7.05E-06	1.00E-04	6.83E-07	7.90E-03	3.17E-05	4.72E-03	1.12E-05	6.38E-02	2.02E-05	1.07E+01
C14111T7	3.27E-07	5.62E-08	3.87E-05	2.53E-06	3.21E-05	6.08E-07	2.82E-03	9.51E-06	2.22E-04	7.66E-07	4.43E-02	5.29E-06	5.64E+01
C14111T8	1.40E-06	1.07E-07	2.18E-04	5.49E-06	4.79E-05	4.65E-07	4.14E-03	1.32E-05	6.88E-04	1.49E-06	6.90E-02	1.07E-05	4.15E+01
C14111T9	1.36E-05	3.97E-07	1.66E-04	4.24E-06	1.08E-04	8.63E-07	8.81E-03	2.72E-05	4.41E-03	4.94E-06	4.00E-02	1.08E-05	8.00E+00
V-65 #30													
C14110T1	5.68E-05	7.11E-07	2.59E-04	4.06E-06	1.14E-04	7.74E-07	8.58E-03	4.01E-05	1.74E-02	6.18E-05	5.45E-02	2.82E-05	2.68E+00
C14110T3	3.23E-05	4.42E-07	4.02E-04	6.61E-06	9.56E-05	8.74E-07	7.53E-03	2.38E-05	1.02E-02	8.51E-06	7.50E-02	2.64E-05	5.55E+00
C14110T4	3.23E-05	4.42E-07	4.02E-04	6.61E-06	9.56E-05	8.74E-07	7.53E-03	2.38E-05	1.02E-02	8.51E-06	7.50E-02	2.64E-05	5.55E+00
C14110T5	7.39E-06	1.86E-07	3.15E-04	7.55E-06	8.50E-05	6.32E-07	6.99E-03	2.15E-05	2.71E-03	2.68E-06	7.51E-02	1.20E-05	1.94E+01
C14110TR	5.26E-05	6.42E-07	1.34E-04	3.73E-06	2.63E-05	3.06E-07	1.33E-03	6.94E-06	1.56E-02	7.06E-05	-1.13E-01	-3.47E-04	-9.61E-01

Table C.2: Inverse isochron data and apparent ages from **feldspar total fusion** measurements of V-45 and V-65.

Measurement	J	± J	Age (ka)	± Age (ka)	$^{39}Ar/^{40}Ar$	± $^{39}Ar/^{40}Ar$	$^{36}Ar/^{40}Ar$	± $^{36}Ar/^{40}Ar$	ρ
V-279V-45 #20									
C14113T1	9.76E-04	9.08E-06	43	90	9.80	0.21	2.56E-03	1.65E-03	0.0300
C14113T2	9.76E-04	9.08E-06	33	45	12.17	0.19	2.60E-03	1.02E-03	0.0330
C14113T3	9.76E-04	9.08E-06	125	173	11.87	0.24	5.69E-04	3.84E-03	0.0027
C14113T4	9.76E-04	9.08E-06	71	91	7.88	0.10	2.31E-03	1.34E-03	0.0108
V-279V-45 #30									
C1411210	9.78E-04	9.39E-06	90	20	8.05	0.09	1.99E-03	3.00E-04	0.0457
C1411211	9.78E-04	9.39E-06	94	51	3.13	0.03	2.80E-03	2.96E-04	0.0273
C1411212	9.78E-04	9.39E-06	99	44	14.79	0.23	6.14E-04	1.20E-03	0.0063
C1411213	9.78E-04	9.39E-06	71	47	3.33	0.03	2.91E-03	2.92E-04	0.0255
C1411214	9.78E-04	9.39E-06	69	28	6.32	0.06	2.54E-03	3.33E-04	0.0317
C1411215	9.78E-04	9.39E-06	79	38	13.01	0.30	1.42E-03	9.33E-04	0.0263
C14112T1	9.78E-04	9.39E-06	71	66	1.27	0.01	3.18E-03	1.57E-04	0.0187
C14112T2	9.78E-04	9.39E-06	83	39	2.59	0.02	2.95E-03	1.87E-04	0.0225
C14112T3	9.78E-04	9.39E-06	100	21	15.01	0.28	5.48E-04	5.96E-04	0.0145
C14112T4	9.78E-04	9.39E-06	88	61	2.87	0.02	2.88E-03	3.29E-04	0.0161
C14112T5	9.78E-04	9.39E-06	70	63	4.58	0.04	2.75E-03	5.36E-04	0.0165
C14112T6	9.78E-04	9.39E-06	71	78	0.72	0.01	3.25E-03	1.04E-04	0.1471
C14112T7	9.78E-04	9.39E-06	96	75	7.10	0.08	2.07E-03	9.92E-04	0.0135
C14112T8	9.78E-04	9.39E-06	84	14	7.58	0.09	2.16E-03	2.04E-04	0.0700
C14112T9	9.78E-04	9.39E-06	95	42	5.30	0.05	2.40E-03	4.19E-04	0.0270
V-279V-65 #20									
C1411110	9.84E-04	7.04E-06	129	38	3.43	0.05	2.53E-03	2.43E-04	0.0785
C1411111	9.84E-04	7.04E-06	81	76	2.03	0.01	3.04E-03	2.88E-04	0.0080
C1411112	9.84E-04	7.04E-06	135	56	2.06	0.02	2.83E-03	2.16E-04	0.0343
C1411113	9.84E-04	7.04E-06	63	74	0.71	0.00	3.27E-03	9.76E-05	0.0173
C1411114	9.84E-04	7.04E-06	132	83	0.90	0.01	3.13E-03	1.39E-04	0.0138
C1411115	9.84E-04	7.04E-06	105	25	7.24	0.08	1.94E-03	3.32E-04	0.0324
C14111T1	9.84E-04	7.04E-06	114	94	4.40	0.04	2.42E-03	7.65E-04	0.0137
C14111T2	9.84E-04	7.04E-06	116	21	7.10	0.07	1.82E-03	2.79E-04	0.0352
C14111T3	9.84E-04	7.04E-06	97	58	3.95	0.04	2.64E-03	4.29E-04	0.0263
C14111T4	9.84E-04	7.04E-06	116	136	0.63	0.00	3.21E-03	1.60E-04	0.0248
C14111T5	9.84E-04	7.04E-06	138	78	0.55	0.00	3.21E-03	8.01E-05	0.0272
C14111T6	9.84E-04	7.04E-06	115	57	1.67	0.02	2.99E-03	1.77E-04	0.0438
C14111T7	9.84E-04	7.04E-06	80	22	12.84	0.18	1.44E-03	5.12E-04	0.0315
C14111T8	9.84E-04	7.04E-06	124	28	6.04	0.06	1.95E-03	3.13E-04	0.0297
C14111T9	9.84E-04	7.04E-06	72	49	2.00	0.01	3.08E-03	1.81E-04	0.0195
V-279V-65 #30									
C14110T1	9.89E-04	6.93E-06	99	94	0.49	0.01	3.26E-03	8.50E-05	0.1654
C14110T3	9.89E-04	6.93E-06	136	64	0.74	0.00	3.16E-03	8.71E-05	0.0176
C14110T4	9.89E-04	6.93E-06	136	64	0.74	0.00	3.16E-03	8.71E-05	0.0176
C14110T5	9.89E-04	6.93E-06	136	29	2.58	0.02	2.70E-03	1.38E-04	0.0242
C14110TR	9.89E-04	6.93E-06	-204	559	0.09	0.00	3.38E-03	8.80E-05	0.2289

Table C.3: Ion beam intensities (in V) from **feldspar total fusion** of V-81 and V-111.

Measurement	^{36}Ar	$\pm$ ^{36}Ar	^{37}Ar	$\pm$ ^{37}Ar	^{38}Ar	$\pm$ ^{38}Ar	^{39}Ar	$\pm$ ^{39}Ar	^{40}Ar	$\pm$ ^{40}Ar	$^{40}Ar^*/^{39}Ar_K$	$\pm^{40}Ar^*/^{39}Ar_K$	$\%^{40}Ar^*$
V-81 #20													
C14109T1	6.74E-06	1.40E-07	5.56E-06	2.41E-06	2.71E-05	3.78E-07	2.25E-03	7.46E-06	2.15E-03	5.43E-06	6.21E-02	2.33E-05	6.49E+00
C14109T2	1.34E-05	2.40E-07	9.72E-06	2.50E-06	5.68E-05	4.37E-07	4.56E-03	1.42E-05	4.34E-03	4.49E-06	7.52E-02	2.38E-05	7.90E+00
C14109T3	2.29E-05	3.28E-07	2.80E-05	2.19E-06	6.15E-05	6.80E-07	4.71E-03	1.46E-05	7.12E-03	7.04E-06	5.96E-02	2.49E-05	3.94E+00
V-81 #30													
C1410810	5.13E-06	1.32E-07	3.26E-05	2.15E-06	9.80E-05	7.93E-07	8.20E-03	2.50E-05	2.16E-03	2.61E-06	7.66E-02	7.44E-06	2.91E+01
C1410811	1.14E-05	2.29E-07	8.76E-05	2.74E-06	9.66E-05	7.68E-07	7.94E-03	2.46E-05	4.00E-03	3.31E-06	7.46E-02	1.29E-05	1.48E+01
C1410812	4.74E-05	6.52E-07	2.50E-05	2.46E-06	8.40E-05	6.66E-07	6.28E-03	2.08E-05	1.49E-02	1.23E-05	1.21E-01	7.53E-05	5.10E+00
C1410813	1.50E-05	2.26E-07	1.16E-04	3.44E-06	9.81E-05	7.99E-07	7.95E-03	2.42E-05	5.05E-03	5.02E-06	7.09E-02	1.21E-05	1.12E+01
C1410814	7.21E-06	1.58E-07	2.13E-05	1.72E-06	9.37E-05	6.85E-07	7.67E-03	2.39E-05	2.77E-03	2.04E-06	8.05E-02	9.93E-06	2.23E+01
C1410816	7.10E-07	1.14E-07	6.54E-05	3.40E-06	8.22E-05	7.06E-07	6.92E-03	2.14E-05	7.33E-04	1.25E-06	7.54E-02	7.47E-06	7.12E+01
C14108T1	7.54E-06	1.62E-07	3.07E-05	2.83E-06	1.12E-04	7.75E-07	9.19E-03	2.85E-05	2.98E-03	3.39E-06	7.94E-02	8.44E-06	2.44E+01
C14108T2	7.69E-06	1.39E-07	2.89E-05	2.12E-06	9.49E-05	7.41E-07	7.84E-03	2.43E-05	2.86E-03	2.50E-06	7.16E-02	7.67E-06	1.96E+01
C14108T3	1.87E-05	2.89E-07	2.00E-05	2.07E-06	7.71E-05	5.61E-07	6.08E-03	1.89E-05	6.17E-03	5.42E-06	9.87E-02	2.82E-05	9.71E+00
C14108T4	8.34E-06	1.90E-07	2.18E-05	2.73E-06	7.71E-05	7.58E-07	6.30E-03	1.93E-05	3.02E-03	2.86E-06	8.30E-02	1.50E-05	1.73E+01
C14108T6	3.18E-06	9.54E-08	2.50E-05	2.48E-06	1.01E-04	8.07E-07	8.47E-03	2.65E-05	1.59E-03	1.90E-06	7.49E-02	5.10E-06	3.99E+01
C14108T7	1.99E-05	4.48E-07	5.08E-05	1.83E-06	9.03E-05	7.81E-07	7.19E-03	2.23E-05	6.56E-03	7.89E-06	8.44E-02	3.15E-05	9.25E+00
C14108T8	1.60E-06	1.12E-07	4.61E-05	2.40E-06	8.95E-05	7.98E-07	7.58E-03	2.39E-05	1.01E-03	1.35E-06	7.05E-02	6.28E-06	5.27E+01
C14108T9	4.46E-06	9.41E-08	2.50E-05	2.81E-06	1.12E-04	9.89E-07	9.32E-03	2.84E-05	2.02E-03	1.63E-06	7.35E-02	4.50E-06	3.39E+01
V-111 #20													
C1410710	4.80E-06	1.85E-07	6.26E-04	9.91E-06	7.59E-05	6.36E-07	6.26E-03	1.92E-05	2.01E-03	1.69E-06	9.97E-02	1.77E-05	3.10E+01
C1410711	9.40E-07	8.66E-08	4.39E-04	7.47E-06	8.80E-05	9.24E-07	7.33E-03	2.25E-05	9.31E-04	1.57E-06	9.28E-02	6.63E-06	7.30E+01
C1410712	1.85E-06	8.03E-08	2.69E-04	5.68E-06	1.10E-04	8.95E-07	9.20E-03	2.79E-05	1.42E-03	1.76E-06	9.57E-02	5.09E-06	6.20E+01
C1410713	9.89E-06	2.20E-07	6.65E-04	7.77E-06	1.78E-04	1.47E-06	1.49E-02	4.50E-05	4.39E-03	3.51E-06	9.91E-02	8.81E-06	3.36E+01
C14107T1	2.25E-06	8.07E-08	3.15E-04	5.50E-06	7.78E-05	6.31E-07	6.55E-03	2.13E-05	1.30E-03	1.23E-06	9.97E-02	7.43E-06	5.01E+01
C14107T2	1.23E-05	2.14E-07	7.11E-04	8.87E-06	1.25E-04	1.20E-06	1.03E-02	3.17E-05	4.59E-03	4.83E-06	9.29E-02	1.16E-05	2.09E+01
C14107T3	1.80E-06	9.09E-08	6.83E-05	3.66E-06	1.28E-05	2.60E-07	1.14E-03	4.01E-06	7.24E-04	1.47E-06	1.68E-01	8.02E-05	2.63E+01
C14107T4	1.96E-05	3.76E-07	1.12E-03	1.67E-05	1.58E-04	1.37E-06	1.30E-02	3.92E-05	7.14E-03	5.57E-06	1.05E-01	1.83E-05	1.91E+01
C14107T5	5.55E-06	1.63E-07	4.15E-04	6.26E-06	1.11E-04	7.53E-07	9.20E-03	2.88E-05	2.45E-03	1.43E-06	8.92E-02	9.49E-06	3.35E+01
C14107T6	4.88E-06	1.53E-07	6.09E-04	7.37E-06	1.08E-04	8.95E-07	8.95E-03	2.77E-05	2.24E-03	2.75E-06	9.22E-02	9.46E-06	3.68E+01
C14107T7	1.84E-06	1.25E-07	6.51E-04	9.49E-06	9.98E-05	8.15E-07	8.26E-03	2.66E-05	1.30E-03	1.52E-06	9.68E-02	8.85E-06	6.13E+01
C14107T8	1.12E-05	2.33E-07	3.90E-04	8.12E-06	9.23E-05	8.42E-07	7.53E-03	2.32E-05	4.04E-03	4.56E-06	9.63E-02	1.79E-05	1.79E+01
C14107T9	1.63E-05	2.35E-07	4.65E-04	6.20E-06	1.18E-04	8.72E-07	9.63E-03	2.96E-05	5.72E-03	6.56E-06	9.26E-02	1.36E-05	1.56E+01
V-111 #30													
C14106T1	1.72E-05	2.62E-07	6.31E-04	8.83E-06	1.50E-04	1.12E-06	1.24E-02	3.78E-05	6.38E-03	6.24E-06	1.04E-01	1.33E-05	2.03E+01
C14106T2	2.12E-05	3.60E-07	6.09E-04	8.75E-06	1.41E-04	1.22E-06	1.15E-02	3.59E-05	7.48E-03	7.03E-06	1.02E-01	1.92E-05	1.57E+01
V-111 #45													
C14105T1	1.17E-05	2.37E-07	4.12E-04	6.85E-06	9.74E-05	1.06E-06	7.86E-03	2.85E-05	4.21E-03	1.08E-05	9.59E-02	1.75E-05	1.79E+01
C14105T2	4.76E-06	2.07E-07	3.73E-04	6.11E-06	9.11E-05	6.84E-07	7.45E-03	2.61E-05	2.07E-03	4.54E-06	8.97E-02	1.50E-05	3.23E+01
C14105T3	1.28E-06	7.16E-08	2.90E-04	5.54E-06	7.76E-05	6.79E-07	6.30E-03	2.41E-05	9.35E-04	2.22E-06	9.06E-02	6.26E-06	6.11E+01
C14105T4	1.03E-05	2.48E-07	3.73E-04	6.66E-06	7.76E-05	6.36E-07	6.26E-03	1.96E-05	3.65E-03	4.47E-06	9.73E-02	2.31E-05	1.67E+01
V-111B #20													
C14104T1	1.45E-05	2.19E-07	1.98E-04	3.49E-06	6.24E-05	4.74E-07	5.06E-03	1.55E-05	4.87E-03	3.85E-06	1.09E-01	2.83E-05	1.13E+01
C14104T2	1.34E-05	2.69E-07	3.87E-04	5.02E-06	9.12E-05	7.56E-07	7.43E-03	2.29E-05	4.72E-03	4.34E-06	9.86E-02	2.14E-05	1.55E+01
V-111B #30													
C14103T1	4.64E-06	1.24E-07	3.43E-04	6.78E-06	1.10E-04	1.00E-06	9.08E-03	2.75E-05	2.14E-03	1.75E-06	8.52E-02	6.99E-06	3.62E+01
C14103T2	6.36E-06	1.16E-07	4.93E-04	7.12E-06	1.47E-04	1.22E-06	1.24E-02	3.76E-05	2.96E-03	3.32E-06	8.86E-02	5.08E-06	3.70E+01
C14103T3	1.84E-05	2.74E-07	4.22E-04	7.83E-06	1.07E-04	8.80E-07	8.74E-03	2.66E-05	6.12E-03	3.77E-06	7.55E-02	1.42E-05	1.08E+01
C14103T4	7.19E-05	9.24E-07	5.87E-04	8.82E-06	1.45E-04	1.24E-06	1.11E-02	3.50E-05	2.31E-02	2.58E-05	1.49E-01	7.47E-05	7.13E+00
C14103T5	5.50E-05	7.88E-07	5.59E-04	8.20E-06	1.71E-04	1.57E-06	1.38E-02	4.17E-05	1.81E-02	6.75E-06	1.22E-01	4.18E-05	9.35E+00
C14103T6	1.67E-05	3.20E-07	3.22E-04	5.36E-06	1.09E-04	9.56E-07	8.86E-03	2.78E-05	5.92E-03	5.83E-06	1.07E-01	2.32E-05	1.61E+01
C14103T7	6.61E-06	1.12E-07	4.53E-04	6.08E-06	1.12E-04	9.87E-07	9.43E-03	2.86E-05	2.82E-03	3.68E-06	9.24E-02	6.70E-06	3.09E+01
V-111B #45													
C14102T1	6.30E-06	1.31E-07	3.74E-04	7.09E-06	1.02E-04	8.60E-07	8.46E-03	2.56E-05	2.69E-03	1.84E-06	9.82E-02	9.15E-06	3.09E+01
C14102T2	5.42E-06	1.43E-07	1.77E-04	2.97E-06	5.55E-05	6.91E-07	4.61E-03	1.52E-05	2.03E-03	3.71E-06	9.20E-02	1.71E-05	2.09E+01

Table C.4: Inverse isochron data and apparent ages from **feldspar total fusion** measurements of V-81 and V-111.

Measurement	J	± J	Age (ka)	± Age (ka)	$^{39}Ar/^{40}Ar$	± $^{39}Ar/^{40}Ar$	$^{36}Ar/^{40}Ar$	± $^{36}Ar/^{40}Ar$	ρ
V-81 #20									
C14109T1	9.91E-04	7.63E-06	113	68	1.05	0.01	3.13E-03	1.31E-04	0.0749
C14109T2	9.91E-04	7.63E-06	136	57	1.05	0.01	3.08E-03	1.11E-04	0.0212
C14109T3	9.91E-04	7.63E-06	108	76	0.66	0.00	3.22E-03	9.24E-05	0.0225
V-81 #30									
C1410810	9.67E-04	1.00E-05	136	17	3.80	0.03	2.37E-03	1.23E-04	0.0414
C1410811	9.67E-04	1.00E-05	132	31	1.99	0.01	2.85E-03	1.15E-04	0.0203
C1410812	9.67E-04	1.00E-05	214	110	0.42	0.00	3.18E-03	8.77E-05	0.0151
C1410813	9.67E-04	1.00E-05	126	30	1.58	0.01	2.97E-03	8.99E-05	0.0285
C1410814	9.67E-04	1.00E-05	142	22	2.77	0.02	2.60E-03	1.14E-04	0.0247
C1410816	9.67E-04	1.00E-05	133	18	9.49	0.10	9.51E-04	3.13E-04	0.0209
C14108T1	9.67E-04	1.00E-05	140	19	3.09	0.02	2.53E-03	1.09E-04	0.0379
C14108T2	9.67E-04	1.00E-05	127	19	2.75	0.02	2.69E-03	9.80E-05	0.0328
C14108T3	9.67E-04	1.00E-05	175	51	0.99	0.01	3.02E-03	9.40E-05	0.0185
C14108T4	9.67E-04	1.00E-05	147	32	2.09	0.01	2.77E-03	1.27E-04	0.0216
C14108T6	9.67E-04	1.00E-05	133	12	5.35	0.04	2.01E-03	1.21E-04	0.0519
C14108T7	9.67E-04	1.00E-05	149	66	1.10	0.01	3.04E-03	1.37E-04	0.0219
C14108T8	9.67E-04	1.00E-05	125	16	7.52	0.07	1.57E-03	2.23E-04	0.0347
C14108T9	9.67E-04	1.00E-05	130	11	4.63	0.03	2.21E-03	9.39E-05	0.0545
V-111 #20									
C1410710	9.79E-04	8.91E-06	179	32	3.12	0.02	2.31E-03	1.85E-04	0.0171
C1410711	9.79E-04	8.91E-06	166	13	7.91	0.08	8.90E-04	1.87E-04	0.0267
C1410712	9.79E-04	8.91E-06	171	10	6.52	0.06	1.26E-03	1.14E-04	0.0456
C1410713	9.79E-04	8.91E-06	178	16	3.40	0.02	2.22E-03	1.01E-04	0.0334
C14107T1	9.79E-04	8.91E-06	179	13	5.04	0.04	1.67E-03	1.24E-04	0.0349
C14107T2	9.79E-04	8.91E-06	166	22	2.25	0.02	2.65E-03	9.37E-05	0.0329
C14107T3	9.79E-04	8.91E-06	300	86	1.57	0.01	2.47E-03	2.52E-04	0.0217
C14107T4	9.79E-04	8.91E-06	188	31	1.82	0.01	2.71E-03	1.06E-04	0.0187
C14107T5	9.79E-04	8.91E-06	160	19	3.76	0.03	2.22E-03	1.33E-04	0.0257
C14107T6	9.79E-04	8.91E-06	165	18	4.00	0.03	2.11E-03	1.37E-04	0.0350
C14107T7	9.79E-04	8.91E-06	173	16	6.36	0.05	1.29E-03	1.94E-04	0.0253
C14107T8	9.79E-04	8.91E-06	172	33	1.86	0.01	2.75E-03	1.16E-04	0.0262
C14107T9	9.79E-04	8.91E-06	166	26	1.69	0.01	2.83E-03	8.27E-05	0.0366
V-111 #30									
C14106T1	9.86E-04	8.14E-06	189	23	1.95	0.01	2.67E-03	8.25E-05	0.0314
C14106T2	9.86E-04	8.14E-06	185	34	1.54	0.01	2.82E-03	9.67E-05	0.0226
V-111 #45									
C14105T1	9.95E-04	7.41E-06	175	33	1.87	0.02	2.75E-03	1.13E-04	0.0769
C14105T2	9.95E-04	7.41E-06	163	30	3.61	0.03	2.26E-03	2.02E-04	0.0360
C14105T3	9.95E-04	7.41E-06	165	13	6.77	0.07	1.29E-03	1.54E-04	0.0425
C14105T4	9.95E-04	7.41E-06	177	43	1.72	0.01	2.79E-03	1.36E-04	0.0239
V-111B #20									
C14104T1	9.98E-04	7.39E-06	199	47	1.04	0.01	2.97E-03	9.02E-05	0.0167
C14104T2	9.98E-04	7.39E-06	180	40	1.58	0.01	2.83E-03	1.14E-04	0.0191
V-111B #30									
C14103T1	9.98E-04	7.38E-06	156	15	4.26	0.03	2.13E-03	1.16E-04	0.0381
C14103T2	9.98E-04	7.38E-06	162	10	4.18	0.03	2.11E-03	7.91E-05	0.0611
C14103T3	9.98E-04	7.38E-06	138	34	1.43	0.01	2.99E-03	8.98E-05	0.0152
C14103T4	9.98E-04	7.38E-06	272	92	0.48	0.00	3.11E-03	8.04E-05	0.0296
C14103T5	9.98E-04	7.38E-06	223	62	0.76	0.00	3.04E-03	8.72E-05	0.0054
C14103T6	9.98E-04	7.38E-06	196	40	1.50	0.01	2.81E-03	1.08E-04	0.0210
C14103T7	9.98E-04	7.38E-06	169	13	3.36	0.02	2.31E-03	8.05E-05	0.0579
V-111B #45									
C14102T1	1.00E-03	8.82E-06	180	17	3.15	0.02	2.31E-03	9.78E-05	0.0303
C14102T2	1.00E-03	8.82E-06	169	34	2.27	0.02	2.65E-03	1.41E-04	0.0408

Table C.5: Ion beam intensities (in V) from **feldspar total fusion** of V-145 and V-209a.

Measurement	^{36}Ar	$\pm$ ^{36}Ar	^{37}Ar	$\pm$ ^{37}Ar	^{38}Ar	$\pm$ ^{38}Ar	^{39}Ar	$\pm$ ^{39}Ar	^{40}Ar	$\pm$ ^{40}Ar	$^{40}Ar^*/^{39}Ar_K$	$\pm^{40}Ar^*/^{39}Ar_K$	$\%^{40}Ar^*$
V-145 #20													
C14101T1	9.42E-07	8.93E-08	1.15E-05	1.76E-06	3.32E-05	4.65E-07	2.76E-03	9.02E-06	6.01E-04	1.13E-06	1.15E-01	2.23E-05	5.31E+01
C14101T2	5.89E-07	4.89E-08	6.28E-06	1.52E-06	2.00E-05	2.99E-07	1.70E-03	5.17E-06	3.45E-04	4.33E-07	9.90E-02	1.70E-05	4.88E+01
C14101T3	8.24E-07	8.94E-08	9.35E-06	1.23E-06	3.10E-05	3.70E-07	2.60E-03	9.19E-06	5.10E-04	1.20E-06	1.01E-01	2.09E-05	5.16E+01
C14101T4	7.73E-07	1.82E-07	4.02E-05	2.50E-06	3.93E-05	4.75E-07	3.28E-03	1.28E-05	5.37E-04	3.68E-06	9.35E-02	3.11E-05	5.72E+01
C14101T5	1.89E-06	3.00E-07	9.97E-05	2.60E-06	7.30E-05	5.41E-07	6.02E-03	2.51E-05	1.25E-03	5.01E-06	1.15E-01	3.43E-05	5.53E+01
C14101T6	2.13E-06	1.03E-07	1.87E-05	1.62E-06	4.37E-05	4.57E-07	3.57E-03	1.78E-05	1.01E-03	5.57E-06	1.06E-01	1.85E-05	3.73E+01
V-145 #30													
C14100T1	1.41E-06	1.20E-07	4.28E-05	2.65E-06	6.52E-05	6.16E-07	5.32E-03	1.74E-05	8.91E-04	1.56E-06	8.86E-02	1.20E-05	5.29E+01
C14100T2	1.84E-06	8.68E-08	3.75E-05	2.90E-06	8.52E-05	7.78E-07	7.21E-03	2.38E-05	1.22E-03	2.30E-06	9.35E-02	7.11E-06	5.50E+01
C14100T3	1.09E-06	6.28E-08	2.33E-05	1.45E-06	4.51E-05	5.67E-07	3.78E-03	1.23E-05	7.12E-04	1.51E-06	1.02E-01	1.02E-05	5.43E+01
C14100T4	5.74E-05	6.90E-07	3.55E-05	1.26E-06	8.25E-05	7.31E-07	5.93E-03	1.85E-05	1.78E-02	1.36E-05	1.13E-01	7.90E-05	3.76E+00
C14100T5	8.20E-06	1.90E-07	7.57E-05	2.29E-06	5.85E-05	6.13E-07	4.82E-03	1.60E-05	2.98E-03	4.71E-06	1.10E-01	2.61E-05	1.79E+01
V-145 #45													
C14099T1	4.01E-06	1.05E-07	6.62E-05	2.59E-06	9.70E-05	7.97E-07	8.19E-03	2.50E-05	2.11E-03	3.87E-06	1.11E-01	8.63E-06	4.31E+01
V-209a #20													
C1409810	7.63E-07	6.76E-08	1.35E-04	3.59E-06	8.47E-05	8.36E-07	7.18E-03	2.27E-05	1.37E-03	1.51E-06	1.60E-01	9.28E-06	8.38E+01
C1409811	2.63E-06	1.32E-07	7.45E-04	1.00E-05	5.82E-05	6.35E-07	4.87E-03	1.65E-05	1.56E-03	3.04E-06	1.72E-01	2.79E-05	5.34E+01
C1409812	1.65E-06	5.42E-08	7.69E-04	1.08E-05	6.49E-05	5.96E-07	5.46E-03	1.81E-05	1.37E-03	2.06E-06	1.70E-01	1.05E-05	6.82E+01
C1409813	1.55E-06	9.44E-08	2.63E-04	4.66E-06	6.14E-05	5.31E-07	5.17E-03	1.67E-05	1.34E-03	1.75E-06	1.72E-01	1.90E-05	6.67E+01
C1409814	4.13E-05	5.77E-07	8.56E-04	1.20E-05	7.46E-05	6.67E-07	5.64E-03	1.78E-05	1.34E-02	1.39E-05	1.98E-01	1.21E-04	8.33E+00
C1409815	2.62E-06	1.31E-07	3.50E-04	7.26E-06	3.52E-05	4.98E-07	2.94E-03	1.08E-05	1.24E-03	2.47E-06	1.64E-01	4.40E-05	3.90E+01
C14098T1	1.22E-06	8.89E-08	1.95E-04	5.98E-06	3.76E-05	4.45E-07	3.16E-03	1.07E-05	8.80E-04	2.07E-06	1.68E-01	2.83E-05	6.02E+01
C14098T2	9.04E-07	1.08E-07	9.98E-05	3.04E-06	9.35E-05	7.11E-07	7.87E-03	2.41E-05	1.51E-03	2.78E-06	1.58E-01	1.31E-05	8.23E+01
C14098T3	9.12E-07	2.23E-07	8.73E-05	4.35E-06	6.21E-05	5.44E-07	5.26E-03	1.63E-05	1.03E-03	1.42E-06	1.45E-01	3.66E-05	7.39E+01
C14098T4	7.15E-07	6.70E-08	3.81E-04	7.23E-06	3.39E-05	3.92E-07	2.77E-03	8.61E-06	6.23E-04	1.10E-06	1.58E-01	2.29E-05	7.02E+01
C14098T5	3.43E-06	9.42E-08	2.36E-04	4.15E-06	7.96E-05	6.40E-07	6.60E-03	2.09E-05	2.17E-03	2.23E-06	1.76E-01	1.53E-05	5.36E+01
C14098T6	2.23E-06	1.39E-07	3.98E-04	6.92E-06	4.14E-05	4.84E-07	3.41E-03	1.07E-05	1.22E-03	1.57E-06	1.72E-01	4.18E-05	4.79E+01
C14098T7	8.28E-07	1.73E-07	1.22E-04	4.35E-06	1.02E-04	7.67E-07	8.45E-03	2.60E-05	1.55E-03	2.01E-06	1.55E-01	1.90E-05	8.43E+01
C14098T8	8.88E-06	2.25E-07	3.50E-04	5.07E-06	3.63E-05	3.17E-07	2.89E-03	9.91E-06	3.11E-03	4.98E-06	1.68E-01	7.88E-05	1.56E+01
C14098T9	7.17E-07	7.29E-08	3.28E-04	6.05E-06	7.83E-05	7.04E-07	6.60E-03	2.06E-05	1.28E-03	2.22E-06	1.64E-01	1.11E-05	8.49E+01
V-209a #30													
C14097T1	6.71E-06	1.26E-07	6.73E-04	7.71E-06	1.17E-04	1.11E-06	9.86E-03	3.03E-05	3.58E-03	3.64E-06	1.65E-01	1.28E-05	4.54E+01
C14097T2	8.96E-06	1.91E-07	5.93E-04	6.26E-06	9.40E-05	8.98E-07	7.65E-03	2.38E-05	3.95E-03	3.62E-06	1.72E-01	2.58E-05	3.33E+01
C14097T3	5.44E-06	1.64E-07	3.29E-04	6.55E-06	1.03E-04	7.73E-07	8.54E-03	2.63E-05	3.00E-03	3.81E-06	1.64E-01	1.90E-05	4.66E+01
C14097T4	1.93E-06	8.14E-08	5.43E-04	6.21E-06	8.58E-05	7.66E-07	7.17E-03	2.22E-05	1.68E-03	2.18E-06	1.60E-01	1.11E-05	6.80E+01
C14097T5	1.17E-06	1.06E-07	2.61E-04	6.02E-06	7.60E-05	6.26E-07	6.29E-03	1.94E-05	1.29E-03	1.60E-06	1.52E-01	1.55E-05	7.42E+01

Table C.6: Inverse isochron data and apparent ages from **feldspar total fusion** measurements of V-145 and V-209a.

Measurement	J	± J	Age (ka)	± Age (ka)	$^{39}Ar/^{40}Ar$	± $^{39}Ar/^{40}Ar$	$^{36}Ar/^{40}Ar$	± $^{36}Ar/^{40}Ar$	ρ
V-145 #20									
C14101T1	1.00E-03	1.02E-05	212	35	4.61	0.04	1.57E-03	2.98E-04	0.0177
C14101T2	1.00E-03	1.02E-05	182	32	4.95	0.04	1.71E-03	2.84E-04	0.0178
C14101T3	1.00E-03	1.02E-05	186	38	5.11	0.05	1.62E-03	3.52E-04	0.0193
C14101T4	1.00E-03	1.02E-05	172	61	6.14	0.10	1.43E-03	6.82E-04	0.0271
C14101T5	1.00E-03	1.02E-05	211	55	4.83	0.06	1.49E-03	4.81E-04	0.0203
C14101T6	1.00E-03	1.02E-05	194	32	3.53	0.05	2.10E-03	2.04E-04	0.0880
V-145 #30									
C14100T1	9.85E-04	7.98E-06	160	24	6.00	0.05	1.57E-03	2.70E-04	0.0239
C14100T2	9.85E-04	7.98E-06	169	14	5.91	0.15	1.50E-03	1.43E-04	0.0161
C14100T3	9.85E-04	7.98E-06	185	18	5.33	0.05	1.52E-03	1.77E-04	0.0360
C14100T4	9.85E-04	7.98E-06	204	126	0.33	0.00	3.22E-03	7.78E-05	0.0157
C14100T5	9.85E-04	7.98E-06	199	43	1.62	0.01	2.75E-03	1.28E-04	0.0338
V-145 #45									
C14099T1	9.80E-04	7.10E-06	199	14	3.90	0.03	1.90E-03	1.00E-04	0.0578
V-209a #20									
C1409810	9.91E-04	6.32E-06	291	10	5.25	0.04	5.32E-04	9.88E-05	0.0158
C1409811	9.91E-04	6.32E-06	311	30	3.12	0.03	1.56E-03	1.69E-04	0.0243
C1409812	9.91E-04	6.32E-06	309	11	4.01	0.03	1.06E-03	8.00E-05	0.0332
C1409813	9.91E-04	6.32E-06	313	20	3.88	0.03	1.11E-03	1.42E-04	0.0174
C1409814	9.91E-04	6.32E-06	358	111	0.42	0.00	3.07E-03	8.65E-05	0.0238
C1409815	9.91E-04	6.32E-06	298	49	2.38	0.02	2.04E-03	2.13E-04	0.0221
C14098T1	9.91E-04	6.32E-06	304	31	3.60	0.03	1.33E-03	2.03E-04	0.0232
C14098T2	9.91E-04	6.32E-06	287	15	5.22	0.04	5.82E-04	1.43E-04	0.0156
C14098T3	9.91E-04	6.32E-06	263	46	5.12	0.04	8.65E-04	4.34E-04	0.0063
C14098T4	9.91E-04	6.32E-06	286	26	4.46	0.04	9.90E-04	2.16E-04	0.0149
C14098T5	9.91E-04	6.32E-06	320	16	3.04	0.02	1.55E-03	8.70E-05	0.0262
C14098T6	9.91E-04	6.32E-06	311	44	2.80	0.02	1.74E-03	2.27E-04	0.0127
C14098T7	9.91E-04	6.32E-06	280	22	5.47	0.04	5.16E-04	2.24E-04	0.0077
C14098T8	9.91E-04	6.32E-06	305	85	0.93	0.01	2.83E-03	1.45E-04	0.0277
C14098T9	9.91E-04	6.32E-06	298	12	5.19	0.04	4.96E-04	1.15E-04	0.0157
V-209a #30									
C14097T1	9.97E-04	6.18E-06	301	14	2.76	0.02	1.82E-03	7.04E-05	0.0350
C14097T2	9.97E-04	6.18E-06	313	27	1.94	0.01	2.23E-03	9.73E-05	0.0203
C14097T3	9.97E-04	6.18E-06	299	21	2.85	0.02	1.79E-03	1.10E-04	0.0275
C14097T4	9.97E-04	6.18E-06	291	13	4.27	0.03	1.07E-03	9.72E-05	0.0277
C14097T5	9.97E-04	6.18E-06	277	19	4.90	0.04	8.56E-04	1.66E-04	0.0149

Table C.7: Ion beam intensities (in V) from **feldspar total fusion** of V-221a and V-254.

Measurement	^{36}Ar	$\pm$ ^{36}Ar	^{37}Ar	$\pm$ ^{37}Ar	^{38}Ar	$\pm$ ^{38}Ar	^{39}Ar	$\pm$ ^{39}Ar	^{40}Ar	$\pm$ ^{40}Ar	$^{40}Ar^*/^{39}Ar_K$	$\pm^{40}Ar^*/^{39}Ar_K$	$\%^{40}Ar^*$
V-221a #20													
C1409615	3.06E-06	1.56E-07	6.75E-04	8.53E-06	7.61E-05	6.62E-07	6.43E-03	2.08E-05	1.89E-03	3.23E-06	1.60E-01	2.33E-05	5.43E+01
C1409613	1.88E-06	1.99E-07	3.52E-04	6.69E-06	4.78E-05	4.46E-07	4.07E-03	1.45E-05	1.19E-03	2.20E-06	1.60E-01	4.69E-05	5.49E+01
C14096T7	1.22E-06	1.03E-07	5.60E-04	8.98E-06	6.43E-05	5.69E-07	5.50E-03	1.76E-05	1.23E-03	1.86E-06	1.65E-01	1.86E-05	7.38E+01
C14096T6	8.70E-07	3.31E-08	2.94E-04	6.16E-06	4.71E-05	4.95E-07	4.01E-03	1.31E-05	9.13E-04	1.98E-06	1.68E-01	8.78E-06	7.38E+01
C1409612	1.77E-06	1.57E-07	6.04E-04	9.09E-06	5.81E-05	5.79E-07	4.93E-03	1.67E-05	1.32E-03	1.54E-06	1.69E-01	3.23E-05	6.32E+01
C14096T1	1.75E-06	6.93E-08	6.53E-04	8.00E-06	9.71E-05	8.92E-07	8.13E-03	2.47E-05	1.87E-03	1.76E-06	1.72E-01	9.08E-06	7.46E+01
C14096T5	9.47E-06	1.53E-07	1.04E-03	1.34E-05	1.27E-04	9.17E-07	1.05E-02	3.22E-05	4.55E-03	2.43E-06	1.72E-01	1.52E-05	3.95E+01
C1409614	2.35E-06	5.38E-08	4.90E-04	6.77E-06	9.98E-05	8.19E-07	8.33E-03	2.58E-05	2.10E-03	2.65E-06	1.72E-01	7.13E-06	6.82E+01
C14096T8	1.89E-06	1.02E-07	4.49E-04	5.13E-06	5.14E-05	4.94E-07	4.27E-03	1.42E-05	1.28E-03	1.58E-06	1.75E-01	2.50E-05	5.84E+01
C14096T3	2.29E-06	1.26E-07	1.30E-03	1.58E-05	6.34E-05	7.16E-07	5.36E-03	1.76E-05	1.52E-03	2.30E-06	1.76E-01	2.49E-05	6.17E+01
C1409610	1.69E-06	1.49E-07	1.63E-03	1.98E-05	5.30E-05	5.00E-07	4.50E-03	1.47E-05	1.18E-03	1.52E-06	1.78E-01	3.53E-05	6.79E+01
C14096T2	5.45E-06	1.53E-07	7.22E-04	8.35E-06	9.88E-05	7.73E-07	8.30E-03	2.54E-05	3.10E-03	3.80E-06	1.84E-01	2.05E-05	4.92E+01
C1409611	4.99E-06	1.60E-07	3.78E-04	6.11E-06	4.11E-05	5.33E-07	3.35E-03	1.14E-05	2.08E-03	4.02E-06	1.86E-01	5.35E-05	2.98E+01
C14096T9	6.24E-06	1.05E-07	1.21E-03	1.49E-05	5.67E-05	5.94E-07	4.72E-03	1.56E-05	2.65E-03	5.59E-06	1.87E-01	2.54E-05	3.32E+01
C14096T4	3.27E-06	8.03E-08	1.16E-03	1.43E-05	6.62E-05	5.74E-07	5.39E-03	2.88E-05	1.87E-03	7.50E-06	1.82E-01	1.75E-05	5.25E+01
V-221a #30													
C14095T1	6.58E-05	8.66E-07	9.36E-04	1.21E-05	1.48E-04	1.26E-06	1.13E-02	3.61E-05	2.19E-02	2.32E-05	2.08E-01	9.61E-05	1.07E+01
C14095T2	5.58E-06	1.08E-07	8.03E-04	8.80E-06	1.14E-04	9.25E-07	9.52E-03	2.95E-05	3.27E-03	3.33E-06	1.74E-01	1.21E-05	5.08E+01
C14095T3	6.96E-06	1.79E-07	8.65E-04	1.14E-05	9.35E-05	7.72E-07	7.76E-03	2.37E-05	3.32E-03	1.39E-06	1.68E-01	2.34E-05	3.93E+01
C14095T4	4.96E-06	1.42E-07	8.21E-04	9.84E-06	1.25E-04	8.55E-07	1.04E-02	3.25E-05	3.14E-03	2.65E-06	1.65E-01	1.37E-05	5.46E+01
C14095T5	1.06E-05	1.36E-07	9.35E-04	1.17E-05	1.08E-04	1.07E-06	8.79E-03	2.69E-05	4.58E-03	4.88E-06	1.70E-01	1.61E-05	3.27E+01
V-254 #20													
C1409410	2.13E-06	1.15E-07	2.52E-04	3.34E-06	9.21E-05	8.37E-07	7.61E-03	2.36E-05	2.25E-03	2.08E-06	2.14E-01	1.96E-05	7.23E+01
C1409411	6.87E-06	1.31E-07	3.76E-04	5.74E-06	9.60E-05	6.78E-07	7.95E-03	2.41E-05	3.75E-03	3.61E-06	2.17E-01	2.17E-05	4.59E+01
C1409412	3.00E-06	1.30E-07	2.50E-04	4.10E-06	9.87E-05	7.01E-07	8.30E-03	2.53E-05	2.70E-03	2.71E-06	2.19E-01	2.08E-05	6.74E+01
C1409413	2.01E-05	4.11E-07	3.45E-04	6.06E-06	1.26E-04	9.40E-07	1.04E-02	3.15E-05	8.30E-03	5.97E-06	2.22E-01	5.26E-05	2.78E+01
C14094T1	3.47E-06	2.42E-07	2.59E-04	5.82E-06	6.63E-05	6.28E-07	5.55E-03	2.10E-05	2.21E-03	1.82E-06	2.14E-01	5.58E-05	5.38E+01
C14094T2	1.55E-06	1.42E-07	3.02E-04	4.27E-06	5.85E-05	5.21E-07	4.82E-03	1.50E-05	1.51E-03	1.99E-06	2.23E-01	3.95E-05	7.08E+01
C14094T3	1.67E-06	8.23E-08	3.34E-04	6.40E-06	1.01E-04	8.30E-07	8.38E-03	2.52E-05	2.34E-03	2.10E-06	2.22E-01	1.35E-05	7.95E+01
C14094T4	1.33E-06	1.11E-07	1.63E-04	4.01E-06	6.96E-05	6.66E-07	5.85E-03	1.79E-05	1.65E-03	3.98E-06	2.16E-01	2.49E-05	7.65E+01
C14094T5	2.83E-06	1.02E-07	3.22E-04	5.41E-06	8.80E-05	5.64E-07	7.36E-03	2.27E-05	2.36E-03	2.36E-06	2.09E-01	1.76E-05	6.51E+01
C14094T6	2.62E-06	1.15E-07	3.22E-04	5.42E-06	8.80E-05	5.64E-07	7.36E-03	2.27E-05	2.36E-03	2.36E-06	2.17E-01	2.06E-05	6.78E+01
C14094T7	2.84E-07	8.11E-08	8.97E-05	3.06E-06	2.95E-05	3.38E-07	2.48E-03	7.75E-06	6.11E-04	1.58E-06	2.14E-01	4.19E-05	8.70E+01
C14094T8	7.03E-07	8.72E-08	2.05E-04	4.26E-06	5.88E-05	5.57E-07	4.88E-03	1.47E-05	1.25E-03	1.95E-06	2.17E-01	2.34E-05	8.43E+01
C14094T9	1.63E-06	8.33E-08	3.04E-04	6.27E-06	1.04E-04	8.18E-07	8.68E-03	2.68E-05	2.33E-03	2.59E-06	2.15E-01	1.28E-05	7.99E+01
V-254 #30													
C14092T1	1.30E-05	2.43E-07	4.33E-04	6.64E-06	1.12E-04	9.76E-07	9.19E-03	2.90E-05	5.86E-03	4.75E-06	2.19E-01	3.49E-05	3.43E+01
C14092T2	1.57E-05	2.67E-07	4.67E-04	6.96E-06	1.29E-04	8.85E-07	1.06E-02	3.33E-05	7.20E-03	6.67E-06	2.38E-01	3.60E-05	3.51E+01
C14092T3	8.88E-06	2.67E-07	5.23E-04	1.54E-05	1.14E-04	8.85E-07	9.61E-03	2.90E-05	4.87E-03	4.05E-06	2.34E-01	3.90E-05	4.62E+01
C14092T4	2.40E-05	3.15E-07	5.62E-04	1.58E-05	1.33E-04	1.20E-06	1.08E-02	3.43E-05	9.67E-03	7.77E-06	2.36E-01	4.14E-05	2.64E+01
C14092T5	4.33E-06	1.04E-07	5.07E-04	1.59E-05	1.13E-04	1.18E-06	9.43E-03	3.46E-05	3.41E-03	3.06E-06	2.29E-01	1.58E-05	6.31E+01
C14092T6	1.16E-05	2.29E-07	5.26E-04	6.99E-06	1.37E-04	9.81E-07	1.13E-02	3.42E-05	5.94E-03	4.17E-06	2.23E-01	2.73E-05	4.23E+01
C14092T7	4.83E-06	1.84E-07	4.35E-04	5.36E-06	1.11E-04	7.11E-07	9.23E-03	2.83E-05	3.43E-03	3.80E-06	2.18E-01	2.62E-05	5.87E+01
C14092T8	3.47E-06	1.55E-07	4.08E-04	5.58E-06	1.11E-04	9.55E-07	9.20E-03	2.80E-05	3.06E-03	1.47E-06	2.22E-01	2.27E-05	6.69E+01

Table C.8: Inverse isochron data and apparent ages from **feldspar total fusion** measurements of V-221a and V-254.

Measurement	J	± J	Age (ka)	± Age (ka)	$^{39}Ar/^{40}Ar$	± $^{39}Ar/^{40}Ar$	$^{36}Ar/^{40}Ar$	± $^{36}Ar/^{40}Ar$	ρ
V-221a #20									
C1409615	1.00E-03	6.33E-06	292	27	2232.72	242.80	6.55E+02	7.12E+01	0.9974
C1409613	1.00E-03	6.33E-06	293	54	2277.57	508.02	6.64E+02	1.48E+02	0.9993
C14096T7	1.00E-03	6.33E-06	303	21	5128.26	983.38	1.15E+03	2.20E+02	0.9991
C14096T6	1.00E-03	6.33E-06	308	10	5053.79	423.87	1.15E+03	9.62E+01	0.9947
C1409612	1.00E-03	6.33E-06	310	35	3053.25	594.70	8.16E+02	1.59E+02	0.9992
C14096T1	1.00E-03	6.33E-06	314	10	5169.14	457.37	1.19E+03	1.05E+02	0.9966
C14096T5	1.00E-03	6.33E-06	314	16	1138.57	38.55	4.94E+02	1.65E+01	0.9813
C1409614	1.00E-03	6.33E-06	315	8	3756.67	184.19	9.44E+02	4.61E+01	0.9884
C14096T8	1.00E-03	6.33E-06	320	26	2414.49	277.97	7.21E+02	8.29E+01	0.9978
C14096T3	1.00E-03	6.33E-06	321	26	2759.58	358.80	7.83E+02	1.02E+02	0.9982
C1409610	1.00E-03	6.33E-06	325	36	3587.27	855.61	9.35E+02	2.23E+02	0.9995
C14096T2	1.00E-03	6.33E-06	337	20	1578.80	92.17	5.89E+02	3.43E+01	0.9929
C1409611	1.00E-03	6.33E-06	340	53	683.77	45.07	4.26E+02	2.80E+01	0.9927
C14096T9	1.00E-03	6.33E-06	342	25	796.30	28.72	4.47E+02	1.60E+01	0.9753
C14096T4	1.00E-03	6.33E-06	333	18	1817.84	100.63	6.29E+02	3.46E+01	0.9697
V-221a #30									
C14095T1	1.00E-03	6.72E-06	381	85	0.51	0.00	2.99E-03	7.93E-05	0.0260
C14095T2	1.00E-03	6.72E-06	320	13	2.92	0.02	1.65E-03	6.63E-05	0.0353
C14095T3	1.00E-03	6.72E-06	309	26	2.34	0.02	2.03E-03	1.08E-04	0.0127
C14095T4	1.00E-03	6.72E-06	303	15	3.32	0.02	1.52E-03	9.10E-05	0.0245
C14095T5	1.00E-03	6.72E-06	313	17	1.92	0.01	2.25E-03	5.98E-05	0.0399
V-254 #20									
C1409410	1.01E-03	6.84E-06	394	17	3.39	0.02	9.21E-04	1.02E-04	0.0143
C1409411	1.01E-03	6.84E-06	399	18	2.12	0.01	1.81E-03	7.00E-05	0.0264
C1409412	1.01E-03	6.84E-06	404	17	3.08	0.02	1.09E-03	9.63E-05	0.0171
C1409413	1.01E-03	6.84E-06	408	44	1.25	0.01	2.42E-03	9.92E-05	0.0121
C14094T1	1.01E-03	6.84E-06	393	48	2.52	0.02	1.55E-03	2.20E-04	0.0061
C14094T2	1.01E-03	6.84E-06	410	33	3.19	0.02	9.71E-04	1.89E-04	0.0098
C14094T3	1.01E-03	6.84E-06	409	11	3.59	0.02	6.79E-04	7.06E-05	0.0165
C14094T4	1.01E-03	6.84E-06	398	21	3.55	0.03	7.81E-04	1.35E-04	0.0221
C14094T5	1.01E-03	6.84E-06	384	16	3.13	0.02	1.16E-03	8.68E-05	0.0204
C14094T6	1.01E-03	6.84E-06	400	17	3.13	0.02	1.08E-03	9.78E-05	0.0167
C14094T7	1.01E-03	6.84E-06	394	36	4.08	0.04	4.27E-04	2.66E-04	0.0069
C14094T8	1.01E-03	6.84E-06	399	20	3.90	0.03	5.18E-04	1.39E-04	0.0099
C14094T9	1.01E-03	6.84E-06	396	11	3.73	0.03	6.66E-04	7.16E-05	0.0184
V-254 #30									
C14092T1	1.00E-03	1.11E-05	400	29	1.57	0.01	2.20E-03	8.32E-05	0.0171
C14092T2	1.00E-03	1.11E-05	435	28	1.48	0.01	2.17E-03	7.43E-05	0.0217
C14092T3	1.00E-03	1.11E-05	428	30	1.98	0.01	1.80E-03	1.10E-04	0.0137
C14092T4	1.00E-03	1.11E-05	431	32	1.12	0.01	2.46E-03	6.54E-05	0.0196
C14092T5	1.00E-03	1.11E-05	418	13	2.77	0.02	1.23E-03	6.14E-05	0.0213
C14092T6	1.00E-03	1.11E-05	408	22	1.90	0.01	1.93E-03	7.73E-05	0.0172
C14092T7	1.00E-03	1.11E-05	399	22	2.70	0.02	1.38E-03	1.08E-04	0.0183
C14092T8	1.00E-03	1.11E-05	407	19	3.02	0.02	1.10E-03	1.02E-04	0.0115

Table C.9: Ion beam intensities (in V) from **feldspar total fusion** of V-279.

Measurement	^{36}Ar	± ^{36}Ar	^{37}Ar	± ^{37}Ar	^{38}Ar	± ^{38}Ar	^{39}Ar	± ^{39}Ar	^{40}Ar	± ^{40}Ar	$^{40}Ar^*/^{39}Ar_K$	$\pm^{40}Ar^*/^{39}Ar_K$	$\%^{40}Ar^*$
V-279 #20													
C1409310	2.21E-06	6.89E-08	1.37E-04	4.44E-06	3.85E-05	3.93E-07	3.16E-03	1.01E-05	1.57E-03	2.18E-06	2.92E-01	3.87E-05	5.86E+01
C1409311	1.88E-06	6.55E-08	1.29E-04	3.21E-06	2.98E-05	3.07E-07	2.47E-03	7.72E-06	1.30E-03	2.03E-06	3.02E-01	4.85E-05	5.74E+01
C1409312	1.78E-06	9.40E-08	1.94E-04	3.92E-06	1.89E-05	2.11E-07	1.59E-03	4.99E-06	9.76E-04	1.52E-06	2.88E-01	1.02E-04	4.69E+01
C1409313	4.37E-06	1.61E-07	1.18E-04	3.11E-06	4.48E-05	5.05E-07	3.70E-03	1.19E-05	2.33E-03	2.54E-06	2.80E-01	7.31E-05	4.43E+01
C1409314	1.50E-06	8.09E-08	8.18E-05	3.16E-06	3.74E-05	3.73E-07	3.13E-03	9.96E-06	1.31E-03	1.59E-06	2.79E-01	4.35E-05	6.63E+01
C14093T1	1.68E-06	1.28E-07	1.07E-04	2.50E-06	3.53E-05	4.61E-07	2.96E-03	9.62E-06	1.40E-03	1.96E-06	3.04E-01	7.91E-05	6.45E+01
C14093T2	1.46E-06	9.64E-08	9.33E-05	2.42E-06	3.64E-05	3.05E-07	3.04E-03	9.78E-06	1.27E-03	1.53E-06	2.77E-01	5.29E-05	6.62E+01
C14093T3	2.51E-06	1.94E-07	1.40E-04	2.48E-06	4.36E-05	4.07E-07	3.64E-03	1.13E-05	1.72E-03	1.87E-06	2.69E-01	8.60E-05	5.69E+01
C14093T4	8.08E-07	7.28E-08	8.36E-05	2.05E-06	3.15E-05	3.05E-07	2.59E-03	8.69E-06	9.80E-04	1.95E-06	2.87E-01	4.87E-05	7.59E+01
C14093T5	7.03E-06	3.57E-07	1.02E-04	1.24E-05	4.56E-05	1.36E-06	5.11E-03	2.35E-04	3.57E-03	5.80E-05	2.88E-01	1.56E-04	4.13E+01
C14093T6	4.24E-06	4.04E-07	1.26E-04	2.90E-06	2.44E-05	2.03E-07	1.97E-03	8.46E-06	1.63E-03	1.12E-05	1.87E-01	2.30E-04	2.27E+01
C14093T7	1.43E-06	1.17E-07	6.28E-05	2.08E-06	3.21E-05	3.30E-07	2.68E-03	8.89E-06	1.21E-03	1.48E-06	2.93E-01	7.65E-05	6.51E+01
C14093T8	5.04E-07	4.97E-08	2.06E-04	5.35E-06	5.23E-05	4.65E-07	4.36E-03	1.38E-05	1.38E-03	1.60E-06	2.86E-01	2.04E-05	9.01E+01
C14093T9	1.08E-06	1.16E-07	5.63E-05	1.86E-06	1.85E-05	2.25E-07	1.55E-03	5.44E-06	7.59E-04	1.87E-06	2.83E-01	1.27E-04	5.78E+01
V-279 #30													
C14091T5	7.53E-06	1.88E-07	2.64E-04	4.21E-06	8.68E-05	7.92E-07	7.12E-03	2.21E-05	4.21E-03	2.29E-06	2.77E-01	4.41E-05	4.69E+01
C14091T4	4.31E-06	1.31E-07	3.50E-04	5.62E-06	9.06E-05	7.99E-07	7.46E-03	2.28E-05	3.34E-03	2.20E-06	2.78E-01	2.97E-05	6.21E+01
C14091T3	1.17E-05	2.09E-07	4.74E-04	6.13E-06	9.61E-05	7.51E-07	7.85E-03	2.41E-05	5.70E-03	5.67E-06	2.84E-01	4.56E-05	3.91E+01
C14091T2	4.35E-06	1.23E-07	3.71E-04	5.66E-06	9.34E-05	7.36E-07	7.66E-03	2.42E-05	3.45E-03	3.92E-06	2.84E-01	2.80E-05	6.31E+01
C14091T1	6.09E-06	2.30E-07	4.40E-04	6.15E-06	9.78E-05	9.50E-07	7.96E-03	2.52E-05	4.07E-03	2.48E-06	2.87E-01	4.98E-05	5.60E+01
C14091T6	8.14E-06	2.44E-07	2.93E-04	4.48E-06	1.06E-04	9.95E-07	8.78E-03	2.68E-05	4.93E-03	2.99E-06	2.87E-01	4.81E-05	5.11E+01
C14091T7	5.09E-06	1.44E-07	3.80E-04	5.68E-06	1.06E-04	7.46E-07	8.78E-03	2.67E-05	4.02E-03	4.43E-06	2.88E-01	2.89E-05	6.28E+01

Table C.10: Inverse isochron data and apparent ages from **feldspar total fusion** measurements of V-279.

Measurement	J	± J	Age (ka)	± Age (ka)	$^{39}Ar/^{40}Ar$	± $^{39}Ar/^{40}Ar$	$^{36}Ar/^{40}Ar$	± $^{36}Ar/^{40}Ar$	ρ
V-279 #20									
C1409310	1.01E-03	6.97E-06	538	24	2.01	0.01	1.39E-03	8.79E-05	0.0229
C1409311	1.01E-03	6.97E-06	557	30	1.90	0.01	1.42E-03	1.01E-04	0.0241
C1409312	1.01E-03	6.97E-06	532	65	1.63	0.01	1.78E-03	1.93E-04	0.0148
C1409313	1.01E-03	6.97E-06	516	48	1.59	0.01	1.86E-03	1.38E-04	0.0126
C1409314	1.01E-03	6.97E-06	514	29	2.38	0.02	1.13E-03	1.23E-04	0.0125
C14093T1	1.01E-03	6.97E-06	561	48	2.12	0.02	1.18E-03	1.84E-04	0.0097
C14093T2	1.01E-03	6.97E-06	511	35	2.39	0.02	1.13E-03	1.52E-04	0.0101
C14093T3	1.01E-03	6.97E-06	496	59	2.12	0.01	1.44E-03	2.26E-04	0.0073
C14093T4	1.01E-03	6.97E-06	530	31	2.65	0.02	8.03E-04	1.49E-04	0.0138
C14093T5	1.01E-03	6.97E-06	531	100	1.44	0.14	1.97E-03	2.10E-04	0.1016
C14093T6	1.01E-03	6.97E-06	345	227	1.21	0.02	2.59E-03	4.98E-04	0.0611
C14093T7	1.01E-03	6.97E-06	541	48	2.22	0.02	1.17E-03	1.93E-04	0.0077
C14093T8	1.01E-03	6.97E-06	527	13	3.16	0.02	3.26E-04	7.22E-05	0.0076
C14093T9	1.01E-03	6.97E-06	522	83	2.05	0.02	1.41E-03	3.07E-04	0.0144
V-279 #30									
C14091T5	1.00E-03	9.77E-06	508	29	1.69	0.01	1.78E-03	8.96E-05	0.0096
C14091T4	1.00E-03	9.77E-06	509	20	2.24	0.01	1.27E-03	7.88E-05	0.0126
C14091T3	1.00E-03	9.77E-06	520	29	1.38	0.01	2.04E-03	7.36E-05	0.0222
C14091T2	1.00E-03	9.77E-06	521	18	2.22	0.02	1.23E-03	7.16E-05	0.0211
C14091T1	1.00E-03	9.77E-06	526	32	1.96	0.01	1.47E-03	1.13E-04	0.0080
C14091T6	1.00E-03	9.77E-06	526	31	1.78	0.01	1.64E-03	9.92E-05	0.0093
C14091T7	1.00E-03	9.77E-06	527	18	2.19	0.01	1.24E-03	7.18E-05	0.0209

Table C.11: Ion beam intensities (in V) from **feldspar stepwise heating measurements** of V-36, V-149, V-184, and V-299. LO abbreviates the laser output in W.

Measure-ment	LO	^{36}Ar	$\pm$ ^{36}Ar	^{37}Ar	$\pm$ ^{37}Ar	^{38}Ar	$\pm$ ^{38}Ar	^{39}Ar	$\pm$ ^{39}Ar	^{40}Ar	$\pm$ ^{40}Ar	$^{40}Ar^*/^{39}Ar_K$	$\pm^{40}Ar^*/^{39}Ar_K$	$\%^{40}Ar^*$	% cum. ^{39}Ar
V-36															
C1502801	0.7	1.77E-07	1.16E-07	1.63E-06	3.27E-06	2.99E-08	9.70E-08	1.89E-08	3.26E-07	-9.35E-05	-4.86E-06	2.02E+03	1.34E+06	43	0
C1502802	1.2	6.40E-06	3.75E-07	-2.92E-06	-5.64E-06	5.88E-06	3.00E-07	3.44E-04	2.22E-06	2.21E-03	1.88E-05	8.62E-01	5.69E-03	13	0
C1502803	1.6	6.53E-06	2.80E-07	4.94E-05	6.60E-06	3.36E-05	4.34E-07	2.71E-03	1.34E-05	2.24E-03	2.07E-05	1.07E-01	6.78E-05	13	2
C1502804	2.0	4.40E-06	2.32E-07	6.84E-05	1.28E-05	9.61E-05	1.82E-06	8.01E-03	3.74E-05	1.62E-03	8.76E-06	3.82E-02	6.67E-06	19	5
C1502805	2.7	3.28E-06	8.45E-08	1.27E-04	3.53E-05	3.01E-04	2.93E-06	2.58E-02	1.15E-04	1.74E-03	7.32E-06	2.94E-02	6.54E-07	43	16
C1502806	3.3	1.35E-06	1.45E-07	2.20E-04	4.30E-05	4.00E-04	4.04E-06	3.46E-02	1.65E-04	1.42E-03	6.98E-06	2.93E-02	7.85E-07	71	21
C1502807	3.9	7.63E-07	1.41E-07	1.70E-04	2.06E-05	3.52E-04	3.41E-06	3.00E-02	1.53E-04	1.05E-03	3.39E-06	2.74E-02	8.06E-07	78	18
C1502808	4.5	7.64E-07	2.26E-07	1.18E-04	1.67E-05	2.73E-04	2.71E-06	2.33E-02	1.11E-04	7.98E-04	3.71E-06	2.42E-02	1.42E-06	71	14
C1502809	5.1	4.70E-07	1.19E-07	1.28E-04	2.83E-05	2.30E-04	2.32E-06	1.96E-02	1.00E-04	6.40E-04	1.10E-05	2.54E-02	9.89E-07	78	12
C1502810	5.8	3.44E-07	1.37E-07	4.37E-05	1.99E-05	1.42E-04	1.61E-06	1.20E-02	6.32E-05	4.26E-04	2.87E-06	2.67E-02	1.85E-06	75	7
C1502811	6.6	8.85E-08	1.22E-07	1.22E-05	4.21E-06	3.68E-05	4.56E-07	3.14E-03	1.59E-05	1.37E-04	2.66E-06	3.50E-02	8.12E-06	80	2
C1502812	7.5	2.37E-07	1.15E-07	3.13E-05	7.60E-06	3.53E-05	5.69E-07	2.96E-03	1.49E-05	1.74E-04	2.67E-06	3.49E-02	8.13E-06	60	2
V-149															
C1503301	0.9	4.48E-06	2.85E-07	-4.51E-06	-6.04E-06	1.32E-06	1.43E-07	1.54E-05	4.73E-07	1.49E-03	1.17E-05	1.00E+01	1.12E+00	10	0
C1503302	1.3	5.68E-06	2.11E-07	7.95E-06	8.03E-06	1.06E-05	2.61E-07	7.18E-04	5.16E-06	1.82E-03	1.01E-05	1.73E-01	3.08E-04	7	1
C1503303	1.7	5.66E-06	3.96E-07	3.07E-05	7.94E-06	3.41E-05	6.49E-07	2.63E-03	1.65E-05	1.89E-03	4.94E-05	7.52E-02	7.34E-05	10	2
C1503304	2.2	4.14E-06	3.28E-07	3.96E-05	1.85E-05	7.91E-05	1.26E-06	6.27E-03	3.39E-05	1.90E-03	8.24E-06	1.06E-01	3.33E-05	35	5
C1503305	2.7	2.35E-06	3.02E-07	4.04E-05	9.51E-06	9.34E-05	1.09E-06	7.81E-03	3.58E-05	1.41E-03	4.72E-06	9.08E-02	2.10E-05	50	6
C1503306	3.3	1.86E-06	2.71E-07	1.22E-04	1.62E-05	1.47E-04	1.44E-06	1.19E-02	6.79E-05	1.78E-03	9.80E-06	1.03E-01	1.42E-05	69	9
C1503307	3.9	1.16E-06	1.66E-07	1.10E-04	1.56E-05	1.78E-04	1.99E-06	1.47E-02	6.52E-05	1.84E-03	3.55E-06	1.01E-01	6.92E-06	81	12
C1503308	4.5	1.05E-06	1.49E-07	9.76E-05	2.36E-05	1.81E-04	1.88E-06	1.52E-02	7.04E-05	1.82E-03	5.40E-06	9.88E-02	5.95E-06	83	12
C1503309	5.1	1.01E-06	2.02E-07	1.51E-04	2.17E-05	2.60E-04	2.51E-06	2.19E-02	1.00E-04	2.48E-03	6.19E-06	9.94E-02	5.64E-06	88	17
C1503310	5.8	4.78E-07	2.68E-07	8.11E-05	2.97E-05	2.32E-04	2.14E-06	1.97E-02	8.89E-05	2.10E-03	4.46E-06	9.91E-02	8.16E-06	93	16
C1503311	6.5	6.60E-07	3.72E-07	6.21E-05	1.90E-05	1.40E-04	1.59E-06	1.15E-02	5.38E-05	1.24E-03	4.12E-06	9.01E-02	1.74E-05	84	9
C1503312	7.2	2.22E-07	2.22E-07	1.47E-05	1.52E-05	8.62E-05	1.00E-06	6.96E-03	3.15E-05	7.85E-04	3.78E-06	1.03E-01	1.97E-05	91	6
C1503313	7.9	1.78E-07	1.52E-07	2.97E-05	1.16E-05	7.48E-05	8.80E-07	6.10E-03	2.78E-05	6.99E-04	3.80E-06	1.06E-01	1.58E-05	92	5
V-184															
C1503201	0.9	2.09E-05	5.18E-07	1.18E-04	1.29E-04	4.52E-06	1.82E-07	4.21E-05	5.29E-07	6.70E-03	1.34E-05	1.09E+01	8.07E-01	7	0
C1503202	1.0	9.62E-06	4.09E-07	1.02E-04	1.34E-04	6.71E-06	2.75E-07	3.94E-04	2.20E-06	3.16E-03	4.81E-06	7.55E-01	4.70E-03	9	1
C1503203	1.2	1.32E-05	3.16E-07	3.61E-04	9.64E-05	3.10E-05	4.62E-07	2.38E-03	1.11E-05	4.24E-03	1.80E-05	1.37E-01	1.11E-04	8	5
C1503204	1.3	7.30E-06	2.56E-07	5.19E-04	2.34E-04	6.24E-05	7.70E-07	4.97E-03	2.36E-05	2.91E-03	1.43E-05	1.55E-01	4.98E-05	26	11
C1503205	1.5	5.57E-06	2.79E-07	1.84E-03	1.42E-04	7.97E-05	9.06E-07	6.43E-03	3.02E-05	2.53E-03	1.20E-05	1.56E-01	4.13E-05	40	14
C1503206	1.8	1.93E-05	4.06E-07	1.84E-03	2.07E-04	9.22E-05	9.67E-07	7.20E-03	3.26E-05	6.66E-03	1.32E-05	1.44E-01	4.93E-05	16	15
C1503207	1.9	1.67E-06	3.44E-07	6.74E-04	2.23E-04	5.21E-05	8.77E-07	4.38E-03	1.98E-05	1.01E-03	4.55E-06	1.28E-01	6.10E-05	55	9
C1503208	2.0	1.33E-06	1.80E-07	1.52E-03	3.36E-04	4.65E-05	8.10E-07	3.83E-03	2.22E-05	7.91E-04	4.39E-06	1.33E-01	4.20E-05	64	8
C1503209	2.1	9.34E-07	1.63E-07	1.65E-03	2.49E-04	3.98E-05	7.10E-07	3.33E-03	1.67E-05	6.26E-04	4.12E-06	1.43E-01	4.53E-05	76	7
C1503210	2.2	8.85E-07	1.53E-07	5.89E-04	1.78E-04	3.62E-05	8.81E-07	3.13E-03	1.51E-05	6.41E-04	4.39E-06	1.34E-01	4.12E-05	66	7
C1503211	2.3	7.77E-07	1.71E-07	6.74E-04	3.02E-04	3.57E-05	5.42E-07	3.09E-03	1.39E-05	5.83E-04	4.79E-06	1.30E-01	4.75E-05	69	7
C1503212	2.4	4.31E-07	1.51E-07	2.66E-04	1.99E-04	2.36E-05	5.22E-07	2.05E-03	1.25E-05	3.79E-04	3.34E-06	1.32E-01	6.13E-05	71	4
C1503213	3.6	6.91E-07	2.64E-07	9.88E-04	1.37E-04	3.07E-05	6.37E-07	2.67E-03	1.21E-05	4.84E-04	3.05E-06	1.32E-01	7.91E-05	73	6
C1503214	5.2	7.23E-07	1.84E-07	1.32E-03	2.89E-04	3.41E-05	4.64E-07	2.97E-03	1.34E-05	5.36E-04	3.43E-06	1.42E-01	5.69E-05	79	6
V-299															
C1502901	0.2	1.47E-05	3.98E-07	2.53E-05	8.34E-06	3.23E-06	1.69E-07	1.92E-05	4.83E-07	4.66E-03	5.23E-06	1.33E+01	8.32E-01	5	0
C1502902	0.7	1.31E-05	4.20E-07	7.67E-04	3.28E-05	8.23E-06	2.07E-07	4.38E-04	5.60E-06	4.12E-03	2.36E-05	5.85E-01	1.71E-03	6	8
C1502903	1.2	5.84E-06	1.99E-07	3.17E-03	7.51E-05	1.26E-05	2.39E-07	9.61E-04	5.14E-06	2.47E-03	1.61E-05	1.02E+00	6.60E-04	39	18
C1502904	1.7	4.10E-06	2.22E-07	4.26E-03	7.69E-05	1.21E-05	2.76E-07	9.71E-04	5.09E-06	2.30E-03	7.41E-06	1.45E+00	1.01E-03	61	18
C1502905	2.4	2.17E-06	1.22E-07	2.50E-03	5.42E-05	5.22E-06	1.53E-07	4.65E-04	2.91E-06	9.53E-04	3.93E-06	1.08E+00	8.62E-04	52	9
C1502906	3.1	1.75E-06	1.61E-07	2.74E-03	8.80E-05	5.45E-06	1.91E-07	4.46E-04	2.79E-06	1.27E-03	3.66E-06	2.17E+00	2.41E-03	76	8
C1502907	3.8	1.47E-06	1.50E-07	2.41E-03	6.60E-05	4.30E-06	1.87E-07	3.47E-04	1.76E-06	5.27E-04	5.08E-06	8.06E-01	1.06E-03	53	6
C1502908	4.5	1.35E-06	1.96E-07	3.06E-03	7.30E-05	5.12E-06	1.65E-07	4.30E-04	2.22E-06	8.14E-04	4.14E-06	1.52E+00	2.11E-03	80	8
C1502910	5.2	1.03E-06	1.04E-07	1.36E-03	4.99E-05	2.62E-06	1.28E-07	2.07E-04	1.66E-06	5.95E-04	3.18E-06	1.92E+00	2.94E-03	66	4
C1502911	6.9	1.75E-06	1.70E-07	2.32E-03	5.82E-05	4.70E-06	2.87E-07	3.73E-04	2.18E-06	8.70E-04	3.32E-06	1.43E+00	1.97E-03	61	7
C1502912	7.6	9.03E-07	1.28E-07	1.12E-03	3.87E-05	2.21E-06	1.81E-07	1.85E-04	1.42E-06	4.39E-04	2.74E-06	1.39E+00	2.92E-03	59	3
C1502913	8.3	1.35E-06	1.60E-07	1.17E-03	4.35E-05	2.40E-06	1.68E-07	2.01E-04	1.70E-06	7.56E-04	5.73E-06	2.22E+00	5.37E-03	59	4
C1502914	9.0	1.16E-06	1.62E-07	1.51E-03	3.59E-05	4.04E-06	1.71E-07	3.29E-04	2.14E-06	9.32E-04	5.20E-06	2.15E+00	3.20E-03	75	6

Table C.12: Inverse isochron data and apparent ages from **feldspar stepwise heating** measurements of V-36, V-149, V-184, and V-299.

Measurement	J	± J	Age (ka)	± Age (ka)	$^{39}Ar/^{40}Ar$	± $^{39}Ar/^{40}Ar$	$^{36}Ar/^{40}Ar$	± $^{36}Ar/^{40}Ar$	ρ
V-36									
C1502801	1.04E-03	1.60E-05	2071892	40408651	0.00	0.01	1.90E-03	2.49E-03	0.000
C1502802	1.04E-03	1.60E-05	1637	1253	0.16	0.00	2.90E-03	3.43E-04	0.115
C1502803	1.04E-03	1.60E-05	203	121	1.21	0.03	2.92E-03	2.56E-04	0.186
C1502804	1.04E-03	1.60E-05	73	33	4.97	0.07	2.71E-03	2.89E-04	0.085
C1502805	1.04E-03	1.60E-05	56	4	14.91	0.26	1.88E-03	1.02E-04	0.235
C1502806	1.04E-03	1.60E-05	56	5	24.72	0.61	9.24E-04	2.08E-04	0.092
C1502807	1.04E-03	1.60E-05	52	6	28.98	0.77	6.94E-04	2.73E-04	0.058
C1502808	1.04E-03	1.60E-05	46	11	29.79	0.83	9.37E-04	5.79E-04	0.040
C1502809	1.04E-03	1.60E-05	48	7	31.22	1.39	6.96E-04	3.81E-04	0.077
C1502810	1.04E-03	1.60E-05	51	13	28.60	0.83	7.96E-04	6.57E-04	0.031
C1502811	1.04E-03	1.60E-05	66	44	23.22	1.04	6.31E-04	1.80E-03	0.015
C1502812	1.04E-03	1.60E-05	66	44	17.23	0.61	1.33E-03	1.34E-03	0.033
V-149									
C1503301	1.03E-03	2.60E-05	18828	20957	0.01	0.00	3.00E-03	3.85E-04	0.030
C1503302	1.03E-03	2.60E-05	327	336	0.39	0.01	3.12E-03	2.35E-04	0.091
C1503303	1.03E-03	2.60E-05	142	184	1.39	0.08	3.00E-03	4.49E-04	0.341
C1503304	1.03E-03	2.60E-05	200	59	3.30	0.05	2.18E-03	3.46E-04	0.037
C1503305	1.03E-03	2.60E-05	172	44	5.55	0.07	1.66E-03	4.30E-04	0.021
C1503306	1.03E-03	2.60E-05	195	26	6.72	0.11	1.03E-03	3.07E-04	0.031
C1503307	1.03E-03	2.60E-05	191	13	8.05	0.09	6.20E-04	1.81E-04	0.017
C1503308	1.03E-03	2.60E-05	187	11	8.40	0.11	5.69E-04	1.65E-04	0.022
C1503309	1.03E-03	2.60E-05	188	11	8.88	0.11	3.94E-04	1.64E-04	0.015
C1503310	1.03E-03	2.60E-05	187	16	9.43	0.12	2.19E-04	2.57E-04	0.005
C1503311	1.03E-03	2.60E-05	170	37	9.37	0.13	5.24E-04	6.06E-04	0.007
C1503312	1.03E-03	2.60E-05	194	36	8.91	0.14	2.79E-04	5.70E-04	0.005
C1503313	1.03E-03	2.60E-05	200	28	8.78	0.14	2.44E-04	4.38E-04	0.006
V-184									
C1503201	9.70E-04	1.37E-05	19232	13019	0.01	0.00	3.12E-03	1.55E-04	0.012
C1503202	9.70E-04	1.37E-05	1339	1104	0.12	0.00	3.03E-03	2.60E-04	0.009
C1503203	9.70E-04	1.37E-05	243	144	0.56	0.01	3.09E-03	1.52E-04	0.116
C1503204	9.70E-04	1.37E-05	275	57	1.71	0.02	2.46E-03	1.83E-04	0.096
C1503205	9.70E-04	1.37E-05	277	47	2.55	0.03	2.02E-03	2.24E-04	0.063
C1503206	9.70E-04	1.37E-05	255	61	1.08	0.01	2.83E-03	1.24E-04	0.038
C1503207	9.70E-04	1.37E-05	227	85	4.35	0.06	1.49E-03	6.95E-04	0.015
C1503208	9.70E-04	1.37E-05	236	56	4.85	0.08	1.18E-03	5.10E-04	0.020
C1503209	9.70E-04	1.37E-05	253	56	5.33	0.09	7.99E-04	5.65E-04	0.016
C1503210	9.70E-04	1.37E-05	239	54	4.90	0.08	1.14E-03	5.00E-04	0.027
C1503211	9.70E-04	1.37E-05	231	65	5.32	0.10	1.03E-03	6.49E-04	0.024
C1503212	9.70E-04	1.37E-05	234	83	5.43	0.12	9.55E-04	8.45E-04	0.017
C1503213	9.70E-04	1.37E-05	235	106	5.54	0.09	8.95E-04	1.11E-03	0.009
C1503214	9.70E-04	1.37E-05	252	71	5.56	0.09	7.05E-04	7.45E-04	0.011
V-299									
C1502901	1.05E-03	1.25E-05	25394	11782	0.00	0.00	3.17E-03	8.57E-05	0.002
C1502902	1.05E-03	1.25E-05	1120	560	0.11	0.00	3.14E-03	1.04E-04	0.071
C1502903	1.05E-03	1.25E-05	1950	124	0.39	0.00	2.03E-03	8.21E-05	0.125
C1502904	1.05E-03	1.25E-05	2778	134	0.42	0.00	1.30E-03	9.75E-05	0.023
C1502905	1.05E-03	1.25E-05	2063	153	0.49	0.00	1.59E-03	1.29E-04	0.028
C1502906	1.05E-03	1.25E-05	4156	213	0.35	0.00	8.09E-04	1.29E-04	0.008
C1502907	1.05E-03	1.25E-05	1544	252	0.65	0.01	1.58E-03	2.87E-04	0.047
C1502908	1.05E-03	1.25E-05	2918	265	0.53	0.00	6.64E-04	2.43E-04	0.010
C1502910	1.05E-03	1.25E-05	3670	293	0.35	0.00	1.12E-03	1.76E-04	0.019
C1502911	1.05E-03	1.25E-05	2729	264	0.43	0.00	1.31E-03	1.97E-04	0.014
C1502912	1.05E-03	1.25E-05	2670	401	0.42	0.00	1.38E-03	2.94E-04	0.019
C1502913	1.05E-03	1.25E-05	4249	462	0.27	0.00	1.38E-03	2.13E-04	0.033
C1502914	1.05E-03	1.25E-05	4108	285	0.35	0.00	8.22E-04	1.74E-04	0.017

Table C.13: Ion beam intensities (in V) from **glass stepwise heating measurements** of V-45, V-57b and V-65. LO abbreviates the laser output in W. The symbol † marks repeated analyses after a tripped measurement.All samples were preheated for 35 seconds at 1.2 % of the maximum CO_2 laser output (60 W). Note that all uncertainties represent two standard deviations. Chapter 5 discusses only one standard deviation in order to guarantee the visibility of the data in diagrams.

Measurement	LO	^{36}Ar	$\pm$ ^{36}Ar	^{37}Ar	$\pm$ ^{37}Ar	^{38}Ar	$\pm$ ^{38}Ar	^{39}Ar	$\pm$ ^{39}Ar	^{40}Ar	$\pm$ ^{40}Ar	$^{40}Ar^*/^{39}Ar_K$	$\pm^{40}Ar^*/^{39}Ar_K$	$\%^{40}Ar^*$	$\%$ ^{39}Ar cum.
V-45															
C1502101	0.2	1.54E-05	8.43E-07	1.70E-04	6.23E-05	6.63E-06	2.56E-07	3.16E-04	4.69E-06	4.65E-03	7.39E-05	1.86E-01	1.55E-03	1.27	1.17
C1502102	0.4	1.18E-05	1.03E-07	2.35E-04	5.47E-05	1.27E-05	1.74E-07	8.40E-04	5.07E-06	3.53E-03	7.27E-05	2.94E-02	2.78E-05	0.70	3.11
C1502103	0.5	2.12E-05	8.77E-07	3.80E-04	8.53E-05	1.90E-05	5.32E-07	1.19E-03	1.58E-05	6.40E-03	9.30E-05	7.78E-02	1.82E-04	1.44	4.41
C1502104	0.7	1.36E-05	4.57E-07	1.12E-04	1.37E-04	1.95E-05	2.05E-07	1.27E-03	1.15E-05	4.12E-03	3.29E-05	3.99E-02	4.46E-05	1.23	4.69
C1502105	0.7	1.63E-05	9.33E-07	1.68E-04	1.49E-04	2.52E-05	4.29E-07	1.65E-03	2.00E-05	4.89E-03	6.28E-05	2.68E-02	4.65E-05	0.90	6.10
C1502106	0.9	1.39E-05	3.17E-07	2.31E-04	1.45E-04	4.20E-05	6.79E-07	2.90E-03	4.08E-05	4.18E-03	6.12E-05	1.41E-02	5.53E-06	0.98	10.76
C1502107	1.2	1.30E-05	3.97E-07	2.27E-04	1.41E-04	3.21E-05	5.99E-07	2.15E-03	2.43E-05	4.04E-03	5.15E-05	8.78E-02	5.30E-05	4.67	7.98
C1502108	1.4	3.01E-05	8.89E-07	3.27E-04	1.40E-04	3.85E-05	4.48E-07	2.56E-03	2.39E-05	9.09E-03	8.00E-05	4.78E-02	5.18E-05	1.35	9.51
C1502109	1.4	2.27E-05	5.60E-07	2.47E-04	1.37E-04	3.42E-05	6.15E-07	2.30E-03	2.37E-05	6.86E-03	6.16E-05	4.83E-02	3.76E-05	1.62	8.54
C1502110	1.7	4.50E-05	9.26E-07	3.12E-04	1.31E-04	4.31E-05	5.82E-07	2.64E-03	2.45E-05	1.36E-02	1.29E-04	5.02E-02	5.82E-05	0.98	9.81
C1502111	1.9	1.12E-04	2.36E-07	3.13E-04	1.43E-04	6.69E-05	1.18E-06	3.40E-03	2.80E-05	3.36E-02	2.26E-04	2.83E-02	2.06E-05	0.29	12.62
C1502112	2.0	5.11E-05	4.28E-07	2.94E-04	1.34E-04	4.32E-05	8.04E-07	2.60E-03	1.54E-05	1.56E-02	1.30E-04	1.34E-01	9.55E-05	2.23	9.63
C1502113	2.2	6.60E-05	9.24E-07	3.79E-04	1.49E-04	3.56E-05	5.02E-07	1.87E-03	1.02E-05	1.98E-02	9.67E-05	8.44E-02	1.33E-04	0.80	6.93
C1502114	2.4	1.86E-05	5.39E-07	8.21E-05	1.36E-04	1.97E-05	3.23E-07	1.28E-03	9.82E-06	5.64E-03	4.07E-05	7.17E-02	9.36E-05	1.62	4.73
V-57b															
C1503101	0.2	8.55E-05	9.37E-07	3.53E-04	2.07E-04	1.67E-05	2.60E-07	4.40E-05	5.57E-07	2.55E-02	9.90E-05	1.28E+00	8.80E-02	0.22	0.29
C1503102	0.2	9.79E-05	4.94E-07	2.83E-04	1.77E-04	2.07E-05	3.63E-07	1.70E-04	2.64E-06	2.93E-02	1.57E-04	2.75E-01	3.64E-03	0.16	1.14
C1503103	0.5	5.19E-05	1.77E-06	1.67E-05	8.43E-06	1.73E-05	3.46E-07	3.99E-04	3.96E-06	1.56E-02	7.02E-05	2.13E-01	2.85E-03	0.55	2.69
C1503104	0.7	2.93E-05	2.55E-07	1.60E-05	9.03E-06	1.52E-05	2.24E-07	6.84E-04	5.86E-06	8.79E-03	8.19E-05	5.82E-02	9.63E-05	0.45	4.61
C1503105	0.8	4.83E-05	6.37E-07	1.35E-05	9.04E-06	1.60E-05	4.19E-07	4.89E-04	2.63E-06	1.45E-02	9.97E-05	1.39E-01	6.17E-04	0.47	3.29
C1503107A †	1.1	1.57E-04	1.66E-06	1.27E-06	6.93E-06	4.32E-05	4.46E-07	9.06E-04	1.78E-06	4.69E-02	1.59E-04	3.31E-02	1.93E-04	0.06	6.10
C1503108	1.2	5.36E-05	9.85E-07	1.35E-05	8.82E-06	1.89E-05	4.65E-07	6.08E-04	5.58E-07	1.61E-02	6.03E-05	1.28E-01	6.38E-04	0.49	4.09
C1503109	1.4	1.28E-04	1.27E-06	4.77E-06	8.58E-06	6.03E-05	6.21E-07	2.48E-03	1.72E-05	3.84E-02	2.12E-04	3.91E-02	6.94E-05	0.25	16.69
C1503110	1.5	1.29E-04	9.55E-07	1.82E-05	1.34E-05	6.08E-05	1.57E-06	2.62E-03	1.32E-05	3.84E-02	2.27E-04	1.08E-02	1.55E-05	0.07	17.62
C1503111	1.6	1.20E-04	5.45E-07	1.17E-05	1.33E-05	5.69E-05	2.75E-07	2.52E-03	1.50E-05	3.59E-02	1.91E-04	2.64E-02	2.75E-05	0.19	16.94
C1503112	1.7	5.89E-05	5.40E-07	1.46E-05	1.34E-05	2.06E-05	5.32E-07	6.53E-04	2.00E-06	1.76E-02	1.12E-04	5.86E-02	1.79E-04	0.22	4.40
C1503113	1.9	5.77E-05	5.52E-07	6.44E-06	6.92E-06	1.86E-05	5.34E-07	5.43E-04	1.40E-06	1.73E-02	8.31E-05	8.46E-02	2.93E-04	0.27	3.66
C1503114	2.1	1.54E-04	1.43E-06	1.61E-05	6.85E-06	5.62E-05	1.02E-06	2.10E-03	5.50E-06	4.61E-02	2.24E-04	4.17E-02	9.71E-05	0.19	14.16
C1503115	2.2	5.85E-05	5.74E-07	1.07E-05	7.21E-06	2.04E-05	5.40E-07	6.42E-04	1.85E-06	1.75E-02	1.32E-04	7.16E-02	2.45E-04	0.26	4.32
V-65															
C1502201	0.2	7.71E-05	1.04E-06	2.86E-04	1.12E-04	1.80E-05	6.55E-07	3.47E-04	2.73E-06	2.30E-02	7.79E-05	-6.63E-02	-6.18E-04	-0.10	2.15
C1502202	0.5	8.40E-06	2.67E-07	1.18E-04	8.80E-05	1.16E-05	3.91E-07	8.02E-04	9.07E-06	2.55E-03	3.20E-05	6.65E-02	7.15E-05	2.09	4.97
C1502203	0.7	7.59E-05	5.91E-07	2.74E-04	1.30E-04	2.65E-05	6.16E-07	9.45E-04	1.08E-05	2.28E-02	2.81E-04	1.84E-01	6.54E-04	0.76	5.86
C1502204	0.7	1.55E-05	7.87E-07	2.10E-04	8.21E-05	1.76E-05	1.90E-07	1.22E-03	1.82E-05	4.66E-03	7.22E-05	4.33E-02	8.76E-05	1.13	7.56
C1502205	0.9	7.78E-05	7.41E-07	2.11E-04	8.13E-05	3.39E-05	2.96E-07	1.54E-03	1.45E-05	2.33E-02	2.00E-04	6.35E-02	1.24E-04	0.42	9.57
C1502206	1.2	9.23E-05	7.06E-07	2.62E-04	6.91E-05	4.85E-05	5.03E-07	2.49E-03	2.54E-05	2.78E-02	2.78E-04	1.01E-01	1.44E-04	0.91	15.44
C1502207	1.4	6.97E-05	9.99E-07	2.67E-04	1.14E-04	3.29E-05	5.64E-07	1.58E-03	1.21E-05	2.10E-02	1.60E-04	9.52E-02	2.05E-04	0.72	9.83
C1502208	1.7	6.85E-05	1.08E-06	2.09E-04	1.10E-04	3.12E-05	7.47E-07	1.45E-03	1.48E-05	2.07E-02	2.06E-04	1.73E-01	4.61E-04	1.21	8.98
C1502209	1.9	3.74E-05	5.44E-07	2.07E-04	1.02E-04	2.59E-05	5.28E-07	1.50E-03	6.69E-06	1.13E-02	4.95E-05	7.72E-02	8.80E-05	1.03	9.34
C1502210	2.1	1.32E-05	3.20E-07	3.72E-04	1.45E-04	1.70E-05	5.03E-07	1.17E-03	7.49E-06	4.01E-03	3.19E-05	7.66E-02	6.69E-05	2.23	7.23
C1502211	2.4	1.55E-05	3.83E-07	1.91E-04	1.39E-04	1.46E-05	4.57E-07	9.31E-04	4.54E-06	4.68E-03	2.85E-05	7.16E-02	9.13E-05	1.43	5.78
C1502212	2.6	2.39E-05	1.75E-07	2.91E-04	1.44E-04	1.91E-05	5.49E-07	1.15E-03	6.66E-06	7.20E-03	4.92E-05	8.13E-02	5.26E-05	1.29	7.10
C1502213	3.1	2.02E-05	2.49E-07	1.25E-04	1.47E-04	1.59E-05	2.62E-07	9.98E-04	6.77E-06	6.06E-03	3.73E-05	3.14E-02	2.67E-05	0.52	6.19

Table C.14: Inverse isochron data and apparent ages from**glass stepwise heating** measurements of V-45, V-57b, and V65. Mass discrimination factor is abbrviated as MDF.

Measurement	J	± J	Age (ka)	± Age (ka)	MDF	± MDF	$^{39}Ar/^{40}Ar$	± $^{39}Ar/^{40}Ar$	$^{36}Ar/^{40}Ar$	± $^{36}Ar/^{40}Ar$	ρ
V-45											
C1502101	9.66E-04	2.72E-05	330	1468	1.0051	0.0002	0.068	1.48E-03	3.31E-03	1.89E-04	0.20
C1502102	9.66E-04	2.72E-05	52	167	1.0051	0.0002	0.238	5.11E-03	3.33E-03	7.46E-05	0.88
C1502103	9.66E-04	2.72E-05	138	414	1.0051	0.0002	0.186	3.65E-03	3.30E-03	1.45E-04	0.24
C1502104	9.66E-04	2.72E-05	71	197	1.0051	0.0002	0.307	3.72E-03	3.31E-03	1.15E-04	0.15
C1502105	9.66E-04	2.72E-05	47	307	1.0051	0.0002	0.337	5.97E-03	3.32E-03	1.96E-04	0.16
C1502106	9.66E-04	2.72E-05	25	69	1.0051	0.0002	0.694	1.41E-02	3.32E-03	9.06E-05	0.39
C1502107	9.66E-04	2.72E-05	155	107	1.0051	0.0002	0.532	9.06E-03	3.19E-03	1.07E-04	0.29
C1502108	9.66E-04	2.72E-05	85	192	1.0051	0.0002	0.282	3.62E-03	3.30E-03	1.02E-04	0.20
C1502109	9.66E-04	2.72E-05	85	138	1.0051	0.0002	0.335	4.58E-03	3.30E-03	8.70E-05	0.22
C1502110	9.66E-04	2.72E-05	89	205	1.0051	0.0002	0.195	2.60E-03	3.32E-03	7.54E-05	0.30
C1502111	9.66E-04	2.72E-05	50	129	1.0051	0.0002	0.101	1.08E-03	3.34E-03	2.36E-05	0.60
C1502112	9.66E-04	2.72E-05	237	126	1.0051	0.0002	0.166	1.70E-03	3.27E-03	3.87E-05	0.57
C1502113	9.66E-04	2.72E-05	149	280	1.0051	0.0002	0.094	6.90E-04	3.32E-03	4.94E-05	0.22
C1502114	9.66E-04	2.72E-05	127	231	1.0051	0.0002	0.226	2.39E-03	3.30E-03	9.86E-05	0.16
V-57b											
C1503101	9.78E-04	3.27E-05	2281	12327	1.0064	0.0002	0.002	2.35E-05	3.34E-03	3.89E-05	0.09
C1503102	9.78E-04	3.27E-05	493	2368	1.0064	0.0002	0.006	9.55E-05	3.34E-03	2.47E-05	0.24
C1503103	9.78E-04	3.27E-05	381	2393	1.0064	0.0002	0.026	2.79E-04	3.33E-03	1.15E-04	0.05
C1503104	9.78E-04	3.27E-05	104	296	1.0064	0.0002	0.078	9.85E-04	3.33E-03	4.25E-05	0.54
C1503105	9.78E-04	3.27E-05	249	794	1.0064	0.0002	0.034	2.95E-04	3.33E-03	4.96E-05	0.36
C1503107A †	9.78E-04	3.27E-05	59	1044	1.0064	0.0002	0.019	7.57E-05	3.35E-03	3.71E-05	0.26
C1503108	9.78E-04	3.27E-05	230	889	1.0064	0.0002	0.038	1.46E-04	3.33E-03	6.25E-05	0.19
C1503109	9.78E-04	3.27E-05	70	318	1.0064	0.0002	0.065	5.74E-04	3.34E-03	3.78E-05	0.30
C1503110	9.78E-04	3.27E-05	19	255	1.0064	0.0002	0.068	5.30E-04	3.35E-03	3.18E-05	0.47
C1503111	9.78E-04	3.27E-05	47	186	1.0064	0.0002	0.070	5.60E-04	3.34E-03	2.34E-05	0.51
C1503112	9.78E-04	3.27E-05	105	546	1.0064	0.0002	0.037	2.61E-04	3.34E-03	3.72E-05	0.51
C1503113	9.78E-04	3.27E-05	151	619	1.0064	0.0002	0.031	1.72E-04	3.34E-03	3.58E-05	0.40
C1503114	9.78E-04	3.27E-05	75	417	1.0064	0.0002	0.046	2.52E-04	3.34E-03	3.50E-05	0.41
C1503115	9.78E-04	3.27E-05	128	612	1.0064	0.0002	0.037	2.95E-04	3.34E-03	4.13E-05	0.57
V-65											
C1502201	9.72E-04	3.87E-05	-118	1658	1.0051	0.0002	0.015	1.30E-04	3.35E-03	4.66E-05	0.10
C1502202	9.72E-04	3.87E-05	118	191	1.0051	0.0002	0.314	5.30E-03	3.28E-03	1.13E-04	0.27
C1502203	9.72E-04	3.87E-05	328	631	1.0051	0.0002	0.041	6.98E-04	3.32E-03	4.85E-05	0.62
C1502204	9.72E-04	3.87E-05	77	359	1.0051	0.0002	0.262	5.62E-03	3.31E-03	1.77E-04	0.21
C1502205	9.72E-04	3.87E-05	113	348	1.0051	0.0002	0.066	8.41E-04	3.34E-03	4.28E-05	0.45
C1502206	9.72E-04	3.87E-05	180	252	1.0051	0.0002	0.090	1.28E-03	3.32E-03	4.18E-05	0.56
C1502207	9.72E-04	3.87E-05	169	383	1.0051	0.0002	0.076	8.16E-04	3.33E-03	5.40E-05	0.33
C1502208	9.72E-04	3.87E-05	308	472	1.0051	0.0002	0.070	9.98E-04	3.31E-03	6.16E-05	0.37
C1502209	9.72E-04	3.87E-05	137	203	1.0051	0.0002	0.134	8.34E-04	3.31E-03	5.05E-05	0.20
C1502210	9.72E-04	3.87E-05	136	155	1.0051	0.0002	0.291	2.97E-03	3.27E-03	8.46E-05	0.24
C1502211	9.72E-04	3.87E-05	127	227	1.0051	0.0002	0.199	1.55E-03	3.30E-03	8.46E-05	0.19
C1502212	9.72E-04	3.87E-05	145	115	1.0051	0.0002	0.159	1.43E-03	3.31E-03	3.36E-05	0.51
C1502213	9.72E-04	3.87E-05	56	151	1.0051	0.0002	0.165	1.51E-03	3.33E-03	4.63E-05	0.30

Table C.15: Ion beam intensities (in V) from **glass stepwise heating measurements** of V-165 and V-209a. LO abbreviates the laser output in W. Note that all uncertainties represent two standard deviations. Chapter 5 discusses only one standard deviation in order to guarantee the visibility of the data in diagrams.

Measurement	LO	^{36}Ar	$\pm$ ^{36}Ar	^{37}Ar	$\pm$ ^{37}Ar	^{38}Ar	$\pm$ ^{38}Ar	^{39}Ar	$\pm$ ^{39}Ar	^{40}Ar	$\pm$ ^{40}Ar	$^{40}Ar^*/^{39}Ar_K$	$\pm^{40}Ar^*/^{39}Ar_K$	$\%^{40}Ar^*$	% cum. $^{39}_{Ar}$
V-165															
C1503001	0.2	2.36E-06	1.65E-07	6.24E-06	7.46E-06	3.36E-07	1.29E-07	1.13E-05	6.39E-07	7.09E-04	1.91E-05	5.31E-01	4.67E+00	0.85	0.03
C1503002	0.3	3.59E-06	2.69E-07	7.73E-06	7.05E-06	1.48E-06	1.16E-07	5.86E-05	7.05E-07	1.03E-03	1.61E-05	-7.61E-01	1.40E+00	-4.34	0.14
C1503003	0.5	3.03E-06	4.55E-07	1.17E-05	6.71E-06	3.43E-06	1.54E-07	1.97E-04	2.96E-06	9.31E-04	1.90E-05	1.36E-01	6.97E-01	2.88	0.47
C1503004	0.7	6.15E-06	3.61E-07	2.39E-05	9.23E-06	1.09E-05	3.67E-07	6.70E-04	1.11E-05	2.01E-03	2.44E-05	2.61E-01	1.65E-01	8.71	1.60
C1503006	0.9	1.03E-05	4.04E-07	6.91E-05	1.56E-05	2.67E-05	4.97E-07	1.69E-03	1.41E-05	3.46E-03	2.66E-05	2.31E-01	7.30E-02	11.29	4.06
C1503008	1.2	1.67E-05	3.76E-07	1.41E-04	1.33E-05	6.30E-05	5.08E-07	3.98E-03	2.60E-05	5.38E-03	3.01E-05	1.03E-01	2.94E-02	7.60	9.53
C1503009	1.4	2.27E-05	3.94E-07	1.05E-04	1.26E-05	8.10E-05	1.24E-06	5.07E-03	3.02E-05	7.30E-03	4.67E-05	1.04E-01	2.51E-02	7.22	12.16
C1503010	1.5	2.56E-05	3.91E-07	1.27E-04	2.48E-05	1.00E-04	1.16E-06	6.35E-03	3.59E-05	8.25E-03	4.72E-05	9.88E-02	2.00E-02	7.61	15.23
C1503011	1.6	2.22E-05	5.44E-07	1.03E-04	1.20E-05	8.16E-05	1.03E-06	5.19E-03	3.14E-05	7.15E-03	4.50E-05	1.00E-01	3.26E-02	7.27	12.43
C1503012	1.9	2.00E-05	8.26E-07	9.35E-05	1.76E-05	7.24E-05	1.64E-06	4.59E-03	3.68E-05	6.39E-03	6.45E-05	9.12E-02	5.56E-02	6.55	11.00
C1503013	2.0	1.07E-05	6.23E-07	6.83E-05	1.63E-05	5.50E-05	8.13E-07	3.59E-03	2.21E-05	3.53E-03	3.18E-05	9.63E-02	5.26E-02	9.79	8.60
C1503014	2.1	9.67E-06	6.98E-07	6.93E-05	2.46E-05	5.50E-05	1.02E-06	3.65E-03	2.45E-05	3.31E-03	2.86E-05	1.18E-01	5.77E-02	13.02	8.74
C1503015	2.4	1.03E-05	5.77E-07	8.52E-05	1.05E-05	5.59E-05	4.07E-07	3.62E-03	2.53E-05	3.43E-03	2.64E-05	9.93E-02	4.82E-02	10.49	8.67
C1503106	2.6	4.90E-06	4.47E-07	5.19E-05	9.67E-06	4.56E-05	1.18E-06	3.07E-03	2.19E-05	1.80E-03	1.99E-05	1.11E-01	4.40E-02	18.85	7.35
V-209a															
C1502001	0.2	3.44E-05	4.78E-07	1.45E-04	8.36E-05	6.90E-06	2.79E-07	2.60E-05	4.49E-07	1.03E-02	4.14E-05	2.02E-01	5.79E+00	0.05	0.16
C1502002	0.3	1.10E-05	4.11E-07	9.46E-05	6.75E-05	3.37E-06	3.15E-07	9.95E-05	1.47E-06	3.36E-03	1.30E-05	8.19E-01	1.24E+00	2.43	0.60
C1502003	0.4	2.47E-05	4.99E-07	3.31E-04	1.02E-04	7.56E-06	2.44E-07	2.27E-04	1.81E-06	7.36E-03	5.30E-05	8.36E-02	7.01E-01	0.26	1.37
C1502004	0.5	5.75E-06	1.22E-07	6.13E-05	8.47E-05	6.64E-06	1.41E-07	4.09E-04	1.28E-06	1.79E-03	8.35E-06	1.82E-01	9.32E-02	4.15	2.46
C1502005	0.6	1.58E-05	5.83E-07	9.90E-05	9.59E-05	1.10E-05	1.69E-07	6.28E-04	2.96E-06	4.77E-03	5.30E-05	8.61E-02	2.91E-01	1.13	3.78
C1502006	0.7	8.79E-06	2.50E-07	1.20E-04	7.58E-05	1.20E-05	2.53E-07	7.91E-04	4.14E-06	2.70E-03	8.09E-06	1.11E-01	9.54E-02	3.24	4.76
C1502007	0.8	5.99E-06	1.07E-07	3.11E-05	7.39E-05	1.11E-05	2.47E-07	7.89E-04	4.11E-06	1.90E-03	4.01E-06	1.48E-01	4.16E-02	6.13	4.75
C1502008	1.0	2.35E-05	4.78E-07	1.24E-04	9.13E-05	1.94E-05	3.57E-07	1.11E-03	4.78E-06	7.22E-03	3.44E-05	1.90E-01	1.34E-01	2.91	6.65
C1502009	1.0	4.99E-05	4.22E-07	4.39E-04	1.76E-04	2.98E-05	1.38E-07	1.58E-03	6.46E-06	1.52E-02	5.37E-05	2.08E-01	8.96E-02	2.16	9.48
C1502010	1.1	4.12E-05	1.27E-06	2.29E-04	1.75E-04	2.13E-05	5.04E-07	9.58E-04	1.75E-06	1.24E-02	4.72E-05	1.64E-01	4.00E-01	1.26	5.76
C1502011	1.2	4.75E-05	8.10E-07	2.71E-04	1.84E-04	2.37E-05	2.90E-07	1.11E-03	4.79E-06	1.42E-02	3.32E-05	5.02E-02	2.23E-01	0.39	6.65
C1502012	1.2	3.01E-05	3.87E-07	9.30E-05	1.10E-04	1.63E-05	2.26E-07	8.39E-04	4.48E-06	9.12E-03	3.66E-05	1.60E-01	1.46E-01	1.47	5.05
C1502013	1.4	6.08E-05	8.10E-07	2.18E-04	1.21E-04	3.30E-05	3.15E-07	1.62E-03	8.13E-06	1.83E-02	4.74E-05	1.36E-01	1.54E-01	1.20	9.75
C1502014	1.5	1.15E-04	1.31E-06	2.54E-04	1.31E-04	3.95E-05	7.72E-07	1.27E-03	1.08E-05	3.43E-02	1.54E-04	5.74E-02	3.35E-01	0.21	7.65
C1502015	1.7	1.16E-04	1.50E-06	2.02E-04	5.49E-05	4.32E-05	4.81E-07	1.59E-03	1.26E-05	3.47E-02	1.30E-04	6.11E-02	2.98E-01	0.28	9.56
C1502016	1.9	9.62E-05	3.98E-07	2.89E-04	4.61E-05	3.86E-05	5.20E-07	1.58E-03	9.60E-06	2.89E-02	1.41E-04	1.49E-01	1.23E-01	0.82	9.51
C1502017	2.1	2.81E-05	1.08E-07	3.15E-04	8.89E-05	2.13E-05	2.43E-07	1.27E-03	1.21E-05	8.55E-03	1.28E-04	1.36E-01	1.04E-01	2.03	7.66
C1502018	2.2	1.56E-05	5.82E-07	9.48E-05	1.36E-04	1.26E-05	3.67E-07	7.37E-04	4.17E-06	4.76E-03	1.07E-04	1.34E-01	2.78E-01	2.07	4.43

Table C.16: Inverse isochron data and apparent ages from**glass stepwise heating** measurements of V-165 and V-209a. Mass discrimination factor is abbrviated as MDF..

Measurement	J	± J	Age (ka)	± Age (ka)	MDF	± MDF	$^{39}Ar/^{40}Ar$	± $^{39}Ar/^{40}Ar$	$^{36}Ar/^{40}Ar$	± $^{36}Ar/^{40}Ar$	ρ
V-165											
C1503001	1.04E-03	4.03E-05	1013	8914	1.0064	0.0002	0.016	9.97E-04	3.32E-03	2.49E-04	0.15
C1503002	1.04E-03	4.03E-05	-1453	2674	1.0064	0.0002	0.057	1.13E-03	3.49E-03	2.68E-04	0.16
C1503003	1.04E-03	4.03E-05	260	1331	1.0064	0.0002	0.211	5.36E-03	3.25E-03	4.93E-04	0.11
C1503004	1.04E-03	4.03E-05	499	315	1.0064	0.0002	0.333	6.85E-03	3.06E-03	1.83E-04	0.12
C1503006	1.04E-03	4.03E-05	440	139	1.0064	0.0002	0.489	5.55E-03	2.97E-03	1.19E-04	0.13
C1503008	1.04E-03	4.03E-05	196	56	1.0064	0.0002	0.740	6.39E-03	3.09E-03	7.21E-05	0.16
C1503009	1.04E-03	4.03E-05	198	48	1.0064	0.0002	0.696	6.10E-03	3.11E-03	5.76E-05	0.25
C1503010	1.04E-03	4.03E-05	189	38	1.0064	0.0002	0.771	6.22E-03	3.09E-03	5.06E-05	0.25
C1503011	1.04E-03	4.03E-05	191	62	1.0064	0.0002	0.725	6.35E-03	3.11E-03	7.85E-05	0.18
C1503012	1.04E-03	4.03E-05	174	106	1.0064	0.0002	0.719	9.28E-03	3.13E-03	1.33E-04	0.19
C1503013	1.04E-03	4.03E-05	184	100	1.0064	0.0002	1.017	1.11E-02	3.02E-03	1.79E-04	0.13
C1503014	1.04E-03	4.03E-05	226	110	1.0064	0.0002	1.101	1.21E-02	2.91E-03	2.12E-04	0.09
C1503015	1.04E-03	4.03E-05	190	92	1.0064	0.0002	1.057	1.10E-02	3.00E-03	1.70E-04	0.10
C1503106	1.04E-03	4.03E-05	211	84	1.0064	0.0002	1.706	2.26E-02	2.72E-03	2.51E-04	0.10
V-209a											
C1502001	9.68E-04	2.98E-05	357	10261	1.0051	0.0002	0.003	4.53E-05	3.35E-03	4.86E-05	0.06
C1502002	9.68E-04	2.98E-05	1451	2202	1.0051	0.0002	0.030	4.53E-04	3.27E-03	1.23E-04	0.03
C1502003	9.68E-04	2.98E-05	148	1241	1.0051	0.0002	0.031	3.31E-04	3.34E-03	7.19E-05	0.22
C1502004	9.68E-04	2.98E-05	322	165	1.0051	0.0002	0.229	1.29E-03	3.21E-03	7.09E-05	0.18
C1502005	9.68E-04	2.98E-05	153	515	1.0051	0.0002	0.132	1.59E-03	3.31E-03	1.28E-04	0.27
C1502006	9.68E-04	2.98E-05	197	169	1.0051	0.0002	0.292	1.77E-03	3.24E-03	9.31E-05	0.05
C1502007	9.68E-04	2.98E-05	262	74	1.0051	0.0002	0.415	2.34E-03	3.14E-03	5.74E-05	0.04
C1502008	9.68E-04	2.98E-05	337	237	1.0051	0.0002	0.153	9.85E-04	3.25E-03	6.81E-05	0.17
C1502009	9.68E-04	2.98E-05	369	159	1.0051	0.0002	0.104	5.62E-04	3.28E-03	3.03E-05	0.25
C1502010	9.68E-04	2.98E-05	290	709	1.0051	0.0002	0.077	3.24E-04	3.31E-03	1.03E-04	0.11
C1502011	9.68E-04	2.98E-05	89	394	1.0051	0.0002	0.078	3.83E-04	3.34E-03	5.76E-05	0.06
C1502012	9.68E-04	2.98E-05	284	259	1.0051	0.0002	0.092	6.15E-04	3.30E-03	4.46E-05	0.18
C1502013	9.68E-04	2.98E-05	240	273	1.0051	0.0002	0.088	4.98E-04	3.31E-03	4.50E-05	0.09
C1502014	9.68E-04	2.98E-05	102	594	1.0051	0.0002	0.037	3.56E-04	3.34E-03	4.11E-05	0.17
C1502015	9.68E-04	2.98E-05	108	527	1.0051	0.0002	0.046	4.02E-04	3.34E-03	4.51E-05	0.12
C1502016	9.68E-04	2.98E-05	265	217	1.0051	0.0002	0.055	4.25E-04	3.32E-03	2.12E-05	0.48
C1502017	9.68E-04	2.98E-05	242	185	1.0051	0.0002	0.149	2.64E-03	3.28E-03	5.07E-05	0.82
C1502018	9.68E-04	2.98E-05	237	492	1.0051	0.0002	0.155	3.59E-03	3.28E-03	1.43E-04	0.50

Appendix D: Ar Isotope Data: Monitor Minerals and Corrections

Ar isotope data of monitor mineral measurements will be provided in this appendix. Data from analysing air and from analysing K and Ca salts is also provided here. An overview of the sample packing and the J-value distribution according to the position in the container is also provided. J-values used for recalculation of the ACs-2 mineral standard are furthermore presented together with the according apparenages and inverse isochron data.

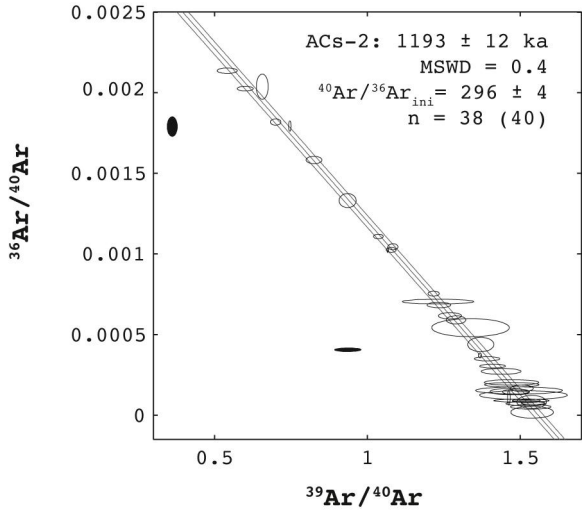

Figure D.1: Inverse isochron of astronimically recalculated ACs-2. All uncertainties stated here represent one standard deviation. Filled ellipses were ignored for the isochron calculation for reasons mentioned in Chapter 6.

Table D.1: Inverse isochron data, J-values, mass discrimination factors, apparent ages and K/Ca ratios from recalculation of ACs-2 mineral standards. Irradiation positions and raw data of the analyses are presented in the following tables of this appendix.

Measurement	$^{39}Ar/^{40}Ar$	$\pm$ $^{39}Ar/^{40}Ar$	$^{36}Ar/^{40}Ar$	$\pm$ $^{36}Ar/^{40}Ar$	ρ	J-val	$\pm$J-val (in %)	MDF	$\pm$MDF (in %)	Age (ka)	$\pm$ Age	K/Ca	$\pm$ K/Ca
MA14003	0.746	0.004	1.79E-03	3.19E-05	1.40E-01	0.0010059	0.9	1.007727	0.1	1146	25	16	0
MA14004	1.368	0.005	3.71E-04	1.47E-05	4.31E-02	0.0010059	0.9	1.007727	0.1	1197	8	52	1
MA14005	1.463	0.004	1.08E-04	4.55E-05	2.07E-03	0.0010059	0.9	1.007727	0.1	1218	18	53	2
MA14006	1.067	0.002	1.02E-03	1.56E-05	5.45E-02	0.0010059	0.9	1.007727	0.1	1198	9	59	1
MA14007	1.078	0.016	1.03E-03	1.47E-05	2.65E-03	0.0009965	1.2	1.007727	0.1	1185	19	65	2
MA14008	1.084	0.016	1.04E-03	1.87E-05	2.71E-03	0.0009965	1.2	1.007727	0.1	1169	20	60	2
MA14009	1.217	0.018	7.54E-04	1.55E-05	1.76E-03	0.0009965	1.2	1.007727	0.1	1172	19	51	1
MA14010	1.036	0.016	1.11E-03	1.41E-05	6.04E-03	0.0009965	1.2	1.007727	0.1	1189	20	61	2
MA14049	1.437	0.065	2.72E-04	1.83E-05	3.57E-04	0.0009953	4.5	1.010407	0.1	1177	54	70	5
MA14050	1.539	0.070	1.80E-05	3.66E-05	2.12E-05	0.0009953	4.5	1.010407	0.1	1190	56	72	6
MA14051	0.935	0.042	4.05E-04	1.10E-05	3.30E-03	0.0009953	4.5	1.010407	0.1	1730	79	46	3
MA14052	0.362	0.016	1.79E-03	5.93E-05	1.41E-03	0.0009953	4.5	1.010407	0.1	2366	140	67	5
MA14045	1.534	0.066	5.16E-05	1.44E-05	1.56E-04	0.0009979	4.2	1.010407	0.1	1181	51	76	5
MA14046	1.465	0.063	1.46E-04	1.93E-05	2.36E-04	0.0009979	4.2	1.010407	0.1	1202	53	80	5
MA14047	0.601	0.026	2.02E-03	1.48E-05	5.24E-03	0.0009979	4.2	1.010407	0.1	1212	54	66	4
MA14048	1.519	0.066	7.14E-05	1.28E-05	9.90E-05	0.0009979	4.2	1.010407	0.1	1186	52	69	5
MA14041	0.542	0.033	2.14E-03	1.70E-05	4.72E-04	0.0009888	6.0	1.010407	0.1	1231	76	57	5
MA14042	1.472	0.089	1.89E-04	1.39E-05	1.39E-04	0.0009888	6.0	1.010407	0.1	1180	72	73	7
MA14043	1.504	0.091	9.03E-05	9.53E-06	1.98E-04	0.0009888	6.0	1.010407	0.1	1191	72	75	7
MA14044	1.472	0.089	2.03E-04	1.70E-05	2.53E-04	0.0009888	6.0	1.010407	0.1	1175	71	73	7
MA14037	1.234	0.039	6.83E-04	1.68E-05	1.14E-03	0.0009430	3.0	1.010407	0.1	1188	38	67	3
MA14038	0.825	0.026	1.58E-03	2.31E-05	7.50E-04	0.0009430	3.0	1.010407	0.1	1176	40	65	3
MA14039	1.537	0.048	8.19E-05	4.05E-05	8.47E-05	0.0009430	3.0	1.010407	0.1	1168	39	75	4
MA14040	1.371	0.043	4.38E-04	4.45E-05	5.35E-04	0.0009430	3.0	1.010407	0.1	1167	41	68	3
MA14033	1.290	0.032	5.91E-04	2.52E-05	1.05E-03	0.0009900	2.3	1.010407	0.1	1175	31	75	4
MA14034	0.700	0.017	1.82E-03	1.95E-05	9.64E-04	0.0009900	2.3	1.010407	0.1	1202	34	66	3
MA14035	1.542	0.038	7.49E-05	9.44E-06	4.79E-04	0.0009900	2.3	1.010407	0.1	1167	29	70	3
MA14036	1.505	0.037	1.66E-04	2.04E-05	2.81E-04	0.0009900	2.3	1.010407	0.1	1162	30	60	2
MA14029	0.656	0.020	2.04E-03	7.80E-05	1.75E-03	0.0009951	2.8	1.010407	0.1	1098	73	66	4
MA14030	1.486	0.044	1.44E-04	1.74E-05	3.06E-04	0.0009951	2.8	1.010407	0.1	1185	36	62	3
MA14031	0.936	0.028	1.33E-03	4.36E-05	1.09E-03	0.0009951	2.8	1.010407	0.1	1186	44	74	4
MA14032	1.519	0.045	8.50E-05	6.61E-06	6.11E-04	0.0009951	2.8	1.010407	0.1	1181	35	73	3
MA14025	1.392	0.042	3.50E-04	1.33E-05	5.92E-04	0.0009877	2.9	1.010407	0.1	1185	36	70	3
MA14026	1.520	0.045	9.05E-05	9.88E-06	4.36E-04	0.0009877	2.9	1.010407	0.1	1178	35	70	3
MA14027	1.270	0.038	6.16E-04	1.97E-05	9.61E-04	0.0009877	2.9	1.010407	0.1	1183	36	65	4
MA14028	1.409	0.042	3.04E-04	1.20E-05	6.11E-04	0.0009877	2.9	1.010407	0.1	1187	36	68	3
MA14021	1.496	0.142	1.53E-04	2.18E-05	7.57E-05	0.0009696	9.5	1.010407	0.1	1174	112	72	10
MA14022	1.511	0.144	1.24E-04	2.77E-05	3.66E-05	0.0009696	9.5	1.010407	0.1	1173	112	71	10
MA14023	1.231	0.117	7.04E-04	1.45E-05	2.95E-04	0.0009696	9.5	1.010407	0.1	1181	112	66	9
MA14024	1.337	0.127	5.43E-04	5.60E-05	1.33E-04	0.0009696	9.5	1.010407	0.1	1154	112	53	7

Table D.2: Sample and monitor positions in irradiation of container PO2CGJ2. J-values are calculated as weighted averages taking the relative distance among two monitor mineral position as the weight. Errors have been propagated accordingly.

Container	Position	Sleeve 1	Base (mm)	Centre (mm)	J ($\times10^{-3}$)	±J ($\times10^{-3}$)	±J in%	Sleeve 2	Base (mm)	Centre (mm)	J ($\times10^{-3}$)	±J ($\times10^{-3}$)	±J in%
PO2CGJ2	13	AC2	25.3	26.0	0.993	0.009	0.89						
PO2CGJ2	12	FC3S	24.0	24.7	0.992	0.008	0.82	AC2	24.8	25.7	1.002	0.012	1.19
PO2CGJ2	11	V-81 #20	22.9	23.4	0.991	0.008	0.76	V-111B #20	23.0	23.9	1.003	0.010	1.02
PO2CGJ2	10	V-65 #30	21.3	22.1	0.989	0.007	0.70	V-111B #45	21.8	22.4	1.002	0.009	0.88
PO2CGJ2	9	FC3S	19.9	20.6	0.988	0.006	0.63	AC2	20.0	20.9	1.002	0.007	0.73
PO2CGJ2	8	AC2	17.5	18.7	0.987	0.005	0.54	V-111B #30	17.8	18.9	1.000	0.007	0.74
PO2CGJ2	7	V-65 #20	13.6	15.5	0.984	0.007	0.72	V-111 #20	15.7	16.8	0.998	0.007	0.74
PO2CGJ2	6	FC3S	11.7	12.6	0.982	0.009	0.88	V-111 #45	14.1	14.9	0.995	0.007	0.75
PO2CGJ2	5	AC2	9.9	10.8	0.980	0.010	0.98	AC2	12.0	13.0	0.992	0.007	0.75
PO2CGJ2	4	V-45 #30	6.7	8.3	0.978	0.009	0.96	V-111 #30	9.3	10.7	0.986	0.008	0.83
PO2CGJ2	3	V-45 #20	4.6	5.6	0.976	0.009	0.93	V-111 #20	6.6	8.0	0.979	0.009	0.91
PO2CGJ2	2	FC3S	2.5	3.5	0.975	0.009	0.91	V-81 #30	2.1	4.4	0.967	0.010	1.04
PO2CGJ2	1	AC2	0.0	1.3	0.973	0.009	0.881	AC2	0.0	1.1	0.954	0.011	1.16
Container	Position	Sleeve 3	Base (mm)	Centre (mm)	J ($\times10^{-3}$)	±J ($\times10^{-3}$)	±J in%	Sleeve 4	Base (mm)	Centre (mm)	J ($\times10^{-3}$)	±J ($\times10^{-3}$)	±J in%
PO2CGJ2	12	AC2	24.8	25.2	1.009	7.047	0.70						
PO2CGJ2	11	V-279 #20	23.2	24.0	1.008	6.974	0.69						
PO2CGJ2	10	V-254 #20	21.1	22.2	1.006	6.857	0.68						
PO2CGJ2	9	V-221a #30	18.8	20.0	1.004	6.717	0.67	AC2	25.4	26.2	1.004	0.008	0.81
PO2CGJ2	8	AC2	17.9	18.3	1.002	6.614	0.66	V-189b #45	23.5	24.4	1.004	0.010	0.98
PO2CGJ2	7	V-221a #20	14.9	16.4	1.000	6.325	0.63	AC2	21.7	22.6	1.004	0.012	1.15
PO2CGJ2	6	V-209a #30	11.8	13.3	0.997	6.184	0.62	V-144 #30	18.5	20.1	1.004	0.011	1.07
PO2CGJ2	5	AC2	9.5	10.7	0.994	5.477	0.55	V-137 #45	15.1	16.8	1.004	0.010	0.97
PO2CGJ2	4	V-209a #20	6.8	8.2	0.991	6.327	0.64	AC2	11.9	13.5	1.003	0.009	0.87
PO2CGJ2	3	V-145 #45	4.6	5.7	0.988	7.159	0.72	V-279 #30	8.4	10.2	1.002	0.010	0.98
PO2CGJ2	2	V-145 #30	2.1	3.4	0.985	7.957	0.81	V-254 #30	3.7	6.0	0.999	0.011	1.11
PO2CGJ2	1	AC2	0.0	1.0	0.982	8.741	0.89	AC2	0.0	1.8	0.996	0.012	1.25

Table D.3: Sample and monitor positions in sleeves from irradiations of containers PO3CG2 and PO2CS2. J-values are calculated as weighted averages taking the relative distance among two monitor mineral position as the weight. Errors have been propagated accordingly. Glasses in sample V-165 † are very clear and transparent, whereas glasses in sample V-165 are blurry to non-transparent.

Container	Position	Sleeve 2	Base (mm)	Centre (mm)	J ($\times10^{-3}$)	±J ($\times10^{-6}$)	±J in%	Sleeve 3	Base (mm)	Centre (mm)	J ($\times10^{-3}$)	±J ($\times10^{-5}$)	±J in%
PO2CS2	8	AC2	18.0	18.8	0.965	0.013	1.31	AC2	16.0	16.8	0.924	0.013	1.38
PO2CS2	7	V-45 G	17.0	17.5	0.966	0.014	1.41	V-137 G	13.9	15.0	0.936	0.015	1.62
PO2CS2	6	V-209a G	14.6	15.8	0.968	0.015	1.55	V-298 G	12.6	13.2	0.947	0.017	1.84
PO2CS2	5	AC 2	11.2	12.9	0.970	0.017	1.78	V-297 G	10.7	11.6	0.955	0.020	2.04
PO2CS2	4	V-165 G	9.8	10.5	0.970	0.016	1.67	AC2	8.7	9.7	0.964	0.022	2.28
PO2CS2	3	V-184 G	7.0	8.4	0.971	0.015	1.58	V-65 G	5.9	7.3	0.972	0.019	1.99
PO2CS2	2	V-184 #30	2.3	4.7	0.970	0.014	1.41	V-57b G	3.0	4.4	0.978	0.016	1.67
PO2CS2	1	AC2	0.0	1.2	0.967	0.012	1.25	AC2	0.0	1.5	0.980	0.013	1.34
Container	**Position**	**Sleeve 1**	**Base (mm)**	**Centre (mm)**	**J ($\times10^{-3}$)**	**±J ($\times10^{-5}$)**	**±J in%**	**Sleeve 2**	**Base (mm)**	**Centre (mm)**	**J ($\times10^{-3}$)**	**±J ($\times10^{-5}$)**	**±J in%**
PO3CG2	14							FC3S	24.4	25.2	1.082	0.016	1.4
PO3CG2	13							Diff. Study	23.0	23.7	1.082	0.015	1.4
PO3CG2	12							Diff. Study	21.4	22.2	1.081	0.014	1.3
PO3CG2	11							Diff. Study	19.5	20.5	1.079	0.013	1.2
PO3CG2	10	AC2	23.1	25.5	1.030	0.020	1.9	Diff. Study	17.7	18.6	1.076	0.012	1.1
PO3CG2	9	V-36 #30	20.6	21.8	1.038	0.016	1.5	FC3S	16.2	16.9	1.073	0.011	1.1
PO3CG2	8	V-227	17.3	18.9	1.042	0.013	1.2	Diff. Study	14.5	15.3	1.070	0.011	1.1
PO3CG2	7	AC2	15.2	16.2	1.045	0.010	0.9	Diff. Study	13.0	13.7	1.066	0.011	1.1
PO3CG2	6	V-299 #30	12.4	13.8	1.047	0.012	1.2	Diff. Study	11.9	12.4	1.063	0.012	1.1
PO3CG2	5	V-289 G	9.4	10.9	1.047	0.015	1.5	FC S 3	9.7	10.8	1.058	0.012	1.1
PO3CG2	4	AC2	7.6	8.5	1.047	0.018	1.7	Ac2	7.6	8.7	1.051	0.028	2.7
PO3CG2	3	V-279 G	4.9	6.3	1.045	0.019	1.8	V-58 G	6.2	6.9	1.044	0.027	2.6
PO3CG2	2	V-165 G †	3.0	4.0	1.043	0.020	1.9	V-146 #30	2.2	4.2	1.032	0.026	2.5
PO3CG2	1	AC2	0.0	1.5	1.040	0.021	2.1	AC2	0.0	1.1	1.018	0.024	2.4

Table D.4: Ion beam intensities (in V) from measurements of **Alder Creek Sanidine monitor minerals**.All uncertainties represent two standard deviations. Listed measurements listed were irradiated in sleeve 1 and sleeve 2 and packed in container PO2CGJ2.The column 'contribution' marks measurements that contributed to the weighted average J-value calculation of the irradiated position.

Container	Sleeve	Position	Contribution	Measurement	^{36}Ar	$\pm^{36}Ar$	^{37}Ar	$\pm^{37}Ar$	^{38}Ar	$\pm^{38}Ar$	^{39}Ar	$\pm^{39}Ar$	^{40}Ar	$\pm^{40}Ar$
PO2CGJ2	1	1	No	MA14065	3.9E-12	1.5E-12	3.1E-05	3.1E-06	4.3E-05	7.9E-07	3.5E-03	2.2E-05	2.6E-03	9.4E-06
PO2CGJ2	1	1	Yes	MA14001	4.7E-06	3.7E-07	3.4E-05	3.1E-06	4.6E-05	7.0E-07	3.8E-03	2.5E-05	4.0E-03	1.1E-01
PO2CGJ2	1	1	Yes	MA14002	2.9E-05	7.9E-07	5.6E-05	2.8E-06	9.1E-05	1.4E-06	7.1E-03	4.3E-05	1.3E-02	3.0E-02
PO2CGJ2	1	1	Yes	MA14066	4.6E-07	1.8E-07	1.0E-04	5.6E-06	1.5E-04	2.1E-06	1.2E-02	7.5E-05	8.3E-03	8.1E-02
PO2CGJ2	1	5	No	MA14062	2.1E-06	2.3E-07	7.0E-05	3.5E-06	1.0E-04	1.5E-06	8.5E-03	5.2E-05	1.2E-02	1.4E-01
PO2CGJ2	1	5	Yes	MA14063	3.8E-06	1.6E-07	5.7E-05	1.9E-06	8.6E-05	1.6E-06	7.4E-03	4.4E-05	6.0E-03	5.7E-02
PO2CGJ2	1	5	Yes	MA14064	2.8E-06	4.5E-07	6.3E-05	3.5E-06	8.7E-05	1.3E-06	7.2E-03	4.5E-05	5.6E-03	2.6E-01
PO2CGJ2	1	5	Yes	MA14061	1.0E-07	2.3E-07	9.3E-05	5.0E-06	1.5E-04	2.3E-06	1.3E-02	9.2E-05	8.4E-03	1.3E-01
PO2CGJ2	1	8	Yes	MA14057	1.5E-06	1.3E-07	1.0E-04	6.2E-06	1.5E-04	2.3E-06	1.3E-02	8.4E-05	8.9E-03	9.0E-02
PO2CGJ2	1	8	Yes	MA14058	1.1E-06	1.7E-07	9.4E-05	6.1E-06	1.6E-04	2.1E-06	1.3E-02	7.9E-05	8.8E-03	9.1E-02
PO2CGJ2	1	8	Yes	MA14059	3.1E-08	9.2E-08	6.7E-05	4.0E-06	1.1E-04	1.5E-06	9.2E-03	5.7E-05	6.0E-03	6.9E-02
PO2CGJ2	1	8	Yes	MA14060	8.1E-07	2.2E-07	7.9E-05	4.3E-06	1.1E-04	1.8E-06	9.5E-03	5.8E-05	6.5E-03	8.2E-02
PO2CGJ2	1	13	Yes	MA14053	1.3E-05	5.2E-07	7.3E-05	3.5E-06	1.0E-04	1.5E-06	8.5E-03	5.3E-05	9.5E-03	4.2E-02
PO2CGJ2	1	13	Yes	MA14054	4.3E-06	2.7E-07	9.6E-05	4.1E-06	1.4E-04	2.1E-06	1.1E-02	6.9E-05	8.6E-03	6.5E-02
PO2CGJ2	1	13	Yes	MA14055	3.8E-06	2.2E-07	7.2E-05	3.3E-06	9.7E-05	1.4E-06	8.2E-03	4.9E-05	6.4E-03	6.5E-02
PO2CGJ2	1	13	No	MA14056	1.8E-07	8.1E-08	3.8E-05	2.9E-06	5.9E-05	1.2E-06	5.0E-03	3.1E-05	7.0E-03	1.0E-01
PO2CGJ2	2	1	Yes	MA14037	6.5E-06	3.5E-07	9.4E-05	3.8E-06	1.3E-04	2.0E-06	1.1E-02	6.7E-05	9.4E-03	7.9E-02
PO2CGJ2	2	1	Yes	MA14038	1.7E-05	6.2E-07	7.3E-05	4.5E-06	1.0E-04	2.0E-06	8.3E-03	5.1E-05	1.1E-02	4.8E-02
PO2CGJ2	2	1	Yes	MA14039	2.5E-07	2.4E-07	3.2E-05	2.3E-06	5.1E-05	7.0E-07	4.3E-03	2.7E-05	3.0E-03	9.6E-02
PO2CGJ2	2	1	Yes	MA14040	1.7E-06	3.4E-07	4.1E-05	2.0E-06	5.7E-05	1.1E-06	4.8E-03	3.0E-05	3.7E-03	1.2E-01
PO2CGJ2	2	5	Yes	MA14041	3.2E-05	8.6E-07	7.8E-05	3.9E-06	9.8E-05	1.5E-06	7.8E-03	4.8E-05	1.5E-02	4.2E-02
PO2CGJ2	2	5	Yes	MA14042	2.1E-06	3.0E-07	1.2E-04	6.5E-06	1.8E-04	2.7E-06	1.5E-02	9.4E-05	1.1E-02	5.0E-02
PO2CGJ2	2	5	Yes	MA14043	7.9E-07	1.6E-07	9.6E-05	5.8E-06	1.5E-04	2.2E-06	1.2E-02	7.9E-05	8.4E-03	9.4E-02
PO2CGJ2	2	5	Yes	MA14044	9.8E-07	1.6E-07	5.4E-05	3.0E-06	8.2E-05	1.6E-06	6.9E-03	4.3E-05	4.7E-03	9.6E-02
PO2CGJ2	2	9	Yes	MA14045	3.9E-07	2.1E-07	8.1E-05	4.6E-06	1.3E-04	2.2E-06	1.1E-02	7.0E-05	7.1E-03	1.2E-01
PO2CGJ2	2	9	Yes	MA14046	9.3E-07	2.4E-07	6.5E-05	4.1E-06	1.1E-04	2.0E-06	9.0E-03	5.5E-05	6.2E-03	9.9E-02
PO2CGJ2	2	9	Yes	MA14047	4.5E-05	1.2E-06	1.1E-04	4.1E-06	1.6E-04	2.6E-06	1.3E-02	8.1E-05	2.2E-02	1.3E-01
PO2CGJ2	2	9	Yes	MA14048	6.1E-07	2.1E-07	1.0E-04	5.4E-06	1.5E-04	2.2E-06	1.2E-02	7.5E-05	8.1E-03	6.2E-02
PO2CGJ2	2	12	Yes	MA14049	1.3E-06	1.7E-07	5.3E-05	2.9E-06	7.7E-05	1.5E-06	6.5E-03	4.0E-05	4.6E-03	8.6E-02
PO2CGJ2	2	12	Yes	MA14050	5.3E-08	1.8E-07	3.0E-05	2.6E-06	4.5E-05	8.6E-07	3.8E-03	2.3E-05	2.5E-03	1.2E-01
PO2CGJ2	2	12	No	MA14051	3.4E-06	2.0E-07	9.4E-05	3.9E-06	9.0E-05	1.3E-06	7.6E-03	4.6E-05	8.1E-03	2.0E-01
PO2CGJ2	2	12	No	MA14052	2.2E-05	1.5E-06	3.8E-05	2.6E-06	5.7E-05	1.2E-06	4.4E-03	2.9E-05	1.2E-02	1.4E-01

Table D.5: Additional isotope ratios from measurements of **Alder Creek Sanidine monitor minerals**.All uncertainties represent two standard deviations. Listed measurements listed were irradiated in sleeve 1 and sleeve 2 and packed in container PO2CGJ2. The column 'contribution' marks measurements that contributed to the weighted average J-value calculation of the irradiated position.

Container	Sleelve	Position	Contribution	Measurement	$\frac{^{40}Ar^*}{^{39}Ar_K}$	$\pm\frac{^{40}Ar^*}{^{39}Ar_K}$	J	$\pm$ J	%40Ar*	%39Ar$_K$	$\frac{Ca}{K}$	$\pm\frac{Ca}{K}$
PO2CGJ2	1	1	No	MA14065	7.0E-01	2.0E-04	9.2E-04	1.8E-05	95.6	13.2	63.8	6.3
PO2CGJ2	1	1	Yes	MA14001	6.8E-01	2.9E-02	9.6E-04	4.1E-05	64.8	14.4	65.1	6.0
PO2CGJ2	1	1	Yes	MA14002	6.6E-01	3.4E-02	9.8E-04	5.0E-05	35.2	26.6	73.0	3.7
PO2CGJ2	1	1	Yes	MA14066	6.7E-01	6.1E-03	9.7E-04	8.9E-06	98.3	45.8	69.8	3.9
PO2CGJ2	1	5	No	MA14062	1.3E+00	1.2E-02	4.9E-04	4.4E-06	94.8	23.9	68.9	3.5
PO2CGJ2	1	5	Yes	MA14063	6.6E-01	7.7E-03	9.9E-04	1.2E-05	81.1	20.7	73.3	2.5
PO2CGJ2	1	5	Yes	MA14064	6.6E-01	1.9E-02	9.8E-04	2.9E-05	85.1	20.2	65.3	3.6
PO2CGJ2	1	5	Yes	MA14061	6.7E-01	7.6E-03	9.7E-04	1.1E-05	99.6	35.2	77.0	4.2
PO2CGJ2	1	8	Yes	MA14057	6.6E-01	5.5E-03	9.9E-04	8.2E-06	95.0	29.0	71.0	4.3
PO2CGJ2	1	8	Yes	MA14058	6.6E-01	5.9E-03	9.8E-04	8.8E-06	96.4	29.0	77.7	5.0
PO2CGJ2	1	8	Yes	MA14059	6.5E-01	5.2E-03	9.9E-04	7.9E-06	99.8	20.8	78.8	4.8
PO2CGJ2	1	8	Yes	MA14060	6.6E-01	8.0E-03	9.8E-04	1.2E-05	96.3	21.3	68.4	3.7
PO2CGJ2	1	13	Yes	MA14053	6.5E-01	1.9E-02	1.0E-03	2.8E-05	58.4	25.9	66.1	3.1
PO2CGJ2	1	13	Yes	MA14054	6.5E-01	8.2E-03	9.9E-04	1.2E-05	85.0	34.1	66.5	2.8
PO2CGJ2	1	13	Yes	MA14055	6.5E-01	9.0E-03	9.9E-04	1.4E-05	82.6	24.8	64.5	3.0
PO2CGJ2	1	13	No	MA14056	1.4E+00	1.0E-02	4.7E-04	3.5E-06	99.2	15.1	73.9	5.6
PO2CGJ2	2	1	Yes	MA14037	6.8E-01	1.1E-02	9.5E-04	1.5E-05	79.3	38.6	66.3	2.7
PO2CGJ2	2	1	Yes	MA14038	6.7E-01	2.3E-02	9.6E-04	3.3E-05	52.2	29.2	64.2	3.9
PO2CGJ2	2	1	Yes	MA14039	6.7E-01	1.8E-02	9.6E-04	2.5E-05	97.4	15.1	75.0	5.3
PO2CGJ2	2	1	Yes	MA14040	6.7E-01	2.1E-02	9.6E-04	3.1E-05	86.7	17.1	67.8	3.4
PO2CGJ2	2	5	Yes	MA14041	6.7E-01	3.3E-02	9.7E-04	4.9E-05	35.5	18.3	56.9	2.8
PO2CGJ2	2	5	Yes	MA14042	6.5E-01	7.2E-03	1.0E-03	1.1E-05	94.2	36.3	72.8	3.9
PO2CGJ2	2	5	Yes	MA14043	6.6E-01	5.9E-03	9.9E-04	8.9E-06	97.2	29.3	74.2	4.5
PO2CGJ2	2	5	Yes	MA14044	6.5E-01	8.4E-03	1.0E-03	1.3E-05	93.8	16.1	72.3	4.0
PO2CGJ2	2	9	Yes	MA14045	6.4E-01	7.3E-03	1.0E-03	1.1E-05	98.3	23.8	75.4	4.3
PO2CGJ2	2	9	Yes	MA14046	6.6E-01	9.1E-03	9.9E-04	1.4E-05	95.5	20.0	79.5	5.1
PO2CGJ2	2	9	Yes	MA14047	6.5E-01	2.8E-02	9.9E-04	4.2E-05	38.9	29.0	65.6	2.4
PO2CGJ2	2	9	Yes	MA14048	6.5E-01	6.6E-03	1.0E-03	1.0E-05	97.7	27.1	69.1	3.7
PO2CGJ2	2	12	Yes	MA14049	6.4E-01	8.9E-03	1.0E-03	1.4E-05	91.7	29.2	69.7	3.8
PO2CGJ2	2	12	Yes	MA14050	6.5E-01	1.5E-02	9.9E-04	2.3E-05	99.4	17.0	71.6	6.3
PO2CGJ2	2	12	No	MA14051	9.5E-01	1.1E-02	6.8E-04	7.7E-06	87.7	34.0	45.6	1.9
PO2CGJ2	2	12	No	MA14052	1.3E+00	1.1E-01	5.1E-04	4.2E-05	46.0	19.8	66.5	4.6

Table D.6: Ion beam intensities (in V) from measurements of **Alder Creek Sanidine monitor minerals**.All uncertainties represent two standard deviations. Listed measurements listed were irradiated in sleeve 3 and sleeve 4 and packed in container PO2CGJ2.The column 'contribution' marks measurements that contributed to the weighted average J-value calculation of the irradiated position.

Container	Sleelve	Position	Contribution	Measurement	^{36}Ar	$\pm^{36}$Ar	^{37}Ar	$\pm^{37}$Ar	^{38}Ar	$\pm^{38}$Ar	^{39}Ar	$\pm^{39}$Ar	^{40}Ar	$\pm^{40}$Ar
PO2CGJ2	3	1	Yes	MA14021	6.5E-07	1.8E-07	4.7E-05	4.5E-06	7.1E-05	1.8E-06	6.0E-03	3.7E-05	4.1E-03	8.0E-02
PO2CGJ2	3	1	Yes	MA14022	5.8E-07	2.5E-07	5.3E-05	4.0E-06	7.8E-05	1.3E-06	6.5E-03	4.0E-05	4.5E-03	6.2E-02
PO2CGJ2	3	1	Yes	MA14023	6.2E-06	2.9E-07	8.9E-05	4.0E-06	1.2E-04	1.9E-06	1.0E-02	6.2E-05	8.7E-03	5.6E-02
PO2CGJ2	3	1	Yes	MA14024	2.3E-06	5.2E-07	5.6E-05	1.8E-06	6.3E-05	1.0E-06	5.2E-03	3.6E-05	4.0E-03	1.0E-01
PO2CGJ2	3	5	Yes	MA14025	3.9E-06	3.1E-07	1.2E-04	5.0E-06	1.8E-04	2.8E-06	1.5E-02	9.3E-05	1.1E-02	5.9E-02
PO2CGJ2	3	5	Yes	MA14026	6.9E-07	1.5E-07	8.9E-05	4.7E-06	1.3E-04	1.7E-06	1.1E-02	6.7E-05	7.3E-03	1.0E-01
PO2CGJ2	3	5	Yes	MA14027	3.3E-06	2.2E-07	5.8E-05	4.2E-06	7.9E-05	1.1E-06	6.6E-03	4.0E-05	5.2E-03	8.0E-02
PO2CGJ2	3	5	Yes	MA14028	2.8E-06	2.2E-07	1.0E-04	6.3E-06	1.5E-04	2.6E-06	1.2E-02	7.5E-05	8.9E-03	6.2E-02
PO2CGJ2	3	8	Yes	MA14029	1.7E-05	1.3E-06	4.6E-05	3.7E-06	6.7E-05	8.2E-07	5.3E-03	3.2E-05	8.1E-03	1.4E-01
PO2CGJ2	3	8	Yes	MA14030	5.6E-07	1.3E-07	5.1E-05	3.5E-06	6.7E-05	1.2E-06	5.5E-03	3.4E-05	3.7E-03	8.5E-02
PO2CGJ2	3	8	Yes	MA14031	6.5E-06	4.5E-07	3.4E-05	2.6E-06	5.5E-05	1.0E-06	4.5E-03	2.9E-05	4.8E-03	9.5E-02
PO2CGJ2	3	8	Yes	MA14032	7.9E-07	1.2E-07	1.1E-04	3.1E-06	1.6E-04	2.1E-06	1.3E-02	8.3E-05	8.9E-03	1.0E-01
PO2CGJ2	3	12	Yes	MA14033	3.0E-06	2.6E-07	4.8E-05	3.6E-06	7.7E-05	1.3E-06	6.4E-03	4.0E-05	5.0E-03	9.1E-02
PO2CGJ2	3	12	Yes	MA14034	3.2E-05	9.9E-07	1.1E-04	5.0E-06	1.5E-04	2.1E-06	1.2E-02	7.4E-05	1.8E-02	4.2E-02
PO2CGJ2	3	12	Yes	MA14035	6.2E-07	1.5E-07	9.8E-05	6.0E-06	1.4E-04	1.9E-06	1.2E-02	7.4E-05	7.9E-03	1.0E-01
PO2CGJ2	3	12	Yes	MA14036	1.0E-06	2.5E-07	8.6E-05	3.3E-06	1.1E-04	1.6E-06	9.1E-03	5.5E-05	6.1E-03	6.9E-02
PO2CGJ2	4	1	Yes	MA14003	3.9E-05	1.6E-06	5.8E-04	1.5E-05	2.1E-04	3.4E-06	1.6E-02	1.6E-04	2.2E-02	3.7E-01
PO2CGJ2	4	1	Yes	MA14004	2.7E-06	2.2E-07	1.1E-04	4.9E-06	1.2E-04	1.6E-06	1.0E-02	8.2E-05	7.3E-03	2.5E-01
PO2CGJ2	4	1	Yes	MA14005	2.2E-07	1.8E-07	3.1E-05	2.7E-06	3.5E-05	5.2E-07	2.9E-03	2.2E-05	2.0E-03	1.5E-01
PO2CGJ2	4	1	Yes	MA14006	1.4E-05	5.1E-07	1.4E-04	3.8E-06	1.8E-04	2.4E-06	1.4E-02	9.3E-05	1.3E-02	1.2E-01
PO2CGJ2	4	4	Yes	MA14007	1.8E-05	6.7E-07	1.7E-04	6.1E-06	2.3E-04	3.6E-06	1.9E-02	1.2E-04	1.8E-02	6.2E-02
PO2CGJ2	4	4	Yes	MA14008	1.7E-05	7.1E-07	1.6E-04	5.1E-06	2.1E-04	3.1E-06	1.7E-02	1.1E-04	1.6E-02	7.3E-02
PO2CGJ2	4	4	Yes	MA14009	1.1E-05	5.0E-07	2.0E-04	7.3E-06	2.1E-04	3.3E-06	1.7E-02	1.1E-04	1.4E-02	5.5E-02
PO2CGJ2	4	4	Yes	MA14010	1.6E-05	5.3E-07	1.4E-04	4.3E-06	1.7E-04	2.5E-06	1.4E-02	8.9E-05	1.4E-02	9.9E-02
PO2CGJ2	4	7	Yes	MA14011	5.0E-06	2.1E-07	1.4E-04	5.7E-06	1.1E-04	1.7E-06	9.0E-03	7.3E-05	7.3E-03	6.7E-02
PO2CGJ2	4	7	Yes	MA14012	1.4E-05	6.5E-07	1.2E-04	3.6E-06	1.2E-04	1.7E-06	1.0E-02	6.3E-05	1.1E-02	8.6E-02
PO2CGJ2	4	7	Yes	MA14013	1.2E-07	1.6E-07	4.3E-05	2.7E-06	3.4E-05	7.6E-07	2.9E-03	1.8E-05	1.9E-03	1.4E-01
PO2CGJ2	4	7	Yes	MA14015	5.9E-07	1.9E-07	2.3E-05	2.8E-06	4.1E-05	1.0E-06	3.4E-03	2.2E-05	2.4E-03	1.5E-01
PO2CGJ2	4	7	Yes	MA1404	1.2E-05	4.5E-07	7.6E-05	3.1E-06	8.5E-05	1.2E-06	6.9E-03	4.2E-05	8.1E-03	8.7E-02
PO2CGJ2	4	9	Yes	MA14017	4.7E-06	3.2E-07	1.5E-04	4.8E-06	1.6E-04	2.3E-06	1.3E-02	9.3E-05	9.8E-03	6.1E-02
PO2CGJ2	4	9	Yes	MA14018	6.8E-06	3.3E-07	1.7E-04	8.3E-06	1.7E-04	2.3E-06	1.4E-02	1.0E-04	1.1E-02	6.3E-02
PO2CGJ2	4	9	Yes	MA14019	9.4E-06	4.6E-07	1.3E-04	5.2E-06	1.5E-04	1.8E-06	1.2E-02	6.7E-05	1.1E-02	5.7E-02
PO2CGJ2	4	9	Yes	MA14020	1.2E-05	5.6E-07	1.0E-04	5.8E-06	1.2E-04	1.6E-06	9.7E-03	5.4E-05	1.0E-02	1.1E-01

Table D.7: Additional isotope ratios from measurements of **Alder Creek Sanidine monitor minerals.** All uncertainties represent two standard deviations. Listed measurements listed were irradiated in sleeve 3 and sleeve 4 and packed in container PO2CGJ2. The column 'contribution' marks measurements that contributed to the weighted average J-value calculation of the irradiated position.

Container	Sleelve	Position	Contribution	Measurement	$\frac{^{40}Ar^*}{^{39}Ar_K}$	$\pm\frac{^{40}Ar^*}{^{39}Ar_K}$	J	$\pm$ J	%40Ar*	%39Ar$_K$	$\frac{Ca}{K}$	$\pm\frac{Ca}{K}$
PO2CGJ2	3	1	Yes	MA14021	6.6E-01	1.0E-02	9.8E-04	1.5E-05	95.3	21.3	71.8	6.9
PO2CGJ2	3	1	Yes	MA14022	6.6E-01	1.2E-02	9.8E-04	1.8E-05	96.2	23.4	71.0	5.4
PO2CGJ2	3	1	Yes	MA14023	6.6E-01	9.3E-03	9.8E-04	1.4E-05	78.7	36.8	66.1	3.0
PO2CGJ2	3	1	Yes	MA14024	6.4E-01	3.0E-02	1.0E-03	4.8E-05	82.9	18.5	52.4	1.7
PO2CGJ2	3	5	Yes	MA14025	6.5E-01	7.4E-03	9.9E-04	1.1E-05	89.4	33.7	69.8	2.8
PO2CGJ2	3	5	Yes	MA14026	6.5E-01	5.9E-03	1.0E-03	9.0E-06	97.2	24.3	70.1	3.7
PO2CGJ2	3	5	Yes	MA14027	6.5E-01	1.1E-02	1.0E-03	1.7E-05	81.3	14.6	64.8	4.7
PO2CGJ2	3	5	Yes	MA14028	6.5E-01	6.8E-03	9.9E-04	1.0E-05	90.7	27.4	67.4	4.1
PO2CGJ2	3	8	Yes	MA14029	5.9E-01	7.5E-02	1.1E-03	1.4E-04	38.5	18.3	65.6	5.3
PO2CGJ2	3	8	Yes	MA14030	6.5E-01	8.3E-03	1.0E-03	1.3E-05	95.6	19.2	61.4	4.2
PO2CGJ2	3	8	Yes	MA14031	6.5E-01	3.0E-02	1.0E-03	4.7E-05	59.8	15.6	73.9	5.6
PO2CGJ2	3	8	Yes	MA14032	6.5E-01	5.1E-03	1.0E-03	7.8E-06	97.3	46.9	72.8	2.2
PO2CGJ2	3	12	Yes	MA14033	6.5E-01	1.3E-02	1.0E-03	2.0E-05	82.1	16.1	75.0	5.6
PO2CGJ2	3	12	Yes	MA14034	6.5E-01	2.5E-02	9.9E-04	3.8E-05	45.1	30.7	65.4	3.1
PO2CGJ2	3	12	Yes	MA14035	6.4E-01	5.7E-03	1.0E-03	9.0E-06	97.6	30.2	69.4	4.2
PO2CGJ2	3	12	Yes	MA14036	6.4E-01	9.3E-03	1.0E-03	1.5E-05	94.9	22.9	59.9	2.3
PO2CGJ2	4	1	Yes	MA14003	6.2E-01	3.2E-02	1.0E-03	5.3E-05	46.4	37.3	15.9	0.4
PO2CGJ2	4	1	Yes	MA14004	6.5E-01	9.3E-03	1.0E-03	1.4E-05	88.9	23.2	52.3	2.4
PO2CGJ2	4	1	Yes	MA14005	6.6E-01	1.9E-02	9.8E-04	2.9E-05	96.7	6.7	52.7	4.6
PO2CGJ2	4	1	Yes	MA14006	6.5E-01	1.2E-02	1.0E-03	1.8E-05	69.4	32.9	59.2	1.7
PO2CGJ2	4	4	Yes	MA14007	6.5E-01	1.1E-02	1.0E-03	1.7E-05	69.3	28.1	65.4	2.4
PO2CGJ2	4	4	Yes	MA14008	6.4E-01	1.3E-02	1.0E-03	2.0E-05	68.8	25.4	60.3	1.9
PO2CGJ2	4	4	Yes	MA14009	6.4E-01	9.6E-03	1.0E-03	1.5E-05	77.4	25.3	50.5	1.9
PO2CGJ2	4	4	Yes	MA14010	6.5E-01	1.2E-02	9.9E-04	1.8E-05	66.9	21.2	60.5	2.0
PO2CGJ2	4	7	Yes	MA14011	6.4E-01	8.8E-03	1.0E-03	1.4E-05	79.5	27.7	37.3	1.6
PO2CGJ2	4	7	Yes	MA14012	6.4E-01	1.9E-02	1.0E-03	3.0E-05	61.8	31.6	50.8	1.6
PO2CGJ2	4	7	Yes	MA14013	6.4E-01	1.7E-02	1.0E-03	2.7E-05	98.2	8.9	38.8	2.4
PO2CGJ2	4	7	Yes	MA14015	6.6E-01	1.7E-02	9.8E-04	2.5E-05	92.7	10.6	84.4	10.1
PO2CGJ2	4	7	Yes	MA1404	6.5E-01	2.0E-02	9.9E-04	3.0E-05	55.4	21.2	51.6	2.1
PO2CGJ2	4	9	Yes	MA14017	6.5E-01	8.9E-03	1.0E-03	1.4E-05	85.5	26.6	49.9	1.6
PO2CGJ2	4	9	Yes	MA14018	6.4E-01	8.7E-03	1.0E-03	1.4E-05	81.3	28.2	45.2	2.2
PO2CGJ2	4	9	Yes	MA14019	6.5E-01	1.2E-02	1.0E-03	1.8E-05	73.9	25.2	55.7	2.3
PO2CGJ2	4	9	Yes	MA14020	6.5E-01	1.8E-02	1.0E-03	2.7E-05	63.1	20.1	53.4	3.0

Table D.8: Ion beam intensities (in V) from measurements of **Alder Creek Sanidine monitor minerals**.All uncertainties represent two standard deviations. Listed measurements listed were irradiated in sleeve 2 and sleeve 3 and packed in container PO2CS2.The column 'contribution' marks measurements that contributed to the weighted average J-value calculation of the irradiated position.

Container	Sleelve	Position	Contribution	Measurement	^{36}Ar	$\pm^{36}$Ar	^{37}Ar	$\pm^{37}$Ar	^{38}Ar	$\pm^{38}$Ar	^{39}Ar	$\pm^{39}$Ar	^{40}Ar	$\pm^{40}$Ar
PO2CS2	2	1	Yes	M15068	5.0E-05	2.0E-06	1.2E-04	2.1E-04	1.9E-04	4.1E-06	1.6E-02	1.7E-04	2.5E-02	3.4E-01
PO2CS2	2	1	Yes	M15070	6.6E-07	3.9E-07	-1.1E-04	-2.3E-04	8.0E-05	1.7E-06	6.6E-03	7.2E-05	4.8E-03	3.0E-01
PO2CS2	2	1	Yes	M15071	1.7E-06	3.6E-07	5.9E-05	2.7E-04	1.2E-04	2.6E-06	9.6E-03	1.0E-04	6.9E-03	2.7E-01
PO2CS2	2	1	Yes	M15072	2.9E-07	1.5E-07	4.0E-05	2.9E-04	1.7E-04	4.0E-06	1.4E-02	1.7E-04	9.7E-03	4.2E-01
PO2CS2	2	5	Yes	MA140421	7.1E-07	4.1E-07	2.9E-05	1.1E-04	5.4E-05	1.4E-06	4.5E-03	4.6E-05	3.2E-03	1.8E-01
PO2CS2	2	5	Yes	MA140422	1.9E-05	8.3E-07	1.3E-04	1.2E-04	1.0E-04	2.3E-06	8.0E-03	8.3E-05	1.1E-02	1.4E-01
PO2CS2	2	5	Yes	MA140423	1.6E-06	4.8E-07	3.3E-05	8.5E-05	1.4E-04	3.0E-06	1.2E-02	1.2E-04	8.3E-03	1.9E-01
PO2CS2	2	9	Yes	MA140424	5.9E-06	3.4E-07	1.3E-04	8.4E-05	9.9E-05	2.2E-06	8.1E-03	8.2E-05	7.2E-03	6.9E-02
PO2CS2	2	9	Yes	MA140425	1.5E-05	6.9E-07	2.2E-04	1.0E-04	1.9E-04	4.0E-06	1.5E-02	1.6E-04	1.5E-02	8.5E-02
PO2CS2	2	9	Yes	MA140426	2.1E-06	3.6E-07	1.9E-04	7.3E-05	8.3E-05	1.9E-06	6.8E-03	7.0E-05	5.3E-03	1.5E-01
PO2CS2	3	1	Yes	MA140427	2.1E-06	4.4E-07	7.0E-05	1.7E-04	1.9E-04	4.2E-06	1.6E-02	1.6E-04	1.1E-02	5.7E-02
PO2CS2	3	1	Yes	MA140428	1.8E-05	9.7E-07	8.1E-05	1.2E-04	1.5E-04	3.7E-06	1.3E-02	1.3E-04	1.4E-02	9.7E-02
PO2CS2	3	1	Yes	MA140429	3.0E-06	3.5E-07	5.0E-05	1.3E-04	5.9E-05	1.3E-06	4.9E-03	4.9E-05	4.2E-03	1.5E-01
PO2CS2	3	4	Yes	MA140430	1.5E-05	9.0E-07	8.6E-05	9.7E-05	1.2E-04	2.5E-06	9.3E-03	9.4E-05	1.1E-02	2.0E-01
PO2CS2	3	4	Yes	MA140431	1.8E-05	8.8E-07	7.9E-05	1.0E-04	8.3E-05	2.0E-06	6.6E-03	6.9E-05	9.8E-03	1.7E-01
PO2CS2	3	4	Yes	MA140432	7.2E-06	3.8E-07	4.4E-05	1.4E-04	8.6E-05	1.9E-06	6.9E-03	7.1E-05	6.9E-03	1.4E-01
PO2CS2	3	8	Yes	M15065	4.4E-08	2.3E-07	1.5E-04	2.2E-04	3.0E-05	9.6E-07	2.6E-03	3.1E-05	1.9E-03	3.8E-01
PO2CS2	3	8	Yes	M15066	7.5E-07	3.0E-07	1.3E-04	2.4E-04	6.2E-05	2.1E-06	5.2E-03	7.5E-05	3.9E-03	5.9E-01
PO2CS2	3	8	Yes	M15067	5.1E-07	2.7E-07	-2.6E-04	-1.7E-04	9.8E-05	2.0E-06	8.0E-03	8.8E-05	5.8E-03	3.1E-01
PO2CS2	3	8	Yes	M15069	7.8E-06	5.3E-07	8.2E-05	2.4E-04	1.0E-04	3.2E-06	8.3E-03	1.2E-04	8.4E-03	5.8E-01

Table D.9: Additional isotope ratios from measurements of **Alder Creek Sanidine monitor minerals**.All uncertainties represent two standard deviations. Listed measurements listed were irradiated in sleeve 2 and sleeve 3 and packed in container PO2CS2. The column 'contribution' marks measurements that contributed to the weighted average J-value calculation of the irradiated position.

Container	Sleelve	Position	Contribution	Measurement	$\frac{^{40}Ar^*}{^{39}Ar_K}$	$\pm\frac{^{40}Ar^*}{^{39}Ar_K}$	J	± J	%40Ar*	%39Ar$_K$	$\frac{Ca}{K}$	$\pm\frac{Ca}{K}$
PO2CS2	2	1	Yes	M15068	6.8E-01	4.0E-02	9.5E-04	5.6E-05	41.7	33.7	76.3	134.6
PO2CS2	2	1	Yes	M15070	6.8E-01	2.0E-02	9.5E-04	2.7E-05	95.5	14.4	-33.2	68.3
PO2CS2	2	1	Yes	M15071	6.7E-01	1.4E-02	9.6E-04	2.0E-05	92.5	20.7	91.8	416.0
PO2CS2	2	1	Yes	M15072	6.6E-01	1.0E-02	9.8E-04	1.5E-05	99.0	31.2	204.0	1447.1
PO2CS2	2	5	Yes	MA140421	6.7E-01	2.8E-02	9.7E-04	4.1E-05	93.4	18.5	88.3	343.3
PO2CS2	2	5	Yes	MA140422	6.6E-01	3.2E-02	9.8E-04	4.8E-05	48.3	33.1	34.5	30.8
PO2CS2	2	5	Yes	MA140423	6.7E-01	1.4E-02	9.7E-04	2.1E-05	94.2	48.4	204.8	535.0
PO2CS2	2	9	Yes	MA140424	6.8E-01	1.4E-02	9.6E-04	2.0E-05	75.5	26.6	35.0	22.4
PO2CS2	2	9	Yes	MA140425	6.8E-01	1.5E-02	9.6E-04	2.1E-05	70.8	51.0	39.6	18.4
PO2CS2	2	9	Yes	MA140426	6.9E-01	1.8E-02	9.4E-04	2.4E-05	88.2	22.4	20.3	7.7
PO2CS2	3	1	Yes	MA140427	6.7E-01	1.1E-02	9.8E-04	1.6E-05	94.4	48.3	132.9	329.2
PO2CS2	3	1	Yes	MA140428	6.7E-01	2.4E-02	9.8E-04	3.6E-05	61.1	37.3	88.6	132.4
PO2CS2	3	1	Yes	MA140429	6.8E-01	2.3E-02	9.7E-04	3.3E-05	78.5	14.4	55.0	144.0
PO2CS2	3	4	Yes	MA140430	6.7E-01	3.0E-02	9.8E-04	4.4E-05	57.6	40.8	61.7	69.5
PO2CS2	3	4	Yes	MA140431	6.6E-01	4.1E-02	1.0E-03	6.1E-05	44.4	28.9	47.8	60.3
PO2CS2	3	4	Yes	MA140432	6.9E-01	1.8E-02	9.5E-04	2.5E-05	68.9	30.3	90.0	280.7
PO2CS2	3	8	Yes	M15065	7.2E-01	3.0E-02	9.1E-04	3.8E-05	99.8	10.7	9.8	14.4
PO2CS2	3	8	Yes	M15066	7.1E-01	2.2E-02	9.2E-04	2.9E-05	94.5	21.6	23.3	43.4
PO2CS2	3	8	Yes	M15067	7.0E-01	1.3E-02	9.3E-04	1.8E-05	97.0	33.2	-17.7	11.5
PO2CS2	3	8	Yes	M15069	7.2E-01	2.5E-02	9.1E-04	3.1E-05	72.2	34.5	58.2	170.9

Table D.10: Ion beam intensities (in V) from measurements of **Alder Creek Sanidine monitor minerals**.All uncertainties represent two standard deviations. Listed measurements listed were irradiated in sleeve 1 and sleeve 2 and packed in container PO3CG2.The column 'contribution' marks measurements that contributed to the weighted average J-value calculation of the irradiated position.

Container	Sleelve	Position	Contribution	Measurement	^{36}Ar	$\pm^{36}Ar$	^{37}Ar	$\pm^{37}Ar$	^{38}Ar	$\pm^{38}Ar$	^{39}Ar	$\pm^{39}Ar$	^{40}Ar	$\pm^{40}Ar$
PO3CG2	1	1	Yes	M15046	9.7E-07	3.2E-07	2.9E-05	2.0E-05	4.8E-05	9.4E-07	4.0E-03	3.7E-05	2.9E-03	1.9E-01
PO3CG2	1	1	No	M15047	1.8E-05	8.1E-07	1.3E-04	2.3E-05	1.3E-04	3.7E-06	1.1E-02	9.5E-05	1.1E-02	7.2E-02
PO3CG2	1	1	Yes	M15048	8.4E-06	4.1E-07	1.1E-04	1.4E-05	1.5E-04	3.5E-06	1.3E-02	1.2E-04	1.1E-02	6.9E-02
PO3CG2	1	1	Yes	M15049	5.4E-06	5.4E-07	7.5E-05	1.1E-05	9.1E-05	2.4E-06	7.6E-03	6.7E-05	6.4E-03	9.5E-02
PO3CG2	1	4	No	M15050	2.5E-05	9.3E-07	6.6E-05	6.9E-06	1.1E-04	2.3E-06	8.9E-03	7.9E-05	1.3E-02	6.5E-02
PO3CG2	1	4	Yes	M15051	1.4E-05	6.3E-07	1.1E-04	1.4E-05	1.2E-04	2.3E-06	9.5E-03	8.7E-05	1.0E-02	1.3E-01
PO3CG2	1	4	No	M15052	1.5E-06	1.9E-07	9.5E-05	2.9E-05	1.2E-04	2.6E-06	1.0E-02	9.0E-05	6.3E-03	1.7E-01
PO3CG2	1	7	Yes	M15053	5.4E-07	2.2E-07	5.0E-05	3.0E-05	7.2E-05	1.4E-06	6.0E-03	5.3E-05	3.8E-03	2.1E-01
PO3CG2	1	7	Yes	M15054	8.8E-05	3.2E-06	9.3E-05	1.2E-05	1.2E-04	2.6E-06	8.3E-03	7.4E-05	3.2E-02	1.1E-01
PO3CG2	1	7	Yes	M15055	2.2E-07	1.6E-07	7.2E-05	2.8E-05	1.1E-04	2.8E-06	8.9E-03	8.0E-05	5.6E-03	9.8E-02
PO3CG2	1	7	Yes	M15057	6.7E-07	2.8E-07	1.2E-04	2.9E-05	1.4E-04	2.9E-06	1.2E-02	1.1E-04	7.7E-03	5.7E-02
PO3CG2	1	10	Yes	M15057	8.1E-07	6.1E-07	1.2E-04	2.9E-05	1.4E-04	2.9E-06	1.2E-02	1.1E-04	7.7E-03	6.4E-01
PO3CG2	1	10	Yes	M15058	5.6E-05	2.0E-06	1.9E-04	2.3E-05	2.4E-04	4.8E-06	1.9E-02	1.7E-04	2.9E-02	1.9E-01
PO3CG2	1	10	Yes	M15059	9.6E-05	3.4E-06	2.2E-04	1.4E-05	2.5E-04	4.6E-06	2.0E-02	1.7E-04	4.1E-02	1.3E-01
PO3CG2	1	10	Yes	M15060	1.6E-05	8.8E-07	1.4E-04	1.5E-05	1.8E-04	3.2E-06	1.4E-02	1.3E-04	1.4E-02	3.6E-01
PO3CG2	2	1	Yes	M15042	2.0E-05	1.1E-06	9.6E-05	2.0E-05	1.1E-04	2.3E-06	8.6E-03	7.9E-05	1.2E-02	6.3E-02
PO3CG2	2	1	Yes	M15043	2.9E-05	1.2E-06	6.6E-05	1.3E-05	6.9E-05	1.8E-06	5.4E-03	4.8E-05	1.2E-02	1.1E-01
PO3CG2	2	1	Yes	M15044	1.9E-05	7.5E-07	9.7E-05	2.0E-05	1.2E-04	2.6E-06	1.0E-02	8.9E-05	1.2E-02	1.1E-01
PO3CG2	2	1	Yes	M15045	1.7E-06	5.4E-07	5.9E-05	2.4E-05	7.8E-05	1.9E-06	6.5E-03	5.8E-05	4.7E-03	1.4E-01
PO3CG2	2	4	No	M15061	3.7E-08	2.5E-07	2.1E-05	2.3E-05	5.7E-05	1.5E-06	4.7E-03	5.1E-05	3.0E-03	3.3E-01
PO3CG2	2	4	Yes	M15062	1.8E-06	5.6E-07	4.0E-05	2.2E-05	4.3E-05	1.3E-06	3.7E-03	4.2E-05	2.8E-03	4.7E-01
PO3CG2	2	4	Yes	M15063	2.6E-05	1.5E-06	2.9E-05	1.6E-05	5.1E-05	1.1E-06	3.9E-03	6.2E-05	1.0E-02	5.0E-01
PO3CG2	2	4	Yes	M15064	1.1E-06	3.0E-07	6.9E-05	3.0E-05	7.1E-05	1.8E-06	5.8E-03	8.5E-05	4.0E-03	3.9E-01
PO3CG2	2	5	Yes	M15073	2.1E-06	7.4E-07	1.8E-05	2.0E-05	2.5E-05	1.1E-06	2.1E-03	2.2E-05	3.1E-02	2.1E-01
PO3CG2	2	5	Yes	M15080	1.2E-08	8.0E-07	1.6E-06	1.7E-05	9.8E-06	1.1E-06	9.2E-04	1.3E-05	1.3E-02	1.0E-01
PO3CG2	2	5	Yes	M15082	2.0E-06	1.8E-06	1.4E-05	1.6E-05	1.6E-05	9.9E-07	1.2E-03	1.4E-05	1.7E-02	3.5E-01
PO3CG2	2	9	Yes	M15081	6.1E-07	4.6E-07	2.4E-05	1.9E-05	5.5E-06	9.6E-07	6.3E-04	7.5E-06	9.3E-03	1.7E-01
PO3CG2	2	9	Yes	M15083	5.5E-07	4.6E-07	9.0E-06	1.4E-05	6.9E-06	8.8E-07	6.5E-04	7.5E-06	9.6E-03	1.4E-01
PO3CG2	2	9	Yes	M15084	3.0E-07	5.2E-07	4.6E-06	1.9E-05	9.1E-06	1.1E-06	8.6E-04	8.6E-06	1.2E-02	1.9E-01
PO3CG2	2	14	Yes	M15085	3.4E-07	3.8E-07	1.6E-05	1.7E-05	9.9E-06	9.4E-07	9.7E-04	1.1E-05	1.4E-02	3.0E-01
PO3CG2	2	14	Yes	M15086	4.3E-08	3.5E-07	1.3E-05	1.9E-05	9.6E-06	1.5E-06	8.6E-04	7.9E-06	1.2E-02	9.9E-02

Table D.11: Additional isotope ratios from measurements of **Alder Creek Sanidine monitor minerals**.All uncertainties represent two standard deviations. Listed measurements listed were irradiated in sleeve 1 and sleeve 2 and packed in container PO3CG2. The column 'contribution' marks measurements that contributed to the weighted average J-value calculation of the irradiated position.

Container	Sleelve	Position	Contribution	Measurement	$\frac{^{40}Ar^*}{^{39}Ar_K}$	$\pm\frac{^{40}Ar^*}{^{39}Ar_K}$	J	± J	%40Ar*	%39Ar$_K$	$\frac{Ca}{K}$	$\pm\frac{Ca}{K}$
PO3CG2	1	1	Yes	M15046	6.4E-01	2.4E-02	1.0E-03	3.8E-05	89.9	11.4	78.6	53.7
PO3CG2	1	1	No	M15047	5.7E-01	2.3E-02	1.1E-03	4.7E-05	53.6	30.3	48.2	8.9
PO3CG2	1	1	Yes	M15048	6.2E-01	1.1E-02	1.0E-03	1.9E-05	76.2	36.8	68.8	9.0
PO3CG2	1	1	Yes	M15049	6.3E-01	2.2E-02	1.0E-03	3.6E-05	74.5	21.5	57.9	8.3
PO3CG2	1	4	No	M15050	5.7E-01	3.2E-02	1.1E-03	6.3E-05	40.6	25.8	77.2	8.1
PO3CG2	1	4	Yes	M15051	6.2E-01	2.1E-02	1.0E-03	3.4E-05	57.9	27.5	47.6	5.8
PO3CG2	1	4	No	M15052	5.8E-01	7.8E-03	1.1E-03	1.5E-05	92.7	29.4	61.4	18.6
PO3CG2	1	7	Yes	M15053	6.2E-01	1.2E-02	1.0E-03	2.1E-05	95.8	17.2	68.6	41.5
PO3CG2	1	7	Yes	M15054	6.5E-01	1.2E-01	9.9E-04	1.8E-04	17.0	28.3	50.5	6.7
PO3CG2	1	7	Yes	M15055	6.2E-01	7.8E-03	1.0E-03	1.3E-05	98.8	30.5	70.7	27.7
PO3CG2	1	7	Yes	M15057	6.2E-01	8.9E-03	1.0E-03	1.5E-05	97.4	41.3	57.9	14.2
PO3CG2	1	10	Yes	M15057	6.2E-01	1.8E-02	1.0E-03	3.0E-05	96.9	18.6	57.5	13.9
PO3CG2	1	10	Yes	M15058	6.5E-01	3.3E-02	1.0E-03	5.1E-05	42.5	29.0	56.9	6.8
PO3CG2	1	10	Yes	M15059	6.5E-01	5.3E-02	1.0E-03	8.2E-05	30.8	30.4	50.3	3.2
PO3CG2	1	10	Yes	M15060	6.3E-01	2.0E-02	1.0E-03	3.4E-05	65.0	22.0	56.5	5.8
PO3CG2	2	1	Yes	M15042	6.4E-01	3.7E-02	1.0E-03	6.0E-05	47.5	28.2	51.3	10.5
PO3CG2	2	1	Yes	M15043	6.4E-01	6.9E-02	1.0E-03	1.1E-04	28.5	17.5	46.0	9.4
PO3CG2	2	1	Yes	M15044	6.3E-01	2.3E-02	1.0E-03	3.8E-05	52.7	33.0	59.0	12.4
PO3CG2	2	1	Yes	M15045	6.4E-01	2.5E-02	1.0E-03	4.0E-05	89.1	21.3	63.6	26.6
PO3CG2	2	4	No	M15061	6.3E-01	1.7E-02	1.0E-03	2.8E-05	99.6	26.2	127.1	135.9
PO3CG2	2	4	Yes	M15062	6.3E-01	4.6E-02	1.0E-03	7.7E-05	81.5	20.4	53.0	28.7
PO3CG2	2	4	Yes	M15063	6.3E-01	1.2E-01	1.0E-03	2.0E-04	23.8	21.2	75.8	42.3
PO3CG2	2	4	Yes	M15064	6.2E-01	1.9E-02	1.0E-03	3.1E-05	92.1	32.2	48.5	20.9
PO3CG2	2	5	Yes	M15073	1.5E+01	1.9E-01	1.1E-03	1.4E-05	98.0	50.3	68.2	75.0
PO3CG2	2	5	Yes	M15080	1.5E+01	3.4E-01	1.1E-03	2.4E-05	100.0	21.8	336.2	3723.4
PO3CG2	2	5	Yes	M15082	1.4E+01	4.9E-01	1.1E-03	3.7E-05	96.6	27.9	47.8	53.2
PO3CG2	2	9	Yes	M15081	1.4E+01	2.9E-01	1.1E-03	2.1E-05	98.0	29.3	15.1	12.1
PO3CG2	2	9	Yes	M15083	1.4E+01	2.7E-01	1.1E-03	2.0E-05	98.3	30.5	41.3	62.0
PO3CG2	2	9	Yes	M15084	1.4E+01	2.4E-01	1.1E-03	1.8E-05	99.3	40.2	106.7	435.9
PO3CG2	2	14	Yes	M15085	1.4E+01	2.2E-01	1.1E-03	1.7E-05	99.3	53.0	34.3	36.0
PO3CG2	2	14	Yes	M15086	1.4E+01	1.8E-01	1.1E-03	1.4E-05	99.9	47.0	37.9	56.0

Table D.12: Ion beam intensities (in V) from **total fusion measurements of Fish Canyon Tuff Sanidine** (FC3) single crystals.

Measurement	^{36}Ar	$\pm$ ^{36}Ar	^{37}Ar	$\pm$ ^{37}Ar	^{38}Ar	$\pm$ ^{38}Ar	^{39}Ar	$\pm$ ^{39}Ar	^{40}Ar	$\pm$ ^{40}Ar	$\frac{^{40}Ar^*}{^{39}Ar_K}$	$\pm\frac{^{40}Ar^*}{^{39}Ar_K}$	% ^{40}Ar*
M14110	3.08E-09	9.05E-08	9.55E-06	2.32E-06	9.22E-06	8.99E-08	7.87E-04	3.21E-06	1.25E-02	8.82E-06	15.93	0.02	28.21
M14111	1.60E-07	9.09E-08	8.21E-06	2.07E-06	1.17E-05	1.88E-07	1.01E-03	3.29E-06	1.59E-02	1.01E-05	15.71	0.02	27.81
M14112	-1.59E-08	-5.43E-08	3.62E-06	9.95E-07	9.10E-06	2.27E-07	7.88E-04	2.76E-06	1.24E-02	8.51E-06	15.73	0.02	27.86
M14113	-1.23E-07	-1.04E-07	7.32E-06	1.26E-06	1.10E-05	1.77E-07	9.50E-04	3.00E-06	1.49E-02	6.04E-06	15.72	0.02	27.83
M14114	-8.04E-09	-8.08E-08	6.60E-06	8.49E-07	1.12E-05	2.92E-07	9.39E-04	3.91E-06	1.48E-02	6.00E-06	15.72	0.02	28.22
M14115	4.36E-10	7.98E-08	8.57E-06	1.93E-06	1.21E-05	2.16E-07	1.07E-03	3.91E-06	1.69E-02	9.27E-06	15.68	0.06	28.14
M14116	1.61E-07	8.28E-08	1.11E-05	9.89E-07	1.99E-05	1.89E-07	1.68E-03	5.40E-06	2.65E-02	1.12E-05	15.66	0.06	28.11
M14117	1.49E-07	8.47E-08	6.21E-05	2.49E-06	3.81E-05	4.03E-07	3.23E-03	1.01E-05	2.32E-02	1.71E-05	7.12	0.01	12.84
M14118	-2.59E-07	-1.26E-07	5.32E-06	1.78E-06	1.33E-05	2.58E-07	1.13E-03	4.02E-06	1.75E-02	1.09E-05	15.55	0.02	27.91
M14119	-3.00E-07	-7.45E-08	1.45E-07	1.96E-06	1.15E-05	1.86E-07	1.02E-03	4.38E-06	1.55E-02	8.79E-06	15.39	0.02	27.63
M14120	-3.48E-07	-7.60E-08	-9.31E-07	-1.69E-06	8.88E-06	1.30E-07	7.90E-04	2.80E-06	1.22E-02	8.10E-06	15.52	0.05	27.87
M14121	-4.17E-07	-9.93E-08	-3.56E-07	-2.35E-06	8.23E-06	1.72E-07	7.46E-04	3.38E-06	1.15E-02	5.36E-06	15.54	0.05	27.90
M14122	-4.06E-07	-1.24E-07	5.00E-06	3.45E-06	9.00E-06	1.63E-07	8.09E-04	3.51E-06	1.18E-02	1.09E-05	14.71	0.02	26.51
M14123	-5.91E-07	-1.73E-07	3.58E-06	4.52E-06	1.01E-05	1.81E-07	9.22E-04	3.63E-06	1.40E-02	8.29E-06	15.41	0.03	27.77
M14124	-3.47E-07	-1.31E-07	3.88E-06	3.58E-06	1.76E-05	2.33E-07	1.52E-03	5.65E-06	2.38E-02	1.28E-05	15.68	0.02	28.24
M14125	-4.40E-07	-1.39E-07	-5.95E-06	-3.49E-06	3.73E-06	1.82E-07	3.57E-04	1.72E-06	5.42E-03	5.67E-06	15.52	0.04	27.97

Table D.13: Inverse isochron data and apparent ages from **total fusion measurements of Fish Canyon Tuff Sanidine** (FC3) single crystals.

Measurement	J	± J	Age (Ma)	± Age (Ma)	$^{39}Ar/^{40}Ar$	± $^{39}Ar/^{40}Ar$	$^{36}Ar/^{40}Ar$	± $^{36}Ar/^{40}Ar$	ρ
M14110	0.975	0.009	28.21	0.26	0.0628	0.0005	4.48E-08	1.44E-05	7.43E-07
M14111	0.975	0.009	27.81	0.21	0.0635	0.0004	9.94E-06	1.15E-05	2.11E-04
M14112	0.975	0.009	27.86	0.21	0.0636	0.0005	-1.36E-06	8.75E-06	4.10E-05
M14113	0.975	0.009	27.83	0.21	0.0638	0.0004	-8.40E-06	1.39E-05	6.25E-05
M14114	0.988	0.006	28.22	0.25	0.0636	0.0005	-6.62E-07	1.09E-05	4.80E-06
M14115	0.988	0.006	28.14	0.69	0.0638	0.0016	-1.08E-07	9.46E-06	5.64E-07
M14116	0.988	0.006	28.11	0.68	0.0637	0.0015	5.96E-06	6.25E-06	2.83E-05
M14117	0.988	0.006	12.84	0.31	0.1402	0.0034	5.72E-06	7.29E-06	7.02E-05
M14118	0.988	0.006	27.91	0.23	0.0646	0.0005	-1.49E-05	1.44E-05	2.22E-04
M14119	0.988	0.006	27.63	0.25	0.0653	0.0006	-1.93E-05	9.58E-06	2.97E-04
M14120	0.988	0.006	27.87	0.54	0.0650	0.0012	-2.86E-05	1.25E-05	2.12E-04
M14121	0.988	0.006	27.90	0.57	0.0650	0.0013	-3.64E-05	1.73E-05	9.20E-05
M14122	0.992	0.008	26.51	0.28	0.0687	0.0006	-3.46E-05	2.10E-05	6.37E-04
M14123	0.992	0.008	27.77	0.30	0.0657	0.0005	-4.22E-05	2.46E-05	3.00E-04
M14124	0.992	0.008	28.24	0.23	0.0641	0.0005	-1.46E-05	1.10E-05	2.08E-04
M14125	0.992	0.008	27.97	0.50	0.0660	0.0006	-8.10E-05	5.15E-05	7.02E-04

Table D.14: Air shot analyses and calculated mass discrimination factors (MDF).

Air Shot	^{36}Ar	^{38}Ar	^{40}Ar	$\frac{^{40}Ar}{^{36}Ar}$	$\pm\frac{^{40}Ar}{^{36}Ar}$	$\frac{^{38}Ar}{^{36}Ar}$	$\pm\frac{^{38}Ar}{^{36}Ar}$	MDF	± MDF	Weighted Mean								
										$\frac{^{38}Ar}{^{36}Ar}$	$\pm\frac{^{38}Ar}{^{36}Ar}$	$\frac{^{40}Ar}{^{36}Ar}$	$\pm\frac{^{40}Ar}{^{36}Ar}$	MSWD	n	MDF	± MDF	Date
A0711141	5.72E-05	1.05E-05	0.0165	288	4	0.184	0.005	1.009	0.004									
A0811142	5.83E-05	1.08E-05	0.0167	286	2	0.184	0.003	1.011	0.002									
A0811144	5.63E-05	1.05E-05	0.0162	287	3	0.187	0.004	1.010	0.003	0.1852	0.0020	286.6	1.2	0.6	3	1.0104	0.0020	08 November 2014
A2711141	5.45E-05	1.02E-05	0.0158	290	4	0.187	0.004	1.007	0.004									
A2711142	5.39E-05	1.02E-05	0.0157	291	3	0.188	0.005	1.007	0.003									
A2711143	5.44E-05	1.03E-05	0.0157	289	2	0.190	0.003	1.008	0.002	0.1889	0.0020	289.6	1.4	0.4	3	1.0077	0.0021	27 November 2014
A2007151	5.04E-05	9.71E-06	0.0148	294	9	0.193	0.012	1.004	0.016									
A2007152	5.25E-05	9.29E-06	0.0152	290	11	0.177	0.009	1.008	0.019									
A2007153	5.19E-05	9.70E-06	0.0152	293	8	0.187	0.010	1.004	0.015	0.1842	0.0181	293	5	0.7	3	1.0051	0.0098	20 July 2015
A1308153	5.06E-05	9.50E-06	0.0147	291	7	0.188	0.008	1.006	0.012									
A1308154	5.19E-05	9.88E-06	0.0151	291	8	0.190	0.010	1.006	0.015									
A1308155	5.10E-05	9.51E-06	0.0149	292	11	0.187	0.012	1.006	0.019	0.1883	0.0055	291	5	0.0	3	1.006	0.009	13 August 2015

Table D.15: Correction parameters on Ca and K from irradiations of PO2CGJ2, PO2CS2 and PO3CG2. Note that the analysis K14006 resulted in unusual high $^{40}Ar/^{39}Ar$ ratios. $^{40}Ar/^{39}Ar$ corrections were conducted by taking the results from measurement K14004 in this study. The value is indistinguishable from K14005 and considers the maximum of observed uncertainties. Its value and its uncertainty are typical for OSR TRIGA reactor following Wijbrans et al. (1995) and Renne et al. (1998). All other correction parameters that have been applied in this study are weighted averages from the three measurements.

Measurement	$\frac{^{39}Ar}{^{37}Ar}$	$\pm\frac{^{39}Ar}{^{37}Ar}$	$\frac{^{36}Ar}{^{37}Ar}$	$\pm\frac{^{36}Ar}{^{37}Ar}$
CA14004	0.00070	0.00005	0.000270	0.000006
CA14005	0.00068	0.00012	0.000252	0.000011
CA14006	0.00066	0.00012	0.000256	0.000011
w. ave.	0.00070	0.00004	0.000263	0.000005
Measurement	$\frac{^{40}Ar}{^{39}Ar}$	$\pm\frac{^{40}Ar}{^{39}Ar}$	$\frac{^{38}Ar}{^{39}Ar}$	$\pm\frac{^{38}Ar}{^{39}Ar}$
K14004	0.00068	0.000416	0.01205	0.00005
K14005	0.00069	0.000004	0.02472	0.00013
K14006	0.01729	0.000129	0.01204	0.00004
w. ave.	0.00071	0.000004	0.01272	0.00003

Appendix E: XRF Data

Table E.1: Major element XRF data in wt%. The sum includes H_2O and CO_2 and trace element concentrations (Table E.2). Median values between top and base of the volcaniclastic layers are listed as approximate stratigraphic depth. The loss of ignition (LOI) is the difference in mass before and after fusing the sample. It is listed for comparison to to the CO_2 and H_2O contents.

V-ID	Depth	SiO_2	TiO_2	Al_2O_3	Fe_2O_3	FeO	MnO	MgO	CaO	Na_2O	K_2O	P_2O_5	SO_3	CO_2	H_2O	Sum	LOI
V-36	23.28	66.2	0.24	12.7	2.23	1.03	0.055	0.92	1.3	5.0	4.5	0.045	0.41	1.67	2.96	99.4	4.6
V-43	26.25	54.4	0.25	12.7	2.85	1.01	0.071	2.81	4.2	4.9	4.1	0.080	0.40	5.66	5.61	99.2	11.3
V-45	26.66	59.5	0.36	14.7	3.14	1.58	0.072	1.15	3.0	5.5	4.2	0.074	1.67	0.96	3.18	99.3	4.1
V-57b	33.74	60.7	0.37	15.9	4.13	1.64	0.158	0.41	0.9	7.8	5.0	0.059	0.48	0.44	1.16	99.3	1.6
V-58	33.87	60.4	0.39	15.5	3.63	1.96	0.154	0.65	1.5	7.3	4.8	0.075	0.47	0.69	1.50	99.2	2.2
V-65	43.38	63.2	0.48	15.1	3.46	2.56	0.198	0.17	1.6	6.2	4.8	0.082	0.38	0.11	0.91	99.5	1.0
V-67#	45.68	59.8	0.84	15.9	3.27	4.43	0.183	1.00	3.3	5.5	2.7	0.281	0.12	0.28	1.54	99.3	1.8
V-81	53.33	68.0	0.27	12.6	0.71	3.22	0.098	0.16	0.7	5.7	4.7	0.023	0.61	0.26	2.06	99.2	2.3
V-111	68.15	61.6	0.58	14.9	5.47	0.00	0.174	0.48	2.0	5.5	5.2	0.104	0.50	0.39	2.69	99.7	3.1
V-111B	68.51	62.1	0.46	14.4	2.71	2.09	0.161	0.44	1.7	5.5	5.2	0.067	0.21	0.93	3.27	99.3	4.2
V-113	70.42	66.8	0.34	12.9	3.72	0.00	0.068	0.59	1.4	4.7	4.5	0.056	0.41	0.84	3.00	99.5	3.8
V-114	71.14	68.8	0.24	12.5	2.24	0.77	0.057	0.46	1.1	4.6	4.7	0.035	0.40	0.48	2.97	99.4	3.5
V-137	86.24	64.5	0.24	11.2	2.17	1.28	0.083	1.30	2.8	4.7	4.2	0.046	0.33	2.50	3.81	99.3	6.3
V-138b	86.43	53.8	0.37	11.6	2.81	1.12	0.082	3.35	7.9	3.0	2.6	0.098	0.49	7.24	5.06	99.6	12.3
V-139b	86.99	65.3	0.23	11.0	2.28	1.00	0.082	1.07	2.7	4.5	4.2	0.035	0.28	2.50	4.04	99.3	6.5
V-140	87.09	69.9	0.20	11.6	2.18	1.12	0.079	0.27	0.7	4.9	4.5	0.019	0.21	0.44	3.18	99.4	3.6
V-144	87.56	70.0	0.20	11.3	1.87	1.21	0.073	0.40	1.1	4.9	4.5	0.021	0.18	0.86	2.59	99.4	3.5
V-145	87.76	59.3	0.20	9.7	1.90	0.98	0.072	2.58	6.2	4.0	3.6	0.057	0.26	5.89	4.32	99.3	10.2
V-146	87.91	68.7	0.21	11.2	1.95	1.08	0.070	0.41	1.6	4.7	4.3	0.039	0.19	1.71	3.20	99.5	4.9
V-149	88.64	67.8	0.21	11.2	1.39	1.72	0.068	0.88	2.0	4.5	4.2	0.070	0.32	1.70	3.10	99.3	4.8
V-153	91.72	65.6	0.15	11.8	1.04	0.56	0.040	0.58	1.8	3.3	4.1	0.054	0.12	6.17	4.26	99.7	10.4
V-156	93.91	68.9	0.11	12.5	0.94	0.67	0.059	0.97	2.5	3.6	4.2	0.052	0.18	1.97	3.03	99.7	5.0
V-165	95.77	68.3	0.22	11.1	2.07	1.07	0.060	0.66	2.0	4.6	4.2	0.036	0.18	1.67	3.02	99.4	4.7
V-166	96.04	69.8	0.13	12.9	1.09	0.71	0.064	1.09	1.7	3.9	4.1	0.047	0.30	0.91	2.90	99.7	3.8
V-174a	102.65	58.5	0.21	10.4	1.52	1.10	0.068	1.45	7.2	3.9	3.9	0.058	0.34	6.72	3.76	99.2	10.5
V-180	113.00	64.8	0.32	14.2	1.97	1.87	0.087	0.22	1.7	4.8	4.7	0.053	1.38	0.18	2.99	99.4	3.2
V-184	115.46	62.1	0.47	14.6	0.97	3.68	0.105	0.35	1.9	5.4	4.4	0.091	1.37	0.34	3.22	99.2	3.6
V-189b	117.12	57.0	0.71	17.5	4.09	1.79	0.071	0.64	4.0	5.7	2.8	0.255	1.61	0.31	2.91	99.4	3.2
V-206	123.21	55.1	0.37	12.7	2.51	1.63	0.109	2.42	5.8	4.2	4.2	0.081	0.58	5.20	4.33	99.2	9.5
V-209a	131.36	60.8	0.52	15.7	2.36	3.49	0.185	0.26	2.0	5.9	5.0	0.129	0.93	0.16	1.73	99.3	1.9
V-210a	133.19	59.2	0.31	13.7	2.07	2.79	0.150	0.63	2.5	6.1	4.8	0.044	0.63	2.31	3.64	99.0	6.0
V-212	134.04	61.3	0.32	13.8	1.63	3.32	0.142	0.47	2.1	6.0	5.0	0.040	0.80	1.36	2.65	99.0	4.0
V-221a	136.84	61.3	0.44	15.9	0.00	4.91	0.107	0.47	2.2	5.5	4.9	0.104	1.14	0.47	2.30	99.2	2.8
V-225	138.05	62.3	0.37	14.4	2.84	1.55	0.089	0.40	2.8	4.7	5.1	0.076	0.99	0.74	2.90	99.4	3.6
V-227	139.60	61.3	0.67	16.0	3.24	1.64	0.062	0.31	2.5	4.8	4.6	0.171	0.96	0.27	2.76	99.5	3.0
V-248	156.13	60.8	0.39	14.5	1.78	2.47	0.113	0.91	2.3	5.1	4.8	0.071	1.45	0.94	3.57	99.3	4.5
V-253	161.00	60.0	0.60	15.6	0.83	3.83	0.105	0.53	1.9	5.6	4.8	0.123	1.26	0.28	3.40	99.1	3.7
V-254t	161.92	58.7	0.75	16.3	1.08	4.59	0.127	0.70	3.1	5.3	4.2	0.169	1.47	0.45	2.16	99.2	2.6
V-254b	162.28	60.5	0.45	15.2	2.27	2.41	0.111	0.32	1.6	5.7	5.1	0.081	1.67	0.36	3.30	99.3	3.7
V-263	175.42	37.9	0.74	10.3	0.00	7.06	0.107	5.65	13.8	2.9	1.7	0.256	3.66	11.79	4.94	98.7	16.7
V-269	186.63	48.0	2.26	15.8	3.91	7.54	0.124	1.88	6.8	4.0	1.6	0.578	4.04	0.63	1.78	99.0	2.4
V-276	189.21	56.8	0.67	13.6	5.36	2.57	0.131	0.96	3.2	4.8	3.5	0.253	3.05	0.47	3.88	99.4	4.4
V-279#	191.27	63.3	0.36	14.9	1.86	1.70	0.097	0.19	1.8	5.7	4.9	0.056	0.17	1.37	2.67	99.2	4.0
V-279	191.29	61.9	0.39	14.5	1.83	1.87	0.099	0.33	2.6	5.5	4.7	0.071	0.22	2.43	2.57	99.2	5.0
V-281	192.94	60.0	0.63	14.8	1.68	3.55	0.117	0.54	3.5	5.1	3.7	0.162	0.56	1.15	3.45	99.0	4.6
V-288	197.42	51.8	2.30	17.1	4.53	5.14	0.154	2.69	6.9	4.6	1.9	0.725	0.18	0.32	0.79	99.2	1.1
V-289	198.38	58.7	1.11	16.2	3.14	3.15	0.119	1.17	3.9	5.0	3.1	0.486	0.29	0.32	2.38	99.2	2.7
V-297	209.67	53.6	1.52	14.3	3.25	7.47	0.216	2.18	5.5	4.2	2.0	0.494	0.13	1.84	2.02	98.9	3.9
V-299	210.39	54.7	1.69	15.3	3.21	6.97	0.201	2.60	4.7	4.8	2.0	0.537	0.14	0.33	1.65	98.9	2.0

Table E.2: Trace element XRF data in ppm. Median values between top and base of the volcaniclastic layers are listed as approximate stratigraphic depth. Concentrations given as < 10 have been less than the detection limit.

V-ID	Depth	Ba	Cr	Ga	Nb	Ni	Rb	Sr	V	Y	Zn	Zr
V-36	23.28	105	<10	28	45	12	191	50	17	86	129	774
V-43	26.25	348	23	20	31	36	149	220	16	56	87	642
V-45	26.66	927	<10	20	24	18	111	174	<10	49	90	477
V-57b	33.74	35	<10	32	78	<10	236	18	<10	85	167	1330
V-58	33.87	126	<10	31	72	13	222	57	<10	84	155	1234
V-65	43.38	965	<10	24	25	<10	81	46	<10	48	109	382
V-67#	45.68	430	<10	26	29	10	67	268	<10	54	133	511
V-81	53.33	30	<10	31	52	<10	204	22	<10	98	147	996
V-111	68.15	288	13	24	29	<10	97	45	<10	51	108	574
V-111B	68.51	79	<10	26	37	13	114	36	<10	59	112	785
V-113	70.42	91	<10	26	55	14	203	65	12	90	127	783
V-114	71.14	62	<10	26	58	16	224	47	<10	97	133	701
V-137	86.24	67	18	28	45	27	165	157	12	92	148	897
V-138b	86.43	223	122	14	12	51	85	305	60	27	60	162
V-139b	86.99	43	18	29	48	21	168	150	11	93	152	916
V-140	87.09	27	<10	30	56	<10	204	32	<10	108	158	1081
V-144	87.56	25	<10	30	52	<10	187	53	<10	96	160	1000
V-145	87.76	68	23	23	39	29	142	348	12	78	134	761
V-146	87.91	35	<10	29	48	<10	181	96	<10	97	152	964
V-149	88.64	52	15	28	46	24	176	101	13	89	144	888
V-153	91.72	221	<10	14	10	12	135	85	<10	28	40	95
V-156	93.91	78	41	16	13	38	180	110	12	37	45	81
V-165	95.77	69	12	28	45	14	184	117	11	99	147	958
V-166	96.04	99	44	16	15	43	183	64	12	40	48	90
V-174a	102.65	117	11	22	34	15	147	474	<10	74	106	549
V-180	113.00	580	<10	25	31	10	142	97	<10	67	96	642
V-184	115.46	709	<10	21	32	<10	125	137	<10	61	92	648
V-189b	117.12	462	<10	23	24	14	73	397	11	40	83	373
V-206	123.21	465	31	24	31	35	121	296	29	58	102	564
V-209a	131.36	1217	<10	24	28	<10	99	63	<10	45	109	422
V-210a	133.19	62	<10	28	49	14	169	109	<10	80	154	868
V-212	134.04	55	<10	26	47	10	173	77	<10	78	154	851
V-221a	136.84	1071	<10	23	33	<10	127	166	<10	52	100	548
V-225	138.05	566	<10	23	39	11	171	128	<10	66	109	764
V-227	139.60	952	<10	22	34	<10	145	210	<10	58	99	902
V-248	156.13	528	<10	24	35	20	148	124	<10	57	109	631
V-253	161.00	728	<10	22	35	<10	145	131	<10	51	101	661
V-254t	161.92	846	<10	22	28	13	110	228	15	41	95	498
V-254b	162.28	409	<10	23	38	10	158	68	12	54	105	717
V-263	175.42	366	96	13	16	57	40	781	49	30	76	252
V-269	186.63	303	<10	19	16	19	34	422	114	36	100	275
V-276	189.21	521	<10	21	33	<10	89	176	17	54	103	588
V-279#	191.27	431	<10	26	40	<10	122	75	<10	63	122	899
V-279	191.29	428	<10	26	39	<10	121	114	<10	64	135	881
V-281	192.94	538	<10	27	32	16	105	207	<10	63	140	665
V-288	197.42	330	<10	24	22	79	48	498	111	42	122	372
V-289	198.38	494	<10	22	25	12	100	326	26	50	116	531
V-297	209.67	373	28	20	26	24	54	317	33	47	129	304
V-299	210.39	320	<10	20	23	<10	52	358	45	47	117	367

Appendix F: XRD Data 2Θ-Scans

Interpreted peaks in XRD 2Θ-scans are displayed in the following figures. The assigned peaks are colour-coded and the list of reflecting minerals and their major peak positions is provided beneath the 2Θ-scan.

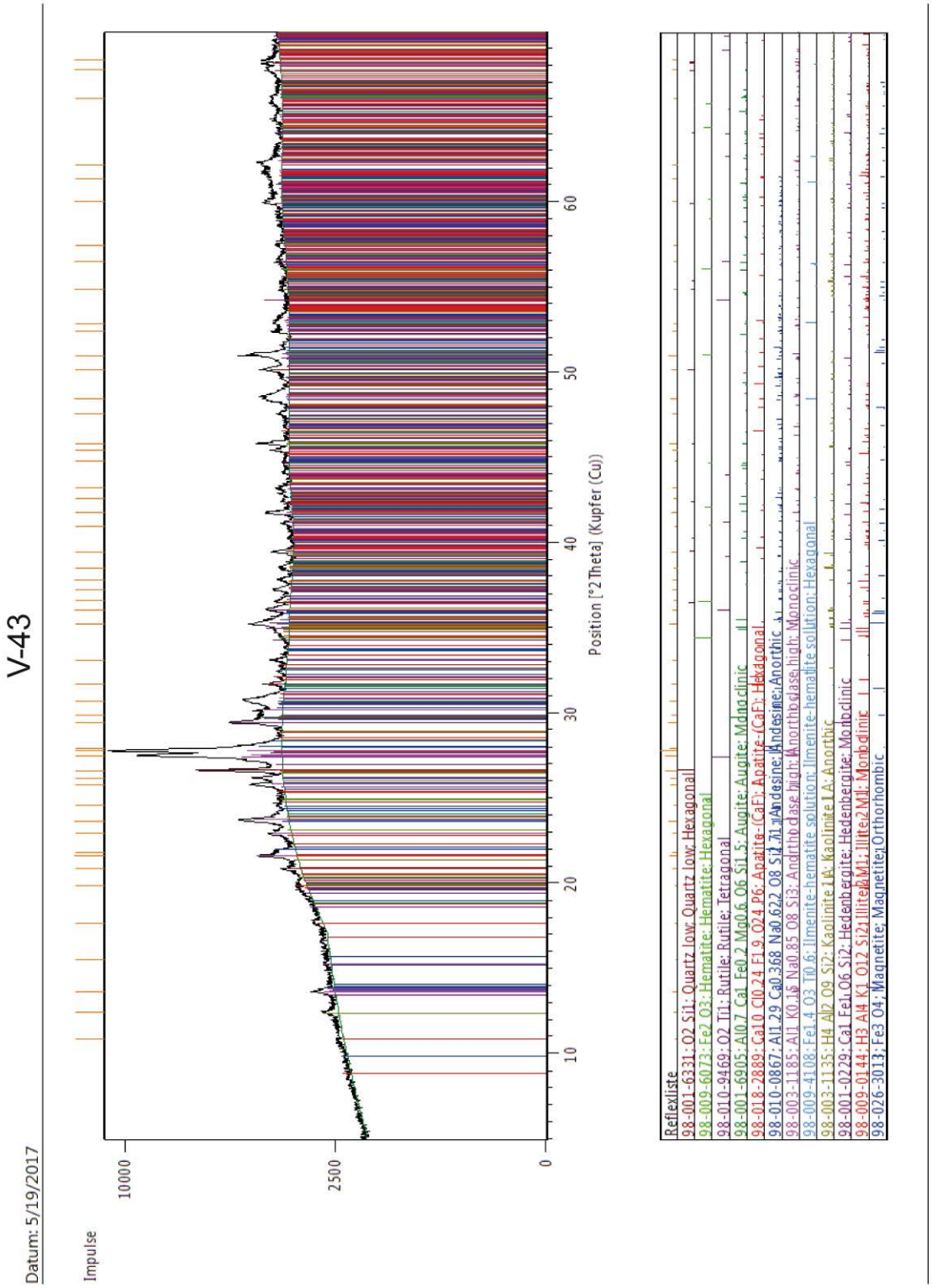

Figure F.1: 2Θ-scan V-43.

Datum: 12/12/2017

V-114

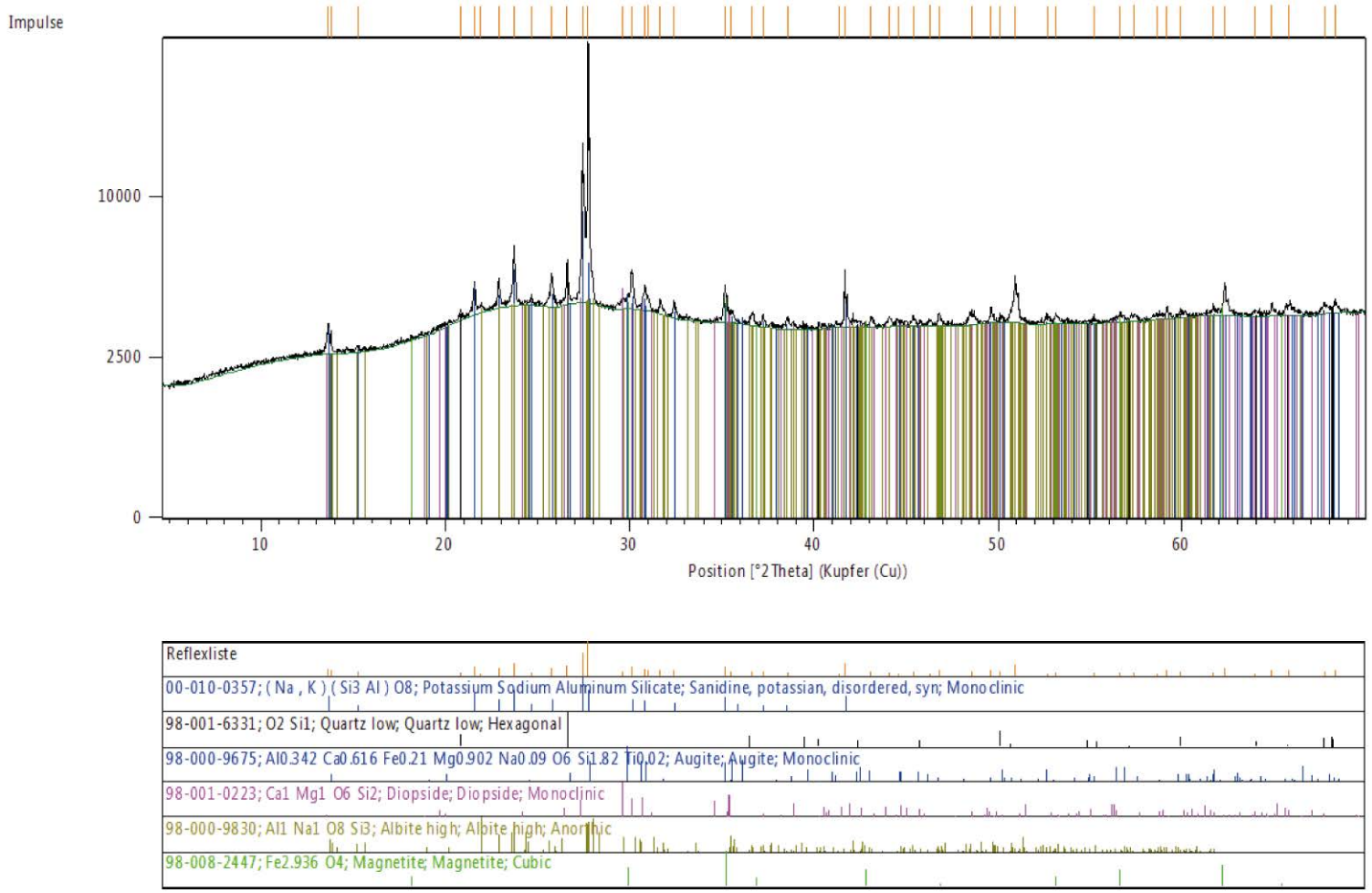

Figure F.2: 2Θ-scan V-114.

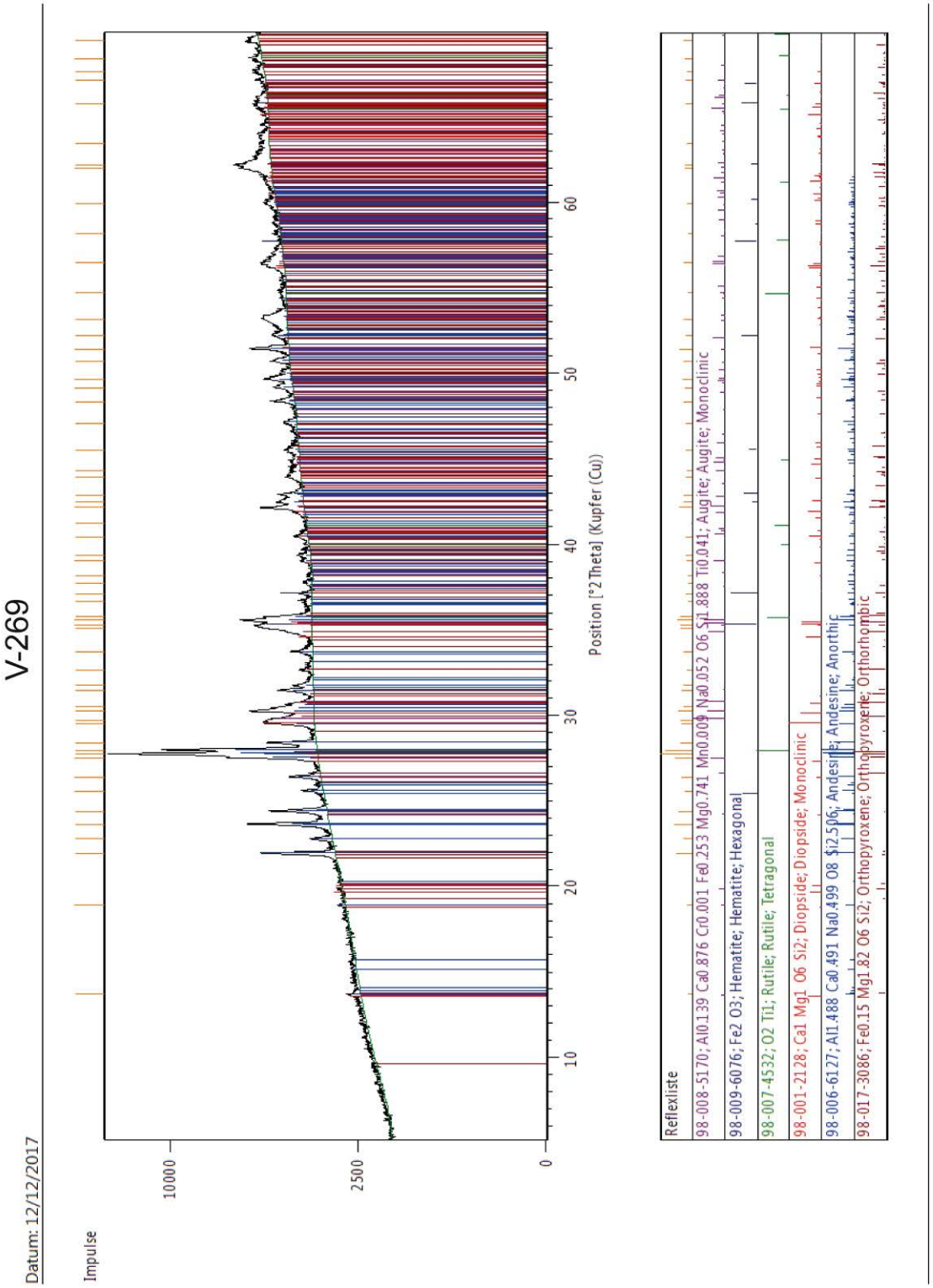

Figure F.3: 2Θ-scan V-269.

Datum: 12/12/2017

V-299

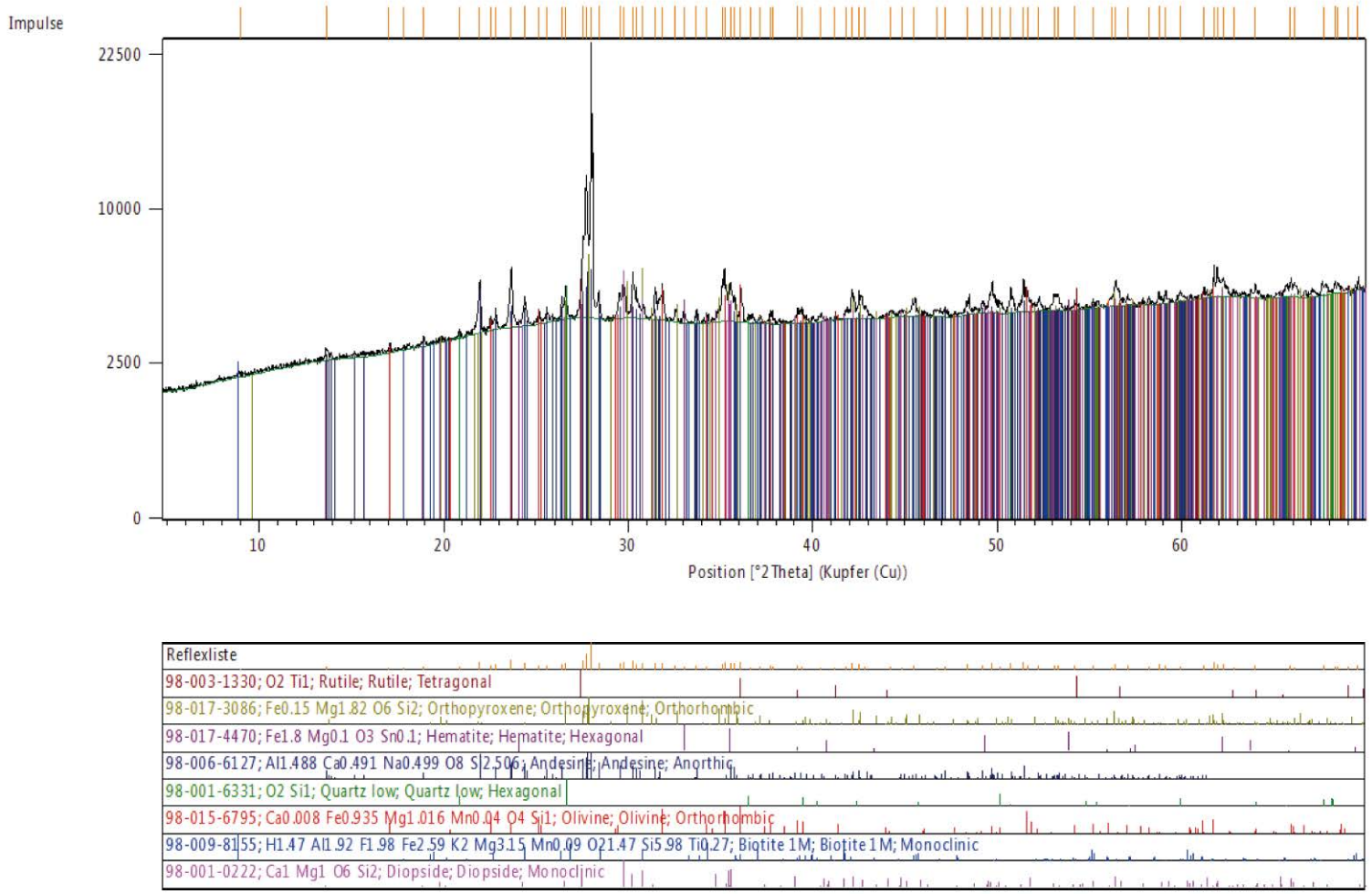

Figure F.4: 2Θ-scan V-299.

Appendix G: Recalibrated Ages

The following two tables provide a recalibration of all $^{40}Ar/^{39}Ar$ ages relative to ages from the Fish Canyon sanidine (FCs) with both full external and minimal uncertainties. A recalibration of the Alder Creek relative to the FCs with an age of 28.03 ± 0.16 Ma from Jourdan and Renne (2007) bases on primary K-Ar standards and allows to calculate the full external uncertainties. Kuiper et al. (2008) provided an age for the FCs of 28.201 ± 0.023 Ma. This age relies on astronomical calibration and no uncaterinties from deay constants contribute to the monitor age. Thus a minimal uncertainty calculation is possible using this age.

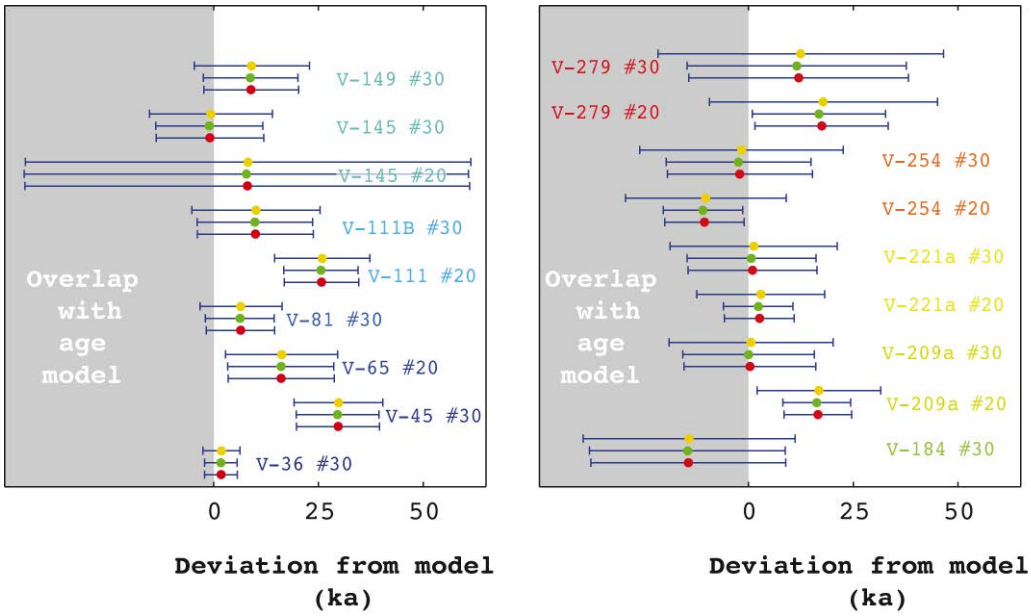

Figure G.1: Summary of inverse isochron ages from calculations relative to AC sanidine using an age from Jicha et al. (2016) (red dots), from recalibration to FCs using an age of 28.201 Ma from Kuiper et al. (2008) (green dots), and from recalibration to FC sanidine using an age from Jourdan and Renne (2007) of 28.03 Ma (yellow dots). The latter one assumes an according age of 1.193 Ma for Alder Creek sanidine from Nomade et al. (2005). Inverse isochron ages of V-45 #30, V-65 #20, V-111 #20 and V-209 #20 deviate model constraints irrespective of absolute or minimal external error propagation. Relevant values are stated in Table G.1.

Table G.1: Comparison of inverse isochron ages from feldspars. All ages are recalibrated relative to Fish Canyon Sanidine. Two recalibrations are presented in this table. A recalibration relative to an age from Jourdan and Renne (2007) represents an inter-calibration to primary standards and provides full external error propagation (including propagated branched decay activities). The recalibration to the astronomical age from Kuiper et al. (2008) considers no uncertainties from decay constants in the errors stated. R_{AC}^{FC} from Niespolo et al. (2017) served for calculating the recalibartion using the age from Kuiper et al. (2008). Nomade et al. (2005) offered an R_{AC}^{FC} value that allowed the recalculation of the ages relative to the primary standards using the fish canyon age from textciteJourdan2007. All uncertainties represent two standard deviations.

			Jourdan and Renne (2007)		Kuiper et al. (2008)	
Sample	Fraction	Analysis	Age (ka)	± Age (ka)	Age (ka)	± Age (ka)
V-36	#30	SWH	50.3	4.4	50.2	3.9
V-45	#30	MGTF	88.8	10.6	88.6	9.9
V-65	#20	SGTF	104.2	13.4	104.0	12.7
V-81	#30	MGTF	136.1	12.2	127.2	8.2
V-111	#20	SGTF	169.9	11.4	169.6	8.9
V-111B	#30	MGTF	154.1	15.3	153.8	13.8
V-145	#20	SGTF	180.2	53.7	179.8	53.1
V-145	#30	MGTF	171.3	14.7	170.9	12.8
V-149	#30	SWH	187.1	13.8	186.8	11.3
V-184	#30	SWH	235.8	25.3	235.4	23.4
V-209a	#20	SGTF	295.8	14.8	295.3	8.1
V-209a	#30	MGTF	279.6	19.6	279.0	15.7
V-221a	#20	SGTF	306.9	15.3	306.3	8.3
V-221a	#30	MGTF	315.3	17.0	304.7	15.4
V-254	#20	SGTF	401.2	19.3	398.1	9.5
V-254	#30	MGTF	399.2	24.9	406.6	17.3
V-279	#20	SGTF	533.6	27.7	524.8	15.9
V-279	#30	MGTF	519.5	34.0	519.5	26.2

Table G.2: Comparison of inverse isochron ages from volcanic glass. All ages are recalibrated relative to Fish Canyon Sanidine. Two recalibrations are presented in this table and are organized as in Table G.1. All uncertainties represent one standard deviations for reasons explained in 5.

			Jourdan and Renne (2007)		Kuiper et al. (2008)	
Sample	Fraction	Analysis	Age Calculation	Age (ka)	± Age (ka)	Age (ka)	± Age (ka)
V-45	#30	SWH	Inverse Isochron	63.7	16.7	63.2	16.5
V-57b	#30	SWH	Plateau Age	71.5	55.0	71.0	54.5
V-65	#30	SWH	Inverse Isochron	105.2	44.6	104.4	44.1
V-165	#30	SWH	Plateau Age	195.3	12.0	193.8	10.6
V-209a	#30	SWH	Plateau Age	270.1	25.7	268.0	24.5

Appendix H: EMPA Feldspar Data

This appendix presents all EMPA analyses on zoned fledspars from volcaniclastics of the AR record. After listing all analyses on PO-type feldspars, measurements on C-type and R-type crystals are presented. Plagioclase compositions that served for calculations of feldspar thermometers in chapter 8 are also presented. All analyses are presented as atoms per formula unit (apfu) of feldspar. The electronic supplementary of the published chapter 4 (Engelhardt et al., 2017) presents an exemplar of the calculation of apfu feldspar and includes the according error propagation. Uncertainties are not stated in this appendix, but are exemplarily presented in the electronic supplementary in (Engelhardt et al., 2017). The range of available uncertainties is furthermore presented iat the end of this appendix. JFE compiled a Matlab script that conducted all calculations (error propagation of apfu). All calculations used the atomic weights and their uncertainties from represent IUPAC recommendations (Wieser et al., 2013).

Table H.1: IUPAC atomic weights for calculating atoms per formula units (Wieser et al., 2013). AMU abbreviates atom mass units.

Element	AMU	± AMU
O	15.999	0.008
Na	22.98976928	0.00000004
Al	26.9815385	0.00000014
Ti	47.867	0.002
Fe	55.845	0.004
K	39.0983	0.0002
Si	28.085	0.004
Mg	24.305	0.004
Mn	54.938044	0.000006
Ba	137.327	0.014
Sr	87.62	0.02
Ca	40.078	0.008
Oxide	**AMU**	**± AMU**
Na_2O	61.979	0.008
Al_2O_3	101.961	0.024
TiO_2	79.865	0.016
FeO	71.844	0.009
K_2O	94.196	0.008
SiO_2	60.083	0.017
MgO	40.304	0.009
MnO	70.937	0.008
BaO	153.326	0.016
SrO	103.619	0.022
CaO	56.077	0.011

Table H.2: EMPA data of PO-type feldspar in V-279. Data is presented in atoms per formula unit and in fractions of solid solution end member. The end members are: albite (X_{Ab}), anorthite (X_{An}), orthoclase (X_{Or}), and celsian (X_{Cs}). Distances of the line scans are directed from core towards the rim of the crystal.

V-ID	Analyses ID	Distance (μm)	Na	Al	Ti	Fe	K	Si	Mg	Mn	Ca	Sr	Ba	Sum	X_{Ab}	X_{An}	X_{Or}	X_{Cs}	Ca/K
V-279	Line 1_1322_FSP_5_CS	1	0.630	1.027	0.001	0.007	0.341	2.969	0.000	0.000	0.025	0.000	0.003	5.002	0.631	0.025	0.341	0.003	0.07
	Line 2_1322_FSP_5_CS	23	0.618	1.036	0.000	0.006	0.340	2.966	0.000	0.001	0.026	0.000	0.003	4.995	0.626	0.026	0.344	0.003	0.08
	Line 3_1322_FSP_5_CS	44	0.629	1.035	0.001	0.007	0.340	2.962	0.000	0.000	0.026	0.000	0.003	5.004	0.630	0.026	0.341	0.003	0.08
	Line 4_1322_FSP_5_CS	66	0.625	1.032	0.001	0.006	0.346	2.966	0.000	0.000	0.024	0.000	0.003	5.003	0.626	0.024	0.347	0.003	0.07
	Line 5_1322_FSP_5_CS	88	0.629	1.030	0.000	0.007	0.338	2.967	0.000	0.000	0.027	0.000	0.003	5.001	0.632	0.027	0.339	0.003	0.08
	Line 6_1322_FSP_5_CS	109	0.616	1.027	0.000	0.006	0.341	2.973	0.000	0.000	0.025	0.000	0.002	4.992	0.625	0.026	0.346	0.003	0.07
	Line 7_1322_FSP_5_CS	131	0.626	1.034	0.000	0.006	0.332	2.967	0.000	0.000	0.027	0.000	0.002	4.995	0.635	0.027	0.336	0.003	0.08
	Line 8_1322_FSP_5_CS	152	0.631	1.030	0.001	0.007	0.347	2.964	0.000	0.001	0.026	0.000	0.003	5.009	0.627	0.026	0.344	0.003	0.08
	Line 9_1322_FSP_5_CS	174	0.672	1.049	0.001	0.006	0.278	2.947	0.001	0.000	0.043	0.000	0.005	5.003	0.673	0.043	0.279	0.005	0.15
	Line 10_1322_FSP_5_CS	196	0.655	1.053	0.001	0.005	0.282	2.947	0.000	0.000	0.045	0.000	0.005	4.994	0.663	0.046	0.286	0.005	0.16
	Line 11_1322_FSP_5_CS	217	0.678	1.049	0.000	0.006	0.282	2.949	0.000	0.000	0.039	0.000	0.004	5.007	0.677	0.039	0.281	0.004	0.14
	Line 12_1322_FSP_5_CS	239	0.656	1.047	0.000	0.006	0.292	2.953	0.000	0.000	0.040	0.000	0.004	4.998	0.662	0.040	0.294	0.004	0.14
	Line 13_1322_FSP_5_CS	261	0.662	1.038	0.000	0.006	0.305	2.954	0.002	0.001	0.037	0.000	0.005	5.011	0.656	0.037	0.302	0.004	0.12
	Line 14_1322_FSP_5_CS	282	0.639	1.043	0.001	0.007	0.310	2.957	0.000	0.000	0.036	0.000	0.004	4.996	0.646	0.037	0.313	0.004	0.12
	Line 15_1322_FSP_5_CS	304	0.648	1.043	0.001	0.007	0.293	2.956	0.000	0.000	0.040	0.000	0.004	4.992	0.657	0.041	0.298	0.004	0.14
	Line 16_1322_FSP_5_CS	325	0.645	1.050	0.001	0.005	0.290	2.952	0.000	0.000	0.043	0.000	0.004	4.990	0.657	0.044	0.295	0.004	0.15
	Line 17_1322_FSP_5_CS	347	0.658	1.051	0.001	0.006	0.284	2.947	0.001	0.000	0.045	0.000	0.004	4.997	0.663	0.045	0.287	0.005	0.16
	Line 18_1322_FSP_5_CS	369	0.680	1.046	0.001	0.007	0.276	2.947	0.000	0.000	0.046	0.000	0.004	5.007	0.675	0.046	0.274	0.004	0.17
	Line 19_1322_FSP_5_CS	390	0.655	1.051	0.000	0.006	0.286	2.948	0.001	0.000	0.045	0.000	0.004	4.997	0.662	0.045	0.289	0.004	0.16
	Line 20_1322_FSP_5_CS	412	0.643	1.053	0.000	0.006	0.292	2.949	0.000	0.000	0.044	0.000	0.004	4.992	0.654	0.045	0.297	0.004	0.15
V-279	Line 1 1322_FSP_2_CS	1	0.639	1.034	0.001	0.006	0.320	2.965	0.000	0.000	0.030	0.000	0.002	4.997	0.645	0.030	0.322	0.002	0.09
	Line 2_1322_FSP_2_CS	8	0.633	1.036	0.001	0.007	0.321	2.964	0.001	0.000	0.030	0.000	0.003	4.995	0.641	0.030	0.326	0.003	0.09
	Line 3_1322_FSP_2_CS	15	0.642	1.032	0.001	0.005	0.323	2.964	0.000	0.001	0.031	0.000	0.003	5.002	0.643	0.031	0.323	0.003	0.10
	Line 4_1322_FSP_2_CS	22	0.634	1.030	0.001	0.008	0.324	2.967	0.000	0.000	0.030	0.000	0.003	4.996	0.640	0.030	0.327	0.003	0.09
	Line 5_1322_FSP_2_CS	29	0.634	1.036	0.000	0.007	0.320	2.963	0.000	0.000	0.031	0.000	0.003	4.995	0.641	0.032	0.324	0.003	0.10
	Line 6_1322_FSP_2_CS	36	0.626	1.038	0.000	0.007	0.316	2.965	0.000	0.000	0.031	0.000	0.002	4.987	0.642	0.032	0.324	0.002	0.10
	Line 7_1322_FSP_2_CS	42	0.625	1.026	0.001	0.007	0.321	2.973	0.000	0.000	0.030	0.000	0.003	4.986	0.639	0.030	0.328	0.003	0.09
	Line 8_1322_FSP_2_CS	49	0.629	1.032	0.001	0.007	0.322	2.967	0.000	0.000	0.031	0.000	0.003	4.991	0.639	0.031	0.327	0.003	0.10
	Line 9_1322_FSP_2_CS	56	0.641	1.031	0.000	0.006	0.323	2.965	0.000	0.000	0.032	0.000	0.003	5.002	0.642	0.032	0.324	0.003	0.10
	Line 10_1322_FSP_2_CS	63	0.625	1.036	0.001	0.006	0.319	2.966	0.000	0.000	0.032	0.000	0.002	4.988	0.639	0.032	0.326	0.003	0.10
	Line 11_1322_FSP_2_CS	70	0.647	1.039	0.001	0.007	0.321	2.957	0.000	0.000	0.033	0.000	0.002	5.007	0.645	0.033	0.321	0.002	0.10
	Line 12_1322_FSP_2_CS	77	0.645	1.032	0.001	0.007	0.325	2.962	0.000	0.000	0.033	0.000	0.003	5.007	0.641	0.033	0.323	0.003	0.10
	Line 13_1322_FSP_2_CS	84	0.628	1.030	0.000	0.008	0.321	2.968	0.000	0.000	0.033	0.000	0.003	4.991	0.638	0.034	0.326	0.003	0.10
	Line 14_1322_FSP_2_CS	91	0.629	1.041	0.000	0.006	0.318	2.960	0.000	0.001	0.034	0.000	0.003	4.993	0.639	0.035	0.323	0.003	0.11
	Line 15_1322_FSP_2_CS	98	0.637	1.042	0.001	0.007	0.321	2.957	0.000	0.000	0.033	0.000	0.003	5.000	0.640	0.033	0.323	0.003	0.10
	Line 16_1322_FSP_2_CS	105	0.639	1.040	0.001	0.006	0.325	2.956	0.000	0.001	0.033	0.000	0.003	5.005	0.639	0.033	0.325	0.003	0.10
	Line 17_1322_FSP_2_CS	111	0.641	1.039	0.000	0.007	0.319	2.958	0.000	0.000	0.033	0.000	0.003	5.002	0.644	0.033	0.321	0.003	0.10
	Line 18_1322_FSP_2_CS	118	0.641	1.038	0.002	0.006	0.324	2.958	0.000	0.000	0.033	0.000	0.003	5.004	0.640	0.033	0.324	0.003	0.10
	Line 19_1322_FSP_2_CS	125	0.634	1.036	0.000	0.007	0.318	2.964	0.000	0.000	0.033	0.000	0.002	4.994	0.642	0.033	0.322	0.002	0.10
	Line 20_1322_FSP_2_CS	132	0.635	1.042	0.001	0.006	0.322	2.958	0.000	0.000	0.033	0.000	0.003	4.999	0.640	0.033	0.324	0.003	0.10

Table H.3: EMPA data of PO-type feldspar in V-279. Data is presented in atoms per formula unit and in fractions of solid solution end member. The end members are: albite (X_{Ab}), anorthite (X_{An}), orthoclase (X_{Or}), and celsian (X_{Cs}). Distances of the line scans are directed from core towards the rim of the crystal.

V-ID	Analyses ID	Distance (μm)	Na	Al	Ti	Fe	K	Si	Mg	Mn	Ca	Sr	Ba	Sum	X_{Ab}	X_{An}	X_{Or}	X_{Cs}	Ca/K
V-279	Line_1_ELV_1322_FSP1_zoning_1	0	0.588	1.024	0.001	0.008	0.334	2.981	0.000	0.001	0.024	0.000	0.001	4.963	0.620	0.026	0.352	0.001	0.07
	Line_2 _ELV_1322_FSP1_zoning_1	6	0.587	1.013	0.001	0.007	0.338	2.989	0.000	0.000	0.024	0.000	0.001	4.961	0.618	0.025	0.356	0.001	0.07
	Line_3_ELV_1322_FSP1_zoning_1	12	0.597	1.017	0.001	0.006	0.336	2.984	0.000	0.000	0.026	0.000	0.002	4.969	0.621	0.027	0.349	0.002	0.08
	Line_4_ELV_1322_FSP1_zoning_1	17	0.600	1.028	0.000	0.007	0.332	2.976	0.000	0.000	0.029	0.000	0.002	4.972	0.623	0.030	0.345	0.002	0.09
	Line_5_ELV_1322_FSP1_zoning_1	23	0.596	1.022	0.000	0.008	0.333	2.980	0.000	0.000	0.026	0.000	0.002	4.967	0.623	0.027	0.347	0.002	0.08
	Line_6_ELV_1322_FSP1_zoning_1	29	0.592	1.033	0.001	0.007	0.335	2.971	0.000	0.000	0.029	0.000	0.002	4.970	0.618	0.031	0.350	0.002	0.09
	Line_7_ELV_1322_FSP1_zoning_1	35	0.614	1.032	0.001	0.006	0.330	2.967	0.001	0.000	0.030	0.000	0.003	4.983	0.629	0.030	0.338	0.003	0.09
	Line_8_ELV_1322_FSP1_zoning_1	41	0.582	1.025	0.000	0.006	0.332	2.979	0.000	0.000	0.031	0.000	0.003	4.959	0.614	0.033	0.350	0.003	0.09
	Line_9_ELV_1322_FSP1_zoning_1	46	0.591	1.032	0.001	0.006	0.330	2.974	0.000	0.000	0.027	0.000	0.002	4.964	0.622	0.029	0.347	0.002	0.08
	Line_10_ELV_1322_FSP1_zoning_1	52	0.594	1.033	0.001	0.005	0.329	2.973	0.000	0.000	0.028	0.000	0.002	4.967	0.623	0.029	0.345	0.003	0.08
	Line_11_ELV_1322_FSP1_zoning_1	58	0.583	1.035	0.001	0.006	0.334	2.971	0.000	0.000	0.030	0.000	0.002	4.964	0.614	0.031	0.352	0.003	0.09
	Line_12_ELV_1322_FSP1_zoning_1	64	0.581	1.021	0.001	0.007	0.335	2.983	0.000	0.000	0.028	0.000	0.001	4.958	0.615	0.029	0.355	0.001	0.08
	Line_13_ELV_1322_FSP1_zoning_1	70	0.573	1.033	0.000	0.005	0.332	2.977	0.000	0.001	0.030	0.000	0.003	4.954	0.611	0.032	0.354	0.003	0.09
	Line_14_ELV_1322_FSP1_zoning_1	75	0.577	1.028	0.001	0.007	0.332	2.978	0.000	0.001	0.030	0.000	0.003	4.957	0.613	0.032	0.352	0.003	0.09
	Line_15_ELV_1322_FSP1_zoning_1	81	0.588	1.033	0.001	0.006	0.332	2.972	0.000	0.000	0.030	0.000	0.003	4.965	0.617	0.032	0.348	0.003	0.09
	Line_16_ELV_1322_FSP1_zoning_1	87	0.584	1.036	0.001	0.006	0.328	2.972	0.000	0.000	0.030	0.000	0.004	4.960	0.618	0.032	0.347	0.004	0.09
	Line_17_ELV_1322_FSP1_zoning_1	93	0.587	1.029	0.000	0.007	0.332	2.975	0.000	0.000	0.030	0.000	0.002	4.964	0.617	0.032	0.349	0.002	0.09
	Line_18_ELV_1322_FSP1_zoning_1	99	0.576	1.039	0.001	0.006	0.331	2.971	0.000	0.000	0.031	0.000	0.002	4.957	0.612	0.033	0.352	0.002	0.09
	Line_19_ELV_1322_FSP1_zoning_1	104	0.575	1.029	0.002	0.006	0.329	2.978	0.000	0.000	0.030	0.000	0.003	4.951	0.614	0.032	0.351	0.003	0.09
	Line_20_ELV_1322_FSP1_zoning_1	110	0.593	1.040	0.000	0.005	0.327	2.966	0.000	0.001	0.032	0.000	0.003	4.968	0.621	0.034	0.343	0.003	0.10
	Line_21_ELV_1322_FSP1_zoning_1	116	0.574	1.042	0.000	0.006	0.331	2.970	0.000	0.000	0.032	0.000	0.003	4.957	0.611	0.034	0.352	0.003	0.10
	Line_22_ELV_1322_FSP1_zoning_1	122	0.583	1.030	0.000	0.007	0.332	2.976	0.000	0.000	0.030	0.000	0.003	4.961	0.615	0.032	0.351	0.003	0.09
	Line_23_ELV_1322_FSP1_zoning_1	128	0.579	1.031	0.001	0.007	0.334	2.976	0.000	0.000	0.029	0.000	0.003	4.960	0.612	0.031	0.354	0.003	0.09
	Line_24_ELV_1322_FSP1_zoning_1	133	0.600	1.021	0.001	0.006	0.329	2.979	0.000	0.000	0.029	0.000	0.002	4.968	0.624	0.030	0.343	0.002	0.09
	Line_25_ELV_1322_FSP1_zoning_1	139	0.585	1.034	0.000	0.006	0.332	2.974	0.000	0.000	0.030	0.000	0.003	4.963	0.616	0.032	0.349	0.003	0.09
	Line_26_ELV_1322_FSP1_zoning_1	145	0.596	1.028	0.000	0.006	0.326	2.975	0.000	0.000	0.031	0.000	0.003	4.966	0.623	0.033	0.341	0.003	0.10
	Line_27_ELV_1322_FSP1_zoning_1	151	0.604	1.035	0.001	0.007	0.327	2.966	0.000	0.000	0.031	0.000	0.003	4.976	0.626	0.032	0.339	0.003	0.09
	Line_28_ELV_1322_FSP1_zoning_1	157	0.592	1.037	0.001	0.008	0.329	2.967	0.000	0.000	0.031	0.000	0.003	4.969	0.620	0.032	0.345	0.003	0.09
	Line_29_ELV_1322_FSP1_zoning_1	162	0.592	1.036	0.000	0.005	0.324	2.970	0.000	0.000	0.032	0.000	0.003	4.963	0.622	0.034	0.341	0.003	0.10
	Line_30_ELV_1322_FSP1_zoning_1	168	0.589	1.028	0.000	0.006	0.331	2.976	0.000	0.000	0.031	0.000	0.003	4.965	0.617	0.033	0.347	0.003	0.09
V-279	ELV_1322_FSPS_7	0	0.587	1.023	0.000	0.007	0.357	2.975	0.000	0.000	0.026	0.000	0.004	4.979	0.602	0.027	0.367	0.004	0.07
	ELV_1322_FSPS_7	11	0.557	1.030	0.002	0.006	0.354	2.978	0.000	0.000	0.023	0.000	0.004	4.956	0.593	0.025	0.378	0.004	0.07
	ELV_1322_FSPS_7	22	0.575	1.036	0.001	0.007	0.359	2.968	0.001	0.001	0.024	0.000	0.004	4.975	0.598	0.025	0.373	0.004	0.07
	ELV_1322_FSPS_7	32	0.569	1.030	0.001	0.007	0.354	2.975	0.000	0.000	0.023	0.000	0.004	4.965	0.599	0.025	0.372	0.004	0.07
	ELV_1322_FSPS_7	43	0.577	1.027	0.001	0.007	0.357	2.976	0.000	0.000	0.022	0.000	0.004	4.971	0.601	0.023	0.372	0.004	0.06
	ELV_1322_FSPS_7	54	0.572	1.027	0.001	0.007	0.355	2.977	0.000	0.000	0.023	0.000	0.004	4.966	0.599	0.025	0.372	0.004	0.07
	ELV_1322_FSPS_7	65	0.568	1.028	0.001	0.006	0.359	2.977	0.000	0.000	0.023	0.000	0.004	4.967	0.595	0.024	0.376	0.004	0.06
	ELV_1322_FSPS_7	75	0.552	1.024	0.001	0.006	0.365	2.982	0.000	0.002	0.022	0.000	0.003	4.958	0.586	0.023	0.387	0.004	0.06
	ELV_1322_FSPS_7	86	0.554	1.026	0.000	0.006	0.364	2.983	0.000	0.001	0.022	0.000	0.003	4.959	0.588	0.024	0.385	0.003	0.06
	ELV_1322_FSPS_7	97	0.564	1.028	0.000	0.006	0.362	2.980	0.001	0.000	0.020	0.000	0.003	4.965	0.595	0.021	0.382	0.003	0.05
	ELV_1322_FSPS_7	108	0.566	1.029	0.002	0.006	0.359	2.976	0.000	0.000	0.023	0.000	0.003	4.964	0.595	0.025	0.377	0.003	0.07
	ELV_1322_FSPS_7	118	0.550	1.027	0.002	0.007	0.371	2.981	0.000	0.000	0.020	0.000	0.003	4.959	0.583	0.021	0.393	0.003	0.05
	ELV_1322_FSPS_7	129	0.574	1.030	0.001	0.007	0.373	2.974	0.000	0.000	0.019	0.000	0.002	4.979	0.593	0.019	0.385	0.002	0.05
	ELV_1322_FSPS_7	140	0.573	1.027	0.001	0.007	0.365	2.977	0.000	0.000	0.018	0.000	0.003	4.972	0.598	0.019	0.380	0.003	0.05
	ELV_1322_FSPS_7	151	0.574	1.022	0.000	0.007	0.370	2.980	0.000	0.000	0.020	0.000	0.002	4.976	0.594	0.021	0.383	0.003	0.05
	ELV_1322_FSPS_7	161	0.546	1.025	0.000	0.007	0.372	2.986	0.000	0.000	0.019	0.000	0.002	4.955	0.582	0.020	0.396	0.002	0.05
	ELV_1322_FSPS_7	172	0.557	1.018	0.000	0.007	0.371	2.987	0.001	0.000	0.020	0.000	0.002	4.963	0.587	0.021	0.390	0.002	0.05
	ELV_1322_FSPS_7	183	0.553	1.018	0.000	0.006	0.370	2.989	0.000	0.000	0.020	0.000	0.002	4.958	0.586	0.021	0.391	0.002	0.05
	ELV_1322_FSPS_7	194	0.549	1.018	0.000	0.006	0.367	2.992	0.000	0.000	0.018	0.000	0.002	4.952	0.587	0.019	0.392	0.002	0.05
	ELV_1322_FSPS_7	204	0.558	1.029	0.001	0.006	0.373	2.978	0.000	0.000	0.020	0.000	0.002	4.966	0.585	0.021	0.391	0.002	0.05
	ELV_1322_FSPS_7	215	0.546	1.029	0.001	0.006	0.370	2.981	0.000	0.000	0.021	0.000	0.002	4.957	0.582	0.022	0.394	0.002	0.06
	ELV_1322_FSPS_7	226	0.545	1.019	0.000	0.006	0.370	2.991	0.000	0.000	0.019	0.000	0.002	4.953	0.582	0.020	0.396	0.003	0.05

Table H.4: EMPA data of PO-type feldspar in V-254 and V-149. Data is presented in atoms per formula unit and in fractions of solid solution end member. The end members are: albite (X_{Ab}), anorthite (X_{An}), orthoclase (X_{Or}), and celsian (X_{Cs}). Distances of the line scans are directed from core towards the rim of the crystal.

V-ID	Analyses ID	Distance (μm)	Na	Al	Ti	Fe	K	Si	Mg	Mn	Ca	Sr	Ba	Sum	X_{Ab}	X_{An}	X_{Or}	X_{Cs}	Ca/K
V-254	Line 1 1319_FSP_7_CS	1	0.553	1.017	0.001	0.005	0.431	2.977	0.000	0.000	0.021	0.000	0.001	5.005	0.550	0.020	0.429	0.001	0.05
	Line 2 1319_FSP_7_CS	6	0.556	1.025	0.001	0.005	0.434	2.971	0.000	0.000	0.019	0.000	0.001	5.011	0.550	0.019	0.430	0.001	0.04
	Line 3 1319_FSP_7_CS	11	0.582	1.026	0.001	0.006	0.426	2.964	0.000	0.000	0.021	0.000	0.001	5.027	0.565	0.020	0.414	0.001	0.05
	Line 4 1319_FSP_7_CS	16	0.580	1.030	0.000	0.004	0.402	2.969	0.000	0.000	0.021	0.000	0.000	5.007	0.578	0.021	0.401	0.000	0.05
	Line 5 1319_FSP_7_CS	21	0.611	1.027	0.000	0.005	0.374	2.966	0.000	0.000	0.027	0.000	0.000	5.012	0.603	0.027	0.369	0.000	0.07
	Line 6 1319_FSP_7_CS	26	0.590	1.033	0.000	0.003	0.381	2.967	0.001	0.000	0.026	0.000	0.001	5.002	0.591	0.026	0.382	0.001	0.07
	Line 7 1319_FSP_7_CS	31	0.601	1.033	0.001	0.005	0.377	2.962	0.000	0.001	0.027	0.000	0.000	5.009	0.598	0.027	0.375	0.000	0.07
	Line 8 1319_FSP_7_CS	36	0.597	1.037	0.000	0.006	0.388	2.959	0.001	0.000	0.025	0.000	0.001	5.015	0.590	0.025	0.384	0.001	0.06
	Line 9 1319_FSP_7_CS	40	0.602	1.038	0.001	0.005	0.397	2.956	0.000	0.000	0.025	0.000	0.000	5.024	0.588	0.025	0.388	0.000	0.06
	Line 10 1319_FSP_7_CS	45	0.588	1.022	0.000	0.005	0.408	2.970	0.000	0.000	0.023	0.000	0.000	5.017	0.577	0.022	0.400	0.000	0.06
	Line 11 1319_FSP_7_CS	50	0.574	1.023	0.000	0.005	0.402	2.974	0.000	0.001	0.023	0.000	0.000	5.002	0.574	0.023	0.403	0.000	0.06
	Line 12 1319_FSP_7_CS	55	0.604	1.031	0.001	0.005	0.388	2.963	0.000	0.000	0.025	0.000	0.000	5.017	0.594	0.024	0.382	0.000	0.06
	Line 13 1319_FSP_7_CS	60	0.582	1.031	0.001	0.005	0.406	2.963	0.000	0.001	0.026	0.000	0.001	5.015	0.574	0.025	0.400	0.001	0.06
	Line 14 1319_FSP_7_CS	65	0.572	1.026	0.000	0.005	0.401	2.971	0.000	0.001	0.025	0.000	0.001	5.002	0.573	0.025	0.402	0.001	0.06
	Line 15 1319_FSP_7_CS	70	0.589	1.034	0.000	0.005	0.391	2.963	0.000	0.000	0.026	0.000	0.001	5.010	0.585	0.026	0.388	0.001	0.07
	Line 16 1319_FSP_7_CS	75	0.584	1.035	0.001	0.005	0.380	2.965	0.001	0.000	0.027	0.000	0.001	4.999	0.589	0.027	0.383	0.001	0.07
	Line 17 1319_FSP_7_CS	80	0.599	1.029	0.001	0.005	0.381	2.965	0.000	0.000	0.029	0.000	0.001	5.010	0.594	0.029	0.377	0.001	0.08
	Line 18 1319_FSP_7_CS	85	0.585	1.037	0.001	0.004	0.376	2.963	0.000	0.001	0.029	0.000	0.001	4.997	0.591	0.030	0.379	0.001	0.08
	Line 19 1319_FSP_7_CS	90	0.587	1.034	0.001	0.005	0.382	2.964	0.000	0.000	0.029	0.000	0.000	5.003	0.588	0.029	0.383	0.000	0.08
	Line 20 1319_FSP_7_CS	95	0.599	1.032	0.000	0.006	0.373	2.965	0.000	0.001	0.028	0.000	0.000	5.004	0.599	0.028	0.373	0.000	0.08
	Line 21 1319_FSP_7_CS	100	0.622	1.030	0.000	0.004	0.369	2.961	0.001	0.001	0.030	0.000	0.000	5.019	0.609	0.029	0.361	0.000	0.08
	Line 22 1319_FSP_7_CS	105	0.622	1.031	0.000	0.006	0.367	2.963	0.000	0.000	0.028	0.000	0.000	5.016	0.612	0.027	0.361	0.000	0.08
	Line 23 1319_FSP_7_CS	109	0.599	1.031	0.001	0.005	0.375	2.964	0.001	0.000	0.028	0.000	0.001	5.006	0.597	0.028	0.374	0.001	0.08
	Line 24 1319_FSP_7_CS	114	0.619	1.029	0.000	0.007	0.373	2.964	0.000	0.000	0.025	0.000	0.001	5.018	0.608	0.025	0.366	0.001	0.07
	Line 25 1319_FSP_7_CS	119	0.604	1.027	0.001	0.007	0.379	2.967	0.000	0.000	0.024	0.000	0.001	5.010	0.600	0.024	0.376	0.001	0.06
	Line 26 1319_FSP_7_CS	124	0.611	1.035	0.001	0.006	0.374	2.960	0.000	0.000	0.027	0.000	0.001	5.014	0.604	0.027	0.369	0.001	0.07
	Line 27 1319_FSP_7_CS	129	0.600	1.036	0.000	0.004	0.378	2.962	0.000	0.000	0.027	0.000	0.001	5.009	0.597	0.026	0.376	0.001	0.07
	Line 28 1319_FSP_7_CS	134	0.594	1.037	0.001	0.004	0.378	2.962	0.000	0.000	0.027	0.000	0.001	5.004	0.594	0.027	0.378	0.001	0.07
	Line 29 1319_FSP_7_CS	139	0.591	1.039	0.001	0.004	0.376	2.960	0.000	0.000	0.029	0.000	0.001	5.002	0.592	0.030	0.377	0.001	0.08
	Line 30 1319_FSP_7_CS	144	0.600	1.038	0.001	0.005	0.385	2.958	0.000	0.000	0.028	0.000	0.001	5.015	0.592	0.027	0.380	0.001	0.07
	Line 31 1319_FSP_7_CS	149	0.599	1.036	0.001	0.004	0.388	2.960	0.000	0.000	0.025	0.000	0.001	5.015	0.591	0.024	0.383	0.001	0.06
	Line 32 1319_FSP_7_CS	154	0.578	1.034	0.000	0.004	0.397	2.965	0.000	0.001	0.024	0.000	0.001	5.005	0.579	0.024	0.397	0.001	0.06
	Line 33 1319_FSP_7_CS	159	0.591	1.035	0.001	0.003	0.396	2.962	0.000	0.001	0.024	0.000	0.001	5.013	0.584	0.024	0.392	0.001	0.06
	Line 34 1319_FSP_7_CS	164	0.583	1.044	0.000	0.004	0.394	2.958	0.000	0.000	0.024	0.000	0.001	5.008	0.582	0.024	0.394	0.001	0.06
	Line 35 1319_FSP_7_CS	169	0.590	1.032	0.001	0.004	0.401	2.964	0.000	0.000	0.022	0.000	0.001	5.015	0.582	0.022	0.395	0.001	0.05
	Line 36 1319_FSP_7_CS	174	0.578	1.026	0.001	0.006	0.398	2.972	0.000	0.000	0.021	0.000	0.000	5.003	0.580	0.021	0.399	0.000	0.05
	Line 37 1319_FSP_7_CS	178	0.557	1.029	0.000	0.005	0.408	2.974	0.000	0.000	0.020	0.000	0.001	4.994	0.565	0.020	0.414	0.001	0.05
	Line 38 1319_FSP_7_CS	183	0.556	1.020	0.000	0.006	0.415	2.979	0.000	0.000	0.019	0.000	0.000	4.996	0.562	0.019	0.419	0.000	0.05
	Line 39 1319_FSP_7_CS	188	0.577	1.029	0.000	0.006	0.417	2.967	0.000	0.000	0.018	0.000	0.000	5.015	0.570	0.018	0.412	0.000	0.04
	Line 40 1319_FSP_7_CS	193	0.560	1.029	0.000	0.006	0.417	2.971	0.001	0.000	0.018	0.000	0.000	5.003	0.562	0.018	0.419	0.000	0.04
	Line 41 1319_FSP_7_CS	198	0.565	1.020	0.000	0.007	0.415	2.976	0.000	0.000	0.019	0.000	0.000	5.004	0.565	0.019	0.415	0.000	0.05
	Line 42 1319_FSP_7_CS	203	0.570	1.023	0.001	0.006	0.421	2.972	0.000	0.000	0.018	0.000	0.000	5.011	0.565	0.018	0.417	0.000	0.04
	Line 43 1319_FSP_7_CS	208	0.570	1.023	0.000	0.006	0.425	2.971	0.000	0.000	0.018	0.000	0.001	5.015	0.562	0.018	0.419	0.001	0.04
	Line 44 1319_FSP_7_CS	213	0.556	1.026	0.000	0.006	0.424	2.972	0.000	0.000	0.018	0.000	0.001	5.005	0.557	0.018	0.424	0.001	0.04
	Line 45 1319_FSP_7_CS	218	0.589	1.027	0.001	0.006	0.407	2.966	0.000	0.000	0.020	0.000	0.001	5.017	0.580	0.019	0.400	0.001	0.05
	Line 46 1319_FSP_7_CS	223	0.584	1.031	0.000	0.006	0.393	2.967	0.000	0.000	0.023	0.000	0.001	5.005	0.583	0.023	0.393	0.001	0.06
	Line 47 1319_FSP_7_CS	228	0.587	1.034	0.000	0.005	0.398	2.965	0.000	0.000	0.021	0.000	0.000	5.011	0.583	0.021	0.396	0.000	0.05
	Line 48 1319_FSP_7_CS	233	0.579	1.027	0.001	0.006	0.394	2.972	0.000	0.001	0.021	0.000	0.000	5.000	0.582	0.021	0.396	0.000	0.05
	Line 49 1319_FSP_7_CS	238	0.615	1.030	0.001	0.007	0.376	2.963	0.001	0.000	0.025	0.000	0.000	5.018	0.605	0.025	0.370	0.000	0.07
	Line 50 1319_FSP_7_CS	243	0.583	1.019	0.000	0.006	0.398	2.977	0.000	0.000	0.019	0.000	0.000	5.003	0.582	0.019	0.398	0.000	0.05
V-149	Line 1 1409_FSP_3_CS	1	0.639	0.991	0.000	0.013	0.323	3.008	0.000	0.000	0.003	0.000	0.000	4.978	0.662	0.003	0.335	0.000	0.01
	1409_FSP_3_CS	13	0.629	0.982	0.000	0.012	0.323	3.017	0.000	0.001	0.003	0.000	0.000	4.967	0.658	0.003	0.339	0.000	0.01
	1409_FSP_3_CS	25	0.627	0.988	0.000	0.012	0.323	3.014	0.000	0.000	0.003	0.000	0.000	4.967	0.658	0.003	0.339	0.000	0.01
	1409_FSP_3_CS	38	0.630	0.989	0.001	0.014	0.327	3.010	0.000	0.000	0.003	0.000	0.000	4.974	0.657	0.003	0.341	0.000	0.01
	1409_FSP_3_CS	50	0.631	0.990	0.001	0.015	0.328	3.009	0.000	0.000	0.002	0.000	0.000	4.974	0.657	0.002	0.341	0.000	0.01
	1409_FSP_3_CS	62	0.629	0.988	0.001	0.013	0.326	3.011	0.000	0.000	0.003	0.000	0.000	4.972	0.657	0.003	0.340	0.000	0.01
	1409_FSP_3_CS	74	0.635	0.983	0.001	0.013	0.323	3.014	0.000	0.000	0.003	0.000	0.000	4.972	0.661	0.003	0.336	0.000	0.01
	1409_FSP_3_CS	87	0.627	0.985	0.000	0.014	0.328	3.014	0.000	0.000	0.002	0.000	0.000	4.970	0.655	0.002	0.343	0.000	0.01
	1409_FSP_3_CS	99	0.627	0.987	0.001	0.013	0.325	3.013	0.001	0.000	0.003	0.000	0.000	4.969	0.656	0.003	0.340	0.000	0.01
	1409_FSP_3_CS	111	0.633	0.985	0.000	0.013	0.328	3.013	0.000	0.000	0.003	0.000	0.000	4.975	0.656	0.003	0.341	0.000	0.01

Table H.5: EMPA data of PO-type feldspar in V-111. Data is presented in atoms per formula unit and in fractions of solid solution end member. The end members are: albite (X_{Ab}), anorthite (X_{An}), orthoclase (X_{Or}), and celsian (X_{Cs}). Distances of the line scans are directed from core towards the rim of the crystal.

V-ID	Analyses ID	Distance (μm)	Na	Al	Ti	Fe	K	Si	Mg	Mn	Ca	Sr	Ba	Sum	X_{Ab}	X_{An}	X_{Or}	X_{Cs}	Ca/K
V-111	Line 1 1305_FSP_6_CS	1	0.554	1.042	0.002	0.006	0.416	2.956	0.000	0.000	0.027	0.000	0.002	5.006	0.555	0.027	0.417	0.002	0.07
	Line 2 1305_FSP_6_CS	5	0.535	1.032	0.002	0.007	0.418	2.968	0.000	0.000	0.026	0.000	0.001	4.991	0.545	0.027	0.427	0.001	0.06
	Line 3 1305_FSP_6_CS	10	0.551	1.037	0.003	0.007	0.420	2.960	0.000	0.000	0.025	0.000	0.001	5.004	0.552	0.025	0.421	0.001	0.06
	Line 4 1305_FSP_6_CS	14	0.528	1.037	0.002	0.008	0.427	2.965	0.000	0.000	0.024	0.000	0.001	4.992	0.539	0.024	0.436	0.001	0.06
	Line 5 1305_FSP_6_CS	18	0.549	1.034	0.002	0.008	0.426	2.962	0.000	0.001	0.023	0.000	0.001	5.006	0.549	0.023	0.427	0.001	0.05
	Line 6 1305_FSP_6_CS	23	0.525	1.039	0.002	0.005	0.432	2.964	0.000	0.001	0.026	0.000	0.001	4.994	0.534	0.026	0.439	0.001	0.06
	Line 7 1305_FSP_6_CS	27	0.506	1.045	0.001	0.005	0.436	2.963	0.000	0.000	0.026	0.000	0.001	4.984	0.522	0.027	0.450	0.001	0.06
	Line 8 1305_FSP_6_CS	31	0.524	1.042	0.002	0.006	0.434	2.959	0.000	0.000	0.030	0.000	0.001	4.998	0.530	0.030	0.439	0.001	0.07
	Line 9 1305_FSP_6_CS	36	0.529	1.036	0.002	0.005	0.422	2.965	0.000	0.000	0.029	0.000	0.001	4.990	0.539	0.030	0.430	0.001	0.07
	Line 10 1305_FSP_6_CS	40	0.539	1.048	0.001	0.006	0.414	2.954	0.000	0.000	0.033	0.000	0.001	4.997	0.547	0.033	0.419	0.001	0.08
	Line 11 1305_FSP_6_CS	44	0.539	1.045	0.002	0.006	0.410	2.957	0.000	0.000	0.034	0.000	0.001	4.993	0.548	0.034	0.417	0.001	0.08
	Line 12 1305_FSP_6_CS	49	0.559	1.040	0.003	0.005	0.403	2.958	0.000	0.000	0.032	0.000	0.001	5.001	0.562	0.032	0.405	0.001	0.08
	Line 13 1305_FSP_6_CS	53	0.558	1.053	0.001	0.005	0.395	2.950	0.000	0.001	0.035	0.000	0.001	4.999	0.564	0.036	0.399	0.001	0.09
	Line 14 1305_FSP_6_CS	57	0.566	1.040	0.002	0.006	0.397	2.955	0.000	0.000	0.037	0.000	0.001	5.004	0.565	0.037	0.397	0.001	0.09
	Line 15 1305_FSP_6_CS	61	0.551	1.037	0.001	0.006	0.410	2.962	0.000	0.000	0.030	0.000	0.001	4.998	0.555	0.030	0.414	0.001	0.07
	Line 16 1305_FSP_6_CS	66	0.568	1.039	0.001	0.006	0.410	2.957	0.000	0.000	0.030	0.000	0.001	5.012	0.564	0.029	0.406	0.001	0.07
	Line 17 1305_FSP_6_CS	70	0.572	1.053	0.002	0.007	0.379	2.948	0.000	0.000	0.038	0.000	0.001	5.000	0.578	0.039	0.383	0.001	0.10
	Line 18 1305_FSP_6_CS	74	0.557	1.055	0.001	0.006	0.379	2.951	0.001	0.000	0.039	0.000	0.001	4.989	0.571	0.040	0.388	0.001	0.10
	Line 19 1305_FSP_6_CS	79	0.567	1.052	0.001	0.006	0.385	2.950	0.000	0.000	0.037	0.000	0.001	4.999	0.573	0.037	0.389	0.001	0.10
	Line 20 1305_FSP_6_CS	83	0.576	1.057	0.002	0.007	0.386	2.943	0.000	0.000	0.038	0.000	0.001	5.009	0.576	0.038	0.386	0.001	0.10
	Line 21 1305_FSP_6_CS	87	0.563	1.040	0.001	0.007	0.397	2.960	0.000	0.000	0.029	0.000	0.001	4.999	0.569	0.029	0.401	0.001	0.07
	Line 22 1305_FSP_6_CS	92	0.564	1.042	0.001	0.008	0.400	2.958	0.001	0.000	0.027	0.000	0.001	5.002	0.569	0.027	0.404	0.001	0.07
	Line 23 1305_FSP_6_CS	96	0.553	1.031	0.001	0.007	0.409	2.968	0.000	0.000	0.025	0.001	0.001	4.997	0.559	0.025	0.414	0.001	0.06
	Line 24 1305_FSP_6_CS	100	0.550	1.030	0.001	0.007	0.411	2.969	0.000	0.000	0.026	0.000	0.001	4.996	0.556	0.027	0.416	0.001	0.06
	Line 25 1305_FSP_6_CS	105	0.547	1.035	0.001	0.008	0.408	2.965	0.000	0.000	0.029	0.000	0.002	4.994	0.555	0.029	0.414	0.002	0.07
	Line 26 1305_FSP_6_CS	109	0.547	1.042	0.001	0.009	0.403	2.958	0.001	0.000	0.032	0.000	0.002	4.995	0.556	0.033	0.410	0.002	0.08
	Line 27 1305_FSP_6_CS	113	0.546	1.053	0.002	0.009	0.395	2.947	0.000	0.001	0.041	0.000	0.002	4.995	0.555	0.042	0.401	0.002	0.10
	Line 28 1305_FSP_6_CS	118	0.547	1.050	0.001	0.008	0.401	2.949	0.000	0.000	0.040	0.000	0.003	4.999	0.552	0.040	0.405	0.003	0.10
	Line 29 1305_FSP_6_CS	122	0.552	1.058	0.001	0.006	0.402	2.942	0.000	0.000	0.041	0.000	0.003	5.005	0.553	0.041	0.402	0.003	0.10
	Line 30 1305_FSP_6_CS	126	0.547	1.053	0.001	0.008	0.401	2.947	0.000	0.000	0.040	0.000	0.002	5.000	0.552	0.040	0.405	0.003	0.10
V-111	Line 1 1305_FSP_3_CS	1	0.558	1.038	0.002	0.006	0.393	2.962	0.000	0.000	0.032	0.000	0.002	4.992	0.567	0.032	0.400	0.002	0.08
	Line 2 1305_FSP_3_CS	5	0.561	1.039	0.002	0.007	0.391	2.959	0.000	0.000	0.034	0.000	0.002	4.995	0.568	0.035	0.395	0.002	0.09
	Line 3 1305_FSP_3_CS	9	0.567	1.040	0.001	0.008	0.388	2.958	0.000	0.000	0.033	0.000	0.003	4.998	0.572	0.033	0.392	0.003	0.09
	Line 4 1305_FSP_3_CS	13	0.587	1.057	0.002	0.005	0.362	2.941	0.000	0.000	0.047	0.000	0.003	5.003	0.588	0.047	0.362	0.003	0.13
	Line 5 1305_FSP_3_CS	17	0.582	1.065	0.001	0.005	0.359	2.937	0.000	0.000	0.047	0.000	0.003	4.999	0.587	0.047	0.362	0.003	0.13
	Line 6 1305_FSP_3_CS	21	0.575	1.053	0.001	0.006	0.375	2.947	0.000	0.000	0.042	0.000	0.002	5.001	0.579	0.043	0.377	0.002	0.11
	Line 7 1305_FSP_3_CS	25	0.593	1.053	0.001	0.007	0.370	2.945	0.000	0.000	0.041	0.000	0.001	5.009	0.590	0.040	0.369	0.001	0.11
	Line 8 1305_FSP_3_CS	29	0.577	1.052	0.001	0.006	0.373	2.948	0.000	0.001	0.043	0.000	0.001	5.000	0.581	0.043	0.376	0.001	0.11
	Line 9 1305_FSP_3_CS	33	0.572	1.054	0.001	0.004	0.370	2.949	0.000	0.001	0.041	0.000	0.001	4.994	0.581	0.042	0.376	0.001	0.11
	Line 10 1305_FSP_3_CS	37	0.591	1.057	0.000	0.006	0.352	2.944	0.000	0.000	0.047	0.000	0.001	4.999	0.596	0.047	0.355	0.001	0.13
	Line 11 1305_FSP_3_CS	41	0.563	1.050	0.001	0.006	0.384	2.953	0.000	0.000	0.037	0.000	0.001	4.995	0.571	0.038	0.390	0.001	0.10
	Line 12 1305_FSP_3_CS	45	0.570	1.050	0.002	0.005	0.375	2.950	0.000	0.000	0.040	0.000	0.001	4.995	0.578	0.041	0.380	0.001	0.11
	Line 13 1305_FSP_3_CS	49	0.578	1.050	0.002	0.005	0.381	2.947	0.000	0.001	0.040	0.000	0.001	5.006	0.578	0.040	0.381	0.001	0.10
	Line 14 1305_FSP_3_CS	53	0.574	1.049	0.002	0.006	0.374	2.950	0.000	0.000	0.042	0.000	0.001	4.998	0.580	0.042	0.378	0.001	0.11
	Line 15 1305_FSP_3_CS	57	0.575	1.051	0.000	0.005	0.375	2.951	0.000	0.000	0.040	0.000	0.001	4.999	0.580	0.041	0.378	0.001	0.11
	Line 16 1305_FSP_3_CS	61	0.572	1.058	0.001	0.007	0.375	2.945	0.000	0.001	0.040	0.000	0.001	4.999	0.579	0.041	0.379	0.001	0.11
	Line 17 1305_FSP_3_CS	65	0.564	1.051	0.002	0.006	0.372	2.952	0.000	0.000	0.041	0.000	0.001	4.989	0.576	0.042	0.380	0.001	0.11
	Line 18 1305_FSP_3_CS	69	0.576	1.051	0.000	0.005	0.371	2.951	0.000	0.000	0.041	0.000	0.000	4.996	0.583	0.042	0.375	0.000	0.11
	Line 19 1305_FSP_3_CS	73	0.589	1.052	0.001	0.004	0.374	2.945	0.000	0.000	0.041	0.000	0.001	5.009	0.586	0.041	0.372	0.001	0.11
	Line 20 1305_FSP_3_CS	77	0.564	1.052	0.001	0.007	0.373	2.951	0.001	0.000	0.041	0.000	0.001	4.990	0.576	0.042	0.381	0.001	0.11
	Line 21 1305_FSP_3_CS	81	0.578	1.055	0.001	0.005	0.366	2.948	0.001	0.000	0.041	0.000	0.001	4.996	0.586	0.042	0.371	0.001	0.11
	Line 22 1305_FSP_3_CS	85	0.591	1.050	0.002	0.006	0.371	2.946	0.001	0.000	0.041	0.000	0.001	5.008	0.589	0.041	0.370	0.001	0.11
	Line 23 1305_FSP_3_CS	89	0.584	1.050	0.001	0.007	0.368	2.949	0.000	0.000	0.041	0.000	0.001	5.001	0.588	0.041	0.370	0.001	0.11
	Line 24 1305_FSP_3_CS	93	0.564	1.054	0.001	0.006	0.363	2.951	0.001	0.000	0.044	0.000	0.001	4.984	0.580	0.045	0.374	0.001	0.12
	Line 25 1305_FSP_3_CS	97	0.599	1.053	0.001	0.006	0.360	2.943	0.000	0.000	0.045	0.000	0.001	5.009	0.596	0.045	0.358	0.001	0.13
	Line 26 1305_FSP_3_CS	101	0.576	1.054	0.001	0.006	0.360	2.948	0.000	0.000	0.045	0.000	0.001	4.992	0.586	0.046	0.367	0.001	0.12
	Line 27 1305_FSP_3_CS	105	0.601	1.057	0.001	0.006	0.363	2.938	0.001	0.000	0.044	0.000	0.001	5.014	0.595	0.044	0.360	0.001	0.12
	Line 28 1305_FSP_3_CS	109	0.596	1.056	0.000	0.005	0.362	2.942	0.001	0.000	0.045	0.000	0.002	5.009	0.593	0.045	0.360	0.002	0.12
	Line 29 1305_FSP_3_CS	113	0.576	1.060	0.002	0.006	0.367	2.941	0.001	0.000	0.045	0.000	0.001	4.998	0.583	0.045	0.371	0.001	0.12
	Line 30 1305_FSP_3_CS	117	0.588	1.054	0.001	0.005	0.363	2.945	0.000	0.000	0.044	0.000	0.001	5.003	0.590	0.044	0.365	0.001	0.12

Table H.6: EMPA data of PO-type feldspar in V-81. Data is presented in atoms per formula unit and in fractions of solid solution end member. The end members are: albite (X_{Ab}), anorthite (X_{An}), orthoclase (X_{Or}), and celsian (X_{Cs}). Distances of the line scans are directed from core towards the rim of the crystal.

V-ID	Analyses ID	Distance (μm)	Na	Al	Ti	Fe	K	Si	Mg	Mn	Ca	Sr	Ba	Sum	X_{Ab}	X_{An}	X_{Or}	X_{Cs}	Ca/K
V-81	Line 1 1304_FSP_1_CS	1	0.616	0.983	0.000	0.016	0.341	3.015	0.000	0.000	0.001	0.000	0.000	4.972	0.643	0.001	0.356	0.000	0.002
	Line 2 1304_FSP_1_CS	9	0.635	0.972	0.001	0.017	0.343	3.016	0.001	0.001	0.001	0.000	0.000	4.987	0.648	0.001	0.351	0.000	0.004
	Line 3 1304_FSP_1_CS	17	0.628	0.970	0.001	0.017	0.344	3.020	0.000	0.000	0.001	0.000	0.000	4.980	0.646	0.001	0.353	0.000	0.002
	Line 4 1304_FSP_1_CS	25	0.632	0.975	0.000	0.016	0.344	3.016	0.000	0.000	0.001	0.000	0.000	4.984	0.647	0.001	0.352	0.000	0.003
	Line 5 1304_FSP_1_CS	33	0.627	0.986	0.000	0.016	0.341	3.010	0.000	0.000	0.001	0.000	0.000	4.981	0.647	0.001	0.352	0.000	0.002
	Line 6 1304_FSP_1_CS	41	0.628	0.977	0.001	0.016	0.345	3.013	0.000	0.001	0.001	0.000	0.000	4.984	0.645	0.001	0.354	0.000	0.002
	Line 7 1304_FSP_1_CS	49	0.613	0.976	0.001	0.017	0.343	3.019	0.000	0.000	0.001	0.000	0.000	4.970	0.640	0.001	0.359	0.000	0.003
	Line 8 1304_FSP_1_CS	57	0.633	0.970	0.000	0.017	0.344	3.018	0.000	0.001	0.001	0.000	0.000	4.985	0.647	0.001	0.352	0.000	0.002
	Line 9 1304_FSP_1_CS	65	0.623	0.981	0.001	0.017	0.343	3.013	0.000	0.000	0.001	0.000	0.000	4.979	0.645	0.001	0.354	0.000	0.002
	Line 10 1304_FSP_1_CS	73	0.631	0.977	0.000	0.018	0.343	3.014	0.000	0.000	0.001	0.000	0.000	4.984	0.648	0.001	0.351	0.000	0.002
	Line 11 1304_FSP_1_CS	81	0.635	0.976	0.000	0.015	0.346	3.014	0.000	0.000	0.001	0.000	0.000	4.988	0.646	0.001	0.353	0.000	0.003
	Line 12 1304_FSP_1_CS	89	0.631	0.977	0.000	0.016	0.345	3.014	0.000	0.000	0.001	0.000	0.000	4.985	0.646	0.001	0.353	0.000	0.004
	Line 13 1304_FSP_1_CS	97	0.627	0.976	0.000	0.018	0.349	3.014	0.000	0.000	0.001	0.000	0.000	4.986	0.641	0.001	0.357	0.000	0.003
	Line 14 1304_FSP_1_CS	105	0.627	0.973	0.001	0.017	0.347	3.017	0.000	0.000	0.001	0.000	0.000	4.983	0.643	0.001	0.356	0.000	0.003
	Line 15 1304_FSP_1_CS	113	0.607	0.976	0.001	0.021	0.345	3.018	0.000	0.000	0.002	0.000	0.000	4.969	0.637	0.002	0.362	0.000	0.005
	Line 16 1304_FSP_1_CS	121	0.635	0.983	0.000	0.013	0.345	3.009	0.001	0.000	0.001	0.000	0.000	4.989	0.647	0.001	0.351	0.000	0.004
	Line 17 1304_FSP_1_CS	129	0.628	0.982	0.001	0.012	0.345	3.012	0.000	0.001	0.002	0.000	0.000	4.983	0.644	0.002	0.354	0.000	0.007
	Line 18 1304_FSP_1_CS	137	0.622	0.982	0.000	0.012	0.346	3.013	0.001	0.001	0.002	0.000	0.000	4.980	0.641	0.002	0.357	0.000	0.006
	Line 19 1304_FSP_1_CS	145	0.622	0.984	0.001	0.012	0.345	3.012	0.000	0.000	0.002	0.000	0.000	4.979	0.642	0.002	0.356	0.000	0.006
	Line 20 1304_FSP_1_CS	153	0.633	0.979	0.001	0.015	0.346	3.012	0.000	0.000	0.002	0.000	0.000	4.987	0.645	0.002	0.353	0.000	0.005
	Line 21 1304_FSP_1_CS	161	0.639	0.976	0.000	0.017	0.344	3.012	0.000	0.000	0.002	0.000	0.000	4.991	0.649	0.002	0.349	0.000	0.005
	Line 22 1304_FSP_1_CS	169	0.639	0.980	0.000	0.015	0.344	3.010	0.000	0.000	0.002	0.000	0.000	4.991	0.649	0.002	0.349	0.000	0.005
	Line 23 1304_FSP_1_CS	177	0.618	0.978	0.002	0.015	0.346	3.015	0.000	0.001	0.002	0.000	0.000	4.977	0.639	0.003	0.358	0.000	0.007
	Line 24 1304_FSP_1_CS	185	0.626	0.983	0.000	0.013	0.347	3.011	0.000	0.000	0.002	0.000	0.000	4.983	0.642	0.002	0.356	0.000	0.005
	Line 25 1304_FSP_1_CS	193	0.621	0.982	0.000	0.015	0.351	3.011	0.001	0.001	0.003	0.000	0.000	4.985	0.637	0.003	0.360	0.000	0.008
	Line 26 1304_FSP_1_CS	202	0.614	0.986	0.001	0.012	0.348	3.012	0.000	0.000	0.003	0.000	0.000	4.976	0.636	0.003	0.361	0.000	0.007
	Line 27 1304_FSP_1_CS	210	0.631	0.983	0.000	0.011	0.350	3.011	0.000	0.000	0.002	0.000	0.000	4.988	0.642	0.002	0.356	0.000	0.006
	Line 28 1304_FSP_1_CS	218	0.626	0.978	0.000	0.016	0.349	3.013	0.000	0.000	0.002	0.000	0.000	4.985	0.641	0.002	0.358	0.000	0.005
	Line 29 1304_FSP_1_CS	226	0.627	0.982	0.001	0.014	0.350	3.010	0.000	0.000	0.002	0.000	0.000	4.986	0.640	0.002	0.357	0.000	0.006
	Line 30 1304_FSP_1_CS	234	0.611	0.979	0.000	0.014	0.350	3.017	0.000	0.000	0.002	0.000	0.000	4.974	0.634	0.002	0.364	0.000	0.005
	Line 31 1304_FSP_1_CS	242	0.627	0.975	0.001	0.013	0.349	3.015	0.001	0.000	0.001	0.000	0.000	4.984	0.642	0.001	0.357	0.000	0.003
	Line 32 1304_FSP_1_CS	250	0.627	0.983	0.000	0.014	0.347	3.011	0.000	0.001	0.002	0.000	0.000	4.984	0.643	0.002	0.356	0.000	0.004
	Line 33 1304_FSP_1_CS	258	0.624	0.980	0.001	0.014	0.351	3.013	0.001	0.000	0.002	0.000	0.000	4.984	0.639	0.002	0.359	0.000	0.005
	Line 34 1304_FSP_1_CS	266	0.625	0.983	0.001	0.013	0.349	3.011	0.001	0.000	0.002	0.000	0.000	4.984	0.641	0.002	0.358	0.000	0.005
	Line 35 1304_FSP_1_CS	274	0.611	0.981	0.001	0.014	0.353	3.015	0.000	0.000	0.002	0.000	0.000	4.976	0.633	0.002	0.365	0.000	0.004
	Line 36 1304_FSP_1_CS	282	0.641	0.980	0.001	0.014	0.350	3.008	0.000	0.000	0.002	0.000	0.000	4.996	0.645	0.002	0.352	0.000	0.006
	Line 37 1304_FSP_1_CS	290	0.620	0.981	0.001	0.014	0.351	3.013	0.000	0.000	0.002	0.000	0.000	4.981	0.638	0.002	0.361	0.000	0.004
	Line 38 1304_FSP_1_CS	298	0.632	0.985	0.000	0.015	0.348	3.008	0.000	0.000	0.001	0.000	0.000	4.990	0.644	0.001	0.354	0.000	0.004
	Line 39 1304_FSP_1_CS	306	0.617	0.978	0.000	0.015	0.351	3.015	0.000	0.000	0.001	0.000	0.000	4.979	0.636	0.002	0.362	0.000	0.004
	Line 40 1304_FSP_1_CS	314	0.619	0.981	0.001	0.014	0.347	3.014	0.000	0.000	0.002	0.000	0.000	4.978	0.640	0.002	0.358	0.000	0.005
	Line 41 1304_FSP_1_CS	322	0.618	0.974	0.000	0.013	0.349	3.020	0.000	0.000	0.002	0.000	0.000	4.976	0.638	0.002	0.360	0.000	0.005
	Line 42 1304_FSP_1_CS	330	0.625	0.980	0.001	0.013	0.346	3.014	0.000	0.000	0.001	0.000	0.000	4.981	0.642	0.002	0.356	0.000	0.004
	Line 43 1304_FSP_1_CS	338	0.611	0.983	0.000	0.013	0.349	3.015	0.000	0.000	0.001	0.000	0.000	4.973	0.635	0.001	0.363	0.000	0.003
	Line 44 1304_FSP_1_CS	346	0.620	0.976	0.001	0.013	0.351	3.017	0.000	0.001	0.002	0.000	0.000	4.980	0.637	0.002	0.361	0.000	0.005
	Line 45 1304_FSP_1_CS	354	0.628	0.985	0.001	0.014	0.348	3.009	0.000	0.000	0.001	0.000	0.000	4.986	0.642	0.001	0.356	0.000	0.003
	Line 46 1304_FSP_1_CS	362	0.611	0.980	0.001	0.014	0.351	3.015	0.001	0.001	0.002	0.000	0.000	4.976	0.633	0.002	0.364	0.000	0.005
	Line 47 1304_FSP_1_CS	370	0.609	0.989	0.000	0.015	0.354	3.009	0.000	0.000	0.002	0.000	0.000	4.978	0.631	0.002	0.367	0.000	0.005
	Line 48 1304_FSP_1_CS	378	0.618	0.984	0.001	0.013	0.356	3.011	0.000	0.000	0.001	0.000	0.000	4.984	0.633	0.001	0.365	0.000	0.003
	Line 49 1304_FSP_1_CS	386	0.636	0.984	0.001	0.013	0.353	3.006	0.000	0.001	0.002	0.000	0.000	4.995	0.642	0.002	0.356	0.000	0.004
	Line 50 1304_FSP_1_CS	394	0.631	0.985	0.000	0.013	0.347	3.008	0.000	0.000	0.002	0.002	0.001	4.989	0.643	0.002	0.354	0.001	0.005

Table H.7: EMPA data of PO-type feldspar inV-81. Data is presented in atoms per formula unit and in fractions of solid solution end member. The end members are: albite (X_{Ab}), anorthite (X_{An}), orthoclase (X_{Or}), and celsian (X_{Cs}). Distances of the line scans are directed from core towards the rim of the crystal.

V-ID	Analyses ID	Distance (μm)	Na	Al	Ti	Fe	K	Si	Mg	Mn	Ca	Sr	Ba	Sum	X_{Ab}	X_{An}	X_{Or}	X_{Cs}	Ca/K
V-81	Line 1 1304_FSP_3_CS	1	0.618	0.987	0.001	0.010	0.353	3.009	0.001	0.001	0.002	0.000	0.000	4.981	0.635	0.002	0.363	0.000	0.005
	Line 2 1304_FSP_3_CS	14	0.616	0.989	0.000	0.008	0.352	3.010	0.000	0.001	0.003	0.000	0.000	4.980	0.634	0.004	0.362	0.000	0.010
	Line 3 1304_FSP_3_CS	27	0.613	0.996	0.001	0.009	0.350	3.006	0.000	0.000	0.003	0.000	0.000	4.977	0.634	0.003	0.363	0.000	0.008
	Line 4 1304_FSP_3_CS	40	0.618	0.991	0.000	0.010	0.348	3.009	0.000	0.000	0.003	0.000	0.000	4.979	0.637	0.003	0.359	0.000	0.009
	Line 5 1304_FSP_3_CS	52	0.621	0.983	0.000	0.011	0.353	3.012	0.000	0.000	0.002	0.000	0.001	4.983	0.636	0.002	0.362	0.001	0.005
	Line 6 1304_FSP_3_CS	65	0.618	0.991	0.000	0.010	0.357	3.006	0.000	0.000	0.003	0.000	0.000	4.986	0.632	0.003	0.365	0.000	0.008
	Line 7 1304_FSP_3_CS	78	0.618	0.996	0.000	0.011	0.351	3.004	0.000	0.000	0.003	0.000	0.000	4.983	0.635	0.003	0.361	0.000	0.008
	Line 8 1304_FSP_3_CS	91	0.623	0.987	0.001	0.012	0.355	3.007	0.000	0.001	0.002	0.000	0.000	4.987	0.635	0.002	0.362	0.000	0.006
	Line 9 1304_FSP_3_CS	104	0.620	0.989	0.000	0.011	0.353	3.007	0.001	0.000	0.002	0.000	0.000	4.984	0.636	0.002	0.362	0.000	0.006
	Line 10 1304_FSP_3_CS	117	0.621	0.977	0.001	0.012	0.360	3.015	0.000	0.000	0.002	0.000	0.000	4.987	0.632	0.002	0.366	0.000	0.005
	Line 11 1304_FSP_3_CS	129	0.627	0.982	0.000	0.013	0.356	3.010	0.000	0.000	0.002	0.000	0.000	4.990	0.637	0.002	0.361	0.000	0.005
	Line 12 1304_FSP_3_CS	142	0.627	0.976	0.001	0.018	0.346	3.014	0.000	0.000	0.001	0.000	0.000	4.983	0.644	0.001	0.355	0.000	0.002
	Line 13 1304_FSP_3_CS	155	0.639	0.978	0.001	0.018	0.347	3.010	0.000	0.000	0.001	0.000	0.000	4.993	0.647	0.001	0.351	0.000	0.004
	Line 14 1304_FSP_3_CS	168	0.618	0.971	0.001	0.019	0.338	3.022	0.000	0.000	0.001	0.000	0.000	4.969	0.646	0.001	0.353	0.000	0.002
	Line 15 1304_FSP_3_CS	181	0.619	0.970	0.000	0.022	0.340	3.021	0.000	0.000	0.001	0.000	0.000	4.973	0.644	0.001	0.354	0.000	0.004
	Line 16 1304_FSP_3_CS	194	0.620	0.965	0.000	0.023	0.343	3.024	0.001	0.000	0.001	0.000	0.000	4.975	0.643	0.001	0.356	0.000	0.003
	Line 17 1304_FSP_3_CS	206	0.622	0.970	0.001	0.020	0.341	3.021	0.000	0.000	0.000	0.000	0.000	4.975	0.646	0.000	0.354	0.000	0.001
	Line 18 1304_FSP_3_CS	219	0.622	0.973	0.001	0.019	0.347	3.016	0.000	0.001	0.000	0.001	0.000	4.981	0.641	0.000	0.358	0.000	0.001
	Line 19 1304_FSP_3_CS	232	0.617	0.968	0.001	0.019	0.350	3.022	0.000	0.000	0.001	0.000	0.000	4.977	0.638	0.001	0.362	0.000	0.002
	Line 20 1304_FSP_3_CS	245	0.617	0.969	0.001	0.019	0.345	3.022	0.000	0.000	0.001	0.000	0.000	4.974	0.641	0.001	0.358	0.000	0.002
	Line 21 1304_FSP_3_CS	258	0.617	0.961	0.001	0.024	0.352	3.024	0.000	0.001	0.001	0.000	0.000	4.979	0.636	0.001	0.363	0.000	0.002
	Line 22 1304_FSP_3_CS	271	0.625	0.969	0.000	0.021	0.351	3.018	0.000	0.001	0.000	0.000	0.000	4.986	0.640	0.000	0.360	0.000	0.001
	Line 23 1304_FSP_3_CS	283	0.604	0.972	0.000	0.022	0.351	3.021	0.000	0.000	0.001	0.000	0.000	4.970	0.632	0.001	0.367	0.000	0.002
	Line 24 1304_FSP_3_CS	296	0.615	0.974	0.000	0.020	0.349	3.018	0.000	0.001	0.001	0.000	0.000	4.977	0.637	0.001	0.362	0.000	0.003
	Line 25 1304_FSP_3_CS	309	0.619	0.976	0.001	0.020	0.348	3.015	0.000	0.000	0.000	0.000	0.000	4.980	0.640	0.000	0.360	0.000	0.001
	Line 26 1304_FSP_3_CS	322	0.603	0.971	0.001	0.022	0.350	3.022	0.000	0.000	0.001	0.000	0.000	4.969	0.632	0.001	0.367	0.000	0.002
	Line 27 1304_FSP_3_CS	335	0.630	0.969	0.000	0.019	0.345	3.020	0.000	0.000	0.001	0.000	0.000	4.984	0.645	0.001	0.353	0.000	0.003
	Line 28 1304_FSP_3_CS	348	0.621	0.965	0.000	0.018	0.350	3.024	0.000	0.000	0.001	0.000	0.000	4.979	0.639	0.001	0.360	0.000	0.002
	Line 29 1304_FSP_3_CS	361	0.626	0.970	0.001	0.018	0.353	3.017	0.000	0.000	0.001	0.000	0.000	4.986	0.639	0.001	0.360	0.000	0.002
	Line 30 1304_FSP_3_CS	373	0.613	0.967	0.001	0.024	0.352	3.021	0.000	0.000	0.001	0.000	0.000	4.978	0.635	0.001	0.365	0.000	0.002
	Line 31 1304_FSP_3_CS	386	0.617	0.973	0.000	0.019	0.352	3.018	0.000	0.000	0.001	0.000	0.000	4.980	0.636	0.001	0.363	0.000	0.003
	Line 32 1304_FSP_3_CS	399	0.616	0.970	0.000	0.021	0.348	3.020	0.001	0.000	0.000	0.000	0.000	4.977	0.639	0.000	0.361	0.000	0.001
	Line 33 1304_FSP_3_CS	412	0.621	0.967	0.000	0.019	0.348	3.023	0.000	0.001	0.001	0.000	0.000	4.979	0.640	0.001	0.359	0.000	0.002
	Line 34 1304_FSP_3_CS	425	0.631	0.961	0.000	0.021	0.348	3.023	0.000	0.000	0.001	0.000	0.000	4.986	0.644	0.001	0.355	0.000	0.002
	Line 35 1304_FSP_3_CS	438	0.624	0.969	0.001	0.021	0.349	3.018	0.000	0.000	0.001	0.000	0.000	4.983	0.640	0.001	0.359	0.000	0.003
	Line 36 1304_FSP_3_CS	450	0.620	0.971	0.000	0.021	0.351	3.018	0.000	0.000	0.001	0.000	0.000	4.983	0.638	0.001	0.361	0.000	0.003
	Line 37 1304_FSP_3_CS	463	0.635	0.984	0.000	0.015	0.352	3.006	0.000	0.000	0.001	0.000	0.000	4.995	0.642	0.001	0.356	0.000	0.004
	Line 38 1304_FSP_3_CS	476	0.645	0.979	0.000	0.014	0.345	3.010	0.000	0.002	0.002	0.000	0.000	4.995	0.650	0.002	0.348	0.000	0.005
	Line 39 1304_FSP_3_CS	489	0.619	0.982	0.001	0.016	0.350	3.011	0.000	0.000	0.001	0.000	0.000	4.981	0.638	0.001	0.361	0.000	0.004
	Line 40 1304_FSP_3_CS	502	0.635	0.990	0.000	0.011	0.345	3.004	0.000	0.000	0.005	0.000	0.000	4.991	0.645	0.005	0.350	0.000	0.014
	Line 41 1304_FSP_3_CS	515	0.603	0.984	0.001	0.011	0.352	3.016	0.001	0.000	0.002	0.000	0.000	4.969	0.631	0.002	0.368	0.000	0.005
	Line 42 1304_FSP_3_CS	527	0.618	0.977	0.000	0.020	0.352	3.013	0.000	0.000	0.002	0.000	0.001	4.984	0.636	0.002	0.362	0.001	0.005
	Line 43 1304_FSP_3_CS	540	0.609	0.975	0.000	0.020	0.349	3.019	0.000	0.000	0.001	0.000	0.000	4.973	0.635	0.001	0.364	0.000	0.003
	Line 44 1304_FSP_3_CS	553	0.621	0.977	0.000	0.017	0.352	3.015	0.000	0.000	0.001	0.000	0.000	4.983	0.638	0.001	0.361	0.000	0.002
	Line 45 1304_FSP_3_CS	566	0.618	0.981	0.000	0.016	0.349	3.014	0.000	0.000	0.001	0.000	0.000	4.980	0.638	0.001	0.361	0.000	0.003
	Line 46 1304_FSP_3_CS	579	0.625	0.981	0.001	0.016	0.352	3.011	0.000	0.000	0.001	0.000	0.000	4.987	0.639	0.001	0.359	0.001	0.003
	Line 47 1304_FSP_3_CS	592	0.613	0.971	0.001	0.016	0.351	3.022	0.000	0.000	0.001	0.000	0.000	4.974	0.635	0.001	0.364	0.000	0.003
	Line 48 1304_FSP_3_CS	604	0.624	0.978	0.000	0.015	0.347	3.015	0.000	0.000	0.001	0.000	0.000	4.981	0.642	0.001	0.357	0.000	0.003
	Line 49 1304_FSP_3_CS	617	0.613	0.968	0.000	0.022	0.348	3.022	0.000	0.001	0.001	0.000	0.000	4.974	0.637	0.001	0.362	0.000	0.002

Table H.8: EMPA data of PO-type feldspar in V-81 and V-65. Data is presented in atoms per formula unit and in fractions of solid solution end member. The end members are: albite (X_{Ab}), anorthite (X_{An}), orthoclase (X_{Or}), and celsian (X_{Cs}). Distances of the line scans are directed from core towards the rim of the crystal.

V-ID	Analyses ID	Distance (μm)	Na	Al	Ti	Fe	K	Si	Mg	Mn	Ca	Sr	Ba	Sum	X_{Ab}	X_{An}	X_{Or}	X_{Cs}	Ca/K
V-81	Line 1 1304_FSP_2_CS	225	0.600	0.953	0.000	0.036	0.364	3.026	0.000	0.000	0.000	0.000	0.000	4.979	0.622	0.000	0.377	0.000	0.001
	Line 2 1304_FSP_2_CS	217	0.605	0.952	0.000	0.035	0.362	3.026	0.000	0.001	0.000	0.000	0.000	4.982	0.626	0.000	0.374	0.000	0.001
	Line 3 1304_FSP_2_CS	209	0.601	0.953	0.001	0.035	0.366	3.025	0.000	0.000	0.001	0.000	0.000	4.982	0.621	0.001	0.378	0.000	0.002
	Line 4 1304_FSP_2_CS	201	0.616	0.963	0.000	0.030	0.365	3.017	0.000	0.000	0.001	0.000	0.000	4.991	0.627	0.001	0.372	0.000	0.002
	Line 5 1304_FSP_2_CS	194	0.600	0.958	0.001	0.031	0.363	3.025	0.000	0.000	0.000	0.000	0.000	4.977	0.623	0.000	0.377	0.000	0.001
	Line 6 1304_FSP_2_CS	186	0.606	0.958	0.000	0.028	0.362	3.025	0.000	0.000	0.001	0.000	0.000	4.980	0.626	0.001	0.373	0.000	0.001
	Line 7 1304_FSP_2_CS	178	0.616	0.960	0.000	0.027	0.361	3.022	0.000	0.000	0.001	0.000	0.000	4.986	0.630	0.001	0.369	0.000	0.002
	Line 8 1304_FSP_2_CS	171	0.619	0.960	0.000	0.028	0.357	3.022	0.000	0.000	0.001	0.000	0.000	4.986	0.634	0.001	0.365	0.000	0.002
	Line 9 1304_FSP_2_CS	163	0.600	0.957	0.000	0.031	0.363	3.025	0.000	0.000	0.000	0.000	0.000	4.977	0.623	0.000	0.377	0.000	0.000
	Line 10 1304_FSP_2_CS	155	0.608	0.956	0.001	0.032	0.354	3.025	0.000	0.000	0.000	0.000	0.000	4.976	0.632	0.000	0.368	0.000	0.001
	Line 11 1304_FSP_2_CS	147	0.616	0.954	0.000	0.035	0.351	3.024	0.000	0.001	0.000	0.000	0.000	4.982	0.637	0.000	0.362	0.000	0.001
	Line 12 1304_FSP_2_CS	140	0.623	0.950	0.000	0.039	0.354	3.023	0.000	0.001	0.000	0.000	0.000	4.991	0.637	0.000	0.362	0.000	0.000
	Line 13 1304_FSP_2_CS	132	0.606	0.952	0.001	0.032	0.353	3.028	0.000	0.000	0.000	0.000	0.000	4.974	0.632	0.000	0.368	0.000	0.000
	Line 14 1304_FSP_2_CS	124	0.610	0.973	0.001	0.021	0.362	3.016	0.000	0.000	0.001	0.000	0.000	4.983	0.627	0.001	0.372	0.000	0.002
	Line 15 1304_FSP_2_CS	117	0.622	0.967	0.000	0.020	0.359	3.018	0.000	0.000	0.001	0.000	0.000	4.989	0.633	0.001	0.366	0.000	0.002
	Line 16 1304_FSP_2_CS	109	0.601	0.968	0.000	0.020	0.359	3.023	0.000	0.000	0.000	0.000	0.000	4.973	0.626	0.000	0.374	0.000	0.001
	Line 17 1304_FSP_2_CS	101	0.621	0.978	0.000	0.019	0.358	3.011	0.000	0.000	0.001	0.000	0.001	4.990	0.633	0.001	0.365	0.001	0.003
	Line 18 1304_FSP_2_CS	94	0.605	0.971	0.000	0.017	0.360	3.021	0.000	0.000	0.000	0.000	0.000	4.975	0.626	0.000	0.373	0.000	0.001
	Line 19 1304_FSP_2_CS	86	0.607	0.973	0.000	0.018	0.365	3.017	0.001	0.000	0.001	0.000	0.000	4.982	0.623	0.001	0.375	0.000	0.003
	Line 20 1304_FSP_2_CS	78	0.613	0.969	0.000	0.018	0.367	3.019	0.000	0.000	0.001	0.000	0.000	4.987	0.625	0.001	0.374	0.000	0.002
	Line 21 1304_FSP_2_CS	70	0.600	0.964	0.001	0.018	0.367	3.024	0.001	0.000	0.001	0.000	0.000	4.976	0.620	0.001	0.379	0.000	0.003
	Line 22 1304_FSP_2_CS	63	0.591	0.963	0.001	0.017	0.362	3.029	0.000	0.000	0.000	0.000	0.000	4.965	0.620	0.000	0.380	0.000	0.001
	Line 23 1304_FSP_2_CS	55	0.611	0.973	0.000	0.020	0.352	3.019	0.000	0.000	0.001	0.000	0.000	4.976	0.634	0.001	0.365	0.000	0.001
	Line 24 1304_FSP_2_CS	47	0.628	0.975	0.000	0.019	0.352	3.014	0.000	0.000	0.001	0.000	0.000	4.988	0.640	0.001	0.359	0.000	0.002
	Line 25 1304_FSP_2_CS	40	0.617	0.963	0.001	0.019	0.352	3.024	0.000	0.000	0.001	0.000	0.000	4.978	0.636	0.001	0.363	0.000	0.002
	Line 26 1304_FSP_2_CS	32	0.605	0.971	0.000	0.020	0.356	3.020	0.000	0.000	0.001	0.000	0.000	4.974	0.629	0.001	0.370	0.000	0.003
	Line 27 1304_FSP_2_CS	24	0.609	0.970	0.001	0.020	0.355	3.020	0.000	0.000	0.001	0.000	0.000	4.976	0.632	0.001	0.368	0.000	0.002
	Line 28 1304_FSP_2_CS	16	0.635	0.971	0.000	0.017	0.353	3.015	0.000	0.000	0.001	0.000	0.000	4.993	0.642	0.001	0.357	0.000	0.002
	Line 29 1304_FSP_2_CS	9	0.627	0.971	0.001	0.016	0.352	3.017	0.000	0.001	0.000	0.000	0.000	4.986	0.640	0.000	0.359	0.000	0.001
	Line 30 1304_FSP_2_CS	1	0.607	0.973	0.001	0.021	0.347	3.020	0.000	0.000	0.001	0.000	0.000	4.970	0.635	0.001	0.364	0.000	0.003
V-65	Line 1 1303_FSP_7_CS	1	0.604	1.011	0.000	0.012	0.345	2.992	0.000	0.000	0.012	0.000	0.000	4.977	0.628	0.012	0.359	0.000	0.03
	Line 2 1303_FSP_7_CS	12	0.598	1.014	0.001	0.010	0.348	2.990	0.000	0.000	0.012	0.000	0.000	4.975	0.624	0.013	0.363	0.000	0.03
	Line 3 1303_FSP_7_CS	22	0.603	1.017	0.001	0.012	0.346	2.985	0.000	0.001	0.014	0.000	0.001	4.980	0.625	0.015	0.359	0.001	0.04
	Line 4 1303_FSP_7_CS	33	0.594	1.014	0.001	0.011	0.352	2.990	0.000	0.000	0.012	0.000	0.001	4.975	0.620	0.013	0.367	0.001	0.04
	Line 5 1303_FSP_7_CS	43	0.597	1.012	0.001	0.011	0.350	2.992	0.001	0.000	0.010	0.000	0.000	4.975	0.623	0.011	0.366	0.000	0.03
	Line 6 1303_FSP_7_CS	54	0.593	1.009	0.001	0.012	0.352	2.995	0.000	0.000	0.009	0.000	0.000	4.972	0.621	0.010	0.368	0.000	0.03
	Line 7 1303_FSP_7_CS	64	0.574	1.012	0.000	0.012	0.356	2.998	0.000	0.000	0.009	0.000	0.000	4.961	0.611	0.010	0.379	0.000	0.03
	Line 8 1303_FSP_7_CS	75	0.577	1.010	0.001	0.011	0.353	2.998	0.000	0.001	0.009	0.000	0.000	4.961	0.614	0.009	0.376	0.000	0.02
	Line 9 1303_FSP_7_CS	85	0.585	1.018	0.001	0.012	0.349	2.990	0.000	0.000	0.010	0.000	0.001	4.966	0.619	0.011	0.370	0.001	0.03
	Line 10 1303_FSP_7_CS	96	0.595	0.997	0.001	0.014	0.354	3.003	0.000	0.000	0.007	0.000	0.000	4.972	0.622	0.007	0.370	0.000	0.02
	Line 11 1303_FSP_7_CS	106	0.592	0.999	0.002	0.014	0.353	3.001	0.000	0.001	0.008	0.000	0.000	4.970	0.622	0.008	0.370	0.000	0.02
	Line 12 1303_FSP_7_CS	117	0.583	1.007	0.001	0.015	0.353	2.998	0.001	0.000	0.007	0.000	0.000	4.965	0.618	0.007	0.374	0.000	0.02
	Line 13 1303_FSP_7_CS	127	0.593	1.000	0.000	0.015	0.355	3.001	0.000	0.001	0.007	0.000	0.000	4.973	0.621	0.007	0.372	0.000	0.02
	Line 14 1303_FSP_7_CS	138	0.577	1.003	0.001	0.014	0.356	3.002	0.000	0.000	0.006	0.000	0.000	4.962	0.614	0.007	0.379	0.000	0.02
	Line 15 1303_FSP_7_CS	148	0.584	0.995	0.001	0.015	0.357	3.007	0.000	0.000	0.005	0.000	0.000	4.965	0.617	0.006	0.378	0.000	0.01
	Line 16 1303_FSP_7_CS	159	0.593	0.998	0.001	0.016	0.357	3.002	0.000	0.001	0.005	0.000	0.000	4.974	0.620	0.006	0.374	0.000	0.02
	Line 17 1303_FSP_7_CS	169	0.588	0.998	0.001	0.016	0.360	3.002	0.000	0.000	0.006	0.000	0.000	4.972	0.616	0.006	0.378	0.000	0.02
	Line 18 1303_FSP_7_CS	180	0.577	0.997	0.002	0.018	0.356	3.005	0.000	0.000	0.006	0.000	0.000	4.961	0.614	0.007	0.379	0.000	0.02
	Line 19 1303_FSP_7_CS	190	0.574	0.999	0.001	0.016	0.356	3.006	0.000	0.000	0.007	0.000	0.000	4.959	0.612	0.008	0.380	0.000	0.02
	Line 20 1303_FSP_7_CS	201	0.577	0.987	0.002	0.017	0.359	3.012	0.000	0.000	0.007	0.000	0.000	4.961	0.612	0.007	0.381	0.000	0.02
	Line 21 1303_FSP_7_CS	211	0.577	1.000	0.000	0.018	0.359	3.003	0.001	0.000	0.007	0.000	0.000	4.964	0.612	0.007	0.381	0.000	0.02
	Line 22 1303_FSP_7_CS	222	0.575	1.000	0.002	0.016	0.360	3.002	0.000	0.000	0.007	0.000	0.000	4.963	0.611	0.007	0.382	0.000	0.02
	Line 23 1303_FSP_7_CS	232	0.588	0.997	0.001	0.019	0.360	3.000	0.000	0.001	0.006	0.000	0.000	4.974	0.616	0.007	0.377	0.000	0.02
	Line 24 1303_FSP_7_CS	243	0.578	0.994	0.001	0.020	0.362	3.005	0.000	0.000	0.006	0.000	0.000	4.967	0.611	0.007	0.382	0.000	0.02
	Line 25 1303_FSP_7_CS	253	0.572	1.003	0.002	0.016	0.358	3.001	0.001	0.000	0.008	0.000	0.000	4.961	0.610	0.009	0.382	0.000	0.02

Table H.9: EMPA data of PO-type feldspar inV-65. Data is presented in atoms per formula unit and in fractions of solid solution end member. The end members are: albite (X_{Ab}), anorthite (X_{An}), orthoclase (X_{Or}), and celsian (X_{Cs}). Distances of the line scans are directed from core towards the rim of the crystal.

V-ID	Analyses ID	Distance (μm)	Na	Al	Ti	Fe	K	Si	Mg	Mn	Ca	Sr	Ba	Sum	X_{Ab}	X_{An}	X_{Or}	X_{Cs}	Ca/K
V-65	Line 1 1303_FSP_3c_CS1	882	0.578	1.036	0.001	0.011	0.346	2.968	0.000	0.001	0.030	0.000	0.004	4.975	0.603	0.031	0.361	0.005	0.09
	Line 2 1303_FSP_3c_CS1	860	0.573	1.045	0.002	0.010	0.343	2.959	0.000	0.000	0.036	0.000	0.007	4.974	0.598	0.037	0.358	0.007	0.10
	Line 3 1303_FSP_3c_CS1	837	0.558	1.057	0.002	0.007	0.338	2.953	0.000	0.000	0.042	0.000	0.009	4.965	0.590	0.044	0.357	0.009	0.12
	Line 4 1303_FSP_3c_CS1	815	0.572	1.034	0.001	0.008	0.357	2.973	0.000	0.000	0.028	0.000	0.002	4.974	0.597	0.029	0.372	0.002	0.08
	Line 5 1303_FSP_3c_CS1	792	0.571	1.036	0.001	0.008	0.358	2.971	0.000	0.000	0.029	0.000	0.001	4.975	0.595	0.030	0.373	0.001	0.08
	Line 6 1303_FSP_3c_CS1	769	0.559	1.022	0.001	0.010	0.367	2.986	0.000	0.000	0.021	0.000	0.000	4.966	0.590	0.022	0.387	0.001	0.06
	Line 7 1303_FSP_3c_CS1	747	0.548	1.021	0.001	0.010	0.369	2.988	0.000	0.000	0.020	0.000	0.001	4.959	0.584	0.021	0.393	0.001	0.05
	Line 8 1303_FSP_3c_CS1	724	0.561	1.015	0.001	0.010	0.372	2.990	0.000	0.001	0.019	0.000	0.001	4.968	0.589	0.020	0.391	0.001	0.05
	Line 9 1303_FSP_3c_CS1	702	0.571	1.020	0.001	0.013	0.370	2.983	0.001	0.000	0.018	0.000	0.000	4.977	0.595	0.019	0.385	0.000	0.05
	Line 10 1303_FSP_3c_CS1	679	0.561	1.023	0.000	0.009	0.368	2.985	0.000	0.000	0.020	0.000	0.001	4.967	0.591	0.021	0.387	0.001	0.05
	Line 11 1303_FSP_3c_CS1	656	0.560	1.019	0.001	0.010	0.366	2.988	0.001	0.000	0.019	0.000	0.001	4.964	0.592	0.020	0.387	0.001	0.05
	Line 12 1303_FSP_3c_CS1	634	0.547	1.019	0.001	0.010	0.367	2.991	0.001	0.001	0.019	0.000	0.000	4.955	0.586	0.021	0.393	0.000	0.05
	Line 13 1303_FSP_3c_CS1	611	0.573	1.014	0.001	0.010	0.368	2.989	0.000	0.000	0.019	0.000	0.000	4.974	0.597	0.020	0.383	0.000	0.05
	Line 14 1303_FSP_3c_CS1	589	0.573	1.019	0.001	0.009	0.365	2.984	0.001	0.000	0.020	0.000	0.000	4.974	0.597	0.021	0.381	0.000	0.06
	Line 15 1303_FSP_3c_CS1	566	0.564	1.017	0.001	0.010	0.358	2.991	0.000	0.001	0.020	0.000	0.001	4.961	0.598	0.021	0.380	0.001	0.06
	Line 16 1303_FSP_3c_CS1	543	0.556	1.025	0.000	0.010	0.364	2.986	0.000	0.000	0.018	0.000	0.001	4.961	0.592	0.020	0.388	0.001	0.05
	Line 17 1303_FSP_3c_CS1	521	0.575	1.023	0.000	0.010	0.356	2.983	0.000	0.000	0.023	0.000	0.001	4.971	0.602	0.024	0.373	0.001	0.06
	Line 18 1303_FSP_3c_CS1	498	0.565	1.028	0.000	0.008	0.354	2.983	0.000	0.000	0.022	0.000	0.001	4.962	0.600	0.023	0.376	0.001	0.06
	Line 19 1303_FSP_3c_CS1	476	0.571	1.022	0.001	0.008	0.351	2.985	0.001	0.000	0.023	0.000	0.001	4.963	0.604	0.024	0.371	0.001	0.07
	Line 20 1303_FSP_3c_CS1	453	0.583	1.027	0.001	0.009	0.353	2.978	0.001	0.001	0.022	0.000	0.000	4.975	0.608	0.023	0.368	0.000	0.06
	Line 21 1303_FSP_3c_CS1	430	0.571	1.023	0.002	0.010	0.351	2.984	0.000	0.000	0.022	0.000	0.001	4.964	0.604	0.023	0.372	0.001	0.06
	Line 22 1303_FSP_3c_CS1	408	0.583	1.022	0.002	0.010	0.351	2.980	0.000	0.000	0.024	0.000	0.001	4.974	0.608	0.025	0.366	0.001	0.07
	Line 23 1303_FSP_3c_CS1	385	0.576	1.020	0.001	0.011	0.360	2.985	0.000	0.000	0.020	0.000	0.000	4.973	0.603	0.021	0.376	0.000	0.05
	Line 24 1303_FSP_3c_CS1	363	0.563	1.017	0.001	0.009	0.353	2.992	0.000	0.000	0.022	0.000	0.001	4.957	0.600	0.023	0.376	0.001	0.06
	Line 25 1303_FSP_3c_CS1	340	0.583	1.016	0.001	0.008	0.354	2.986	0.000	0.001	0.022	0.000	0.001	4.973	0.607	0.023	0.368	0.001	0.06
	Line 26 1303_FSP_3c_CS1	317	0.578	1.024	0.002	0.008	0.355	2.982	0.000	0.000	0.021	0.000	0.001	4.970	0.605	0.022	0.371	0.001	0.06
	Line 27 1303_FSP_3c_CS1	295	0.572	1.026	0.001	0.009	0.355	2.981	0.000	0.000	0.022	0.000	0.001	4.968	0.602	0.024	0.374	0.001	0.06
	Line 28 1303_FSP_3c_CS1	272	0.577	1.025	0.001	0.008	0.354	2.982	0.000	0.001	0.021	0.000	0.001	4.970	0.605	0.022	0.372	0.001	0.06
	Line 29 1303_FSP_3c_CS1	250	0.571	1.018	0.002	0.008	0.353	2.988	0.000	0.000	0.022	0.000	0.001	4.963	0.603	0.023	0.373	0.001	0.06
	Line 30 1303_FSP_3c_CS1	227	0.563	1.021	0.001	0.008	0.353	2.989	0.000	0.000	0.021	0.000	0.001	4.957	0.600	0.023	0.376	0.001	0.06
	Line 31 1303_FSP_3c_CS1	204	0.578	1.025	0.001	0.008	0.353	2.982	0.000	0.000	0.023	0.000	0.001	4.970	0.606	0.024	0.370	0.001	0.06
	Line 32 1303_FSP_3c_CS1	182	0.571	1.021	0.001	0.008	0.357	2.987	0.001	0.000	0.022	0.000	0.001	4.967	0.601	0.023	0.376	0.001	0.06
	Line 33 1303_FSP_3c_CS1	159	0.569	1.019	0.002	0.009	0.354	2.988	0.000	0.000	0.021	0.000	0.000	4.962	0.603	0.022	0.375	0.000	0.06
	Line 34 1303_FSP_3c_CS1	137	0.479	1.163	0.004	0.042	0.404	2.868	0.000	0.000	0.028	0.000	0.000	4.989	0.525	0.031	0.443	0.000	0.07
	Line 35 1303_FSP_3c_CS1	114	0.583	1.018	0.000	0.009	0.354	2.987	0.000	0.000	0.020	0.000	0.001	4.973	0.609	0.021	0.370	0.001	0.06
	Line 36 1303_FSP_3c_CS1	91	0.578	1.016	0.001	0.009	0.356	2.987	0.000	0.001	0.022	0.000	0.001	4.970	0.604	0.023	0.372	0.001	0.06
	Line 37 1303_FSP_3c_CS1	69	0.569	1.021	0.001	0.009	0.353	2.987	0.000	0.000	0.022	0.000	0.001	4.963	0.602	0.024	0.374	0.001	0.06
	Line 38 1303_FSP_3c_CS1	46	0.578	1.021	0.001	0.008	0.352	2.986	0.000	0.000	0.022	0.000	0.000	4.968	0.607	0.023	0.370	0.001	0.06
	Line 39 1303_FSP_3c_CS1	24	0.584	1.023	0.001	0.009	0.348	2.982	0.000	0.000	0.023	0.000	0.001	4.970	0.611	0.024	0.364	0.001	0.07
	Line 40 1303_FSP_3c_CS1	1	0.567	1.019	0.001	0.009	0.354	2.990	0.000	0.000	0.019	0.000	0.000	4.959	0.603	0.020	0.376	0.000	0.05

Table H.10: EMPA data of PO-type feldspar in V-65. Data is presented in atoms per formula unit and in fractions of solid solution end member. The end members are: albite (X_{Ab}), anorthite (X_{An}), orthoclase (X_{Or}), and celsian (X_{Cs}). Distances of the line scans are directed from core towards the rim of the crystal.

V-ID	Analyses ID	Distance (μm)	Na	Al	Ti	Fe	K	Si	Mg	Mn	Ca	Sr	Ba	Sum	X_{Ab}	X_{An}	X_{Or}	X_{Cs}	Ca/K
V-65	Line 1 1303_FSP_3c_CS2	250	0.575	1.016	0.001	0.010	0.361	2.989	0.000	0.000	0.016	0.000	0.000	4.969	0.603	0.017	0.379	0.000	0.05
	Line 2 1303_FSP_3c_CS2	241	0.574	1.018	0.002	0.010	0.361	2.986	0.000	0.000	0.018	0.000	0.001	4.970	0.602	0.019	0.378	0.001	0.05
	Line 3 1303_FSP_3c_CS2	232	0.563	1.031	0.002	0.008	0.354	2.977	0.001	0.002	0.026	0.001	0.000	4.964	0.597	0.027	0.375	0.000	0.07
	Line 4 1303_FSP_3c_CS2	224	0.565	1.028	0.002	0.009	0.357	2.978	0.000	0.000	0.025	0.000	0.000	4.966	0.596	0.027	0.377	0.000	0.07
	Line 5 1303_FSP_3c_CS2	215	0.570	1.019	0.001	0.009	0.359	2.988	0.000	0.000	0.019	0.000	0.000	4.966	0.600	0.021	0.379	0.000	0.05
	Line 6 1303_FSP_3c_CS2	207	0.582	1.022	0.001	0.009	0.352	2.984	0.000	0.001	0.020	0.000	0.000	4.970	0.610	0.020	0.369	0.000	0.06
	Line 7 1303_FSP_3c_CS2	198	0.571	1.023	0.001	0.010	0.352	2.986	0.000	0.000	0.019	0.000	0.001	4.963	0.606	0.020	0.373	0.001	0.05
	Line 8 1303_FSP_3c_CS2	190	0.585	1.023	0.002	0.009	0.354	2.981	0.000	0.001	0.020	0.000	0.000	4.975	0.609	0.021	0.369	0.000	0.06
	Line 9 1303_FSP_3c_CS2	181	0.572	1.028	0.001	0.010	0.353	2.980	0.000	0.000	0.022	0.000	0.001	4.968	0.603	0.023	0.372	0.001	0.06
	Line 10 1303_FSP_3c_CS2	172	0.552	1.024	0.001	0.009	0.349	2.991	0.000	0.000	0.021	0.000	0.000	4.947	0.599	0.023	0.379	0.000	0.06
	Line 11 1303_FSP_3c_CS2	164	0.579	1.008	0.001	0.009	0.352	2.995	0.000	0.000	0.021	0.000	0.000	4.966	0.608	0.022	0.370	0.000	0.06
	Line 12 1303_FSP_3c_CS2	155	0.571	1.012	0.002	0.010	0.353	2.993	0.000	0.001	0.018	0.000	0.000	4.961	0.606	0.019	0.375	0.001	0.05
	Line 13 1303_FSP_3c_CS2	147	0.584	1.012	0.001	0.011	0.351	2.992	0.000	0.000	0.017	0.000	0.000	4.968	0.613	0.018	0.369	0.000	0.05
	Line 14 1303_FSP_3c_CS2	138	0.578	1.013	0.001	0.011	0.351	2.992	0.001	0.000	0.018	0.000	0.000	4.965	0.610	0.019	0.371	0.000	0.05
	Line 15 1303_FSP_3c_CS2	130	0.595	1.008	0.001	0.009	0.349	2.994	0.000	0.000	0.016	0.000	0.000	4.973	0.619	0.017	0.363	0.000	0.05
	Line 16 1303_FSP_3c_CS2	121	0.569	1.015	0.001	0.010	0.349	2.995	0.000	0.000	0.018	0.000	0.000	4.956	0.608	0.019	0.373	0.000	0.05
	Line 17 1303_FSP_3c_CS2	112	0.572	1.012	0.001	0.010	0.346	2.998	0.000	0.000	0.017	0.000	0.000	4.955	0.612	0.018	0.370	0.000	0.05
	Line 18 1303_FSP_3c_CS2	104	0.571	1.015	0.001	0.010	0.347	2.994	0.000	0.001	0.018	0.000	0.000	4.957	0.610	0.019	0.370	0.000	0.05
	Line 19 1303_FSP_3c_CS2	95	0.574	1.015	0.000	0.010	0.348	2.995	0.000	0.000	0.018	0.000	0.000	4.958	0.611	0.019	0.370	0.000	0.05
	Line 20 1303_FSP_3c_CS2	87	0.577	1.010	0.000	0.009	0.348	2.997	0.000	0.000	0.018	0.000	0.001	4.960	0.612	0.019	0.369	0.001	0.05
	Line 21 1303_FSP_3c_CS2	78	0.563	1.019	0.001	0.009	0.349	2.992	0.000	0.002	0.020	0.000	0.000	4.954	0.604	0.022	0.374	0.000	0.06
	Line 22 1303_FSP_3c_CS2	70	0.582	1.018	0.001	0.008	0.347	2.989	0.000	0.000	0.021	0.000	0.000	4.966	0.613	0.022	0.365	0.000	0.06
	Line 23 1303_FSP_3c_CS2	61	0.579	1.027	0.001	0.008	0.342	2.983	0.000	0.000	0.024	0.000	0.001	4.963	0.612	0.026	0.361	0.001	0.07
	Line 24 1303_FSP_3c_CS2	52	0.583	1.022	0.002	0.007	0.347	2.984	0.000	0.000	0.023	0.000	0.001	4.968	0.612	0.024	0.364	0.001	0.06
	Line 25 1303_FSP_3c_CS2	44	0.578	1.023	0.001	0.009	0.342	2.985	0.000	0.000	0.024	0.000	0.001	4.962	0.612	0.025	0.362	0.001	0.07
	Line 26 1303_FSP_3c_CS2	35	0.569	1.029	0.002	0.010	0.338	2.981	0.000	0.000	0.026	0.000	0.001	4.956	0.609	0.028	0.362	0.001	0.08
	Line 27 1303_FSP_3c_CS2	27	0.194	1.044	0.002	0.008	0.255	3.085	0.000	0.000	0.027	0.000	0.001	4.616	0.407	0.056	0.534	0.002	0.10
	Line 28 1303_FSP_3c_CS2	18	0.101	1.057	0.002	0.007	0.149	3.128	0.000	0.000	0.022	0.000	0.001	4.467	0.370	0.081	0.545	0.003	0.15
	Line 29 1303_FSP_3c_CS2	10	0.591	1.035	0.001	0.008	0.344	2.972	0.000	0.000	0.025	0.000	0.001	4.977	0.615	0.026	0.358	0.001	0.07
	Line 30 1303_FSP_3c_CS2	1	0.590	1.028	0.001	0.009	0.340	2.977	0.000	0.001	0.025	0.000	0.001	4.973	0.617	0.026	0.356	0.001	0.07

Table H.11: EMPA data of PO-type feldspar inV-65. Data is presented in atoms per formula unit and in fractions of solid solution end member. The end members are: albite (X_{Ab}), anorthite (X_{An}), orthoclase (X_{Or}), and celsian (X_{Cs}). Distances of the line scans are directed from core towards the rim of the crystal.

V-ID	Analyses ID	Distance (μm)	Na	Al	Ti	Fe	K	Si	Mg	Mn	Ca	Sr	Ba	Sum	X_{Ab}	X_{An}	X_{Or}	X_{Cs}	Ca/K
V-65	Line 1 1303_FSP_4d_CS	1	0.603	1.005	0.001	0.013	0.347	2.998	0.000	0.000	0.007	0.000	0.001	4.974	0.630	0.007	0.362	0.001	0.02
	Line 2 1303_FSP_4d_CS	12	0.598	1.005	0.001	0.016	0.346	2.996	0.000	0.002	0.007	0.001	0.000	4.972	0.629	0.007	0.364	0.000	0.02
	Line 3 1303_FSP_4d_CS	23	0.596	1.001	0.001	0.016	0.343	3.002	0.001	0.000	0.007	0.000	0.000	4.967	0.629	0.007	0.363	0.001	0.02
	Line 4 1303_FSP_4d_CS	33	0.602	1.009	0.001	0.015	0.346	2.994	0.000	0.001	0.007	0.000	0.000	4.974	0.630	0.007	0.362	0.000	0.02
	Line 5 1303_FSP_4d_CS	44	0.603	0.998	0.002	0.016	0.345	3.001	0.000	0.000	0.006	0.000	0.000	4.972	0.632	0.006	0.362	0.000	0.02
	Line 6 1303_FSP_4d_CS	55	0.592	1.006	0.001	0.013	0.351	2.997	0.000	0.000	0.007	0.000	0.000	4.970	0.622	0.008	0.370	0.000	0.02
	Line 7 1303_FSP_4d_CS	66	0.599	1.011	0.000	0.014	0.347	2.994	0.000	0.000	0.007	0.000	0.000	4.973	0.629	0.007	0.364	0.000	0.02
	Line 8 1303_FSP_4d_CS	77	0.597	1.012	0.001	0.013	0.344	2.995	0.000	0.001	0.006	0.000	0.000	4.969	0.630	0.006	0.363	0.000	0.02
	Line 9 1303_FSP_4d_CS	87	0.610	1.007	0.002	0.013	0.347	2.994	0.000	0.000	0.006	0.000	0.000	4.980	0.633	0.007	0.360	0.000	0.02
	Line 10 1303_FSP_4d_CS	98	0.609	0.997	0.000	0.014	0.344	3.003	0.000	0.000	0.007	0.000	0.001	4.975	0.634	0.007	0.358	0.001	0.02
	Line 11 1303_FSP_4d_CS	109	0.595	1.002	0.000	0.014	0.345	3.003	0.000	0.000	0.006	0.000	0.000	4.966	0.629	0.006	0.365	0.000	0.02
	Line 12 1303_FSP_4d_CS	120	0.599	1.002	0.001	0.016	0.345	3.001	0.000	0.000	0.006	0.000	0.000	4.969	0.631	0.006	0.363	0.000	0.02
	Line 13 1303_FSP_4d_CS	130	0.597	1.006	0.000	0.016	0.343	3.000	0.000	0.000	0.005	0.000	0.000	4.967	0.632	0.005	0.363	0.000	0.01
	Line 14 1303_FSP_4d_CS	141	0.599	1.003	0.001	0.017	0.344	2.999	0.000	0.000	0.006	0.000	0.000	4.969	0.631	0.006	0.363	0.000	0.02
	Line 15 1303_FSP_4d_CS	152	0.598	0.994	0.002	0.016	0.346	3.006	0.000	0.000	0.006	0.000	0.000	4.968	0.629	0.006	0.365	0.000	0.02
	Line 16 1303_FSP_4d_CS	163	0.591	1.002	0.001	0.017	0.344	3.003	0.000	0.000	0.006	0.000	0.000	4.963	0.628	0.007	0.365	0.000	0.02
	Line 17 1303_FSP_4d_CS	174	0.603	1.000	0.000	0.017	0.342	3.001	0.000	0.000	0.006	0.000	0.000	4.971	0.634	0.006	0.360	0.000	0.02
	Line 18 1303_FSP_4d_CS	184	0.584	1.010	0.000	0.016	0.345	2.999	0.000	0.000	0.007	0.000	0.000	4.961	0.624	0.007	0.369	0.000	0.02
	Line 19 1303_FSP_4d_CS	195	0.594	1.005	0.001	0.015	0.344	3.000	0.000	0.000	0.007	0.000	0.000	4.965	0.629	0.007	0.364	0.000	0.02
	Line 20 1303_FSP_4d_CS	206	0.584	1.006	0.001	0.015	0.342	3.002	0.000	0.000	0.007	0.000	0.000	4.957	0.625	0.008	0.367	0.000	0.02
	Line 21 1303_FSP_4d_CS	217	0.604	1.006	0.001	0.014	0.342	2.995	0.001	0.000	0.008	0.000	0.000	4.973	0.633	0.008	0.359	0.000	0.02
	Line 22 1303_FSP_4d_CS	228	0.600	1.006	0.001	0.013	0.342	2.999	0.000	0.000	0.007	0.000	0.000	4.968	0.632	0.008	0.360	0.000	0.02
	Line 23 1303_FSP_4d_CS	238	0.600	1.004	0.002	0.014	0.343	2.998	0.000	0.000	0.008	0.000	0.000	4.969	0.631	0.008	0.361	0.000	0.02
	Line 24 1303_FSP_4d_CS	249	0.598	1.005	0.000	0.016	0.346	2.998	0.001	0.001	0.007	0.000	0.000	4.971	0.629	0.008	0.363	0.000	0.02
	Line 25 1303_FSP_4d_CS	260	0.602	1.009	0.000	0.014	0.346	2.995	0.000	0.000	0.008	0.000	0.000	4.974	0.630	0.008	0.362	0.000	0.02

Table H.12: EMPA data of C-type feldspar inV-254. Data is presented in atoms per formula unit and in fractions of solid solution end member. The end members are: albite (X_{Ab}), anorthite (X_{An}), orthoclase (X_{Or}), and celsian (X_{Cs}). Distances of the line scans are directed from core towards the rim of the crystal.

V-ID	Analyses ID	Distance (μm)	Na	Al	Ti	Fe	K	Si	Mg	Mn	Ca	Sr	Ba	Sum	X_{Ab}	X_{An}	X_{Or}	X_{Cs}	Ca/K
V-254	Line 1 1319_FSP_8_CS	1	0.531	1.059	0.002	0.005	0.442	2.933	0.000	0.000	0.039	0.000	0.011	5.022	0.519	0.038	0.432	0.011	0.09
	Line 2 1319_FSP_8_CS	11	0.516	1.061	0.001	0.004	0.429	2.939	0.000	0.000	0.039	0.000	0.012	5.002	0.517	0.040	0.431	0.012	0.09
	Line 3 1319_FSP_8_CS	22	0.523	1.054	0.001	0.005	0.438	2.942	0.000	0.000	0.037	0.000	0.012	5.011	0.518	0.037	0.434	0.012	0.09
	Line 4 1319_FSP_8_CS	32	0.529	1.065	0.002	0.005	0.417	2.931	0.000	0.000	0.045	0.000	0.012	5.007	0.527	0.045	0.416	0.012	0.11
	Line 5 1319_FSP_8_CS	42	0.538	1.075	0.002	0.005	0.401	2.922	0.001	0.001	0.053	0.000	0.011	5.008	0.537	0.053	0.400	0.011	0.13
	Line 6 1319_FSP_8_CS	53	0.561	1.085	0.001	0.004	0.377	2.914	0.000	0.000	0.059	0.000	0.011	5.012	0.556	0.059	0.374	0.011	0.16
	Line 7 1319_FSP_8_CS	63	0.564	1.089	0.002	0.005	0.345	2.908	0.001	0.000	0.075	0.000	0.011	5.000	0.567	0.075	0.346	0.011	0.22
	Line 8 1319_FSP_8_CS	73	0.595	1.099	0.000	0.005	0.323	2.890	0.002	0.000	0.093	0.000	0.011	5.019	0.582	0.091	0.316	0.011	0.29
	Line 9 1319_FSP_8_CS	83	0.617	1.111	0.001	0.005	0.294	2.880	0.001	0.000	0.098	0.000	0.010	5.018	0.605	0.096	0.289	0.010	0.33
	Line 10 1319_FSP_8_CS	94	0.629	1.107	0.002	0.004	0.274	2.883	0.001	0.000	0.104	0.000	0.008	5.013	0.620	0.102	0.270	0.008	0.38
	Line 11 1319_FSP_8_CS	104	0.632	1.124	0.001	0.005	0.252	2.869	0.001	0.001	0.119	0.000	0.007	5.010	0.626	0.117	0.250	0.007	0.47
	Line 12 1319_FSP_8_CS	114	0.655	1.125	0.001	0.004	0.238	2.863	0.001	0.000	0.124	0.001	0.007	5.019	0.640	0.121	0.232	0.007	0.52
	Line 13 1319_FSP_8_CS	125	0.616	1.097	0.001	0.005	0.298	2.899	0.000	0.000	0.085	0.000	0.009	5.009	0.612	0.084	0.296	0.008	0.28
	Line 14 1319_FSP_8_CS	135	0.618	1.107	0.001	0.004	0.283	2.890	0.000	0.000	0.094	0.000	0.008	5.006	0.616	0.094	0.282	0.008	0.33
	Line 15 1319_FSP_8_CS	145	0.636	1.130	0.000	0.005	0.247	2.867	0.001	0.000	0.116	0.000	0.007	5.009	0.632	0.115	0.245	0.007	0.47
	Line 16 1319_FSP_8_CS	156	0.643	1.115	0.001	0.004	0.238	2.872	0.001	0.000	0.129	0.000	0.006	5.010	0.632	0.127	0.234	0.006	0.54
	Line 17 1319_FSP_8_CS	166	0.646	1.117	0.002	0.006	0.256	2.868	0.002	0.000	0.118	0.000	0.007	5.023	0.629	0.115	0.250	0.007	0.46
	Line 18 1319_FSP_8_CS	176	0.658	1.123	0.000	0.006	0.251	2.863	0.002	0.001	0.121	0.000	0.007	5.030	0.635	0.116	0.242	0.007	0.48
	Line 19 1319_FSP_8_CS	187	0.626	1.135	0.002	0.006	0.242	2.863	0.001	0.000	0.120	0.000	0.007	5.001	0.630	0.120	0.243	0.007	0.50
	Line 20 1319_FSP_8_CS	197	0.658	1.137	0.000	0.005	0.236	2.856	0.001	0.001	0.121	0.000	0.007	5.022	0.644	0.118	0.231	0.007	0.51
	Line 21 1319_FSP_8_CS	207	0.655	1.135	0.000	0.005	0.230	2.860	0.000	0.001	0.121	0.000	0.007	5.015	0.646	0.120	0.227	0.007	0.53
	Line 22 1319_FSP_8_CS	218	0.665	1.141	0.001	0.005	0.221	2.855	0.000	0.000	0.123	0.000	0.006	5.016	0.655	0.122	0.217	0.006	0.56
	Line 23 1319_FSP_8_CS	228	0.655	1.128	0.001	0.004	0.238	2.867	0.000	0.000	0.114	0.000	0.006	5.015	0.646	0.113	0.235	0.006	0.48
	Line 24 1319_FSP_8_CS	238	0.586	1.085	0.001	0.004	0.347	2.913	0.000	0.000	0.066	0.000	0.008	5.010	0.582	0.065	0.344	0.008	0.19
	Line 25 1319_FSP_8_CS	248	0.638	1.106	0.001	0.006	0.284	2.886	0.001	0.000	0.093	0.000	0.007	5.021	0.624	0.091	0.278	0.007	0.33
	Line 26 1319_FSP_8_CS	259	0.661	1.127	0.001	0.004	0.254	2.867	0.001	0.000	0.106	0.000	0.006	5.026	0.644	0.103	0.247	0.006	0.42
	Line 27 1319_FSP_8_CS	269	0.652	1.131	0.001	0.005	0.231	2.865	0.000	0.000	0.118	0.000	0.006	5.010	0.647	0.117	0.230	0.006	0.51
	Line 28 1319_FSP_8_CS	279	0.651	1.131	0.001	0.006	0.241	2.865	0.000	0.000	0.113	0.000	0.007	5.015	0.644	0.111	0.238	0.007	0.47
	Line 29 1319_FSP_8_CS	290	0.642	1.119	0.002	0.005	0.258	2.874	0.000	0.000	0.107	0.000	0.007	5.014	0.633	0.106	0.254	0.007	0.42
	Line 30 1319_FSP_8_CS	300	0.658	1.120	0.001	0.006	0.253	2.873	0.000	0.000	0.104	0.000	0.007	5.021	0.644	0.101	0.247	0.007	0.41
	Line 31 1319_FSP_8_CS	310	0.649	1.128	0.000	0.005	0.239	2.870	0.001	0.000	0.110	0.000	0.006	5.009	0.645	0.110	0.238	0.006	0.46
	Line 32 1319_FSP_8_CS	321	0.644	1.121	0.000	0.006	0.240	2.878	0.001	0.000	0.108	0.000	0.006	5.003	0.646	0.108	0.241	0.006	0.45
	Line 33 1319_FSP_8_CS	331	0.647	1.105	0.001	0.006	0.261	2.889	0.001	0.001	0.096	0.000	0.006	5.011	0.641	0.095	0.259	0.006	0.37
	Line 34 1319_FSP_8_CS	341	0.637	1.111	0.001	0.007	0.267	2.886	0.000	0.000	0.094	0.000	0.007	5.010	0.634	0.093	0.266	0.006	0.35
	Line 35 1319_FSP_8_CS	352	0.638	1.108	0.001	0.005	0.286	2.887	0.000	0.000	0.089	0.000	0.006	5.020	0.626	0.087	0.281	0.006	0.31
	Line 36 1319_FSP_8_CS	362	0.619	1.096	0.001	0.006	0.310	2.898	0.000	0.000	0.081	0.000	0.006	5.017	0.610	0.080	0.305	0.006	0.26
	Line 37 1319_FSP_8_CS	372	0.567	1.084	0.002	0.005	0.364	2.916	0.000	0.000	0.061	0.000	0.007	5.006	0.568	0.061	0.364	0.007	0.17
	Line 38 1319_FSP_8_CS	382	0.608	1.083	0.001	0.006	0.343	2.910	0.001	0.001	0.063	0.000	0.007	5.023	0.595	0.062	0.336	0.007	0.18
	Line 39 1319_FSP_8_CS	393	0.584	1.078	0.001	0.005	0.343	2.921	0.001	0.000	0.064	0.000	0.007	5.003	0.586	0.064	0.344	0.007	0.19
	Line 40 1319_FSP_8_CS	403	0.575	1.072	0.001	0.006	0.364	2.925	0.001	0.000	0.057	0.000	0.007	5.007	0.573	0.056	0.363	0.007	0.16

Table H.13: EMPA data of C-type feldspar inV-254. Data is presented in atoms per formula unit and in fractions of solid solution end member. The end members are: albite (X_{Ab}), anorthite (X_{An}), orthoclase (X_{Or}), and celsian (X_{Cs}). Distances of the line scans are directed from core towards the rim of the crystal.

V-ID	Analyses ID	Distance (μm)	Na	Al	Ti	Fe	K	Si	Mg	Mn	Ca	Sr	Ba	Sum	X_{Ab}	X_{An}	X_{Or}	X_{Cs}	Ca/K
V-254	Line 1 1319_FSP_5_CS	1	0.681	1.164	0.001	0.007	0.177	2.829	0.000	0.000	0.149	0.000	0.009	5.017	0.670	0.146	0.174	0.009	0.84
	Line 2 1319_FSP_5_CS	5	0.663	1.163	0.001	0.005	0.180	2.837	0.000	0.000	0.146	0.000	0.008	5.002	0.665	0.146	0.181	0.008	0.81
	Line 3 1319_FSP_5_CS	8	0.670	1.165	0.000	0.004	0.185	2.832	0.000	0.000	0.147	0.000	0.009	5.012	0.663	0.146	0.183	0.009	0.80
	Line 4 1319_FSP_5_CS	12	0.680	1.159	0.002	0.005	0.183	2.833	0.000	0.001	0.147	0.000	0.009	5.018	0.667	0.144	0.180	0.009	0.80
	Line 5 1319_FSP_5_CS	15	0.678	1.156	0.001	0.006	0.185	2.836	0.000	0.000	0.145	0.000	0.009	5.016	0.666	0.143	0.182	0.009	0.79
	Line 6 1319_FSP_5_CS	19	0.666	1.162	0.001	0.006	0.187	2.834	0.000	0.000	0.145	0.000	0.010	5.011	0.661	0.144	0.186	0.010	0.77
	Line 7 1319_FSP_5_CS	22	0.652	1.160	0.001	0.005	0.191	2.833	0.002	0.000	0.153	0.001	0.010	5.007	0.649	0.152	0.190	0.009	0.80
	Line 8 1319_FSP_5_CS	26	0.666	1.166	0.001	0.005	0.188	2.832	0.000	0.000	0.144	0.000	0.009	5.011	0.661	0.143	0.187	0.009	0.77
	Line 9 1319_FSP_5_CS	29	0.673	1.157	0.003	0.006	0.186	2.836	0.000	0.001	0.144	0.000	0.009	5.013	0.665	0.142	0.184	0.009	0.77
	Line 10 1319_FSP_5_CS	33	0.673	1.156	0.001	0.005	0.185	2.838	0.000	0.000	0.143	0.000	0.010	5.012	0.665	0.142	0.183	0.010	0.77
	Line 11 1319_FSP_5_CS	36	0.673	1.151	0.001	0.006	0.183	2.841	0.000	0.000	0.144	0.001	0.010	5.010	0.667	0.143	0.181	0.010	0.79
	Line 12 1319_FSP_5_CS	40	0.678	1.155	0.002	0.005	0.183	2.837	0.000	0.000	0.145	0.000	0.009	5.014	0.668	0.143	0.180	0.009	0.79
	Line 13 1319_FSP_5_CS	43	0.668	1.160	0.001	0.005	0.184	2.839	0.000	0.000	0.139	0.000	0.009	5.006	0.668	0.139	0.184	0.009	0.75
	Line 14 1319_FSP_5_CS	47	0.659	1.127	0.002	0.005	0.233	2.866	0.000	0.001	0.114	0.000	0.009	5.015	0.650	0.112	0.229	0.009	0.49
	Line 15 1319_FSP_5_CS	50	0.624	1.109	0.000	0.005	0.280	2.889	0.000	0.000	0.090	0.001	0.011	5.009	0.620	0.090	0.278	0.011	0.32
	Line 16 1319_FSP_5_CS	54	0.590	1.088	0.001	0.006	0.332	2.908	0.000	0.001	0.071	0.000	0.012	5.008	0.587	0.070	0.330	0.012	0.21
	Line 17 1319_FSP_5_CS	57	0.563	1.079	0.001	0.004	0.366	2.919	0.000	0.000	0.060	0.000	0.014	5.005	0.561	0.060	0.365	0.014	0.16
	Line 18 1319_FSP_5_CS	61	0.558	1.077	0.001	0.005	0.382	2.920	0.000	0.000	0.055	0.000	0.014	5.011	0.553	0.055	0.378	0.014	0.14
	Line 19 1319_FSP_5_CS	64	0.565	1.077	0.001	0.005	0.376	2.918	0.001	0.000	0.056	0.000	0.014	5.013	0.559	0.056	0.371	0.014	0.15
	Line 20 1319_FSP_5_CS	68	0.573	1.082	0.000	0.005	0.370	2.913	0.000	0.001	0.059	0.000	0.014	5.017	0.564	0.058	0.364	0.013	0.16
	Line 21 1319_FSP_5_CS	71	0.544	1.075	0.000	0.004	0.380	2.926	0.000	0.000	0.055	0.000	0.014	4.998	0.547	0.055	0.383	0.014	0.14
	Line 22 1319_FSP_5_CS	75	0.555	1.077	0.002	0.004	0.373	2.920	0.001	0.000	0.058	0.000	0.014	5.003	0.555	0.058	0.373	0.014	0.16
	Line 23 1319_FSP_5_CS	78	0.545	1.072	0.002	0.004	0.386	2.925	0.000	0.000	0.054	0.000	0.015	5.003	0.545	0.054	0.386	0.015	0.14
	Line 24 1319_FSP_5_CS	82	0.550	1.082	0.001	0.004	0.375	2.918	0.000	0.000	0.058	0.000	0.015	5.003	0.552	0.058	0.375	0.015	0.16
	Line 25 1319_FSP_5_CS	85	0.568	1.087	0.000	0.005	0.364	2.911	0.000	0.000	0.062	0.000	0.014	5.012	0.564	0.061	0.361	0.014	0.17
	Line 26 1319_FSP_5_CS	89	0.577	1.091	0.000	0.004	0.365	2.906	0.000	0.000	0.062	0.000	0.013	5.019	0.567	0.061	0.359	0.013	0.17
	Line 27 1319_FSP_5_CS	93	0.560	1.069	0.001	0.004	0.392	2.926	0.000	0.000	0.051	0.000	0.012	5.015	0.552	0.050	0.386	0.012	0.13
	Line 28 1319_FSP_5_CS	96	0.545	1.060	0.002	0.004	0.400	2.935	0.000	0.000	0.048	0.000	0.010	5.005	0.543	0.047	0.399	0.010	0.12
	Line 29 1319_FSP_5_CS	100	0.527	1.069	0.001	0.005	0.412	2.934	0.000	0.001	0.043	0.000	0.009	5.001	0.532	0.044	0.416	0.009	0.10
	Line 30 1319_FSP_5_CS	103	0.544	1.063	0.000	0.004	0.399	2.937	0.000	0.000	0.049	0.000	0.008	5.003	0.545	0.049	0.399	0.008	0.12
	Line 31 1319_FSP_5_CS	107	0.549	1.056	0.001	0.004	0.402	2.941	0.000	0.000	0.044	0.000	0.006	5.005	0.548	0.044	0.401	0.006	0.11
	Line 32 1319_FSP_5_CS	110	0.544	1.051	0.001	0.006	0.410	2.945	0.000	0.001	0.041	0.000	0.006	5.005	0.543	0.041	0.410	0.006	0.10
	Line 33 1319_FSP_5_CS	114	0.553	1.047	0.001	0.004	0.416	2.946	0.000	0.000	0.040	0.000	0.006	5.013	0.545	0.039	0.410	0.006	0.10
	Line 34 1319_FSP_5_CS	117	0.545	1.058	0.001	0.005	0.417	2.939	0.000	0.000	0.042	0.000	0.006	5.012	0.540	0.041	0.413	0.006	0.10
	Line 35 1319_FSP_5_CS	121	0.556	1.061	0.001	0.006	0.405	2.935	0.001	0.000	0.044	0.000	0.006	5.014	0.550	0.044	0.401	0.006	0.11
	Line 36 1319_FSP_5_CS	124	0.562	1.063	0.000	0.003	0.408	2.933	0.000	0.000	0.046	0.000	0.006	5.020	0.550	0.045	0.399	0.006	0.11
	Line 37 1319_FSP_5_CS	128	0.544	1.053	0.000	0.005	0.408	2.945	0.000	0.000	0.044	0.000	0.006	5.005	0.543	0.044	0.407	0.006	0.11
	Line 38 1319_FSP_5_CS	131	0.545	1.060	0.000	0.004	0.408	2.939	0.001	0.000	0.044	0.000	0.006	5.008	0.544	0.044	0.407	0.006	0.11
	Line 39 1319_FSP_5_CS	135	0.551	1.060	0.002	0.004	0.406	2.937	0.000	0.000	0.043	0.000	0.005	5.010	0.548	0.043	0.404	0.005	0.11
	Line 40 1319_FSP_5_CS	138	0.551	1.062	0.002	0.005	0.402	2.935	0.000	0.000	0.046	0.000	0.006	5.009	0.548	0.046	0.400	0.005	0.11

Table H.14: EMPA data of C-type feldspar inV-221a. Data is presented in atoms per formula unit and in fractions of solid solution end member. The end members are: albite (X_{Ab}), anorthite (X_{An}), orthoclase (X_{Or}), and celsian (X_{Cs}). Distances of the line scans are directed from core towards the rim of the crystal.

V-ID	Analyses ID	Distance (μm)	Na	Al	Ti	Fe	K	Si	Mg	Mn	Ca	Sr	Ba	Sum	X_{Ab}	X_{An}	X_{Or}	X_{Cs}	Ca/K
V-221a	Line 1 1316_FSP_10_SCAN_1_VC	96	0.633	1.154	0.001	0.008	0.213	2.847	0.000	0.000	0.132	0.000	0.011	4.999	0.640	0.133	0.216	0.011	0.62
	Line 2 1316_FSP_10_SCAN_1_VC	92	0.644	1.117	0.001	0.006	0.213	2.874	0.000	0.000	0.130	0.001	0.010	4.995	0.646	0.130	0.213	0.010	0.61
	Line 3 1316_FSP_10_SCAN_1_VC	88	0.651	1.134	0.001	0.008	0.223	2.861	0.000	0.000	0.121	0.000	0.010	5.008	0.648	0.120	0.222	0.010	0.54
	Line 4 1316_FSP_10_SCAN_1_VC	84	0.636	1.137	0.001	0.007	0.220	2.862	0.001	0.000	0.123	0.000	0.009	4.996	0.644	0.125	0.223	0.009	0.56
	Line 5 1316_FSP_10_SCAN_1_VC	80	0.642	1.130	0.001	0.007	0.221	2.865	0.000	0.000	0.123	0.001	0.010	5.001	0.644	0.124	0.222	0.010	0.56
	Line 6 1316_FSP_10_SCAN_1_VC	76	0.614	1.135	0.001	0.006	0.225	2.868	0.000	0.000	0.124	0.000	0.009	4.983	0.631	0.128	0.232	0.010	0.55
	Line 7 1316_FSP_10_SCAN_1_VC	72	0.647	1.153	0.002	0.006	0.226	2.844	0.000	0.000	0.125	0.000	0.011	5.014	0.641	0.124	0.224	0.011	0.55
	Line 8 1316_FSP_10_SCAN_1_VC	68	0.631	1.135	0.000	0.007	0.223	2.864	0.000	0.000	0.123	0.002	0.009	4.996	0.640	0.125	0.226	0.009	0.55
	Line 9 1316_FSP_10_SCAN_1_VC	64	0.640	1.138	0.001	0.008	0.232	2.858	0.000	0.000	0.121	0.000	0.010	5.008	0.638	0.121	0.231	0.010	0.52
	Line 10 1316_FSP_10_SCAN_1_VC	60	0.623	1.130	0.001	0.008	0.229	2.870	0.000	0.000	0.119	0.000	0.010	4.990	0.635	0.121	0.233	0.010	0.52
	Line 11 1316_FSP_10_SCAN_1_VC	56	0.659	1.142	0.000	0.007	0.228	2.851	0.001	0.000	0.120	0.002	0.010	5.021	0.648	0.118	0.224	0.010	0.53
	Line 12 1316_FSP_10_SCAN_1_VC	52	0.652	1.136	0.002	0.006	0.230	2.858	0.000	0.000	0.120	0.000	0.009	5.013	0.645	0.118	0.227	0.009	0.52
	Line 13 1316_FSP_10_SCAN_1_VC	48	0.572	1.087	0.001	0.007	0.360	2.911	0.000	0.001	0.059	0.000	0.013	5.010	0.570	0.059	0.358	0.012	0.17
	Line 14 1316_FSP_10_SCAN_1_VC	44	0.558	1.080	0.002	0.006	0.385	2.917	0.001	0.000	0.051	0.000	0.013	5.012	0.554	0.051	0.382	0.013	0.13
	Line 15 1316_FSP_10_SCAN_1_VC	40	0.557	1.069	0.001	0.007	0.394	2.924	0.000	0.000	0.050	0.000	0.014	5.016	0.549	0.049	0.388	0.014	0.13
	Line 16 1316_FSP_10_SCAN_1_VC	36	0.542	1.072	0.001	0.006	0.407	2.922	0.001	0.000	0.049	0.000	0.014	5.014	0.535	0.048	0.402	0.014	0.12
	Line 17 1316_FSP_10_SCAN_1_VC	32	0.560	1.086	0.001	0.006	0.395	2.910	0.000	0.000	0.052	0.000	0.014	5.024	0.548	0.051	0.387	0.014	0.13
V-221a	Line 1 1316_FSP_1_CS	1	0.650	1.116	0.001	0.007	0.238	2.879	0.000	0.000	0.108	0.000	0.006	5.005	0.649	0.107	0.237	0.006	0.45
	Line 2 1316_FSP_1_CS	29	0.635	1.119	0.000	0.006	0.234	2.880	0.000	0.001	0.113	0.000	0.006	4.994	0.643	0.114	0.237	0.006	0.48
	Line 3 1316_FSP_1_CS	57	0.655	1.112	0.002	0.007	0.235	2.882	0.000	0.000	0.107	0.000	0.005	5.005	0.654	0.107	0.234	0.005	0.46
	Line 4 1316_FSP_1_CS	85	0.640	1.100	0.000	0.006	0.256	2.896	0.001	0.000	0.097	0.000	0.006	5.002	0.641	0.097	0.256	0.006	0.38
	Line 5 1316_FSP_1_CS	113	0.645	1.093	0.002	0.007	0.265	2.900	0.000	0.000	0.089	0.000	0.006	5.007	0.641	0.089	0.264	0.006	0.34
	Line 6 1316_FSP_1_CS	141	0.632	1.109	0.001	0.006	0.253	2.890	0.000	0.000	0.099	0.000	0.007	4.997	0.638	0.100	0.255	0.007	0.39
	Line 7 1316_FSP_1_CS	169	0.629	1.102	0.001	0.007	0.265	2.895	0.000	0.000	0.094	0.000	0.006	5.000	0.633	0.094	0.266	0.006	0.35
	Line 8 1316_FSP_1_CS	197	0.595	1.071	0.001	0.005	0.327	2.926	0.000	0.000	0.065	0.000	0.007	4.998	0.598	0.066	0.329	0.007	0.20
	Line 9 1316_FSP_1_CS	224	0.547	1.052	0.001	0.006	0.392	2.944	0.000	0.000	0.047	0.000	0.008	4.998	0.550	0.047	0.394	0.008	0.12
	Line 10 1316_FSP_1_CS	252	0.557	1.064	0.001	0.006	0.363	2.937	0.000	0.000	0.055	0.001	0.007	4.991	0.567	0.056	0.369	0.007	0.15
	Line 11 1316_FSP_1_CS	280	0.638	1.091	0.001	0.006	0.282	2.900	0.001	0.000	0.089	0.000	0.006	5.013	0.629	0.087	0.278	0.006	0.31
	Line 12 1316_FSP_1_CS	308	0.546	1.054	0.002	0.006	0.377	2.946	0.000	0.000	0.051	0.000	0.006	4.987	0.557	0.052	0.385	0.007	0.13
	Line 13 1316_FSP_1_CS	336	0.570	1.048	0.001	0.005	0.380	2.945	0.001	0.000	0.049	0.000	0.006	5.005	0.567	0.049	0.378	0.006	0.13
	Line 14 1316_FSP_1_CS	364	0.518	1.039	0.001	0.005	0.415	2.961	0.000	0.000	0.040	0.000	0.006	4.986	0.529	0.041	0.424	0.006	0.10
	Line 15 1316_FSP_1_CS	392	0.534	1.047	0.001	0.005	0.417	2.952	0.000	0.000	0.038	0.000	0.005	4.999	0.537	0.038	0.419	0.006	0.09
	Line 16 1316_FSP_1_CS	420	0.532	1.041	0.001	0.005	0.409	2.958	0.000	0.000	0.040	0.000	0.005	4.992	0.540	0.040	0.415	0.005	0.10
	Line 17 1316_FSP_1_CS	448	0.534	1.034	0.001	0.004	0.415	2.962	0.001	0.000	0.037	0.000	0.005	4.994	0.539	0.037	0.418	0.005	0.09
	Line 18 1316_FSP_1_CS	476	0.319	0.821	0.011	0.112	0.321	3.126	0.008	0.005	0.047	0.000	0.001	4.772	0.463	0.069	0.466	0.002	0.15
	Line 19 1316_FSP_1_CS	504	0.607	1.083	0.001	0.006	0.303	2.915	0.000	0.000	0.078	0.000	0.005	4.998	0.611	0.078	0.305	0.005	0.26
	Line 20 1316_FSP_1_CS	532	0.558	1.053	0.001	0.005	0.389	2.944	0.000	0.001	0.045	0.000	0.006	5.002	0.559	0.045	0.390	0.006	0.12
	Line 21 1316_FSP_1_CS	560	0.560	1.058	0.001	0.006	0.380	2.940	0.001	0.001	0.049	0.000	0.005	5.000	0.563	0.050	0.382	0.006	0.13
	Line 22 1316_FSP_1_CS	588	0.552	1.047	0.002	0.005	0.402	2.948	0.000	0.000	0.041	0.000	0.006	5.003	0.552	0.041	0.401	0.006	0.10
	Line 23 1316_FSP_1_CS	615	0.533	1.044	0.001	0.005	0.415	2.954	0.000	0.000	0.039	0.000	0.005	4.996	0.537	0.039	0.418	0.005	0.09
	Line 24 1316_FSP_1_CS	643	0.554	1.047	0.000	0.006	0.388	2.950	0.000	0.000	0.047	0.000	0.005	4.998	0.557	0.048	0.390	0.005	0.12
	Line 25 1316_FSP_1_CS	671	0.546	1.048	0.001	0.006	0.406	2.947	0.000	0.000	0.043	0.000	0.005	5.003	0.546	0.043	0.406	0.005	0.11
	Line 26 1316_FSP_1_CS	699	0.533	1.047	0.000	0.005	0.419	2.953	0.000	0.000	0.037	0.000	0.005	4.999	0.536	0.037	0.422	0.005	0.09
	Line 27 1316_FSP_1_CS	727	0.556	1.058	0.001	0.005	0.384	2.941	0.000	0.000	0.048	0.000	0.005	4.999	0.560	0.048	0.387	0.005	0.12
	Line 28 1316_FSP_1_CS	755	0.547	1.051	0.001	0.005	0.399	2.945	0.001	0.000	0.048	0.000	0.004	5.001	0.548	0.048	0.400	0.004	0.12
	Line 29 1316_FSP_1_CS	783	0.546	1.051	0.001	0.004	0.420	2.945	0.000	0.000	0.040	0.000	0.004	5.012	0.540	0.040	0.416	0.004	0.10
	Line 30 1316_FSP_1_CS	811	0.512	1.037	0.002	0.006	0.432	2.961	0.000	0.001	0.035	0.000	0.004	4.991	0.520	0.036	0.439	0.004	0.08

Table H.15: EMPA data of C-type feldspar inV-221a. Data is presented in atoms per formula unit and in fractions of solid solution end member. The end members are: albite (X_{Ab}), anorthite (X_{An}), orthoclase (X_{Or}), and celsian (X_{Cs}). Distances of the line scans are directed from core towards the rim of the crystal.

V-ID	Analyses ID	Distance (μm)	Na	Al	Ti	Fe	K	Si	Mg	Mn	Ca	Sr	Ba	Sum	X_{Ab}	X_{An}	X_{Or}	X_{Cs}	Ca/K
V-221a	Line 1 1316_FSP_4_CS	1	0.554	1.047	0.000	0.005	0.411	2.950	0.000	0.001	0.037	0.000	0.004	5.009	0.551	0.037	0.408	0.004	0.09
	Line 2 1316_FSP_4_CS	39	0.536	1.053	0.001	0.004	0.397	2.951	0.000	0.000	0.043	0.000	0.004	4.989	0.547	0.044	0.405	0.004	0.11
	Line 3 1316_FSP_4_CS	77	0.577	1.054	0.000	0.005	0.380	2.942	0.000	0.000	0.047	0.000	0.004	5.009	0.572	0.046	0.377	0.004	0.12
	Line 4 1316_FSP_4_CS	116	0.577	1.066	0.000	0.006	0.349	2.932	0.000	0.000	0.063	0.000	0.005	4.998	0.580	0.063	0.351	0.005	0.18
	Line 5 1316_FSP_4_CS	154	0.550	1.058	0.001	0.006	0.367	2.947	0.000	0.001	0.048	0.000	0.005	4.983	0.566	0.050	0.378	0.005	0.13
	Line 6 1316_FSP_4_CS	192	0.641	1.098	0.000	0.006	0.272	2.897	0.001	0.001	0.090	0.000	0.005	5.010	0.636	0.089	0.270	0.005	0.33
	Line 7 1316_FSP_4_CS	230	0.651	1.105	0.001	0.005	0.247	2.890	0.000	0.000	0.101	0.000	0.005	5.005	0.649	0.101	0.246	0.005	0.41
	Line 8 1316_FSP_4_CS	268	0.656	1.114	0.001	0.006	0.235	2.882	0.001	0.000	0.106	0.000	0.005	5.006	0.655	0.106	0.235	0.005	0.45
	Line 9 1316_FSP_4_CS	307	0.654	1.117	0.001	0.007	0.240	2.879	0.000	0.001	0.105	0.002	0.005	5.009	0.651	0.104	0.239	0.005	0.44
	Line 10 1316_FSP_4_CS	345	0.656	1.106	0.001	0.006	0.246	2.887	0.000	0.000	0.104	0.000	0.005	5.010	0.649	0.103	0.243	0.005	0.42
	Line 11 1316_FSP_4_CS	383	0.629	1.097	0.002	0.006	0.266	2.899	0.001	0.000	0.094	0.000	0.006	4.999	0.632	0.094	0.267	0.006	0.35
	Line 12 1316_FSP_4_CS	421	0.612	1.083	0.001	0.007	0.298	2.912	0.001	0.000	0.080	0.000	0.006	5.000	0.615	0.080	0.299	0.006	0.27
	Line 13 1316_FSP_4_CS	460	0.611	1.083	0.001	0.006	0.305	2.912	0.001	0.002	0.077	0.000	0.007	5.004	0.611	0.078	0.305	0.007	0.25
	Line 14 1316_FSP_4_CS	498	0.597	1.079	0.001	0.005	0.323	2.919	0.001	0.000	0.070	0.000	0.006	5.001	0.600	0.070	0.324	0.006	0.22
	Line 15 1316_FSP_4_CS	536	0.667	1.121	0.000	0.007	0.220	2.873	0.000	0.001	0.116	0.000	0.005	5.010	0.662	0.115	0.218	0.005	0.53
	Line 16 1316_FSP_4_CS	574	0.653	1.131	0.001	0.005	0.210	2.873	0.000	0.000	0.115	0.000	0.004	4.992	0.665	0.117	0.214	0.004	0.55
	Line 17 1316_FSP_4_CS	612	0.671	1.134	0.001	0.006	0.200	2.861	0.000	0.000	0.129	0.000	0.005	5.006	0.668	0.128	0.199	0.005	0.64
	Line 18 1316_FSP_4_CS	651	0.665	1.133	0.002	0.007	0.203	2.861	0.001	0.000	0.127	0.000	0.005	5.005	0.665	0.127	0.203	0.005	0.63
	Line 19 1316_FSP_4_CS	689	0.669	1.130	0.001	0.007	0.210	2.863	0.000	0.001	0.123	0.000	0.005	5.010	0.664	0.123	0.209	0.005	0.59
	Line 20 1316_FSP_4_CS	727	0.655	1.133	0.002	0.005	0.216	2.865	0.000	0.000	0.121	0.000	0.006	5.002	0.656	0.121	0.217	0.006	0.56
	Line 21 1316_FSP_4_CS	765	0.654	1.122	0.002	0.006	0.235	2.872	0.000	0.000	0.112	0.000	0.005	5.009	0.650	0.112	0.233	0.005	0.48
	Line 22 1316_FSP_4_CS	803	0.639	1.115	0.001	0.006	0.243	2.883	0.000	0.000	0.107	0.000	0.006	5.000	0.642	0.107	0.245	0.006	0.44
	Line 23 1316_FSP_4_CS	842	0.682	1.133	0.001	0.007	0.189	2.859	0.001	0.000	0.133	0.000	0.005	5.010	0.676	0.132	0.188	0.005	0.70
	Line 24 1316_FSP_4_CS	880	0.676	1.146	0.002	0.007	0.187	2.848	0.000	0.000	0.139	0.000	0.005	5.009	0.672	0.138	0.185	0.005	0.75
	Line 25 1316_FSP_4_CS	918	0.664	1.151	0.002	0.006	0.185	2.845	0.000	0.000	0.143	0.000	0.006	5.002	0.666	0.144	0.185	0.006	0.77
	Line 26 1316_FSP_4_CS	956	0.661	1.140	0.002	0.006	0.194	2.855	0.000	0.000	0.138	0.000	0.005	5.001	0.663	0.138	0.194	0.005	0.71
	Line 27 1316_FSP_4_CS	994	0.637	1.158	0.002	0.006	0.198	2.848	0.000	0.000	0.133	0.000	0.006	4.988	0.654	0.136	0.204	0.006	0.67
	Line 28 1316_FSP_4_CS	1033	0.660	1.140	0.002	0.007	0.200	2.855	0.000	0.001	0.133	0.000	0.006	5.003	0.661	0.133	0.201	0.006	0.66
	Line 29 1316_FSP_4_CS	1071	0.654	1.143	0.001	0.008	0.197	2.853	0.000	0.000	0.139	0.000	0.006	5.000	0.657	0.140	0.198	0.006	0.71
	Line 30 1316_FSP_4_CS	1109	0.653	1.135	0.001	0.008	0.203	2.865	0.000	0.000	0.124	0.000	0.006	4.995	0.662	0.126	0.206	0.006	0.61
	Line 31 1316_FSP_4_CS	1147	0.663	1.139	0.002	0.006	0.207	2.857	0.000	0.001	0.127	0.000	0.006	5.007	0.661	0.127	0.206	0.006	0.61
	Line 32 1316_FSP_4_CS	1186	0.663	1.142	0.001	0.006	0.201	2.856	0.000	0.000	0.130	0.000	0.006	5.005	0.664	0.130	0.201	0.006	0.65
	Line 33 1316_FSP_4_CS	1224	0.670	1.135	0.001	0.006	0.205	2.861	0.001	0.000	0.124	0.000	0.005	5.008	0.667	0.123	0.204	0.005	0.60
	Line 34 1316_FSP_4_CS	1262	0.645	1.136	0.001	0.006	0.216	2.866	0.000	0.000	0.120	0.000	0.006	4.996	0.653	0.122	0.219	0.006	0.56
	Line 35 1316_FSP_4_CS	1300	0.666	1.124	0.002	0.007	0.212	2.869	0.000	0.000	0.120	0.000	0.006	5.006	0.663	0.120	0.211	0.006	0.57
	Line 36 1316_FSP_4_CS	1338	0.664	1.130	0.002	0.007	0.205	2.864	0.000	0.001	0.125	0.003	0.005	5.004	0.665	0.125	0.205	0.005	0.61
	Line 37 1316_FSP_4_CS	1377	0.656	1.119	0.001	0.006	0.234	2.874	0.001	0.000	0.112	0.002	0.007	5.010	0.650	0.111	0.232	0.006	0.48
	Line 38 1316_FSP_4_CS	1415	0.659	1.120	0.001	0.004	0.225	2.876	0.000	0.001	0.112	0.000	0.006	5.005	0.658	0.112	0.225	0.006	0.50
	Line 39 1316_FSP_4_CS	1453	0.624	1.113	0.002	0.006	0.255	2.885	0.000	0.001	0.102	0.000	0.007	4.995	0.632	0.103	0.258	0.007	0.40
	Line 40 1316_FSP_4_CS	1491	0.653	1.114	0.002	0.007	0.236	2.878	0.000	0.000	0.109	0.000	0.007	5.007	0.650	0.108	0.235	0.007	0.46
	Line 41 1316_FSP_4_CS	1529	0.644	1.102	0.002	0.007	0.270	2.891	0.000	0.001	0.090	0.000	0.007	5.013	0.637	0.089	0.267	0.007	0.33
	Line 42 1316_FSP_4_CS	1568	0.639	1.104	0.001	0.006	0.246	2.891	0.000	0.000	0.105	0.000	0.007	4.999	0.641	0.105	0.247	0.007	0.42
	Line 43 1316_FSP_4_CS	1606	0.666	1.122	0.001	0.007	0.213	2.874	0.000	0.000	0.116	0.000	0.005	5.004	0.666	0.116	0.213	0.005	0.54
	Line 44 1316_FSP_4_CS	1644	0.641	1.114	0.001	0.006	0.245	2.884	0.000	0.000	0.103	0.000	0.005	5.001	0.644	0.104	0.247	0.005	0.42
	Line 45 1316_FSP_4_CS	1682	0.639	1.107	0.002	0.008	0.236	2.887	0.001	0.001	0.108	0.002	0.005	4.995	0.647	0.109	0.239	0.005	0.46
	Line 46 1316_FSP_4_CS	1720	0.638	1.108	0.001	0.007	0.253	2.888	0.000	0.000	0.099	0.000	0.006	5.002	0.641	0.099	0.255	0.006	0.39
	Line 47 1316_FSP_4_CS	1759	0.671	1.122	0.002	0.006	0.231	2.871	0.000	0.001	0.109	0.000	0.006	5.017	0.660	0.107	0.227	0.006	0.47
	Line 48 1316_FSP_4_CS	1797	0.650	1.110	0.001	0.007	0.237	2.886	0.001	0.000	0.103	0.001	0.006	5.002	0.653	0.104	0.238	0.006	0.44
	Line 49 1316_FSP_4_CS	1835	0.641	1.108	0.001	0.005	0.259	2.886	0.001	0.001	0.099	0.000	0.007	5.008	0.637	0.099	0.257	0.007	0.38
	Line 50 1316_FSP_4_CS	1873	0.655	1.112	0.001	0.006	0.237	2.882	0.000	0.000	0.108	0.000	0.006	5.007	0.651	0.107	0.235	0.006	0.46
	Line 51 1316_FSP_4_CS	1912	0.644	1.125	0.002	0.006	0.222	2.873	0.000	0.001	0.116	0.000	0.006	4.996	0.651	0.118	0.224	0.006	0.52
	Line 52 1316_FSP_4_CS	1950	0.646	1.130	0.000	0.008	0.212	2.870	0.000	0.000	0.122	0.000	0.006	4.994	0.655	0.124	0.215	0.006	0.57
	Line 53 1316_FSP_4_CS	1988	0.653	1.122	0.001	0.007	0.215	2.871	0.001	0.000	0.122	0.001	0.007	5.001	0.655	0.122	0.216	0.007	0.57
	Line 54 1316_FSP_4_CS	2026	0.649	1.114	0.002	0.006	0.231	2.882	0.000	0.000	0.108	0.000	0.006	4.999	0.653	0.109	0.232	0.006	0.47
	Line 55 1316_FSP_4_CS	2064	0.589	1.058	0.001	0.007	0.350	2.934	0.000	0.000	0.058	0.000	0.008	5.005	0.586	0.058	0.348	0.008	0.17
	Line 56 1316_FSP_4_CS	2103	0.572	1.070	0.002	0.005	0.345	2.930	0.000	0.000	0.063	0.000	0.006	4.992	0.581	0.064	0.350	0.006	0.18
	Line 57 1316_FSP_4_CS	2141	0.520	1.033	0.001	0.005	0.429	2.965	0.000	0.000	0.034	0.000	0.005	4.992	0.526	0.034	0.434	0.005	0.08
	Line 58 1316_FSP_4_CS	2179	0.547	1.050	0.001	0.005	0.398	2.946	0.001	0.000	0.047	0.000	0.004	5.000	0.549	0.047	0.399	0.005	0.12
	Line 59 1316_FSP_4_CS	2217	0.523	1.035	0.001	0.004	0.431	2.963	0.000	0.000	0.035	0.000	0.004	4.996	0.527	0.035	0.434	0.004	0.08
	Line 60 1316_FSP_4_CS	2255	0.513	1.021	0.000	0.006	0.434	2.977	0.000	0.000	0.031	0.000	0.003	4.985	0.523	0.032	0.442	0.003	0.07

Table H.16: EMPA data of C-type feldspar inV-221a. Data is presented in atoms per formula unit and in fractions of solid solution end member. The end members are: albite (X_{Ab}), anorthite (X_{An}), orthoclase (X_{Or}), and celsian (X_{Cs}). Distances of the line scans are directed from core towards the rim of the crystal.

V-ID	Analyses ID	Distance (μm)	Na	Al	Ti	Fe	K	Si	Mg	Mn	Ca	Sr	Ba	Sum	X_{Ab}	X_{An}	X_{Or}	X_{Cs}	Ca/K
V-221a	Line 1 1316_FSP_1_CS	1	0.650	1.116	0.001	0.007	0.238	2.879	0.000	0.000	0.108	0.000	0.006	5.005	0.649	0.107	0.237	0.006	0.45
	Line 2 1316_FSP_1_CS	29	0.635	1.119	0.000	0.006	0.234	2.880	0.000	0.001	0.113	0.000	0.006	4.994	0.643	0.114	0.237	0.006	0.48
	Line 3 1316_FSP_1_CS	57	0.655	1.112	0.002	0.007	0.235	2.882	0.000	0.000	0.107	0.000	0.005	5.005	0.654	0.107	0.234	0.005	0.46
	Line 4 1316_FSP_1_CS	85	0.640	1.100	0.000	0.006	0.256	2.896	0.001	0.000	0.097	0.000	0.006	5.002	0.641	0.097	0.256	0.006	0.38
	Line 5 1316_FSP_1_CS	113	0.645	1.093	0.002	0.007	0.265	2.900	0.000	0.000	0.089	0.000	0.006	5.007	0.641	0.089	0.264	0.006	0.34
	Line 6 1316_FSP_1_CS	141	0.632	1.109	0.001	0.006	0.253	2.890	0.000	0.000	0.099	0.000	0.007	4.997	0.638	0.100	0.255	0.007	0.39
	Line 7 1316_FSP_1_CS	169	0.629	1.102	0.001	0.007	0.265	2.895	0.000	0.000	0.094	0.000	0.006	5.000	0.633	0.094	0.266	0.006	0.35
	Line 8 1316_FSP_1_CS	197	0.595	1.071	0.001	0.005	0.327	2.926	0.000	0.000	0.065	0.000	0.007	4.998	0.598	0.066	0.329	0.007	0.20
	Line 9 1316_FSP_1_CS	224	0.547	1.052	0.001	0.006	0.392	2.944	0.000	0.000	0.047	0.000	0.008	4.998	0.550	0.047	0.394	0.008	0.12
	Line 10 1316_FSP_1_CS	252	0.557	1.064	0.001	0.006	0.363	2.937	0.000	0.000	0.055	0.001	0.007	4.991	0.567	0.056	0.369	0.007	0.15
	Line 11 1316_FSP_1_CS	280	0.638	1.091	0.001	0.006	0.282	2.900	0.001	0.000	0.089	0.000	0.006	5.013	0.629	0.087	0.278	0.006	0.31
	Line 12 1316_FSP_1_CS	308	0.546	1.054	0.002	0.006	0.377	2.946	0.000	0.000	0.051	0.000	0.006	4.987	0.557	0.052	0.385	0.007	0.13
	Line 13 1316_FSP_1_CS	336	0.570	1.048	0.001	0.005	0.380	2.945	0.001	0.000	0.049	0.000	0.006	5.005	0.567	0.049	0.378	0.006	0.13
	Line 14 1316_FSP_1_CS	364	0.518	1.039	0.001	0.005	0.415	2.961	0.000	0.000	0.040	0.000	0.006	4.986	0.529	0.041	0.424	0.006	0.10
	Line 15 1316_FSP_1_CS	392	0.534	1.047	0.001	0.005	0.417	2.952	0.000	0.000	0.038	0.000	0.005	4.999	0.537	0.038	0.419	0.006	0.09
	Line 16 1316_FSP_1_CS	420	0.532	1.041	0.001	0.005	0.409	2.958	0.000	0.000	0.040	0.000	0.005	4.992	0.540	0.040	0.415	0.005	0.10
	Line 17 1316_FSP_1_CS	448	0.534	1.034	0.001	0.004	0.415	2.962	0.001	0.000	0.037	0.000	0.005	4.994	0.539	0.037	0.418	0.005	0.09
	Line 18 1316_FSP_1_CS	476	0.319	0.821	0.011	0.112	0.321	3.126	0.008	0.005	0.047	0.000	0.001	4.772	0.463	0.069	0.466	0.002	0.15
	Line 19 1316_FSP_1_CS	504	0.607	1.083	0.001	0.006	0.303	2.915	0.000	0.000	0.078	0.000	0.005	4.998	0.611	0.078	0.305	0.005	0.26
	Line 20 1316_FSP_1_CS	532	0.558	1.053	0.001	0.005	0.389	2.944	0.000	0.001	0.045	0.000	0.006	5.002	0.559	0.045	0.390	0.006	0.12
	Line 21 1316_FSP_1_CS	560	0.560	1.058	0.001	0.006	0.380	2.940	0.001	0.001	0.049	0.000	0.005	5.000	0.563	0.050	0.382	0.006	0.13
	Line 22 1316_FSP_1_CS	588	0.552	1.047	0.002	0.005	0.402	2.948	0.000	0.000	0.041	0.000	0.006	5.003	0.552	0.041	0.401	0.006	0.10
	Line 23 1316_FSP_1_CS	615	0.533	1.044	0.001	0.005	0.415	2.954	0.000	0.000	0.039	0.000	0.005	4.996	0.537	0.039	0.418	0.005	0.09
	Line 24 1316_FSP_1_CS	643	0.554	1.047	0.000	0.006	0.388	2.950	0.000	0.000	0.047	0.000	0.005	4.998	0.557	0.048	0.390	0.005	0.12
	Line 25 1316_FSP_1_CS	671	0.546	1.048	0.001	0.006	0.406	2.947	0.000	0.000	0.043	0.000	0.005	5.003	0.546	0.043	0.406	0.005	0.11
	Line 26 1316_FSP_1_CS	699	0.533	1.047	0.000	0.005	0.419	2.953	0.000	0.000	0.037	0.000	0.005	4.999	0.536	0.037	0.422	0.005	0.09
	Line 27 1316_FSP_1_CS	727	0.556	1.058	0.001	0.005	0.384	2.941	0.000	0.000	0.048	0.000	0.005	4.999	0.560	0.048	0.387	0.005	0.12
	Line 28 1316_FSP_1_CS	755	0.547	1.051	0.001	0.005	0.399	2.945	0.001	0.000	0.048	0.000	0.004	5.001	0.548	0.048	0.400	0.004	0.12
	Line 29 1316_FSP_1_CS	783	0.546	1.051	0.001	0.004	0.420	2.945	0.000	0.000	0.040	0.000	0.004	5.012	0.540	0.040	0.416	0.004	0.10
	Line 30 1316_FSP_1_CS	811	0.512	1.037	0.002	0.006	0.432	2.961	0.000	0.001	0.035	0.000	0.004	4.991	0.520	0.036	0.439	0.004	0.08
V-221a	Line 1 1316_FSP_4_CS	1	0.665	1.212	0.002	0.009	0.110	2.788	0.001	0.000	0.202	0.000	0.004	4.992	0.679	0.206	0.112	0.004	1.84
	Line 2 1316_FSP_4_CS	16	0.674	1.209	0.002	0.009	0.114	2.783	0.001	0.002	0.203	0.003	0.005	5.005	0.677	0.204	0.115	0.005	1.77
	Line 3 1316_FSP_4_CS	32	0.665	1.204	0.002	0.008	0.114	2.795	0.000	0.000	0.195	0.001	0.004	4.990	0.679	0.199	0.117	0.005	1.71
	Line 4 1316_FSP_4_CS	47	0.683	1.194	0.000	0.007	0.125	2.802	0.000	0.000	0.188	0.001	0.005	5.005	0.683	0.188	0.125	0.005	1.50
	Line 5 1316_FSP_4_CS	63	0.670	1.186	0.002	0.008	0.140	2.813	0.000	0.001	0.175	0.000	0.005	4.998	0.677	0.177	0.142	0.005	1.25
	Line 6 1316_FSP_4_CS	78	0.672	1.153	0.002	0.007	0.185	2.841	0.000	0.000	0.142	0.002	0.006	5.010	0.669	0.141	0.184	0.006	0.77
	Line 7 1316_FSP_4_CS	94	0.646	1.119	0.002	0.007	0.228	2.877	0.000	0.000	0.115	0.001	0.006	5.000	0.649	0.116	0.229	0.006	0.51
	Line 8 1316_FSP_4_CS	109	0.615	1.104	0.000	0.006	0.270	2.895	0.000	0.000	0.096	0.001	0.008	4.995	0.622	0.097	0.273	0.008	0.36
	Line 9 1316_FSP_4_CS	125	0.650	1.151	0.002	0.007	0.193	2.848	0.000	0.001	0.138	0.001	0.006	4.997	0.659	0.140	0.196	0.006	0.72
	Line 10 1316_FSP_4_CS	140	0.619	1.152	0.001	0.008	0.212	2.853	0.000	0.001	0.135	0.000	0.006	4.986	0.637	0.139	0.218	0.006	0.64
	Line 11 1316_FSP_4_CS	156	0.642	1.111	0.002	0.009	0.245	2.885	0.001	0.000	0.101	0.000	0.007	5.002	0.645	0.102	0.247	0.007	0.41
	Line 12 1316_FSP_4_CS	171	0.650	1.119	0.001	0.007	0.233	2.876	0.000	0.000	0.112	0.000	0.007	5.005	0.649	0.112	0.233	0.007	0.48
	Line 13 1316_FSP_4_CS	187	0.650	1.136	0.002	0.008	0.219	2.862	0.000	0.001	0.119	0.001	0.006	5.003	0.654	0.120	0.221	0.006	0.54
	Line 14 1316_FSP_4_CS	202	0.655	1.116	0.001	0.007	0.232	2.877	0.001	0.000	0.111	0.000	0.007	5.008	0.652	0.110	0.231	0.007	0.48
	Line 15 1316_FSP_4_CS	218	0.672	1.156	0.002	0.007	0.177	2.836	0.000	0.000	0.152	0.000	0.005	5.008	0.668	0.151	0.176	0.005	0.86
	Line 16 1316_FSP_4_CS	233	0.682	1.178	0.000	0.007	0.145	2.818	0.000	0.000	0.173	0.000	0.004	5.007	0.680	0.172	0.144	0.004	1.19
	Line 17 1316_FSP_4_CS	249	0.635	1.118	0.001	0.007	0.237	2.880	0.000	0.000	0.112	0.000	0.007	4.996	0.641	0.113	0.240	0.007	0.47
	Line 18 1316_FSP_4_CS	264	0.635	1.113	0.002	0.007	0.246	2.884	0.000	0.000	0.105	0.000	0.007	4.998	0.640	0.105	0.248	0.007	0.43
	Line 19 1316_FSP_4_CS	280	0.643	1.124	0.001	0.007	0.242	2.874	0.000	0.000	0.107	0.000	0.007	5.005	0.644	0.107	0.242	0.007	0.44
	Line 20 1316_FSP_4_CS	295	0.626	1.122	0.001	0.007	0.246	2.879	0.000	0.001	0.105	0.000	0.007	4.994	0.637	0.106	0.250	0.007	0.43
	Line 21 1316_FSP_4_CS	311	0.631	1.118	0.001	0.007	0.248	2.881	0.000	0.000	0.104	0.000	0.007	4.998	0.638	0.105	0.250	0.007	0.42
	Line 22 1316_FSP_4_CS	326	0.672	1.164	0.001	0.008	0.167	2.830	0.000	0.000	0.157	0.002	0.005	5.007	0.672	0.157	0.167	0.005	0.94
	Line 23 1316_FSP_4_CS	342	0.637	1.123	0.000	0.007	0.231	2.876	0.000	0.000	0.114	0.000	0.006	4.995	0.645	0.115	0.234	0.006	0.49
	Line 24 1316_FSP_4_CS	357	0.667	1.130	0.002	0.007	0.216	2.862	0.000	0.001	0.122	0.000	0.006	5.013	0.660	0.120	0.214	0.006	0.56
	Line 25 1316_FSP_4_CS	373	0.661	1.141	0.002	0.008	0.201	2.854	0.001	0.000	0.131	0.000	0.005	5.004	0.662	0.131	0.201	0.005	0.65
	Line 26 1316_FSP_4_CS	388	0.649	1.139	0.001	0.009	0.197	2.860	0.001	0.000	0.132	0.000	0.006	4.993	0.660	0.134	0.200	0.006	0.67
	Line 27 1316_FSP_4_CS	404	0.661	1.132	0.001	0.007	0.221	2.865	0.000	0.000	0.117	0.000	0.006	5.009	0.658	0.116	0.220	0.005	0.53
	Line 28 1316_FSP_4_CS	419	0.648	1.116	0.001	0.007	0.237	2.878	0.001	0.000	0.110	0.000	0.006	5.005	0.648	0.109	0.237	0.006	0.46
	Line 29 1316_FSP_4_CS	435	0.650	1.130	0.000	0.008	0.208	2.866	0.000	0.000	0.129	0.000	0.006	4.998	0.654	0.130	0.210	0.006	0.62
	Line 30 1316_FSP_4_CS	450	0.637	1.108	0.002	0.007	0.259	2.886	0.000	0.000	0.099	0.000	0.007	5.006	0.635	0.099	0.258	0.007	0.38

Table H.17: EMPA data of C-type feldspar inV-221a. Data is presented in atoms per formula unit and in fractions of solid solution end member. The end members are: albite (X_{Ab}), anorthite (X_{An}), orthoclase (X_{Or}), and celsian (X_{Cs}). Distances of the line scans are directed from core towards the rim of the crystal.

V-ID	Analyses ID	Distance (μm)	Na	Al	Ti	Fe	K	Si	Mg	Mn	Ca	Sr	Ba	Sum	X_{Ab}	X_{An}	X_{Or}	X_{Cs}	Ca/K
V-221a	Line 1 1316_FSP_4_CS	1	0.665	1.212	0.002	0.009	0.110	2.788	0.001	0.000	0.202	0.000	0.004	4.992	0.679	0.206	0.112	0.004	1.84
	Line 2 1316_FSP_4_CS	16	0.674	1.209	0.002	0.009	0.114	2.783	0.001	0.002	0.203	0.003	0.005	5.005	0.677	0.204	0.115	0.005	1.77
	Line 3 1316_FSP_4_CS	32	0.665	1.204	0.002	0.008	0.114	2.795	0.000	0.000	0.195	0.001	0.004	4.990	0.679	0.199	0.117	0.005	1.71
	Line 4 1316_FSP_4_CS	47	0.683	1.194	0.000	0.007	0.125	2.802	0.000	0.000	0.188	0.001	0.005	5.005	0.683	0.188	0.125	0.005	1.50
	Line 5 1316_FSP_4_CS	63	0.670	1.186	0.002	0.008	0.140	2.813	0.000	0.001	0.175	0.000	0.005	4.998	0.677	0.177	0.142	0.005	1.25
	Line 6 1316_FSP_4_CS	78	0.672	1.153	0.002	0.007	0.185	2.841	0.000	0.000	0.142	0.002	0.006	5.010	0.669	0.141	0.184	0.006	0.77
	Line 7 1316_FSP_4_CS	94	0.646	1.119	0.002	0.007	0.228	2.877	0.000	0.000	0.115	0.001	0.006	5.000	0.649	0.116	0.229	0.006	0.51
	Line 8 1316_FSP_4_CS	109	0.615	1.104	0.000	0.006	0.270	2.895	0.000	0.000	0.096	0.001	0.008	4.995	0.622	0.097	0.273	0.008	0.36
	Line 9 1316_FSP_4_CS	125	0.650	1.151	0.002	0.007	0.193	2.848	0.000	0.001	0.138	0.001	0.006	4.997	0.659	0.140	0.196	0.006	0.72
	Line 10 1316_FSP_4_CS	140	0.619	1.152	0.001	0.008	0.212	2.853	0.000	0.001	0.135	0.000	0.006	4.986	0.637	0.139	0.218	0.006	0.64
	Line 11 1316_FSP_4_CS	156	0.642	1.111	0.002	0.009	0.245	2.885	0.001	0.000	0.101	0.000	0.007	5.002	0.645	0.102	0.247	0.007	0.41
	Line 12 1316_FSP_4_CS	171	0.650	1.119	0.001	0.007	0.233	2.876	0.000	0.000	0.112	0.000	0.007	5.005	0.649	0.112	0.233	0.007	0.48
	Line 13 1316_FSP_4_CS	187	0.650	1.136	0.002	0.008	0.219	2.862	0.000	0.001	0.119	0.001	0.006	5.003	0.654	0.120	0.221	0.006	0.54
	Line 14 1316_FSP_4_CS	202	0.655	1.116	0.001	0.007	0.232	2.877	0.001	0.000	0.111	0.000	0.007	5.008	0.652	0.110	0.231	0.007	0.48
	Line 15 1316_FSP_4_CS	218	0.672	1.156	0.002	0.007	0.177	2.836	0.000	0.000	0.152	0.000	0.005	5.008	0.668	0.151	0.176	0.005	0.86
	Line 16 1316_FSP_4_CS	233	0.682	1.178	0.000	0.007	0.145	2.818	0.000	0.000	0.173	0.000	0.004	5.007	0.680	0.172	0.144	0.004	1.19
	Line 17 1316_FSP_4_CS	249	0.635	1.118	0.001	0.007	0.237	2.880	0.000	0.000	0.112	0.000	0.007	4.996	0.641	0.113	0.240	0.007	0.47
	Line 18 1316_FSP_4_CS	264	0.635	1.113	0.002	0.007	0.246	2.884	0.000	0.000	0.105	0.000	0.007	4.998	0.640	0.105	0.248	0.007	0.43
	Line 19 1316_FSP_4_CS	280	0.643	1.124	0.001	0.007	0.242	2.874	0.000	0.000	0.107	0.000	0.007	5.005	0.644	0.107	0.242	0.007	0.44
	Line 20 1316_FSP_4_CS	295	0.626	1.122	0.001	0.007	0.246	2.879	0.000	0.001	0.105	0.000	0.007	4.994	0.637	0.106	0.250	0.007	0.43
	Line 21 1316_FSP_4_CS	311	0.631	1.118	0.001	0.007	0.248	2.881	0.000	0.000	0.104	0.000	0.007	4.998	0.638	0.105	0.250	0.007	0.42
	Line 22 1316_FSP_4_CS	326	0.672	1.164	0.001	0.008	0.167	2.830	0.000	0.000	0.157	0.002	0.005	5.007	0.672	0.157	0.167	0.005	0.94
	Line 23 1316_FSP_4_CS	342	0.637	1.123	0.000	0.007	0.231	2.876	0.000	0.000	0.114	0.000	0.006	4.995	0.645	0.115	0.234	0.006	0.49
	Line 24 1316_FSP_4_CS	357	0.667	1.130	0.002	0.007	0.216	2.862	0.000	0.001	0.122	0.000	0.006	5.013	0.660	0.120	0.214	0.006	0.56
	Line 25 1316_FSP_4_CS	373	0.661	1.141	0.002	0.008	0.201	2.854	0.001	0.000	0.131	0.000	0.005	5.004	0.662	0.131	0.201	0.005	0.65
	Line 26 1316_FSP_4_CS	388	0.649	1.139	0.001	0.009	0.197	2.860	0.001	0.000	0.132	0.000	0.006	4.993	0.660	0.134	0.200	0.006	0.67
	Line 27 1316_FSP_4_CS	404	0.661	1.132	0.001	0.007	0.221	2.865	0.000	0.000	0.117	0.000	0.006	5.009	0.658	0.116	0.220	0.005	0.53
	Line 28 1316_FSP_4_CS	419	0.648	1.116	0.001	0.007	0.237	2.878	0.001	0.000	0.110	0.000	0.006	5.005	0.648	0.109	0.237	0.006	0.46
	Line 29 1316_FSP_4_CS	435	0.650	1.130	0.000	0.008	0.208	2.866	0.000	0.000	0.129	0.000	0.006	4.998	0.654	0.130	0.210	0.006	0.62
	Line 30 1316_FSP_4_CS	450	0.637	1.108	0.002	0.007	0.259	2.886	0.000	0.000	0.099	0.000	0.007	5.006	0.635	0.099	0.258	0.007	0.38
V-221a	Line 1 1316_FSP_21_CS_A	1	0.617	1.076	0.001	0.007	0.318	2.919	0.000	0.000	0.068	0.000	0.004	5.009	0.613	0.067	0.316	0.004	0.21
	Line 2 1316_FSP_21_CS_A	10	0.602	1.072	0.002	0.005	0.331	2.924	0.000	0.000	0.064	0.000	0.005	5.005	0.601	0.064	0.331	0.005	0.19
	Line 3 1316_FSP_21_CS_A	18	0.569	1.058	0.003	0.006	0.370	2.938	0.000	0.000	0.052	0.000	0.004	5.000	0.572	0.052	0.372	0.004	0.14
	Line 4 1316_FSP_21_CS_A	27	0.593	1.058	0.001	0.007	0.350	2.933	0.000	0.000	0.061	0.000	0.005	5.008	0.588	0.061	0.347	0.005	0.18
	Line 5 1316_FSP_21_CS_A	35	0.588	1.060	0.001	0.006	0.349	2.934	0.001	0.000	0.059	0.000	0.004	5.003	0.588	0.059	0.349	0.004	0.17
	Line 6 1316_FSP_21_CS_A	44	0.615	1.083	0.001	0.007	0.309	2.914	0.000	0.000	0.073	0.000	0.004	5.007	0.614	0.073	0.309	0.004	0.24
	Line 7 1316_FSP_21_CS_A	53	0.654	1.099	0.001	0.007	0.257	2.894	0.000	0.000	0.094	0.000	0.004	5.011	0.648	0.093	0.254	0.004	0.37
	Line 8 1316_FSP_21_CS_A	61	0.652	1.097	0.001	0.006	0.263	2.896	0.000	0.000	0.091	0.000	0.004	5.011	0.645	0.090	0.261	0.004	0.35
	Line 9 1316_FSP_21_CS_A	70	0.659	1.094	0.000	0.006	0.247	2.900	0.000	0.001	0.094	0.000	0.004	5.006	0.656	0.093	0.246	0.004	0.38
	Line 10 1316_FSP_21_CS_A	78	0.619	1.088	0.000	0.006	0.273	2.911	0.000	0.000	0.087	0.000	0.005	4.991	0.629	0.088	0.278	0.005	0.32
	Line 11 1316_FSP_21_CS_A	87	0.631	1.101	0.002	0.006	0.265	2.898	0.000	0.000	0.089	0.000	0.005	4.997	0.637	0.090	0.267	0.005	0.34
	Line 12 1316_FSP_21_CS_A	95	0.610	1.075	0.001	0.006	0.324	2.920	0.000	0.001	0.067	0.000	0.006	5.009	0.606	0.066	0.322	0.006	0.21
	Line 13 1316_FSP_21_CS_A	104	0.641	1.101	0.001	0.008	0.258	2.893	0.000	0.001	0.098	0.000	0.004	5.005	0.640	0.098	0.258	0.004	0.38
	Line 14 1316_FSP_21_CS_A	113	0.639	1.105	0.001	0.006	0.259	2.892	0.000	0.000	0.096	0.000	0.005	5.004	0.640	0.096	0.259	0.005	0.37
	Line 15 1316_FSP_21_CS_A	121	0.633	1.079	0.001	0.006	0.296	2.911	0.000	0.000	0.080	0.000	0.006	5.013	0.623	0.079	0.292	0.006	0.27
	Line 16 1316_FSP_21_CS_A	130	0.634	1.092	0.001	0.006	0.283	2.904	0.000	0.000	0.084	0.000	0.005	5.008	0.630	0.083	0.281	0.005	0.30
	Line 17 1316_FSP_21_CS_A	138	0.608	1.091	0.002	0.006	0.301	2.907	0.000	0.000	0.079	0.000	0.006	5.000	0.612	0.080	0.303	0.006	0.26
	Line 18 1316_FSP_21_CS_A	147	0.641	1.097	0.001	0.006	0.259	2.898	0.000	0.000	0.094	0.000	0.004	5.002	0.642	0.095	0.260	0.004	0.36
	Line 19 1316_FSP_21_CS_A	156	0.602	1.067	0.001	0.006	0.334	2.929	0.000	0.000	0.060	0.000	0.005	5.004	0.601	0.060	0.333	0.005	0.18
	Line 20 1316_FSP_21_CS_A	164	0.642	1.098	0.001	0.006	0.260	2.898	0.000	0.000	0.094	0.000	0.004	5.003	0.642	0.094	0.260	0.004	0.36
	Line 21 1316_FSP_21_CS_A	173	0.527	1.047	0.001	0.006	0.417	2.953	0.000	0.000	0.039	0.000	0.005	4.995	0.533	0.039	0.422	0.005	0.09
	Line 22 1316_FSP_21_CS_A	181	0.555	1.055	0.001	0.007	0.391	2.941	0.000	0.001	0.048	0.000	0.005	5.004	0.556	0.048	0.391	0.005	0.12
	Line 23 1316_FSP_21_CS_A	190	0.552	1.055	0.001	0.007	0.381	2.944	0.000	0.000	0.049	0.000	0.004	4.994	0.559	0.050	0.386	0.004	0.13
	Line 24 1316_FSP_21_CS_A	198	0.554	1.048	0.002	0.006	0.396	2.946	0.000	0.000	0.047	0.000	0.005	5.003	0.553	0.047	0.396	0.005	0.12
	Line 25 1316_FSP_21_CS_A	207	0.558	1.054	0.001	0.005	0.381	2.942	0.000	0.000	0.053	0.000	0.005	4.999	0.560	0.053	0.383	0.005	0.14
	Line 26 1316_FSP_21_CS_A	216	0.555	1.046	0.002	0.007	0.385	2.948	0.000	0.000	0.049	0.000	0.004	4.996	0.559	0.049	0.387	0.004	0.13
	Line 27 1316_FSP_21_CS_A	224	0.560	1.058	0.000	0.006	0.375	2.940	0.000	0.001	0.054	0.000	0.004	4.998	0.564	0.054	0.378	0.004	0.14
	Line 28 1316_FSP_21_CS_A	233	0.528	1.045	0.001	0.006	0.421	2.956	0.000	0.001	0.035	0.000	0.003	4.996	0.535	0.036	0.426	0.004	0.08
	Line 29 1316_FSP_21_CS_A	241	0.535	1.036	0.001	0.006	0.424	2.959	0.000	0.000	0.037	0.000	0.003	5.002	0.536	0.037	0.424	0.003	0.09
	Line 30 1316_FSP_21_CS_A	250	0.525	1.040	0.001	0.006	0.426	2.958	0.000	0.000	0.037	0.000	0.003	4.996	0.529	0.037	0.430	0.003	0.09

Table H.18: EMPA data of C-type feldspar inV-221a and V-209a. Data is presented in atoms per formula unit and in fractions of solid solution end member. The end members are: albite (X_{Ab}), anorthite (X_{An}), orthoclase (X_{Or}), and celsian (X_{Cs}). Distances of the line scans are directed from core towards the rim of the crystal.

V-ID	Analyses ID	Distance (μm)	Na	Al	Ti	Fe	K	Si	Mg	Mn	Ca	Sr	Ba	Sum	X_{Ab}	X_{An}	X_{Or}	X_{Cs}	Ca/K
V-221a	Line 1 1326_FSP_1_SCAN_1b_VC	4	0.674	1.183	0.001	0.008	0.115	2.824	0.000	0.000	0.167	0.000	0.006	4.978	0.700	0.174	0.120	0.006	1.45
_VC	8		0.692	1.181	0.001	0.008	0.115	2.822	0.000	0.000	0.165	0.002	0.005	4.990	0.709	0.169	0.118	0.005	1.43
	Line 3 1326_FSP_1_SCAN_1b_VC	12	0.697	1.172	0.002	0.008	0.117	2.824	0.000	0.001	0.168	0.000	0.005	4.995	0.706	0.170	0.119	0.005	1.43
	Line 4 1326_FSP_1_SCAN_1b_VC	16	0.682	1.178	0.001	0.008	0.115	2.824	0.000	0.000	0.171	0.000	0.005	4.984	0.701	0.176	0.118	0.005	1.49
	Line 5 1326_FSP_1_SCAN_1b_VC	20	0.701	1.172	0.000	0.008	0.111	2.827	0.000	0.000	0.170	0.000	0.005	4.994	0.711	0.172	0.112	0.005	1.53
	Line 6 1326_FSP_1_SCAN_1b_VC	24	0.690	1.179	0.001	0.007	0.111	2.821	0.001	0.000	0.173	0.001	0.005	4.989	0.704	0.177	0.113	0.005	1.56
	Line 7 1326_FSP_1_SCAN_1b_VC	28	0.710	1.182	0.001	0.009	0.110	2.813	0.000	0.000	0.174	0.000	0.005	5.005	0.711	0.174	0.110	0.005	1.57
	Line 8 1326_FSP_1_SCAN_1b_VC	32	0.432	0.939	0.007	0.087	0.207	3.031	0.003	0.002	0.100	0.001	0.003	4.812	0.583	0.134	0.278	0.005	0.48
	Line 9 1326_FSP_1_SCAN_1b_VC	36	0.632	1.074	0.001	0.014	0.233	2.920	0.000	0.001	0.091	0.001	0.009	4.974	0.655	0.094	0.242	0.009	0.39
	Line 10 1326_FSP_1_SCAN_1b_VC	40	0.665	1.101	0.000	0.007	0.241	2.893	0.000	0.001	0.091	0.000	0.010	5.009	0.660	0.090	0.240	0.010	0.38
	Line 11 1326_FSP_1_SCAN_1b_VC	44	0.643	1.101	0.000	0.008	0.260	2.898	0.000	0.000	0.082	0.000	0.011	5.003	0.645	0.082	0.261	0.011	0.32
	Line 12 1326_FSP_1_SCAN_1b_VC	48	0.668	1.106	0.001	0.006	0.245	2.888	0.000	0.000	0.089	0.000	0.010	5.014	0.661	0.088	0.242	0.010	0.36
	Line 13 1326_FSP_1_SCAN_1b_VC	52	0.662	1.108	0.001	0.007	0.246	2.887	0.000	0.000	0.090	0.000	0.010	5.012	0.656	0.090	0.244	0.010	0.37
	Line 14 1326_FSP_1_SCAN_1b_VC	56	0.643	1.102	0.001	0.005	0.238	2.899	0.000	0.000	0.092	0.000	0.010	4.989	0.655	0.094	0.242	0.010	0.39
V-209a	Line 1 1315_FSP_12_CS	1	0.557	1.108	0.001	0.007	0.317	2.901	0.000	0.001	0.076	0.000	0.013	4.981	0.579	0.079	0.329	0.013	0.24
	Line 2 1315_FSP_12_CS	5	0.559	1.110	0.002	0.007	0.309	2.899	0.001	0.001	0.078	0.000	0.013	4.978	0.583	0.081	0.322	0.014	0.25
	Line 3 1315_FSP_12_CS	9	0.577	1.117	0.002	0.009	0.290	2.888	0.000	0.001	0.086	0.000	0.014	4.985	0.596	0.089	0.300	0.014	0.30
	Line 4 1315_FSP_12_CS	13	0.574	1.115	0.002	0.007	0.294	2.891	0.000	0.000	0.087	0.000	0.014	4.984	0.592	0.090	0.304	0.014	0.30
	Line 5 1315_FSP_12_CS	17	0.591	1.124	0.001	0.007	0.290	2.881	0.000	0.000	0.088	0.000	0.014	4.996	0.602	0.089	0.295	0.014	0.30
	Line 6 1315_FSP_12_CS	21	0.591	1.137	0.002	0.008	0.253	2.868	0.000	0.000	0.112	0.000	0.013	4.983	0.610	0.116	0.261	0.013	0.44
	Line 7 1315_FSP_12_CS	25	0.600	1.160	0.001	0.008	0.219	2.849	0.000	0.000	0.131	0.000	0.012	4.980	0.624	0.136	0.227	0.013	0.60
	Line 8 1315_FSP_12_CS	29	0.587	1.153	0.003	0.007	0.224	2.856	0.000	0.000	0.126	0.001	0.014	4.971	0.617	0.133	0.235	0.015	0.56
	Line 9 1315_FSP_12_CS	33	0.574	1.123	0.001	0.007	0.290	2.883	0.000	0.000	0.089	0.000	0.019	4.986	0.590	0.092	0.299	0.019	0.31
	Line 10 1315_FSP_12_CS	37	0.611	1.187	0.002	0.007	0.194	2.816	0.001	0.000	0.156	0.001	0.017	4.991	0.625	0.160	0.198	0.017	0.80
	Line 11 1315_FSP_12_CS	41	0.600	1.200	0.002	0.009	0.190	2.805	0.000	0.000	0.161	0.002	0.019	4.988	0.618	0.166	0.196	0.020	0.85
	Line 12 1315_FSP_12_CS	45	0.606	1.170	0.001	0.008	0.218	2.833	0.001	0.000	0.135	0.001	0.020	4.993	0.619	0.138	0.223	0.020	0.62
	Line 13 1315_FSP_12_CS	49	0.610	1.189	0.002	0.007	0.204	2.816	0.000	0.000	0.145	0.000	0.020	4.994	0.623	0.148	0.209	0.020	0.71
	Line 14 1315_FSP_12_CS	53	0.607	1.192	0.001	0.009	0.206	2.813	0.001	0.000	0.146	0.000	0.020	4.996	0.621	0.149	0.210	0.020	0.71
	Line 15 1315_FSP_12_CS	57	0.611	1.180	0.002	0.006	0.220	2.826	0.000	0.000	0.135	0.000	0.019	4.998	0.620	0.137	0.223	0.020	0.61
	Line 16 1315_FSP_12_CS	61	0.586	1.167	0.002	0.006	0.234	2.842	0.000	0.000	0.122	0.005	0.019	4.983	0.610	0.127	0.243	0.020	0.52
	Line 17 1315_FSP_12_CS	65	0.597	1.144	0.002	0.008	0.243	2.861	0.000	0.001	0.112	0.001	0.018	4.985	0.616	0.116	0.250	0.018	0.46
	Line 18 1315_FSP_12_CS	69	0.591	1.151	0.002	0.008	0.244	2.856	0.000	0.000	0.114	0.003	0.016	4.984	0.612	0.119	0.253	0.017	0.47
	Line 19 1315_FSP_12_CS	73	0.588	1.138	0.002	0.007	0.266	2.870	0.001	0.000	0.099	0.000	0.016	4.986	0.607	0.102	0.275	0.016	0.37
	Line 20 1315_FSP_12_CS	77	0.572	1.127	0.002	0.008	0.266	2.884	0.000	0.001	0.094	0.001	0.014	4.969	0.604	0.100	0.282	0.014	0.35

Table H.19: EMPA data of C-type feldspar in V-209a. Data is presented in atoms per formula unit and in fractions of solid solution end member. The end members are: albite (X_{Ab}), anorthite (X_{An}), orthoclase (X_{Or}), and celsian (X_{Cs}). Distances of the line scans are directed from core towards the rim of the crystal.

V-ID	Analyses ID	Distance (μm)	Na	Al	Ti	Fe	K	Si	Mg	Mn	Ca	Sr	Ba	Sum	X_{Ab}	X_{An}	X_{Or}	X_{Cs}	Ca/K
V-209a	Line 2 1315_FSP_8_CS	5	0.583	1.133	0.000	0.007	0.267	2.877	0.000	0.000	0.099	0.000	0.016	4.982	0.604	0.103	0.277	0.017	0.37
	Line 3 1315_FSP_8_CS	9	0.601	1.136	0.002	0.006	0.254	2.869	0.000	0.000	0.105	0.000	0.015	4.989	0.616	0.107	0.261	0.016	0.41
	Line 4 1315_FSP_8_CS	13	0.600	1.140	0.002	0.008	0.248	2.866	0.000	0.000	0.110	0.000	0.013	4.986	0.618	0.113	0.255	0.014	0.44
	Line 5 1315_FSP_8_CS	17	0.605	1.147	0.001	0.007	0.244	2.861	0.001	0.000	0.112	0.000	0.011	4.989	0.622	0.115	0.251	0.012	0.46
	Line 6 1315_FSP_8_CS	21	0.606	1.137	0.002	0.008	0.240	2.868	0.001	0.000	0.116	0.000	0.008	4.985	0.625	0.120	0.247	0.008	0.48
	Line 7 1315_FSP_8_CS	25	0.548	1.076	0.002	0.008	0.363	2.928	0.000	0.000	0.056	0.000	0.007	4.988	0.563	0.057	0.373	0.007	0.15
	Line 8 1315_FSP_8_CS	29	0.550	1.075	0.002	0.007	0.351	2.931	0.001	0.000	0.059	0.000	0.005	4.980	0.570	0.062	0.363	0.005	0.17
	Line 9 1315_FSP_8_CS	33	0.540	1.074	0.001	0.007	0.359	2.934	0.000	0.002	0.056	0.000	0.004	4.977	0.563	0.058	0.375	0.004	0.15
	Line 10 1315_FSP_8_CS	37	0.568	1.060	0.000	0.007	0.369	2.940	0.000	0.000	0.050	0.000	0.005	4.999	0.573	0.050	0.372	0.005	0.14
	Line 11 1315_FSP_8_CS	41	0.549	1.070	0.001	0.008	0.361	2.935	0.000	0.000	0.053	0.000	0.005	4.983	0.567	0.055	0.372	0.005	0.15
	Line 12 1315_FSP_8_CS	45	0.555	1.074	0.002	0.007	0.350	2.931	0.000	0.000	0.057	0.000	0.005	4.981	0.574	0.059	0.362	0.005	0.16
	Line 13 1315_FSP_8_CS	49	0.543	1.068	0.001	0.007	0.371	2.938	0.000	0.000	0.051	0.000	0.005	4.984	0.560	0.053	0.383	0.005	0.14
	Line 14 1315_FSP_8_CS	53	0.544	1.067	0.001	0.007	0.367	2.939	0.000	0.001	0.051	0.000	0.004	4.982	0.562	0.053	0.380	0.005	0.14
	Line 15 1315_FSP_8_CS	57	0.553	1.066	0.002	0.008	0.382	2.935	0.000	0.000	0.046	0.000	0.006	4.998	0.560	0.047	0.387	0.006	0.12
	Line 16 1315_FSP_8_CS	61	0.527	1.063	0.002	0.007	0.371	2.945	0.000	0.001	0.050	0.000	0.006	4.971	0.552	0.052	0.389	0.006	0.13
	Line 17 1315_FSP_8_CS	65	0.552	1.067	0.002	0.007	0.372	2.936	0.000	0.000	0.049	0.000	0.007	4.991	0.563	0.050	0.380	0.007	0.13
	Line 18 1315_FSP_8_CS	69	0.531	1.063	0.002	0.007	0.379	2.942	0.000	0.001	0.047	0.000	0.008	4.980	0.550	0.049	0.393	0.008	0.12
	Line 19 1315_FSP_8_CS	73	0.532	1.064	0.001	0.007	0.380	2.942	0.001	0.000	0.046	0.000	0.008	4.981	0.551	0.047	0.393	0.008	0.12
	Line 20 1315_FSP_8_CS	77	0.537	1.062	0.002	0.008	0.371	2.942	0.000	0.000	0.049	0.000	0.008	4.979	0.556	0.051	0.384	0.008	0.13
	Line 21 1315_FSP_8_CS	81	0.545	1.068	0.001	0.007	0.365	2.940	0.000	0.000	0.049	0.000	0.008	4.981	0.564	0.051	0.377	0.008	0.13
	Line 22 1315_FSP_8_CS	85	0.549	1.068	0.001	0.008	0.359	2.936	0.000	0.001	0.054	0.000	0.007	4.983	0.567	0.056	0.370	0.008	0.15
	Line 23 1315_FSP_8_CS	89	0.554	1.062	0.001	0.007	0.369	2.939	0.000	0.000	0.050	0.000	0.008	4.991	0.565	0.051	0.376	0.008	0.14
	Line 24 1315_FSP_8_CS	93	0.580	1.104	0.001	0.009	0.301	2.900	0.001	0.000	0.083	0.000	0.009	4.988	0.596	0.085	0.310	0.009	0.28
	Line 25 1315_FSP_8_CS	97	0.582	1.096	0.001	0.006	0.301	2.909	0.000	0.000	0.079	0.000	0.010	4.983	0.599	0.081	0.310	0.010	0.26
	Line 26 1315_FSP_8_CS	101	0.574	1.098	0.002	0.006	0.301	2.908	0.000	0.000	0.080	0.000	0.009	4.978	0.595	0.083	0.313	0.009	0.26
	Line 27 1315_FSP_8_CS	105	0.596	1.100	0.001	0.006	0.294	2.902	0.002	0.000	0.082	0.000	0.010	4.992	0.607	0.083	0.300	0.010	0.28
	Line 28 1315_FSP_8_CS	109	0.574	1.113	0.002	0.007	0.291	2.897	0.000	0.000	0.083	0.000	0.011	4.978	0.599	0.087	0.304	0.011	0.28
	Line 29 1315_FSP_8_CS	113	0.585	1.104	0.002	0.008	0.295	2.898	0.001	0.000	0.085	0.001	0.010	4.988	0.600	0.087	0.303	0.010	0.29
	Line 30 1315_FSP_8_CS	117	0.567	1.114	0.001	0.006	0.298	2.899	0.000	0.000	0.081	0.000	0.010	4.976	0.593	0.085	0.312	0.011	0.27

Table H.20: EMPA data of C-type feldspar in V-65. Data is presented in atoms per formula unit and in fractions of solid solution end member. The end members are: albite (X_{Ab}), anorthite (X_{An}), orthoclase (X_{Or}), and celsian (X_{Cs}). Distances of the line scans are directed from core towards the rim of the crystal.

V-ID	Analyses ID	Distance (μm)	Na	Al	Ti	Fe	K	Si	Mg	Mn	Ca	Sr	Ba	Sum	X_{Ab}	X_{An}	X_{Or}	X_{Cs}	Ca/K
V-65	1303_FSP_1_CS	0	0.629	1.068	0.001	0.007	0.280	2.926	0.001	0.000	0.068	0.000	0.008	4.988	0.638	0.069	0.284	0.008	0.24
	1303_FSP_1_CS	6	0.622	1.076	0.002	0.008	0.274	2.922	0.000	0.000	0.069	0.000	0.008	4.981	0.639	0.070	0.282	0.009	0.25
	1303_FSP_1_CS	12	0.626	1.080	0.001	0.007	0.272	2.918	0.001	0.000	0.071	0.000	0.008	4.985	0.640	0.073	0.278	0.009	0.26
	1303_FSP_1_CS	18	0.646	1.072	0.002	0.008	0.269	2.919	0.001	0.000	0.070	0.000	0.009	4.996	0.650	0.071	0.271	0.009	0.26
	1303_FSP_1_CS	24	0.604	1.079	0.000	0.007	0.281	2.924	0.000	0.000	0.068	0.000	0.009	4.972	0.628	0.071	0.291	0.010	0.24
	1303_FSP_1_CS	30	0.623	1.063	0.001	0.007	0.275	2.931	0.000	0.001	0.069	0.000	0.009	4.981	0.638	0.071	0.282	0.009	0.25
	1303_FSP_1_CS	36	0.625	1.079	0.001	0.006	0.276	2.920	0.000	0.001	0.068	0.000	0.009	4.985	0.639	0.069	0.283	0.009	0.24
	1303_FSP_1_CS	42	0.610	1.051	0.001	0.006	0.302	2.948	0.000	0.001	0.049	0.000	0.008	4.976	0.630	0.050	0.312	0.008	0.16
	1303_FSP_1_CS	48	0.633	1.072	0.001	0.008	0.261	2.926	0.000	0.001	0.070	0.000	0.007	4.978	0.652	0.072	0.269	0.007	0.27
	1303_FSP_1_CS	54	0.644	1.116	0.001	0.007	0.205	2.887	0.001	0.000	0.103	0.000	0.008	4.972	0.671	0.107	0.213	0.008	0.50
	1303_FSP_1_CS	60	0.613	1.117	0.003	0.006	0.208	2.893	0.000	0.000	0.102	0.000	0.009	4.951	0.658	0.110	0.223	0.010	0.49
	1303_FSP_1_CS	66	0.649	1.114	0.001	0.007	0.213	2.883	0.000	0.000	0.105	0.000	0.011	4.983	0.664	0.108	0.218	0.011	0.49
	1303_FSP_1_CS	72	0.638	1.118	0.001	0.007	0.217	2.884	0.001	0.000	0.102	0.000	0.010	4.978	0.660	0.106	0.224	0.010	0.47
	1303_FSP_1_CS	78	0.636	1.107	0.001	0.008	0.219	2.892	0.000	0.000	0.102	0.000	0.010	4.975	0.658	0.106	0.226	0.010	0.47
	1303_FSP_1_CS	84	0.652	1.123	0.002	0.006	0.213	2.877	0.000	0.000	0.103	0.000	0.010	4.987	0.666	0.106	0.218	0.011	0.48
	1303_FSP_1_CS	90	0.651	1.113	0.000	0.006	0.211	2.885	0.000	0.000	0.105	0.000	0.010	4.982	0.666	0.108	0.216	0.011	0.50
	1303_FSP_1_CS	96	0.637	1.119	0.001	0.008	0.213	2.884	0.000	0.000	0.103	0.000	0.009	4.976	0.662	0.107	0.222	0.010	0.48
	1303_FSP_1_CS	103	0.668	1.112	0.001	0.007	0.214	2.879	0.000	0.000	0.106	0.000	0.011	4.998	0.669	0.106	0.214	0.011	0.49
	1303_FSP_1_CS	109	0.635	1.104	0.001	0.006	0.215	2.897	0.001	0.000	0.102	0.000	0.010	4.970	0.660	0.106	0.223	0.011	0.47
	1303_FSP_1_CS	115	0.644	1.114	0.003	0.006	0.222	2.884	0.000	0.001	0.101	0.000	0.010	4.983	0.660	0.103	0.227	0.010	0.45
	1303_FSP_1_CS	121	0.647	1.111	0.001	0.009	0.218	2.886	0.000	0.001	0.101	0.000	0.010	4.984	0.662	0.104	0.224	0.010	0.46
	1303_FSP_1_CS	127	0.659	1.115	0.001	0.008	0.216	2.882	0.000	0.001	0.100	0.000	0.010	4.992	0.669	0.101	0.219	0.011	0.46
	1303_FSP_1_CS	133	0.628	1.116	0.001	0.008	0.221	2.890	0.000	0.000	0.097	0.000	0.009	4.970	0.658	0.101	0.231	0.010	0.44
	1303_FSP_1_CS	139	0.622	1.102	0.001	0.007	0.217	2.904	0.000	0.000	0.097	0.000	0.010	4.959	0.657	0.103	0.229	0.011	0.45
	1303_FSP_1_CS	145	0.627	1.107	0.003	0.008	0.220	2.893	0.001	0.000	0.101	0.000	0.011	4.969	0.654	0.105	0.230	0.011	0.46
	1303_FSP_1_CS	151	0.625	1.103	0.001	0.007	0.217	2.901	0.001	0.000	0.097	0.000	0.010	4.961	0.659	0.102	0.229	0.010	0.45
	1303_FSP_1_CS	157	0.682	1.102	0.002	0.007	0.211	2.887	0.000	0.000	0.100	0.000	0.010	5.001	0.680	0.100	0.210	0.010	0.47
	1303_FSP_1_CS	163	0.635	1.105	0.002	0.007	0.214	2.896	0.000	0.000	0.101	0.000	0.010	4.970	0.661	0.105	0.223	0.011	0.47
	1303_FSP_1_CS	169	0.675	1.118	0.000	0.008	0.210	2.877	0.000	0.000	0.102	0.000	0.010	5.001	0.677	0.102	0.210	0.010	0.49
	1303_FSP_1_CS	175	0.637	1.111	0.002	0.008	0.214	2.887	0.001	0.000	0.105	0.000	0.010	4.975	0.659	0.108	0.221	0.011	0.49
	1303_FSP_1_CS	181	0.632	1.121	0.001	0.007	0.207	2.882	0.000	0.000	0.107	0.000	0.011	4.969	0.660	0.112	0.217	0.011	0.52
	1303_FSP_1_CS	187	0.642	1.112	0.002	0.007	0.207	2.884	0.000	0.002	0.111	0.000	0.010	4.977	0.662	0.114	0.213	0.010	0.54
	1303_FSP_1_CS	193	0.635	1.115	0.002	0.007	0.200	2.885	0.001	0.000	0.112	0.000	0.010	4.967	0.664	0.117	0.208	0.011	0.56
	1303_FSP_1_CS	199	0.650	1.119	0.002	0.007	0.206	2.878	0.001	0.000	0.113	0.000	0.011	4.984	0.664	0.115	0.210	0.011	0.55
	1303_FSP_1_CS	205	0.644	1.129	0.002	0.006	0.206	2.871	0.001	0.000	0.113	0.000	0.011	4.981	0.662	0.116	0.212	0.011	0.55
	1303_FSP_1_CS	211	0.624	1.116	0.001	0.007	0.212	2.886	0.000	0.000	0.110	0.000	0.011	4.968	0.652	0.115	0.221	0.012	0.52
	1303_FSP_1_CS	217	0.627	1.119	0.002	0.008	0.211	2.883	0.000	0.000	0.108	0.000	0.011	4.969	0.655	0.113	0.221	0.011	0.51
	1303_FSP_1_CS	223	0.643	1.123	0.000	0.007	0.208	2.878	0.001	0.000	0.110	0.000	0.011	4.980	0.662	0.113	0.214	0.011	0.53
	1303_FSP_1_CS	229	0.628	1.124	0.003	0.009	0.208	2.879	0.000	0.000	0.109	0.000	0.010	4.969	0.658	0.114	0.218	0.010	0.53
	1303_FSP_1_CS	235	0.659	1.117	0.001	0.007	0.211	2.877	0.000	0.000	0.111	0.000	0.011	4.993	0.665	0.112	0.213	0.011	0.53

Table H.21: EMPA data of C-type feldspar inV-65. Data is presented in atoms per formula unit and in fractions of solid solution end member. The end members are: albite (X_{Ab}), anorthite (X_{An}), orthoclase (X_{Or}), and celsian (X_{Cs}). Distances of the line scans are directed from core towards the rim of the crystal.

V-ID	Analyses ID	Distance (μm)	Na	Al	Ti	Fe	K	Si	Mg	Mn	Ca	Sr	Ba	Sum	X_{Ab}	X_{An}	X_{Or}	X_{Cs}	Ca/K
V-65	Line 1 ELV_1303_FSP_3b	0	0.636	1.096	0.001	0.009	0.259	2.891	0.000	0.001	0.101	0.006	0.008	5.008	0.634	0.100	0.258	0.008	0.39
	Line 2 ELV_1303_FSP_3b	8	0.641	1.119	0.002	0.009	0.219	2.876	0.000	0.000	0.110	0.006	0.010	4.993	0.654	0.113	0.224	0.010	0.50
	Line 3 ELV_1303_FSP_3b	17	0.664	1.106	0.001	0.008	0.255	2.888	0.000	0.000	0.082	0.006	0.009	5.019	0.657	0.081	0.253	0.009	0.32
	Line 4 ELV_1303_FSP_3b	25	0.638	1.095	0.000	0.007	0.282	2.903	0.000	0.000	0.071	0.005	0.009	5.010	0.639	0.071	0.282	0.009	0.25
	Line 5 ELV_1303_FSP_3b	33	0.643	1.097	0.002	0.007	0.273	2.898	0.000	0.000	0.075	0.006	0.009	5.010	0.643	0.075	0.273	0.009	0.27
	Line 6 ELV_1303_FSP_3b	42	0.611	1.083	0.001	0.008	0.273	2.917	0.000	0.000	0.075	0.006	0.009	4.983	0.631	0.078	0.282	0.009	0.28
	Line 7 ELV_1303_FSP_3b	50	0.604	1.094	0.001	0.007	0.277	2.909	0.000	0.001	0.075	0.006	0.010	4.983	0.626	0.077	0.286	0.010	0.27
	Line 8 ELV_1303_FSP_3b	59	0.634	1.105	0.001	0.007	0.259	2.896	0.000	0.000	0.081	0.000	0.009	4.991	0.645	0.082	0.263	0.010	0.31
	Line 9 ELV_1303_FSP_3b	67	0.601	1.116	0.003	0.007	0.258	2.892	0.000	0.000	0.085	0.000	0.010	4.971	0.630	0.089	0.270	0.011	0.33
	Line 10 ELV_1303_FSP_3b	75	0.623	1.108	0.001	0.008	0.262	2.894	0.000	0.001	0.083	0.000	0.010	4.989	0.637	0.085	0.268	0.010	0.32
	Line 11 ELV_1303_FSP_3b	84	0.620	1.099	0.001	0.008	0.278	2.900	0.000	0.000	0.077	0.000	0.010	4.993	0.629	0.078	0.282	0.010	0.28
	Line 12 ELV_1303_FSP_3b	92	0.601	1.078	0.002	0.006	0.297	2.927	0.000	0.000	0.055	0.000	0.009	4.976	0.625	0.057	0.309	0.009	0.19
	Line 13 ELV_1303_FSP_3b	100	0.654	1.116	0.001	0.006	0.246	2.882	0.000	0.000	0.087	0.000	0.010	5.002	0.656	0.088	0.246	0.010	0.36
	Line 14 ELV_1303_FSP_3b	109	0.636	1.108	0.002	0.008	0.256	2.891	0.001	0.001	0.082	0.000	0.010	4.993	0.647	0.083	0.260	0.010	0.32
	Line 15 ELV_1303_FSP_3b	117	0.658	1.111	0.002	0.008	0.259	2.883	0.000	0.000	0.081	0.000	0.010	5.012	0.653	0.081	0.257	0.010	0.31
	Line 16 ELV_1303_FSP_3b	125	0.641	1.101	0.001	0.009	0.258	2.898	0.000	0.000	0.079	0.000	0.010	4.995	0.649	0.080	0.261	0.010	0.31
	Line 17 ELV_1303_FSP_3b	134	0.637	1.103	0.002	0.008	0.258	2.894	0.000	0.001	0.080	0.000	0.010	4.993	0.647	0.082	0.262	0.010	0.31
	Line 18 ELV_1303_FSP_3b	142	0.637	1.100	0.001	0.008	0.260	2.900	0.000	0.000	0.078	0.000	0.010	4.992	0.647	0.079	0.264	0.010	0.30
	Line 19 ELV_1303_FSP_3b	150	0.622	1.109	0.001	0.008	0.266	2.895	0.002	0.000	0.075	0.000	0.010	4.988	0.639	0.077	0.274	0.010	0.28
	Line 20 ELV_1303_FSP_3b	159	0.624	1.101	0.002	0.009	0.263	2.901	0.000	0.000	0.075	0.000	0.009	4.985	0.642	0.077	0.271	0.010	0.28
	Line 21 ELV_1303_FSP_3b	167	0.652	1.113	0.001	0.008	0.266	2.885	0.000	0.000	0.077	0.000	0.009	5.011	0.649	0.077	0.265	0.009	0.29
	Line 22 ELV_1303_FSP_3b	176	0.614	1.105	0.002	0.007	0.265	2.900	0.000	0.000	0.077	0.000	0.008	4.979	0.637	0.080	0.275	0.008	0.29
	Line 23 ELV_1303_FSP_3b	184	0.620	1.096	0.002	0.009	0.265	2.905	0.001	0.000	0.076	0.000	0.008	4.982	0.640	0.079	0.273	0.008	0.29
	Line 24 ELV_1303_FSP_3b	192	0.641	1.120	0.001	0.008	0.226	2.880	0.000	0.001	0.102	0.000	0.007	4.986	0.657	0.104	0.231	0.008	0.45
	Line 25 ELV_1303_FSP_3b	201	0.633	1.078	0.002	0.007	0.288	2.921	0.000	0.000	0.057	0.000	0.007	4.993	0.643	0.058	0.292	0.007	0.20
	Line 26 ELV_1303_FSP_3b	209	0.597	1.087	0.002	0.006	0.287	2.920	0.000	0.000	0.064	0.000	0.008	4.970	0.625	0.067	0.300	0.008	0.22
	Line 27 ELV_1303_FSP_3b	217	0.626	1.093	0.002	0.010	0.282	2.907	0.000	0.000	0.066	0.000	0.008	4.994	0.637	0.067	0.287	0.008	0.23
	Line 28 ELV_1303_FSP_3b	226	0.621	1.083	0.002	0.008	0.280	2.915	0.000	0.000	0.067	0.000	0.008	4.986	0.636	0.069	0.287	0.008	0.24
	Line 29 ELV_1303_FSP_3b	234	0.607	1.091	0.002	0.008	0.279	2.914	0.000	0.000	0.068	0.000	0.007	4.976	0.631	0.071	0.291	0.007	0.24
	Line 30 ELV_1303_FSP_3b	242	0.635	1.093	0.002	0.009	0.279	2.906	0.000	0.000	0.068	0.000	0.006	4.997	0.643	0.069	0.282	0.006	0.24
	Line 31 ELV_1303_FSP_3b	251	0.628	1.086	0.001	0.008	0.278	2.913	0.000	0.000	0.070	0.000	0.006	4.991	0.639	0.072	0.283	0.006	0.25
	Line 32 ELV_1303_FSP_3b	259	0.630	1.090	0.002	0.008	0.277	2.907	0.001	0.002	0.071	0.000	0.006	4.994	0.640	0.072	0.281	0.006	0.26
	Line 33 ELV_1303_FSP_3b	268	0.635	1.088	0.002	0.007	0.277	2.910	0.000	0.000	0.068	0.000	0.006	4.994	0.644	0.069	0.280	0.007	0.25
	Line 34 ELV_1303_FSP_3b	276	0.643	1.104	0.002	0.008	0.277	2.897	0.001	0.000	0.066	0.000	0.006	5.003	0.648	0.066	0.280	0.006	0.24
	Line 35 ELV_1303_FSP_3b	284	0.623	1.090	0.001	0.007	0.280	2.914	0.000	0.000	0.067	0.000	0.006	4.987	0.638	0.068	0.287	0.007	0.24
	Line 36 ELV_1303_FSP_3b	293	0.626	1.092	0.002	0.007	0.278	2.909	0.000	0.000	0.067	0.000	0.006	4.989	0.640	0.069	0.285	0.006	0.24
	Line 37 ELV_1303_FSP_3b	301	0.599	1.093	0.001	0.008	0.285	2.915	0.000	0.000	0.066	0.000	0.006	4.975	0.626	0.069	0.298	0.007	0.23
	Line 38 ELV_1303_FSP_3b	309	0.609	1.097	0.001	0.006	0.284	2.910	0.000	0.000	0.068	0.000	0.007	4.981	0.629	0.070	0.293	0.007	0.24
	Line 39 ELV_1303_FSP_3b	318	0.626	1.091	0.002	0.007	0.283	2.909	0.000	0.000	0.068	0.000	0.007	4.993	0.636	0.069	0.288	0.007	0.24
	Line 40 ELV_1303_FSP_3b	326	0.620	1.090	0.002	0.006	0.281	2.912	0.000	0.001	0.067	0.000	0.006	4.986	0.636	0.069	0.288	0.006	0.24
	Line 41 ELV_1303_FSP_3b	334	0.619	1.090	0.001	0.008	0.289	2.911	0.000	0.001	0.065	0.000	0.007	4.992	0.631	0.066	0.295	0.007	0.22
	Line 42 ELV_1303_FSP_3b	343	0.609	1.092	0.001	0.007	0.281	2.914	0.000	0.000	0.067	0.000	0.008	4.979	0.631	0.070	0.291	0.008	0.24
	Line 43 ELV_1303_FSP_3b	351	0.598	1.084	0.002	0.008	0.279	2.919	0.001	0.000	0.072	0.000	0.007	4.971	0.625	0.076	0.292	0.007	0.26
	Line 44 ELV_1303_FSP_3b	359	0.614	1.086	0.002	0.007	0.281	2.917	0.000	0.000	0.065	0.000	0.008	4.980	0.634	0.067	0.290	0.008	0.23
	Line 45 ELV_1303_FSP_3b	368	0.632	1.090	0.002	0.008	0.278	2.908	0.000	0.000	0.069	0.000	0.007	4.994	0.641	0.070	0.282	0.007	0.25
	Line 46 ELV_1303_FSP_3b	376	0.606	1.095	0.001	0.008	0.285	2.912	0.000	0.000	0.066	0.000	0.007	4.979	0.629	0.068	0.295	0.008	0.23
	Line 47 ELV_1303_FSP_3b	385	0.630	1.099	0.001	0.007	0.279	2.902	0.000	0.000	0.069	0.000	0.007	4.995	0.640	0.070	0.283	0.007	0.25
	Line 48 ELV_1303_FSP_3b	393	0.593	1.094	0.002	0.006	0.280	2.916	0.000	0.001	0.066	0.000	0.007	4.966	0.627	0.070	0.296	0.007	0.24
	Line 49 ELV_1303_FSP_3b	401	0.622	1.088	0.002	0.008	0.278	2.913	0.000	0.001	0.067	0.000	0.008	4.986	0.638	0.069	0.285	0.008	0.24
	Line 50 ELV_1303_FSP_3b	410	0.626	1.091	0.000	0.007	0.282	2.912	0.000	0.000	0.065	0.000	0.007	4.991	0.638	0.066	0.288	0.008	0.23

Table H.22: EMPA data of C-type feldspar inV-65. Data is presented in atoms per formula unit and in fractions of solid solution end member. The end members are: albite (X_{Ab}), anorthite (X_{An}), orthoclase (X_{Or}), and celsian (X_{Cs}). Distances of the line scans are directed from core towards the rim of the crystal.

V-ID	Analyses ID	Distance (μm)	Na	Al	Ti	Fe	K	Si	Mg	Mn	Ca	Sr	Ba	Sum	X_{Ab}	X_{An}	X_{Or}	X_{Cs}	Ca/K
V-65	Line 51 ELV_1303_FSP_3b	418	0.636	1.091	0.001	0.008	0.285	2.908	0.000	0.000	0.065	0.000	0.007	5.000	0.641	0.065	0.288	0.007	0.23
	Line 52 ELV_1303_FSP_3b	426	0.609	1.101	0.001	0.007	0.287	2.906	0.000	0.000	0.066	0.000	0.006	4.984	0.629	0.068	0.296	0.007	0.23
	Line 53 ELV_1303_FSP_3b	435	0.604	1.090	0.002	0.009	0.280	2.915	0.000	0.000	0.065	0.000	0.007	4.973	0.632	0.068	0.293	0.007	0.23
	Line 54 ELV_1303_FSP_3b	443	0.592	1.085	0.001	0.007	0.286	2.922	0.000	0.000	0.067	0.000	0.007	4.968	0.622	0.070	0.301	0.007	0.23
	Line 55 ELV_1303_FSP_3b	451	0.606	1.087	0.001	0.007	0.287	2.918	0.000	0.000	0.066	0.000	0.007	4.979	0.627	0.068	0.297	0.007	0.23
	Line 56 ELV_1303_FSP_3b	460	0.607	1.091	0.003	0.008	0.292	2.913	0.001	0.000	0.062	0.000	0.008	4.984	0.627	0.064	0.301	0.008	0.21
	Line 57 ELV_1303_FSP_3b	468	0.612	1.084	0.001	0.008	0.294	2.918	0.001	0.000	0.060	0.000	0.008	4.986	0.628	0.062	0.302	0.009	0.20
	Line 58 ELV_1303_FSP_3b	477	0.600	1.085	0.001	0.007	0.290	2.922	0.000	0.000	0.062	0.000	0.007	4.973	0.626	0.065	0.302	0.007	0.21
	Line 59 ELV_1303_FSP_3b	485	0.621	1.082	0.002	0.007	0.296	2.916	0.000	0.000	0.061	0.000	0.007	4.993	0.630	0.062	0.300	0.007	0.21
	Line 60 ELV_1303_FSP_3b	493	0.610	1.086	0.001	0.006	0.293	2.918	0.000	0.000	0.061	0.000	0.008	4.985	0.628	0.063	0.301	0.008	0.21
	Line 61 ELV_1303_FSP_3b	502	0.621	1.101	0.001	0.008	0.294	2.904	0.000	0.000	0.060	0.000	0.008	4.996	0.632	0.061	0.299	0.008	0.20
	Line 62 ELV_1303_FSP_3b	510	0.602	1.083	0.001	0.007	0.290	2.924	0.000	0.000	0.060	0.000	0.007	4.975	0.627	0.063	0.302	0.008	0.21
	Line 63 ELV_1303_FSP_3b	518	0.596	1.091	0.001	0.008	0.289	2.915	0.000	0.001	0.065	0.000	0.008	4.975	0.622	0.068	0.301	0.009	0.23
	Line 64 ELV_1303_FSP_3b	527	0.594	1.102	0.001	0.007	0.288	2.908	0.000	0.001	0.065	0.000	0.008	4.974	0.622	0.068	0.301	0.008	0.23
	Line 65 ELV_1303_FSP_3b	535	0.627	1.089	0.001	0.009	0.287	2.910	0.001	0.000	0.064	0.000	0.009	4.996	0.636	0.065	0.291	0.009	0.22
	Line 66 ELV_1303_FSP_3b	543	0.616	1.083	0.001	0.009	0.289	2.917	0.000	0.000	0.062	0.000	0.009	4.987	0.631	0.063	0.296	0.010	0.21
	Line 67 ELV_1303_FSP_3b	552	0.617	1.101	0.002	0.007	0.284	2.903	0.001	0.000	0.066	0.000	0.010	4.990	0.632	0.068	0.291	0.010	0.23
	Line 68 ELV_1303_FSP_3b	560	0.618	1.099	0.001	0.008	0.261	2.903	0.001	0.000	0.081	0.000	0.009	4.981	0.638	0.084	0.269	0.009	0.31
	Line 69 ELV_1303_FSP_3b	568	0.628	1.094	0.000	0.008	0.259	2.908	0.000	0.000	0.077	0.000	0.009	4.983	0.645	0.079	0.266	0.010	0.30
	Line 70 ELV_1303_FSP_3b	577	0.635	1.095	0.002	0.007	0.264	2.901	0.000	0.001	0.076	0.000	0.009	4.992	0.645	0.077	0.268	0.009	0.29
	Line 71 ELV_1303_FSP_3b	585	0.639	1.114	0.001	0.008	0.252	2.890	0.000	0.000	0.078	0.000	0.009	4.992	0.653	0.080	0.257	0.010	0.31
	Line 72 ELV_1303_FSP_3b	594	0.619	1.107	0.002	0.007	0.260	2.896	0.001	0.000	0.081	0.000	0.010	4.983	0.638	0.083	0.268	0.010	0.31
	Line 73 ELV_1303_FSP_3b	602	0.631	1.100	0.002	0.007	0.267	2.902	0.000	0.001	0.073	0.000	0.009	4.991	0.644	0.075	0.272	0.009	0.27
	Line 74 ELV_1303_FSP_3b	610	0.610	1.114	0.001	0.009	0.266	2.894	0.000	0.000	0.076	0.000	0.009	4.981	0.634	0.079	0.276	0.010	0.29
	Line 75 ELV_1303_FSP_3b	619	0.647	1.107	0.002	0.007	0.271	2.890	0.001	0.000	0.075	0.000	0.009	5.008	0.646	0.075	0.270	0.009	0.28
	Line 76 ELV_1303_FSP_3b	627	0.654	1.104	0.001	0.008	0.266	2.892	0.000	0.000	0.074	0.000	0.010	5.009	0.651	0.074	0.265	0.010	0.28
	Line 77 ELV_1303_FSP_3b	635	0.614	1.109	0.000	0.008	0.263	2.898	0.000	0.000	0.077	0.000	0.009	4.979	0.637	0.080	0.273	0.010	0.29
	Line 78 ELV_1303_FSP_3b	644	0.625	1.105	0.002	0.008	0.260	2.897	0.000	0.001	0.081	0.000	0.009	4.986	0.642	0.083	0.267	0.009	0.31
	Line 79 ELV_1303_FSP_3b	652	0.627	1.097	0.001	0.008	0.271	2.903	0.000	0.000	0.073	0.000	0.010	4.991	0.639	0.075	0.276	0.010	0.27
	Line 80 ELV_1303_FSP_3b	660	0.627	1.106	0.002	0.007	0.268	2.895	0.000	0.001	0.078	0.000	0.010	4.993	0.638	0.079	0.272	0.010	0.29
	Line 81 ELV_1303_FSP_3b	669	0.608	1.103	0.003	0.007	0.273	2.901	0.000	0.000	0.075	0.000	0.009	4.979	0.630	0.077	0.283	0.010	0.27
	Line 82 ELV_1303_FSP_3b	677	0.605	1.101	0.001	0.008	0.276	2.904	0.000	0.000	0.073	0.000	0.010	4.979	0.627	0.075	0.286	0.011	0.26
	Line 83 ELV_1303_FSP_3b	686	0.611	1.090	0.001	0.008	0.303	2.913	0.000	0.000	0.059	0.000	0.009	4.993	0.623	0.060	0.308	0.009	0.19
	Line 84 ELV_1303_FSP_3b	694	0.601	1.097	0.001	0.008	0.288	2.910	0.000	0.000	0.063	0.000	0.010	4.979	0.624	0.065	0.300	0.010	0.22
	Line 85 ELV_1303_FSP_3b	702	0.642	1.118	0.001	0.008	0.247	2.884	0.001	0.000	0.087	0.000	0.008	4.996	0.652	0.089	0.251	0.008	0.35
	Line 86 ELV_1303_FSP_3b	711	0.609	1.109	0.002	0.008	0.255	2.898	0.000	0.000	0.081	0.000	0.009	4.972	0.638	0.085	0.267	0.009	0.32
	Line 87 ELV_1303_FSP_3b	719	0.641	1.101	0.002	0.010	0.256	2.894	0.001	0.000	0.081	0.000	0.009	4.996	0.650	0.082	0.259	0.009	0.32
	Line 88 ELV_1303_FSP_3b	727	0.614	1.103	0.001	0.009	0.260	2.902	0.001	0.000	0.077	0.000	0.009	4.976	0.640	0.080	0.271	0.009	0.30
	Line 89 ELV_1303_FSP_3b	736	0.602	1.105	0.001	0.009	0.258	2.902	0.000	0.000	0.081	0.000	0.010	4.969	0.633	0.085	0.272	0.010	0.31
	Line 90 ELV_1303_FSP_3b	744	0.617	1.110	0.001	0.008	0.245	2.895	0.000	0.000	0.087	0.000	0.010	4.973	0.644	0.090	0.255	0.010	0.35
	Line 91 ELV_1303_FSP_3b	752	0.627	1.106	0.001	0.007	0.259	2.898	0.000	0.000	0.079	0.000	0.008	4.985	0.645	0.081	0.266	0.008	0.30
	Line 92 ELV_1303_FSP_3b	761	0.593	1.111	0.002	0.008	0.262	2.901	0.001	0.000	0.076	0.000	0.009	4.964	0.631	0.081	0.279	0.009	0.29
	Line 93 ELV_1303_FSP_3b	769	0.647	1.098	0.001	0.008	0.268	2.896	0.000	0.000	0.076	0.000	0.009	5.004	0.647	0.076	0.268	0.009	0.28
	Line 94 ELV_1303_FSP_3b	777	0.613	1.117	0.002	0.009	0.269	2.890	0.001	0.001	0.074	0.000	0.009	4.984	0.635	0.077	0.279	0.009	0.28
	Line 95 ELV_1303_FSP_3b	786	0.634	1.098	0.002	0.007	0.274	2.899	0.000	0.001	0.074	0.000	0.009	4.998	0.639	0.075	0.277	0.010	0.27
	Line 96 ELV_1303_FSP_3b	794	0.623	1.094	0.003	0.008	0.274	2.903	0.000	0.000	0.073	0.000	0.010	4.990	0.635	0.075	0.280	0.010	0.27
	Line 97 ELV_1303_FSP_3b	803	0.631	1.104	0.001	0.007	0.277	2.895	0.001	0.000	0.074	0.000	0.010	5.000	0.636	0.074	0.279	0.010	0.27
	Line 98 ELV_1303_FSP_3b	811	0.602	1.113	0.002	0.008	0.277	2.893	0.000	0.001	0.076	0.000	0.010	4.982	0.624	0.078	0.287	0.011	0.27
	Line 99 ELV_1303_FSP_3b	819	0.607	1.101	0.000	0.008	0.286	2.906	0.001	0.001	0.066	0.000	0.009	4.985	0.627	0.068	0.296	0.009	0.23
	Line 100 ELV_1303_FSP_3b	828	0.610	1.089	0.002	0.009	0.292	2.915	0.000	0.000	0.060	0.000	0.008	4.985	0.629	0.061	0.301	0.008	0.20

Table H.23: EMPA data of C-type feldspar inV-45. Data is presented in atoms per formula unit and in fractions of solid solution end member. The end members are: albite (X_{Ab}), anorthite (X_{An}), orthoclase (X_{Or}), and celsian (X_{Cs}). Distances of the line scans are directed from core towards the rim of the crystal.

V-ID	Analyses ID	Distance (μm)	Na	Al	Ti	Fe	K	Si	Mg	Mn	Ca	Sr	Ba	Sum	X_{Ab}	X_{An}	X_{Or}	X_{Cs}	Ca/K
V-45	Line 1 1301_FSP_18_CS	121	0.684	1.117	0.001	0.008	0.199	2.876	0.000	0.000	0.114	0.000	0.008	5.007	0.681	0.114	0.198	0.008	0.57
	Line 2 1301_FSP_18_CS	108	0.693	1.122	0.000	0.007	0.187	2.871	0.001	0.000	0.120	0.000	0.007	5.007	0.688	0.119	0.186	0.007	0.64
	Line 3 1301_FSP_18_CS	95	0.716	1.128	0.000	0.006	0.156	2.868	0.000	0.001	0.124	0.001	0.004	5.004	0.716	0.124	0.156	0.004	0.80
	Line 4 1301_FSP_18_CS	81	0.714	1.153	0.001	0.007	0.124	2.843	0.001	0.000	0.151	0.000	0.004	4.998	0.719	0.152	0.125	0.004	1.22
	Line 5 1301_FSP_18_CS	68	0.719	1.160	0.000	0.007	0.116	2.833	0.000	0.000	0.163	0.002	0.003	5.004	0.718	0.163	0.116	0.003	1.41
	Line 6 1301_FSP_18_CS	54	0.722	1.161	0.001	0.007	0.107	2.832	0.000	0.001	0.167	0.000	0.003	5.001	0.722	0.167	0.108	0.003	1.55
	Line 7 1301_FSP_18_CS	41	0.719	1.173	0.000	0.007	0.101	2.821	0.000	0.000	0.178	0.000	0.003	5.003	0.718	0.178	0.101	0.003	1.76
	Line 8 1301_FSP_18_CS	28	0.715	1.176	0.001	0.008	0.093	2.815	0.000	0.000	0.188	0.000	0.003	5.000	0.716	0.188	0.093	0.003	2.01
	Line 9 1301_FSP_18_CS	14	0.710	1.175	0.001	0.008	0.099	2.819	0.000	0.001	0.181	0.000	0.003	4.997	0.715	0.183	0.099	0.003	1.84
	Line 10 1301_FSP_18_CS	1	0.714	1.171	0.000	0.006	0.099	2.821	0.001	0.000	0.183	0.001	0.003	5.000	0.715	0.183	0.099	0.003	1.85
V-45	Line 1 1301_FSP_3_CS	1	0.703	1.187	0.000	0.007	0.106	2.812	0.000	0.000	0.179	0.000	0.004	4.999	0.709	0.180	0.107	0.004	1.68
	Line 2 1301_FSP_3_CS	8	0.727	1.180	0.001	0.007	0.103	2.812	0.000	0.000	0.180	0.001	0.003	5.013	0.718	0.178	0.101	0.003	1.75
	Line 3 1301_FSP_3_CS	16	0.710	1.175	0.001	0.007	0.103	2.820	0.000	0.001	0.179	0.000	0.003	4.998	0.714	0.180	0.103	0.003	1.74
	Line 4 1301_FSP_3_CS	23	0.706	1.141	0.001	0.012	0.129	2.851	0.000	0.000	0.151	0.000	0.003	4.995	0.714	0.153	0.130	0.003	1.18
	Line 5 1301_FSP_3_CS	31	0.675	1.119	0.001	0.007	0.203	2.880	0.000	0.000	0.110	0.000	0.006	4.999	0.680	0.110	0.204	0.006	0.54
	Line 6 1301_FSP_3_CS	38	0.671	1.116	0.001	0.007	0.212	2.882	0.001	0.000	0.104	0.000	0.008	5.001	0.675	0.105	0.213	0.008	0.49
	Line 7 1301_FSP_3_CS	46	0.669	1.104	0.001	0.007	0.229	2.890	0.001	0.001	0.096	0.000	0.008	5.006	0.668	0.096	0.228	0.008	0.42
	Line 8 1301_FSP_3_CS	53	0.644	1.075	0.000	0.007	0.273	2.922	0.000	0.000	0.070	0.000	0.009	4.999	0.647	0.070	0.274	0.009	0.26
	Line 9 1301_FSP_3_CS	61	0.664	1.089	0.001	0.007	0.239	2.906	0.000	0.000	0.087	0.000	0.008	5.000	0.666	0.087	0.239	0.008	0.36
	Line 10 1301_FSP_3_CS	68	0.654	1.096	0.000	0.007	0.250	2.902	0.000	0.000	0.086	0.000	0.008	5.002	0.656	0.086	0.250	0.008	0.34
	Line 11 1301_FSP_3_CS	76	0.669	1.107	0.001	0.005	0.212	2.892	0.000	0.000	0.102	0.000	0.006	4.994	0.676	0.103	0.214	0.006	0.48
V-45	Line 1 1301_FSP_9_CS	1	0.659	1.057	0.000	0.009	0.269	2.934	0.001	0.001	0.067	0.000	0.005	5.001	0.659	0.067	0.269	0.005	0.25
	Line 2 1301_FSP_9_CS	5	0.673	1.064	0.000	0.007	0.258	2.930	0.000	0.000	0.066	0.000	0.005	5.003	0.672	0.066	0.258	0.005	0.25
	Line 3 1301_FSP_9_CS	9	0.669	1.053	0.001	0.008	0.253	2.943	0.001	0.000	0.060	0.000	0.005	4.991	0.678	0.061	0.257	0.005	0.24
	Line 4 1301_FSP_9_CS	13	0.676	1.082	0.000	0.006	0.239	2.912	0.001	0.000	0.083	0.000	0.005	5.004	0.674	0.083	0.238	0.005	0.35
	Line 5 1301_FSP_9_CS	17	0.669	1.082	0.001	0.007	0.234	2.915	0.000	0.000	0.081	0.000	0.005	4.994	0.677	0.082	0.236	0.005	0.35
	Line 6 1301_FSP_9_CS	21	0.681	1.096	0.001	0.006	0.221	2.896	0.000	0.000	0.100	0.000	0.006	5.007	0.675	0.099	0.219	0.006	0.45
	Line 7 1301_FSP_9_CS	25	0.670	1.111	0.001	0.006	0.209	2.882	0.000	0.000	0.115	0.000	0.007	5.002	0.669	0.115	0.209	0.007	0.55
	Line 8 1301_FSP_9_CS	29	0.656	1.123	0.000	0.005	0.201	2.878	0.000	0.000	0.116	0.001	0.007	4.989	0.669	0.118	0.205	0.007	0.58
	Line 9 1301_FSP_9_CS	33	0.680	1.108	0.001	0.007	0.197	2.883	0.000	0.001	0.116	0.000	0.006	5.000	0.681	0.116	0.197	0.006	0.59
	Line 10 1301_FSP_9_CS	37	0.682	1.117	0.001	0.006	0.195	2.876	0.000	0.000	0.120	0.000	0.006	5.004	0.679	0.120	0.195	0.006	0.62
	Line 11 1301_FSP_9_CS	41	0.680	1.122	0.001	0.008	0.188	2.872	0.001	0.000	0.121	0.001	0.006	5.000	0.683	0.122	0.189	0.006	0.65
	Line 12 1301_FSP_9_CS	45	0.687	1.117	0.001	0.005	0.182	2.876	0.001	0.001	0.122	0.000	0.006	4.999	0.689	0.122	0.182	0.006	0.67
	Line 13 1301_FSP_9_CS	49	0.691	1.121	0.000	0.007	0.179	2.873	0.000	0.000	0.125	0.000	0.005	5.001	0.691	0.125	0.179	0.005	0.70
	Line 14 1301_FSP_9_CS	53	0.704	1.114	0.001	0.004	0.180	2.878	0.000	0.000	0.121	0.000	0.005	5.007	0.697	0.120	0.178	0.005	0.67
	Line 15 1301_FSP_9_CS	57	0.687	1.117	0.001	0.006	0.175	2.881	0.000	0.000	0.120	0.000	0.005	4.992	0.696	0.121	0.177	0.005	0.68
	Line 16 1301_FSP_9_CS	61	0.687	1.110	0.001	0.007	0.170	2.886	0.000	0.000	0.121	0.000	0.005	4.987	0.699	0.123	0.173	0.005	0.71
	Line 17 1301_FSP_9_CS	65	0.697	1.115	0.002	0.006	0.177	2.879	0.001	0.000	0.118	0.000	0.005	4.999	0.699	0.118	0.178	0.005	0.66
	Line 18 1301_FSP_9_CS	69	0.693	1.111	0.000	0.007	0.192	2.883	0.000	0.000	0.110	0.000	0.006	5.004	0.692	0.110	0.192	0.006	0.57
	Line 19 1301_FSP_9_CS	73	0.695	1.102	0.001	0.007	0.202	2.889	0.000	0.000	0.107	0.000	0.006	5.008	0.688	0.106	0.200	0.006	0.53
	Line 20 1301_FSP_9_CS	77	0.681	1.104	0.001	0.007	0.196	2.893	0.000	0.000	0.107	0.000	0.005	4.993	0.689	0.108	0.198	0.005	0.55

Table H.24: EMPA data of C-type feldspar inV-45. Data is presented in atoms per formula unit and in fractions of solid solution end member. The end members are: albite (X_{Ab}), anorthite (X_{An}), orthoclase (X_{Or}), and celsian (X_{Cs}). Distances of the line scans are directed from core towards the rim of the crystal.

V-ID	Analyses ID	Distance (μm)	Na	Al	Ti	Fe	K	Si	Mg	Mn	Ca	Sr	Ba	Sum	X_{Ab}	X_{An}	X_{Or}	X_{Cs}	Ca/K
V-45	Line 1 1301_FSP_18_CS	121	0.684	1.117	0.001	0.008	0.199	2.876	0.000	0.000	0.114	0.000	0.008	5.007	0.681	0.114	0.198	0.008	0.57
	Line 2 1301_FSP_18_CS	108	0.693	1.122	0.000	0.007	0.187	2.871	0.001	0.000	0.120	0.000	0.007	5.007	0.688	0.119	0.186	0.007	0.64
	Line 3 1301_FSP_18_CS	95	0.716	1.128	0.000	0.006	0.156	2.868	0.000	0.001	0.124	0.001	0.004	5.004	0.716	0.124	0.156	0.004	0.80
	Line 4 1301_FSP_18_CS	81	0.714	1.153	0.001	0.007	0.124	2.843	0.001	0.000	0.151	0.000	0.004	4.998	0.719	0.152	0.125	0.004	1.22
	Line 5 1301_FSP_18_CS	68	0.719	1.160	0.000	0.007	0.116	2.833	0.000	0.000	0.163	0.002	0.003	5.004	0.718	0.163	0.116	0.003	1.41
	Line 6 1301_FSP_18_CS	54	0.722	1.161	0.001	0.007	0.107	2.832	0.000	0.001	0.167	0.000	0.003	5.001	0.722	0.167	0.108	0.003	1.55
	Line 7 1301_FSP_18_CS	41	0.719	1.173	0.000	0.007	0.101	2.821	0.000	0.000	0.178	0.000	0.003	5.003	0.718	0.178	0.101	0.003	1.76
	Line 8 1301_FSP_18_CS	28	0.715	1.176	0.001	0.008	0.093	2.815	0.000	0.000	0.188	0.000	0.003	5.000	0.716	0.188	0.093	0.003	2.01
	Line 9 1301_FSP_18_CS	14	0.710	1.175	0.001	0.008	0.099	2.819	0.000	0.001	0.181	0.000	0.003	4.997	0.715	0.183	0.099	0.003	1.84
	Line 10 1301_FSP_18_CS	1	0.714	1.171	0.000	0.006	0.099	2.821	0.001	0.000	0.183	0.001	0.003	5.000	0.715	0.183	0.099	0.003	1.85
	Line 1 1301_FSP_3_CS	1	0.703	1.187	0.000	0.007	0.106	2.812	0.000	0.000	0.179	0.000	0.004	4.999	0.709	0.180	0.107	0.004	1.68
	Line 2 1301_FSP_3_CS	8	0.727	1.180	0.001	0.007	0.103	2.812	0.000	0.000	0.180	0.001	0.003	5.013	0.718	0.178	0.101	0.003	1.75
	Line 3 1301_FSP_3_CS	16	0.710	1.175	0.001	0.007	0.103	2.820	0.000	0.001	0.179	0.000	0.003	4.998	0.714	0.180	0.103	0.003	1.74
	Line 4 1301_FSP_3_CS	23	0.706	1.141	0.001	0.012	0.129	2.851	0.000	0.000	0.151	0.000	0.003	4.995	0.714	0.153	0.130	0.003	1.18
	Line 5 1301_FSP_3_CS	31	0.675	1.119	0.001	0.007	0.203	2.880	0.000	0.000	0.110	0.000	0.006	4.999	0.680	0.110	0.204	0.006	0.54
	Line 6 1301_FSP_3_CS	38	0.671	1.116	0.001	0.007	0.212	2.882	0.001	0.000	0.104	0.000	0.008	5.001	0.675	0.105	0.213	0.008	0.49
	Line 7 1301_FSP_3_CS	46	0.669	1.104	0.001	0.007	0.229	2.890	0.001	0.001	0.096	0.000	0.008	5.006	0.668	0.096	0.228	0.008	0.42
	Line 8 1301_FSP_3_CS	53	0.644	1.075	0.000	0.007	0.273	2.922	0.000	0.000	0.070	0.000	0.009	4.999	0.647	0.070	0.274	0.009	0.26
	Line 9 1301_FSP_3_CS	61	0.664	1.089	0.001	0.007	0.239	2.906	0.000	0.000	0.087	0.000	0.008	5.000	0.666	0.087	0.239	0.008	0.36
	Line 10 1301_FSP_3_CS	68	0.654	1.096	0.000	0.007	0.250	2.902	0.000	0.000	0.086	0.000	0.008	5.002	0.656	0.086	0.250	0.008	0.34
	Line 11 1301_FSP_3_CS	76	0.669	1.107	0.001	0.005	0.212	2.892	0.000	0.000	0.102	0.000	0.006	4.994	0.676	0.103	0.214	0.006	0.48
V-45	Line 1 1301_FSP_9_CS	1	0.659	1.057	0.000	0.009	0.269	2.934	0.001	0.001	0.067	0.000	0.005	5.001	0.659	0.067	0.269	0.005	0.25
	Line 2 1301_FSP_9_CS	5	0.673	1.064	0.000	0.007	0.258	2.930	0.000	0.000	0.066	0.000	0.005	5.003	0.672	0.066	0.258	0.005	0.25
	Line 3 1301_FSP_9_CS	9	0.669	1.053	0.001	0.008	0.253	2.943	0.001	0.000	0.060	0.000	0.005	4.991	0.678	0.061	0.257	0.005	0.24
	Line 4 1301_FSP_9_CS	13	0.676	1.082	0.000	0.006	0.239	2.912	0.001	0.000	0.083	0.000	0.005	5.004	0.674	0.083	0.238	0.005	0.35
	Line 5 1301_FSP_9_CS	17	0.669	1.082	0.001	0.007	0.234	2.915	0.000	0.000	0.081	0.000	0.005	4.994	0.677	0.082	0.236	0.005	0.35
	Line 6 1301_FSP_9_CS	21	0.681	1.096	0.001	0.006	0.221	2.896	0.000	0.000	0.100	0.000	0.006	5.007	0.675	0.099	0.219	0.006	0.45
	Line 7 1301_FSP_9_CS	25	0.670	1.111	0.001	0.006	0.209	2.882	0.000	0.000	0.115	0.000	0.007	5.002	0.669	0.115	0.209	0.007	0.55
	Line 8 1301_FSP_9_CS	29	0.656	1.123	0.000	0.005	0.201	2.878	0.000	0.000	0.116	0.001	0.007	4.989	0.669	0.118	0.205	0.007	0.58
	Line 9 1301_FSP_9_CS	33	0.680	1.108	0.001	0.007	0.197	2.883	0.000	0.001	0.116	0.000	0.006	5.000	0.681	0.116	0.197	0.006	0.59
	Line 10 1301_FSP_9_CS	37	0.682	1.117	0.001	0.006	0.195	2.876	0.000	0.000	0.120	0.000	0.006	5.004	0.679	0.120	0.195	0.006	0.62
	Line 11 1301_FSP_9_CS	41	0.680	1.122	0.001	0.008	0.188	2.872	0.001	0.000	0.121	0.001	0.006	5.000	0.683	0.122	0.189	0.006	0.65
	Line 12 1301_FSP_9_CS	45	0.687	1.117	0.001	0.005	0.182	2.876	0.001	0.001	0.122	0.000	0.006	4.999	0.689	0.122	0.182	0.006	0.67
	Line 13 1301_FSP_9_CS	49	0.691	1.121	0.000	0.007	0.179	2.873	0.000	0.000	0.125	0.000	0.005	5.001	0.691	0.125	0.179	0.005	0.70
	Line 14 1301_FSP_9_CS	53	0.704	1.114	0.001	0.004	0.180	2.878	0.000	0.000	0.121	0.000	0.005	5.007	0.697	0.120	0.178	0.005	0.67
	Line 15 1301_FSP_9_CS	57	0.687	1.117	0.001	0.006	0.175	2.881	0.000	0.000	0.120	0.000	0.005	4.992	0.696	0.121	0.177	0.005	0.68
	Line 16 1301_FSP_9_CS	61	0.687	1.110	0.001	0.007	0.170	2.886	0.000	0.000	0.121	0.000	0.005	4.987	0.699	0.123	0.173	0.005	0.71
	Line 17 1301_FSP_9_CS	65	0.697	1.115	0.002	0.006	0.177	2.879	0.001	0.000	0.118	0.000	0.005	4.999	0.699	0.118	0.178	0.005	0.66
	Line 18 1301_FSP_9_CS	69	0.693	1.111	0.000	0.007	0.192	2.883	0.000	0.000	0.110	0.000	0.006	5.004	0.692	0.110	0.192	0.006	0.57
	Line 19 1301_FSP_9_CS	73	0.695	1.102	0.001	0.007	0.202	2.889	0.000	0.000	0.107	0.000	0.006	5.008	0.688	0.106	0.200	0.006	0.53
	Line 20 1301_FSP_9_CS	77	0.681	1.104	0.001	0.007	0.196	2.893	0.000	0.000	0.107	0.000	0.005	4.993	0.689	0.108	0.198	0.005	0.55

Table H.25: EMPA data of C-type feldspar inV-45. Data is presented in atoms per formula unit and in fractions of solid solution end member. The end members are: albite (X_{Ab}), anorthite (X_{An}), orthoclase (X_{Or}), and celsian (X_{Cs}). Distances of the line scans are directed from core towards the rim of the crystal.

V-ID	Analyses ID	Distance (μm)	Na	Al	Ti	Fe	K	Si	Mg	Mn	Ca	Sr	Ba	Sum	X_{Ab}	X_{An}	X_{Or}	X_{Cs}	Ca/K
V-45	Line 1 1301_FSP_12_CS	1	0.665	1.092	0.001	0.007	0.238	2.900	0.000	0.001	0.091	0.000	0.008	5.004	0.663	0.090	0.238	0.008	0.38
	Line 2 1301_FSP_12_CS	11	0.665	1.097	0.001	0.006	0.233	2.899	0.000	0.000	0.090	0.000	0.008	5.000	0.668	0.091	0.234	0.008	0.39
	Line 3 1301_FSP_12_CS	20	0.664	1.099	0.000	0.007	0.221	2.896	0.000	0.000	0.098	0.003	0.008	4.997	0.670	0.099	0.223	0.008	0.44
	Line 4 1301_FSP_12_CS	30	0.659	1.098	0.001	0.006	0.220	2.898	0.000	0.000	0.100	0.000	0.008	4.991	0.668	0.101	0.223	0.008	0.45
	Line 5 1301_FSP_12_CS	40	0.679	1.099	0.001	0.006	0.218	2.893	0.000	0.000	0.099	0.000	0.008	5.005	0.676	0.099	0.217	0.008	0.46
	Line 6 1301_FSP_12_CS	50	0.659	1.108	0.001	0.005	0.208	2.891	0.000	0.000	0.106	0.000	0.008	4.988	0.671	0.108	0.212	0.008	0.51
	Line 7 1301_FSP_12_CS	59	0.687	1.116	0.001	0.006	0.201	2.876	0.001	0.000	0.114	0.000	0.008	5.009	0.680	0.113	0.199	0.007	0.57
	Line 8 1301_FSP_12_CS	69	0.679	1.120	0.002	0.007	0.186	2.875	0.000	0.000	0.119	0.001	0.007	4.996	0.685	0.120	0.188	0.007	0.64
	Line 9 1301_FSP_12_CS	79	0.676	1.121	0.001	0.006	0.188	2.876	0.000	0.000	0.119	0.000	0.006	4.995	0.683	0.120	0.190	0.007	0.63
	Line 10 1301_FSP_12_CS	89	0.685	1.116	0.001	0.007	0.188	2.880	0.000	0.000	0.114	0.000	0.007	4.998	0.689	0.115	0.189	0.007	0.61
	Line 11 1301_FSP_12_CS	98	0.699	1.119	0.001	0.007	0.185	2.873	0.000	0.000	0.117	0.000	0.007	5.008	0.694	0.116	0.183	0.007	0.63
	Line 12 1301_FSP_12_CS	108	0.685	1.113	0.001	0.006	0.186	2.880	0.002	0.000	0.117	0.000	0.007	4.998	0.688	0.118	0.187	0.007	0.63
	Line 13 1301_FSP_12_CS	118	0.676	1.107	0.001	0.004	0.201	2.891	0.000	0.001	0.105	0.000	0.007	4.993	0.684	0.106	0.203	0.007	0.52
	Line 14 1301_FSP_12_CS	128	0.695	1.205	0.001	0.006	0.086	2.791	0.000	0.000	0.210	0.001	0.002	4.996	0.699	0.211	0.087	0.002	2.43
	Line 15 1301_FSP_12_CS	137	0.718	1.177	0.001	0.006	0.097	2.816	0.000	0.000	0.184	0.000	0.003	5.002	0.717	0.184	0.097	0.003	1.89
	Line 16 1301_FSP_12_CS	147	0.719	1.189	0.001	0.007	0.090	2.801	0.000	0.001	0.198	0.000	0.002	5.008	0.713	0.196	0.089	0.002	2.21
	Line 17 1301_FSP_12_CS	157	0.694	1.128	0.001	0.007	0.171	2.866	0.000	0.001	0.128	0.000	0.005	5.001	0.696	0.128	0.171	0.005	0.75
	Line 18 1301_FSP_12_CS	167	0.651	1.052	0.003	0.018	0.190	2.929	0.000	0.001	0.116	0.000	0.004	4.963	0.678	0.120	0.198	0.004	0.61
	Line 19 1301_FSP_12_CS	176	0.690	1.089	0.002	0.007	0.215	2.901	0.001	0.000	0.094	0.000	0.007	5.006	0.686	0.094	0.214	0.007	0.44
	Line 20 1301_FSP_12_CS	186	0.678	1.103	0.000	0.007	0.206	2.891	0.000	0.000	0.106	0.000	0.007	4.999	0.680	0.106	0.207	0.007	0.51
	Line 21 1301_FSP_12_CS	196	0.339	0.790	0.008	0.109	0.289	3.160	0.004	0.003	0.047	0.000	0.002	4.751	0.502	0.070	0.426	0.002	0.16
	Line 22 1301_FSP_12_CS	206	0.668	1.102	0.001	0.009	0.215	2.896	0.001	0.000	0.094	0.000	0.007	4.993	0.679	0.095	0.219	0.007	0.44
	Line 23 1301_FSP_12_CS	215	0.659	1.105	0.001	0.007	0.211	2.890	0.001	0.001	0.105	0.006	0.006	4.992	0.671	0.107	0.215	0.006	0.50
	Line 24 1301_FSP_12_CS	225	0.718	1.179	0.001	0.007	0.091	2.808	0.001	0.000	0.198	0.001	0.003	5.006	0.711	0.196	0.090	0.003	2.18
	Line 25 1301_FSP_12_CS	235	0.696	1.134	0.001	0.006	0.154	2.861	0.000	0.000	0.139	0.001	0.005	4.996	0.701	0.140	0.155	0.005	0.90
	Line 26 1301_FSP_12_CS	245	0.669	1.087	0.000	0.007	0.227	2.906	0.001	0.000	0.095	0.000	0.007	4.999	0.670	0.095	0.228	0.007	0.42
	Line 27 1301_FSP_12_CS	254	0.682	1.085	0.000	0.005	0.203	2.906	0.001	0.000	0.106	0.000	0.006	4.994	0.683	0.106	0.204	0.007	0.52
	Line 28 1301_FSP_12_CS	264	0.705	1.151	0.001	0.007	0.135	2.843	0.001	0.000	0.154	0.000	0.004	5.001	0.706	0.154	0.136	0.004	1.14
	Line 29 1301_FSP_12_CS	274	0.696	1.141	0.000	0.006	0.141	2.854	0.000	0.000	0.152	0.000	0.004	4.994	0.701	0.153	0.142	0.004	1.08
	Line 30 1301_FSP_12_CS	283	0.680	1.193	0.001	0.005	0.099	2.807	0.001	0.000	0.197	0.001	0.002	4.986	0.695	0.201	0.101	0.002	1.99
	Line 31 1301_FSP_12_CS	293	0.678	1.130	0.001	0.007	0.160	2.866	0.000	0.000	0.137	0.001	0.006	4.986	0.691	0.140	0.163	0.006	0.85
	Line 32 1301_FSP_12_CS	303	0.656	1.109	0.001	0.005	0.209	2.894	0.000	0.001	0.101	0.000	0.007	4.983	0.674	0.104	0.215	0.007	0.48
	Line 33 1301_FSP_12_CS	313	0.681	1.105	0.001	0.006	0.197	2.891	0.000	0.000	0.106	0.000	0.006	4.995	0.688	0.107	0.199	0.006	0.54
	Line 34 1301_FSP_12_CS	322	0.674	1.107	0.001	0.005	0.203	2.891	0.000	0.000	0.105	0.000	0.007	4.993	0.682	0.106	0.206	0.007	0.52
	Line 35 1301_FSP_12_CS	332	0.667	1.113	0.001	0.007	0.191	2.884	0.001	0.001	0.114	0.000	0.007	4.986	0.681	0.117	0.195	0.007	0.60
	Line 36 1301_FSP_12_CS	342	0.682	1.121	0.002	0.005	0.187	2.874	0.000	0.001	0.119	0.000	0.007	4.998	0.685	0.120	0.188	0.007	0.64
	Line 37 1301_FSP_12_CS	352	0.671	1.111	0.000	0.005	0.197	2.886	0.001	0.000	0.112	0.001	0.007	4.992	0.680	0.113	0.200	0.008	0.56
	Line 38 1301_FSP_12_CS	361	0.665	1.099	0.000	0.005	0.222	2.896	0.000	0.000	0.101	0.000	0.009	4.999	0.667	0.101	0.223	0.009	0.45
	Line 39 1301_FSP_12_CS	371	0.691	1.083	0.000	0.008	0.223	2.905	0.000	0.000	0.093	0.000	0.008	5.011	0.681	0.092	0.220	0.008	0.42
	Line 40 1301_FSP_12_CS	381	0.670	1.090	0.001	0.007	0.223	2.901	0.000	0.000	0.100	0.000	0.008	5.000	0.670	0.100	0.222	0.008	0.45

Table H.26: EMPA data of C-type feldspar inV-45. Data is presented in atoms per formula unit and in fractions of solid solution end member. The end members are: albite (X_{Ab}), anorthite (X_{An}), orthoclase (X_{Or}), and celsian (X_{Cs}). Distances of the line scans are directed from core towards the rim of the crystal.

V-ID	Analyses ID	Distance (μm)	Na	Al	Ti	Fe	K	Si	Mg	Mn	Ca	Sr	Ba	Sum	X_{Ab}	X_{An}	X_{Or}	X_{Cs}	Ca/K
V-45	Line 1 ELV_1301_FSP_12b	0	0.661	1.120	0.001	0.011	0.201	2.878	0.000	0.000	0.108	0.000	0.007	4.986	0.676	0.110	0.206	0.007	0.53
	Line 2 ELV_1301_FSP_12b	4	0.650	1.104	0.001	0.010	0.236	2.893	0.000	0.000	0.091	0.000	0.007	4.992	0.661	0.092	0.239	0.008	0.39
	Line 3 ELV_1301_FSP_12b	8	0.619	1.085	0.002	0.021	0.264	2.904	0.000	0.002	0.081	0.000	0.008	4.987	0.637	0.084	0.272	0.008	0.31
	Line 4 ELV_1301_FSP_12b	13	0.515	0.957	0.005	0.059	0.286	3.011	0.001	0.002	0.062	0.000	0.005	4.902	0.593	0.072	0.329	0.006	0.22
	Line 5 ELV_1301_FSP_12b	17	0.477	0.928	0.005	0.069	0.273	3.039	0.002	0.001	0.064	0.000	0.003	4.861	0.584	0.078	0.334	0.003	0.23
	Line 6 ELV_1301_FSP_12b	21	0.557	1.039	0.002	0.034	0.221	2.957	0.001	0.000	0.089	0.000	0.004	4.905	0.640	0.102	0.254	0.005	0.40
	Line 7 ELV_1301_FSP_12b	25	0.623	1.066	0.000	0.024	0.217	2.924	0.000	0.000	0.095	0.000	0.005	4.957	0.662	0.101	0.231	0.005	0.44
	Line 8 ELV_1301_FSP_12b	29	0.378	0.794	0.009	0.109	0.285	3.147	0.004	0.001	0.045	0.000	0.000	4.772	0.533	0.064	0.402	0.000	0.16
	Line 9 ELV_1301_FSP_12b	34	0.606	1.046	0.002	0.023	0.248	2.943	0.001	0.001	0.079	0.000	0.006	4.955	0.645	0.084	0.264	0.006	0.32
	Line 10 ELV_1301_FSP_12b	38	0.630	1.112	0.000	0.009	0.236	2.893	0.000	0.000	0.092	0.000	0.007	4.979	0.653	0.095	0.245	0.007	0.39
	Line 11 ELV_1301_FSP_12b	42	0.625	1.125	0.001	0.009	0.239	2.882	0.000	0.000	0.092	0.000	0.007	4.981	0.649	0.095	0.248	0.008	0.38
	Line 12 ELV_1301_FSP_12b	46	0.611	1.118	0.001	0.008	0.273	2.890	0.000	0.000	0.076	0.000	0.009	4.986	0.631	0.078	0.282	0.009	0.28
	Line 13 ELV_1301_FSP_12b	50	0.601	1.094	0.001	0.012	0.282	2.908	0.000	0.000	0.072	0.001	0.009	4.980	0.623	0.075	0.292	0.010	0.26
	Line 14 ELV_1301_FSP_12b	54	0.602	1.108	0.002	0.008	0.279	2.898	0.000	0.000	0.074	0.001	0.009	4.980	0.625	0.076	0.289	0.009	0.26
	Line 15 ELV_1301_FSP_12b	59	0.604	1.111	0.001	0.008	0.264	2.898	0.000	0.000	0.080	0.000	0.009	4.974	0.632	0.083	0.276	0.009	0.30
	Line 16 ELV_1301_FSP_12b	63	0.578	1.118	0.001	0.008	0.254	2.896	0.000	0.000	0.090	0.001	0.009	4.954	0.621	0.096	0.273	0.010	0.35
	Line 17 ELV_1301_FSP_12b	67	0.622	1.132	0.001	0.010	0.242	2.872	0.000	0.001	0.101	0.000	0.008	4.988	0.639	0.104	0.249	0.008	0.42
	Line 18 ELV_1301_FSP_12b	71	0.636	1.135	0.001	0.009	0.207	2.872	0.000	0.000	0.109	0.000	0.005	4.974	0.665	0.113	0.216	0.005	0.52
	Line 19 ELV_1301_FSP_12b	75	0.658	1.137	0.001	0.010	0.187	2.871	0.000	0.001	0.108	0.000	0.004	4.977	0.687	0.113	0.196	0.004	0.58
	Line 20 ELV_1301_FSP_12b	80	0.616	1.106	0.002	0.011	0.267	2.898	0.001	0.000	0.078	0.000	0.005	4.983	0.638	0.081	0.276	0.005	0.29
	Line 21 ELV_1301_FSP_12b	84	0.628	1.111	0.001	0.008	0.233	2.895	0.001	0.000	0.092	0.000	0.004	4.973	0.656	0.096	0.244	0.004	0.39
	Line 22 ELV_1301_FSP_12b	88	0.638	1.125	0.000	0.006	0.223	2.882	0.001	0.000	0.100	0.000	0.004	4.979	0.661	0.103	0.231	0.004	0.45
	Line 23 ELV_1301_FSP_12b	92	0.660	1.132	0.001	0.010	0.202	2.874	0.000	0.000	0.102	0.000	0.004	4.985	0.681	0.105	0.209	0.004	0.50
	Line 24 ELV_1301_FSP_12b	96	0.675	1.123	0.001	0.008	0.196	2.880	0.000	0.000	0.101	0.000	0.003	4.988	0.692	0.103	0.201	0.003	0.51
	Line 25 ELV_1301_FSP_12b	101	0.663	1.120	0.001	0.009	0.196	2.888	0.000	0.000	0.095	0.000	0.003	4.975	0.692	0.100	0.205	0.003	0.49
	Line 26 ELV_1301_FSP_12b	105	0.670	1.111	0.000	0.009	0.211	2.892	0.000	0.001	0.089	0.000	0.003	4.988	0.688	0.092	0.217	0.004	0.42
	Line 27 ELV_1301_FSP_12b	109	0.667	1.122	0.000	0.009	0.209	2.880	0.000	0.000	0.100	0.000	0.004	4.991	0.680	0.102	0.214	0.004	0.48
	Line 28 ELV_1301_FSP_12b	113	0.646	1.142	0.001	0.008	0.194	2.866	0.001	0.000	0.112	0.000	0.006	4.976	0.674	0.117	0.202	0.006	0.58
	Line 29 ELV_1301_FSP_12b	117	0.640	1.161	0.002	0.007	0.180	2.854	0.001	0.001	0.117	0.000	0.006	4.969	0.679	0.124	0.191	0.006	0.65
	Line 30 ELV_1301_FSP_12b	122	0.673	1.144	0.001	0.008	0.170	2.862	0.000	0.000	0.118	0.000	0.005	4.980	0.697	0.122	0.176	0.005	0.69

Table H.27: EMPA data of R-type feldspar inV-279. Data is presented in atoms per formula unit and in fractions of solid solution end member. The end members are: albite (X_{Ab}), anorthite (X_{An}), orthoclase (X_{Or}), and celsian (X_{Cs}). Distances of the line scans are directed from core towards the rim of the crystal.

V-ID	Analyses ID	Distance (μm)	Na	Al	Ti	Fe	K	Si	Mg	Mn	Ca	Sr	Ba	Sum	X_{Ab}	X_{An}	X_{Or}	X_{Cs}	Ca/K
V-279	Line 1 1322_P_1_CS	1	0.713	1.095	0.001	0.007	0.191	2.899	0.000	0.001	0.091	0.000	0.005	5.004	0.713	0.091	0.191	0.005	0.488
	Line 2 1322_P_1_CS	12	0.716	1.102	0.001	0.006	0.187	2.896	0.000	0.000	0.091	0.000	0.004	5.004	0.717	0.091	0.187	0.004	0.462
	Line 3 1322_P_1_CS	24	0.719	1.094	0.000	0.007	0.192	2.901	0.000	0.000	0.089	0.000	0.005	5.007	0.716	0.088	0.191	0.005	0.465
	Line 4 1322_P_1_CS	35	0.709	1.098	0.001	0.007	0.193	2.900	0.000	0.000	0.090	0.000	0.004	5.001	0.712	0.090	0.194	0.004	0.471
	Line 5 1322_P_1_CS	46	0.714	1.096	0.000	0.006	0.192	2.901	0.000	0.000	0.090	0.000	0.004	5.004	0.714	0.090	0.192	0.004	0.444
	Line 6 1322_P_1_CS	57	0.712	1.090	0.001	0.007	0.195	2.907	0.000	0.000	0.086	0.000	0.004	5.001	0.714	0.087	0.195	0.004	0.382
	Line 7 1322_P_1_CS	69	0.720	1.089	0.001	0.007	0.205	2.907	0.000	0.000	0.078	0.000	0.004	5.011	0.715	0.078	0.203	0.004	0.340
	Line 8 1322_P_1_CS	80	0.700	1.085	0.000	0.006	0.216	2.915	0.000	0.000	0.074	0.001	0.003	5.000	0.705	0.074	0.218	0.004	0.163
	Line 9 1322_P_1_CS	91	0.663	1.056	0.001	0.006	0.281	2.943	0.001	0.000	0.046	0.000	0.004	5.000	0.667	0.046	0.283	0.004	0.126
	Line 10 1322_P_1_CS	102	0.649	1.041	0.000	0.006	0.308	2.955	0.000	0.000	0.039	0.000	0.004	5.003	0.649	0.039	0.308	0.004	0.179
	Line 11 1322_P_1_CS	114	0.661	1.056	0.001	0.006	0.271	2.945	0.000	0.000	0.049	0.000	0.004	4.993	0.672	0.049	0.275	0.004	0.181
	Line 12 1322_P_1_CS	125	0.665	1.058	0.000	0.006	0.273	2.942	0.000	0.000	0.049	0.000	0.004	4.998	0.671	0.050	0.275	0.004	0.117
	Line 13 1322_P_1_CS	136	0.628	1.047	0.000	0.007	0.312	2.956	0.000	0.000	0.037	0.000	0.004	4.991	0.640	0.037	0.318	0.004	0.159
	Line 14 1322_P_1_CS	147	0.652	1.056	0.001	0.005	0.288	2.944	0.000	0.000	0.046	0.001	0.004	4.997	0.659	0.046	0.291	0.004	0.157
	Line 15 1322_P_1_CS	159	0.659	1.059	0.001	0.005	0.287	2.940	0.000	0.000	0.045	0.002	0.004	5.003	0.662	0.045	0.288	0.004	0.119
	Line 16 1322_P_1_CS	170	0.658	1.038	0.001	0.007	0.311	2.954	0.000	0.002	0.037	0.000	0.004	5.011	0.651	0.037	0.308	0.004	0.101
	Line 17 1322_P_1_CS	181	0.649	1.031	0.001	0.005	0.320	2.963	0.000	0.000	0.032	0.000	0.004	5.005	0.645	0.032	0.319	0.004	0.090
	Line 18 1322_P_1_CS	192	0.613	1.040	0.000	0.005	0.329	2.965	0.001	0.000	0.030	0.000	0.004	4.986	0.629	0.030	0.337	0.004	0.100
	Line 19 1322_P_1_CS	204	0.628	1.040	0.001	0.006	0.328	2.959	0.000	0.001	0.033	0.000	0.003	4.998	0.633	0.033	0.330	0.003	0.095
	Line 20 1322_P_1_CS	215	0.638	1.038	0.001	0.007	0.331	2.958	0.000	0.000	0.031	0.000	0.003	5.007	0.636	0.031	0.330	0.003	0.602
V-279	Line 1 1322_FSP_22_CS	1	0.711	1.114	0.002	0.009	0.176	2.882	0.000	0.000	0.106	0.000	0.003	5.003	0.713	0.107	0.177	0.003	0.448
	Line 2 1322_FSP_22_CS	16	0.728	1.086	0.002	0.008	0.194	2.905	0.000	0.000	0.087	0.000	0.003	5.011	0.719	0.086	0.192	0.003	0.569
	Line 3 1322_FSP_22_CS	31	0.718	1.097	0.001	0.008	0.173	2.899	0.000	0.000	0.098	0.000	0.003	4.997	0.724	0.099	0.174	0.003	0.442
	Line 4 1322_FSP_22_CS	46	0.701	1.087	0.002	0.005	0.192	2.913	0.000	0.001	0.085	0.000	0.003	4.988	0.715	0.087	0.196	0.003	0.409
	Line 5 1322_FSP_22_CS	61	0.719	1.085	0.000	0.006	0.196	2.912	0.000	0.000	0.080	0.000	0.003	5.003	0.720	0.080	0.196	0.003	0.344
	Line 6 1322_FSP_22_CS	76	0.719	1.076	0.001	0.008	0.212	2.918	0.000	0.001	0.073	0.000	0.004	5.010	0.713	0.072	0.211	0.004	0.402
	Line 7 1322_FSP_22_CS	91	0.722	1.079	0.000	0.008	0.196	2.916	0.000	0.000	0.079	0.000	0.004	5.004	0.721	0.079	0.196	0.004	0.349
	Line 8 1322_FSP_22_CS	106	0.708	1.084	0.001	0.007	0.208	2.916	0.001	0.000	0.073	0.000	0.004	5.000	0.713	0.073	0.210	0.004	1.753
	Line 9 1322_FSP_22_CS	121	0.751	1.170	0.000	0.007	0.092	2.827	0.001	0.000	0.161	0.000	0.002	5.010	0.747	0.160	0.091	0.002	2.061
	Line 10 1322_FSP_22_CS	137	0.747	1.178	0.001	0.006	0.083	2.819	0.001	0.000	0.171	0.000	0.001	5.007	0.745	0.171	0.083	0.001	1.035
	Line 11 1322_FSP_22_CS	152	0.754	1.138	0.001	0.008	0.128	2.853	0.000	0.000	0.132	0.001	0.002	5.017	0.742	0.130	0.126	0.002	0.259
	Line 12 1322_FSP_22_CS	167	0.677	1.066	0.001	0.006	0.238	2.935	0.000	0.000	0.062	0.000	0.004	4.988	0.691	0.063	0.242	0.004	0.280
	Line 13 1322_FSP_22_CS	182	0.703	1.076	0.000	0.006	0.232	2.922	0.000	0.000	0.065	0.000	0.003	5.007	0.701	0.065	0.231	0.003	0.362
	Line 14 1322_FSP_22_CS	197	0.728	1.083	0.000	0.007	0.209	2.910	0.000	0.001	0.076	0.000	0.004	5.017	0.716	0.074	0.205	0.004	0.292
	Line 15 1322_FSP_22_CS	212	0.689	1.070	0.001	0.008	0.227	2.929	0.000	0.000	0.066	0.000	0.004	4.994	0.699	0.067	0.230	0.004	0.455
	Line 16 1322_FSP_22_CS	227	0.704	1.100	0.000	0.007	0.195	2.900	0.000	0.001	0.089	0.000	0.004	5.000	0.710	0.089	0.196	0.004	0.262
	Line 17 1322_FSP_22_CS	242	0.507	0.985	0.013	0.138	0.272	2.942	0.006	0.005	0.071	0.000	0.003	4.942	0.595	0.084	0.319	0.003	0.425
	Line 18 1322_FSP_22_CS	257	0.705	1.092	0.001	0.007	0.192	2.910	0.000	0.001	0.081	0.000	0.003	4.992	0.718	0.083	0.195	0.003	0.336
	Line 19 1322_FSP_22_CS	272	0.710	1.080	0.000	0.006	0.213	2.918	0.000	0.000	0.071	0.000	0.005	5.003	0.711	0.072	0.213	0.005	0.227
	Line 20 1322_FSP_22_CS	287	0.691	1.067	0.001	0.007	0.247	2.930	0.001	0.000	0.056	0.000	0.005	5.004	0.692	0.056	0.247	0.005	0.156
	Line 21 1322_FSP_22_CS	302	0.672	1.047	0.002	0.007	0.284	2.946	0.000	0.000	0.044	0.000	0.005	5.007	0.668	0.044	0.282	0.005	0.161
	Line 22 1322_FSP_22_CS	317	0.684	1.050	0.001	0.007	0.276	2.943	0.000	0.000	0.044	0.000	0.005	5.011	0.678	0.044	0.274	0.005	0.130
	Line 23 1322_FSP_22_CS	332	0.659	1.045	0.000	0.006	0.295	2.953	0.000	0.000	0.038	0.000	0.004	5.001	0.661	0.039	0.297	0.004	0.111
	Line 24 1322_FSP_22_CS	347	0.657	1.042	0.000	0.007	0.307	2.955	0.000	0.000	0.034	0.000	0.004	5.006	0.656	0.034	0.307	0.004	0.107
	Line 25 1322_FSP_22_CS	362	0.657	1.046	0.001	0.006	0.312	2.951	0.000	0.000	0.033	0.000	0.003	5.010	0.653	0.033	0.310	0.003	0.105
	Line 26 1322_FSP_22_CS	378	0.629	1.044	0.001	0.007	0.315	2.957	0.000	0.001	0.033	0.000	0.004	4.992	0.641	0.034	0.321	0.004	0.081
	Line 27 1322_FSP_22_CS	393	0.621	1.029	0.001	0.006	0.339	2.969	0.000	0.000	0.027	0.000	0.003	4.996	0.627	0.028	0.342	0.003	0.074
	Line 28 1322_FSP_22_CS	408	0.620	1.024	0.000	0.006	0.344	2.973	0.000	0.001	0.026	0.000	0.003	4.997	0.625	0.026	0.347	0.003	0.076
	Line 29 1322_FSP_22_CS	423	0.609	1.033	0.001	0.006	0.349	2.967	0.001	0.000	0.026	0.000	0.002	4.995	0.617	0.027	0.353	0.002	0.075
	Line 30 1322_FSP_22_CS	438	0.607	1.035	0.001	0.005	0.353	2.965	0.000	0.000	0.026	0.000	0.003	4.996	0.614	0.027	0.357	0.003	0.103

Table H.28: EMPA data of R-type feldspar inV-254. Data is presented in atoms per formula unit and in fractions of solid solution end member. The end members are: albite (X_{Ab}), anorthite (X_{An}), orthoclase (X_{Or}), and celsian (X_{Cs}). Distances of the line scans are directed from core towards the rim of the crystal.

V-ID	Analyses ID	Distance (μm)	Na	Al	Ti	Fe	K	Si	Mg	Mn	Ca	Sr	Ba	Sum	X_{Ab}	X_{An}	X_{Or}	X_{Cs}	Ca/K
V-254	Line 1 1319_FSP_2_CS	1	0.576	1.075	0.001	0.004	0.361	2.919	0.000	0.000	0.054	0.000	0.021	5.011	0.569	0.053	0.357	0.021	0.153
	Line 2 1319_FSP_2_CS	13	0.588	1.068	0.002	0.005	0.360	2.920	0.000	0.000	0.055	0.000	0.019	5.018	0.576	0.054	0.352	0.019	0.136
	Line 3 1319_FSP_2_CS	25	0.579	1.064	0.002	0.005	0.364	2.928	0.000	0.000	0.049	0.000	0.018	5.010	0.573	0.049	0.360	0.018	0.140
	Line 4 1319_FSP_2_CS	37	0.584	1.070	0.002	0.006	0.354	2.925	0.000	0.001	0.049	0.001	0.015	5.007	0.582	0.049	0.353	0.015	0.127
	Line 5 1319_FSP_2_CS	49	0.571	1.059	0.002	0.005	0.377	2.934	0.000	0.000	0.048	0.000	0.013	5.008	0.566	0.047	0.374	0.013	0.110
	Line 6 1319_FSP_2_CS	61	0.577	1.048	0.002	0.004	0.385	2.944	0.000	0.000	0.042	0.000	0.008	5.011	0.570	0.042	0.380	0.008	0.098
	Line 7 1319_FSP_2_CS	73	0.536	1.047	0.001	0.004	0.399	2.955	0.001	0.000	0.039	0.000	0.007	4.988	0.546	0.040	0.407	0.007	0.105
	Line 8 1319_FSP_2_CS	85	0.557	1.044	0.002	0.004	0.391	2.953	0.000	0.000	0.041	0.000	0.005	4.997	0.561	0.041	0.393	0.005	0.107
	Line 9 1319_FSP_2_CS	98	0.572	1.046	0.001	0.004	0.391	2.950	0.000	0.000	0.042	0.000	0.004	5.008	0.567	0.041	0.388	0.004	0.110
	Line 10 1319_FSP_2_CS	110	0.581	1.045	0.001	0.005	0.381	2.948	0.000	0.000	0.042	0.000	0.005	5.009	0.576	0.042	0.378	0.005	0.103
	Line 11 1319_FSP_2_CS	122	0.564	1.050	0.002	0.005	0.396	2.946	0.000	0.000	0.041	0.000	0.005	5.008	0.561	0.041	0.394	0.005	0.160
	Line 12 1319_FSP_2_CS	134	0.605	1.063	0.000	0.005	0.345	2.932	0.000	0.000	0.055	0.000	0.005	5.011	0.599	0.055	0.341	0.004	0.111
	Line 13 1319_FSP_2_CS	146	0.577	1.049	0.001	0.005	0.382	2.947	0.001	0.000	0.042	0.000	0.004	5.008	0.574	0.042	0.380	0.004	0.132
	Line 14 1319_FSP_2_CS	158	0.590	1.044	0.001	0.005	0.364	2.948	0.001	0.001	0.048	0.000	0.003	5.005	0.587	0.048	0.362	0.003	0.131
	Line 15 1319_FSP_2_CS	170	0.577	1.055	0.002	0.003	0.361	2.945	0.000	0.001	0.047	0.000	0.004	4.995	0.583	0.048	0.365	0.004	0.165
	Line 16 1319_FSP_2_CS	182	0.627	1.056	0.000	0.004	0.336	2.935	0.000	0.000	0.056	0.000	0.003	5.018	0.614	0.054	0.329	0.003	0.185
	Line 17 1319_FSP_2_CS	194	0.616	1.066	0.000	0.005	0.326	2.931	0.000	0.000	0.060	0.000	0.002	5.007	0.613	0.060	0.324	0.002	0.193
	Line 18 1319_FSP_2_CS	206	0.604	1.068	0.002	0.003	0.321	2.930	0.000	0.001	0.062	0.002	0.002	4.996	0.611	0.063	0.324	0.002	0.187
	Line 19 1319_FSP_2_CS	218	0.619	1.068	0.002	0.004	0.324	2.927	0.000	0.000	0.061	0.001	0.002	5.009	0.616	0.060	0.322	0.002	0.159
	Line 20 1319_FSP_2_CS	230	0.614	1.056	0.001	0.005	0.335	2.940	0.000	0.000	0.053	0.000	0.002	5.005	0.611	0.053	0.334	0.002	2.784
V-254	Line 1 1319_FSP_4_CS	1	0.515	1.058	0.001	0.004	0.414	2.948	0.000	0.001	0.043	0.000	0.002	4.987	0.529	0.044	0.425	0.002	0.086
	Line 2 1319_FSP_4_CS	28	0.491	1.057	0.001	0.004	0.431	2.954	0.000	0.000	0.037	0.000	0.003	4.978	0.510	0.039	0.448	0.003	0.106
	Line 3 1319_FSP_4_CS	55	0.521	1.065	0.000	0.005	0.401	2.945	0.000	0.000	0.043	0.000	0.003	4.983	0.538	0.044	0.415	0.003	0.102
	Line 4 1319_FSP_4_CS	81	0.508	1.065	0.001	0.005	0.403	2.948	0.000	0.000	0.041	0.000	0.002	4.974	0.532	0.043	0.422	0.002	0.175
	Line 5 1319_FSP_4_CS	108	0.575	1.077	0.000	0.005	0.337	2.931	0.000	0.000	0.059	0.000	0.003	4.987	0.590	0.061	0.346	0.003	0.155
	Line 6 1319_FSP_4_CS	135	0.553	1.074	0.000	0.005	0.357	2.935	0.000	0.000	0.055	0.000	0.003	4.982	0.572	0.057	0.368	0.003	0.140
	Line 7 1319_FSP_4_CS	162	0.552	1.065	0.001	0.004	0.364	2.942	0.001	0.000	0.051	0.000	0.003	4.982	0.569	0.053	0.376	0.003	0.208
	Line 8 1319_FSP_4_CS	189	0.591	1.083	0.001	0.005	0.319	2.922	0.001	0.000	0.067	0.000	0.003	4.991	0.603	0.068	0.326	0.003	0.138
	Line 9 1319_FSP_4_CS	215	0.545	1.063	0.001	0.004	0.374	2.942	0.001	0.001	0.052	0.000	0.003	4.985	0.560	0.053	0.384	0.003	0.138
	Line 10 1319_FSP_4_CS	242	0.538	1.070	0.001	0.004	0.375	2.939	0.000	0.000	0.052	0.000	0.003	4.981	0.556	0.053	0.388	0.003	0.113
	Line 11 1319_FSP_4_CS	269	0.531	1.068	0.000	0.004	0.392	2.942	0.000	0.000	0.044	0.000	0.003	4.985	0.547	0.046	0.404	0.003	0.123
	Line 12 1319_FSP_4_CS	296	0.531	1.075	0.001	0.004	0.381	2.938	0.000	0.000	0.047	0.000	0.003	4.979	0.552	0.049	0.396	0.003	0.137
	Line 13 1319_FSP_4_CS	323	0.535	1.069	0.000	0.004	0.373	2.942	0.000	0.000	0.051	0.000	0.003	4.977	0.556	0.053	0.388	0.003	0.150
	Line 14 1319_FSP_4_CS	350	0.549	1.079	0.001	0.004	0.359	2.932	0.000	0.001	0.054	0.000	0.003	4.982	0.569	0.056	0.372	0.003	0.167
	Line 15 1319_FSP_4_CS	376	0.560	1.084	0.001	0.005	0.350	2.926	0.000	0.000	0.058	0.000	0.003	4.986	0.576	0.060	0.360	0.003	0.187
	Line 16 1319_FSP_4_CS	403	0.568	1.092	0.000	0.004	0.335	2.920	0.000	0.000	0.063	0.000	0.003	4.985	0.586	0.065	0.346	0.003	0.192
	Line 17 1319_FSP_4_CS	430	0.565	1.083	0.001	0.005	0.327	2.928	0.000	0.000	0.063	0.000	0.003	4.975	0.590	0.066	0.341	0.003	0.184
	Line 18 1319_FSP_4_CS	457	0.586	1.075	0.001	0.004	0.337	2.928	0.000	0.000	0.062	0.000	0.003	4.995	0.594	0.063	0.341	0.003	0.191
	Line 19 1319_FSP_4_CS	484	0.561	1.083	0.002	0.005	0.330	2.928	0.000	0.000	0.063	0.000	0.003	4.974	0.586	0.066	0.345	0.003	0.177
	Line 20 1319_FSP_4_CS	510	0.572	1.083	0.001	0.005	0.343	2.924	0.000	0.000	0.061	0.000	0.003	4.991	0.585	0.062	0.350	0.003	1.761

Table H.29: EMPA data of R-type feldspar inV-254. Data is presented in atoms per formula unit and in fractions of solid solution end member. The end members are: albite (X_{Ab}), anorthite (X_{An}), orthoclase (X_{Or}), and celsian (X_{Cs}). Distances of the line scans are directed from core towards the rim of the crystal.

V-ID	Analyses ID	Distance (μm)	Na	Al	Ti	Fe	K	Si	Mg	Mn	Ca	Sr	Ba	Sum	X_{Ab}	X_{An}	X_{Or}	X_{Cs}	Ca/K
V-254	Line 1 1319_FSP_3_CS	1	0.731	1.178	0.001	0.005	0.100	2.816	0.000	0.000	0.176	0.001	0.003	5.010	0.724	0.174	0.099	0.003	1.787
	Line 2 1319_FSP_3_CS	9	0.727	1.169	0.001	0.006	0.098	2.823	0.000	0.000	0.175	0.001	0.002	5.004	0.725	0.175	0.098	0.002	2.147
	Line 3 1319_FSP_3_CS	17	0.739	1.186	0.000	0.006	0.088	2.805	0.000	0.000	0.189	0.000	0.002	5.016	0.726	0.186	0.087	0.002	1.948
	Line 4 1319_FSP_3_CS	24	0.737	1.190	0.000	0.006	0.095	2.802	0.000	0.000	0.185	0.000	0.002	5.018	0.723	0.182	0.093	0.002	1.786
	Line 5 1319_FSP_3_CS	32	0.702	1.182	0.000	0.006	0.099	2.820	0.001	0.000	0.176	0.001	0.003	4.990	0.716	0.180	0.101	0.003	1.894
	Line 6 1319_FSP_3_CS	40	0.743	1.181	0.001	0.007	0.095	2.809	0.000	0.000	0.180	0.000	0.003	5.019	0.728	0.176	0.093	0.002	1.774
	Line 7 1319_FSP_3_CS	48	0.748	1.184	0.000	0.004	0.099	2.808	0.000	0.000	0.176	0.003	0.002	5.024	0.729	0.172	0.097	0.002	1.943
	Line 8 1319_FSP_3_CS	56	0.718	1.186	0.001	0.006	0.094	2.811	0.000	0.000	0.182	0.000	0.003	5.001	0.720	0.183	0.094	0.003	1.719
	Line 9 1319_FSP_3_CS	64	0.734	1.175	0.000	0.006	0.101	2.818	0.000	0.000	0.173	0.003	0.002	5.012	0.727	0.171	0.100	0.002	1.433
	Line 10 1319_FSP_3_CS	71	0.714	1.161	0.000	0.007	0.114	2.836	0.000	0.000	0.163	0.001	0.003	4.997	0.719	0.164	0.114	0.003	1.036
	Line 11 1319_FSP_3_CS	79	0.716	1.151	0.000	0.006	0.139	2.846	0.000	0.001	0.144	0.000	0.003	5.005	0.715	0.144	0.139	0.003	0.655
	Line 12 1319_FSP_3_CS	87	0.677	1.133	0.000	0.006	0.191	2.865	0.000	0.000	0.125	0.000	0.005	5.003	0.678	0.125	0.192	0.005	0.582
	Line 13 1319_FSP_3_CS	95	0.676	1.126	0.001	0.006	0.204	2.870	0.000	0.000	0.119	0.000	0.006	5.007	0.673	0.118	0.203	0.006	0.455
	Line 14 1319_FSP_3_CS	103	0.683	1.109	0.001	0.004	0.231	2.881	0.000	0.001	0.105	0.000	0.006	5.021	0.667	0.102	0.225	0.006	0.419
	Line 15 1319_FSP_3_CS	111	0.659	1.112	0.000	0.004	0.242	2.884	0.001	0.001	0.102	0.000	0.005	5.010	0.653	0.101	0.240	0.005	0.392
	Line 16 1319_FSP_3_CS	118	0.640	1.112	0.001	0.006	0.255	2.883	0.000	0.001	0.100	0.004	0.006	5.007	0.640	0.100	0.254	0.006	0.373
	Line 17 1319_FSP_3_CS	126	0.648	1.106	0.001	0.004	0.255	2.890	0.000	0.000	0.095	0.001	0.007	5.008	0.645	0.095	0.254	0.007	0.369
	Line 18 1319_FSP_3_CS	134	0.644	1.104	0.002	0.004	0.258	2.892	0.000	0.000	0.095	0.000	0.006	5.005	0.642	0.095	0.257	0.006	0.382
	Line 19 1319_FSP_3_CS	142	0.659	1.109	0.000	0.005	0.253	2.885	0.000	0.001	0.097	0.000	0.006	5.016	0.649	0.095	0.249	0.006	0.425
	Line 20 1319_FSP_3_CS	150	0.651	1.101	0.001	0.007	0.238	2.893	0.000	0.000	0.101	0.001	0.005	4.999	0.654	0.101	0.239	0.005	0.381
	Line 21 1319_FSP_3_CS	158	0.648	1.105	0.002	0.004	0.255	2.891	0.000	0.000	0.097	0.000	0.005	5.006	0.645	0.097	0.254	0.005	0.418
	Line 22 1319_FSP_3_CS	165	0.666	1.104	0.000	0.005	0.239	2.890	0.000	0.000	0.100	0.000	0.005	5.010	0.660	0.099	0.237	0.005	0.049
	Line 23 1319_FSP_3_CS	173	0.438	1.045	0.001	0.006	0.523	2.953	0.001	0.000	0.026	0.000	0.011	5.003	0.439	0.026	0.524	0.011	0.559
	Line 24 1319_FSP_3_CS	181	0.688	1.111	0.001	0.005	0.200	2.883	0.001	0.000	0.112	0.000	0.004	5.005	0.685	0.111	0.199	0.004	0.491
	Line 25 1319_FSP_3_CS	189	0.672	1.116	0.001	0.006	0.221	2.879	0.001	0.000	0.109	0.000	0.004	5.009	0.668	0.108	0.220	0.004	0.417
	Line 26 1319_FSP_3_CS	197	0.676	1.103	0.001	0.005	0.237	2.889	0.000	0.000	0.099	0.000	0.005	5.015	0.665	0.097	0.233	0.005	0.320
	Line 27 1319_FSP_3_CS	205	0.608	1.100	0.000	0.005	0.280	2.903	0.000	0.000	0.090	0.000	0.004	4.991	0.620	0.091	0.285	0.004	0.427
	Line 28 1319_FSP_3_CS	212	0.660	1.111	0.001	0.006	0.233	2.888	0.000	0.000	0.100	0.001	0.004	5.003	0.662	0.100	0.234	0.004	0.441
	Line 29 1319_FSP_3_CS	220	0.654	1.111	0.001	0.006	0.239	2.885	0.000	0.000	0.105	0.000	0.003	5.005	0.653	0.105	0.239	0.003	0.419
	Line 30 1319_FSP_3_CS	228	0.666	1.101	0.001	0.006	0.239	2.893	0.001	0.000	0.100	0.000	0.003	5.009	0.661	0.099	0.237	0.003	0.383
	Line 31 1319_FSP_3_CS	236	0.664	1.093	0.000	0.004	0.240	2.904	0.000	0.000	0.092	0.001	0.003	5.001	0.665	0.092	0.240	0.003	0.100
	Line 32 1319_FSP_3_CS	244	0.519	1.055	0.000	0.004	0.435	2.943	0.000	0.000	0.043	0.000	0.007	5.006	0.517	0.043	0.433	0.007	0.076
	Line 33 1319_FSP_3_CS	252	0.496	1.043	0.000	0.004	0.467	2.953	0.000	0.000	0.036	0.000	0.007	5.006	0.493	0.035	0.464	0.007	0.081
	Line 34 1319_FSP_3_CS	259	0.490	1.045	0.001	0.004	0.460	2.953	0.000	0.001	0.037	0.000	0.007	4.999	0.492	0.038	0.463	0.007	0.081
	Line 35 1319_FSP_3_CS	267	0.495	1.049	0.001	0.004	0.460	2.950	0.000	0.000	0.037	0.000	0.006	5.002	0.496	0.038	0.460	0.006	0.081
	Line 36 1319_FSP_3_CS	275	0.502	1.049	0.001	0.004	0.454	2.950	0.000	0.000	0.037	0.000	0.006	5.003	0.503	0.037	0.455	0.006	0.080
	Line 37 1319_FSP_3_CS	283	0.519	1.047	0.000	0.004	0.455	2.947	0.000	0.000	0.037	0.001	0.006	5.017	0.510	0.036	0.448	0.006	0.083
	Line 38 1319_FSP_3_CS	291	0.502	1.053	0.000	0.004	0.452	2.947	0.000	0.000	0.038	0.000	0.007	5.004	0.502	0.038	0.452	0.007	0.091
	Line 39 1319_FSP_3_CS	299	0.505	1.046	0.002	0.004	0.443	2.951	0.000	0.000	0.040	0.000	0.008	4.998	0.507	0.040	0.445	0.008	0.082
	Line 40 1319_FSP_3_CS	306	0.495	1.052	0.001	0.004	0.454	2.948	0.000	0.000	0.037	0.000	0.007	4.999	0.498	0.038	0.457	0.007	0.088

Table H.30: EMPA data of R-type feldspar inV-254. Data is presented in atoms per formula unit and in fractions of solid solution end member. The end members are: albite (X_{Ab}), anorthite (X_{An}), orthoclase (X_{Or}), and celsian (X_{Cs}). Distances of the line scans are directed from core towards the rim of the crystal.

V-ID	Analyses ID	Distance (μm)	Na	Al	Ti	Fe	K	Si	Mg	Mn	Ca	Sr	Ba	Sum	X_{Ab}	X_{An}	X_{Or}	X_{Cs}	Ca/K
V-254	Line 1 1319_FSP_8_CS	1	0.531	1.059	0.002	0.005	0.442	2.933	0.000	0.000	0.039	0.000	0.011	5.022	0.519	0.038	0.432	0.011	0.092
	Line 2 1319_FSP_8_CS	11	0.516	1.061	0.001	0.004	0.429	2.939	0.000	0.000	0.039	0.000	0.012	5.002	0.517	0.040	0.431	0.012	0.085
	Line 3 1319_FSP_8_CS	22	0.523	1.054	0.001	0.005	0.438	2.942	0.000	0.000	0.037	0.000	0.012	5.011	0.518	0.037	0.434	0.012	0.108
	Line 4 1319_FSP_8_CS	32	0.529	1.065	0.002	0.005	0.417	2.931	0.000	0.000	0.045	0.000	0.012	5.007	0.527	0.045	0.416	0.012	0.131
	Line 5 1319_FSP_8_CS	42	0.538	1.075	0.002	0.005	0.401	2.922	0.001	0.001	0.053	0.000	0.011	5.008	0.537	0.053	0.400	0.011	0.158
	Line 6 1319_FSP_8_CS	53	0.561	1.085	0.001	0.004	0.377	2.914	0.000	0.000	0.059	0.000	0.011	5.012	0.556	0.059	0.374	0.011	0.217
	Line 7 1319_FSP_8_CS	63	0.564	1.089	0.002	0.005	0.345	2.908	0.001	0.000	0.075	0.000	0.011	5.000	0.567	0.075	0.346	0.011	0.288
	Line 8 1319_FSP_8_CS	73	0.595	1.099	0.000	0.005	0.323	2.890	0.002	0.000	0.093	0.000	0.011	5.019	0.582	0.091	0.316	0.011	0.334
	Line 9 1319_FSP_8_CS	83	0.617	1.111	0.001	0.005	0.294	2.880	0.001	0.000	0.098	0.000	0.010	5.018	0.605	0.096	0.289	0.010	0.379
	Line 10 1319_FSP_8_CS	94	0.629	1.107	0.002	0.004	0.274	2.883	0.001	0.000	0.104	0.000	0.008	5.013	0.620	0.102	0.270	0.008	0.470
	Line 11 1319_FSP_8_CS	104	0.632	1.124	0.001	0.005	0.252	2.869	0.001	0.001	0.119	0.000	0.007	5.010	0.626	0.117	0.250	0.007	0.522
	Line 12 1319_FSP_8_CS	114	0.655	1.125	0.001	0.004	0.238	2.863	0.001	0.000	0.124	0.001	0.007	5.019	0.640	0.121	0.232	0.007	0.284
	Line 13 1319_FSP_8_CS	125	0.616	1.097	0.001	0.005	0.298	2.899	0.000	0.000	0.085	0.000	0.009	5.009	0.612	0.084	0.296	0.008	0.334
	Line 14 1319_FSP_8_CS	135	0.618	1.107	0.001	0.004	0.283	2.890	0.000	0.000	0.094	0.000	0.008	5.006	0.616	0.094	0.282	0.008	0.470
	Line 15 1319_FSP_8_CS	145	0.636	1.130	0.000	0.005	0.247	2.867	0.001	0.000	0.116	0.000	0.007	5.009	0.632	0.115	0.245	0.007	0.541
	Line 16 1319_FSP_8_CS	156	0.643	1.115	0.001	0.004	0.238	2.872	0.001	0.000	0.129	0.000	0.006	5.010	0.632	0.127	0.234	0.006	0.461
	Line 17 1319_FSP_8_CS	166	0.646	1.117	0.002	0.006	0.256	2.868	0.002	0.000	0.118	0.000	0.007	5.023	0.629	0.115	0.250	0.007	0.481
	Line 18 1319_FSP_8_CS	176	0.658	1.123	0.000	0.006	0.251	2.863	0.002	0.001	0.121	0.000	0.007	5.030	0.635	0.116	0.242	0.007	0.495
	Line 19 1319_FSP_8_CS	187	0.626	1.135	0.002	0.006	0.242	2.863	0.001	0.000	0.120	0.000	0.007	5.001	0.630	0.120	0.243	0.007	0.512
	Line 20 1319_FSP_8_CS	197	0.658	1.137	0.000	0.005	0.236	2.856	0.001	0.001	0.121	0.000	0.007	5.022	0.644	0.118	0.231	0.007	0.525
	Line 21 1319_FSP_8_CS	207	0.655	1.135	0.000	0.005	0.230	2.860	0.000	0.001	0.121	0.000	0.007	5.015	0.646	0.120	0.227	0.007	0.559
	Line 22 1319_FSP_8_CS	218	0.665	1.141	0.001	0.005	0.221	2.855	0.000	0.000	0.123	0.000	0.006	5.016	0.655	0.122	0.217	0.006	0.479
	Line 23 1319_FSP_8_CS	228	0.655	1.128	0.001	0.004	0.238	2.867	0.000	0.000	0.114	0.000	0.006	5.015	0.646	0.113	0.235	0.006	0.190
	Line 24 1319_FSP_8_CS	238	0.586	1.085	0.001	0.004	0.347	2.913	0.000	0.000	0.066	0.000	0.008	5.010	0.582	0.065	0.344	0.008	0.329
	Line 25 1319_FSP_8_CS	248	0.638	1.106	0.001	0.006	0.284	2.886	0.001	0.000	0.093	0.000	0.007	5.021	0.624	0.091	0.278	0.007	0.417
	Line 26 1319_FSP_8_CS	259	0.661	1.127	0.001	0.004	0.254	2.867	0.001	0.000	0.106	0.000	0.006	5.026	0.644	0.103	0.247	0.006	0.510
	Line 27 1319_FSP_8_CS	269	0.652	1.131	0.001	0.005	0.231	2.865	0.000	0.000	0.118	0.000	0.006	5.010	0.647	0.117	0.230	0.006	0.467
	Line 28 1319_FSP_8_CS	279	0.651	1.131	0.001	0.006	0.241	2.865	0.000	0.000	0.113	0.000	0.007	5.015	0.644	0.111	0.238	0.007	0.415
	Line 29 1319_FSP_8_CS	290	0.642	1.119	0.002	0.005	0.258	2.874	0.000	0.000	0.107	0.000	0.007	5.014	0.633	0.106	0.254	0.007	0.410
	Line 30 1319_FSP_8_CS	300	0.658	1.120	0.001	0.006	0.253	2.873	0.000	0.000	0.104	0.000	0.007	5.021	0.644	0.101	0.247	0.007	0.461
	Line 31 1319_FSP_8_CS	310	0.649	1.128	0.000	0.005	0.239	2.870	0.001	0.000	0.110	0.000	0.006	5.009	0.645	0.110	0.238	0.006	0.448
	Line 32 1319_FSP_8_CS	321	0.644	1.121	0.000	0.006	0.240	2.878	0.001	0.000	0.108	0.000	0.006	5.003	0.646	0.108	0.241	0.006	0.367
	Line 33 1319_FSP_8_CS	331	0.647	1.105	0.001	0.006	0.261	2.889	0.001	0.001	0.096	0.000	0.006	5.011	0.641	0.095	0.259	0.006	0.351
	Line 34 1319_FSP_8_CS	341	0.637	1.111	0.001	0.007	0.267	2.886	0.000	0.000	0.094	0.000	0.007	5.010	0.634	0.093	0.266	0.006	0.309
	Line 35 1319_FSP_8_CS	352	0.638	1.108	0.001	0.005	0.286	2.887	0.000	0.000	0.089	0.000	0.006	5.020	0.626	0.087	0.281	0.006	0.261
	Line 36 1319_FSP_8_CS	362	0.619	1.096	0.001	0.006	0.310	2.898	0.000	0.000	0.081	0.000	0.006	5.017	0.610	0.080	0.305	0.006	0.168
	Line 37 1319_FSP_8_CS	372	0.567	1.084	0.002	0.005	0.364	2.916	0.000	0.000	0.061	0.000	0.007	5.006	0.568	0.061	0.364	0.007	0.184
	Line 38 1319_FSP_8_CS	382	0.608	1.083	0.001	0.006	0.343	2.910	0.001	0.001	0.063	0.000	0.007	5.023	0.595	0.062	0.336	0.007	0.186
	Line 39 1319_FSP_8_CS	393	0.584	1.078	0.001	0.005	0.343	2.921	0.001	0.000	0.064	0.000	0.007	5.003	0.586	0.064	0.344	0.007	0.155
	Line 40 1319_FSP_8_CS	403	0.575	1.072	0.001	0.006	0.364	2.925	0.001	0.000	0.057	0.000	0.007	5.007	0.573	0.056	0.363	0.007	0.150

Table H.31: EMPA data of R-type feldspar inV-221a. Data is presented in atoms per formula unit and in fractions of solid solution end member. The end members are: albite (X_{Ab}), anorthite (X_{An}), orthoclase (X_{Or}), and celsian (X_{Cs}). Distances of the line scans are directed from core towards the rim of the crystal.

V-ID	Analyses ID	Distance (μm)	Na	Al	Ti	Fe	K	Si	Mg	Mn	Ca	Sr	Ba	Sum	X_{Ab}	X_{An}	X_{Or}	X_{Cs}	Ca/K
V-221a	Line 1 1316_P_3_CS	1	0.687	1.243	0.001	0.009	0.085	2.749	0.000	0.000	0.237	0.002	0.002	5.014	0.680	0.234	0.084	0.002	5.618
	Line 2 1316_P_3_CS	26	0.633	1.322	0.001	0.008	0.056	2.672	0.001	0.000	0.315	0.001	0.001	5.010	0.629	0.313	0.056	0.001	5.628
	Line 3 1316_P_3_CS	51	0.625	1.319	0.002	0.009	0.055	2.677	0.000	0.000	0.312	0.002	0.002	5.002	0.629	0.314	0.056	0.002	0.948
	Line 4 1316_P_3_CS	76	0.668	1.164	0.001	0.008	0.169	2.829	0.000	0.000	0.160	0.001	0.005	5.006	0.666	0.160	0.169	0.005	1.784
	Line 5 1316_P_3_CS	101	0.671	1.201	0.000	0.008	0.112	2.796	0.001	0.001	0.199	0.003	0.003	4.994	0.681	0.202	0.113	0.003	0.365
	Line 6 1316_P_3_CS	126	0.643	1.107	0.002	0.007	0.257	2.889	0.000	0.000	0.094	0.000	0.007	5.005	0.642	0.094	0.257	0.007	0.357
	Line 7 1316_P_3_CS	151	0.642	1.100	0.001	0.007	0.263	2.894	0.000	0.000	0.094	0.000	0.007	5.008	0.639	0.093	0.261	0.007	0.372
	Line 8 1316_P_3_CS	176	0.641	1.099	0.001	0.007	0.259	2.895	0.000	0.000	0.096	0.000	0.007	5.004	0.640	0.096	0.258	0.007	0.244
	Line 9 1316_P_3_CS	201	0.597	1.079	0.001	0.005	0.305	2.922	0.000	0.000	0.074	0.000	0.004	4.988	0.609	0.076	0.311	0.004	0.233
	Line 10 1316_P_3_CS	226	0.612	1.072	0.001	0.006	0.310	2.923	0.000	0.001	0.072	0.000	0.004	5.001	0.613	0.072	0.311	0.004	0.292
	Line 11 1316_P_3_CS	251	0.616	1.090	0.001	0.007	0.280	2.911	0.002	0.000	0.082	0.000	0.004	4.991	0.628	0.083	0.285	0.004	0.145
	Line 12 1316_P_3_CS	276	0.551	1.059	0.001	0.005	0.364	2.944	0.000	0.000	0.053	0.000	0.005	4.983	0.566	0.054	0.374	0.005	0.194
	Line 13 1316_P_3_CS	301	0.604	1.076	0.001	0.006	0.332	2.921	0.000	0.000	0.064	0.000	0.004	5.009	0.601	0.064	0.331	0.004	0.242
	Line 14 1316_P_3_CS	326	0.611	1.081	0.001	0.008	0.308	2.915	0.000	0.000	0.075	0.000	0.005	5.003	0.612	0.075	0.309	0.005	0.145
	Line 15 1316_P_3_CS	351	0.557	1.060	0.001	0.006	0.367	2.941	0.000	0.001	0.053	0.000	0.005	4.990	0.568	0.054	0.373	0.005	0.168
	Line 16 1316_P_3_CS	376	0.588	1.063	0.002	0.007	0.351	2.931	0.000	0.000	0.059	0.000	0.004	5.005	0.587	0.059	0.350	0.004	0.168
	Line 17 1316_P_3_CS	401	0.586	1.059	0.000	0.005	0.354	2.937	0.000	0.000	0.059	0.000	0.004	5.003	0.584	0.059	0.353	0.004	0.212
	Line 18 1316_P_3_CS	427	0.592	1.070	0.001	0.007	0.325	2.927	0.000	0.000	0.069	0.000	0.004	4.995	0.598	0.069	0.328	0.004	0.154
	Line 19 1316_P_3_CS	452	0.579	1.061	0.001	0.005	0.365	2.934	0.001	0.000	0.056	0.000	0.005	5.007	0.576	0.056	0.363	0.005	0.143
	Line 20 1316_P_3_CS	477	0.558	1.058	0.001	0.007	0.370	2.941	0.000	0.000	0.053	0.000	0.005	4.993	0.566	0.054	0.375	0.005	0.213
V-221a	Line 1 1316_FSP_21_CS_A	1	0.617	1.076	0.001	0.007	0.318	2.919	0.000	0.000	0.068	0.000	0.004	5.009	0.613	0.067	0.316	0.004	0.194
	Line 2 1316_FSP_21_CS_A	10	0.602	1.072	0.002	0.005	0.331	2.924	0.000	0.000	0.064	0.000	0.005	5.005	0.601	0.064	0.331	0.005	0.139
	Line 3 1316_FSP_21_CS_A	18	0.569	1.058	0.003	0.006	0.370	2.938	0.000	0.000	0.052	0.000	0.004	5.000	0.572	0.052	0.372	0.004	0.175
	Line 4 1316_FSP_21_CS_A	27	0.593	1.058	0.001	0.007	0.350	2.933	0.000	0.000	0.061	0.000	0.005	5.008	0.588	0.061	0.347	0.005	0.169
	Line 5 1316_FSP_21_CS_A	35	0.588	1.060	0.001	0.006	0.349	2.934	0.001	0.000	0.059	0.000	0.004	5.003	0.588	0.059	0.349	0.004	0.237
	Line 6 1316_FSP_21_CS_A	44	0.615	1.083	0.001	0.007	0.309	2.914	0.000	0.000	0.073	0.000	0.004	5.007	0.614	0.073	0.309	0.004	0.367
	Line 7 1316_FSP_21_CS_A	53	0.654	1.099	0.001	0.007	0.257	2.894	0.000	0.000	0.094	0.000	0.004	5.011	0.648	0.093	0.254	0.004	0.345
	Line 8 1316_FSP_21_CS_A	61	0.652	1.097	0.001	0.006	0.263	2.896	0.000	0.000	0.091	0.000	0.004	5.011	0.645	0.090	0.261	0.004	0.380
	Line 9 1316_FSP_21_CS_A	70	0.659	1.094	0.000	0.006	0.247	2.900	0.000	0.001	0.094	0.000	0.004	5.006	0.656	0.093	0.246	0.004	0.317
	Line 10 1316_FSP_21_CS_A	78	0.619	1.088	0.000	0.006	0.273	2.911	0.000	0.000	0.087	0.000	0.005	4.991	0.629	0.088	0.278	0.005	0.338
	Line 11 1316_FSP_21_CS_A	87	0.631	1.101	0.002	0.006	0.265	2.898	0.000	0.000	0.089	0.000	0.005	4.997	0.637	0.090	0.267	0.005	0.206
	Line 12 1316_FSP_21_CS_A	95	0.610	1.075	0.001	0.006	0.324	2.920	0.000	0.001	0.067	0.000	0.006	5.009	0.606	0.066	0.322	0.006	0.380
	Line 13 1316_FSP_21_CS_A	104	0.641	1.101	0.001	0.008	0.258	2.893	0.000	0.001	0.098	0.000	0.004	5.005	0.640	0.098	0.258	0.004	0.370
	Line 14 1316_FSP_21_CS_A	113	0.639	1.105	0.001	0.006	0.259	2.892	0.000	0.000	0.096	0.000	0.005	5.004	0.640	0.096	0.259	0.005	0.272
	Line 15 1316_FSP_21_CS_A	121	0.633	1.079	0.001	0.006	0.296	2.911	0.000	0.000	0.080	0.000	0.006	5.013	0.623	0.079	0.292	0.006	0.296
	Line 16 1316_FSP_21_CS_A	130	0.634	1.092	0.001	0.006	0.283	2.904	0.000	0.000	0.084	0.000	0.005	5.008	0.630	0.083	0.281	0.005	0.264
	Line 17 1316_FSP_21_CS_A	138	0.608	1.091	0.002	0.006	0.301	2.907	0.000	0.000	0.079	0.000	0.006	5.000	0.612	0.080	0.303	0.006	0.364
	Line 18 1316_FSP_21_CS_A	147	0.641	1.097	0.001	0.006	0.259	2.898	0.000	0.000	0.094	0.000	0.004	5.002	0.642	0.095	0.260	0.004	0.181
	Line 19 1316_FSP_21_CS_A	156	0.602	1.067	0.001	0.006	0.334	2.929	0.000	0.000	0.060	0.000	0.005	5.004	0.601	0.060	0.333	0.005	0.363
	Line 20 1316_FSP_21_CS_A	164	0.642	1.098	0.001	0.006	0.260	2.898	0.000	0.000	0.094	0.000	0.004	5.003	0.642	0.094	0.260	0.004	0.092
	Line 21 1316_FSP_21_CS_A	173	0.527	1.047	0.001	0.006	0.417	2.953	0.000	0.000	0.039	0.000	0.005	4.995	0.533	0.039	0.422	0.005	0.122
	Line 22 1316_FSP_21_CS_A	181	0.555	1.055	0.001	0.007	0.391	2.941	0.000	0.001	0.048	0.000	0.005	5.004	0.556	0.048	0.391	0.005	0.129
	Line 23 1316_FSP_21_CS_A	190	0.552	1.055	0.001	0.007	0.381	2.944	0.000	0.000	0.049	0.000	0.004	4.994	0.559	0.050	0.386	0.004	0.118
	Line 24 1316_FSP_21_CS_A	198	0.554	1.048	0.002	0.006	0.396	2.946	0.000	0.000	0.047	0.000	0.005	5.003	0.553	0.047	0.396	0.005	0.138
	Line 25 1316_FSP_21_CS_A	207	0.558	1.054	0.001	0.005	0.381	2.942	0.000	0.000	0.053	0.000	0.005	4.999	0.560	0.053	0.383	0.005	0.127
	Line 26 1316_FSP_21_CS_A	216	0.555	1.046	0.002	0.007	0.385	2.948	0.000	0.000	0.049	0.000	0.004	4.996	0.559	0.049	0.387	0.004	0.143
	Line 27 1316_FSP_21_CS_A	224	0.560	1.058	0.000	0.006	0.375	2.940	0.000	0.001	0.054	0.000	0.004	4.998	0.564	0.054	0.378	0.004	0.083
	Line 28 1316_FSP_21_CS_A	233	0.528	1.045	0.001	0.006	0.421	2.956	0.000	0.001	0.035	0.000	0.003	4.996	0.535	0.036	0.426	0.004	0.087
	Line 29 1316_FSP_21_CS_A	241	0.535	1.036	0.001	0.006	0.424	2.959	0.000	0.000	0.037	0.000	0.003	5.002	0.536	0.037	0.424	0.003	0.087
	Line 30 1316_FSP_21_CS_A	250	0.525	1.040	0.001	0.006	0.426	2.958	0.000	0.000	0.037	0.000	0.003	4.996	0.529	0.037	0.430	0.003	0.187

Table H.32: EMPA data of R-type feldspar inV-209a. Data is presented in atoms per formula unit and in fractions of solid solution end member. The end members are: albite (X_{Ab}), anorthite (X_{An}), orthoclase (X_{Or}), and celsian (X_{Cs}). Distances of the line scans are directed from core towards the rim of the crystal.

V-ID	Analyses ID	Distance (μm)	Na	Al	Ti	Fe	K	Si	Mg	Mn	Ca	Sr	Ba	Sum	X_{Ab}	X_{An}	X_{Or}	X_{Cs}	Ca/K
V-209a	Line 1 1315_FSP_13_CS	1	0.551	1.073	0.003	0.007	0.341	2.931	0.000	0.000	0.064	0.000	0.005	4.975	0.574	0.066	0.355	0.005	0.181
	Line 2 1315_FSP_13_CS	16	0.556	1.076	0.001	0.007	0.340	2.931	0.000	0.000	0.062	0.000	0.005	4.978	0.578	0.064	0.353	0.005	0.193
	Line 3 1315_FSP_13_CS	31	0.548	1.081	0.001	0.007	0.337	2.928	0.000	0.001	0.065	0.000	0.005	4.973	0.574	0.068	0.353	0.005	0.178
	Line 4 1315_FSP_13_CS	46	0.556	1.077	0.002	0.007	0.345	2.929	0.001	0.000	0.061	0.000	0.005	4.982	0.574	0.063	0.357	0.005	0.155
	Line 5 1315_FSP_13_CS	60	0.562	1.070	0.000	0.008	0.348	2.937	0.000	0.000	0.054	0.000	0.004	4.982	0.581	0.056	0.359	0.004	0.148
	Line 6 1315_FSP_13_CS	75	0.565	1.065	0.001	0.007	0.352	2.940	0.000	0.000	0.052	0.000	0.004	4.986	0.580	0.054	0.362	0.004	0.142
	Line 7 1315_FSP_13_CS	90	0.561	1.059	0.002	0.008	0.355	2.943	0.000	0.000	0.051	0.000	0.004	4.984	0.578	0.052	0.366	0.004	0.122
	Line 8 1315_FSP_13_CS	105	0.539	1.053	0.000	0.007	0.365	2.956	0.000	0.000	0.045	0.000	0.004	4.970	0.566	0.047	0.383	0.004	0.122
	Line 9 1315_FSP_13_CS	120	0.543	1.058	0.001	0.006	0.368	2.950	0.000	0.000	0.045	0.000	0.004	4.976	0.566	0.047	0.383	0.004	0.124
	Line 10 1315_FSP_13_CS	135	0.529	1.058	0.001	0.008	0.368	2.953	0.000	0.000	0.045	0.000	0.004	4.966	0.559	0.048	0.389	0.004	0.139
	Line 11 1315_FSP_13_CS	149	0.543	1.069	0.000	0.007	0.358	2.942	0.001	0.000	0.050	0.000	0.003	4.974	0.570	0.052	0.375	0.003	0.152
	Line 12 1315_FSP_13_CS	164	0.563	1.062	0.001	0.007	0.348	2.943	0.001	0.000	0.053	0.000	0.004	4.980	0.582	0.055	0.360	0.004	0.150
	Line 13 1315_FSP_13_CS	179	0.549	1.069	0.002	0.007	0.352	2.940	0.000	0.000	0.053	0.000	0.004	4.974	0.573	0.055	0.368	0.004	0.122
	Line 14 1315_FSP_13_CS	194	0.548	1.056	0.001	0.008	0.360	2.952	0.000	0.000	0.044	0.000	0.004	4.973	0.573	0.046	0.377	0.004	0.135
	Line 15 1315_FSP_13_CS	209	0.543	1.057	0.002	0.007	0.360	2.950	0.000	0.000	0.049	0.000	0.004	4.971	0.568	0.051	0.377	0.004	0.160
	Line 16 1315_FSP_13_CS	224	0.570	1.067	0.000	0.009	0.344	2.937	0.000	0.000	0.055	0.000	0.003	4.986	0.586	0.057	0.354	0.004	0.154
	Line 17 1315_FSP_13_CS	238	0.560	1.065	0.000	0.008	0.350	2.940	0.000	0.000	0.054	0.000	0.004	4.981	0.579	0.056	0.362	0.004	0.156
	Line 18 1315_FSP_13_CS	253	0.547	1.075	0.001	0.007	0.348	2.936	0.000	0.001	0.054	0.000	0.004	4.973	0.574	0.057	0.365	0.004	0.139
	Line 19 1315_FSP_13_CS	268	0.548	1.061	0.001	0.007	0.357	2.947	0.000	0.001	0.050	0.000	0.004	4.975	0.572	0.052	0.373	0.004	0.145
	Line 20 1315_FSP_13_CS	283	0.535	1.062	0.001	0.007	0.357	2.948	0.001	0.000	0.052	0.000	0.004	4.966	0.564	0.055	0.377	0.004	0.165
	Line 21 1315_FSP_13_CS	298	0.554	1.064	0.002	0.008	0.349	2.940	0.000	0.000	0.057	0.000	0.003	4.977	0.575	0.060	0.362	0.003	0.173
	Line 22 1315_FSP_13_CS	313	0.551	1.070	0.002	0.008	0.345	2.936	0.000	0.000	0.060	0.000	0.003	4.975	0.574	0.062	0.360	0.004	0.179
	Line 23 1315_FSP_13_CS	327	0.563	1.077	0.001	0.007	0.340	2.929	0.001	0.000	0.061	0.000	0.004	4.982	0.582	0.063	0.351	0.004	0.174
	Line 24 1315_FSP_13_CS	342	0.560	1.074	0.001	0.007	0.343	2.932	0.001	0.000	0.060	0.000	0.004	4.981	0.580	0.062	0.355	0.004	0.185
	Line 25 1315_FSP_13_CS	357	0.562	1.076	0.001	0.006	0.341	2.929	0.000	0.000	0.063	0.000	0.004	4.983	0.579	0.065	0.352	0.004	0.192
	Line 26 1315_FSP_13_CS	372	0.560	1.082	0.002	0.008	0.335	2.924	0.000	0.000	0.064	0.000	0.004	4.980	0.581	0.067	0.348	0.004	0.191
	Line 27 1315_FSP_13_CS	387	0.557	1.075	0.002	0.009	0.339	2.929	0.000	0.000	0.065	0.000	0.004	4.980	0.577	0.067	0.352	0.004	0.174
	Line 28 1315_FSP_13_CS	402	0.541	1.077	0.002	0.007	0.350	2.932	0.000	0.000	0.061	0.000	0.004	4.974	0.566	0.064	0.366	0.004	0.161
	Line 29 1315_FSP_13_CS	417	0.557	1.065	0.001	0.007	0.354	2.939	0.001	0.000	0.057	0.000	0.004	4.984	0.573	0.059	0.365	0.004	0.161
	Line 30 1315_FSP_13_CS	431	0.564	1.066	0.001	0.009	0.346	2.939	0.000	0.000	0.056	0.000	0.003	4.982	0.582	0.058	0.357	0.003	0.165

Table H.33: EMPA data of R-type feldspar inV-209a. Data is presented in atoms per formula unit and in fractions of solid solution end member. The end members are: albite (X_{Ab}), anorthite (X_{An}), orthoclase (X_{Or}), and celsian (X_{Cs}). Distances of the line scans are directed from core towards the rim of the crystal.

V-ID	Analyses ID	Distance (μm)	Na	Al	Ti	Fe	K	Si	Mg	Mn	Ca	Sr	Ba	Sum	X_{Ab}	X_{An}	X_{Or}	X_{Cs}	Ca/K
V-209a	Line 1 1315_FSP_7_CS	1	0.568	1.084	0.001	0.008	0.341	2.924	0.000	0.001	0.056	0.000	0.004	4.988	0.585	0.058	0.352	0.004	0.169
	Line 2 1315_FSP_7_CS	10	0.568	1.084	0.002	0.007	0.337	2.924	0.001	0.001	0.057	0.000	0.004	4.985	0.589	0.059	0.348	0.004	0.173
	Line 3 1315_FSP_7_CS	19	0.563	1.080	0.001	0.007	0.329	2.931	0.000	0.001	0.057	0.000	0.004	4.973	0.591	0.060	0.345	0.005	0.171
	Line 4 1315_FSP_7_CS	28	0.573	1.079	0.000	0.008	0.328	2.931	0.000	0.001	0.056	0.000	0.004	4.980	0.597	0.058	0.341	0.004	0.175
	Line 5 1315_FSP_7_CS	36	0.573	1.078	0.001	0.007	0.332	2.930	0.000	0.000	0.058	0.000	0.004	4.983	0.593	0.060	0.344	0.004	0.184
	Line 6 1315_FSP_7_CS	45	0.565	1.080	0.002	0.007	0.327	2.929	0.000	0.000	0.060	0.000	0.005	4.975	0.590	0.063	0.342	0.005	0.182
	Line 7 1315_FSP_7_CS	54	0.558	1.078	0.001	0.007	0.331	2.931	0.001	0.000	0.060	0.000	0.005	4.973	0.584	0.063	0.347	0.006	0.177
	Line 8 1315_FSP_7_CS	63	0.574	1.083	0.001	0.008	0.334	2.923	0.000	0.001	0.059	0.000	0.005	4.988	0.591	0.061	0.343	0.005	0.189
	Line 9 1315_FSP_7_CS	72	0.579	1.082	0.002	0.008	0.326	2.924	0.000	0.000	0.062	0.000	0.004	4.986	0.596	0.063	0.336	0.004	0.185
	Line 10 1315_FSP_7_CS	81	0.558	1.089	0.002	0.008	0.328	2.924	0.001	0.000	0.061	0.000	0.004	4.973	0.587	0.064	0.345	0.005	0.170
	Line 11 1315_FSP_7_CS	90	0.567	1.075	0.001	0.007	0.338	2.932	0.000	0.000	0.058	0.000	0.005	4.982	0.586	0.059	0.350	0.005	0.197
	Line 12 1315_FSP_7_CS	98	0.574	1.079	0.001	0.007	0.328	2.925	0.001	0.000	0.065	0.000	0.005	4.985	0.591	0.066	0.338	0.005	0.186
	Line 13 1315_FSP_7_CS	107	0.578	1.081	0.002	0.007	0.326	2.925	0.000	0.000	0.061	0.000	0.005	4.985	0.597	0.063	0.336	0.005	0.178
	Line 14 1315_FSP_7_CS	116	0.569	1.086	0.001	0.008	0.333	2.922	0.001	0.000	0.059	0.000	0.005	4.985	0.589	0.061	0.344	0.005	0.177
	Line 15 1315_FSP_7_CS	125	0.562	1.076	0.002	0.008	0.332	2.933	0.000	0.000	0.059	0.000	0.004	4.975	0.587	0.061	0.347	0.004	0.169
	Line 16 1315_FSP_7_CS	134	0.562	1.084	0.002	0.007	0.333	2.928	0.000	0.000	0.056	0.000	0.004	4.976	0.589	0.059	0.348	0.004	0.166
	Line 17 1315_FSP_7_CS	143	0.563	1.074	0.002	0.007	0.337	2.935	0.001	0.000	0.056	0.000	0.004	4.977	0.587	0.058	0.351	0.004	0.172
	Line 18 1315_FSP_7_CS	152	0.561	1.074	0.002	0.008	0.332	2.935	0.000	0.000	0.057	0.000	0.004	4.973	0.588	0.060	0.348	0.005	0.168
	Line 19 1315_FSP_7_CS	160	0.576	1.071	0.001	0.008	0.336	2.933	0.000	0.000	0.056	0.000	0.004	4.986	0.593	0.058	0.346	0.004	0.171
	Line 20 1315_FSP_7_CS	169	0.579	1.075	0.001	0.009	0.334	2.929	0.000	0.000	0.057	0.000	0.004	4.989	0.594	0.059	0.343	0.004	0.167
	Line 21 1315_FSP_7_CS	178	0.572	1.080	0.001	0.006	0.339	2.928	0.000	0.000	0.057	0.000	0.004	4.987	0.589	0.058	0.349	0.004	0.164
	Line 22 1315_FSP_7_CS	187	0.569	1.073	0.000	0.008	0.340	2.934	0.000	0.000	0.056	0.001	0.003	4.984	0.587	0.058	0.351	0.003	0.166
	Line 23 1315_FSP_7_CS	196	0.573	1.072	0.001	0.006	0.338	2.934	0.000	0.000	0.056	0.000	0.003	4.984	0.590	0.058	0.349	0.004	0.168
	Line 24 1315_FSP_7_CS	205	0.568	1.081	0.002	0.007	0.338	2.927	0.000	0.000	0.057	0.000	0.003	4.983	0.588	0.059	0.350	0.003	0.162
	Line 25 1315_FSP_7_CS	214	0.580	1.071	0.001	0.007	0.341	2.933	0.000	0.000	0.055	0.000	0.003	4.991	0.592	0.056	0.348	0.003	0.151
	Line 26 1315_FSP_7_CS	223	0.556	1.065	0.001	0.007	0.344	2.944	0.000	0.001	0.052	0.000	0.002	4.973	0.583	0.054	0.361	0.002	0.132
	Line 27 1315_FSP_7_CS	231	0.563	1.054	0.002	0.009	0.354	2.949	0.000	0.000	0.047	0.000	0.002	4.980	0.583	0.048	0.367	0.002	0.116
	Line 28 1315_FSP_7_CS	240	0.568	1.057	0.000	0.008	0.367	2.947	0.000	0.001	0.043	0.000	0.001	4.991	0.580	0.044	0.375	0.001	0.113
	Line 29 1315_FSP_7_CS	249	0.554	1.045	0.001	0.008	0.368	2.959	0.000	0.000	0.041	0.000	0.001	4.978	0.574	0.043	0.381	0.001	0.112
	Line 30 1315_FSP_7_CS	258	0.552	1.050	0.002	0.009	0.369	2.953	0.001	0.001	0.042	0.000	0.002	4.981	0.572	0.043	0.383	0.002	0.118
	Line 31 1315_FSP_7_CS	267	0.550	1.059	0.000	0.008	0.364	2.950	0.000	0.000	0.043	0.000	0.002	4.977	0.573	0.045	0.380	0.002	0.135
	Line 32 1315_FSP_7_CS	276	0.554	1.067	0.000	0.008	0.365	2.939	0.001	0.000	0.049	0.000	0.003	4.987	0.570	0.051	0.375	0.003	0.134
	Line 33 1315_FSP_7_CS	285	0.546	1.066	0.001	0.008	0.363	2.942	0.001	0.000	0.049	0.000	0.003	4.979	0.568	0.051	0.378	0.003	0.130
	Line 34 1315_FSP_7_CS	293	0.550	1.064	0.002	0.008	0.363	2.942	0.000	0.000	0.047	0.000	0.004	4.980	0.570	0.049	0.377	0.004	0.126
	Line 35 1315_FSP_7_CS	302	0.552	1.064	0.002	0.008	0.367	2.940	0.000	0.000	0.046	0.000	0.004	4.985	0.569	0.048	0.379	0.004	0.124
	Line 36 1315_FSP_7_CS	311	0.560	1.057	0.001	0.007	0.372	2.944	0.000	0.000	0.046	0.000	0.005	4.992	0.570	0.047	0.378	0.005	0.133
	Line 37 1315_FSP_7_CS	320	0.550	1.070	0.001	0.009	0.369	2.935	0.000	0.000	0.049	0.000	0.004	4.989	0.565	0.051	0.379	0.005	0.128
	Line 38 1315_FSP_7_CS	329	0.544	1.072	0.002	0.009	0.367	2.935	0.000	0.000	0.047	0.000	0.004	4.982	0.565	0.049	0.381	0.004	0.130
	Line 39 1315_FSP_7_CS	338	0.551	1.060	0.001	0.009	0.367	2.944	0.000	0.001	0.048	0.000	0.004	4.984	0.568	0.049	0.379	0.004	0.128
	Line 40 1315_FSP_7_CS	347	0.548	1.060	0.001	0.009	0.371	2.943	0.001	0.000	0.048	0.000	0.004	4.985	0.565	0.049	0.382	0.004	0.016

Table H.34: EMPA data of R-type feldspar inV-149. Data is presented in atoms per formula unit and in fractions of solid solution end member. The end members are: albite (X_{Ab}), anorthite (X_{An}), orthoclase (X_{Or}), and celsian (X_{Cs}). Distances of the line scans are directed from core towards the rim of the crystal.

V-ID	Analyses ID	Distance (μm)	Na	Al	Ti	Fe	K	Si	Mg	Mn	Ca	Sr	Ba	Sum	X_{Ab}	X_{An}	X_{Or}	X_{Cs}	Ca/K
V-149	Line 2 1409_FSP_6_CS	74	0.678	0.997	0.000	0.013	0.290	3.008	0.000	0.001	0.005	0.000	0.000	4.993	0.697	0.005	0.298	0.000	0.017
	Line 3 1409_FSP_6_CS	89	0.665	1.000	0.000	0.012	0.291	3.010	0.000	0.001	0.005	0.000	0.000	4.984	0.692	0.005	0.303	0.000	0.014
	Line 4 1409_FSP_6_CS	103	0.665	0.995	0.001	0.013	0.292	3.013	0.000	0.000	0.004	0.000	0.000	4.983	0.692	0.004	0.304	0.000	0.012
	Line 5 1409_FSP_6_CS	118	0.662	1.002	0.001	0.012	0.298	3.007	0.001	0.000	0.004	0.000	0.000	4.987	0.687	0.004	0.309	0.000	0.014
	Line 6 1409_FSP_6_CS	133	0.639	0.995	0.000	0.012	0.297	3.018	0.001	0.000	0.004	0.000	0.000	4.967	0.680	0.005	0.315	0.000	0.016
	Line 7 1409_FSP_6_CS	147	0.663	1.001	0.001	0.011	0.295	3.008	0.001	0.000	0.005	0.000	0.000	4.984	0.689	0.005	0.306	0.000	0.027
	Line 8 1409_FSP_6_CS	162	0.660	1.011	0.000	0.009	0.290	3.003	0.001	0.000	0.008	0.000	0.000	4.981	0.690	0.008	0.302	0.000	0.015
	Line 9 1409_FSP_6_CS	177	0.619	0.995	0.001	0.011	0.316	3.019	0.000	0.000	0.005	0.000	0.000	4.966	0.659	0.005	0.336	0.000	0.016
	Line 10 1409_FSP_6_CS	191	0.644	1.003	0.000	0.011	0.310	3.009	0.000	0.000	0.005	0.000	0.000	4.981	0.672	0.005	0.323	0.000	0.018
	Line 11 1409_FSP_6_CS	206	0.647	1.004	0.000	0.009	0.324	3.004	0.000	0.000	0.006	0.000	0.000	4.995	0.662	0.006	0.332	0.000	0.017
	Line 12 1409_FSP_6_CS	220	0.622	1.008	0.001	0.010	0.324	3.006	0.000	0.001	0.006	0.000	0.000	4.978	0.654	0.006	0.340	0.000	0.012
	Line 13 1409_FSP_6_CS	235	0.636	1.007	0.000	0.011	0.335	3.002	0.000	0.000	0.004	0.000	0.000	4.995	0.652	0.004	0.344	0.000	0.013
	Line 14 1409_FSP_6_CS	250	0.612	0.998	0.000	0.013	0.336	3.013	0.000	0.000	0.004	0.000	0.000	4.977	0.643	0.005	0.353	0.000	0.014
	Line 15 1409_FSP_6_CS	264	0.610	1.001	0.001	0.012	0.344	3.009	0.000	0.000	0.005	0.000	0.000	4.982	0.636	0.005	0.359	0.000	0.012
	Line 16 1409_FSP_6_CS	279	0.622	1.000	0.001	0.012	0.349	3.005	0.000	0.000	0.004	0.000	0.000	4.994	0.637	0.004	0.358	0.000	0.011
	Line 17 1409_FSP_6_CS	294	0.596	1.005	0.000	0.013	0.361	3.006	0.000	0.000	0.004	0.000	0.000	4.985	0.620	0.004	0.376	0.000	0.015
	Line 18 1409_FSP_6_CS	308	0.611	1.010	0.001	0.012	0.333	3.004	0.000	0.000	0.005	0.000	0.001	4.976	0.643	0.005	0.351	0.001	0.016
	Line 19 1409_FSP_6_CS	323	0.627	1.010	0.001	0.012	0.340	3.009	0.000	0.000	0.005	0.000	0.000	5.004	0.644	0.006	0.350	0.000	0.070
	Line 20 1409_FSP_6_CS	337	0.661	1.023	0.001	0.007	0.269	3.003	0.001	0.000	0.019	0.000	0.000	4.984	0.697	0.020	0.284	0.000	0.065
	Line 21 1409_FSP_6_CS	352	0.663	1.025	0.001	0.008	0.273	3.001	0.000	0.000	0.018	0.000	0.000	4.989	0.695	0.019	0.286	0.000	0.068
	Line 22 1409_FSP_6_CS	367	0.668	1.023	0.001	0.007	0.277	3.000	0.000	0.000	0.019	0.000	0.000	4.995	0.693	0.020	0.287	0.000	0.062
	Line 23 1409_FSP_6_CS	381	0.677	1.018	0.001	0.007	0.290	2.991	0.000	0.000	0.018	0.000	0.000	5.002	0.687	0.018	0.294	0.000	0.059
	Line 24 1409_FSP_6_CS	396	0.647	1.023	0.001	0.005	0.298	2.994	0.000	0.000	0.018	0.000	0.000	4.985	0.672	0.018	0.310	0.000	0.058
	Line 25 1409_FSP_6_CS	411	0.658	1.021	0.001	0.005	0.296	2.993	0.000	0.000	0.017	0.000	0.000	4.992	0.677	0.018	0.305	0.000	0.062
	Line 26 1409_FSP_6_CS	425	0.648	1.018	0.001	0.007	0.288	2.999	0.000	0.000	0.018	0.000	0.000	4.979	0.679	0.019	0.302	0.000	0.059
	Line 27 1409_FSP_6_CS	440	0.667	1.017	0.000	0.007	0.288	2.996	0.000	0.000	0.017	0.000	0.000	4.993	0.686	0.017	0.297	0.000	0.064
	Line 28 1409_FSP_6_CS	455	0.645	1.014	0.001	0.009	0.286	3.002	0.000	0.000	0.018	0.000	0.000	4.976	0.679	0.019	0.301	0.000	0.062
	Line 29 1409_FSP_6_CS	469	0.669	1.019	0.000	0.007	0.289	2.994	0.000	0.000	0.018	0.000	0.001	4.996	0.685	0.018	0.296	0.001	0.064
	Line 30 1409_FSP_6_CS	484	0.657	1.021	0.001	0.007	0.287	2.994	0.000	0.000	0.018	0.000	0.000	4.987	0.683	0.019	0.298	0.000	0.011
V-149	Line 1 1409_P_1_CS	1	0.625	0.995	0.000	0.012	0.321	3.009	0.000	0.000	0.004	0.000	0.000	4.966	0.658	0.004	0.338	0.000	0.011
	Line 2 1409_P_1_CS	22	0.625	0.982	0.001	0.013	0.330	3.015	0.000	0.000	0.004	0.000	0.000	4.970	0.652	0.004	0.344	0.000	0.009
	Line 3 1409_P_1_CS	43	0.629	0.990	0.001	0.010	0.327	3.011	0.001	0.000	0.003	0.000	0.000	4.971	0.656	0.003	0.341	0.000	0.010
	Line 4 1409_P_1_CS	64	0.637	0.986	0.000	0.012	0.325	3.012	0.000	0.001	0.003	0.000	0.000	4.976	0.660	0.003	0.337	0.000	0.011
	Line 5 1409_P_1_CS	85	0.630	0.991	0.000	0.012	0.323	3.011	0.000	0.000	0.004	0.000	0.000	4.970	0.659	0.004	0.338	0.000	0.011
	Line 6 1409_P_1_CS	106	0.648	0.995	0.000	0.012	0.315	3.005	0.000	0.000	0.003	0.000	0.000	4.980	0.670	0.004	0.326	0.000	0.012
	Line 7 1409_P_1_CS	128	0.650	0.989	0.000	0.012	0.309	3.009	0.001	0.001	0.004	0.000	0.000	4.976	0.675	0.004	0.321	0.000	0.012
	Line 8 1409_P_1_CS	149	0.665	0.984	0.001	0.012	0.295	3.014	0.000	0.000	0.004	0.000	0.000	4.974	0.690	0.004	0.306	0.000	0.013
	Line 9 1409_P_1_CS	170	0.654	0.988	0.000	0.011	0.305	3.012	0.000	0.000	0.004	0.000	0.000	4.974	0.679	0.004	0.317	0.000	0.013
	Line 10 1409_P_1_CS	191	0.655	0.987	0.001	0.012	0.312	3.009	0.000	0.001	0.004	0.000	0.000	4.981	0.674	0.004	0.322	0.000	0.059

Table H.35: EMPA data of R-type feldspar inV-111. Data is presented in atoms per formula unit and in fractions of solid solution end member. The end members are: albite (X_{Ab}), anorthite (X_{An}), orthoclase (X_{Or}), and celsian (X_{Cs}). Distances of the line scans are directed from core towards the rim of the crystal.

V-ID	Analyses ID	Distance (μm)	Na	Al	Ti	Fe	K	Si	Mg	Mn	Ca	Sr	Ba	Sum	X_{Ab}	X_{An}	X_{Or}	X_{Cs}	Ca/K
V-111	Line 1 1305_FSP_5_CS	1	0.539	1.031	0.001	0.007	0.432	2.967	0.000	0.000	0.025	0.000	0.000	5.002	0.541	0.025	0.434	0.000	0.060
	Line 2 1305_FSP_5_CS	10	0.538	1.036	0.001	0.006	0.433	2.964	0.000	0.000	0.026	0.000	0.000	5.003	0.539	0.026	0.434	0.000	0.058
	Line 3 1305_FSP_5_CS	19	0.527	1.032	0.000	0.006	0.434	2.970	0.000	0.000	0.025	0.000	0.000	4.994	0.534	0.026	0.440	0.000	0.059
	Line 4 1305_FSP_5_CS	27	0.528	1.034	0.001	0.006	0.434	2.966	0.000	0.002	0.025	0.000	0.000	4.996	0.535	0.026	0.439	0.000	0.058
	Line 5 1305_FSP_5_CS	36	0.513	1.038	0.001	0.007	0.436	2.967	0.000	0.000	0.025	0.000	0.000	4.987	0.526	0.026	0.447	0.000	0.062
	Line 6 1305_FSP_5_CS	45	0.534	1.036	0.000	0.006	0.434	2.964	0.000	0.000	0.027	0.000	0.000	5.002	0.537	0.027	0.436	0.000	0.064
	Line 7 1305_FSP_5_CS	54	0.529	1.044	0.001	0.006	0.430	2.959	0.000	0.000	0.027	0.000	0.000	4.997	0.536	0.028	0.436	0.000	0.072
	Line 8 1305_FSP_5_CS	62	0.533	1.036	0.000	0.005	0.428	2.963	0.001	0.001	0.031	0.000	0.002	4.999	0.536	0.031	0.431	0.002	0.122
	Line 9 1305_FSP_5_CS	71	0.563	1.054	0.002	0.007	0.377	2.946	0.000	0.000	0.046	0.000	0.001	4.995	0.571	0.046	0.382	0.001	0.110
	Line 10 1305_FSP_5_CS	80	0.559	1.061	0.001	0.007	0.383	2.943	0.000	0.000	0.042	0.000	0.001	4.997	0.568	0.043	0.388	0.001	0.108
	Line 11 1305_FSP_5_CS	89	0.549	1.054	0.001	0.006	0.389	2.949	0.000	0.000	0.042	0.000	0.001	4.992	0.560	0.043	0.396	0.001	0.111
	Line 12 1305_FSP_5_CS	97	0.567	1.055	0.001	0.006	0.386	2.944	0.000	0.000	0.043	0.000	0.000	5.003	0.569	0.043	0.387	0.000	0.111
	Line 13 1305_FSP_5_CS	106	0.567	1.053	0.001	0.006	0.382	2.948	0.000	0.000	0.042	0.000	0.001	4.999	0.571	0.043	0.386	0.001	0.114
	Line 14 1305_FSP_5_CS	115	0.572	1.054	0.001	0.004	0.379	2.947	0.000	0.000	0.043	0.000	0.001	5.000	0.575	0.043	0.381	0.001	0.110
	Line 15 1305_FSP_5_CS	124	0.550	1.062	0.000	0.005	0.388	2.944	0.000	0.000	0.043	0.000	0.001	4.994	0.560	0.043	0.396	0.001	0.110
	Line 16 1305_FSP_5_CS	132	0.574	1.056	0.000	0.006	0.384	2.944	0.000	0.000	0.042	0.000	0.001	5.007	0.573	0.042	0.384	0.001	0.109
	Line 17 1305_FSP_5_CS	141	0.566	1.055	0.001	0.006	0.385	2.946	0.000	0.001	0.042	0.000	0.001	5.002	0.569	0.042	0.388	0.001	0.110
	Line 18 1305_FSP_5_CS	150	0.552	1.057	0.002	0.006	0.387	2.946	0.001	0.000	0.042	0.000	0.001	4.993	0.562	0.043	0.394	0.001	0.109
	Line 19 1305_FSP_5_CS	159	0.541	1.047	0.001	0.005	0.386	2.958	0.000	0.000	0.042	0.000	0.000	4.981	0.558	0.043	0.399	0.000	0.111
	Line 20 1305_FSP_5_CS	167	0.565	1.062	0.001	0.006	0.386	2.939	0.001	0.000	0.043	0.000	0.001	5.004	0.568	0.043	0.388	0.001	0.108
	Line 21 1305_FSP_5_CS	176	0.556	1.059	0.001	0.006	0.389	2.944	0.000	0.000	0.042	0.000	0.000	4.999	0.563	0.043	0.394	0.000	0.110
	Line 22 1305_FSP_5_CS	185	0.550	1.054	0.003	0.005	0.391	2.947	0.000	0.000	0.043	0.000	0.001	4.994	0.558	0.044	0.397	0.001	0.099
	Line 23 1305_FSP_5_CS	194	0.559	1.055	0.001	0.007	0.393	2.946	0.000	0.001	0.039	0.000	0.000	5.001	0.564	0.039	0.396	0.000	0.100
	Line 24 1305_FSP_5_CS	202	0.554	1.053	0.001	0.006	0.391	2.949	0.000	0.001	0.039	0.000	0.000	4.996	0.562	0.040	0.397	0.000	0.101
	Line 25 1305_FSP_5_CS	211	0.551	1.053	0.001	0.007	0.393	2.950	0.000	0.000	0.040	0.000	0.001	4.995	0.560	0.040	0.399	0.001	0.100
	Line 26 1305_FSP_5_CS	220	0.562	1.050	0.003	0.007	0.392	2.947	0.000	0.000	0.039	0.000	0.000	5.002	0.566	0.039	0.395	0.000	0.102
	Line 27 1305_FSP_5_CS	229	0.553	1.052	0.001	0.007	0.394	2.949	0.000	0.000	0.040	0.000	0.001	4.998	0.560	0.041	0.399	0.001	0.097
	Line 28 1305_FSP_5_CS	237	0.555	1.050	0.001	0.007	0.396	2.950	0.001	0.000	0.038	0.000	0.001	4.999	0.560	0.039	0.400	0.001	0.103
	Line 29 1305_FSP_5_CS	246	0.548	1.053	0.001	0.007	0.392	2.950	0.000	0.000	0.041	0.000	0.000	4.993	0.559	0.041	0.400	0.000	0.103
	Line 30 1305_FSP_5_CS	255	0.581	1.051	0.001	0.008	0.389	2.944	0.000	0.001	0.040	0.000	0.000	5.015	0.575	0.040	0.385	0.000	0.162

Table H.36: EMPA data of R-type feldspar inV-111. Data is presented in atoms per formula unit and in fractions of solid solution end member. The end members are: albite (X_{Ab}), anorthite (X_{An}), orthoclase (X_{Or}), and celsian (X_{Cs}). Distances of the line scans are directed from core towards the rim of the crystal.

V-ID	Analyses ID	Distance (μm)	Na	Al	Ti	Fe	K	Si	Mg	Mn	Ca	Sr	Ba	Sum	X_{Ab}	X_{An}	X_{Or}	X_{Cs}	Ca/K
V-111	Line 1 1305_FSP_4_CS	1	0.608	1.066	0.003	0.007	0.320	2.934	0.000	0.000	0.052	0.000	0.003	4.993	0.619	0.053	0.326	0.003	0.157
	Line 2 1305_FSP_4_CS	12	0.612	1.070	0.002	0.005	0.321	2.931	0.001	0.001	0.050	0.001	0.003	4.998	0.620	0.051	0.326	0.003	0.156
	Line 3 1305_FSP_4_CS	23	0.623	1.071	0.001	0.006	0.323	2.929	0.000	0.000	0.050	0.000	0.003	5.007	0.623	0.050	0.323	0.003	0.164
	Line 4 1305_FSP_4_CS	34	0.617	1.068	0.001	0.007	0.317	2.932	0.000	0.001	0.052	0.000	0.004	5.000	0.623	0.053	0.320	0.005	0.171
	Line 5 1305_FSP_4_CS	45	0.614	1.073	0.001	0.004	0.314	2.931	0.001	0.000	0.054	0.000	0.004	4.996	0.622	0.054	0.319	0.005	0.162
	Line 6 1305_FSP_4_CS	57	0.607	1.075	0.001	0.006	0.321	2.930	0.001	0.000	0.052	0.000	0.004	4.996	0.617	0.053	0.326	0.004	0.159
	Line 7 1305_FSP_4_CS	68	0.630	1.065	0.001	0.007	0.322	2.931	0.000	0.000	0.051	0.000	0.004	5.012	0.625	0.051	0.320	0.004	0.095
	Line 8 1305_FSP_4_CS	79	0.575	1.052	0.003	0.007	0.372	2.949	0.000	0.000	0.035	0.000	0.003	4.996	0.584	0.036	0.378	0.003	0.064
	Line 9 1305_FSP_4_CS	90	0.563	1.035	0.002	0.007	0.395	2.965	0.000	0.000	0.025	0.000	0.001	4.994	0.572	0.026	0.401	0.001	0.070
	Line 10 1305_FSP_4_CS	101	0.577	1.036	0.002	0.006	0.387	2.962	0.000	0.000	0.027	0.000	0.002	4.999	0.581	0.027	0.389	0.002	0.114
	Line 11 1305_FSP_4_CS	112	0.606	1.054	0.001	0.006	0.348	2.945	0.000	0.000	0.040	0.000	0.003	5.004	0.608	0.040	0.349	0.003	0.151
	Line 12 1305_FSP_4_CS	123	0.601	1.068	0.002	0.005	0.327	2.936	0.000	0.000	0.050	0.000	0.003	4.992	0.612	0.050	0.334	0.003	0.154
	Line 13 1305_FSP_4_CS	134	0.613	1.070	0.002	0.007	0.323	2.931	0.000	0.000	0.050	0.000	0.003	5.000	0.620	0.050	0.327	0.003	0.152
	Line 14 1305_FSP_4_CS	146	0.616	1.071	0.002	0.005	0.321	2.931	0.000	0.000	0.049	0.000	0.004	5.000	0.623	0.049	0.324	0.004	0.163
	Line 15 1305_FSP_4_CS	157	0.612	1.071	0.002	0.006	0.316	2.932	0.000	0.001	0.052	0.000	0.003	4.995	0.623	0.052	0.322	0.003	0.167
	Line 16 1305_FSP_4_CS	168	0.610	1.073	0.002	0.006	0.312	2.932	0.000	0.000	0.052	0.000	0.003	4.990	0.625	0.053	0.319	0.003	0.164
	Line 17 1305_FSP_4_CS	179	0.620	1.068	0.003	0.007	0.314	2.932	0.000	0.001	0.052	0.000	0.003	4.999	0.627	0.052	0.318	0.003	0.174
	Line 18 1305_FSP_4_CS	190	0.614	1.068	0.002	0.006	0.308	2.934	0.000	0.001	0.054	0.000	0.003	4.991	0.628	0.055	0.315	0.003	0.169
	Line 19 1305_FSP_4_CS	201	0.641	1.060	0.002	0.005	0.313	2.933	0.001	0.001	0.053	0.000	0.005	5.012	0.634	0.052	0.309	0.005	0.158
	Line 20 1305_FSP_4_CS	212	0.606	1.072	0.002	0.006	0.324	2.931	0.000	0.001	0.051	0.000	0.005	4.997	0.615	0.052	0.328	0.005	0.155
	Line 21 1305_FSP_4_CS	223	0.607	1.076	0.001	0.007	0.321	2.929	0.000	0.000	0.050	0.000	0.004	4.996	0.619	0.051	0.327	0.004	0.189
	Line 22 1305_FSP_4_CS	235	0.640	1.075	0.001	0.006	0.304	2.923	0.000	0.000	0.057	0.000	0.004	5.011	0.637	0.057	0.302	0.004	0.206
	Line 23 1305_FSP_4_CS	246	0.613	1.083	0.002	0.006	0.294	2.924	0.000	0.000	0.061	0.000	0.004	4.987	0.631	0.062	0.302	0.005	0.214
	Line 24 1305_FSP_4_CS	257	0.619	1.088	0.001	0.006	0.307	2.913	0.000	0.000	0.066	0.000	0.004	5.004	0.622	0.066	0.308	0.004	0.197
	Line 25 1305_FSP_4_CS	268	0.618	1.069	0.001	0.007	0.305	2.931	0.000	0.000	0.060	0.000	0.003	4.995	0.627	0.061	0.309	0.003	0.193
	Line 26 1305_FSP_4_CS	279	0.617	1.081	0.002	0.008	0.310	2.920	0.000	0.001	0.060	0.000	0.002	5.000	0.625	0.060	0.313	0.002	0.167
	Line 27 1305_FSP_4_CS	290	0.623	1.066	0.002	0.009	0.314	2.933	0.000	0.000	0.053	0.000	0.001	5.001	0.629	0.053	0.317	0.001	0.155
	Line 28 1305_FSP_4_CS	301	0.634	1.064	0.001	0.005	0.313	2.937	0.001	0.000	0.048	0.000	0.001	5.004	0.636	0.049	0.315	0.001	0.140
	Line 29 1305_FSP_4_CS	312	0.637	1.063	0.001	0.008	0.316	2.936	0.001	0.001	0.044	0.000	0.001	5.008	0.638	0.044	0.317	0.001	0.140
	Line 30 1305_FSP_4_CS	323	0.642	1.063	0.001	0.008	0.312	2.936	0.001	0.000	0.044	0.000	0.001	5.009	0.643	0.044	0.313	0.001	0.000

Table H.37: EMPA data of volcanic glass from sample V-45. Data is presented in wt%. The oxygen equivalents of F and Cl are calculated by multiplying wt% F by 0.4211 and Cl by 0.2256. The oxygen-equivalents for the F and Cl are subtracted in an addtional sum† from the analytical total followin Deer et al. (2013).

V-ID	Comment	SiO_2	K_2O	CaO	Na_2O	FeO	Al_2O_3	TiO_2	Cl	MgO	MnO	F	P_2O_5	BaO	SO_3	ZnO	Total	F=O	Cl=O	SUM†
V-45 cores	Line 1 JE_1301_1_CORE	73.15	3.84	0.20	5.36	2.65	10.62	0.18	0.01	0.02	0.06	0.00	0.00	0.01	0.00	0.04	96.15	0.00	0.00	96.14
	Line 2 JE_1301_1_CORE	74.17	4.54	0.23	5.26	2.61	10.41	0.10	0.00	0.01	0.01	0.00	0.04	0.00	0.03	0.19	97.61	0.00	0.00	97.61
	Line 3 JE_1301_1_CORE	74.86	4.46	0.18	5.28	2.54	10.65	0.39	0.00	0.02	0.00	0.00	0.05	0.34	0.03	0.00	98.81	0.00	0.00	98.81
	Line 4 JE_1301_1_CORE	73.02	4.21	0.22	5.00	2.69	11.04	0.12	0.00	0.00	0.00	0.11	0.00	0.02	0.00	0.26	96.70	0.05	0.00	96.65
	Line 5 JE_1301_1_CORE	74.91	4.04	0.26	5.09	2.48	10.52	0.16	0.04	0.01	0.00	0.22	0.01	0.03	0.00	0.15	97.92	0.09	0.01	97.81
	Line 6 JE_1301_1_CORE	73.63	4.13	0.14	5.32	2.82	10.60	0.06	0.06	0.00	0.00	0.00	0.00	0.03	0.05	0.00	96.84	0.00	0.01	96.83
	Line 7 JE_1301_1_CORE	73.55	4.45	0.14	5.12	2.44	10.65	0.22	0.06	0.03	0.00	0.06	0.00	0.09	0.05	0.20	97.06	0.03	0.01	97.02
	Line 8 JE_1301_1_CORE	74.81	4.29	0.17	5.33	2.39	10.57	0.10	0.05	0.05	0.02	0.00	0.00	0.23	0.10	0.17	98.27	0.00	0.01	98.26
	Line 9 JE_1301_1_CORE	74.30	4.69	0.22	5.69	2.43	10.56	0.09	0.06	0.00	0.00	0.00	0.10	0.00	0.00	0.09	98.23	0.00	0.01	98.22
	Line 10 JE_1301_1_CORE	74.78	3.99	0.10	5.16	2.59	10.65	0.21	0.00	0.00	0.07	0.00	0.00	0.00	0.05	0.26	97.86	0.00	0.00	97.86
	Line 11 JE_1301_1_CORE	75.45	4.60	0.22	4.98	2.55	10.73	0.06	0.00	0.02	0.06	0.05	0.00	0.43	0.05	0.04	99.25	0.02	0.00	99.23
	Line 12 JE_1301_1_CORE	73.52	4.40	0.19	5.48	2.58	10.38	0.05	0.06	0.02	0.00	0.00	0.32	0.06	0.05	0.13	97.25	0.00	0.01	97.23
	JE_1301_2_core1	75.73	4.60	0.10	5.28	2.71	10.50	0.13	0.02	0.00	0.01	0.15	0.16	0.24	0.00	0.02	99.64	0.06	0.00	99.57
	JE_1301_2_core2	75.54	4.48	0.04	5.37	2.55	10.53	0.11	0.06	0.00	0.02	0.00	0.02	0.02	0.00	0.00	98.74	0.00	0.01	98.73
	JE_1301_2_core3	74.21	4.45	0.07	5.32	2.44	10.39	0.05	0.04	0.00	0.00	0.00	0.00	0.00	0.03	0.00	97.01	0.00	0.01	97.00
	JE_1301_2_core4	75.18	4.53	0.02	5.41	2.64	10.51	0.10	0.05	0.01	0.00	0.00	0.00	0.27	0.19	0.17	99.08	0.00	0.01	99.07
	JE_1301_2_core5	75.24	4.51	0.11	5.41	2.51	10.41	0.13	0.00	0.02	0.00	0.00	0.06	0.05	0.08	0.00	98.53	0.00	0.00	98.53
	JE_1301_2_core6	75.40	4.49	0.04	5.37	2.43	10.58	0.24	0.04	0.04	0.02	0.16	0.04	0.05	0.05	0.00	98.95	0.07	0.01	98.88
	JE_1301_2_core7	75.76	4.51	0.04	5.44	2.64	10.62	0.25	0.03	0.03	0.06	0.00	0.00	0.11	0.05	0.17	99.71	0.00	0.01	99.70
	JE_1301_2_core8	74.64	4.61	0.00	5.22	2.50	10.59	0.13	0.00	0.00	0.02	0.00	0.00	0.13	0.00	0.00	97.85	0.00	0.00	97.85
	JE_1301_2_core9	75.87	4.29	0.00	5.45	2.58	10.79	0.14	0.02	0.01	0.01	0.01	0.00	0.11	0.00	0.04	99.32	0.01	0.00	99.31
	JE_1301_2_core10	75.33	4.73	0.12	5.16	2.45	10.49	0.15	0.00	0.01	0.00	0.00	0.10	0.33	0.00	0.00	98.86	0.00	0.00	98.86
	Line 1 JE_1301_3_core	74.34	4.55	0.14	5.23	2.40	10.80	0.26	0.05	0.00	0.02	0.00	0.22	0.20	0.02	0.00	98.22	0.00	0.01	98.21
	Line 2 JE_1301_3_core	75.04	4.38	0.19	5.46	2.58	10.47	0.17	0.04	0.00	0.00	0.07	0.03	0.00	0.03	0.00	98.45	0.03	0.01	98.41
	Line 3 JE_1301_3_core	74.20	4.11	0.22	4.97	2.51	10.78	0.05	0.08	0.00	0.00	0.00	0.11	0.25	0.02	0.00	97.30	0.00	0.02	97.28
	Line 4 JE_1301_3_core	74.55	4.42	0.18	5.45	2.44	10.68	0.21	0.00	0.02	0.04	0.00	0.03	0.00	0.00	0.02	98.04	0.00	0.00	98.03
	Line 5 JE_1301_3_core	73.41	4.20	0.22	5.00	2.58	10.51	0.10	0.00	0.00	0.00	0.00	0.00	0.24	0.00	0.07	96.33	0.00	0.00	96.33
	Line 6 JE_1301_3_core	74.00	4.08	0.16	5.60	2.51	10.66	0.18	0.02	0.01	0.02	0.05	0.09	0.00	0.05	0.00	97.42	0.02	0.00	97.39
	Line 7 JE_1301_3_core	75.08	4.07	0.18	5.32	2.54	10.45	0.16	0.01	0.00	0.00	0.00	0.00	0.28	0.08	0.00	98.18	0.00	0.00	98.18
	Line 8 JE_1301_3_core	74.49	4.53	0.21	5.41	2.75	10.84	0.06	0.03	0.00	0.02	0.00	0.31	0.12	0.02	0.09	98.89	0.00	0.01	98.88
	Line 9 JE_1301_3_core	74.98	4.34	0.17	5.13	2.63	10.70	0.17	0.14	0.00	0.11	0.00	0.00	0.23	0.08	0.00	98.66	0.00	0.03	98.63
	Line 10 JE_1301_3_core	74.02	4.44	0.17	5.65	2.51	10.39	0.14	0.07	0.01	0.00	0.00	0.00	0.18	0.00	0.24	97.82	0.00	0.02	97.81
V-45 rims	JE_1301_1_rim_1	72.28	4.24	0.13	5.46	2.59	10.23	0.04	0.00	0.00	0.10	0.00	0.01	0.10	0.00	0.15	95.34	0.00	0.00	95.34
	JE_1301_1_rim_2	73.42	4.10	0.21	5.03	2.58	10.52	0.11	0.00	0.00	0.00	0.03	0.07	0.25	0.10	0.00	96.43	0.01	0.00	96.41
	JE_1301_1_rim_3	73.35	4.17	0.17	5.08	2.56	10.12	0.09	0.03	0.00	0.00	0.02	0.04	0.03	0.05	0.15	95.87	0.01	0.01	95.85
	JE_1301_1_rim_4	73.02	4.14	0.13	5.04	2.62	10.19	0.09	0.12	0.00	0.00	0.00	0.00	0.09	0.00	0.00	95.44	0.00	0.03	95.42
	JE_1301_1_rim_5	73.21	4.40	0.17	5.48	2.57	10.52	0.15	0.05	0.00	0.00	0.17	0.15	0.01	0.00	0.00	96.87	0.07	0.01	96.79
	JE_1301_2_rim1	74.15	4.62	0.00	5.31	2.53	10.46	0.24	0.00	0.06	0.04	0.00	0.00	0.12	0.00	0.00	97.54	0.00	0.00	97.54
	JE_1301_2_rim2	75.80	4.43	0.05	4.92	2.71	10.26	0.23	0.03	0.02	0.03	0.00	0.00	0.03	0.06	0.07	98.65	0.00	0.01	98.64
	JE_1301_2_rim3	74.79	4.67	0.00	5.14	2.37	10.29	0.13	0.06	0.00	0.03	0.00	0.00	0.15	0.06	0.00	97.69	0.00	0.01	97.68
	JE_1301_2_rim4	75.21	4.52	0.05	5.49	2.50	10.42	0.13	0.04	0.00	0.02	0.01	0.00	0.00	0.03	0.07	98.50	0.00	0.01	98.49
	JE_1301_2_rim5	73.81	4.50	0.07	5.12	2.44	10.60	0.27	0.04	0.02	0.00	0.09	0.05	0.00	0.00	0.00	97.02	0.04	0.01	96.97
	JE_1301_3_rim1	72.66	4.26	0.24	5.21	2.52	10.49	0.12	0.04	0.00	0.00	0.13	0.00	0.20	0.02	0.24	96.14	0.05	0.01	96.07
	JE_1301_3_rim2	72.54	3.96	0.21	5.50	2.58	10.37	0.18	0.02	0.00	0.00	0.00	0.03	0.39	0.00	0.13	95.91	0.00	0.01	95.91
	JE_1301_3_rim3	73.19	4.17	0.18	5.08	2.39	10.66	0.10	0.05	0.00	0.02	0.00	0.00	0.11	0.06	0.00	96.01	0.00	0.01	96.00
	JE_1301_3_rim4	73.75	4.29	0.15	5.30	2.61	10.47	0.14	0.07	0.04	0.01	0.00	0.01	0.05	0.16	0.00	97.05	0.00	0.02	97.03
	JE_1301_3_rim5	74.37	4.51	0.19	5.16	2.52	10.21	0.10	0.00	0.04	0.00	0.00	0.00	0.02	0.00	0.06	97.18	0.00	0.00	97.18

Table H.38: EMPA data of plagioclase inV-221a. Data is presented in atoms per formula unit and in fractions of solid solution end member. The end members are: albite (X_{Ab}), anorthite (X_{An}), orthoclase (X_{Or}), and celsian (X_{Cs}).

V-ID	Comment	Na	Al	Ti	Fe	K	Si	Mg	Mn	Ba	Sr	Ca	Total	X_{Ab}	X_{Or}	X_{An}	X_{Ce}
V-221a	1316_P1_1	0.644	1.269	0.002	0.008	0.076	2.728	0.002	0.000	0.265	0.000	0.003	4.996	0.652	0.077	0.268	0.003
	1316_P1_2	0.656	1.271	0.001	0.008	0.075	2.723	0.001	0.000	0.267	0.000	0.002	5.006	0.656	0.075	0.267	0.002
	1316_P1_3	0.664	1.254	0.002	0.010	0.078	2.734	0.001	0.000	0.263	0.001	0.003	5.009	0.659	0.077	0.261	0.003
	1316_P1_4	0.662	1.255	0.001	0.009	0.075	2.735	0.001	0.000	0.261	0.005	0.003	5.005	0.661	0.075	0.261	0.003
	1316_P1_5	0.646	1.293	0.001	0.010	0.067	2.696	0.000	0.001	0.288	0.007	0.002	5.013	0.644	0.067	0.287	0.002
	1316_P1_6	0.625	1.299	0.002	0.010	0.066	2.694	0.000	0.001	0.300	0.000	0.002	5.000	0.630	0.066	0.302	0.002
	1316_P1_7	0.635	1.305	0.002	0.009	0.063	2.690	0.000	0.000	0.299	0.000	0.001	5.004	0.636	0.063	0.299	0.001
	1316_P1_8	0.637	1.303	0.001	0.010	0.061	2.690	0.001	0.000	0.299	0.004	0.001	5.007	0.638	0.062	0.300	0.001
	1316_P1_9	0.631	1.310	0.002	0.010	0.061	2.681	0.001	0.000	0.308	0.002	0.002	5.008	0.630	0.061	0.307	0.002
	1316_P1_10	0.635	1.311	0.002	0.010	0.060	2.678	0.001	0.000	0.309	0.005	0.001	5.012	0.632	0.060	0.307	0.001
	1316_P5_1	0.699	1.183	0.001	0.009	0.122	2.807	0.000	0.001	0.184	0.000	0.005	5.011	0.692	0.121	0.182	0.005
	1316_P5_2	0.682	1.189	0.001	0.007	0.119	2.808	0.000	0.001	0.186	0.000	0.005	4.998	0.688	0.120	0.187	0.005
	1316_P5_3	0.698	1.194	0.001	0.009	0.120	2.798	0.001	0.000	0.186	0.002	0.005	5.014	0.692	0.119	0.184	0.005
	1316_P5_4	0.694	1.189	0.001	0.008	0.121	2.803	0.000	0.000	0.186	0.000	0.005	5.008	0.691	0.120	0.185	0.005
	1316_P5_5	0.687	1.196	0.001	0.008	0.120	2.798	0.001	0.000	0.190	0.000	0.005	5.007	0.686	0.120	0.189	0.005
	1316_P5_6	0.690	1.196	0.001	0.008	0.119	2.797	0.000	0.001	0.193	0.000	0.004	5.009	0.686	0.118	0.192	0.004
	1316_P5_7	0.703	1.200	0.001	0.009	0.117	2.792	0.000	0.000	0.192	0.000	0.004	5.017	0.692	0.115	0.189	0.004
	1316_P5_8	0.681	1.196	0.002	0.008	0.114	2.800	0.001	0.000	0.192	0.000	0.004	4.998	0.687	0.115	0.194	0.004
	1316_P5_9	0.675	1.198	0.001	0.007	0.115	2.802	0.000	0.000	0.190	0.002	0.004	4.993	0.686	0.117	0.193	0.004
	1316_P5_10	0.685	1.198	0.001	0.007	0.113	2.799	0.000	0.000	0.194	0.000	0.003	5.000	0.689	0.113	0.195	0.003
	1316_P5_11	0.693	1.194	0.001	0.007	0.121	2.801	0.001	0.000	0.186	0.000	0.004	5.008	0.690	0.121	0.185	0.004
	1316_P5_12	0.703	1.188	0.002	0.008	0.119	2.801	0.001	0.000	0.187	0.002	0.004	5.014	0.694	0.117	0.185	0.003
	1316_P5_13	0.684	1.165	0.001	0.006	0.155	2.828	0.001	0.001	0.162	0.001	0.004	5.009	0.680	0.154	0.161	0.004
	1316_P6_1	0.687	1.243	0.001	0.009	0.085	2.749	0.000	0.000	0.237	0.002	0.002	5.014	0.680	0.084	0.234	0.002
	1316_P6_2	0.633	1.322	0.001	0.008	0.056	2.672	0.001	0.000	0.315	0.001	0.001	5.010	0.629	0.056	0.313	0.001
	1316_P6_3	0.625	1.319	0.002	0.009	0.055	2.677	0.000	0.000	0.312	0.002	0.002	5.002	0.629	0.056	0.314	0.002

Table H.39: EMPA data of plagioclase inV-45. Data is presented in atoms per formula unit and in fractions of solid solution end member. The end members are: albite (X_{Ab}), anorthite (X_{An}), orthoclase (X_{Or}), and celsian (X_{Cs}).

V-ID	Comment	Na	Al	Ti	Fe	K	Si	Mg	Mn	Ba	Sr	Ca	Total	X_{Ab}	X_{Or}	X_{An}	X_{Ce}
V-45	1301_Plag_12_1	0.723	1.163	0.000	0.008	0.107	2.822	0.001	0.000	0.182	0.003	0.004	5.012	0.712	0.105	0.179	0.004
	1301_Plag_12_2	0.720	1.165	0.001	0.007	0.108	2.823	0.000	0.000	0.178	0.000	0.004	5.006	0.713	0.107	0.176	0.004
	1301_Plag_12_3	0.702	1.169	0.002	0.006	0.104	2.824	0.000	0.000	0.183	0.000	0.003	4.992	0.708	0.105	0.184	0.003
	1301_Plag_12_4	0.692	1.185	0.001	0.006	0.093	2.814	0.000	0.000	0.191	0.000	0.003	4.985	0.706	0.095	0.196	0.003
	1301_Plag_12_5	0.697	1.187	0.001	0.007	0.088	2.808	0.000	0.000	0.197	0.003	0.002	4.990	0.708	0.090	0.200	0.002
	1301_Plag_12_6	0.703	1.201	0.000	0.006	0.081	2.792	0.000	0.000	0.211	0.001	0.002	4.999	0.705	0.081	0.211	0.002
	1301_Plag_12_7	0.668	1.182	0.001	0.008	0.085	2.819	0.001	0.000	0.200	0.000	0.002	4.966	0.700	0.089	0.209	0.002
	1301_Plag_12_8	0.700	1.179	0.000	0.006	0.086	2.815	0.001	0.001	0.198	0.000	0.003	4.988	0.709	0.087	0.201	0.003
	1301_Plag_12_9	0.696	1.186	0.000	0.007	0.085	2.812	0.000	0.000	0.196	0.001	0.003	4.986	0.710	0.087	0.200	0.003
	1301_Plag_12_10	0.712	1.181	0.001	0.006	0.088	2.812	0.001	0.001	0.192	0.000	0.002	4.997	0.716	0.089	0.193	0.002
	1301_Plag_12_11	0.706	1.184	0.001	0.004	0.088	2.811	0.000	0.000	0.195	0.000	0.003	4.992	0.712	0.089	0.196	0.003
	1301_Plag_12_12	0.695	1.179	0.001	0.006	0.099	2.818	0.001	0.000	0.186	0.000	0.003	4.988	0.707	0.101	0.190	0.003
	1301_Plag_12_13	0.698	1.168	0.001	0.007	0.098	2.826	0.000	0.001	0.185	0.000	0.003	4.987	0.709	0.100	0.188	0.003
	1301_Plag_12_14	0.706	1.166	0.001	0.006	0.104	2.829	0.000	0.000	0.177	0.000	0.003	4.992	0.713	0.105	0.179	0.003
	1301_Plag_12_15	0.681	1.187	0.001	0.006	0.098	2.806	0.000	0.000	0.205	0.000	0.003	4.989	0.689	0.100	0.208	0.003
	1301_Plag_12_16	0.722	1.177	0.000	0.007	0.097	2.814	0.001	0.001	0.185	0.000	0.003	5.007	0.717	0.096	0.183	0.003
	1301_Plag_12_17	0.703	1.176	0.001	0.007	0.098	2.820	0.000	0.000	0.183	0.001	0.003	4.991	0.712	0.099	0.186	0.003
	1301_Plag_12_18	0.700	1.186	0.001	0.007	0.098	2.811	0.000	0.001	0.188	0.000	0.003	4.994	0.707	0.099	0.190	0.003
	1301_Plag_12_19	0.709	1.171	0.000	0.008	0.102	2.823	0.001	0.000	0.179	0.000	0.004	4.996	0.714	0.103	0.180	0.004
	1301_Plag_12_20	0.692	1.180	0.000	0.005	0.100	2.821	0.001	0.000	0.182	0.000	0.003	4.985	0.707	0.103	0.186	0.003
	1301_Plag_12_21	0.700	1.178	0.001	0.006	0.102	2.821	0.000	0.000	0.179	0.000	0.004	4.991	0.711	0.103	0.182	0.004
	1301_Plag_12_22	0.703	1.170	0.001	0.006	0.105	2.824	0.000	0.001	0.179	0.001	0.004	4.994	0.709	0.106	0.181	0.004
	1301_Plag_12_23	0.691	1.148	0.002	0.006	0.129	2.848	0.000	0.001	0.155	0.001	0.004	4.986	0.706	0.132	0.158	0.004
	1301_Pl5_1	0.695	1.228	0.001	0.008	0.070	2.762	0.001	0.000	0.238	0.000	0.002	5.005	0.691	0.070	0.237	0.002
	1301_Pl5_2	0.675	1.255	0.001	0.008	0.059	2.733	0.001	0.000	0.267	0.004	0.002	5.006	0.673	0.059	0.266	0.002
	1301_Pl5_3	0.669	1.257	0.001	0.008	0.060	2.735	0.001	0.000	0.266	0.001	0.002	5.001	0.671	0.061	0.267	0.002
	1301_Pl5_4	0.704	1.208	0.001	0.009	0.075	2.781	0.001	0.000	0.223	0.001	0.002	5.003	0.702	0.074	0.222	0.002
	1301_Pl5_5	0.704	1.209	0.000	0.008	0.077	2.780	0.000	0.000	0.224	0.000	0.002	5.006	0.700	0.076	0.222	0.002
	1301_Pl5_6	0.697	1.213	0.001	0.008	0.075	2.775	0.000	0.000	0.232	0.002	0.002	5.004	0.693	0.074	0.231	0.002
	1301_Pl5_7	0.707	1.213	0.002	0.008	0.074	2.774	0.002	0.001	0.223	0.002	0.002	5.009	0.702	0.074	0.222	0.002
	1301_Pl5_8	0.704	1.213	0.001	0.007	0.079	2.778	0.000	0.001	0.218	0.002	0.003	5.006	0.702	0.078	0.217	0.003
	1301_Pl5_9	0.686	1.241	0.001	0.009	0.066	2.748	0.000	0.001	0.251	0.000	0.002	5.006	0.682	0.066	0.250	0.002
	1301_Pl5_10	0.696	1.234	0.002	0.008	0.071	2.756	0.001	0.000	0.238	0.000	0.002	5.008	0.691	0.070	0.236	0.002
	1301_Pl5_11	0.685	1.238	0.001	0.008	0.068	2.755	0.000	0.000	0.241	0.001	0.002	5.001	0.688	0.069	0.242	0.002
	1301_Pl5_12	0.713	1.216	0.000	0.007	0.077	2.775	0.001	0.001	0.221	0.000	0.002	5.013	0.704	0.076	0.218	0.002
	1301_Pl5_13	0.695	1.210	0.000	0.008	0.080	2.787	0.001	0.001	0.211	0.000	0.002	4.995	0.703	0.081	0.214	0.003
	1301_Pl5_14	0.718	1.197	0.001	0.007	0.083	2.791	0.001	0.000	0.210	0.001	0.002	5.010	0.709	0.082	0.207	0.002
	1301_Pl5_15	0.728	1.190	0.001	0.006	0.087	2.798	0.001	0.000	0.198	0.001	0.002	5.013	0.717	0.085	0.195	0.002
	1301_Pl5_16	0.685	1.220	0.001	0.009	0.077	2.775	0.001	0.000	0.222	0.002	0.002	4.994	0.695	0.078	0.225	0.002
	1301_Pl5_17	0.699	1.213	0.001	0.008	0.076	2.777	0.001	0.000	0.225	0.002	0.003	5.004	0.698	0.075	0.224	0.003
	1301_Pl5_18	0.700	1.219	0.000	0.007	0.079	2.775	0.000	0.000	0.222	0.000	0.002	5.005	0.698	0.078	0.221	0.002
	1301_Pl5_19	0.695	1.191	0.001	0.007	0.088	2.806	0.001	0.001	0.195	0.002	0.002	4.989	0.709	0.090	0.199	0.002
	1301_Pl5_20	0.711	1.192	0.001	0.009	0.090	2.802	0.000	0.000	0.193	0.000	0.003	5.001	0.714	0.090	0.194	0.003
	1301_FSP_18_1	0.714	1.153	0.001	0.007	0.124	2.843	0.001	0.000	0.151	0.000	0.004	4.998	0.719	0.125	0.152	0.004
	1301_FSP_18_2	0.719	1.160	0.000	0.007	0.116	2.833	0.000	0.000	0.163	0.002	0.003	5.004	0.718	0.116	0.163	0.003
	1301_FSP_18_3	0.722	1.161	0.001	0.007	0.107	2.832	0.000	0.001	0.167	0.000	0.003	5.001	0.722	0.108	0.167	0.003
	1301_FSP_18_4	0.719	1.173	0.000	0.007	0.101	2.821	0.000	0.000	0.178	0.000	0.003	5.003	0.718	0.101	0.178	0.003
	1301_FSP_18_5	0.715	1.176	0.001	0.008	0.093	2.815	0.000	0.000	0.188	0.000	0.003	5.000	0.716	0.093	0.188	0.003
	1301_FSP_18_6	0.710	1.175	0.001	0.008	0.099	2.819	0.000	0.001	0.181	0.000	0.003	4.997	0.715	0.099	0.183	0.003
	1301_FSP_18_7	0.714	1.171	0.000	0.006	0.099	2.821	0.001	0.000	0.183	0.001	0.003	5.000	0.715	0.099	0.183	0.003
	Line_1_1301_FSP_5_1_CS	0.665	1.265	0.000	0.010	0.056	2.728	0.000	0.000	0.272	0.002	0.001	5.000	0.670	0.056	0.273	0.001
	Line_2_1301_FSP_5_1_CS	0.662	1.279	0.001	0.010	0.052	2.712	0.001	0.000	0.284	0.003	0.001	5.005	0.663	0.052	0.284	0.001
	Line_3_1301_FSP_5_1_CS	0.612	1.328	0.000	0.009	0.042	2.665	0.001	0.001	0.337	0.001	0.001	4.998	0.617	0.042	0.340	0.001
	Line_4_1301_FSP_5_1_CS	0.646	1.301	0.001	0.010	0.046	2.690	0.000	0.000	0.306	0.004	0.002	5.005	0.646	0.046	0.306	0.002
	Line_5_1301_FSP_5_1_CS	0.625	1.302	0.000	0.009	0.046	2.691	0.000	0.000	0.318	0.001	0.001	4.994	0.631	0.047	0.321	0.001
	Line_6_1301_FSP_5_1_CS	0.661	1.287	0.001	0.008	0.052	2.699	0.001	0.000	0.298	0.004	0.002	5.013	0.653	0.051	0.294	0.002
	Line_7_1301_FSP_5_1_CS	0.661	1.272	0.000	0.009	0.052	2.718	0.001	0.000	0.289	0.000	0.002	5.003	0.659	0.052	0.288	0.002
	Line_8_1301_FSP_5_1_CS	0.641	1.286	0.001	0.010	0.050	2.705	0.001	0.000	0.303	0.000	0.002	4.997	0.644	0.050	0.304	0.002
	Line_9_1301_FSP_5_1_CS	0.688	1.250	0.000	0.008	0.060	2.740	0.000	0.000	0.259	0.001	0.002	5.009	0.682	0.059	0.257	0.002
	Line_10_1301_FSP_5_1_CS	0.675	1.240	0.001	0.009	0.062	2.753	0.001	0.000	0.250	0.000	0.002	4.995	0.682	0.063	0.253	0.002
	Line_11_1301_FSP_5_1_CS	0.674	1.244	0.000	0.008	0.064	2.752	0.001	0.001	0.247	0.002	0.002	4.995	0.683	0.065	0.250	0.002
	Line_12_1301_FSP_5_1_CS	0.651	1.279	0.001	0.009	0.053	2.710	0.001	0.000	0.292	0.004	0.002	5.002	0.652	0.053	0.292	0.002
	Line_13_1301_FSP_5_1_CS	0.657	1.275	0.001	0.008	0.051	2.714	0.001	0.000	0.290	0.001	0.001	5.001	0.657	0.051	0.290	0.001
	Line_14_1301_FSP_5_1_CS	0.684	1.246	0.001	0.008	0.060	2.743	0.001	0.000	0.261	0.000	0.002	5.005	0.679	0.060	0.259	0.002
	Line_15_1301_FSP_5_1_CS	0.693	1.242	0.002	0.008	0.062	2.746	0.001	0.000	0.251	0.002	0.003	5.009	0.687	0.061	0.249	0.003

Table H.40: Range of uncertainties from EMPA on feldspar. Minimum and maximum uncertainties from 110 EMP analyses on feldspars are presented as standard deviation in % oxides and as a propagated uncertainty of atoms per formula unit. The data is also presented in electronic supplementary of Engelhardt et al. (2017).

Oxide	Na_2O	Al_2O_3	TiO_2	FeO	K_2O	SiO_2	MgO	MnO	CaO	SrO	BaO
min SD oxide in %	2.8	0.7	47	19	1.2	0.4	69	69	1.2	133	7
max SD oxide in %	6	1.6	>100	75	3	0.9	»100	»100	5	»100	»100
Atom	Na	Al	Ti	Fe	K	Si	Mg	Mn	Ba	Sr	Ca
min SD apfu	1.69E-02	8.15E-03	1.01E-03	1.36E-03	3.32E-03	1.25E-02	7.24E-04	8.47E-04	4.98E-04	2.54E-03	8.65E-04
max SD apfu	3.74E-02	1.72E-02	2.27E-03	3.03E-03	1.01E-02	2.64E-02	2.13E-03	2.40E-03	5.84E-04	6.41E-03	1.95E-03

Appendix I: EMPA on Pyroxenes and Olivines

This appendix lists all results from EMP measurements on pyroxenes, and olivines.

Table I.1: EMPA data of pyroxenes from samples V-298, V-297 and V-221a. Data is presented in wt%.

V−ID	Comment	Na_2O	Al_2O_3	MnO	FeO	K_2O	SiO_2	MgO	TiO_2	Cr_2O_3	CaO	SrO	SO_3	BaO	Total
V-298	ELV_13_25_Px_1	0.22	2.8	0.56	17.3	0.00	46.7	9.1	1.06	0.00	20.1	0.00	0.00	0.00	97.8
	ELV_13_25_Px_2	0.32	3.5	0.72	19.6	0.00	46.0	7.8	1.46	0.00	19.1	0.00	0.00	0.00	98.5
	ELV_13_25_Px_inc	0.26	1.7	0.59	17.9	0.00	48.7	9.2	0.61	0.00	19.8	0.00	0.00	0.00	98.6
V-297	ELV_13_24_PX_1	0.30	1.2	0.64	17.6	0.00	46.8	10.0	0.31	0.00	17.1	0.00	0.00	0.00	94.0
	ELV_13_24_PX_2	0.20	1.5	0.59	15.7	0.00	48.2	11.6	0.45	0.00	16.9	0.00	0.00	0.00	95.2
	ELV_13_24_PX_3	0.24	1.4	0.66	18.6	0.00	47.7	10.0	0.39	0.00	16.3	0.00	0.00	0.00	95.3
	ELV_13_24_PX_4	0.33	1.5	0.59	16.1	0.00	48.1	11.3	0.45	0.00	17.3	0.00	0.00	0.00	95.7
	ELV_13_24_PX_5	0.25	1.3	0.75	18.1	0.00	46.2	9.3	0.41	0.00	17.0	0.00	0.00	0.00	93.4
	ELV_13_24_PX_6	0.24	1.1	0.59	17.1	0.00	45.0	9.1	0.31	0.00	18.0	0.00	0.00	0.00	91.5
	ELV_13_24_PX_7	0.30	1.4	0.63	17.7	0.00	46.2	9.9	0.35	0.00	17.2	0.00	0.00	0.00	93.6
	ELV_13_24_PX_7	0.20	1.2	0.59	17.5	0.00	47.0	9.5	0.32	0.00	17.7	0.00	0.00	0.00	94.1
	ELV_13_24_PX_8	0.27	1.4	0.62	16.9	0.00	47.5	10.3	0.46	0.02	17.2	0.00	0.00	0.00	94.7
	ELV_13_24_PX_9	0.24	1.3	0.55	17.1	0.00	47.3	10.3	0.39	0.00	17.4	0.00	0.00	0.00	94.5
	ELV_13_24_PX_10	0.22	1.2	0.59	17.2	0.00	47.7	9.8	0.34	0.00	18.2	0.00	0.00	0.00	95.2
	ELV_13_24_PX_11	0.23	1.2	0.65	17.7	0.00	47.5	9.3	0.36	0.00	18.2	0.00	0.00	0.00	95.2
	ELV_13_24_PX_12	0.40	7.9	0.12	4.5	0.00	46.9	15.8	0.66	0.17	18.6	0.00	0.00	0.00	95.0
	ELV_13_24_PX_13	0.31	1.4	0.66	18.3	0.00	47.4	9.5	0.36	0.02	17.1	0.00	0.00	0.00	95.0
	ELV_13_24_PX_14	0.30	1.3	0.58	16.8	0.00	47.8	10.3	0.31	0.03	17.8	0.00	0.00	0.00	95.1
	1324_PX_1	0.43	1.3	0.66	18.5	0.02	50.8	9.4	0.38	0.00	18.1	0.00	0.00	0.01	99.6
	1324_PX_2	0.02	0.0	1.44	55.7	0.00	32.8	10.6	0.02	0.02	0.2	0.00	0.02	0.00	100.8
	1324_PX_3	0.35	1.1	0.67	17.8	0.00	51.7	9.4	0.35	0.01	18.6	0.00	0.00	0.02	100.1
	1324_PX_4	0.41	1.5	0.60	16.6	0.00	51.1	10.9	0.41	0.00	18.5	0.00	0.00	0.02	100.1
	1324_PX_5	0.00	0.0	1.48	55.8	0.00	32.4	10.7	0.05	0.00	0.2	0.00	0.00	0.00	100.7
	1324_PX_6	0.37	1.3	0.60	17.0	0.01	51.2	10.1	0.37	0.00	18.6	0.00	0.02	0.01	99.6
	1324_PX_7	0.40	1.6	0.61	16.7	0.00	50.8	10.9	0.43	0.01	18.2	0.00	0.02	0.02	99.7
	1324_PX_8	0.42	1.4	0.64	17.9	0.01	51.2	10.9	0.39	0.01	17.2	0.00	0.00	0.00	100.0
	1324_PX_9	0.00	0.0	1.50	56.0	0.00	32.3	10.5	0.00	0.00	0.3	0.00	0.00	0.01	100.6
	1324_PX_10	0.39	1.2	0.65	17.8	0.00	51.2	9.7	0.32	0.01	18.6	0.00	0.00	0.02	100.0
V-221a	1316_PX_1	0.42	1.1	0.89	19.0	0.00	49.4	7.7	0.58	0.00	19.5	0.00	0.00	0.00	98.5
	1316_PX_2	0.41	0.8	0.90	18.3	0.00	50.0	8.4	0.42	0.02	19.9	0.00	0.00	0.00	99.2
	1316_PX_3	0.40	0.9	0.83	18.5	0.00	50.2	7.9	0.46	0.00	20.0	0.00	0.00	0.00	99.1
	1316_PX_4	0.44	1.2	0.84	15.9	0.02	50.5	9.9	0.46	0.00	19.8	0.00	0.00	0.00	99.0
	1316_PX_5	0.44	1.0	0.89	18.3	0.02	50.0	8.2	0.45	0.02	19.8	0.00	0.00	0.00	99.1
	1316_CPX_2	0.44	0.7	1.03	20.8	0.00	49.9	6.0	0.36	0.00	20.0	0.00	0.00	0.00	99.3
	1316_CPX_3	0.42	1.2	1.01	20.9	0.00	48.8	6.0	0.62	0.03	19.5	0.00	0.00	0.00	98.5
	1316_CPX_4	0.67	1.1	1.10	21.8	0.03	48.5	5.6	0.62	0.02	19.2	0.00	0.00	0.00	98.7
	1316_CPX_5	0.60	0.9	1.03	21.9	0.03	49.2	5.4	0.43	0.00	19.6	0.00	0.00	0.00	99.0
	1316_CPX_6	0.40	0.9	0.90	17.6	0.03	50.3	8.8	0.43	0.02	19.9	0.00	0.00	0.00	99.2
	1316_CPX_8	0.39	0.7	1.04	20.7	0.00	49.8	6.5	0.43	0.01	19.7	0.00	0.00	0.00	99.4
	1316_CPX_9	0.34	1.1	0.72	19.6	0.02	49.6	7.9	0.44	0.00	19.2	0.00	0.00	0.00	99.0
	1316_CPX_10	0.36	1.0	0.90	18.8	0.01	49.8	7.5	0.51	0.03	19.7	0.00	0.00	0.00	98.6

Table I.2: EMPA data of pyroxenes from samples V-146, V-111, V-65 and V-45a. Data is presented in wt%.

V-ID	Comment	Na_2O	Al_2O_3	MnO	FeO	K_2O	SiO_2	MgO	TiO_2	Cr_2O_3	CaO	SrO	SO_3	BaO	Total
V-146	1408_CPX_1	0.93	0.2	1.32	28.8	0.01	47.6	0.6	0.27	0.00	18.1	0.00	0.06	0.01	98.0
V-114	Line_1_1404_CPX_1	0.57	0.5	1.17	20.4	0.01	50.0	6.9	0.38	0.00	19.4	0.00	0.01	0.01	99.3
	Line_1_1404_CPX_2	0.60	0.5	1.15	20.2	0.02	49.0	6.7	0.47	0.00	19.3	0.00	0.00	0.04	98.0
	Line_1_1404_CPX_3	0.57	0.5	1.15	19.8	0.01	49.7	7.0	0.43	0.00	19.2	0.00	0.04	0.00	98.4
	Line_1_1404_CPX_4	0.59	0.5	1.15	19.3	0.00	49.7	7.3	0.43	0.00	19.3	0.00	0.02	0.04	98.4
	Line_1_1404_CPX_5	0.55	0.5	1.11	18.8	0.00	49.2	7.7	0.40	0.01	19.4	0.00	0.05	0.02	97.8
	Line_1_1404_CPX_6	0.50	0.6	1.06	17.9	0.00	49.3	8.2	0.42	0.05	19.6	0.00	0.00	0.04	97.7
	Line_1_1404_CPX_7	0.50	0.6	1.07	17.5	0.00	49.2	8.4	0.40	0.00	20.2	0.00	0.05	0.02	97.8
	Line_1_1404_CPX_8	0.45	0.6	1.02	17.4	0.00	50.5	8.6	0.41	0.00	20.0	0.00	0.02	0.02	99.2
V-111	ELV_13_05_I_Px_1	0.26	0.7	1.16	21.6	0.01	48.5	6.4	0.50	0.00	20.6	0.00	0.00	0.00	99.7
	ELV_13_05_II_Px_1	0.25	0.8	1.09	20.6	0.00	48.5	7.4	0.54	0.02	20.2	0.00	0.00	0.00	99.3
	ELV_13_05_III_Px_1	0.27	0.7	1.11	20.9	0.02	48.5	6.8	0.55	0.00	20.6	0.00	0.00	0.00	99.4
	ELV_13_05_IV_Px_1	0.27	0.8	1.31	23.6	0.03	47.4	5.0	0.69	0.01	20.0	0.00	0.00	0.00	99.2
	ELV_13_05_VIII_px_1	0.26	0.7	1.17	21.7	0.01	47.8	6.5	0.57	0.01	20.3	0.00	0.00	0.00	99.0
	ELV_13_05_VIII_px_2	0.26	0.8	1.19	21.3	0.00	48.2	6.7	0.60	0.00	20.4	0.00	0.00	0.00	99.5
	ELV_13_05_IX_px_1	0.28	0.7	1.43	24.0	0.00	47.2	5.0	0.51	0.02	20.0	0.00	0.00	0.00	99.1
	ELV_13_05_X_px_1	0.36	0.6	1.36	25.9	0.02	45.7	3.1	0.63	0.01	20.4	0.00	0.00	0.00	98.2
	ELV_13_05_XI_pxin_inc_2	1.59	7.3	0.93	17.4	2.16	51.7	2.3	0.45	0.01	12.8	0.00	0.00	0.00	96.7
	ELV_13_05_XI_px_Fsp_inc_3	0.88	3.2	1.05	19.6	0.81	49.9	5.1	0.50	0.00	18.2	0.00	0.00	0.00	99.3
	ELV_13_05_XVII_Px_1	0.32	1.1	0.82	17.8	0.01	49.2	10.2	0.59	0.00	19.2	0.00	0.00	0.00	99.2
	ELV_13_05_XVIII_Px_1	0.32	0.7	1.21	23.1	0.00	48.0	5.6	0.55	0.01	20.1	0.00	0.00	0.00	99.6
	ELV_13_05_XIX_Px_1	0.31	0.5	1.31	24.0	0.01	47.6	4.7	0.48	0.00	20.2	0.00	0.00	0.00	99.2
	ELV_13_05_XX_Px_1	0.24	0.6	1.19	22.5	0.00	47.8	5.7	0.47	0.01	20.3	0.00	0.00	0.00	98.8
V-65	1303_cpx_1	0.51	0.8	1.30	23.8	0.01	48.6	3.5	0.62	0.01	20.2	0.00	0.00	0.00	99.4
	1303_cpx_2	0.49	0.7	1.30	24.9	0.00	48.7	3.0	0.69	0.00	20.0	0.00	0.00	0.00	99.8
	1303_cpx_3	0.58	0.6	1.34	25.6	0.00	48.7	2.5	0.70	0.00	19.9	0.00	0.00	0.00	100.0
	1303_cpx_4	0.85	0.2	1.53	28.3	0.00	48.8	0.9	0.54	0.00	19.2	0.00	0.00	0.00	100.3
	1303_cpx_7	0.45	1.0	1.06	17.8	0.00	50.5	7.9	0.60	0.00	20.3	0.00	0.00	0.00	99.6
	1303_cpx_8	0.67	0.7	1.36	26.7	0.00	48.6	1.7	0.68	0.00	19.7	0.00	0.00	0.00	100.1
	1303_cpx_9	0.57	0.8	1.36	25.4	0.00	48.7	2.5	0.76	0.02	20.0	0.00	0.00	0.00	100.1
	1303_cpx_10	0.42	0.6	1.33	25.1	0.00	49.0	2.6	0.63	0.00	20.2	0.00	0.00	0.00	99.8
V-45	1301_CPX_1	0.46	1.1	0.79	24.0	0.01	49.0	4.1	0.54	0.03	19.9	0.00	0.00	0.00	99.9
	1301_CPX_2	0.40	0.5	0.83	26.8	0.00	48.6	1.9	0.42	0.01	19.9	0.00	0.00	0.00	99.3
	1301_CPX_3	0.36	0.7	0.73	21.9	0.00	49.6	5.6	0.45	0.01	20.1	0.00	0.00	0.00	99.4
	1301_CPX_4	0.42	0.8	0.72	21.7	0.01	49.7	5.8	0.38	0.01	20.1	0.00	0.00	0.00	99.6
	1301_CPX_5	0.42	1.1	0.83	23.5	0.00	48.9	4.6	0.63	0.00	19.6	0.00	0.00	0.00	99.5
	1301_CPX_6	0.39	0.9	0.83	24.3	0.00	48.8	4.1	0.57	0.01	19.5	0.00	0.00	0.00	99.3
	1301_CPX_7	0.38	0.5	0.89	26.9	0.01	48.8	2.1	0.40	0.04	20.1	0.00	0.00	0.00	100.1
	1301_CPX_9	0.41	0.9	0.68	21.6	0.01	49.9	6.0	0.48	0.00	20.0	0.00	0.00	0.00	99.9
	1301_CPX_10	0.40	0.7	0.77	22.6	0.02	49.9	5.1	0.33	0.00	20.1	0.00	0.00	0.00	99.8
	1301_CPX_11	0.35	0.7	0.79	22.7	0.01	49.4	4.7	0.38	0.03	20.2	0.00	0.00	0.00	99.3
	1301_CPX_12	0.36	1.2	0.52	11.8	0.00	51.7	12.9	0.52	0.00	20.5	0.00	0.00	0.00	99.4
	1301_CPX_13	0.39	0.7	0.74	21.8	0.00	49.8	5.7	0.34	0.04	20.2	0.00	0.00	0.00	99.7
	1301_CPX_14	0.39	0.8	0.80	23.1	0.00	49.3	4.7	0.41	0.00	19.9	0.00	0.00	0.00	99.4
	1301_CPX_15_in_FSP	0.40	1.1	0.72	22.8	0.01	48.8	4.7	0.72	0.03	19.8	0.00	0.00	0.00	99.2

Table I.3: EMPA data of olivines from samples V-297 and V-298. Data is presented in wt%.

V-ID	Comment	Na_2O	Al_2O_3	MnO	FeO	K_2O	SiO_2	MgO	TiO_2	Cr_2O_3	BaO	SO_3	CaO	SrO	Total
V-297	1324_OL_1	0.05	0.03	1.5	55.2	0.01	32.1	10.7	0.05	0.00	0.00	0.04	0.24	0.00	99.9
	1324_OL_2	0.02	0.00	1.5	55.2	0.00	32.2	10.8	0.05	0.00	0.00	0.01	0.23	0.00	99.9
	1324_OL_3	0.00	0.00	1.4	55.6	0.02	32.2	10.9	0.05	0.00	0.00	0.04	0.28	0.00	100.4
	1324_OL_4	0.02	0.01	1.5	56.0	0.01	32.4	10.8	0.04	0.03	0.00	0.02	0.25	0.00	101.1
	1324_OL_6	0.04	0.01	1.5	55.1	0.00	32.7	10.4	0.03	0.00	0.01	0.02	0.23	0.00	100.1
	1324_OL_7	0.05	0.00	1.5	55.3	0.01	32.4	10.4	0.01	0.00	0.00	0.03	0.27	0.00	100.0
	1324_OL_8	0.05	0.00	1.5	55.3	0.01	32.4	10.7	0.01	0.00	0.01	0.01	0.23	0.00	100.2
	1324_OL_9	0.00	0.01	1.4	55.0	0.00	32.2	10.8	0.09	0.00	0.00	0.01	0.25	0.00	99.9
	1324_OL_10	0.00	0.01	1.5	55.0	0.00	32.4	10.6	0.07	0.01	0.00	0.00	0.26	0.00	99.8
	1324_OL_1	0.00	0.05	1.5	55.0	0.02	32.7	10.8	0.07	0.00	0.00	0.00	0.24	0.00	100.4
	1324_OL_2	0.00	0.03	1.5	55.5	0.00	32.3	10.5	0.00	0.00	0.01	0.00	0.25	0.00	100.1
	1324_OL_3	0.00	0.02	1.5	55.5	0.00	32.4	10.7	0.05	0.00	0.00	0.00	0.25	0.00	100.4
	1324_OL_4	0.02	0.00	1.4	55.2	0.00	32.8	10.6	0.02	0.02	0.00	0.02	0.23	0.00	100.3
	ELV_13_24_II_OL	0.01	0.02	1.5	55.8	0.00	31.0	10.6	0.03	0.00	0.00	0.00	0.22	0.00	99.2
	ELV_13_24_IV_OL	0.03	0.00	1.4	55.5	0.00	31.1	10.7	0.05	0.01	0.00	0.00	0.25	0.00	99.1
	ELV_13_24_V_OL	0.05	0.01	1.4	55.8	0.00	30.9	10.9	0.04	0.00	0.00	0.00	0.25	0.00	99.3
	ELV_13_24_XI_OL	0.00	0.02	0.7	39.7	0.00	34.0	25.7	0.05	0.01	0.00	0.00	0.20	0.00	100.5
	ELV_13_24_XII_OL	0.03	0.00	1.4	56.1	0.00	30.0	10.9	0.02	0.00	0.00	0.00	0.26	0.00	98.7
	ELV_13_24_XIX_OL	0.00	0.00	1.5	56.1	0.00	30.6	10.9	0.03	0.00	0.00	0.00	0.23	0.00	99.3
V-298	ELV_13_25_OL_1	0.02	0.02	2.0	59.1	0.00	31.1	7.9	0.01	0.00	0.00	0.00	0.40	0.00	100.5
	ELV_13_25_IV_OL_1	0.02	0.04	1.6	55.6	0.01	31.7	11.5	0.08	0.00	0.00	0.00	0.40	0.00	100.9
	ELV_13_25_V_OL_1	0.02	0.01	2.0	58.7	0.01	31.0	8.6	0.07	0.02	0.00	0.00	0.42	0.00	100.9
	ELV_13_25_VI_OL_1	0.02	0.01	1.4	51.6	0.00	32.4	14.8	0.04	0.00	0.00	0.00	0.38	0.00	100.6
	ELV_13_25_VII_OL_1	0.02	0.03	1.6	52.3	0.01	31.4	13.4	0.14	0.00	0.00	0.00	0.38	0.00	99.4
	ELV_13_25_VIII_OL_1	0.00	0.01	1.8	55.1	0.00	31.8	10.9	0.05	0.00	0.00	0.00	0.41	0.00	100.1
	ELV_13_25_VIII_OL	0.02	0.03	1.7	56.4	0.00	31.3	10.9	0.03	0.00	0.00	0.00	0.40	0.00	100.8
	ELV_13_25_IX_OL	0.02	0.04	0.9	45.0	0.00	33.9	21.6	0.06	0.00	0.00	0.00	0.22	0.00	101.7
	ELV_13_25_IX_OL	0.00	0.00	0.9	44.7	0.01	33.9	21.9	0.05	0.00	0.00	0.00	0.27	0.00	101.7
	ELV_13_25_XIII_OL	0.02	0.00	1.4	51.6	0.00	32.0	15.0	0.03	0.01	0.00	0.00	0.35	0.00	100.4

Appendix J: EMPA on volcanic glass

This appendix lists all results from EMP measurements on volcanic glasses. Analyses on glass from V-58, V-297 and V-144 were conducted at the University of Potsdam. All other analyses were conducted at the GFZ Potsdam. Details about the analytical equipment and the setting are presented in chapter 3.

Table J.1: EMPA data of of volcanic glass from V-58, V-297 and V-144. Data is presented in wt%.

V-ID	Comment	Na_2O	Al_2O_3	MnO	FeO	K_2O	SiO_2	MgO	TiO_2	Cr_2O_3	BaO	SO_3	CaO	SrO	Total
V-58	1402_shard_1	4.4	15.9	0.18	4.8	5.4	67.9	0.28	0.47	0.00	0.02	0.00	1.02	0.00	100.3
	1402_shard_2	4.4	16.5	0.21	5.9	5.4	65.6	0.20	0.37	0.00	0.01	0.06	0.71	0.00	99.3
	1402_shard_3	3.4	15.5	0.11	4.6	6.3	67.2	0.17	0.49	0.01	0.02	0.04	0.12	0.00	98.0
	1402_shard_4	3.1	15.3	0.17	5.1	5.7	65.9	0.31	0.51	0.01	0.00	0.03	0.75	0.00	96.9
	1402_shard_5	4.6	16.3	0.20	5.7	5.3	66.0	0.20	0.35	0.00	0.00	0.04	0.81	0.00	99.5
	1402_shard_6	4.7	16.5	0.21	6.0	5.4	65.9	0.20	0.38	0.00	0.00	0.05	0.83	0.00	100.1
	1402_shard_7	5.0	16.4	0.22	6.0	5.5	65.6	0.20	0.38	0.02	0.01	0.01	0.81	0.00	100.1
	1402_shard_8	3.7	16.7	0.19	5.8	5.2	65.8	0.22	0.41	0.00	0.01	0.03	0.85	0.00	98.9
	1402_shard_9	0.3	0.6	0.61	62.9	0.1	3.3	0.98	0.49	0.00	0.03	3.44	1.78	0.04	74.5
	1402_shard_10_transparent	4.6	16.4	0.20	5.9	5.2	65.2	0.20	0.40	0.00	0.00	0.02	0.82	0.00	98.9
V-144	1308_Shard1_GM	2.9	11.7	0.05	2.9	4.7	73.3	0.00	0.20	0.00	0.05	0.03	0.21	0.00	96.0
	1308_Shard4_GM	4.0	11.8	0.12	2.8	4.6	73.6	0.00	0.20	0.00	0.00	0.00	0.22	0.00	97.3
	1308_Shard6_GM	3.3	12.0	0.03	3.0	4.8	74.1	0.00	0.24	0.00	0.00	0.02	0.30	0.00	97.8
	1308_Shard_1	3.9	11.9	0.11	3.0	4.6	73.0	0.00	0.21	0.00	0.01	0.00	0.20	0.00	97.0
	1308_Shard_2	4.3	11.5	0.04	2.9	4.6	72.2	0.00	0.20	0.00	0.00	0.02	0.28	0.00	96.0
	1308_Shard_3	4.4	11.9	0.08	2.9	4.7	71.4	0.00	0.13	0.00	0.00	0.00	0.15	0.00	95.7
	1308_Shard_4	4.1	12.0	0.08	3.0	4.7	72.8	0.00	0.17	0.00	0.00	0.00	0.25	0.00	97.1
	1308_Shard_5	4.6	11.2	0.03	2.7	4.5	74.5	0.00	0.13	0.00	0.00	0.00	0.18	0.00	97.8
	1308_Shard_6	4.1	11.9	0.12	3.0	4.7	73.1	0.01	0.23	0.00	0.00	0.00	0.28	0.00	97.5
	1308_GM_5	3.9	11.6	0.05	2.9	4.6	73.5	0.00	0.22	0.00	0.02	0.00	0.21	0.00	97.0
	1308_Shard_9	4.3	11.7	0.05	2.9	4.7	73.7	0.01	0.23	0.00	0.00	0.01	0.28	0.00	97.8
	1308_Shard_7	4.6	11.7	0.10	3.0	4.6	73.3	0.00	0.24	0.00	0.03	0.05	0.25	0.00	97.7
	1308_Shard_4_RIM	4.0	11.7	0.07	2.9	4.5	72.4	0.00	0.23	0.00	0.00	0.00	0.21	0.00	96.0
	1308_Shard_6_RIM	3.8	11.6	0.11	2.9	4.6	72.4	0.01	0.19	0.00	0.00	0.02	0.27	0.00	95.9
	1308_Shard_4_RIM	4.3	11.8	0.04	2.8	4.6	72.1	0.00	0.23	0.00	0.00	0.00	0.23	0.00	96.1
	1308_Shard_5_RIM	4.3	11.1	0.06	2.6	4.4	73.0	0.02	0.12	0.00	0.00	0.00	0.19	0.00	95.9
	1308_Shard_9_RIM	4.3	11.5	0.07	2.9	4.6	72.0	0.00	0.20	0.00	0.00	0.01	0.27	0.00	95.8
	1308_Shard_7_RIM	4.3	11.4	0.16	2.9	4.6	72.1	0.00	0.24	0.00	0.04	0.00	0.26	0.00	96.0
V-146	1408_Shards_2	2.8	11.8	0.10	3.1	4.7	75.7	0.01	0.16	0.00	0.00	0.05	0.21	0.00	98.6
	1408_Shards_3	4.4	12.7	0.00	1.9	5.1	73.3	0.00	0.15	0.00	0.00	0.04	0.16	0.00	97.8
	1408_Shards_4	3.2	11.9	0.06	3.1	4.6	73.9	0.00	0.18	0.01	0.00	0.04	0.26	0.09	97.5
	1408_Shards_	3.2	11.9	0.06	3.2	4.7	73.2	0.00	0.21	0.00	0.00	0.03	0.30	0.00	96.6
	1408_Shards_6	3.6	11.5	0.05	2.9	4.6	76.6	0.00	0.16	0.01	0.00	0.03	0.17	0.00	99.4
	1408_Shards_8	3.5	11.5	0.09	2.7	4.5	76.0	0.00	0.17	0.00	0.00	0.02	0.21	0.00	98.7
	1408_Shards_9	2.8	12.1	0.07	3.2	4.7	73.2	0.00	0.19	0.04	0.00	0.02	0.29	0.00	96.6
	1408_Shards_10	2.5	12.1	0.08	3.1	4.6	71.5	0.01	0.20	0.00	0.00	0.00	0.28	0.00	94.3
	1408_Shard_9_Line_1	2.4	11.6	0.04	3.1	4.4	74.1	0.01	0.20	0.00	0.00	0.03	0.34	0.00	96.2
	1408_Shard_9_Line_2	2.8	11.7	0.08	3.1	4.4	74.3	0.02	0.17	0.00	0.00	0.01	0.32	0.00	96.8
	1408_Shard_9_Line_3	3.0	11.6	0.09	3.0	4.5	73.8	0.00	0.21	0.01	0.00	0.00	0.35	0.00	96.5
	1408_Shard_9_Line_4	2.9	11.7	0.08	3.1	4.6	72.3	0.00	0.20	0.00	0.00	0.02	0.34	0.00	95.3
	1408_Shard_9_Line_5	3.0	12.0	0.05	3.1	4.7	74.8	0.00	0.19	0.02	0.01	0.03	0.35	0.00	98.3
	1408_Shard_9_Line_6	3.0	11.9	0.08	3.1	4.7	70.6	0.00	0.21	0.00	0.00	0.07	0.31	0.00	94.0
	1408_Shard_9_Line_7	3.0	11.9	0.11	3.2	4.7	73.2	0.01	0.21	0.00	0.01	0.01	0.26	0.00	96.6
	1408_Shard_9_Line_8	2.9	11.9	0.05	3.2	4.7	71.4	0.00	0.21	0.00	0.00	0.04	0.30	0.00	94.7
	1408_Shard_9_Line_9	3.1	11.8	0.07	3.1	4.6	74.6	0.00	0.19	0.00	0.02	0.01	0.28	0.00	97.9
	1408_Shard_9_Line_10	3.2	12.0	0.11	3.1	4.7	75.8	0.01	0.17	0.00	0.03	0.04	0.32	0.00	99.4
	1408_Shard_9_Line_11	2.7	11.9	0.07	3.2	4.7	75.5	0.01	0.19	0.00	0.01	0.04	0.33	0.00	98.7
	1408_Shard_9_Line_12	3.2	11.9	0.12	3.2	4.7	71.3	0.00	0.23	0.03	0.00	0.03	0.28	0.00	95.0
	1408_Shard_9_Line_13	2.7	11.9	0.10	3.2	4.8	70.5	0.00	0.19	0.03	0.00	0.04	0.29	0.00	93.6
	1408_Shard_9_Line_14	2.9	12.1	0.13	3.2	4.7	75.0	0.00	0.21	0.00	0.00	0.08	0.34	0.00	98.6
	1408_Shard_9_Line_15	2.7	12.0	0.09	3.1	4.7	75.2	0.00	0.19	0.01	0.01	0.06	0.35	0.00	98.5
	1408_Shard_9_Line_16	2.6	12.1	0.08	3.0	4.6	74.6	0.02	0.19	0.00	0.00	0.07	0.30	0.00	97.5
V-297	1324_Shards_2	3.5	16.5	0.17	8.3	2.5	61.1	1.70	1.19	0.02	0.08	0.05	4.25	0.00	99.4
	1324_Shards_3	4.1	15.6	0.22	10.4	2.0	52.0	3.01	2.38	0.01	0.10	0.14	6.54	0.00	96.6
	1324_Shards_4	6.0	22.9	0.04	2.9	0.6	55.8	0.52	1.23	0.00	0.06	0.07	6.91	0.00	96.9
	1324_Shards_5_transparent	3.1	15.9	0.12	5.2	3.8	67.1	0.39	0.48	0.00	0.04	0.03	2.17	0.00	98.4
	1324_Shards_6_transparent	2.2	15.2	0.07	3.8	3.8	67.9	0.27	0.28	0.00	0.04	0.02	1.50	0.00	95.1
	1324_Shards_7_transparent	2.3	15.3	0.08	3.9	3.7	67.0	0.29	0.33	0.00	0.05	0.01	1.60	0.00	94.6
	1324_Shards_9	6.7	24.3	0.04	1.2	0.7	59.3	0.16	0.20	0.00	0.06	0.00	6.83	0.00	99.4
	1324_Shards_10	5.6	26.9	0.03	1.0	0.4	56.8	0.16	0.27	0.01	0.02	0.03	9.00	0.00	100.3

Table J.2: EMPA data of volcanic glass from sample V-209a. Data is presented in wt%. The oxygen equivalents of F and Cl are calculated by multiplying wt% F by 0.4211 and Cl by 0.2256. The oxygen-equivalents for the F and Cl are subtracted in an addtional sum† from the analytical total followin Deer et al. (2013).

V-ID	Comment	SiO_2	K_2O	CaO	Na_2O	FeO	Al_2O_3	TiO_2	Cl	MgO	MnO	F	P_2O_5	BaO	SO_3	ZnO	Total	F=O	Cl=O	SUM†
V-209a cores	Line_1_JE_1315_1_core	73.28	4.13	0.23	5.36	2.81	11.28	0.25	0.06	0.00	0.01	0.00	0.13	0.13	0.03	0.13	97.85	0.00	0.01	97.84
	Line_2_JE_1315_1_core	73.23	4.67	0.23	5.43	2.88	10.86	0.21	0.00	0.04	0.05	0.00	0.10	0.14	0.05	0.00	97.89	0.00	0.00	97.89
	Line_3_JE_1315_1_core	73.30	4.39	0.27	5.48	2.82	10.82	0.07	0.01	0.00	0.00	0.00	0.00	0.00	0.00	0.15	97.32	0.00	0.00	97.31
	Line_4_JE_1315_1_core	74.70	4.52	0.18	5.58	2.91	11.00	0.20	0.01	0.01	0.03	0.00	0.00	0.00	0.14	0.08	99.35	0.00	0.00	99.34
	Line_5_JE_1315_1_core	72.25	4.25	0.31	5.38	3.01	11.26	0.08	0.06	0.00	0.00	0.00	0.07	0.03	0.11	0.11	96.93	0.00	0.01	96.92
	Line_6_JE_1315_1_core	72.20	4.53	0.26	5.45	2.79	11.10	0.08	0.00	0.00	0.00	0.00	0.00	0.26	0.10	0.00	96.77	0.00	0.00	96.77
	Line_7_JE_1315_1_core	74.17	4.84	0.22	5.87	3.04	11.23	0.11	0.08	0.03	0.00	0.01	0.00	0.00	0.16	0.19	99.94	0.00	0.02	99.92
	Line_8_JE_1315_1_core	73.78	4.12	0.18	5.68	2.96	11.22	0.34	0.02	0.00	0.00	0.09	0.04	0.00	0.05	0.00	98.48	0.04	0.00	98.44
	Line_9_JE_1315_1_core	73.28	4.45	0.28	5.48	3.20	11.30	0.20	0.03	0.02	0.01	0.00	0.12	0.03	0.00	0.08	98.48	0.00	0.01	98.47
	Line_10_JE_1315_1_core	73.23	4.35	0.21	5.61	3.09	10.83	0.29	0.10	0.00	0.02	0.04	0.08	0.00	0.00	0.00	97.84	0.02	0.02	97.80
	Line_1_JE_1315_2_core	72.97	4.40	0.34	5.75	2.68	10.83	0.34	0.08	0.00	0.00	0.00	0.05	0.00	0.00	0.21	97.64	0.00	0.02	97.63
	Line_2_JE_1315_2_core	73.52	4.45	0.24	5.78	2.83	11.18	0.25	0.00	0.00	0.00	0.00	0.00	0.00	0.06	0.00	98.32	0.00	0.00	98.32
	Line_3_JE_1315_2_core	72.90	4.56	0.25	5.73	2.83	10.93	0.14	0.03	0.02	0.01	0.00	0.15	0.00	0.03	0.11	97.68	0.00	0.01	97.68
	Line_4_JE_1315_2_core	74.37	4.82	0.27	5.62	2.97	11.41	0.10	0.03	0.00	0.05	0.00	0.15	0.00	0.06	0.00	99.85	0.00	0.01	99.85
	Line_5_JE_1315_2_core	73.89	4.31	0.28	5.74	2.84	10.92	0.18	0.00	0.00	0.03	0.00	0.00	0.25	0.02	0.13	98.60	0.00	0.00	98.60
	Line_6_JE_1315_2_core	74.95	4.61	0.28	5.27	2.82	11.04	0.15	0.09	0.03	0.02	0.00	0.02	0.02	0.02	0.07	99.38	0.00	0.02	99.36
	Line_7_JE_1315_2_core	74.87	4.65	0.30	5.49	2.80	11.20	0.23	0.00	0.00	0.07	0.00	0.00	0.26	0.00	0.11	99.98	0.00	0.00	99.98
	Line_8_JE_1315_2_core	74.65	4.65	0.23	5.52	3.01	11.23	0.11	0.00	0.02	0.00	0.00	0.05	0.13	0.10	0.17	99.86	0.00	0.00	99.86
	Line_9_JE_1315_2_core	74.00	4.67	0.32	5.69	2.87	11.23	0.10	0.05	0.00	0.03	0.00	0.00	0.23	0.00	0.00	99.20	0.00	0.01	99.19
	Line_10_JE_1315_2_core	74.84	4.79	0.30	5.58	2.85	11.25	0.21	0.00	0.00	0.09	0.00	0.00	0.00	0.10	0.00	100.00	0.00	0.00	100.00
V-209a rims	JE_1315_3_core1	74.41	4.87	0.21	5.59	2.74	11.24	0.16	0.07	0.00	0.00	0.00	0.00	0.00	0.00	0.00	99.29	0.00	0.02	99.28
	JE_1315_3_core2	74.19	4.51	0.09	5.63	2.86	11.16	0.18	0.09	0.00	0.00	0.00	0.25	0.14	0.00	0.06	99.15	0.00	0.02	99.13
	JE_1315_3_core3	73.01	4.66	0.20	5.27	2.62	11.17	0.23	0.01	0.00	0.03	0.04	0.04	0.06	0.02	0.22	97.59	0.02	0.00	97.57
	JE_1315_3_core4	74.99	4.30	0.16	5.34	2.81	11.03	0.22	0.01	0.00	0.00	0.00	0.12	0.28	0.00	0.13	99.39	0.00	0.00	99.39
	JE_1315_3_core5	73.33	4.46	0.18	5.33	2.77	11.00	0.19	0.00	0.00	0.01	0.00	0.07	0.00	0.02	0.13	97.49	0.00	0.00	97.49
	JE_1315_3_core6	72.63	4.57	0.23	5.66	2.90	11.22	0.34	0.00	0.00	0.04	0.00	0.09	0.26	0.13	0.02	98.08	0.00	0.00	98.08
	JE_1315_3_core7	73.61	4.85	0.23	5.88	2.79	11.14	0.13	0.04	0.00	0.00	0.02	0.08	0.28	0.03	0.00	99.09	0.01	0.01	99.07
	JE_1315_3_core8	73.45	4.68	0.19	5.78	2.84	11.25	0.21	0.07	0.02	0.01	0.00	0.08	0.19	0.02	0.17	98.94	0.00	0.02	98.93
	JE_1315_3_core9	72.91	4.64	0.18	5.58	2.65	11.01	0.31	0.04	0.00	0.00	0.00	0.00	0.41	0.00	0.04	97.77	0.00	0.01	97.76
	JE_1315_3_core10	73.79	4.78	0.21	5.65	2.77	10.99	0.19	0.06	0.01	0.04	0.00	0.12	0.13	0.00	0.00	98.75	0.00	0.01	98.73
	JE_1315_1_rim1	71.57	4.39	0.31	5.42	2.78	10.84	0.18	0.03	0.03	0.02	0.00	0.08	0.27	0.02	0.02	95.95	0.00	0.01	95.95
	JE_1315_1_rim2	73.27	4.61	0.29	5.56	2.68	10.91	0.13	0.01	0.02	0.00	0.00	0.00	0.29	0.06	0.04	97.87	0.00	0.00	97.87
	JE_1315_1_rim3	71.99	4.39	0.29	5.42	3.09	11.23	0.24	0.00	0.00	0.00	0.00	0.00	0.12	0.02	0.00	96.78	0.00	0.00	96.78
	JE_1315_1_rim4	71.54	4.33	0.19	5.43	2.94	10.99	0.14	0.06	0.00	0.00	0.00	0.00	0.00	0.00	0.00	95.62	0.00	0.01	95.61
	JE_1315_1_rim5	70.77	4.61	0.34	5.64	2.98	11.03	0.14	0.04	0.00	0.05	0.00	0.10	0.24	0.21	0.00	96.15	0.00	0.01	96.14
	JE_1315_2_rim1	72.27	4.26	0.30	5.49	2.95	10.75	0.25	0.02	0.00	0.00	0.20	0.06	0.15	0.00	0.28	96.98	0.08	0.00	96.89
	JE_1315_2_rim2	73.53	4.57	0.23	5.29	2.85	11.04	0.23	0.07	0.00	0.00	0.24	0.00	0.44	0.00	0.00	98.49	0.10	0.02	98.37
	JE_1315_2_rim3	72.62	4.32	0.32	5.68	2.75	10.92	0.24	0.04	0.02	0.00	0.00	0.11	0.00	0.00	0.04	97.06	0.00	0.01	97.05
	JE_1315_2_rim4	72.08	4.68	0.30	5.73	2.82	10.67	0.20	0.10	0.01	0.05	0.00	0.00	0.00	0.00	0.00	96.63	0.00	0.02	96.61
	JE_1315_2_rim5	73.26	4.39	0.30	5.38	2.79	10.97	0.18	0.06	0.00	0.02	0.00	0.00	0.07	0.11	0.00	97.53	0.00	0.01	97.51
	JE_1315_3_rim1	73.12	4.48	0.15	5.58	2.75	11.29	0.30	0.05	0.00	0.00	0.00	0.00	0.00	0.00	0.02	97.74	0.00	0.01	97.73
	JE_1315_3_rim2	74.06	4.35	0.11	5.59	2.81	10.87	0.16	0.02	0.03	0.01	0.00	0.15	0.00	0.00	0.00	98.16	0.00	0.01	98.16
	JE_1315_3_rim3	72.17	4.71	0.18	5.22	2.98	11.12	0.24	0.03	0.04	0.00	0.00	0.00	0.00	0.05	0.21	96.95	0.00	0.01	96.94
	JE_1315_3_rim4	71.95	4.53	0.12	5.44	2.60	11.15	0.13	0.00	0.02	0.05	0.00	0.03	0.00	0.00	0.07	96.09	0.00	0.00	96.09

Table J.3: EMPA data of volcanic glass from sample V-65. Data is presented in wt%. The oxygen equivalents of F and Cl are calculated by multiplying wt% F by 0.4211 and Cl by 0.2256. The oxygen-equivalents for the F and Cl are subtracted in an addtional sum† from the analytical total followin Deer et al. (2013).

V-ID	Comment	SiO_2	K_2O	CaO	Na_2O	FeO	Al_2O_3	TiO_2	Cl	MgO	MnO	F	P_2O_5	BaO	SO_3	ZnO	Total	F=O	Cl=O	SUM†
V-165 cores	Line 1 JE_1310_1_core	73.41	4.40	0.46	5.96	3.52	11.35	0.13	0.00	0.00	0.01	0.00	0.00	0.00	0.06	0.00	99.30	0.00	0.00	99.30
	Line 2 JE_1310_1_core	72.83	4.70	0.26	5.59	2.96	11.62	0.24	0.00	0.00	0.00	0.13	0.13	0.24	0.13	0.00	98.83	0.06	0.00	98.77
	Line 3 JE_1310_1_core	73.93	4.63	0.19	5.89	2.93	11.43	0.17	0.00	0.00	0.09	0.00	0.00	0.04	0.00	0.30	99.60	0.00	0.00	99.60
	Line 4 JE_1310_1_core	74.16	4.86	0.20	5.62	3.04	11.29	0.19	0.00	0.02	0.00	0.00	0.00	0.00	0.00	0.06	99.43	0.00	0.00	99.43
	Line 5 JE_1310_1_core	72.95	4.32	0.31	5.95	2.94	11.05	0.33	0.09	0.00	0.00	0.00	0.18	0.16	0.00	0.06	98.34	0.00	0.02	98.32
	Line 6 JE_1310_1_core	71.51	4.63	0.23	5.64	3.02	11.38	0.19	0.06	0.01	0.05	0.00	0.00	0.23	0.00	0.00	96.94	0.00	0.01	96.93
	Line 7 JE_1310_1_core	72.51	4.46	0.30	5.58	3.32	11.34	0.21	0.00	0.02	0.01	0.00	0.07	0.00	0.08	0.02	97.91	0.00	0.00	97.91
	Line 8 JE_1310_1_core	72.58	4.51	0.21	5.77	3.02	11.34	0.22	0.06	0.00	0.00	0.00	0.04	0.00	0.00	0.00	97.76	0.00	0.01	97.74
	Line 9 JE_1310_1_core	72.15	4.66	0.31	6.00	2.90	11.33	0.14	0.00	0.02	0.00	0.00	0.03	0.26	0.00	0.02	97.81	0.00	0.00	97.81
	Line 10 JE_1310_1_core	72.26	4.74	0.25	5.68	2.91	11.12	0.25	0.04	0.00	0.06	0.04	0.14	0.06	0.00	0.22	97.78	0.02	0.01	97.75
	Line 11 JE_1310_1_core	74.28	4.40	0.31	5.55	3.18	11.28	0.23	0.01	0.00	0.00	0.00	0.03	0.12	0.02	0.00	99.40	0.00	0.00	99.40
	Line 12 JE_1310_1_core	73.44	4.52	0.21	5.34	3.12	10.81	0.19	0.06	0.00	0.00	0.00	0.00	0.41	0.00	0.04	98.13	0.00	0.01	98.12
	Line 1 13 JE_1310_1_core	72.75	4.11	0.17	5.58	2.85	11.22	0.25	0.03	0.01	0.05	0.00	0.00	0.14	0.05	0.00	97.20	0.00	0.01	97.20
	Line 2 13 JE_1310_1_core	72.58	4.75	0.21	5.80	3.16	11.32	0.23	0.00	0.00	0.00	0.00	0.01	0.00	0.00	0.24	98.29	0.00	0.00	98.29
	Line 3 13 JE_1310_1_core	73.21	4.38	0.39	5.60	3.29	11.06	0.25	0.02	0.00	0.10	0.11	0.03	0.00	0.05	0.00	98.48	0.05	0.01	98.43
	JE_1310_3_core1	74.10	4.28	0.21	6.06	2.97	11.36	0.12	0.00	0.02	0.00	0.00	0.03	0.28	0.00	0.17	99.60	0.00	0.00	99.60
	JE_1310_3_core2	72.79	4.53	0.15	5.47	2.96	11.48	0.22	0.00	0.00	0.00	0.00	0.00	0.21	0.00	0.00	97.82	0.00	0.00	97.82
	JE_1310_3_core3	73.01	4.44	0.27	5.93	2.99	11.39	0.22	0.04	0.02	0.00	0.13	0.03	0.00	0.00	0.15	98.62	0.05	0.01	98.56
	JE_1310_3_core4	73.27	4.34	0.32	5.57	3.12	11.42	0.17	0.06	0.00	0.00	0.26	0.07	0.06	0.10	0.00	98.76	0.11	0.01	98.64
	JE_1310_3_core5	73.07	4.78	0.20	5.75	2.75	11.34	0.23	0.00	0.00	0.00	0.04	0.03	0.00	0.00	0.09	98.29	0.02	0.00	98.27
	JE_1310_3_core6	72.71	4.33	0.27	5.24	3.00	11.24	0.27	0.06	0.00	0.00	0.00	0.09	0.02	0.02	0.00	97.25	0.00	0.01	97.24
	JE_1310_3_core7	74.23	4.74	0.24	5.85	3.10	11.26	0.11	0.00	0.02	0.00	0.30	0.14	0.21	0.00	0.00	100.19	0.13	0.00	100.07
	JE_1310_3_core8	73.44	4.89	0.24	5.84	3.02	11.40	0.25	0.06	0.00	0.01	0.12	0.00	0.00	0.00	0.00	99.27	0.05	0.01	99.20
	JE_1310_3_core9	74.39	4.65	0.27	5.59	2.93	11.37	0.29	0.00	0.02	0.01	0.00	0.01	0.16	0.06	0.24	99.99	0.00	0.00	99.99
	JE_1310_3_core10	72.41	4.63	0.17	5.51	2.87	11.43	0.24	0.06	0.00	0.00	0.00	0.06	0.15	0.13	0.07	97.74	0.00	0.01	97.72
	Line 1 JE_1310_2_core	72.40	4.64	0.21	5.77	3.03	11.22	0.17	0.01	0.03	0.00	0.07	0.00	0.00	0.10	0.00	97.66	0.03	0.00	97.62
	Line 2 JE_1310_2_core	72.98	4.14	0.20	5.54	2.89	11.44	0.16	0.00	0.00	0.02	0.09	0.12	0.00	0.00	0.19	97.76	0.04	0.00	97.73
	Line 3 JE_1310_2_core	71.98	4.58	0.23	5.99	3.03	11.08	0.17	0.03	0.04	0.01	0.17	0.00	0.30	0.00	0.00	97.61	0.07	0.01	97.53
	Line 4 JE_1310_2_core	72.91	4.69	0.26	5.54	3.04	11.47	0.22	0.04	0.01	0.00	0.00	0.00	0.37	0.00	0.00	98.56	0.00	0.01	98.55
	Line 5 JE_1310_2_core	72.64	4.89	0.24	5.82	3.06	11.27	0.06	0.09	0.00	0.05	0.17	0.05	0.41	0.05	0.00	98.80	0.07	0.02	98.71
	Line 6 JE_1310_2_core	72.73	4.64	0.22	5.59	3.21	11.03	0.13	0.05	0.01	0.02	0.00	0.00	0.00	0.00	0.13	97.76	0.00	0.01	97.75
	Line 7 JE_1310_2_core	72.63	4.56	0.11	5.71	3.14	11.48	0.15	0.02	0.03	0.00	0.00	0.00	0.00	0.02	0.06	97.90	0.00	0.00	97.90
	Line 8 JE_1310_2_core	72.34	4.89	0.35	5.78	3.22	11.20	0.25	0.07	0.00	0.00	0.00	0.05	0.29	0.00	0.04	98.49	0.00	0.02	98.47
	Line 9 JE_1310_2_core	71.96	4.59	0.18	5.86	2.78	11.35	0.28	0.00	0.02	0.02	0.00	0.00	0.00	0.03	0.00	97.07	0.00	0.00	97.07
	Line 10 JE_1310_2_core	73.31	4.03	0.30	5.73	3.22	11.37	0.24	0.12	0.00	0.00	0.00	0.00	0.05	0.00	0.19	98.56	0.00	0.03	98.53
	JE_1310_2_core_nl1	72.19	4.44	0.29	5.88	3.12	11.32	0.11	0.04	0.00	0.00	0.00	0.00	0.20	0.00	0.00	97.58	0.00	0.01	97.58
	JE_1310_2_core_nl2	72.71	4.80	0.25	5.76	3.05	11.04	0.20	0.07	0.02	0.02	0.00	0.00	0.33	0.00	0.09	98.34	0.00	0.02	98.32
	JE_1310_2_core_nl3	73.43	4.69	0.21	5.84	2.99	11.44	0.23	0.01	0.00	0.00	0.00	0.00	0.22	0.02	0.15	99.23	0.00	0.00	99.23
	JE_1310_2_core_nl4	71.35	4.67	0.19	5.88	3.26	11.33	0.21	0.04	0.00	0.00	0.06	0.00	0.00	0.00	0.02	97.01	0.03	0.01	96.98
V-165 rims	JE_1310_1_rim1	72.71	4.45	0.32	5.45	3.12	11.51	0.21	0.04	0.00	0.03	0.00	0.00	0.04	0.11	0.13	98.12	0.00	0.01	98.11
	JE_1310_1_rim2	74.23	4.39	0.24	5.51	2.96	11.32	0.22	0.08	0.00	0.00	0.00	0.00	0.24	0.00	0.00	99.20	0.00	0.02	99.18
	JE_1310_1_rim3	73.71	4.61	0.29	5.70	2.90	11.54	0.26	0.00	0.00	0.02	0.00	0.04	0.00	0.05	0.00	99.11	0.00	0.00	99.11
	JE_1310_1_rim4	74.16	4.43	0.16	5.86	2.83	11.52	0.32	0.00	0.01	0.05	0.00	0.04	0.62	0.06	0.00	100.08	0.00	0.00	100.08
	JE_1310_1_rim5	73.35	4.96	0.19	5.69	3.27	11.52	0.14	0.07	0.00	0.03	0.00	0.28	0.30	0.06	0.04	99.89	0.00	0.02	99.88
	JE_1310_1_rim6	73.94	4.55	0.21	5.71	2.92	11.50	0.14	0.00	0.00	0.04	0.14	0.04	0.11	0.00	0.11	99.41	0.06	0.00	99.35
	JE_1310_2_rim1	71.34	4.08	0.26	5.88	2.96	11.68	0.28	0.07	0.00	0.01	0.00	0.04	0.24	0.00	0.00	96.83	0.00	0.01	96.82
	JE_1310_2_rim2	72.47	4.49	0.34	5.40	3.00	11.09	0.19	0.02	0.04	0.03	0.00	0.00	0.00	0.09	0.00	97.17	0.00	0.00	97.16
	JE_1310_2_rim3	71.83	4.46	0.20	5.72	3.05	11.02	0.24	0.06	0.00	0.00	0.00	0.08	0.12	0.00	0.00	96.78	0.00	0.01	96.76
	JE_1310_3_rim1	72.50	4.48	0.24	5.78	2.97	11.21	0.25	0.03	0.00	0.02	0.00	0.00	0.01	0.06	0.00	97.55	0.00	0.01	97.54
	JE_1310_3_rim2	72.30	4.68	0.25	5.75	2.78	11.17	0.09	0.03	0.00	0.07	0.00	0.24	0.19	0.13	0.17	97.84	0.00	0.01	97.83
	JE_1310_3_rim3	71.04	4.26	0.22	5.62	2.76	11.13	0.04	0.00	0.03	0.03	0.00	0.01	0.05	0.00	0.00	95.20	0.00	0.00	95.20
	JE_1310_3_rim4	71.87	4.34	0.14	5.91	2.77	10.82	0.16	0.00	0.00	0.00	0.00	0.09	0.00	0.00	0.00	96.10	0.00	0.00	96.10
	JE_1310_3_rim5	72.81	4.59	0.25	5.76	3.09	11.24	0.18	0.00	0.00	0.02	0.08	0.01	0.03	0.06	0.00	98.13	0.04	0.00	98.10
	JE_1310_2_rim1	71.27	4.92	0.23	5.66	2.88	11.14	0.24	0.07	0.01	0.00	0.00	0.00	0.00	0.00	0.07	96.50	0.00	0.02	96.48
	JE_1310_2_rim2	73.39	4.71	0.16	6.12	2.91	11.45	0.15	0.02	0.00	0.03	0.00	0.08	0.07	0.00	0.04	99.13	0.00	0.01	99.13
	JE_1310_2_rim3	72.27	4.81	0.27	6.11	2.68	11.82	0.14	0.00	0.01	0.00	0.00	0.00	0.00	0.00	0.19	98.29	0.00	0.00	98.29
	JE_1310_2_rim4	71.45	5.17	0.24	5.31	2.95	10.88	0.25	0.06	0.01	0.00	0.09	0.08	0.27	0.00	0.00	96.75	0.04	0.01	96.70
	JE_1310_2_rim5	73.52	4.34	0.18	6.10	2.92	11.44	0.19	0.02	0.00	0.00	0.12	0.04	0.00	0.00	0.13	99.01	0.05	0.00	98.95

Table J.4: EMPA data of volcanic glass from sample V-165. Data is presented in wt%. The oxygen equivalents of F and Cl are calculated by multiplying wt% F by 0.4211 and Cl by 0.2256. The oxygen-equivalents for the F and Cl are subtracted in an addtional sum† from the analytical total followin Deer et al. (2013).

V-ID	Comment	SiO_2	K_2O	CaO	Na_2O	FeO	Al_2O_3	TiO_2	Cl	MgO	MnO	F	P_2O_5	BaO	SO_3	ZnO	Total	F=O	Cl=O	SUM†
V-45 cores	Line_1_JE_1315_1_core	73.28	4.13	0.23	5.36	2.81	11.28	0.25	0.06	0.00	0.01	0.00	0.13	0.13	0.03	0.13	97.85	0.00	0.01	97.84
	Line_2_JE_1315_1_core	73.23	4.67	0.23	5.43	2.88	10.86	0.21	0.00	0.04	0.05	0.00	0.10	0.14	0.05	0.00	97.89	0.00	0.00	97.89
	Line_3_JE_1315_1_core	73.30	4.39	0.27	5.48	2.82	10.82	0.07	0.01	0.00	0.00	0.00	0.00	0.00	0.00	0.15	97.32	0.00	0.00	97.31
	Line_4_JE_1315_1_core	74.70	4.52	0.18	5.58	2.91	11.00	0.20	0.01	0.01	0.03	0.00	0.00	0.00	0.14	0.08	99.35	0.00	0.00	99.34
	Line_5_JE_1315_1_core	72.25	4.25	0.31	5.38	3.01	11.26	0.08	0.06	0.00	0.00	0.00	0.07	0.03	0.11	0.11	96.93	0.00	0.01	96.92
	Line_6_JE_1315_1_core	72.20	4.53	0.26	5.45	2.79	11.10	0.08	0.00	0.00	0.00	0.00	0.00	0.26	0.10	0.00	96.77	0.00	0.00	96.77
	Line_7_JE_1315_1_core	74.17	4.84	0.22	5.87	3.04	11.23	0.11	0.08	0.03	0.00	0.01	0.00	0.00	0.16	0.19	99.94	0.00	0.02	99.92
	Line_8_JE_1315_1_core	73.78	4.12	0.18	5.68	2.96	11.22	0.34	0.02	0.00	0.00	0.09	0.04	0.00	0.05	0.00	98.48	0.04	0.00	98.44
	Line_9_JE_1315_1_core	73.28	4.45	0.28	5.48	3.20	11.30	0.20	0.03	0.02	0.01	0.00	0.12	0.03	0.00	0.08	98.48	0.00	0.01	98.47
	Line_10_JE_1315_1_core	73.23	4.35	0.21	5.61	3.09	10.83	0.29	0.10	0.00	0.02	0.04	0.08	0.00	0.00	0.00	97.84	0.02	0.02	97.80
	Line_1_JE_1315_2_core	72.97	4.40	0.34	5.75	2.68	10.83	0.34	0.08	0.00	0.00	0.00	0.05	0.00	0.00	0.21	97.64	0.00	0.02	97.63
	Line_2_JE_1315_2_core	73.52	4.45	0.24	5.78	2.83	11.18	0.25	0.00	0.00	0.00	0.00	0.00	0.00	0.06	0.00	98.32	0.00	0.00	98.32
	Line_3_JE_1315_2_core	72.90	4.56	0.25	5.73	2.83	10.93	0.14	0.03	0.02	0.01	0.00	0.15	0.00	0.03	0.11	97.68	0.00	0.01	97.68
	Line_4_JE_1315_2_core	74.37	4.82	0.27	5.62	2.97	11.41	0.10	0.03	0.00	0.05	0.00	0.15	0.00	0.06	0.00	99.85	0.00	0.01	99.85
	Line_5_JE_1315_2_core	73.89	4.31	0.28	5.74	2.84	10.92	0.18	0.00	0.00	0.03	0.00	0.00	0.25	0.02	0.13	98.60	0.00	0.00	98.60
	Line_6_JE_1315_2_core	74.95	4.61	0.28	5.27	2.82	11.04	0.15	0.09	0.03	0.02	0.00	0.02	0.02	0.02	0.07	99.38	0.00	0.02	99.36
	Line_7_JE_1315_2_core	74.87	4.65	0.30	5.49	2.80	11.20	0.23	0.00	0.00	0.07	0.00	0.00	0.26	0.00	0.11	99.98	0.00	0.00	99.98
	Line_8_JE_1315_2_core	74.65	4.65	0.23	5.52	3.01	11.23	0.11	0.00	0.02	0.00	0.00	0.05	0.13	0.10	0.17	99.86	0.00	0.00	99.86
	Line_9_JE_1315_2_core	74.00	4.67	0.32	5.69	2.87	11.23	0.10	0.05	0.00	0.03	0.00	0.00	0.23	0.00	0.00	99.20	0.00	0.01	99.19
	Line_10_JE_1315_2_core	74.84	4.79	0.30	5.58	2.85	11.25	0.21	0.00	0.00	0.09	0.00	0.00	0.00	0.10	0.00	100.00	0.00	0.00	100.00
V-45 rims	JE_1315_3_core1	74.41	4.87	0.21	5.59	2.74	11.24	0.16	0.07	0.00	0.00	0.00	0.00	0.00	0.00	0.00	99.29	0.00	0.02	99.28
	JE_1315_3_core2	74.19	4.51	0.09	5.63	2.86	11.16	0.18	0.09	0.00	0.00	0.00	0.25	0.14	0.00	0.06	99.15	0.00	0.02	99.13
	JE_1315_3_core3	73.01	4.66	0.20	5.27	2.62	11.17	0.23	0.01	0.00	0.03	0.04	0.04	0.06	0.02	0.22	97.59	0.02	0.00	97.57
	JE_1315_3_core4	74.99	4.30	0.16	5.34	2.81	11.03	0.22	0.01	0.00	0.00	0.00	0.12	0.28	0.00	0.13	99.39	0.00	0.00	99.39
	JE_1315_3_core5	73.33	4.46	0.18	5.33	2.77	11.00	0.19	0.00	0.00	0.01	0.00	0.07	0.00	0.02	0.13	97.49	0.00	0.00	97.49
	JE_1315_3_core6	72.63	4.57	0.23	5.66	2.90	11.22	0.34	0.00	0.00	0.04	0.00	0.09	0.26	0.13	0.02	98.08	0.00	0.00	98.08
	JE_1315_3_core7	73.61	4.85	0.23	5.88	2.79	11.14	0.13	0.04	0.00	0.00	0.02	0.08	0.28	0.03	0.00	99.09	0.01	0.01	99.07
	JE_1315_3_core8	73.45	4.68	0.19	5.78	2.84	11.25	0.21	0.07	0.02	0.01	0.00	0.08	0.19	0.02	0.17	98.94	0.00	0.02	98.93
	JE_1315_3_core9	72.91	4.64	0.18	5.58	2.65	11.01	0.31	0.04	0.00	0.00	0.00	0.00	0.41	0.00	0.04	97.77	0.00	0.01	97.76
	JE_1315_3_core10	73.79	4.78	0.21	5.65	2.77	10.99	0.19	0.06	0.01	0.04	0.00	0.12	0.13	0.00	0.00	98.75	0.00	0.01	98.73
	JE_1315_1_rim1	71.57	4.39	0.31	5.42	2.78	10.84	0.18	0.03	0.03	0.02	0.00	0.08	0.27	0.02	0.02	95.95	0.00	0.01	95.95
	JE_1315_1_rim2	73.27	4.61	0.29	5.56	2.68	10.91	0.13	0.01	0.02	0.00	0.00	0.00	0.29	0.06	0.04	97.87	0.00	0.00	97.87
	JE_1315_1_rim3	71.99	4.39	0.29	5.42	3.09	11.23	0.24	0.00	0.00	0.00	0.00	0.00	0.12	0.02	0.00	96.78	0.00	0.00	96.78
	JE_1315_1_rim4	71.54	4.33	0.19	5.43	2.94	10.99	0.14	0.06	0.00	0.00	0.00	0.00	0.00	0.00	0.00	95.62	0.00	0.01	95.61
	JE_1315_1_rim5	70.77	4.61	0.34	5.64	2.98	11.03	0.14	0.04	0.00	0.05	0.00	0.10	0.24	0.21	0.00	96.15	0.00	0.01	96.14
	JE_1315_2_rim1	72.27	4.26	0.30	5.49	2.95	10.75	0.25	0.02	0.00	0.00	0.20	0.06	0.15	0.00	0.28	96.98	0.08	0.00	96.89
	JE_1315_2_rim2	73.53	4.57	0.23	5.29	2.85	11.04	0.23	0.07	0.00	0.00	0.24	0.00	0.44	0.00	0.00	98.49	0.10	0.02	98.37
	JE_1315_2_rim3	72.62	4.32	0.32	5.68	2.75	10.92	0.24	0.04	0.02	0.00	0.00	0.11	0.00	0.00	0.04	97.06	0.00	0.01	97.05
	JE_1315_2_rim4	72.08	4.68	0.30	5.73	2.82	10.67	0.20	0.10	0.01	0.05	0.00	0.00	0.00	0.00	0.00	96.63	0.00	0.02	96.61
	JE_1315_2_rim5	73.26	4.39	0.30	5.38	2.79	10.97	0.18	0.06	0.00	0.02	0.00	0.00	0.07	0.11	0.00	97.53	0.00	0.01	97.51
	JE_1315_3_rim1	73.12	4.48	0.15	5.58	2.75	11.29	0.30	0.05	0.00	0.00	0.00	0.00	0.00	0.00	0.02	97.74	0.00	0.01	97.73
	JE_1315_3_rim2	74.06	4.35	0.11	5.59	2.81	10.87	0.16	0.02	0.03	0.01	0.00	0.15	0.00	0.00	0.00	98.16	0.00	0.01	98.16
	JE_1315_3_rim3	72.17	4.71	0.18	5.22	2.98	11.12	0.24	0.03	0.04	0.00	0.00	0.00	0.00	0.05	0.21	96.95	0.00	0.01	96.94
	JE_1315_3_rim4	71.95	4.53	0.12	5.44	2.60	11.15	0.13	0.00	0.02	0.05	0.00	0.03	0.00	0.00	0.07	96.09	0.00	0.00	96.09

Table J.5: EMPA data of volcanic glass from sample V-57b. Data is presented in wt%. The oxygen equivalents of F and Cl are calculated by multiplying wt% F by 0.4211 and Cl by 0.2256. The oxygen-equivalents for the F and Cl are subtracted in an addtional sum† from the analytical total followin Deer et al. (2013).

V-ID	Comment	SiO_2	K_2O	CaO	Na_2O	FeO	Al_2O_3	TiO_2	Cl	MgO	MnO	F	P_2O_5	BaO	SO_3	ZnO	Total	F=O	Cl=O	SUM†
V-57b cores	Line 1 JE_1302_2_core_l1	63.42	5.37	0.90	9.14	5.62	16.32	0.29	0.08	0.04	0.04	0.00	0.11	0.03	0.00	0.00	101.35	0.00	0.02	101.33
	Line 2 JE_1302_2_core_l1	64.94	5.52	0.86	9.14	5.24	15.96	0.37	0.01	0.02	0.01	0.00	0.01	0.00	0.00	0.06	102.14	0.00	0.00	102.13
	Line 3 JE_1302_2_core_l1	62.98	5.04	0.86	9.21	5.19	16.02	0.37	0.08	0.03	0.00	0.08	0.00	0.20	0.00	0.20	100.26	0.03	0.02	100.21
	Line 1 JE_1302_2_core_l2	63.94	5.50	0.69	9.09	5.79	15.90	0.39	0.00	0.00	0.00	0.06	0.00	0.00	0.06	0.17	101.59	0.02	0.00	101.56
	Line 2 JE_1302_2_core_l2	64.83	5.40	0.92	9.05	5.45	15.90	0.27	0.00	0.07	0.00	0.13	0.00	0.10	0.09	0.00	102.21	0.05	0.00	102.16
	Line 3 JE_1302_2_core_l2	64.69	5.17	0.93	8.73	5.42	15.74	0.46	0.00	0.06	0.07	0.11	0.00	0.22	0.02	0.00	101.62	0.04	0.00	101.58
	Line 1 JE_1302_2_core_l3	64.02	5.30	0.83	8.55	5.64	15.88	0.33	0.04	0.02	0.00	0.00	0.30	0.00	0.16	0.00	101.07	0.00	0.01	101.06
	Line 2 JE_1302_2_core_l3	64.54	4.97	0.89	9.02	5.31	15.54	0.40	0.03	0.00	0.03	0.22	0.07	0.00	0.09	0.00	101.12	0.09	0.01	101.02
	Line 3 JE_1302_2_core_l3	64.30	5.06	0.85	9.17	5.41	15.93	0.37	0.00	0.02	0.11	0.05	0.04	0.64	0.05	0.00	101.98	0.02	0.00	101.96
	Line 4 JE_1302_2_core_l3	63.43	5.14	0.67	8.67	5.52	16.44	0.47	0.03	0.03	0.00	0.00	0.00	0.09	0.00	0.04	100.52	0.00	0.01	100.52
	Line 1 JE_1302_3_core_l1	62.83	5.29	0.71	9.36	5.23	15.50	0.29	0.00	0.04	0.00	0.13	0.11	0.00	0.02	0.04	99.55	0.06	0.00	99.49
	Line 2 JE_1302_3_core_l1	63.98	5.65	0.81	9.30	5.52	15.87	0.53	0.09	0.00	0.03	0.07	0.26	0.00	0.00	0.00	102.12	0.03	0.02	102.06
	Line 3 JE_1302_3_core_l1	63.01	5.05	0.88	8.90	5.47	15.90	0.35	0.03	0.00	0.05	0.11	0.09	0.25	0.00	0.00	100.10	0.05	0.01	100.04
	Line 4 JE_1302_3_core_l1	64.42	5.24	0.89	9.03	5.23	15.71	0.35	0.08	0.06	0.03	0.10	0.33	0.28	0.00	0.24	101.99	0.04	0.02	101.92
	Line 1 JE_1302_3_core_l2	62.41	5.62	0.74	9.30	5.47	15.64	0.30	0.00	0.00	0.01	0.11	0.13	0.00	0.00	0.00	99.73	0.05	0.00	99.69
	Line 2 JE_1302_3_core_l2	64.16	5.54	0.76	8.76	5.39	15.67	0.29	0.01	0.00	0.00	0.00	0.02	0.04	0.00	0.00	100.64	0.00	0.00	100.64
	Line 3 JE_1302_3_core_l2	64.00	5.11	0.87	8.88	5.25	15.83	0.41	0.03	0.02	0.00	0.00	0.18	0.05	0.00	0.00	100.64	0.00	0.01	100.63
	Line 4 JE_1302_3_core_l2	64.11	5.15	0.88	9.04	5.39	15.50	0.52	0.04	0.04	0.00	0.12	0.06	0.02	0.03	0.00	100.89	0.05	0.01	100.83
	JE_1302_3_core_nl1	64.88	5.41	0.85	9.11	5.46	15.91	0.45	0.04	0.01	0.00	0.12	0.00	0.35	0.16	0.19	102.92	0.05	0.01	102.86
	JE_1302_3_core_nl2	64.34	5.42	0.75	9.10	5.27	15.72	0.53	0.00	0.07	0.04	0.13	0.08	0.09	0.05	0.00	101.58	0.05	0.00	101.52
	Line 1 JE_1302_4_core_l1	63.91	5.35	0.81	9.35	5.73	15.64	0.31	0.11	0.00	0.06	0.00	0.00	0.02	0.08	0.00	101.37	0.00	0.02	101.35
	Line 2 JE_1302_4_core_l1	63.85	5.15	0.82	9.24	5.47	15.95	0.36	0.03	0.05	0.02	0.00	0.00	0.59	0.00	0.02	101.56	0.00	0.01	101.55
	Line 3 JE_1302_4_core_l1	64.24	5.29	0.72	9.13	5.52	15.87	0.35	0.06	0.00	0.05	0.18	0.03	0.05	0.14	0.11	101.74	0.08	0.01	101.65
	Line 4 JE_1302_4_core_l1	62.83	5.73	0.83	8.69	5.67	15.90	0.52	0.02	0.03	0.00	0.00	0.23	0.11	0.08	0.17	100.81	0.00	0.00	100.80
	Line 5 JE_1302_4_core_l1	63.67	5.21	0.76	9.09	5.32	15.88	0.38	0.00	0.00	0.00	0.00	0.00	0.14	0.00	0.00	100.46	0.00	0.00	100.46
	Line 6 JE_1302_4_core_l1	64.05	5.52	0.78	8.99	5.62	16.12	0.26	0.00	0.04	0.00	0.00	0.00	0.13	0.06	0.02	101.60	0.00	0.00	101.60
	Line 7 JE_1302_4_core_l1	64.70	5.04	0.84	9.02	5.51	15.86	0.44	0.04	0.00	0.01	0.11	0.00	0.20	0.14	0.02	101.94	0.05	0.01	101.88
	Line 8 JE_1302_4_core_l1	63.57	5.10	0.83	8.96	5.38	16.08	0.34	0.12	0.00	0.02	0.00	0.10	0.15	0.11	0.24	100.99	0.00	0.03	100.96
	Line 9 JE_1302_4_core_l1	63.44	5.22	0.72	8.97	5.38	15.63	0.36	0.09	0.04	0.04	0.02	0.02	0.05	0.00	0.00	99.97	0.01	0.02	99.95
	Line 10 JE_1302_4_core_l1	64.46	5.47	0.70	9.26	5.37	15.85	0.34	0.01	0.00	0.00	0.28	0.00	0.06	0.05	0.19	102.04	0.12	0.00	101.91
	Line 1 JE_1302_4_core_le	63.24	5.49	0.81	9.65	5.35	15.75	0.46	0.04	0.01	0.00	0.28	0.27	0.13	0.00	0.11	101.60	0.12	0.01	101.47
	Line 2 JE_1302_4_core_le	64.28	5.47	0.63	9.04	5.46	15.77	0.32	0.02	0.05	0.00	0.10	0.00	0.05	0.00	0.00	101.20	0.04	0.00	101.15
	Line 3 JE_1302_4_core_le	63.65	5.62	0.77	9.13	5.36	15.94	0.36	0.12	0.05	0.04	0.46	0.02	0.28	0.03	0.04	101.86	0.19	0.03	101.64
	Line 4 JE_1302_4_core_le	63.94	5.36	0.77	9.64	5.43	16.05	0.42	0.07	0.05	0.00	0.31	0.00	0.00	0.03	0.11	102.18	0.13	0.01	102.03
V-57v rims	JE_1302_2_rim1	62.91	4.97	0.75	8.79	5.25	15.52	0.35	0.09	0.03	0.09	0.00	0.11	0.00	0.00	0.13	98.98	0.00	0.02	98.96
	JE_1302_2_rim_2	62.61	4.93	0.86	8.66	5.60	15.74	0.36	0.05	0.05	0.05	0.28	0.09	0.12	0.00	0.11	99.51	0.12	0.01	99.38
	JE_1302_2_rim_3	63.85	5.18	0.91	9.25	5.53	15.83	0.29	0.00	0.02	0.00	0.03	0.09	0.54	0.11	0.00	101.63	0.01	0.00	101.61
	JE_1302_2_rim_4	64.78	5.07	0.75	8.99	5.48	16.18	0.34	0.03	0.03	0.00	0.07	0.00	0.03	0.00	0.07	101.83	0.03	0.01	101.79
	JE_1302_2_rim_5	64.57	5.14	0.83	8.77	5.30	15.89	0.47	0.00	0.03	0.00	0.00	0.01	0.28	0.00	0.06	101.34	0.00	0.00	101.34
	JE_1302_3_rim1	64.64	5.30	0.73	8.89	5.23	15.56	0.36	0.07	0.01	0.00	0.00	0.06	0.22	0.06	0.00	101.13	0.00	0.02	101.12
	JE_1302_3_rim2	63.96	5.31	0.76	9.22	5.44	15.80	0.32	0.01	0.06	0.00	0.17	0.11	0.36	0.08	0.09	101.70	0.07	0.00	101.62
	JE_1302_3_rim3	64.56	5.20	0.76	9.38	5.18	15.81	0.44	0.00	0.01	0.00	0.05	0.15	0.00	0.00	0.20	101.74	0.02	0.00	101.72
	JE_1302_3_rim4	64.26	5.31	0.73	10.17	5.37	15.60	0.44	0.00	0.03	0.00	0.09	0.10	0.32	0.09	0.00	102.51	0.04	0.00	102.48
	JE_1302_3_rim5	61.62	5.34	0.64	10.94	5.39	15.68	0.30	0.07	0.03	0.00	0.22	0.09	0.17	0.09	0.15	100.72	0.09	0.01	100.61

Table J.6: EMPA data of volcanic glass from sample V-45. Data is presented in wt%. The oxygen equivalents of F and Cl are calculated by multiplying wt% F by 0.4211 and Cl by 0.2256. The oxygen-equivalents for the F and Cl are subtracted in an addtional sum† from the analytical total followin Deer et al. (2013).

V-ID	Comment	SiO_2	K_2O	CaO	Na_2O	FeO	Al_2O_3	TiO_2	Cl	MgO	MnO	F	P_2O_5	BaO	SO_3	ZnO	Total	F=O	Cl=O	SUM†
V-45 cores	Line 1 JE_1301_1_CORE	73.15	3.84	0.20	5.36	2.65	10.62	0.18	0.01	0.02	0.06	0.00	0.00	0.01	0.00	0.04	96.15	0.00	0.00	96.14
	Line 2 JE_1301_1_CORE	74.17	4.54	0.23	5.26	2.61	10.41	0.10	0.00	0.01	0.01	0.00	0.04	0.00	0.03	0.19	97.61	0.00	0.00	97.61
	Line 3 JE_1301_1_CORE	74.86	4.46	0.18	5.28	2.54	10.65	0.39	0.00	0.02	0.00	0.00	0.05	0.34	0.03	0.00	98.81	0.00	0.00	98.81
	Line 4 JE_1301_1_CORE	73.02	4.21	0.22	5.00	2.69	11.04	0.12	0.00	0.00	0.00	0.11	0.00	0.02	0.00	0.26	96.70	0.05	0.00	96.65
	Line 5 JE_1301_1_CORE	74.91	4.04	0.26	5.09	2.48	10.52	0.16	0.04	0.01	0.00	0.22	0.01	0.03	0.00	0.15	97.92	0.09	0.01	97.81
	Line 6 JE_1301_1_CORE	73.63	4.13	0.14	5.32	2.82	10.60	0.06	0.06	0.00	0.00	0.00	0.00	0.03	0.05	0.00	96.84	0.00	0.01	96.83
	Line 7 JE_1301_1_CORE	73.55	4.45	0.14	5.12	2.44	10.65	0.22	0.06	0.03	0.00	0.06	0.00	0.09	0.05	0.20	97.06	0.03	0.01	97.02
	Line 8 JE_1301_1_CORE	74.81	4.29	0.17	5.33	2.39	10.57	0.10	0.05	0.05	0.02	0.00	0.00	0.23	0.10	0.17	98.27	0.00	0.01	98.26
	Line 9 JE_1301_1_CORE	74.30	4.69	0.22	5.69	2.43	10.56	0.09	0.06	0.00	0.00	0.00	0.10	0.00	0.00	0.09	98.23	0.00	0.01	98.22
	Line 10 JE_1301_1_CORE	74.78	3.99	0.10	5.16	2.59	10.65	0.21	0.00	0.00	0.07	0.00	0.00	0.00	0.05	0.26	97.86	0.00	0.00	97.86
	Line 11 JE_1301_1_CORE	75.45	4.60	0.22	4.98	2.55	10.73	0.06	0.00	0.02	0.06	0.05	0.00	0.43	0.05	0.04	99.25	0.02	0.00	99.23
	Line 12 JE_1301_1_CORE	73.52	4.40	0.19	5.48	2.58	10.38	0.05	0.06	0.02	0.00	0.00	0.32	0.06	0.05	0.13	97.25	0.00	0.01	97.23
	JE_1301_2_core1	75.73	4.60	0.10	5.28	2.71	10.50	0.13	0.02	0.00	0.01	0.15	0.16	0.24	0.00	0.02	99.64	0.06	0.00	99.57
	JE_1301_2_core2	75.54	4.48	0.04	5.37	2.55	10.53	0.11	0.06	0.00	0.02	0.00	0.02	0.02	0.00	0.00	98.74	0.00	0.01	98.73
	JE_1301_2_core3	74.21	4.45	0.07	5.32	2.44	10.39	0.05	0.04	0.00	0.00	0.00	0.00	0.00	0.03	0.00	97.01	0.00	0.01	97.00
	JE_1301_2_core4	75.18	4.53	0.02	5.41	2.64	10.51	0.10	0.05	0.01	0.00	0.00	0.00	0.27	0.19	0.17	99.08	0.00	0.01	99.07
	JE_1301_2_core5	75.24	4.51	0.11	5.41	2.51	10.41	0.13	0.00	0.02	0.00	0.00	0.06	0.05	0.08	0.00	98.53	0.00	0.00	98.53
	JE_1301_2_core6	75.40	4.49	0.04	5.37	2.43	10.58	0.24	0.04	0.04	0.02	0.16	0.04	0.05	0.05	0.00	98.95	0.07	0.01	98.88
	JE_1301_2_core7	75.76	4.51	0.04	5.44	2.64	10.62	0.25	0.03	0.03	0.06	0.00	0.00	0.11	0.05	0.17	99.71	0.00	0.01	99.70
	JE_1301_2_core8	74.64	4.61	0.00	5.22	2.50	10.59	0.13	0.00	0.00	0.02	0.00	0.00	0.13	0.00	0.00	97.85	0.00	0.00	97.85
	JE_1301_2_core9	75.87	4.29	0.00	5.45	2.58	10.79	0.14	0.02	0.01	0.01	0.01	0.00	0.11	0.00	0.04	99.32	0.01	0.00	99.31
	JE_1301_2_core10	75.33	4.73	0.12	5.16	2.45	10.49	0.15	0.00	0.01	0.00	0.00	0.10	0.33	0.00	0.00	98.86	0.00	0.00	98.86
	Line 1 JE_1301_3_core	74.34	4.55	0.14	5.23	2.40	10.80	0.26	0.05	0.00	0.02	0.00	0.22	0.20	0.02	0.00	98.22	0.00	0.01	98.21
	Line 2 JE_1301_3_core	75.04	4.38	0.19	5.46	2.58	10.47	0.17	0.04	0.00	0.00	0.07	0.03	0.00	0.03	0.00	98.45	0.03	0.01	98.41
	Line 3 JE_1301_3_core	74.20	4.11	0.22	4.97	2.51	10.78	0.05	0.08	0.00	0.00	0.00	0.11	0.25	0.02	0.00	97.30	0.00	0.02	97.28
	Line 4 JE_1301_3_core	74.55	4.42	0.18	5.45	2.44	10.68	0.21	0.00	0.02	0.04	0.00	0.03	0.00	0.00	0.02	98.04	0.00	0.00	98.03
	Line 5 JE_1301_3_core	73.41	4.20	0.22	5.00	2.58	10.51	0.10	0.00	0.00	0.00	0.00	0.00	0.24	0.00	0.07	96.33	0.00	0.00	96.33
	Line 6 JE_1301_3_core	74.00	4.08	0.16	5.60	2.51	10.66	0.18	0.02	0.01	0.02	0.05	0.09	0.00	0.05	0.00	97.42	0.02	0.00	97.39
	Line 7 JE_1301_3_core	75.08	4.07	0.18	5.32	2.54	10.45	0.16	0.01	0.00	0.00	0.00	0.00	0.28	0.08	0.00	98.18	0.00	0.00	98.18
	Line 8 JE_1301_3_core	74.49	4.53	0.21	5.41	2.75	10.84	0.06	0.03	0.00	0.02	0.00	0.31	0.12	0.02	0.09	98.89	0.00	0.01	98.88
	Line 9 JE_1301_3_core	74.98	4.34	0.17	5.13	2.63	10.70	0.17	0.14	0.00	0.11	0.00	0.00	0.23	0.08	0.00	98.66	0.00	0.03	98.63
	Line 10 JE_1301_3_core	74.02	4.44	0.17	5.65	2.51	10.39	0.14	0.07	0.01	0.00	0.00	0.00	0.18	0.00	0.24	97.82	0.00	0.02	97.81
V-45 rims	JE_1301_1_rim_1	72.28	4.24	0.13	5.46	2.59	10.23	0.04	0.00	0.00	0.10	0.00	0.01	0.10	0.00	0.15	95.34	0.00	0.00	95.34
	JE_1301_1_rim_2	73.42	4.10	0.21	5.03	2.58	10.52	0.11	0.00	0.00	0.00	0.03	0.07	0.25	0.10	0.00	96.43	0.01	0.00	96.41
	JE_1301_1_rim_3	73.35	4.17	0.17	5.08	2.56	10.12	0.09	0.03	0.00	0.00	0.02	0.04	0.03	0.05	0.15	95.87	0.01	0.01	95.85
	JE_1301_1_rim_4	73.02	4.14	0.13	5.04	2.62	10.19	0.09	0.12	0.00	0.00	0.00	0.00	0.09	0.00	0.00	95.44	0.00	0.03	95.42
	JE_1301_1_rim_5	73.21	4.40	0.17	5.48	2.57	10.52	0.15	0.05	0.00	0.00	0.17	0.15	0.01	0.00	0.00	96.87	0.07	0.01	96.79
	JE_1301_2_rim1	74.15	4.62	0.00	5.31	2.53	10.46	0.24	0.00	0.06	0.04	0.00	0.00	0.12	0.00	0.00	97.54	0.00	0.00	97.54
	JE_1301_2_rim2	75.80	4.43	0.05	4.92	2.71	10.26	0.23	0.03	0.02	0.03	0.00	0.00	0.03	0.06	0.07	98.65	0.00	0.01	98.64
	JE_1301_2_rim3	74.79	4.67	0.00	5.14	2.37	10.29	0.13	0.06	0.00	0.03	0.00	0.00	0.15	0.06	0.00	97.69	0.00	0.01	97.68
	JE_1301_2_rim4	75.21	4.52	0.05	5.49	2.50	10.42	0.13	0.04	0.00	0.02	0.01	0.00	0.00	0.03	0.07	98.50	0.00	0.01	98.49
	JE_1301_2_rim5	73.81	4.50	0.07	5.12	2.44	10.60	0.27	0.04	0.02	0.00	0.09	0.05	0.00	0.00	0.00	97.02	0.04	0.01	96.97
	JE_1301_3_rim1	72.66	4.26	0.24	5.21	2.52	10.49	0.12	0.04	0.00	0.00	0.13	0.00	0.20	0.02	0.24	96.14	0.05	0.01	96.07
	JE_1301_3_rim2	72.54	3.96	0.21	5.50	2.58	10.37	0.18	0.02	0.00	0.00	0.00	0.03	0.39	0.00	0.13	95.91	0.00	0.01	95.91
	JE_1301_3_rim3	73.19	4.17	0.18	5.08	2.39	10.66	0.10	0.05	0.00	0.02	0.00	0.00	0.11	0.06	0.00	96.01	0.00	0.01	96.00
	JE_1301_3_rim4	73.75	4.29	0.15	5.30	2.61	10.47	0.14	0.07	0.04	0.01	0.00	0.01	0.05	0.16	0.00	97.05	0.00	0.02	97.03
	JE_1301_3_rim5	74.37	4.51	0.19	5.16	2.52	10.21	0.10	0.00	0.04	0.00	0.00	0.00	0.02	0.00	0.06	97.18	0.00	0.00	97.18

Appendix K: Ba diffusion couples

Table K.1: Ba contents from grain F12 of V-45.

F12L1			F12O2			F12O3			F12D2		
Ba (apfu)	±Ba	Dist (μ)	Ba (apfu)	±Ba	Dist (μ)	Ba (apfu)	±Ba	Dist (μ)	Ba (apfu)	±Ba	Dist (μ)
0.0035	0.0005	-28.0	0.0070	0.0005	33.5	0.0072	0.0005	31.2	0.0025	0.0005	-30.8
0.0023	0.0005	-20.0	0.0060	0.0005	30.2	0.0073	0.0005	27.9	0.0032	0.0005	-26.4
0.0024	0.0005	-16.0	0.0062	0.0005	26.8	0.0066	0.0005	24.5	0.0029	0.0005	-22.1
0.0024	0.0005	-12.0	0.0066	0.0005	23.4	0.0057	0.0005	21.1	0.0023	0.0005	-17.7
0.0020	0.0005	-8.0	0.0074	0.0005	20.1	0.0060	0.0005	17.8	0.0025	0.0005	-13.4
0.0022	0.0005	-4.0	0.0069	0.0005	16.7	0.0056	0.0005	14.4	0.0029	0.0005	-9.1
0.0046	0.0005	0.0	0.0070	0.0005	13.4	0.0055	0.0005	11.1	0.0023	0.0005	-4.7
0.0067	0.0005	4.0	0.0066	0.0005	10.0	0.0057	0.0005	7.7	0.0050	0.0005	-0.4
0.0065	0.0005	8.0	0.0065	0.0005	6.6	0.0051	0.0005	4.3	0.0077	0.0005	4.0
0.0065	0.0005	12.0	0.0065	0.0005	3.3	0.0044	0.0005	1.0	0.0085	0.0005	8.3
0.0065	0.0005	16.0	0.0044	0.0005	-0.1	0.0030	0.0005	-2.4	0.0072	0.0005	12.7
0.0076	0.0005	20.0	0.0021	0.0005	-3.4	0.0020	0.0005	-5.7	0.0069	0.0005	17.0
			0.0019	0.0005	-6.8	0.0017	0.0005	-9.1	0.0067	0.0005	21.3
			0.0016	0.0005	-10.1	0.0024	0.0005	-12.5			
			0.0016	0.0005	-13.5	0.0021	0.0005	-15.8			
			0.0021	0.0005	-16.9	0.0025	0.0005	-19.2			
			0.0019	0.0005	-20.2	0.0022	0.0005	-22.5			
			0.0025	0.0005	-23.6	0.0025	0.0005	-25.9			
			0.0036	0.0005	-26.9	0.0040	0.0005	-29.2			
			0.0040	0.0005	-30.3	0.0059	0.0005	-32.6			
			0.0023	0.0005	-33.7	0.0060	0.0005	-36.0			
			0.0029	0.0005	-37.0						

Table K.2: Ba contents from grain F9 of V-45.

F9L1			F49O2			F9O3		
Ba (apfu)	±Ba	Dist (μ)	Ba (apfu)	±Ba	Dist (μ)	Ba (apfu)	±Ba	Dist (μ)
0.0047	0.0005	-24.5	0.0051	0.0005	-22.0	0.0048	0.0005	-20.1
0.0053	0.0005	-20.5	0.0042	0.0005	-19.9	0.0048	0.0005	-18.1
0.0049	0.0005	-16.5	0.0050	0.0005	-17.9	0.0047	0.0005	-16.0
0.0046	0.0005	-12.5	0.0045	0.0005	-15.8	0.0046	0.0005	-14.0
0.0042	0.0005	-8.5	0.0046	0.0005	-13.8	0.0046	0.0005	-11.9
0.0047	0.0005	-4.5	0.0043	0.0005	-11.7	0.0045	0.0005	-9.9
0.0050	0.0005	-0.5	0.0044	0.0005	-9.7	0.0046	0.0005	-7.8
0.0061	0.0006	3.5	0.0037	0.0005	-7.6	0.0041	0.0005	-5.8
0.0085	0.0006	7.5	0.0040	0.0005	-5.6	0.0045	0.0005	-3.7
0.0091	0.0006	11.5	0.0048	0.0005	-3.5	0.0056	0.0005	-1.6
0.0088	0.0006	15.5	0.0056	0.0005	-1.4	0.0066	0.0005	0.4
0.0098	0.0006	19.5	0.0065	0.0005	0.6	0.0076	0.0006	2.5
0.0095	0.0006	23.5	0.0075	0.0006	2.7	0.0087	0.0006	4.5
			0.0090	0.0006	4.7	0.0087	0.0006	6.6
			0.0086	0.0006	6.8	0.0082	0.0006	8.6
			0.0095	0.0006	8.8	0.0085	0.0006	10.7
			0.0088	0.0006	10.9	0.0085	0.0006	12.7
			0.0092	0.0006	12.9	0.0077	0.0006	14.8
			0.0093	0.0006	15.0	0.0072	0.0006	16.8
			0.0086	0.0006	17.0	0.0073	0.0005	18.9
			0.0088	0.0006	19.1	0.0069	0.0005	20.9
			0.0082	0.0006	21.2			
			0.0081	0.0006	23.2			

Table K.3: Ba contents from grain F4 of V-221a.

F4S1			F4S2			F4S3		
Ba (apfu)	±Ba	Dist (μ)	Ba (apfu)	±Ba	Dist (μ)	Ba (apfu)	±Ba	Dist (μ)
0.0055	0.0005	60.0	0.0058	0.0005	41.1	0.0056	0.0005	45.5
0.0052	0.0005	56.0	0.0058	0.0005	37.1	0.0055	0.0005	41.5
0.0056	0.0005	52.0	0.0063	0.0006	33.1	0.0059	0.0005	37.5
0.0057	0.0005	48.0	0.0063	0.0006	29.1	0.0063	0.0006	33.5
0.0061	0.0006	44.0	0.0069	0.0006	25.1	0.0065	0.0006	29.5
0.0065	0.0006	40.0	0.0063	0.0006	21.1	0.0062	0.0006	25.5
0.0065	0.0006	36.0	0.0066	0.0006	17.1	0.0066	0.0006	21.5
0.0063	0.0006	32.0	0.0062	0.0006	13.1	0.0070	0.0006	17.5
0.0068	0.0006	28.0	0.0070	0.0006	9.1	0.0067	0.0006	13.5
0.0070	0.0006	24.0	0.0068	0.0006	5.1	0.0065	0.0006	9.5
0.0070	0.0006	20.0	0.0068	0.0006	1.1	0.0065	0.0006	5.5
0.0071	0.0006	16.0	0.0050	0.0005	-2.9	0.0062	0.0005	1.5
0.0074	0.0006	12.0	0.0046	0.0005	-6.9	0.0042	0.0005	-2.5
0.0070	0.0006	8.0	0.0045	0.0005	-10.9	0.0042	0.0005	-6.5
0.0070	0.0006	4.0	0.0049	0.0005	-14.9	0.0045	0.0005	-10.5
0.0060	0.0005	0.0	0.0048	0.0005	-18.9	0.0046	0.0005	-14.5
0.0054	0.0005	-4.0	0.0050	0.0005	-22.9	0.0048	0.0005	-18.5
0.0051	0.0005	-8.0	0.0054	0.0005	-26.9	0.0056	0.0005	-22.5
0.0053	0.0005	-12.0	0.0051	0.0005	-30.9	0.0056	0.0005	-26.5
0.0053	0.0005	-16.0	0.0057	0.0005	-34.9	0.0050	0.0005	-30.5
0.0050	0.0005	-20.0	0.0052	0.0005	-38.9	0.0050	0.0005	-34.5
0.0052	0.0005	-24.0				0.0050	0.0005	-38.5
0.0050	0.0005	-28.0						
0.0050	0.0005	-32.0						
0.0055	0.0005	-36.0						
0.0054	0.0005	-40.0						
0.0054	0.0005	-44.0						
0.0059	0.0005	-48.0						
0.0053	0.0005	-52.0						
0.0053	0.0005	-56.0						
0.0061	0.0005	-60.0						

Table K.4: Ba contents from grain F1 of V-221a.

F1L1			F1O2 -1st set			F1O2 - 2nd set			F1O3 - 1st set			F1O3 - 2nd set		
Ba (apfu)	±Ba	Dist (μ)	Ba (apfu)	±Ba	Dist (μ)	Ba (apfu)	±Ba	Dist (μ)	Ba (apfu)	±Ba	Dist (μ)	Ba (apfu)	±Ba	Dist (μ)
0.0063	0.0007	-94.0	0.0058	0.0005	76.3	0.0048	0.0005	-11.8	0.0056	0.0005	85.3	0.0049	0.0005	-4.2
0.0064	0.0007	-90.0	0.0063	0.0005	74.2	0.0051	0.0005	-13.9	0.0059	0.0005	83.6	0.0051	0.0005	-5.9
0.0065	0.0007	-86.0	0.0063	0.0005	72.0	0.0049	0.0005	-16.1	0.0055	0.0005	81.9	0.0046	0.0005	-7.6
0.0066	0.0007	-82.0	0.0059	0.0005	69.9	0.0055	0.0005	-18.2	0.0057	0.0005	80.2	0.0048	0.0005	-9.4
0.0062	0.0006	-78.0	0.0065	0.0005	67.7	0.0053	0.0005	-20.4	0.0057	0.0005	78.5	0.0051	0.0005	-11.1
0.0064	0.0007	-74.0	0.0066	0.0005	65.6	0.0060	0.0005	-22.5	0.0057	0.0005	76.7	0.0048	0.0005	-12.8
0.0068	0.0007	-70.0	0.0059	0.0005	63.4	0.0057	0.0005	-24.7	0.0056	0.0005	75.0	0.0046	0.0005	-14.5
0.0065	0.0007	-66.0	0.0062	0.0005	61.3	0.0064	0.0005	-26.8	0.0055	0.0005	73.3	0.0051	0.0005	-16.3
0.0068	0.0007	-62.0	0.0065	0.0005	59.1	0.0055	0.0005	-29.0	0.0058	0.0005	71.6	0.0057	0.0005	-18.0
0.0066	0.0007	-58.0	0.0060	0.0005	57.0	0.0058	0.0006	-31.1	0.0063	0.0005	69.8	0.0052	0.0005	-19.7
0.0057	0.0006	-54.0	0.0067	0.0005	54.8	0.0057	0.0005	-33.3	0.0062	0.0005	68.1	0.0048	0.0005	-21.4
0.0065	0.0007	-50.0	0.0072	0.0005	52.7	0.0057	0.0005	-35.4	0.0057	0.0005	66.4	0.0051	0.0005	-23.1
0.0058	0.0006	-46.0	0.0061	0.0005	50.5	0.0059	0.0005	-37.6	0.0065	0.0005	64.7	0.0055	0.0005	-24.9
0.0062	0.0007	-42.0	0.0064	0.0005	48.4	0.0063	0.0005	-39.7	0.0068	0.0005	63.0	0.0055	0.0005	-26.6
0.0047	0.0006	-38.0	0.0071	0.0005	46.2	0.0068	0.0006	-41.9	0.0059	0.0005	61.2	0.0053	0.0005	-28.3
0.0052	0.0007	-34.0	0.0066	0.0005	44.1	0.0057	0.0005	-44.0	0.0066	0.0005	59.5	0.0055	0.0005	-30.0
0.0055	0.0006	-30.0	0.0063	0.0005	41.9	0.0058	0.0006	-46.2	0.0065	0.0005	57.8	0.0057	0.0005	-31.8
0.0051	0.0006	-26.0	0.0065	0.0005	39.8	0.0089	0.0014	-48.3	0.0070	0.0005	56.1	0.0056	0.0005	-33.5
0.0048	0.0006	-22.0	0.0067	0.0005	37.6	0.0063	0.0005	-50.5	0.0070	0.0006	54.3	0.0057	0.0005	-35.2
0.0044	0.0006	-18.0	0.0069	0.0005	35.5	0.0062	0.0005	-52.6	0.0065	0.0006	52.6	0.0058	0.0005	-36.9
0.0051	0.0006	-14.0	0.0072	0.0005	33.3	0.0061	0.0005	-54.8	0.0066	0.0005	50.9	0.0061	0.0005	-38.6
0.0056	0.0006	-10.0	0.0065	0.0005	31.2	0.0064	0.0005	-56.9	0.0067	0.0005	49.2	0.0054	0.0005	-40.4
0.0050	0.0006	-6.0	0.0067	0.0005	29.0	0.0064	0.0005	-59.1	0.0070	0.0006	47.5	0.0052	0.0005	-42.1
0.0052	0.0006	-2.0	0.0071	0.0005	26.9	0.0063	0.0005	-61.2	0.0067	0.0005	45.7	0.0057	0.0005	-43.8
0.0076	0.0007	2.0	0.0070	0.0006	24.7	0.0062	0.0005	-63.4	0.0068	0.0005	44.0	0.0059	0.0005	-45.5
0.0077	0.0007	6.0	0.0066	0.0005	22.6	0.0058	0.0005	-65.5	0.0064	0.0005	42.3	0.0059	0.0005	-47.3
0.0075	0.0007	10.0	0.0066	0.0006	20.4	0.0060	0.0005	-67.7	0.0066	0.0005	40.6	0.0060	0.0005	-49.0
0.0071	0.0007	14.0	0.0068	0.0006	18.3	0.0067	0.0005	-69.8	0.0065	0.0005	38.8	0.0057	0.0005	-50.7
0.0074	0.0007	18.0	0.0066	0.0006	16.2	0.0064	0.0005	-72.0	0.0063	0.0005	37.1	0.0061	0.0005	-52.4
0.0063	0.0007	22.0	0.0076	0.0006	14.0	0.0062	0.0005	-74.1	0.0067	0.0006	35.4	0.0060	0.0005	-54.1
0.0065	0.0007	26.0	0.0073	0.0006	11.9	0.0056	0.0005	-76.3	0.0070	0.0006	33.7	0.0062	0.0005	-55.9
0.0059	0.0007	30.0	0.0075	0.0006	9.7	0.0058	0.0005	-78.4	0.0073	0.0006	32.0	0.0062	0.0005	-57.6
0.0069	0.0007	34.0	0.0068	0.0006	7.6	0.0059	0.0005	-80.6	0.0064	0.0005	30.2	0.0059	0.0005	-59.3
0.0058	0.0007	38.0	0.0069	0.0006	5.4	0.0063	0.0005	-82.7	0.0113	0.0015	28.5	0.0064	0.0005	-61.0
0.0061	0.0007	42.0	0.0065	0.0006	3.3	0.0059	0.0005	-84.9	0.0069	0.0006	26.8	0.0061	0.0005	-62.8
0.0064	0.0007	46.0	0.0065	0.0005	1.1	0.0061	0.0005	-87.0	0.0069	0.0005	25.1	0.0067	0.0005	-64.5
0.0063	0.0007	50.0	0.0056	0.0005	-1.0	0.0055	0.0005	-89.2	0.0073	0.0006	23.3	0.0062	0.0005	-66.2
0.0066	0.0007	54.0	0.0047	0.0005	-3.2	0.0057	0.0005	-91.3	0.0074	0.0005	21.6	0.0063	0.0005	-67.9
			0.0044	0.0005	-5.3	0.0060	0.0005	-93.5	0.0071	0.0005	19.9	0.0061	0.0005	-69.6
			0.0050	0.0005	-7.5	0.0061	0.0005	-95.6	0.0074	0.0006	18.2	0.0061	0.0005	-71.4
			0.0050	0.0005	-9.6	0.0061	0.0005	-97.8	0.0072	0.0006	16.5	0.0066	0.0005	-73.1
									0.0071	0.0006	14.7	0.0061	0.0005	-74.8
									0.0070	0.0006	13.0	0.0060	0.0005	-76.5
									0.0069	0.0006	11.3	0.0060	0.0005	-78.3
									0.0069	0.0005	9.6	0.0068	0.0005	-80.0
									0.0071	0.0006	7.9	0.0061	0.0005	-81.7
									0.0072	0.0006	6.1	0.0062	0.0005	-83.4
									0.0067	0.0006	4.4	0.0064	0.0005	-85.1
									0.0063	0.0005	2.7	0.0065	0.0005	-86.9
									0.0062	0.0005	1.0	0.0067	0.0005	-88.6
									0.0061	0.0005	-0.8	0.0061	0.0005	-90.3
									0.0053	0.0005	-2.5	0.0067	0.0005	-92.0

Table K.5: Ba contents from grain F1 of V-221a.

F1S4			F1S5			F1S6		
Ba (apfu)	±Ba	Dist (μ)	Ba (apfu)	±Ba	Dist (μ)	Ba (apfu)	±Ba	Dist (μ)
0.0073	0.0006	25.9	0.0063	0.0005	-56.0	0.0068	0.0005	-57.9
0.0073	0.0006	21.9	0.0064	0.0005	-52.0	0.0061	0.0005	-53.9
0.0074	0.0006	17.9	0.0068	0.0005	-48.0	0.0058	0.0005	-49.9
0.0073	0.0006	13.9	0.0068	0.0005	-44.0	0.0059	0.0005	-45.9
0.0073	0.0006	9.9	0.0065	0.0005	-40.0	0.0059	0.0005	-41.9
0.0078	0.0006	5.9	0.0064	0.0005	-36.0	0.0059	0.0005	-37.9
0.0073	0.0006	1.9	0.0064	0.0005	-32.0	0.0065	0.0005	-33.9
0.0051	0.0005	-2.1	0.0062	0.0005	-28.0	0.0065	0.0005	-29.9
0.0049	0.0005	-6.1	0.0060	0.0005	-24.0	0.0061	0.0005	-25.9
0.0051	0.0005	-10.1	0.0065	0.0005	-20.0	0.0063	0.0005	-21.9
0.0060	0.0005	-14.1	0.0067	0.0005	-16.0	0.0059	0.0005	-17.9
0.0054	0.0005	-18.1	0.0064	0.0005	-12.0	0.0065	0.0005	-13.9
0.0053	0.0005	-22.1	0.0064	0.0005	-8.0	0.0063	0.0005	-9.9
0.0058	0.0005	-26.1	0.0064	0.0005	-4.0	0.0063	0.0005	-5.9
			0.0076	0.0006	0.0	0.0073	0.0006	-1.9
			0.0090	0.0006	4.0	0.0079	0.0006	2.1
			0.0090	0.0006	8.0	0.0081	0.0006	6.1
			0.0090	0.0006	12.0	0.0086	0.0006	10.1
			0.0093	0.0006	16.0	0.0082	0.0006	14.1
			0.0092	0.0006	20.0	0.0093	0.0006	18.1
			0.0093	0.0006	24.0	0.0086	0.0006	22.1
			0.0089	0.0006	28.0	0.0089	0.0006	26.1
			0.0090	0.0006	32.0	0.0083	0.0006	30.1
			0.0089	0.0006	36.0	0.0080	0.0006	34.1
			0.0090	0.0006	40.0	0.0081	0.0006	38.1
			0.0082	0.0006	44.0	0.0079	0.0006	42.1
			0.0084	0.0006	48.0	0.0075	0.0006	46.1
			0.0081	0.0006	52.0	0.0077	0.0006	50.1
			0.0078	0.0006	56.0	0.0076	0.0006	54.1

Table K.6: Ba contents from grain F1 of V-221a.

F1S7			F1S8			F1S9		
Ba (apfu)	±Ba	Dist (μ)	Ba (apfu)	±Ba	Dist (μ)	Ba (apfu)	±Ba	Dist (μ)
0.0061	0.0005	-58.2	0.0072	0.0006	28.0	0.0072	0.0006	36.6
0.0063	0.0005	-54.2	0.0078	0.0006	24.0	0.0075	0.0006	32.6
0.0064	0.0005	-50.2	0.0084	0.0006	20.0	0.0083	0.0006	28.6
0.0058	0.0005	-46.2	0.0078	0.0006	16.0	0.0084	0.0006	24.6
0.0063	0.0005	-42.2	0.0080	0.0006	12.0	0.0085	0.0006	20.6
0.0060	0.0005	-38.2	0.0083	0.0006	8.0	0.0083	0.0006	16.6
0.0057	0.0005	-34.2	0.0082	0.0006	4.0	0.0081	0.0006	12.6
0.0064	0.0005	-30.2	0.0071	0.0006	0.0	0.0078	0.0006	8.6
0.0060	0.0005	-26.2	0.0057	0.0005	-4.0	0.0081	0.0006	4.6
0.0059	0.0005	-22.2	0.0055	0.0005	-8.0	0.0071	0.0006	0.6
0.0056	0.0005	-18.2	0.0054	0.0005	-12.0	0.0057	0.0005	-3.4
0.0060	0.0005	-14.2	0.0054	0.0005	-16.0	0.0050	0.0005	-7.4
0.0064	0.0005	-10.2	0.0057	0.0005	-20.0	0.0054	0.0005	-11.4
0.0063	0.0005	-6.2	0.0053	0.0005	-24.0	0.0053	0.0005	-15.4
0.0065	0.0006	-2.2	0.0062	0.0005	-28.0	0.0053	0.0005	-19.4
0.0078	0.0005	1.8				0.0047	0.0005	-23.4
0.0079	0.0006	5.8				0.0052	0.0005	-27.4
0.0081	0.0006	9.8				0.0049	0.0005	-31.4
0.0081	0.0006	13.8				0.0060	0.0005	-35.4
0.0082	0.0006	17.8						
0.0087	0.0006	21.8						
0.0088	0.0006	25.8						
0.0078	0.0006	29.8						
0.0079	0.0006	33.8						
0.0082	0.0006	37.8						
0.0079	0.0006	41.8						
0.0080	0.0006	45.8						
0.0074	0.0006	49.8						
0.0073	0.0006	53.8						

Autorenerklärung

Die vorliegende Doktorarbeit habe ich, Jonathan Franz Engelhardt, selbstständig verfasst. Textpassagen, die anderen Quellen im Wortlaut oder im Sinn entnommen wurden, habe ich durch Angaben der Herkunft gekennzeichnet. Ich versichere der Universität Potsdam, dass diese Doktorarbeit an keiner anderen Hochschule eingereicht worden ist.

Potsdam, den 16. Juli 2017 Jonathan Franz Engelhardt